Shaopu Yang
Liqun Chen
Shaohua Li

Dynamics of Vehicle-Road Coupled System

Science Press
Beijing

Springer

Dynamics of Vehicle–Road Coupled System

Shaopu Yang • Liqun Chen • Shaohua Li

Dynamics of Vehicle–Road Coupled System

Science Press
Beijing

Springer

Shaopu Yang
School of Mechanical Engineering
Shijiazhuang Tiedao University
Shijiazhuang
Hebei
China

Shaohua Li
School of Mechanical Engineering
Shijiazhuang Tiedao University
Shijiazhuang Hebei
China

Liqun Chen
Department of Mechanics
Shanghai University
Shanghai
China

ISBN 978-3-662-45956-0 ISBN 978-3-662-45957-7 (eBook)
DOI 10.1007/978-3-662-45957-7
Jointly published with Science Press, Beijing
ISBN: 978-7-03-042528-7 Science Press, Beijing

Library of Congress Control Number: 2015934232

Springer Heidelberg New York Dordrecht London

Printed on acid-free paper

Springer is part of Springer Science+Business Media (www.springer.com)

Abstract

Vehicle dynamics and road dynamics are two separate subjects. In vehicle dynamics, road surface roughness is generally regarded as random excitation to the vehicle, while at the same time handling stability, ride comfort, and vehicle safety are all investigated. In road dynamics, the vehicle is generally regarded as a moving load acting on the pavement, while at the same time the response and lifetime of the pavement and foundation are all studied. This book suggests a new research concept to couple the vehicle and the road together with a three dimensional (3D) tire model. The dynamics of the vehicle, road, and the vehicle–road coupled system were investigated by a theoretical analysis, numerical simulations, and field tests.

Chap 1 gives the state of research in vehicle dynamics, road dynamics and tire dynamics, and proposes the research scheme of vehicle-road coupled system dynamics.

In Chap. 2, the lumped parameter models of two-axle and three-axle vehicle systems are established and the dynamic responses are analyzed.

In Chap. 3, the nonlinear virtual prototype model of a heavy vehicle is set up, and an orthogonal optimization program for the virtual heavy vehicle model is presented to analyze the effect of vehicle parameters on riding comfort and road friendliness according to the design of experiment (DOE) method.

In Chap. 4, the road models of a finite and infinite beam on a nonlinear foundation with viscous damping are established. Based on the Galerkin method and the integral transform method, the numerical and analytical solutions are derived for the dynamic response of the pavement structure subjected to a moving load. Moreover, the vibration characteristics of the pavement structure under a moving load are discussed through some examples. Furthermore, the coupled nonlinear vibration of the vehicle–pavement system is studied based on a finite Timoshenko beam on the foundation subjected to a spring–mass–damper oscillator.

Chap 5 establishes the road model as an infinite double-layer plate on a Kelvin foundation and an elastic half-space. An analytical approach is developed to investigate the dynamic response of the road subjected to moving vehicle loads. The analytical solutions of the dynamic responses in time domain are then derived by integrating the generalized Duhamel integral over the Green's function of the

double-layer plate under the unit impulse load. The vibration characteristics of the road under a moving constant and harmonic load are then analyzed.

In Chap. 6, a 3D finite element model of the road system is established and the time-dependent deflection, stress, and strain of the road are obtained by linking together the road surface roughness, a moving heavy duty vehicle, and a multilayered road system. The road fatigue life is calculated by taking the tensile strain at the bottom of the asphalt surface as the evaluation index.

In Chap. 7, a 2D and 3D vehicle–road coupled systems are built and coupled system responses are simulated with the methods of mode superposition, Galerkin's method, and numerical integration. The differences between the coupled system and the traditional systems are also investigated.

By using the theory of vehicle–pavement coupled system proposed in Chap. 7, effects of system parameters on dynamic characteristics of vehicle and pavement are simulated and analyzed in Chap. 8. Based on the simulation results, some low dynamic design measures are suggested for choosing system parameters, which may contribute to the ride comfort of heavy vehicle and the life of asphalt pavement.

Chapter 9 presents a nonlinear vehicle-road coupled model composed of a seven degree of freedom (DOF) vehicle and a simply supported double-layer rectangular thin plate on a nonlinear viscoelastic foundation. A numerical integration method for solving this coupled system is developed and the nonlinear dynamic behaviors of the system are analyzed. In addition, the simulation results of the nonlinear viscoelastic model are compared to those of the linear or elastic model. The effects of system parameters on vehicle riding comfort and road damage are investigated.

In Chap. 10, a vehicle–road field test section was built on a highway and the responses of a heavy vehicle and the road were measured. This book has constructed a cross-subject research framework referred to as "vehicle-road coupled system dynamics" and will be beneficial to vehicle optimization, road design, construction, and fatigue life prediction.

This book is suitable for university professors, graduate students, and engineers majoring in vehicles, mechanics, highway engineering, and other related areas.

Contents

About the Authors

Dr. Shaopu Yang received his Ph.D. from Tianjin University in 1991. He currently serves as a Professor and Deputy President at Shijiazhuang Tiedao University. He is also a committee member of IFToMM. He is a leading scientist of the National Basic Research Program of China (973 Project). He was in charge of more than 30 projects including three key projects for the National Natural Science Foundation of China, and has published over 150 journal and conference papers. He received the National Science and Technology Award in 2003. His research was funded by the National Outstanding Young Scientist Fund of the National Natural Science Foundation of China. He is also winner of the Science and Technology Award of Hebei Province for three times (2005, 2009, 2013).

Dr. Liqun Chen is the Chang Jiang Chair Professor at Shanghai University. His research was rewarded by the National Outstanding Young Scientist Fund of the National Natural Science Foundation of China. He has co-authored 5 five books, namely Mechanics of Vibrations (1998, 2000, 2011), Nonlinear Dynamics (2000), Nonlinear Vibrations (2001, 2003), Theoretical Mechanics (2006, 2014), and Chaos in Attitude Dynamics of Spacecraft (in English) (2013). He has published over 100 papers in international journals in the fields of nonlinear dynamics and vibration of continua.

Dr. Shaohua Li is a Professor of Mechanical Engineering at Shijiaz huang Tiedao University. She received M.S. (2003) from STDU and Ph.D. (2009) degree from Beijing Jiaotong University. Since 2003, she has been working on the research of vehicle dynamics and control and has published 25 journal papers. As principal investigator, she has completed five projects and is still fulfilling two projects, including "The National Natural Science Foundation of China: Nonlinear dynamics of heavy-duty vehicles under complex conditions" and "Project Supported by New Century Talent Foundation of Ministry of Education, China: Modeling, simulation and control of the driver-vehicle-road system". Her research was funded by the Hebei Outstanding Young Scientist Fund of the Natural Science Foundation of Hebei.

Acknowledgmemts

The authors would like to give special thanks to Professor Wanming Zhai, who has discussed with the authors about the dynamics of the vehicle–road-coupled systems extensively and offered many useful suggestions to us.

The authors also wish to express their sincere thanks and appreciation to the many individuals (students, faculty members, and practicing engineers) who have both directly and indirectly contributed to the contents of this book. The number of such contributors is too large, however, to attempt listing them by name.

Some of those deserving of special recognition are Dr. Ding Hu, Dr. Lu Yongjie, and Dr. Li Haoyu, who have made a large contribution to the contents of the book. Prof. Chen Enli performed a lot of the field test work. Yang Yushi, Ng Jiaqiang (Eldwin) and Paul Joseph German have spent a lot of time in revising and proving the context of the book. The authors express their deep appreciation and thanks to them for a job superbly done.

Chapter 1
Introduction

With the increase in road traffic and vehicle loads, premature damage of the asphalt pavement on expressways has become more prevalent, which has been greatly reducing the pavement's effective lifetime. Much of the damage occurs within the first 2–3 years after the road use [1]. Road damage is seen to cause an increase in dynamic tire forces, which may worsen vehicle vibration and reduce the passenger's ride comfort and safety. Accordingly, the increased vehicle vibration leads to an increased tire force, which may speed up road damage. Hence, the vehicle and road together form a coupled system. Mamlouk [2] put forward the concept that vehicle-road interaction can be applied to weigh-in-motion, pavement design, and vehicle regulation as early as 1997.

However, at present, the vehicle and the pavement are investigated separately in vehicle dynamics and road dynamics. In vehicle dynamics, the road surface roughness is generally regarded as an excitation on a vehicle, where the handling stability, ride comfort, and safety of vehicles are investigated. In road dynamics, the vehicle is generally regarded as a moving load acting on the pavement, and the dynamic response and fatigue life of roads are investigated. The interaction of vehicle and road should however, be investigated simultaneously based on a vehicle-road coupled system. This will be beneficial to vehicle optimization, road design, construction and fatigue life prediction. It is a new cross-subject topic that involves vehicle dynamics, road dynamics, tire dynamics, and nonlinear dynamics, and has important theoretical significance and application value.

1.1 The State of Research in Vehicle Dynamics

In vehicle dynamics, the investigation of vehicle-road interaction began many decades ago. Here, vehicles are taken as research subjects and roads as excitations. The dynamic tire loads and the road-friendly characteristics of vehicles are investigated according to road damage experiential equations. Research topics involve dynamic analysis, studies on the effects of vehicle parameters on road damage, and optimal design of suspensions. In the study of vehicle dynamics, the road system is not modeled and the effect of pavement vibration on vehicle dynamics is also seldom considered. The research models of vehicles have undergone great changes,

S. Yang et al., *Dynamics of Vehicle-Road Coupled System,*
DOI 10.1007/978-3-662-45957-7_1

from the traditional lumped-parameter model to the modern finite-element model, dynamic sub-structure model and multibody dynamic model, and from linear models to nonlinear models with nonlinear stiffness or damping. Figures 1.1–1.4 show these vehicle models. The responses of these models can be obtained theoretically or numerically. Theoretical methods include mode superposition, direct integration, and averaging, while the main methods of numerical integration are the Newmark-β method, the Wilson-θ method, and the Runge-Kutta method.

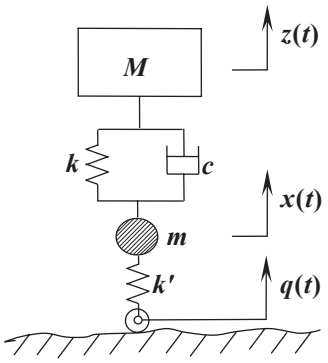

Fig. 1.1 2-DOF quarter-vehicle model

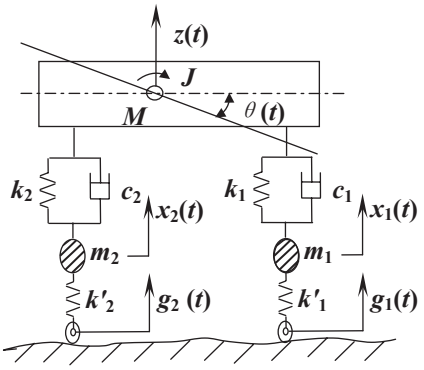

Fig. 1.2 4-DOF half-vehicle model

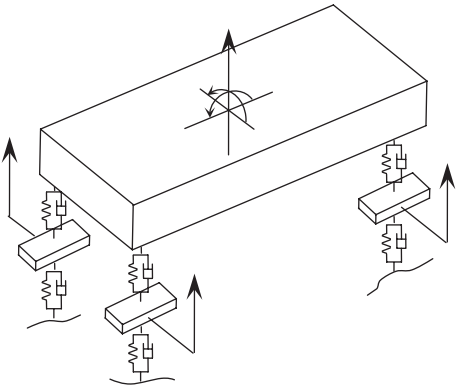

Fig. 1.3 7-DOF full-vehicle model

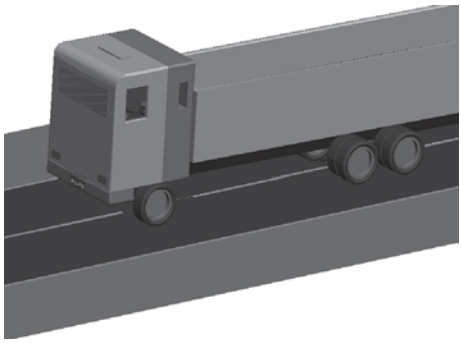

Fig. 1.4 Vehicle model of multibody system dynamics

For the lumped-parameter modeling method, the finite degree-of-freedom (DOF) model of a vehicle system is comprised of mass, spring, and damping elements. Typical examples include a quarter-vehicle model with 2-DOF, a half-vehicle model with 4- or 5-DOF, and a full-vehicle model with 7–18-DOF. At present, these models are popular for researching road-friendly characteristics of vehicles. Cole and Cebon are representative researchers in this area. They investigated the effect of heavy vehicle parameters on tire pressure and road damage, and optimized a passive suspension. It was found that a 15 % reduction in dynamic tire force may lead to a 5.3 % decrease in road damage. Moreover, they proposed the concept of spatial repeatability and believed that the peak forces applied by a heavy vehicle fleet are concentrated at specific locations along the pavement. They also used the 95th percentile fourth-power force to investigate the effect of suspension stiffness and damping on road damage [3-9]. Hardy used the mode-superposition theory and the integral transform to derive an analytical solution of the displacement of a beam on a viscoelastic foundation, and validated it by field experiments [10]. Yi K, optimized active and semiactive heavy vehicle suspensions in order to decrease the pavement damage caused by dynamic vehicle loads [11]. Kenis investigated dynamic tire loads on pavements with different road surface roughness and simulated the dynamic pavement response [12]. Markow and Myers investigated the influence of heavy vehicle characteristics on tire forces and pavement response. They found that the vehicle configuration and suspension system greatly influences tire forces and that the tire pressure has little effect on the dynamic load [13, 14]. Sun optimized a 3-DOF quarter-truck suspension system by minimizing the dynamic pavement load and found that a large tire pressure and a small suspension damping may increase dynamic tire forces [15]. Yu optimized a heavy vehicle suspension with the aim of decreasing road damage and proposed that the main cause of pavement damage is a small damping coefficient [16]. Zhu investigated the effect of vehicle speed, road roughness, wheel track, and tread on tire loads using a 7-DOF model and designed a semiactive suspension to minimize dynamic tire loads [17–18]. Xu revised the fourth-power force and analyzed the influences of the vehicle load, running speed, and suspension parameters on road damage with a revised fourth-power law and optimized suspension parameters [19]. Liu investigated the relationship among road damage, suspension parameters, vehicle load, and road roughness, and proposed that the main reason for road damage is the spatial repeatability of the

dynamic tire force and the vibration of sprung mass [20]. Zheng discussed the effect of vehicle speed and road roughness on random tire force and pavement fatigue stress using a 2-DOF model [21]. Zhang built a function to describe the relationship between the suspension parameters and the vertical tire force and found that a heavy vehicle with a preview-feedback active suspension leads to 23–27 % less road damage and improves riding comfort by more than 90 %. He also presented a full probability evaluation of pavement damage by the vehicle based on the fourth-power law, and analyzed the relativity of vehicle riding comfort to pavement damage [22–25]. Yu investigated the variation of the Dynamic Load Coefficient (DLC) with the road roughness wavelength using a 4-DOF model and concluded that the DLC does not increase with a rise in vehicle speed, but shows resonance with a peak value [26]. Zhang investigated the effect of vehicle speed, road roughness, vehicle load, and suspension stiffness on dynamic tire loads using a single-DOF model [27]. Guo employed a Fourier-superposition method to calculate the amplitude and power spectral density (PSD) of the vehicle dynamic load, and the amplitude factor and PSD of acceleration, and concluded that an increase in vehicle speed and road roughness will increase the DLC [28]. Yan designed an optimal active-suspension controller based on a 2-DOF model and compared road-friendliness between active and passive suspension systems using DLCs, dynamic load stress factors, and 95th percentile fourth-power forces. It was concluded that an active suspension can improve road-friendliness of a heavy vehicle [29].

Since finite element (FE) modeling demands much more calculation time, the FE vehicle model is mainly used for the design of complex parts such as the vehicle body, engine mount, etc. [30–32]. The dynamic substructure approach includes the mechanical admittance method and the modal synthesis method. The modal synthesis method has been successfully applied to study the vehicle vibration noise mechanism and the vibration transfer characteristics of the vehicle chassis and frame [33, 34]. At present, dynamic analysis modeling of the vehicle is usually combined with the lumped mass method, FE method and modal synthesis method.

With the development of computer technology and applied software, Functional Virtual Prototyping (FVP) technology is now used extensively in vehicle modeling. The core content of the FVP is the Multi-Body System Kinematics and Dynamics modeling theory. Since FVP models are good at describing complex structures and dynamic tire-road contact forces, more scholars have begun to analyze vehicle dynamic behaviors based on the FVP vehicle model. Popular multi-body dynamics software include Simpack, ADAMS, and TruckSim, which have developed professional design modules in cooperation with famous vehicle manufacturing companies, such as Ford, BMW, GE, etc. [35–37]. Vaculin optimized a semiactive suspension system based on SIMPACK and Matlab by minimizing the tire dynamic load [38]. Odhams developed a complex multibody model of a heavy-load hinged vehicle using TruckSim and studied the driving safety of a trailer under the operation of an active steering system [39]. Yang investigated vehicle ride comfort using ADAMS software [40]. Lu validated a FVP full-vehicle model with experimental data of a heavy vehicle and discussed the effects of vehicle speed, vehicle load and road surface roughness on tire forces and DLC [41]. Ren built a FVP vehicle model

with ADAMS and studied the interaction between the vehicle and the road, and designed an active suspension which can significantly reduce tire forces [42–43]. Studies of road-friendly vehicles using FVP models have not been sufficient so far and thus need further research.

At the same time, other scholars have modeled the nonlinear characteristics of suspensions and tires, and have studied the nonlinear dynamics and semiactive control of vehicle systems. Stensson analyzed nonlinear phenomena, including multisolutions, subresonance, and parameter sensitivity using numerical simulation, in a SAAB 9000 vehicle suspension [44]. Kim investigated vibration control of a vehicle suspension with magneto-rheological fluid (MRF) damping [45]. Zhu investigated bifurcations and chaos in a vehicle suspension with nonlinear damping and stiffness [46–47]. Li investigated primary resonance, subharmonic resonance and chaos in a hysteretic nonlinear vehicle suspension using Melnikov's method and numerical methods [48–49]. Georgios studied the effect of suspension damping on vehicle ride comfort using a semiactive control based on a nonlinear vehicle model [50]. Oscar modeled the nonlinearity of air suspensions on heavy-duty trucks and numerically analyzed the influence of road roughness on ride comfort [51]. Ji proposed a square nonlinear model to describe tire forces through a dynamic tire test [52]. Qu discussed the effects of nonlinear factors on vehicle steering, dynamic response, and handling stability based on a nonlinear perturbation tire model[53]. Meng considered the nonlinearity of a leaf-spring suspension and tire stiffness, and found that double-period bifurcations existed in some range of frequencies which greatlyincreased the vertical acceleration of the vehicle body [54]. Zhao performed a dynamic test for a l0.00-20-type tire and found that the tire radial stiffness has a nonlinear relationship with displacement, but hardly varied with excitation frequency [55]. Zhu and Xu set up a nonlinear vehicle suspension model for a leaf spring with variable stiffness, and calculated the stochastic response with the statistic nonlinear method, and compared the numerical results with the test data [56, 57]. Yang built a 2-DOF model for a heavy vehicle suspension with a primary and a secondary leaf spring, and optimized the suspension parameters in order to enhance riding comfort [58].

It is to be noted that these investigations on vehicle dynamics generally assumed that the pavement was rigid and stationary and did not take into account the effect of pavement vibration on vehicle response. It is necessary to propose a new vehicle-pavement-foundation coupled model to investigate the vehicle's and the pavement's response simultaneously.

1.2 The State of Research in Road Dynamics

In road dynamics, the vehicle is generally regarded as a moving load acting on the pavement, and the pavement's dynamic response such as stress, strain, and displacements are investigated. In theoretical research, the methods of integral transform, mode superposition, and transfer matrix are used to obtain the analytical solutions

of the system and numerical integrations are used to calculate the distribution of responses. In computational research, the methods of finite element (FE) and boundary element (BE) are used to model the multilayer system of the road, and the road response can then be obtained by numerical integrations. The Strategic Highway Research Program (SHRP) in the US, performed comprehensive research on road dynamics and road damage potential of dynamic wheel loads [59]. The Organization for Economic Co-operation and Development (OECD) in Europe completed the project of Dynamic Interaction between Vehicles and Infrastructure Experiment (DIVINE) and also contributed a lot to the research of road dynamics [60–61]. The dynamic response of roads under traffic loads and the mechanism of road damage have become a hot topic in road research.

In road dynamics, researchers emphasize the road and seldom model the vehicle system. They hardly consider the influence of vehicle vibration on road dynamics. Research models of the road have developed from one-dimensional to two- or three-dimensional, from single to multilayer, from using a linear elastic foundation to a nonlinear elastic foundation, and from linear elastic to nonlinear viscoelastic materials. At present, roads are usually modeled as a beam, a plate, or a multilayer system on an elastic or viscoelastic foundation, as shown in Figs. 1.5–1.8.

The one-dimensional model of a beam on a viscoelastic foundation is simple and practical and is suitable for dynamic analysis of a symmetric road. Early on, this model was widely used by scholars in different countries to research road dynamics under moving loads. Timoshenko investigated the vibration of a simply supported

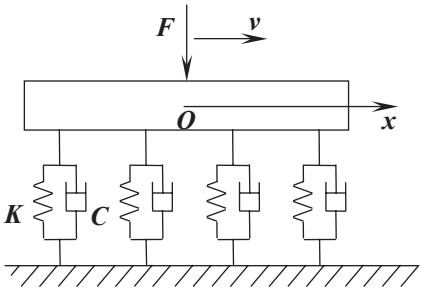

Fig. 1.5 Model of a beam on a viscoelastic foundation

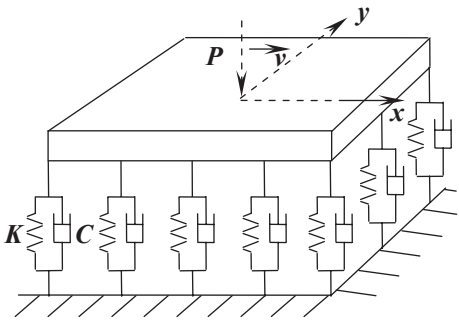

Fig. 1.6 Model of a plate on a viscoelastic foundation

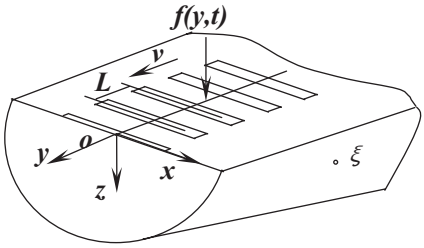

Fig. 1.7 Model of an elastic half space

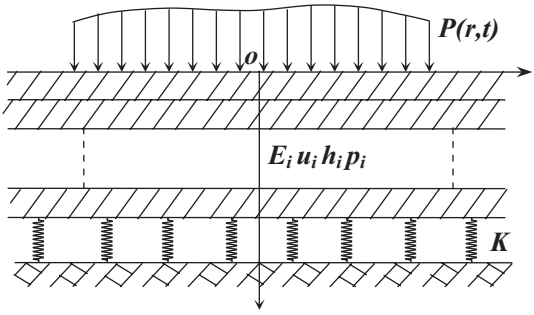

Fig. 1.8 Model of a multilayer on a viscoelastic foundation

beam induced by a moving point load, and obtained a triangular series solution of the beam response [62]. Kenny, Fryba, and Steele investigated the dynamic response of beams of finite and infinite lengths under moving loads [63–65]. Thambiratnam calculated the response of a beam on an elastic foundation via the Newmark numerical integration. He analyzed the effects of load moving speed, foundation stiffness and beam length on beam response [66]. Liu and Sun derived an analytical solution of a beam on a viscoelastic foundation under moving loads using the integral transform method and discussed the influence of road roughness on pavement displacement and strain respectively [67, 68]. Giuseppe studied the response of a beam on a viscoelastic foundation subjected to a single-DOF oscillator. He converted the coupled-system equations to dimensionless ones and calculated the response by the methods of mode superposition and numerical integration [69]. Deng investigated the dynamics of a beam on a Winkler or a Kelvin foundation under moving vehicle loads using an integral transform [70]. Zhou obtained an analytical solution of a beam with infinite length on a Kelvin foundation under moving loads using an integral transform. He proposed that the beam displacement increases with the speed of moving loads when the foundation damping is small, but on the contrary, varies when the foundation damping is large [71–72]. In the last several years, some scholars have investigated the nonlinear dynamics, such as bifurcations and chaos, of beams on a nonlinear elastic foundation. Lenci investigated the chaos of a nonlinear beam on a Winkler foundation under an axial load using the method of Melnikov and found two different paths from bifurcation to chaos [73]. Kargarnovin obtained the responses of infinite beams supported by nonlinear viscoelastic foundations and subjected to harmonic moving loads using a perturbation method and a complex Fourier transform. He investigated the influence of the

load speed and the frequency on the beam response [74]. Santee and Gonçalves investigated the stability of a beam on a nonlinear elastic foundation and the effects of system parameters on the nonlinear vibration of the beam. They obtained the critical boundary of system instability with Melnikov's method [75]. Kang studied the nonlinear behavior of a beam under a distributed axial load with time-dependent terms by Galerkin's discretization and the spectral balance method. He found that the system's motion will turn into chaos after several Hopf bifurcations [76]. Considering material and geometric nonlinearities, Zhang studied the chaotic motions of an axially compressed nonlinear elastic beam subjected to a transverse load using the nonlinear Galerkin and the Melnikov methods and found that chaos may occur in the system when the load parameters satisfy certain conditions [77]. Zhang used Galerkin's method and numerical integration to investigate the nonlinear dynamics of a Timoshenko beam with damage on a viscoelastic foundation, and obtained phase trajectories, a Poincaré section and a bifurcation diagram. She also discussed the effects of beam material, loads, foundation, and damage on the beam's response [78].

The 2-dimenional model of a plate on a viscoelastic foundation has been an active area of research, with research results mainly concentrated on the dynamics of a linear elastic plate on a foundation. Fulton, Sneddon, and Morley solved for the dynamic response of a plate subjected to linear loads using the integral transformation method [79–80]. Liu built a 2-DOF vehicle and a plate on a viscoelastic foundation, and derived the analytical solution of the pavement displacement under moving vehicle loads using an integral transform. He analyzed the effects of road roughness and foundation modulus on pavement displacement and strains, and found that a large foundation modulus may lead to a small strain [81]. Huang investigated the dynamic response of a thin plate on a Winkler foundation under a harmonic moving load. He found that velocity, moving load frequency, foundation stiffness, and tire configuration all affect the dynamic behavior of the plate [82]. Kim studied the dynamic response of a plate on a viscous Winkler foundation under moving loads of varying amplitude using the mode superposition and the integral transform methods. He analyzed the influence of wheel space and driving speed on the plate displacement and stress [83]. Sun studied the response of a plate subjected to a moving point or line load and obtained the analytical solution using Green's function. He discussed the relation of the critical speed and the critical frequency of the moving loads [84]. Wu converted a rectangular plate subjected to a line load into a beam subjected to a point load by the equivalent method, and the conversion was seen to be beneficial for test design and its fulfillment [85]. Cai studied the steady-state response of pavement systems subjected to a moving traffic load employing Kirchhoff's small-deflection thin-plate theory and Biot's fully dynamic poroelastic theory. He also simulated the influences of load speed, soil permeability, and the plate's flexural rigidity on the pavement system's response [86]. Cheng and Zheng investigated the dynamics of a rectangular plate on an elastic foundation by the mode superposition method [87–88]. Deng [17] investigated the dynamics of a pavement under a moving vehicle load using an integral transform and the generalized Duhamel integral based on the plate model on an elastic foundation

[70]. Based on the principle of calculus variation, Yang analyzed the response of a rigid pavement lying on a Winkler foundation and the effects of the main vehicle parameters on the dynamic response [89]. Zhou modeled a rigid pavement as an infinite plate on a Kelvin foundation subjected to moving loads and developed analytical solutions of steady-state displacements using Duhamel's integral for constant or harmonic point, line, and area loads. The effects of velocity and damping on the maximum and the distribution of displacement were also analyzed, and the critical velocity and characteristics of the dynamic response of the plate were found [90–91]. Yan used an integral transform for solving a two-parameter layer foundation mode analytically, and discussed the effects of load moving speed, foundation modulus, foundation damping, the Poisson ratio, plate thickness, and plate elastic modulus of pavement deformation [92]. Additionally, some scholars have put much emphasis on the bifurcation and chaos of plates on a nonlinear elastic foundation. However, this research mainly considers loads with fixed positions and seldom considers moving loads. Gajiendar [93] and Nath [94] investigated the nonlinear vibration of a circular plate on an elastic foundation respectively. Xiao investigated the bifurcation and chaos of a rectangular, moderately thick, cracked plate on an elastic foundation subjected to a periodic load[95]. Qiu analyzed the bifurcation and chaos of a circular plate on a nonlinear elastic foundation [96]. Yang studied nonlinear vibration and singularities of a rectangular, thin plate on a nonlinear elastic foundation with a Melnikov function and Galerkin's method [97–98].

From top to bottom, the pavement system contains a surface course, a base course, a sub-base course, a filled subgrade, and a natural foundation. A three-dimensional multilayered medium on a linear elastic foundation is the best model closest to a real pavement. The analytical method can provide explicit representations and physical interpretations of the subject—this method has thus been widely used and is still important for understanding the nature of the problem. Eason first studied the dynamics of a three-dimensional pavement subjected to a point load moving at a constant speed [99]. De Barros derived the dynamic responses of a viscoelastic-layered half space to a point or a line load moving at a constant speed [100]. Based on the Betti–Rayleigh dynamic reciprocal theorem and Green's function, Cao converted the moving source problem to a fixed source problem with the receiver point moving in an opposite direction and derived the transfer matrix of the multilayered soil medium subjected to a moving load. A Matlab code was developed and employed to perform a case study. The results show that the ground vibration induced by a moving load is of typically low-frequency feature [101]. Deng obtained the theoretical solution of a dynamic response of a multilayer induced by a half-sinusoidal load [70]. Zhong derived the explicit solution of an axisymmetric multilayered half space by means of an integral transform and transfer matrix [102]. Li analyzed the response of an elastic multilayer under traffic loads and considered the material viscoelasticity in his model[103]. On the other hand, numerical methods, such as the finite element method and boundary element method have been used successfully in the dynamic analysis of a layered viscoelastic medium subjected to moving loads. The introduction of numerical methods into the solution process can possibly allow for more complicated and hence more realistic pavement

dynamics problems. Wu considered the interaction between pavements and the underlying soil foundation and investigated the dynamic responses of concrete pavements subjected to moving loads using the 3D finite element method. The effects of finite element division, foundation stiffness and pavement thickness on pavement displacement were also discussed [104]. Markov presented that the key factors influencing a stiff pavement are the configuration of the vehicle and axle, vehicle load, suspension properties, vehicle speed, road roughness and plate bending [105]. Considering the dynamic variation and complex distribution of the tire-pavement contact stress, together with vehicle speed and viscoelastic material properties, Siddharthan developed a 3D-MOVE procedure using the Fourier transformation method and simulated pavement responses to the moving tire loads [106–107]. Wang simulated the road damage caused by different trucks in North America and found that a large vehicle load would exacerbate road damage [108]. Kim studied the stress and strain of pavements with sand or clay foundations under tire loads using the finite-element method. He proposed that there existed a flaw in the flexible pavement design [109]. Metrikine studied the stability of a two-mass oscillator that moves along a beam on a viscoelastic half-space. Using the Laplace and the Fourier integral transforms, he derived expressions for the dynamic stiffness of the beam at the point of contact with the oscillator and concluded that a proper combination of negative damping mechanisms may effectivelystabilize the system [110]. Jeongho modeled the base and subgrade layers as stress-dependent cross-anisotropic materials to assess the pavement response using finite-element (FE) analysis, and established equations correlating the critical strains to layer displacements, axle loading, offset distance, and layer moduli in order to evaluate the accelerated damage potential due to overweight truck loading [111]. Darestani tested road responses under both quasi-static and dynamic truck loads and the resulting test data were used to validate the finite element model developed in ANSYS for further sensitivity study on those parameters affecting the dynamic response of concrete pavements [112]. Using the nonlinear finite element method, Asghar estimated the cracking and failure of rigid pavement slabs and joints as a result of repeated application of the dynamic loads. Simulations were performed for specific gross vehicle loads and tractor–trailer configurations, and it was found that the vehicle speed fluctuated with the DLC and the rise of vehicle load may reduce the DLC [113]. In addition, Chen, Hou, Xie, and Liu also built finite element models for roads and analyzed stress, strain, and other dynamic responses of the road [114–117].

Some problems may exist in the current research field of road dynamics, such as:

1. The loads acting upon the road are not comprehensively treated. In most studies, only the vertical load is considered while the lateral and the longitudinal loads are neglected.
2. Linear elastic materials are usually investigated, but insufficient results are available for nonlinear viscoelastic materials.
3. Research is concentrated on the response of the road, and is hardly concerned with the effects of road vibration on vehicle system dynamics.
4. In research on plates on a nonlinear elastic foundation, an equivalent distributed load at a fixed position is used. Moving or random loads are scarcely applied. Moreover, nonlinear viscoelastic pavement materials are seldom considered.

1.3 The State of Research in Tire Dynamics

Tire dynamics is concerned about the relation of force, deformation, and dynamic responses of a tire under different driving conditions, as shown in Fig. 1.9. For the investigation on vehicle–road interaction, it is important to model the tire's vertical, longitudinal, and lateral forces as well as the aligning moment.

The research of tire dynamics includes the analysis of the extrinsic and intrinsic characteristics of the tire. The extrinsic characteristics are the tire enveloping, slide, and roll characteristics of the tire, which are related to vehicle ride comfort, handling stability, and driving or braking safety. The intrinsic characteristics are the inherent frequency, mode, and dynamic response. Research on vehicle tire mechanics is the key to connecting vehicles and roads. Tire mechanical models can be divided into five categories: the enveloping model, the sliding model, the ring model, the direct-mode model, and the FE model.

The enveloping characteristic model of a tire is used to describe the vertical and longitudinal forces. Tires are modeled as springs, masses, and a low-pass filter. Many enveloping models for tires have been presented, including the single-point-contact model, the fixed-print model, the rigid/flexible-roller-contact model, and the radial spring model, as shown in Fig. 1.10. The simplest is the point-contact tire

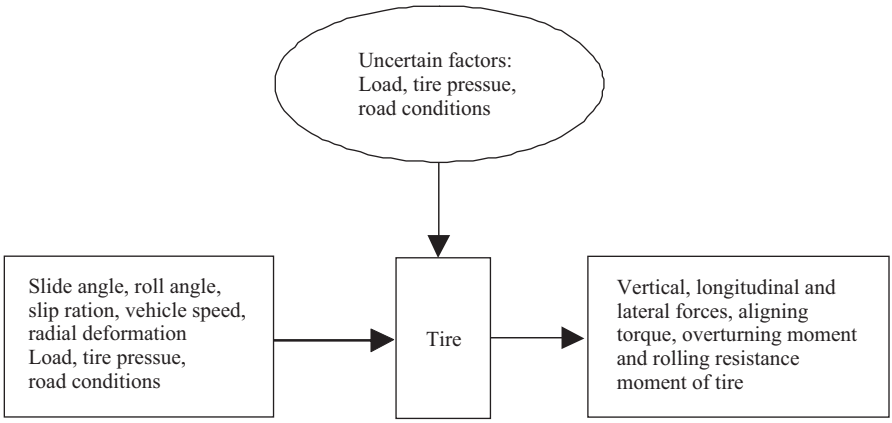

Fig. 1.9 The research task of tire dynamics

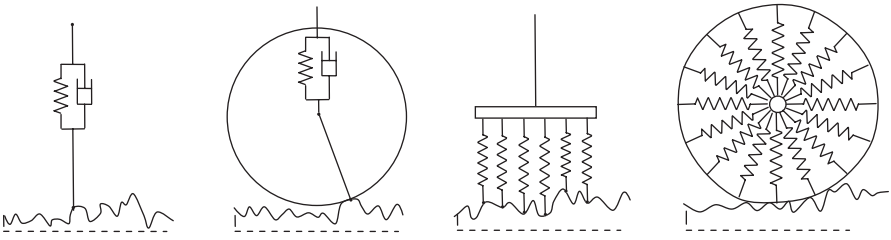

Fig. 1.10 Tire enveloping models

model, which describes the tire's vertical force and is most widely used in both vehicle dynamics and road dynamics. Some scholars have used the fixed-print model to add a line or a surface moving load to the pavement, and thus analyzed the dynamic response of the road. Guo presented a flexible roller-contact tire model, and carried out simulations of a vehicle vibration system based on a rigid- and a flexible- roller-contact tire model. The simulation results showed good agreement with experimental data [118–120]. Huang proposed a new method for measuring the effective road profile to study tire displacement enveloping characteristics [121]. Guan presented a vehicle system with the enveloping tire model to study the performance of an active suspension system [122]. Yang proposed a modified elastic-roller tire model and developed a two-dimensional vehicle-road-subgrade coupled system. The improved elastic-roller line-contact model and the point-contact model of the vehicle-road coupled system are compared [123].

The sliding models aim at describing the relationship among the lateral tire force, aligning torque, sliding angle, and vertical tire load. These models are usually used to analyze vehicle handling stability and are seldom used in road dynamics, and can be divided into: pure physical models, empirical models, and semiempirical models. According to the tire physical structure and working mechanism, the pure physical model is proposed in the form of a mathematical expression used to describe a tire's mechanical characteristics, and is simple and convenient in theoretical research. Pure physical models are expressed by polynomials and include the Fiala, the Gim, and the Dugoff tire models, etc. [124–125]. The empirical model has a higher precision, but has a higher computing cost, and is only used in vehicle dynamics design and simulation. The famous Magic Formula model was proposed by Pacejka based on extensive experiments. It is expressed by inverse tangent functions and can be used to describe a six-directional wheel force in a steady state [126]. The semiempirical model combines the theoretical model with experimental data. Due to the higher precision and shorter computing time, it has been widely used in vehicle simulation and theoretical research. Guo put forward a semiempirical model, named the UniTire Model, which describes a tire's mechanical characteristics in an exponential form. It describes the six-component characteristics of a tire in a variety of working conditions, and has a high precision in simulating complex and extreme conditions [127]. Shiotsuka, Palkovicis, Ren, and Cui all used the manual neural-network theory to develop tire sliding models [128–131].

The ring model and the direct-mode model of tires can account for enveloping and sliding properties, and they have thus attracted much attention in vehicle dynamic simulations. However, they are seldom used in road dynamic research. In order to extend the frequency range of the tire, Pacekja introduced a dynamic rigid-ring model based on the Magic Formula model and proposed a Swift model. The Magic Formula and Swift tire models were developed at Delft University of Technology. They have been implemented in commercial software (ADAMS, SIMPACK and MATLAB/Simulink), and named as MF-Tyre and MF-Swift, respectively. The ring tire model extracts the low-order mode parameters from experimental

measurements. On the other hand, the direct-mode model obtains almost all mode parameters from experimental measurements and additionally considers road roughness. It is more practical, but also more difficult than the ring model, and costs more in experimental expenses. Guan put forward a tire model describing the enveloping and sliding properties with the tire mode parameters [132].

With higher precision and longer computing time, the FE model can model the tire configuration in detail and is widely used in tire design. The FE tire model has been used for static and dynamic analyses, thermal coupling, abrasion, and fatigue life prediction. However, research work on vehicle and road dynamics with FE tire models is still seldom found. Rao used the ABAQUS software to investigate the lateral and longitudinal forces of pneumatic tires during steering and braking and compared the simulated results with test data [133]. Gall built a 3D FE tire model with the tread, and found that the normal stress reaches a maximum value when the friction coefficient is in the vicinity of 0.55 [49], and the distribution of normal stress tends to be stable with an increasing friction coefficient. This model is suitable for the analysis of transient rolling contacts, internal stress, modality, noise, and so on [134]. Mousseau combined a multibody vehicle model and a FE tire model and derived the tire force and displacement [135].

1.4 The Research Scheme of Vehicle-Road Coupled System Dynamics

Over the past couple of decades, the vehicle and the pavement have been investigated separately in vehicle dynamics and road dynamics. In vehicle dynamics, road surface roughness is usually regarded as an excitation to a vehicle, and accordingly, the vibration of the pavement is neglected. In road dynamics, the vehicle is generally regarded as a moving load acting on the pavement, consequently, the characteristics of the vehicle suspension are not considered. It is noted that the coupling action between vehicle and road is seldom considered in the previously published works.

On the other hand, research on vehicle-track coupled dynamics [136–139] and vehicle-bridge coupled dynamics [140–145] has developed rapidly and achieved good results. The research ideas and methods of vehicle-track and vehicle-bridge interaction has inspired us to bring coupled dynamics to vehicle-road systems.

The research scheme of vehicle-road coupled system dynamics is proposed, as shown in Fig. 1.11. The vehicle and the road are linked by tire forces, and the resulting vehicle-road coupled system is composed of a vehicle model, a road model, and a tire model. Based on this coupled system, the vibration of the vehicle and road can be calculated simultaneously and the vehicle-road interaction can be investigated in detail. In recent years, our group has developed a body of research on vehicle-road coupled system dynamics [123, 146–149], which is beneficial to vehicle and road design, road construction, and fatigue life prediction.

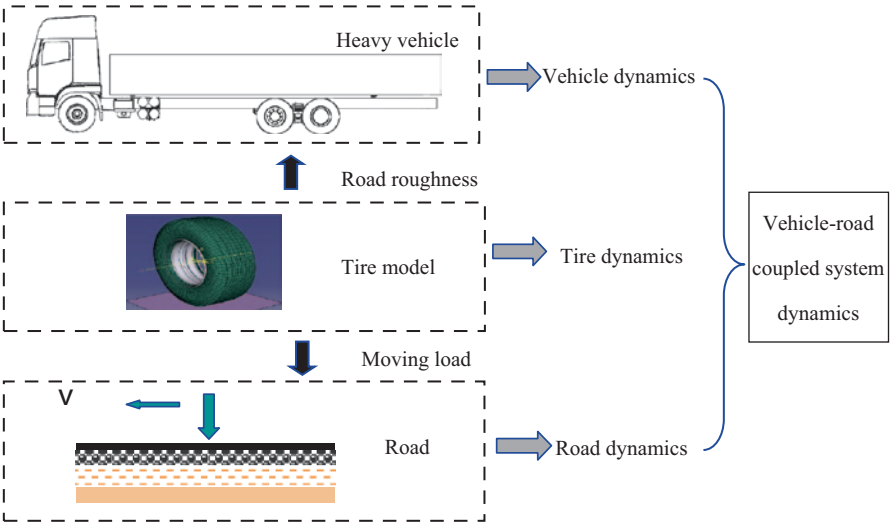

Fig. 1.11 The research scheme of vehicle-road coupled system dynamics

1.5 Outline and the Main Issues of Vehicle-Road Coupled System Dynamics

The main part of this book consists of nine chapters, which may be divided into four parts as follows:

1. *Analysis of vehicle system dynamics* (Chaps. 2 and 3)

The dynamic properties of a leaf-spring and damper system for a heavy truck were measured, and nonlinear stiffness and damping models are proposed. The model parameters are identified from test data. Then, multiple-degree-of-freedom and multibody models of heavy vehicles were constructed, and the dynamics for heavy vehicles are analyzed. The orthogonal optimization and the semiactive control strategy are also presented based on the multibody vehicle model.

2. *Dynamic responses of road systems under vehicle loads* (Chaps. 4, 5, and 6)

A beam on a nonlinear foundation, a double-layer plate on a viscoelastic foundation and elastic half space, and (FE) model are set up for viscoelastic roads. The road dynamic responses under vehicle loads are calculated theoretically and numerically. The natural frequencies and modes of the road system are also calculated with Galerkin's methods, differential quadrature, and so on.

3. *Modeling and dynamic interaction of vehicle-road coupled systems* (Chaps. 7, 8, and 9)

The two-dimensional and three-dimensional vehicle-road coupled systems are built and coupled system responses are simulated with the methods of mode

superposition, Galerkin and numerical integration. The differences between the coupled system and the traditional systems are also investigated. The effects of system parameters, nonlinearity, and viscoelasticity on vehicle riding comfort and road damage were analyzed and the low dynamic design measures of the vehicle-road system parameters are summarized. In addition, the nonlinear dynamics of the vehicle-road coupled system are investigated.

4. *Construction of a highway test section for vehicle-road interaction analysis* (Chap. 10)

In order to obtain reliable data of vehicle and road dynamic responses, a vehicle-road test section was built on a highway and the responses of a heavy vehicle and the road were measured. By comparing simulated results with test data, the validity of the proposed vehicle-road coupled model and the calculation methods were verified.

In vehicle-road coupled system dynamics, further work is needed in the following areas:

1. Modeling of a nonlinear viscoelastic road subjected to 3D moving loads and boundary conditions.
2. Modeling of 3D nonlinear tire forces and 3D coupled vehicle-road systems.
3. The solvable conditions of ordinary and partial differential equations with integral terms.
4. Effective analytical methods and stable convergent numerical integration algorithms to solve high dimensional rigid-flexible coupled systems.
5. Construction of vehicle-road test sections and analysis of test data.

The research on dynamics of vehicle-road coupled system need some more investigation on it. It has been found that the coupling effects in vehicle-road systems are not as strong as those in railway train-track coupled systems, but it will have more effects in loaded “vehicle”-road system, especially on a highway ramp or on a bridge. It will also have more impacts on the vehicle driving safety when taking into account of the coupling effect in the road roughness spectrum which we will work in near future.

References

1. Sha QL. Highway asphalt pavement premature damage and prevention. Beijing: China Communications press; 2001.
2. Mamlouk MS. General outlook of pavement and vehicle dynamics. J Transp Eng. 1997;Nov/Dec:515–7.
3. Cebon D. Theoretical road damage due to dynamic tire forces of heavy vehicles. Proc Inst Mech Eng. 1988;202:103–17.

4. Cole D J, Cebon D. Optimization of passive and semi-active heavy vehicle suspension. SAE 942309, 1994, 567–578.
5. Cebon D. Interaction between heavy vehicles and roads. Warrendale: Society of Automotive Engineers; 1993 (SAE 930001).
6. Collop AC, Cebon D. Parametric study of factors affecting flexible-pavement performance. J Transp Eng. 1995;Nov/Dec:485–94.
7. Cole DJ. Truck suspension design to minimize road damage. Proc Inst Mech Eng. 1996;210(D):95–107.
8. Potter TEC, Cebon D, Cole DJ. Assessing 'Road— friendliness': a review. Proc of the Inst Mech Eng. 1997;2l1(D4):455–75 (Part D)
9. Cole DJ, Cebon D. Spatial repeatability of dynamic tire forces generated by heavy vehicles. Proc Inst Mech Eng, Part D. 1992;206(D):17–27 .
10. Hardy MSA, Cebon D. Response of continuous pavements to moving dynamic loads. J Eng Mech. 1993;119(9):1762–80.
11. Yi K, Hedrick JK. Active and semi-active heavy truck suspensions to reduce pavement damage. Society of Automotive Engineers; 1989. p. 588–95. (SAE 892486).
12. Kenis W, Kulakowski BT, Streit DA. Heavy vehicle pavement loading: a comprehensive testing program. Heavy vehicle and road: technology, safety and policy. London: Thomas Telford; 1992. pp. 260–5.
13. Markow MJ, Brademeyer BD. Analyzing the interactions between dynamic vehicle loads and highway pavements. Transp Res Rec. 1996;1196:161–9
14. Myers L. Measurement of contact stress for different truck tire types to evaluate their influence on near surface cracking and rutting. Transp Res Rec.1999;1655:175–84
15. Sun L, Cai XM, Yang J. Genetic algorithm-based optimum vehicle suspension design using minimum dynamic pavement load as a design criterion. J Sound and Vib. 2007;301:18–27.
16. Yu ZP, Huang XP, Zhang HX. The alleviation of road damage by heavy vehicles—optimization design of vehicle-suspension. China J Highw Transp. 1994;7(3):83–7.
17. Zhu KY. Study on the interaction between the vehicle and road system[D]. Chin Agric Univ. 2001.
18. Zhu KY, Yu Q. Study reality and prospect on the interaction of vehicle and pavement. J Xi'an Highw Univ. 2001;21(2):6–9, 23
19. Xu B, Zheng GT, Fan T. The elements influencing road damage and the optimization of suspension parameters. Automot Eng. 2000;22(6):418–22.
20. Liu Q, Xu B, Lin B. Study of suspension parameters for reduction of road damage due to dynamic load. J Harbin Inst Technol. 2002;34(6):832–37.
21. Zheng Q, Yang FT. Effect of vehicle speed and roadway surface condition on the random dynamic loads of the wheels. J Hefei Univ Technol. 2002;24(1):139–42.
22. Zhang HX, Chen BC, Zhang TZ. Full probability evaluation of a pavement's damage by a vehicle. J Qingdao Univ. 2002;17(1):60–3.
23. Zhang HX, Chen BC, Zhang TZ, et al. Relationship between smoothness of a heavy vehicle and Its caused damage to pavement. Trans Chin Soc Agric Mach. 2002;33(3):1–3, 7.
24. Zhang HX, Yin YC, Mou HB. Simulation of heavy vehicle performance improvement caused by active suspension. J Qingdao Univ. 2003;18(2):1–4.
25. Zhang HX. Study of the relation of heavy vehicle suspension parameter and pavement damage by a vehicle [D]. Changchun: Jilin University; 2002.
26. Yu Q, Cao YW. Vehicle dynamic loads caused by surface evenness. J Chongqing Jiaotong Univ. 2003;22(4):32–4.
27. Zhang J. The research on the dynamic interaction between a heavy vehicle and rigid pavement structure[D]. Changsha: Hunan University; 2003.
28. Guo CC, Tao XH, Wang FM. The influence of vehicle speed and pavement roughness characteristics on vehicle-road interaction. J North China Inst Water Conserv Hydroelectr Power. 2004;25(3):42–5.
29. Yan TY, Liu DW, Chen HM. Road-friendliness of heavy vehicles based on active suspension systems. Chin J Mech Eng. 2007;43(2):163–7.

30. Qu QZ. Analysis and evaluation of car body structure finite element methods. Automot Eng. 1996;18(3):148–51.
31. Lee NK. Design of engine mount using finite element method and optimization technique. Warrendale: Society of Automotive Engineers; 1998 (SAE 980379).
32. Gao YK, et al. FEM calculation and structural modification sensitivity analysis for natural bending vibration characteristics of mini-bus power plant. Automot Eng. 1995;17(6):354–9.
33. He YS. Automotive vibration. Beijing: China Communications Press; 1990.
34. Li CD. The muti-freedoms model and random vibration response analysis of the whole vehicle system. Automot Eng. 1987;9(2):26–41.
35. Li J, Xing JW, Tan WJ. ADAMS tutorial examples. Beijing: Beijing Institute of Technology; 2002.
36. Chen LP. The dynamic analysis of mechanical systems and ADAMS applications. Beijing: Tsinghua University Press; 2004.
37. Yu F, Lin Y. Automotive system dynamics. Beijing: China Machine Press; 2005.
38. Vaculin O, Kortum W. Analysis and design of semi-active damping in truck suspension. Design by simulation, 2007.
39. Odhams AMC, Roebuck RL, Cebon D, et al. Dynamic safety of active trailer steering systems. Proc Inst Mech Eng (Part K: J Multi-body Dyn). 2008;22(4):367–80.
40. Yang Y, Ren WQ, Chen LQ. Study on ride comfort of a tractor with tandem suspension based on Multi-body system dynamics. Appl Math Model. 2009;33(1):11–33.
41. Lu YJ, Yang SP, Li SH. Numerical and experimental investigation on stochastic dynamic load of a heavy duty vehicle. Appl Math Model. 2010;34(10):2698–710.
42. Ren WQ, Zhang YQ, Jin GD. Systematic research method for vehicle-generated road damage. China J Highw Transp. 2005;18(4):111–4.
43. Ren WQ. Virtual prototype in vehicle-road system dynamics -MSC.ADAMS applicant and practice. Beijing: Publishing House of Electronics Industry; 2005.
44. Stensson A, Asplund C, Karlsson L. Nonlinear behavior of a MacPherson strut wheel suspension. Veh Syst Dyn. 1994;23(2):85–106.
45. Kim K, Jeon D. Vibration suppression in an MR fluid damper suspension system. J Intell Mater Syst Struct. 2000;10(10):779–86.
46. Zhu Q, Ishitobi M. Chaos and bifurcations in a nonlinear vehicle model. J Sound Vib. 2004;275(3–5):1136–46. (Aug 23).
47. Zhu Q, Ishitobi M. Chaotic vibration of a nonlinear full-vehicle model. Int J Sol Struct. 2006;43(3–4):747–59.
48. Li SH, Yang SP, Guo WW. Investigation on chaotic motion in hysteretic nonlinear suspension system with multi-frequency excitation. Mech Res Commun. 2004;31:229–36.
49. Li SH, Yang SP. Sub-harmonic resonance and singularity of a nonlinear vehicle suspension system. J Vib Eng. 2007;20(2):168–73.
50. Georgios T, Charles WS, Emanuele G. Hybrid balance control of a magneto rheological truck suspension. J Sound Vib. 2008;317(3–5):514–36.
51. Oscar M, Gonzalez JC, Alejandro L, et al. Effect of road profile on heavy vehicles with air suspension. Int J Heavy Veh Syst. 2007;14(1):98–110.
52. Ji XW, Gao GM, Qiu XD. The dynamic stiffness and damping characteristics of the tire. Automot Eng. 1994;16(5):315–21.
53. Qu QZ, Liu YZ. Vehicle dynamics based on nonlinear characteristics of tires. Chin Q Mech. 2000;21(1):38–44.
54. Meng Q, Wang HL. A study on bifurcations of vehicle systems. Automot Eng. 2004;26(1): 50–3.
55. Zhao DX, Zhu WN, Zhang ZD, et al. Measurement of three-dimensional dynamic stiffness and damping for an engineering tire. China J Highw Transp. 1990;(7):84–7.
56. Zhu B, Zhang LJ, Zou XH. A study on the random response of a nonlinear vehicle suspension system. J Liaoning Techn Univ. 2004;23(2):250–2.
57. Xu B, Shi YB, Wang GD. Suspension nonlinear components influence upon ride comfort and road friendliness. Veh Power Technol. 2005;1:46–51.

58. Yang XL. Nonlinear suspension construction parameters optimization of a heavy truck. Trans Chin Soc Agric Mach. 2007;38(6):23–5.
59. Jorge BS, Joseph C, Carl LM. Summary report on permanent deformation in asphalt concrete. Washington: Transportation Research Board Business Office; 1991.
60. Transportation Research Broad. Strategic highway research program 2 [EB/OL]. http://www.trb.org/SHRP2. 2009. Accessed 3 June 2009.
61. OECD DIVNE. Dynamic interaction between vehicles and infrastructure experiment: technical report. Paris: Organization for Economic Co-operation and Development (OECD). Road Transport Research. Scientific Expert Group; 1998.
62. Timoshenko S. Method of analysis of statical and dynamic stress in rail. Proceedings of the Second International Conference for Applied Mechanics, Zurich, Switzerland; 1926. p. 407–18.
63. Kenny JT. Steady-state vibrations of a beam on an elastic foundation for a moving load. J Appl Mech. 1954;21(4):359–364.
64. Fryba L. Infinite beam on an elastic foundation subjected to a moving load. Aplikace Matematiky. 1957;12(2):105–1132.
65. Steele CR. The finite beam with a moving load. J Appl Mech ASME. 1967;35(4):111–9.
66. Thambiratnam DP, Zhuge Y. Dynamic analysis of beams on an elastic foundation subjected to moving loads. J Sound Vib. 1996;198:149–69.
67. Liu C, Gazis D Surface roughness effect on dynamic response of pavements. J Transp Eng ASCE. 1999;July/Aug:332–7.
68. Sun L. A closed-form solution of a Bernoulli-Euler beam on a viscoelastic foundation under harmonic line loads. J Sound Vib. 2001;242(4):619–27.
69. Giuseppe M, Alessandro P. Response of beams resting on a viscoelastically damped foundation to moving oscillators. Int J Sol Struct. 2007;44:1317–36.
70. Deng XJ, Sun L. Study on the dynamics of a vehicle-ground pavement structure system. Beijing: China Communications Press; 2000.
71. Zhou HF, Jiang JQ, Zhang TQ. Steady-state response of an infinite beam on a Kelvin foundation under moving loads. J Zhejiang Univ. 2004;38(10):1328–33.
72. Zhou HF. Steady-state response of an infinite beam on a Kelvin foundation under moving loads[D]. J Zhejiang Univ (Eng Sci). 2005.
73. Lenci S, Tarantino AM. Chaotic dynamics of an elastic beam resting on a Winkler-type soil. Chaos, Solitons Fractals. 1996;7(10):1601–14.
74. Kargarnovin MH, Younesian D, Thompson DJ. Response of beams on nonlinear viscoelastic foundations to harmonic moving loads. Comp Struct. 2005;83:1865–77.
75. Santee DM, Gonçalves PB. Oscillations of a beam on a non-linear elastic foundation under periodic loads. Shock Vib. 2006;13(4–5):273–84.
76. Kang B, Tan CA. Nonlinear response of a beam under distributed moving contact load. Commun Nonlinear Sci Numer Simul. 2006;11:203–32.
77. Zhang NM, Yang GT. Chaotic belt phenomena in a nonlinear elastic beam. Appl Math Mech. 2003;24(5):450–4.
78. Zhang Y, Sheng DF, Cheng CJ. Dynamic behaviors of viscoelastic beams with damage under finite deformation. Chin Q Mech. 2004;25(2):230–8.
79. Fulton J, Sneddon IN. The dynamic stresses produced in a thick plate by the action of surface forces. Proceedings of the Glasgow Mathematical Association. 1958;3(4):153–163.
80. Morley LSD. Elastic plate with loads travelling at uniform velocity along the bounding surfaces. QUART J MECH APPL MATH , 1962; 15(2): 193–213.
81. Liu C, McCullough BF, Oey HS. Response of a rigid pavement to vehicle-road interaction. J Transp Eng, ASCE. 2000;May/June:237–42
82. Huang MH, Thambiratnam DP. Dynamic response of plates on an elastic foundation to moving loads. J Eng Mech. 2002;128(9):1016–22.
83. Kim SM, McCullough BF. Dynamic response of a plate on a viscous Winkler foundation to moving loads of varying amplitude. Eng Struct. 2003;25:1179–88.
84. Sun L. Dynamics of plate generated by moving harmonic loads. Trans ASME. 2005;72(Sep):772–7.

85. Wu JJ. Dynamic analysis of a rectangular plate under a moving line load using scale beams and scaling laws. Comp Struct. 2005;83:1646–58.
86. Cai YQ, Cao ZG, Sun HL, Xu CJ. Dynamic response of pavements on a poroelastic half-space soil medium to a moving traffic load. Comp Geotech. 2009;36:52–60.
87. Cheng XS. Dynamic response of plates on elastic foundations due to the moving loads. Appl Math Mech. 1987;8(4):3–10.
88. Zheng XP., Wang SW. Dynamic analysis of simply supported rectangular plates on an elastic foundation under moving loads. Acta Aeronaut Et Astronaut Sinica. 1989;10(10):557–60.
89. Yang FT, Yu Q. Study on the dynamic response of a roadway to a moving vehicle. Trans CSAE. 1996;12(2):49–53.
90. Zhou HF, Jiang JQ. Dynamic response of rigid pavements to moving vehicles. China Civ Eng J. 2006;39(8):
91. Jiang JQ, Zhou HF, Zhang TQ. Steady state response of an infinite plate on a viscoelastic foundation subjected to a moving load. China J Highw Transp. 2006;19(1):6–11.
92. Yan KZ. Study on the dynamic response of a thin plate on an elastic foundation[D]. Hangzhou: Zhejiang University; 2005.
93. Gajiendar N. Large amplitude vibrations of plates on an elastic foundation. Int J Nonlinear Mech. 1967;2(1):163–8.
94. Nath Y. Large amplitude response of a circular plate on an elastic foundation. Int J Nonlinear Mech. 1982;17(4):285–96.
95. Xiao YG, Fu YM, Zh XD. Bifurcation and chaos of rectangular moderately thick cracked plates on an elastic foundation subjected to periodic load. Chaos Solitons Fractals. 2008;35(3):460–65.
96. Qiu P, Wang XZ, Ye KY. Bifurcation and chaos of the circular plates on the nonlinear elastic foundation. Appl Math Mech. 2003;24(8):779–84.
97. Yang ZA, Zhao XJ, Xi XY. Effective calculation method of multi-components non-stationary stochastic seismic response. J Vib Shock. 2006;25(5):69–73.
98. Yang ZA, Fan J. Study on 1/3 subharmonic resonance and chaos of a rectangular thin plate with four sides free on the Winkler foundation. J Tangshan Coll. 2006;19(2):87–96.
99. Eason G, Fulton J, Sneddon IN. The generation of waves in an infinite elastic solid by variable body forces. Philosophical transactions of the Royal society of London. 1956, 248: 575–607.
100. De Barros FCP. Luco JE. Response of a layered viscoelastic half-space to a moving point load. Wave Motion. 1994;19:189–210.
101. Cao YM, Xia H, Lombaert G. Solution of moving-load-induced soil vibrations based on the Betti–Rayleigh Dynamic Reciprocal Theorem. Soil Dyn Earthq Eng. 2010;30:470–80.
102. Zhong Y, Sun L, Huang YG. The explicit solution of axisymmetric elastic-dynamic problem for multilayered halfspace. China J Highw Transp. 1998;11(2):24–9.
103. Li HZ. Study on the dynamic load, ruts and reasonable axle load of a vehicle-pavement system. Beijing: China Agricultural university Press; 1999.
104. Wu CP, Shen PA. Dynamic analysis of concrete pavements subjected to moving loads. J Transp Eng ASCE. (Sep/Oct) 1995;367–73.
105. Michael J, Markow J. Hedrick K, Bran D, Brademeyer. Analyzing the Interactions between Dynamic Vehicle Loads and Highway Pavement. Transp Res Rec. 1988;1196:161–169.
106. Zai. Zafur, Raj V Siddharthan, Peter, E. Sebaaly. Dynamic pavement strain histories from moving traffic load. J Transp Eng ASCE. 1994;120(5):821–42.
107. Siddharthan RV, Peter JY, Sebaaly E. Pavement Strain from Moving Dynamic 3D load Distribution. J Transp Eng ASCE. 1998;124(6):557–66.
108. Wang WJ, Kenis W, Liu C. Procedure for NAFTA Truck Overload Simulation. Applications of Advanced Technologies in Transportation Engineering. 2004:475–80.
109. Kim D, Salgado R, Altschaeffl AG. Effects of Super single Tire Loadings on Pavements. J Transp Eng ASCE. (Oct) 2005;732–43.
110. Metrikine AV, Verichev SN, Blaauwendraad J. Stability of a two-mass oscillator moving on a beam supported by a viscoelastic half-space. Int J Solid Struct. 2005;42:1187–207.

111. Jeongho O, Fernando EG, Lytton RL. Evaluation of damage potential for pavements due to overweight truck traffic. J transp Eng. (May) 2007;308–17.
112. Darestani MY, Thambiratnam DP, Nataatmadja A. Structural response of concrete pavements under moving truck loads. J transp Eng. (Dec.) 2007;670–6.
113. Asghar M, Stoner JW. Nonlinear pavement distress model using dynamic vehicle loads. J Infrastruct Syst. 1998;June:71–8.
114. Chen J. Basic research on the vehicle and the road surface interaction. Changchun: Jinlin University; 2002.
115. Hou Y, Sun SP, Guo ZY. Dynamic response sensitivity analysis of a plate on an elastic foundation subjected to moving point loads. J Tongji Univ. 2003;31(1):31–5.
116. Xie SY, Zheng CC. Effects of tire contact pressure on an asphalt pavement structure. J Chang'an Univ. 2004;24(3):12–6.
117. Liu DW, Chen J, Yan TY, et al. Stress characteristics of a half rigid road under dynamic load. J Qingdao Univ. 2006;21(2):59–63.
118. Guo KH. Tire roller contact model for simulation of vehicle vibration input. Soc Automot Eng. 1993;991:45–51 (SAE 932008).
119. Guo KH, Liu Q, Ding GF. Influences of loading and inflation pressure on tire enveloping properties. Trans CSAE. 1998;14(3):53–5.
120. Guo KH, Liu Q, Ding GF. Analysis of tire enveloping properties and its application in modeling of vehicle vibration systems. Automot Eng. 1999;21(2):65–80.
121. Huang XP, Lin MC, Zhao JH. Study of tire displacement enveloping characteristics and calculation method of effective road surface spectrum. Automot Eng. 1991;13(3):161–69.
122. Guan X, Dong B. An active suspension system with enveloping tire model. Automot Eng. 2003;25(4):356–9.
123. Yang SP, Li SH, Lu YJ. Dynamics of a vehicle-pavement coupled system based on a revised flexible roller contact tire model. Sci China, Ser E. 2009;52(3):721–30.
124. Fiala E. Seitenkrafte am rollenden luftreifen. ZVDI. 1954;29(11):81–92.
125. Gim G. Nikravesh PE. A three dimensional tire model for steady-state simulations of vehicles. SAE. 1993;102(2):150–9.
126. Pacejka HB, Sharp RS. Shear force development by pneumatic tyres in steady state conditions: a review of modelling aspects. Veh Syst Dyn. 1991;20(3/4):121–76.
127. Guo Konghui. Vehicle Handling Dynamics Theory [M]. Nanjing: Jiangsu Science and Technology Publishing House; 2011.
128. Shiotsuka T. Adaptive control of a 4WS system by using a neural network. Veh Syst Dyn. 1993;22(5/6):411–24
129. Palkovics L, El-Gindy M. Neural network representation of tire characteristics: the neurotyre. Veh Des. 1993;14(5/6):563–91.
130. Ren WQ, Huang MH, Jing GD. Vehicle handling and stability simulation with an artificial neural networks tire model. Comp Simul. 2000;17(2):46–9.
131. Cui SM, Wang F. Tire cornering characteristics model based on an artificial neural network. Tire Ind. 2000;20(1):11–4.
132. Guan DH, Wu WD. Experimental modal analysis of tire dynamics. Automot Eng. 1995;17(6):328–33.
133. Rao KVN, Kumar RK. Simulation of tire dynamic behavior using various finite element techniques. Comp Methods Eng Sci Mech. 2007;8(5):363–72.
134. Gall R, Tkacik P. On the incorporation of frictional effects on the tire/ground contact area. Tire Sci Technol. 1993;21(1):2–22.
135. Mousseau CW. An analytical and experimental study of a tire rolling over a stepped obstacle at low velocity. Tire Sci Technol. 1994;22(3):162–81.
136. Liang B, Cai Y, Zhu DS. Dynamic analysis on a vehicle-subgrade model of a vertical coupled system. J China Railw Soc. 2000;22(5):65–71.
137. Chen G, Zhai WM, Zuo HF. Vertical lateral model of a vehicle-track coupling system and its verification. J Vib Shock. 2001;20(4):16–21.

138. Wang KY, Zhai WM, Cai CB. The model of locomotive-track spatially coupled dynamics and its verification. J China Railw Soc. 2002;21(4):21–7.
139. Zhai WM. Vehicle-track coupling dynamics. Beijing: China Railway Publishing House; 2002.
140. Xia H, Chen YJ. Analysis of the lateral dynamic interaction in a vehicle-girder-pier system. China Civ Eng J. 1992;25(2):3–12.
141. Xia H. Dynamic interaction of vehicle and structure. Beijing: Science Press; 2002
142. Law SS, Zhu XQ. Bridge dynamic responses due to road surface roughness and braking of a vehicle. J Sound Vib. 2005;282;805–30.
143. Yang YB, Lin CW. Vehicle-bridge interaction dynamics and potential applications. J Sound Vib. 2005;284:205–26.
144. Wang JJ, Zhang W, Wu WX Analysis of dynamic responses of a simply supported girder bridge under heavy moving vehicles. Cent south highw eng. 2005;30(2):55–7.
145. Sheng GG, Li CX, Zhao B. Dynamic analysis of a simply-supported beam subjected to moving vehicles. Eng Mech. 2006;23(12):154–8.
146. Li SH, Yang SP. Investigation of the interaction between a vehicle and the road using the second road excitation on the vehicle. Proc Inst Mech Eng, Part D: J Automob Eng. 2009; 223(7):855–63.
147. Yang SP, Li SH, Lu YJ. Investigation of the dynamic interaction between a heavy vehicle and road pavement. Veh Syst Dyn. 2010;48(8):923–44.
148. Ding H, Chen LQ, Yang SP. Convergence of Galerkin truncation for dynamic response of finite beams on nonlinear foundations under a moving load. J Sound Vib. doi:10.1016/j.jsv.2011.12.036.
149. Li SH, Yang SP, Chen LQ. Effects of parameters on dynamic responses for a heavy vehicle-pavement-foundation coupled system. Int J Heavy Veh Syst. 2012;19(2):207–24.

Chapter 2
Dynamic Analysis of a Heavy Vehicle Using Lumped Parameter Model

The interaction between a vehicle and the road is a very complicated dynamic process, which involves many fields such as vehicle dynamics, pavement dynamics, and tribology. From the aspect of dynamics, the dynamic process between the vehicle and the road can be briefly summarized as follows: (1) when a vehicle is moving on the road surface, the random vibration excited by the uneven road profile is transferred to the vehicle body through the tires and the suspension. (2) The vehicle body vibration is transferred to the road surface through the suspension as well as the tires. The repeated dynamic contact stresses (vertical and lateral) caused by the vehicle load may result in accumulative deformation of the road profile. (3) The changed road profile excites a new round of vibration on the vehicle once again. It is widely believed that contact stress is the main reason for road damage, especially for cracking and rutting. It should be noted that the tire and the suspension are two core transmission parts that define the relationship between the pavement and the vehicle. In this chapter, the damping of the shock absorber and the stiffness of the leaf spring are first obtained in a laboratory experiment. Through experimental data fitting and parameter identification, the nonlinear models for the shock absorbers and the leaf spring are established. Then the lumped parameter models of two-axle and three-axle vehicle systems are established and the dynamic responses are analyzed in detail.

2.1 Experimental Modeling for the Nonlinear Components in Vehicle Suspension

The shock absorber and the leaf springs are both key components of a heavy vehicle suspension. The damping and stiffness characteristics have an important influence on vehicle ride comfort and road friendliness. These parts are usually simplified as a linear model for the sake of convenience of calculation. However, the linear model cannot reflect their nonlinear characteristics and thus the vehicle vibration responses are distorted. So it is necessary to establish nonlinear models for the shock absorber and the leaf spring through experiments.

S. Yang et al., *Dynamics of Vehicle-Road Coupled System,*
DOI 10.1007/978-3-662-45957-7_2

2.1.1 Experimental Damping Characteristics of the Shock Absorber

1. *Theoretical basis and experimental purpose*

The relation of damping force to piston relative velocity can elucidate the damping characteristics of a shock absorber. Furthermore, the relationship between damping force and velocity is nonlinear due to the shock absorber's structural feature of a throttle valve and its working principle. The working principle of the hydraulic shock absorber can be briefly summarized [1] as follows: When a piston is moving back and forth in the cylinder tube, oil in the shell of the shock absorber repeatedly flows from one cavity into the other cavity through some narrow gaps. As a result, a damping force is produced because of the friction among the oil molecules. In theory, a greater damping force attenuates the vehicle suspension vibration faster. However, the damping force is always larger in the tension stage than in the compression stage. The purpose of setting the throttle valve is to make the shock absorber improve vehicle dynamic behaviors. A bidirectional hydraulic shock absorber is studied in this chapter, which could attenuate the vibration in the tension and compression stages and reflects the nonlinear hysteretic characteristics. The shock absorber is a typical nonlinear system and the modeling of its damping force has become a research highlight [2]. Nonlinear modeling methods consist of: parametric models and nonparametric models. Parametric models account for the shock absorber's internal fluid flow and the real structure of throttle, while nonparametric models are mainly based on actual measurements, ignoring its internal structure [3].

At present there are many mathematical models to describe the damping characteristics of a shock absorber. A complex nonlinear shock-absorber model was proposed by Segel [4] and Lang [5], which includes 83 parameters depending on physical features. Although Lang's model is good at describing the distortion problem during high frequency, it has some limitations in practical applications due to many parameters [6, 7]. Karadayi established a simpler and clearer model for describing the hysteresis characteristics of a shock absorber, but it is only suitable for low-frequency working conditions. Besinger and Cole proposed a nonlinear model including seven parameters [8]. They applied the Besinger model to a heavy-duty vehicle suspension shock absorber, and its simulation results are in accordance with experiments when the frequency is less than 10 Hz and the speed is less than 1 m/s [9, 10].

The shock absorber has asymmetrical and hysteretic damping characteristics. Mathematical models for symmetrical hysteresis include the bilinear model and differential hysteresis (such as Bouc–Wen) model. These models are based on the assumption of symmetry, which is not suitable for describing the behavior of the hysteretic system.

In this section, the damping characteristics of the shock absorber are first measured, and the least squares method (LMS) is used to identify the relevant parameters in order to establish a nonlinear, asymmetrical model for the shock absorber.

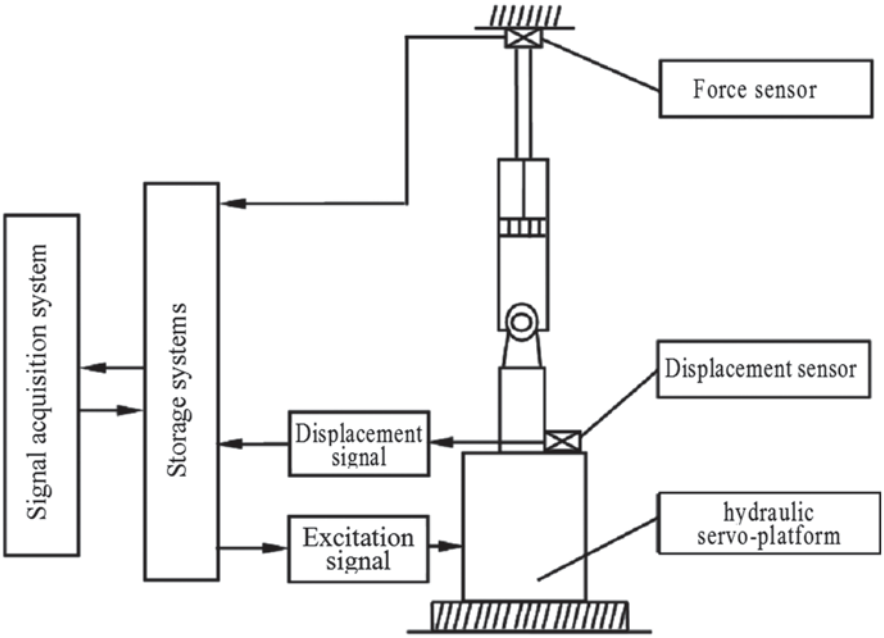

Fig. 2.1 Test principle schematics of a shock absorber. (Reprinted from ref. [11], Copyright 2013, with kind permission from Maxwell Scientific organization)

2. *Testing system and scheme*

In this section, a dynamic material testing system (Hongda HT-911) is chosen to test the damping characteristics of the shock absorber. The principle of the test system is shown in Fig. 2.1 [11].

The test system includes a servo control system, a signal acquisition system, a function generator, a security monitoring system, a digital A/D interface system, a servo-valve driver, and a twin-tube hydraulic shock absorber.

The key specifications of this testing machine are: static and dynamic load rating: 500 – 50,000 kN, actuator nominal displacement range: 0–25 mm, frequency range: 0.05–50 Hz.

The specific testing scheme is designed as follows:

1. Clamping the shock absorber

The lower end of the shock absorber is vertically fixed to the hydraulic servo-platform and the upper end is fastened to a rigid beam equipped with a force sensor. The shock absorber is adjusted along the vertical direction to ensure that the piston does not produce eccentric wear during the loading process. The initial position of the servo-console is also adjusted to ensure that the piston is located in the middle of the effective stroke.

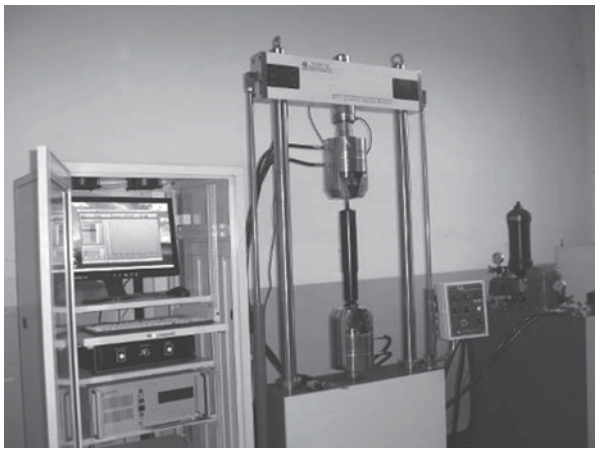

Fig. 2.2 Experimental setup for testing shock absorber. (Reprinted from ref. [11], Copyright 2013, with kind permission from Maxwell Scientific organization)

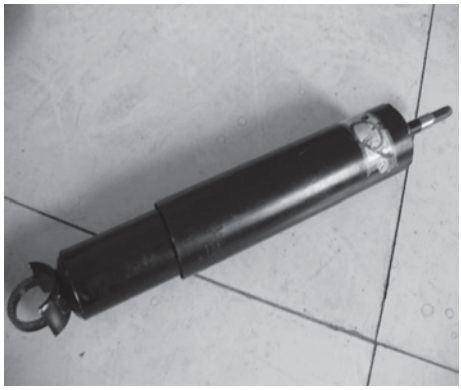

Fig. 2.3 Shock absorber. (Reprinted from ref. [11], Copyright 2013, with kind permission from Maxwell Scientific organization)

2. Loading the shock absorber

The excitation frequency, amplitude and sampling frequency are all input into the computer. A sinusoidal driving signal is produced through a function generator. The signal is amplified by the digital A/D interface to make the servo platform excite the shock absorber with the pre-input frequency and amplitude.

3. Collecting the data

Because the applied driving excitation is a displacement of the shock-absorber piston, the displacement signal can be directly obtained as the pre-input signal. And the damping force can be recorded through the force sensor on the rigid beam.

The test object is a shock absorber in front suspension of the heavy-duty truck DFL1250A9 manufactured by Dongfeng Motor Corporation Ltd, China. Photographs of the testing setup and the shock absorber are shown in Figs. 2.2 and 2.3 respectively.

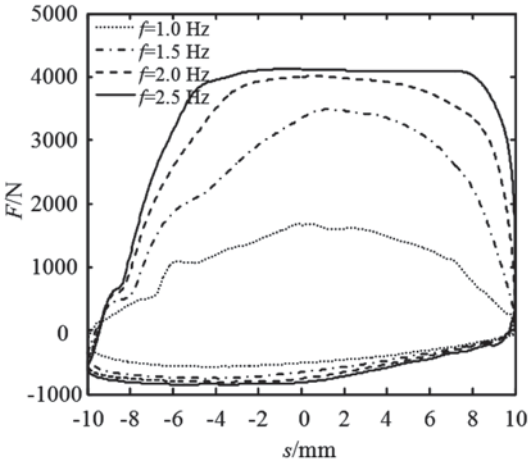

Fig. 2.4 Force–displacement curves for different frequencies. (Reprinted from ref. [11], Copyright 2013, with kind permission from Maxwell Scientific organization)

3. *Testing results for damping characteristics*

To obtain the nonlinear damping characteristics of a shock absorber, it is necessary to do some excitation tests at different excitation frequencies and different amplitudes. The steady-state excitation on the shock absorber is made according to the standard QC/T 545-1999. The excitation frequencies were chosen as 1.0, 1.5, 2.0, 2.5 Hz, and the excitation amplitudes of the piston were chosen as 5, 10, 15, 20 mm.

Because the shock absorber is excited by a sinusoidal displacement, the piston motion is given as

$$S = S_0 \sin(2\pi\omega t) \tag{2.1}$$

Where S_0 is the amplitude of the piston movement and ω is the angular frequency of the displacement. The relative velocity between the piston and the cylinder tube can be deduced as

$$V = 2\pi\omega S_0 \cos(2\pi\omega t) \tag{2.2}$$

Through a series of experiments, the damping characteristic curves of the shock absorber are measured. Then the force–displacement curves for different excitation frequencies and amplitudes are shown in Figs. 2.4 and 2.5, respectively.

From Figs. 2.4 and 2.5, it can be observed that the area of the curves gradually increases with the increasing excitation frequency at the same excitation amplitude. The reason is that the higher external excitation frequency results in a larger damping force and dissipated energy. In addition, the damping force–velocity curves of the shock absorber were also obtained under different frequencies and amplitudes, shown as Figs. 2.6 and 2.7.

Figures 2.6 and 2.7 show that the curves present obvious nonlinear characteristics during both the tension and the compression stages. Furthermore, there also exists a hysteresis phenomenon.

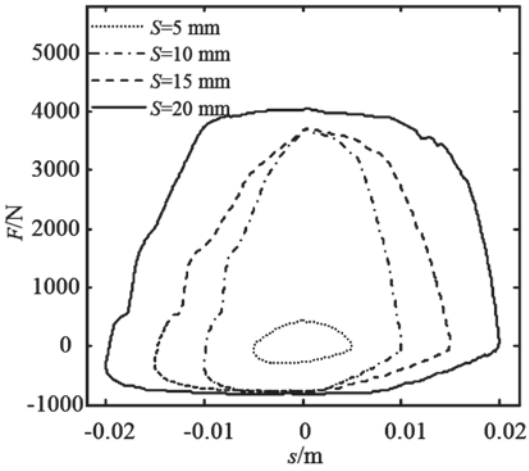

Fig. 2.5 Force–displacement curve for different amplitudes. (Reprinted from ref. [11], Copyright 2013, with kind permission from Maxwell Scientific organization)

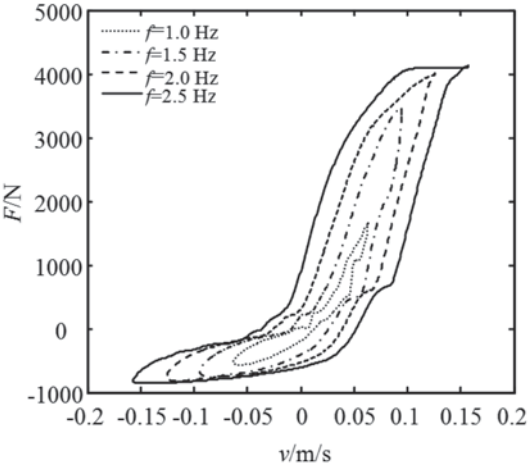

Fig. 2.6 Force–velocity curve for different frequencies. (Reprinted from ref. [11], Copyright 2013, with kind permission from Maxwell Scientific organization)

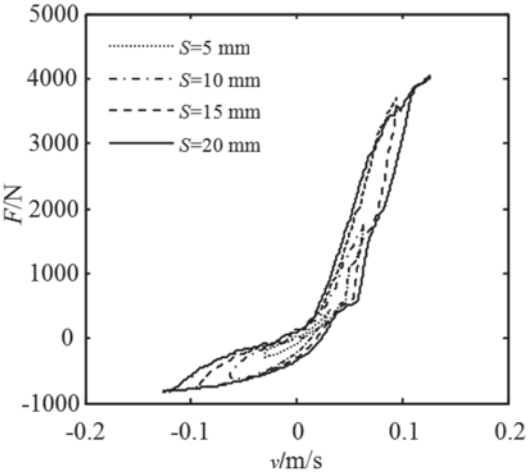

Fig. 2.7 Force–velocity curve for different amplitudes. (Reprinted from ref. [11], Copyright 2013, with kind permission from Maxwell Scientific organization)

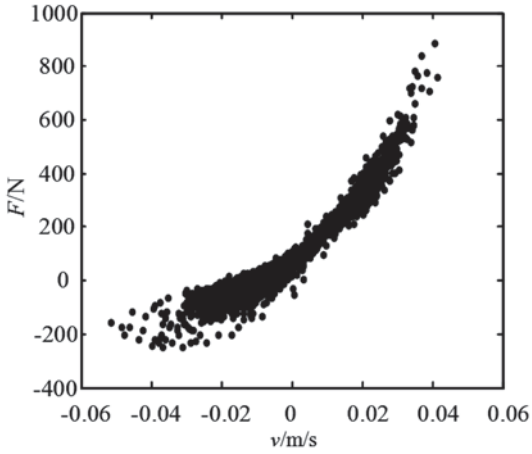

Fig. 2.8 Force–velocity curve for random excitation. (Reprinted from ref. [11], Copyright 2013, with kind permission from Maxwell Scientific organization)

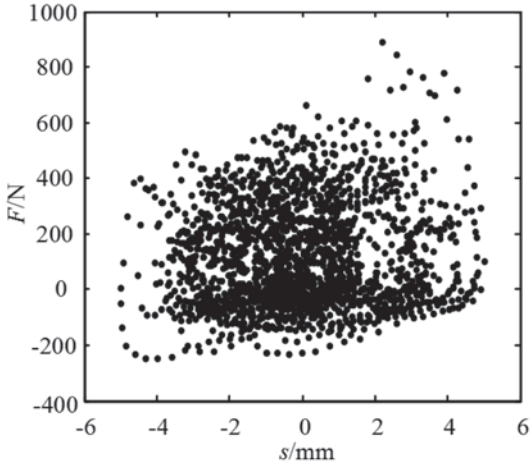

Fig. 2.9 Force–displacement curve for random excitation. (Reprinted from ref. [11], Copyright 2013, with kind permission from Maxwell Scientific organization)

In order to further simulate the actual vibration of a heavy vehicle travelling on an uneven road, a random excitation test is also performed for the shock absorber. Figures 2.8 and 2.9 show the damping characteristics of the shock absorber under random excitation.

Some conclusions can be drawn from Figs. 2.8 and 2.9 as follows:

1. The points feature is an uneven distribution under random excitation but these points are basically located within a region of −6 to 6 mm amplitude and −0.06 to 0.06 m/s velocity.
2. The force–displacement curve presents a “Hamburger” shape and the left and right sides are not completely symmetrical. The damping characteristics curve presents a “Banana” shape. These results once again prove that the shock absorber has indeed features of nonlinearity and asymmetry.

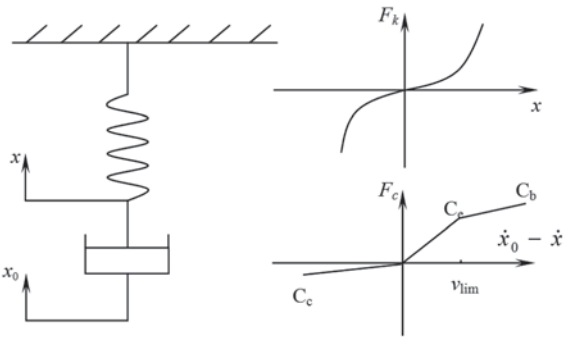

Fig. 2.10 The Besinger model of a shock absorber

4. *Modeling of the shock absorber*

Experimental research is only the beginning in the understanding of the shock absorber's characteristics. Parameter identification should be done to complete the vehicle dynamics research. There are two ways to accomplish system parameter identification: in the time domain and in the frequency domain. The LSM was first proposed by Gauss in 1795, and is a basic and effective method to apply identification theory to a static or dynamic, linear or nonlinear system. Thus the LSM is utilized to identify the shock absorber parameters based on experimental data. In this section, the Besinger model is chosen for the identification of the damping force. A nonlinear springs and a damper are cascaded together in this model, as shown in Fig. 2.10. The model has three features: a nonlinear relationship between the tension and compression stages, a hysteresis loop, and saturation in the tension stage at high speeds.

According to the model in Fig. 2.10, the spring force can be written as

$$F_k = k_1 x + k_2 x^3 \tag{2.3}$$

where k_1 and k_2 are the coefficients of the spring stiffness. The damping force is defined as

$$F_c = \begin{cases} C(v)v & v < v_{\lim} \\ C_e v_{\lim} + C_b(v - v_{\lim}) & v \geq v_{\lim} \end{cases} \tag{2.4}$$

where $C(v) = \dfrac{c_1(v-\alpha)}{\alpha\sqrt{1+\left(\dfrac{v-\alpha}{\alpha}\right)^2}} + c_2$ is a function of v, the piston velocity relative to the cylinder tube, and

$$c_1 = (C_e - C_c)/2\,, \quad c_2 = (C_e - C_c)/2$$

where C_b is the damping coefficient of the shock absorber at the high-speed stage of the tension stage;

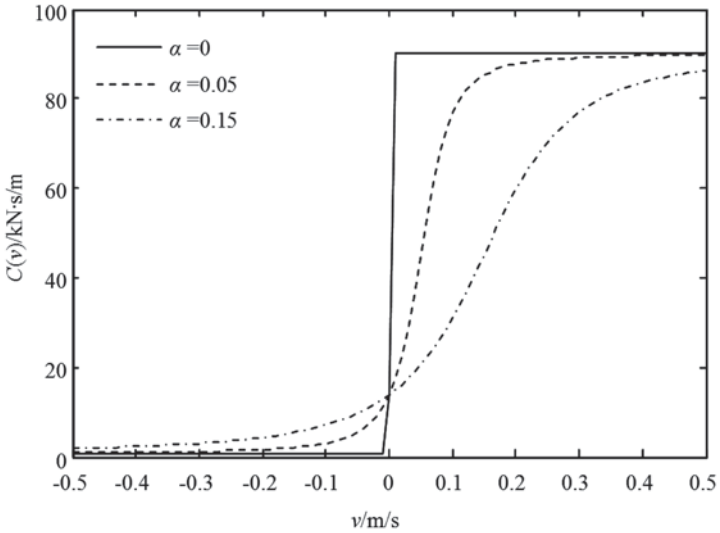

Fig. 2.11 Curve of the damping function C(v). (Reprinted from ref. [11], Copyright 2013, with kind permission from Maxwell Scientific organization)

C_e is the damping coefficient of the shock absorber at the low-speed stage of the tension stroke;

C_c is the damping coefficient of the shock absorber in the compression stage;

v_{lim} is the transition speed between the high- and low-speed stages during the tensile stroke;

α is the transition parameter between the compressive and tensile damping forces.

Figure 2.11 illustrates the trend of C(v) with the relative velocity and the transition parameter.

Combining (2.3) with (2.4), the first-order differential expression of the shock absorber damping force is

$$\dot{x} = \begin{cases} \dfrac{k_1 x + k_2 x^3}{C(v)} + \dot{x}_0 & v < v_{\text{lim}} \\ \dfrac{k_1 x + k_2 x^3}{C_b} + \dfrac{C_e - C_b}{C_b} v_{\text{lim}} + \dot{x}_0 & v \geq v_{\text{lim}} \end{cases} \tag{2.5}$$

5. *Parameter identification of the shock absorber*

According to the Besinger model, when the relative velocity of the piston is relatively low, there is a nonlinear relationship between the damping force and the relative velocity. When the relative velocity of the piston exceeds v_{lim}, there is a piecewise relationship between the damping force and the relative velocity. The Besinger model includes the seven parameters C_c, C_e, C_b, v_{lim}, α, k_1, and k_2.

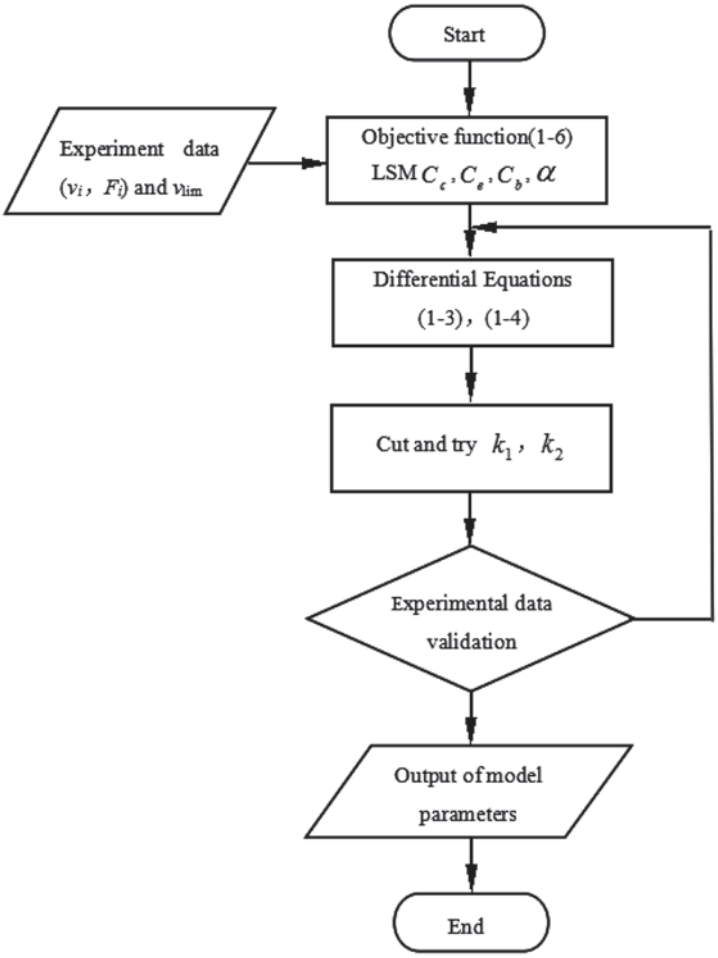

Fig. 2.12 Parameter identification flowchart of the shock absorber. (Reprinted from ref. [11], Copyright 2013, with kind permission from Maxwell Scientific organization)

In order to identify these model parameters from the experimental data, a parameter identification process is designed as Fig. 2.12. For the C_c, C_e, C_b, α parameters of Besinger, the objective function can be defined as

$$J=\begin{cases}\left\{\dfrac{1}{2}\sum\limits_{i-1}^{N}\left[F_i-\dfrac{c_1\left(v_i-\alpha\right)}{\alpha\sqrt{1+\left(\dfrac{v_i-\alpha}{\alpha}\right)^2}}v_i-c_2v_i\right]^2\right. \rightarrow \min & v_i<v_{\lim}\\ \dfrac{1}{2}\sum\limits_{i-1}^{N}\left[F_i-C_ev_{\lim}-C_b(v_i-v_{\lim})\right]^2\rightarrow\min & v_i\geq v_{\lim}\end{cases} \tag{2.6}$$

where F_i and v_i are the shock absorber's damping force and the piston's relative velocity obtained from the experimental data, N are the sampling points, and $v_{\lim}$ can be directly estimated from the experimental results. Combining with Eqs. (2.3) and (2.4), one can determine k_1 and k_2 by the cut-and-try method.

Based on the testing data (frequency 2 Hz, amplitude 10 mm), the LMS method is utilized to identify the damping parameters of the shock absorber. The specific damping coefficients are: $C_c = 5630Ns/m$, $C_e = 31523Ns/m$, $C_b = 2500Ns/m$, $v_{\lim} = 0.123m/s$, $\alpha = 0.0195m/s$, $k_1 = 150N/mm$, and $k_2 = 0.12N/mm^3$.

2.1.2 Experimental Stiffness Characteristics of the Leaf Springs

The stiffness characteristic caused by the vertical deformation of the leaf spring directly affects vehicle ride comfort, integrity of goods and dynamic tire force. Since 2005, due to the continuous development of the domestic automobile industry and transport industry, the demand for large-tonnage heavy commercial vehicles has gradually increased. As an important component part, the leaf spring of a heavy vehicle suspension continues to increase in demand. The demand for heavy leaf springs was about 16 million ton at the end of 2006 and 36 million ton by 2008, which accounted for more than 35% of the total demand for commercial vehicle leaf springs in China. For convenience, the leaf spring is usually simplified to a linear model, generating results that cannot reflect its nonlinear characteristics. Thus, analysis of the vehicle vibration response may be distorted based on a linear model. So it is necessary to establish a nonlinear model for the leaf spring through experiments. The experimental and theoretical study of the leaf spring has had a great significance to improving heavy-vehicle ride comfort.

1. *Theoretical basis and experimental purposes*

There are many nonlinear factors during the leaf spring's actual operation, such as large deformation, contact between leafs and so on. These factors lead to energy loss in the leaf spring and show nonlinear-hysteresis characteristics under dynamic loading. The hysteresis characteristics have an influence on vehicle ride comfort and road friendliness. In recent decades, many scholars have proposed nonlinear mechanical models for the leaf spring. In the initial study, the hysteresis characteristics of the leaf spring are simplified as a parallel linear model. This model is very simple and clear, and it is able to reflect the leaf spring's locking phenomenon. However, Caughey pointed out that this model has poor accuracy. In 1970s, a modified dual linear model formed by a set of parallel linear springs and dampers was proposed [12]. Fancher proposed an index-difference model of the leaf spring, which can more accurately reflect the transient vibration characteristics and hysteresis characteristics of the leaf spring [13]. In recent years, the finite element (FE) method has been widely applied in research on leaf-spring equivalent damping and hysteresis characteristics [14–16].

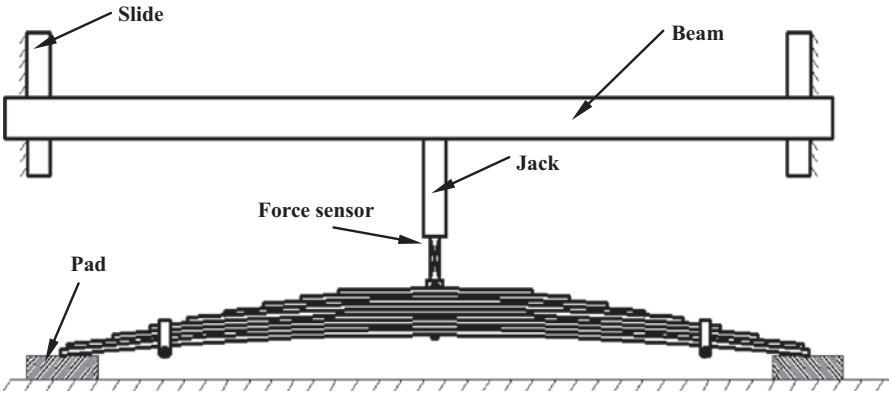

Fig. 2.13 Test principle schematics of a leaf spring

2. *Testing system and scheme*

The leaf spring of a heavy vehicle in this experiment has nine leaves with equal widths as well as thicknesses. The material is steel (60SiMn). The basic geometrical length of each piece ranges from 1600 to 280 mm (1600, 1600, 1412, 1222, 1034, 846, 656, 468, 280 mm). The width and the thickness of each spring are 90 and 25 mm, respectively. The total height of the spring is 220 mm, including 30 mm arc height. The experimental setup includes: a jack (type: YDC240QX-200), a string pressure gauge (type: JM2X-3102), a digital displacement sensor (type: DA-10), and an integrated testing instrument (type: JMZX-300X). The test system is shown in Fig. 2.13.

The specific testing program of the leaf spring stiffness characteristics is as follows:

1. Installation of the leaf spring

Some grease between the spring leaves is spread to reduce the frictional contact resistance. In the experiment, the leaf spring is installed according to the location on the heavy vehicle and is loaded with a jack at the top of the leaf spring. Two pads are used to support the two ends of the spring and the spring can slide along the longitudinal direction.

2. Loading the leaf spring

According to the vehicle leaf spring performance requirements, a 14.4 kN preload on the leaf spring is first loaded. Then the leaf spring is loaded and unloaded gradually along the central vertical direction.

3. Data acquisition

The load and the deformation of the leaf spring are recorded using the pressure gauge and displacement sensors, respectively.

The testing setup and photograph of the leaf spring are shown in Figs. 2.14 and 2.15, respectively.

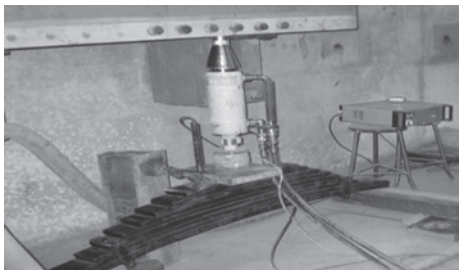

Fig. 2.14 Experimental setup for testing a leaf spring

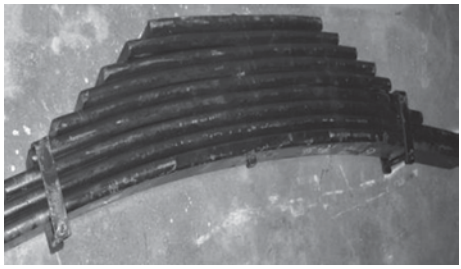

Fig. 2.15 Leaf spring

3. *Analysis of the experimental results*

The results of the loading and unloading experiments of the leaf spring are shown in Table 2.1, which includes 12 experimental variations to determine the stiffness characteristics. The test curve is also shown as solid line in Fig. 2.17. It is clear that when the leaf spring is loaded and unloaded, the envelope curves of the leaf-spring stiffness characteristics basically formed two straight lines with different slopes, showing the hysteretic characteristic.

4. *Modeling for a nonlinear leaf spring*

In order to reflect the actual nonlinear hysteretic characteristic of the leaf spring, the Fancher difference model mentioned previously is chosen to describe the stiffness of the leaf spring. The schematic diagram of the model is showed in Fig. 2.16.

Table 2.1 Experimental results of a leaf spring

Test number	Load/kN	Displacement (loading)/mm	Displacement (unloading)/mm
1	29.5	−12.52	−10.306
2	40.9	−6.914	−2.521
3	43.8	−5.577	−0.931
4	56.5	0.417	4.126
5	64.1	4.040	10.849
6	85.1	14.519	17.799

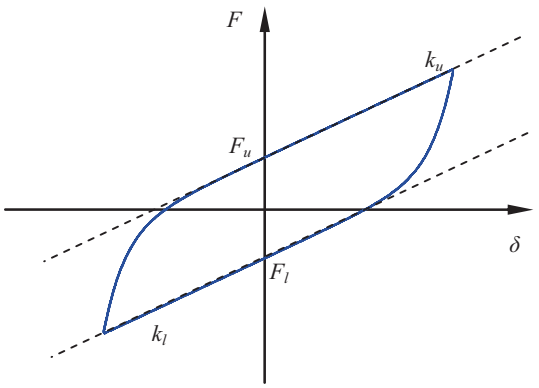

Fig. 2.16 Fancher leaf spring model

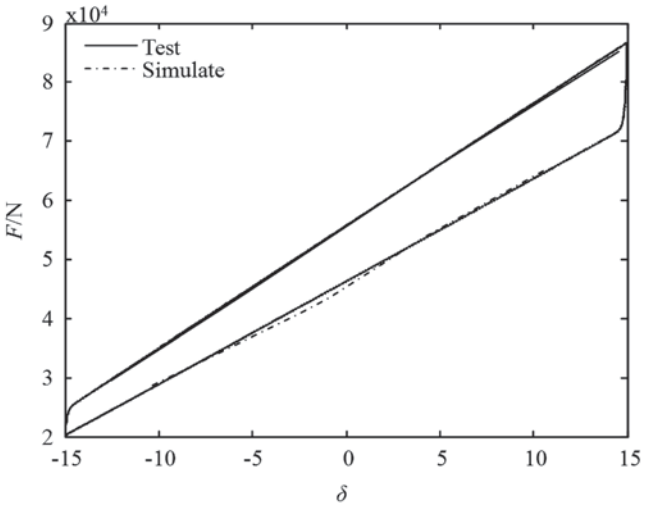

Fig. 2.17 Stiffness comparison chart between test and simulation

In the Fancher model, the restoring force of the spring during the loading process is written as

$$\begin{cases} \dfrac{dF_u(\delta)}{d\delta} = \dfrac{\left[F_{envu} - F_u(\delta)\right]}{\beta} \\ F_{envu} = k_u\delta + F_u \end{cases} \tag{2.7}$$

The restoring force of the leaf spring during the unloading process is

$$\begin{cases} \dfrac{dF_l(\delta)}{d\delta} = \dfrac{F_{envl} - F_l(\delta)}{\beta} \\ F_{envl} = k_l\delta + F \end{cases} \tag{2.8}$$

where δ is the vertical displacement of leaf spring, F_u and F_l are the restoring force of loading and unloading, F_{envu} and F_{envl} are the envelop forces of loading and unloading, k_u and k_l are the stiffnesses of loading and unloading, and β_u is the attenuation coefficient.

The restoring forces of the leaf spring model can also be obtained using the following iterative formula:

$$F_i = F_{envi} + (F_{i-1} - F_{envi})e^{-|\delta_i - \delta_{i-1}|/\beta} \tag{2.9}$$

5. *Parameter identification of the leaf spring stiffness*

LSM is a basic estimation method, which can be applied not only to a static system but also to a dynamic system, not only to a linear system but also to a nonlinear system, not only to an on-line system but also to an off-line system. Therefore, the identification based on the test data of the leaf spring is conducted with the LSM for our test data. After the parameter identification, the model parameters are obtained. $k_u = 2064995\ N/m$, $k_l = 1768096\ N/m$, $F_u = 55394N$, $F_l = 45989N$, $\beta = 0.1\times10^{-3}m$. Comparing the actual test results with the fitted model, the maximum of the error is 2.9%, shown in Fig. 2.17.

2.2 Dynamic Analysis of a Two-Axle Heavy Vehicle

2.2.1 Vehicle Model and Differential Equations of Motion

A vehicle is a complex vibration system. It is rather difficult to establish a complete model to reflect the overall vehicle vibration characteristics. When the mathematical model for analysis is established, the vibration system must be appropriately simplified according to the research objective. A simple "whole-vehicle" model is shown in Fig. 2.18. It is three dimensional, with 8 degrees of freedom.

The symbols in Fig. 2.18 are listed as: m_c —operator and seat mass, z_c —vertical displacement of operator's seat, m_b —vehicle body, z_b —vertical displacement of center of vehicle body; I_θ —pitch moment inertia of vehicle body, θ —pitch angle of vehicle body, I_ϕ —roll moment inertia of vehicle body, ϕ —roll angle of vehicle body, m_{ti} —tire mass($i = 1,2,3,4$), z_{ti} —vertical displacement of tire, q_i —road roughness displacement inputs to the four tires, k_{si} —suspension stiffness, c_{si} —suspension damping, k_{ti} —tire stiffness, c_{ti} —tire damping, k_c —seat spring stiffness, c_c —seat spring damping, d_f —half of front axle spacing, d_r —half of rear axle spacing, l_1 —spacing between the center of vehicle body and front axle, l_2 —spacing between center of vehicle body and rear axle, l_x —longitudinal spacing between center of vehicle body and seat, l_y —transverse spacing between center of vehicle body and seat.

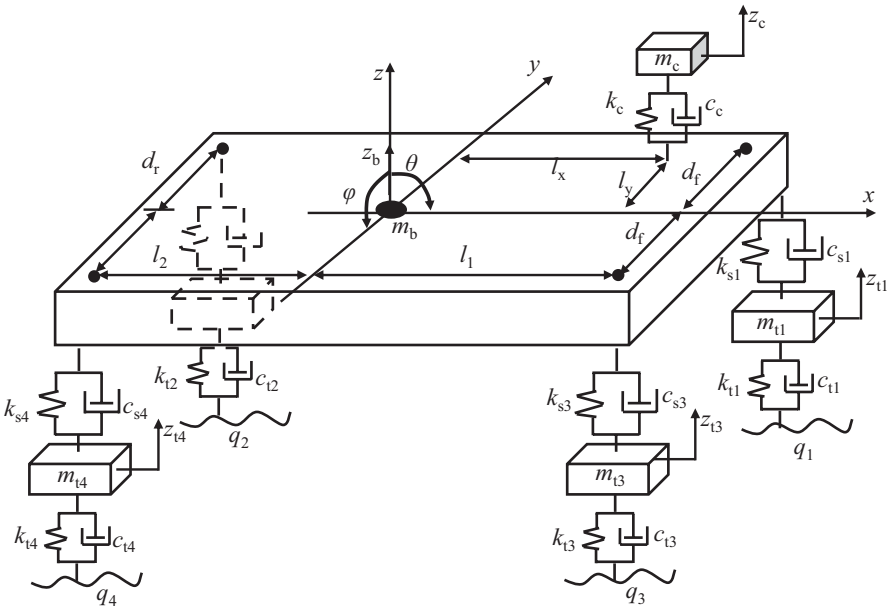

Fig. 2.18 Three-dimensional vehicle model with 8 degrees of freedom

The governing equations of this whole-vehicle model can be derived from the Lagrange equation.

Differential equation of vertical motion of seat

$$m_c\ddot{z}_c - k_c(z_b - l_x\theta + l_y\phi - z_c) - c_c(\dot{z}_b - l_x\dot{\theta} + l_y\dot{\phi} - \dot{z}_c) = 0 \tag{2.10}$$

Differential equation of vertical motion of vehicle body

$$\begin{aligned} &m_b\ddot{z}_b + c_{s1}(\dot{z}_b - l_1\dot{\theta} + d_f\dot{\phi} - \dot{z}_{t1}) + k_{s1}(z_b - l_1\theta + d_f\phi - z_{t1}) \\ &\quad + c_{s2}(\dot{z}_b - l_2\dot{\theta} + d_r\dot{\phi} - \dot{z}_{t2}) + k_{s2}(z_b - l_2\theta + d_r\phi - z_{t2}) \\ &\quad + c_{s3}(\dot{z}_b - l_1\dot{\theta} + d_f\dot{\phi} - \dot{z}_{t3}) + k_{s3}(\dot{z}_b - l_1\theta + d_f\phi - z_{t3}) \\ &\quad + c_{s4}(\dot{z}_b - l_2\dot{\theta} + d_r\dot{\phi} - \dot{z}_{t4}) + k_{s4}(\dot{z}_b - l_2\theta + d_r\phi - z_{t4}) \\ &\quad + c_c(\dot{z}_b - l_x\dot{\theta} + l_y\dot{\phi} - \dot{z}_c) + k_c(z_b - l_x\theta + l_y\phi - z_c) = 0 \end{aligned} \tag{2.11}$$

Differential equation of pitch motion of vehicle body

$$\begin{aligned} &I_\theta\ddot{\theta} - l_1c_{s1}(\dot{z}_b - l_1\dot{\theta} + d_f\dot{\phi} - \dot{z}_{t1}) - l_1k_{s1}(z_b - l_1\theta + d_f\phi - z_{t1}) \\ &\quad + l_2c_{s2}(\dot{z}_b - l_2\dot{\theta} + d_r\dot{\phi} - \dot{z}_{t2}) - l_2k_{s2}(z_b - l_2\theta + d_r\phi - z_{t2}) \\ &\quad - l_1c_{s3}(\dot{z}_b - l_1\dot{\theta} + d_f\dot{\phi} - \dot{z}_{t3}) - l_1k_{s3}(z_b - l_1\theta + d_f\phi - z_{t3}) \\ &\quad + l_2c_{s4}(\dot{z}_b - l_2\dot{\theta} + d_r\dot{\phi} - \dot{z}_{t4}) - l_2k_{s4}(z_b - l_2\theta + d_r\phi - z_{t4}) \\ &\quad - l_xc_c(\dot{z}_b - l_x\dot{\theta} + l_y\dot{\phi} - \dot{z}_c) - l_xk_c(z_b - l_x\theta + l_y\phi - z_c) = 0 \end{aligned} \tag{2.12}$$

Differential equation of roll motion of vehicle body

$$\begin{aligned} &I_\phi\ddot{\phi} + d_f c_{s1}(\dot{z}_b - l_1\dot{\theta} + d_f\dot{\phi} - \dot{z}_{t1}) + d_f k_{s1}(z_b - l_1\theta + d_f\phi - z_{t1}) \\ &+ d_r c_{s2}(\dot{z}_b - l_2\dot{\theta} + d_r\dot{\phi} - \dot{z}_{t2}) + d_r k_{s2}(z_b - l_2\theta + d_r\phi - z_{t2}) \\ &- d_f c_{s3}(\dot{z}_b - l_1\dot{\theta} + d_f\dot{\phi} - \dot{z}_{t3}) + d_f k_{s3}(z_b - l_1\theta + d_f\phi - z_{t3}) \\ &- d_r c_{s4}(\dot{z}_b - l_2\dot{\theta} + d_r\dot{\phi} - \dot{z}_{t4}) + d_r k_{s4}(z_b - l_2\theta + d_r\phi - z_{t4}) \\ &+ l_y c_c(\dot{z}_b - l_x\dot{\theta} + d_f\dot{\phi} - \dot{z}_{t1}) + l_y k_c(z_b - l_x\theta + l_y\phi - z_c) = 0 \end{aligned} \tag{2.13}$$

Differential equation of vertical motion of left-side front tire

$$\begin{aligned} &m_{t1}\ddot{z}_{t1} - c_{s1}(\dot{z}_b - l_1\dot{\theta} + d_f\dot{\phi} - \dot{z}_{t1}) - k_{s1}(z_b - l_1\theta + d_f\phi - z_{t1}) \\ &+ c_{t1}\dot{z}_{t1} + k_{t1}z_{t1} = c_{t1}\dot{q}_1 + k_{t1}q_1 \end{aligned} \tag{2.14}$$

Differential equation of vertical motion of left-side rear tire

$$\begin{aligned} &m_{t2}\ddot{z}_{t2} - c_{s2}(\dot{z}_b - l_2\dot{\theta} + d_r\dot{\phi} - \dot{z}_{t2}) - k_{s2}(z_b - l_2\theta + d_r\phi - z_{t2}) \\ &+ c_{t2}\dot{z}_{t2} + k_{t2}z_{t2} = c_{t2}\dot{q}_2 + k_{t2}q_2 \end{aligned} \tag{2.15}$$

Differential equation of vertical motion of right-side front tire

$$\begin{aligned} &m_{t3}\ddot{z}_{t3} - c_{s3}(\dot{z}_b - l_1\dot{\theta} + d_f\dot{\phi} - \dot{z}_{t3}) - k_{s1}(z_b - l_1\theta + d_f\phi - z_{t3}) \\ &+ c_{t3}\dot{z}_{t3} + k_{t3}z_{t3} = c_{t3}\dot{q}_3 + k_{t3}q_3 \end{aligned} \tag{2.16}$$

Differential equation of vertical motion of right-side rear tire

$$\begin{aligned} &m_{t4}\ddot{z}_{t4} - c_{s4}(\dot{z}_b - l_2\dot{\theta} + d_r\dot{\phi} - \dot{z}_{t4}) - k_{s4}(z_b - l_2\theta + d_r\phi - z_{t4}) \\ &+ c_{t4}\dot{z}_{t4} + k_{t4}z_{t4} = c_{t4}\dot{q}_4 + k_{t4}q_4 \end{aligned} \tag{2.17}$$

It is convenient to rewrite Eqs. (2.10)–(2.17) together in the standard form of a matrix equation

$$[M]\{\ddot{Z}\} + [C]\{\dot{Z}\} + [K]\{Z\} = [K_t]\{Q\} + [C_t]\{Q\} \tag{2.18}$$

where,

$$\{Q\} = [q_1 q_2 q_3 q_4]^T \quad \{Z\} = [z_c z_b \theta \ \phi z_{t1} z_{t2} z_{t3} z_{t4}]^T$$

$$[M] = diag[m_c m_b I_\theta I_\phi m_{t1} m_{t2} m_{t3} m_{t4}]$$

$$
[K] = \begin{bmatrix}
k_c & -k_c & l_x k_c & -l_y k_c & 0 & 0 & 0 & 0 \\
 & \sum_{i=1}^{4} k_{si} + k_c & -k_{s1}l_1 + k_{s2}l_2 - k_{s3}l_1 + k_{s4}l_2 - k_c l_x & k_{s1}d_f + k_{s2}d_r - k_{s3}d_f - k_{s4}d_r + k_c l_y & -k_{s1} & -k_{s2} & -k_{s3} & -k_{s4} \\
 & & k_{s1}l_1^2 k_{s2}l_2^2 + k_{s3}l_1^2 + k_{s4}l_2^2 + k_c l_x^2 & -k_{s1}l_1 d_f + k_{s2}l_2 d_r + k_{s3}l_1 d_f - k_{s4}l_2 d_r - k_c l_x l_y & k_{s1}l_1 & -k_{s2}l_2 & k_{s3}l_1 & -k_{s4}l_2 \\
 & & & k_{s1}d_f^2 + k_{s2}d_r^2 + k_{s3}d_r^2 + k_c l_y^2 & -k_{s1}d_f & -k_{s2}d_r & k_{s3}d_f & k_{s4}d_r \\
 & & & \text{Symmetric} & k_{s1} + k_{t1} & 0 & 0 & 0 \\
 & & & & & k_{s2} + k_{t2} & 0 & 0 \\
 & & & & & & k_{s3} + k_{t3} & 0 \\
 & & & & & & & k_{s4} + k_{t4}
\end{bmatrix}
$$

$$
[C] = \begin{bmatrix}
c_c & -c_c & l_x c_c & -l_y c_c & 0 & 0 & 0 & 0 \\
 & \sum_{i=1}^{4} c_{si} + c_c & -c_{s1}l_1 + c_{s2}l_2 - c_{s3}l_1 + c_{s4}l_2 - c_c l_x & c_{s1}d_f + c_{s2}d_r - c_{s3}d_f - c_{s4}d_r + c_c l_y & -c_{s1} & -c_{s2} & -c_{s3} & -c_{s4} \\
 & & c_{s1}l_1^2 + c_{s2}l_2^2 + c_{s3}l_1^2 + c_{s4}l_2^2 + c_c l_x^2 & -c_{s1}l_1 d_f + c_{s2}l_2 d_r + c_{s3}l_1 d_f - c_{s4}l_2 d_r - c_c l_x l_y & c_{s1}l_1 & -c_{s2}l_2 & c_{s3}l_1 & -c_{s4}l_2 \\
 & & & c_{s1}d_f^2 + c_{s2}d_r^2 c_{s3}d_f^2 + k_c l_y^2 & -c_{s1}d_f & -c_{s2}d_r & c_{s3}d_f & c_{s4}d_r \\
 & & & \text{Symmetric} & c_{s1} + c_{t1} & 0 & 0 & 0 \\
 & & & & & c_{s2} + c_{t2} & 0 & 0 \\
 & & & & & & c_{s3} + c_{t3} & 0 \\
 & & & & & & & c_{s4} + c_{t4}
\end{bmatrix}
$$

$$[K_t]=\begin{bmatrix}0&0&0&0&k_{t1}&0&0&0\\0&0&0&0&0&k_{t2}&0&0\\0&0&0&0&0&0&k_{t3}&0\\0&0&0&0&0&0&0&k_{t4}\end{bmatrix}^T;$$

$$[C_t]=\begin{bmatrix}0&0&0&0&c_{t1}&0&0&0\\0&0&0&0&0&c_{t2}&0&0\\0&0&0&0&0&0&c_{t3}&0\\0&0&0&0&0&0&0&c_{t4}\end{bmatrix}^T$$

2.2.2 Calculation of the Vehicle Response

This simple vehicle model does not contain the detailed suspension nonlinearities that are typical of heavy vehicles, however its response illustrates many of the more important vehicle characteristics. Linear vehicle simulations can be performed efficiently in the frequency domain for random inputs. In this approach, spectral densities of the output variables are calculated directly from a vehicle response transfer function and the road roughness spectral densities.

1. Calculation of displacement, velocity and acceleration

Taking a Fourier transform of both sides of Eq. (2.18)leads to

$$\begin{aligned}&-\omega^2[M]\{Z(\omega)\}+j\omega[C]\{Z(\omega)\}+[K]\{Z(\omega)\}=[K_t]\{Q(\omega)\}\\&+j\omega[C_t]\{Q(\omega)\}\end{aligned}\tag{2.19}$$

The transfer matrix relating the road displacement inputs to the vehicle vibration displacement outputs can be expressed as follows

$$[H_{z-q}(\omega)]=\frac{\{Z(\omega)\}}{Q(\omega)}=\frac{j\omega[C_t]+[K_t]}{-\omega^2[M]+j\omega[C]+[K]}\tag{2.20}$$

where $H_{z-q}(\omega)$ is a matrix of eight rows and four columns, in which angular frequency ω is used as an independent variable.

The spectral density matrix of the displacement response may be calculated using the well-known relationship between the input and the output spectral densities for a linear system

$$[G_z]=[H_{z-q}{}^*(\omega)][G_q][H_{z-q}(\omega)]^T\tag{2.21}$$

where $[G_q]$ is the spectral density matrix of the road profile displacement, $H_{z-q}{}^*(\omega)$ and $[H_{z-q}(\omega)]^T$ are the complex conjugate and transpose of matrix $H_{z-q}(\omega)$, re-

spectively. $[G_z]$ is a matrix of eight rows and eight columns, in which the spectral densities of the vehicle displacements in the *i*th degree of freedom can be extracted from the diagonal elements ($G_{z_i z_i}$, $i = 1$–8) are the direct spectral densities. Following the relation $\omega = 2\pi f$ and substituting the angular frequency with the temporal frequency in Eq. (2.21), the root-mean-square of the vehicle-vibration displacements in the *i*th degree of freedom is given by

$$\sigma_{z_i}^2 = \int_0^\infty G_{z_i z_i}(f)df \tag{2.22}$$

Let $[H_{\dot{z}-q}(\omega)]$ and $[H_{\ddot{z}-q}(\omega)]$ denote the transfer matrices of the velocity and acceleration. Then, from the property of the Fourier transform, we can derive

$$[H_{\dot{z}-q}(\omega)] = j\omega[H_{z-q}(\omega)] = j2\pi f[H_{z-q}(\omega)] \tag{2.23}$$

$$[H_{\ddot{z}-q}(\omega)] = -\omega^2[H_{z-q}(\omega)] = -4\pi^2 f^2[H_{z-q}(\omega)] \tag{2.24}$$

So, the spectral density matrix of the acceleration response is given by

$$[G_{\ddot{z}}] = \omega^4[H_{z-q}{}^*(\omega)][G_q][H_{z-q}(\omega)]^T = (2\pi f)^4[H_{z-q}{}^*(\omega)][G_q][H_{z-q}(\omega)]^T \tag{2.25}$$

Similarly, the diagonal elements $G_{\ddot{z}_i\ddot{z}_i}$ in matrix $\left[G_{\ddot{z}}\right]$ are also the direct spectral densities of the vehicle-vibration accelerations in the *i*th degree of freedom. So, the root-mean-square of the vehicle-vibration accelerations in the *i*th degree of freedom is obtained from

$$\sigma_{\ddot{z}_i}^2 = \int_0^\infty G_{\ddot{z}_i\ddot{z}_i}(f)df \tag{2.26}$$

When evaluating ride comfort, one can obtain the root-mean-square of the seat's vertical acceleration by multiplying Eq. (2.26) by the frequency weighting function $W(f)$, that is

$$\sigma_{\ddot{z}_c}^2 = \int_0^\infty W^2(f)G_{\ddot{z}_c\ddot{z}_c}(f)df \tag{2.27}$$

where, $W(f) = \begin{cases} 0.5 & (0.5 < f \le 2) \\ f/4 & (2 < f \le 4) \\ 1 & (4 < f \le 12.5) \\ 12.5/f & (12.5 < f \le \infty) \end{cases}$

2. Calculation of the dynamic suspension deflection

Let f_{d1} , f_{d2} , f_{d3} and f_{d4} denote the dynamic suspension deflection of the left-side front, left-side rear, right-side front and right-side rear suspensions. Then, from the calculation formula and Fig. 2.18, we can derive

$$\begin{cases} f_{d1} = z_b - l_1\theta + d_f\phi - z_{t1} \\ f_{d2} = z_b + l_2\theta + d_r\phi - z_{t2} \\ f_{d3} = z_b - l_1\theta + d_f\phi - z_{t3} \\ f_{d4} = z_b + l_2\theta - d_r\phi - z_{t4} \end{cases} \tag{2.28}$$

Taking the Fourier transform of both sides of Eq. (2.28) and rewriting in a form of a matrix

$$\{f_d(\omega)\} = [H_{f_d - z}(\omega)]\{Z(\omega)\} \tag{2.29}$$

where,

$$[H_{f_d-z}(\omega)] = \begin{bmatrix} 0 & 1 & -l_1 & d_f & -1 & 0 & 0 & 0 \\ 0 & 1 & l_2 & d_r & 0 & -1 & 0 & 0 \\ 0 & 1 & -l_1 & -d_f & 0 & 0 & -1 & 0 \\ 0 & 1 & l_2 & -d_r & 0 & 0 & 0 & -1 \end{bmatrix};$$

$$\{f_d(\omega)\} = [f_{d1}(\omega) \quad f_{d2}(\omega) \quad f_{d3}(\omega) \quad f_{d4}(\omega)]^T;$$

$$\{Z(\omega)\} = [z_c(\omega) \quad z_b(\omega) \quad \theta(\omega) \quad \phi(\omega) \quad z_{t1}(\omega) \quad z_{t2}(\omega) \quad z_{t3}(\omega) \quad z_{t4}(\omega)]^T$$

Substituting Eq. (2.20) into Eq. (2.29) leads to

$$f_d(\omega) = [H_{f_d-z}(\omega)][H_{z-q}(\omega)]Q(\omega) = [H_{f_d-q}(\omega)]Q(\omega) \tag{2.30}$$

$[H_{f_d-q}(\omega)] = [H_{f_d-z}(\omega)][H_{z-q}(\omega)]$ is the transfer matrix relating the road displacement inputs to the dynamic suspension deflection outputs. So, the spectral density matrix of the dynamic suspension deflection can be expressed as

$$[G_{f_d}] = [H_{f_d-q}{}^*(\omega)][G_q][H_{f_d-q}(w)]^T \tag{2.31}$$

where $[G_{f_d}]$ is a matrix of four rows and four columns, in which the diagonal elements G_{f_d11}, G_{f_d22}, G_{f_d33}, and G_{f_d44} are the direct spectral densities of the dynamic suspension deflection of the left-side front, left-side rear, right-side front and right-side rear suspensions, respectively. So, the root-mean-square of the dynamic suspension deflection is given by

$$\sigma^2_{f_di} = \int_0^\infty G_{f_dii}(f)df \quad i = 1,2,3,4 \tag{2.32}$$

3. Calculation of the stochastic dynamic tire force

The stochastic dynamic tire force generated by a moving vehicle is

$$F_{ti} = k_{ti}(z_{ti} - q_i) + c_{ti}(\dot{z}_{ti} - \dot{q}_i) \quad i = 1,2,3,4 \tag{2.33}$$

By substituting Eqs. (2.14)–(2.17) into Eq. (2.33), we have after some rearrangement

$$\begin{cases} F_{t1} = k_{s1}(z_b - l_1\theta + d_f\phi - z_{t1}) + c_{s1}(\dot{z}_b - l_1\dot{\theta} + d_f\dot{\phi} - \dot{z}_{t1}) - m_{t1}\ddot{z}_{t1} \\ F_{t2} = k_{s2}(z_b + l_2\theta + d_r\phi - z_{t2}) + c_{s2}(\dot{z}_b + l_2\dot{\theta} + d_f\dot{\phi} - \dot{z}_{t2}) - m_{t2}\ddot{z}_{t2} \\ F_{t3} = k_{s1}(z_b - l_1\theta - d_f\phi - z_{t3}) + c_{s3}(\dot{z}_b - l_1\dot{\theta} - d_f\dot{\phi} - \dot{z}_{t3}) - m_{t3}\ddot{z}_{t3} \\ F_{t4} = k_{s4}(z_b + l_2\theta - d_r\phi - z_{t4}) + c_{s4}(\dot{z}_b + l_2\dot{\theta} - d_r\dot{\phi} - \dot{z}_{t4}) - m_{t4}\ddot{z}_{t4} \end{cases} \tag{2.34}$$

Similarly, the following equation can be deduced by the Fourier transform

$$F_t(\omega) = [H_{F_d-z}(\omega)][H_{z-q}(\omega)]Q(\omega) = [H_{F_d-q}(\omega)]Q(\omega) \tag{2.35}$$

in which

$$\left[H_{F_d-z}(\omega)\right] = \begin{bmatrix} 0 & k_{s1} + j\omega c_{s1} & -l_1(k_{s1} + j\omega c_{s1}) & d_f(k_{s1} + j\omega c_{s1}) \\ 0 & k_{s2} + j\omega c_{s2} & l_2(k_{s2} + j\omega c_{s2}) & d_r(k_{s2} + j\omega c_{s2}) \\ 0 & k_{s2} + j\omega c_{s3} & -l_1(k_{s3} + j\omega c_{s3}) & -d_f(k_{s3} + j\omega c_{s3}) \\ 0 & k_{s2} + j\omega c_{s4} & l_2(k_{s4} + j\omega c_{s4}) & -d_r(k_{s4} + j\omega c_{s4}) \end{bmatrix}$$

$$\begin{bmatrix} \omega^2 m_{t1} - k_{s1} - j\omega c_{s1} & 0 & 0 & 0 \\ 0 & \omega^2 m_{t2} - k_{s2} - j\omega c_{s2} & 0 & 0 \\ 0 & 0 & \omega^2 m_{t3} - k_{s3} - j\omega c_{s3} & 0 \\ 0 & 0 & 0 & \omega^2 m_{t4} - k_{s4} - j\omega c_{s4} \end{bmatrix}$$

$$\left\{F_t(\omega)\right\} = [F_{t1}(\omega) \quad F_{t2}(\omega) \quad F_{t3}(\omega) \quad F_{t4}(\omega)]^T$$

$[H_{F_d-q}(\omega)]$ is the transfer matrix relating the road displacement inputs to the stochastic dynamic tire force outputs. So, the spectral density matrix of the stochastic dynamic tire force can be expressed as

$$[G_{F_d}] = [H_{F_d-q}{}^*(w)][G_q][H_{F_d-q}{}^*(w)]^T \tag{2.36}$$

The diagonal elements G_{F_d11}, G_{F_d22}, G_{F_d33}, and G_{F_d44} in matrix $[G_{F_d}]$ are the direct spectral densities of the dynamic tire force of the four tires. So, the root-mean-square of the dynamic tire force is given by

$$\sigma^2_{F_di} = \int_0^\infty G_{F_dii}(f)df \tag{2.37}$$

2.2.3 Analysis of Vehicle-Vibration Response Under Random Excitation

In this section, the distribution of the dynamic tire forces are calculated using Matlab software, and a parametric study then follows to show the effect of the

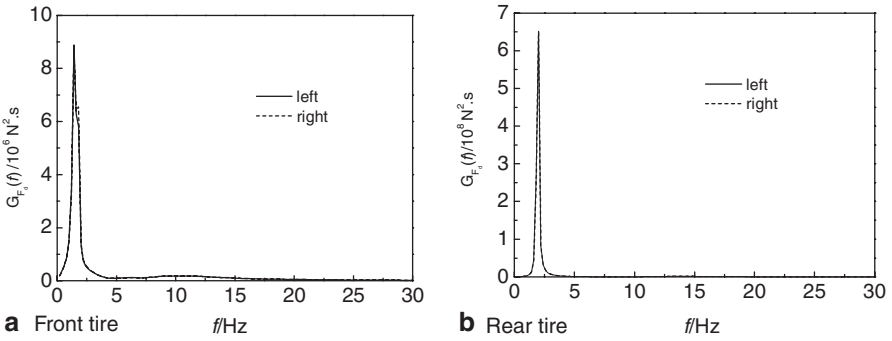

Fig. 2.19 Tire force spectral density

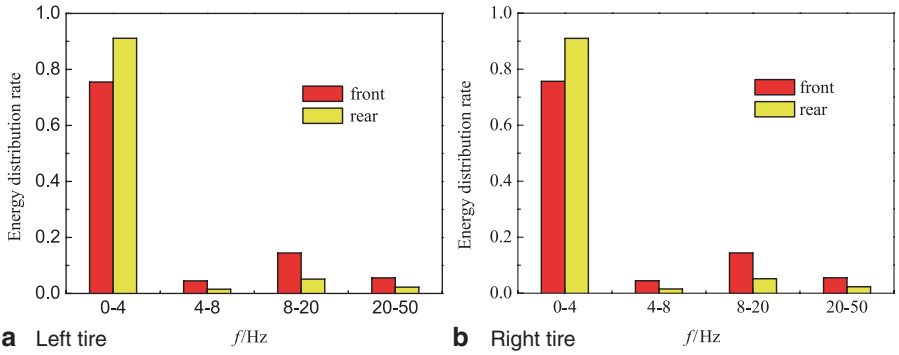

Fig. 2.20 Energy distribution ratio of the dynamic tire force

vehicle system parameters on the dynamic tire force. The heavy vehicle parameters are chosen to be: $m_b = 24900kg$, $I_\theta = 203931kg{\cdot}m^2$, $I_\phi = 22994kg{\cdot}m^2$, $m_{t1} = m_{t3} = 300kg$, $m_{t2} = m_{t4} = 800kg$, $m_c = 90kg$, $k_{s1} = k_{s3} = 400kN/m$, $k_{s2} = k_{s4} = 2500kN/m$, $k_{t1} = k_{t3} = 1000kN/m$, $k_{t2} = k_{t4} = 3000kN/m$, $k_c = 29.9kN/m$, $c_{s1} = c_{s3} = 15kN{\cdot}s/m$, $c_{s2} = c_{s4} = 25kN{\cdot}s/m$, $c_c = 680N{\cdot}s/m$, $c_{t1} = c_{t3} = 1kN{\cdot}s/m$, $c_{t2} = c_{t4} = 3kN{\cdot}s/m$; $d_f = 0.993m$, $d_r = 0.93m$, $l_1 = 4.55m$, $l_2 = 1.8m$, $l_x = 4.4m$, $l_y = 0.8m$, vehicle moving speed $v = 20m/s$. The road grade is B.

Figure 2.19 shows the front and rear tire force spectral density as defined by Eq. (2.36). There are two main spectral peaks in the curve. The two spectral peaks for the front tire are frequencies of approximately 1.5 and 9.5 Hz, and the two spectral peaks for the rear tire are at frequencies of approximately 2 and 14 Hz. The first peak frequency corresponds to the spring-mass resonant frequency, which is related to suspension stiffness. The second peak frequency corresponds to the wheel hop frequency, which is related to tire stiffness. The second peak is relatively small compared to the first one. This also indicates that the suspension parameters have a significant effect on the dynamic tire force.

Figure 2.20 shows the energy distribution ratio of the dynamic tire force in different frequency domains, which can easily be estimated by the formula

$$\Delta EN(f_1 \le f \le f_2) = \frac{\int_{f_1}^{f_2} G_{F_d}(f)df}{\int_0^{90} G_{F_d}(f)df} \tag{2.38}$$

From Fig. 2.20, we can see that the dynamic tire force generated by a heavy vehicle is typically of low frequency. The energy is concentrated primarily in the range of 0–4 Hz, in this frequency range, the energy distribution ratio of the front tire force is 75.6 %, and it is 91 % for the rear tire.

2.2.4 Numerical Results and Discussions

In this section, the effect of vehicle suspension stiffness, suspension damping, tire stiffness, tire damping, road grade, and moving speed on the energy distribution of the dynamic tire force will be examined. The energy distribution of the dynamic tire force for the left-side and the right-side tires is similar, so, only the dynamic tire force of the left-side tire are worked out. In order to clearly observe the distribution of tire force spectral density for different parameters, logarithmic y-axes are used in Figs. 2.21, 2.22, 2.23, 2.24, 2.25, 2.26, 2.27, 2.28, 2.29, and 2.30.

1. The effect of suspension stiffness

The suspension stiffness has a significant effect on the tire force spectral density, affecting both the sprung mass resonant frequency and the wheel hop frequency. Figures 2.21 and 2.22 illustrate the relationship between the suspension stiffness and the tire force spectral density. The variation in the front suspension stiffness has little effect on the rear tire force spectral density, and the variation in the rear suspension stiffness also has little effect on the front tire force spectral density. As the front and rear suspension stiffnesses increase, the first spectral peaks of the front- and the rear-tire force increase in magnitude, while the second spectral peaks decrease in magnitude. The frequencies of both spectral peaks are seen to increase.

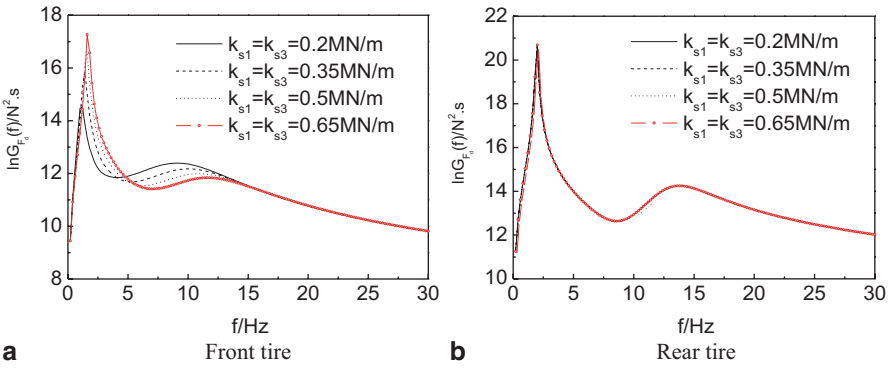

Fig. 2.21 The effect of front suspension stiffness on the tire force spectral density

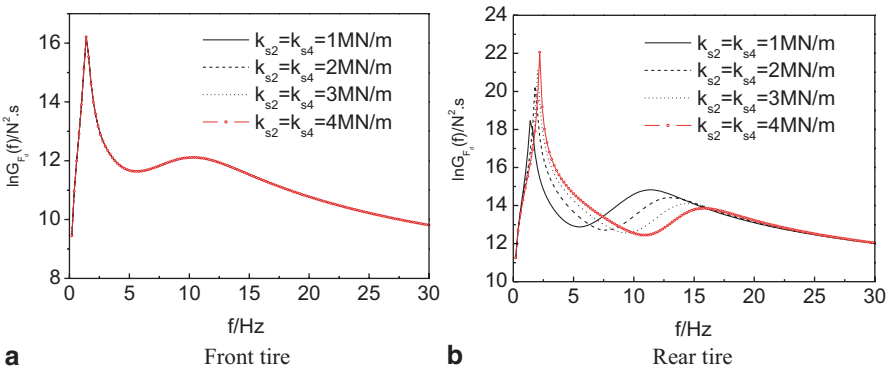

Fig. 2.22 The effect of rear suspension stiffness on the tire force spectral density

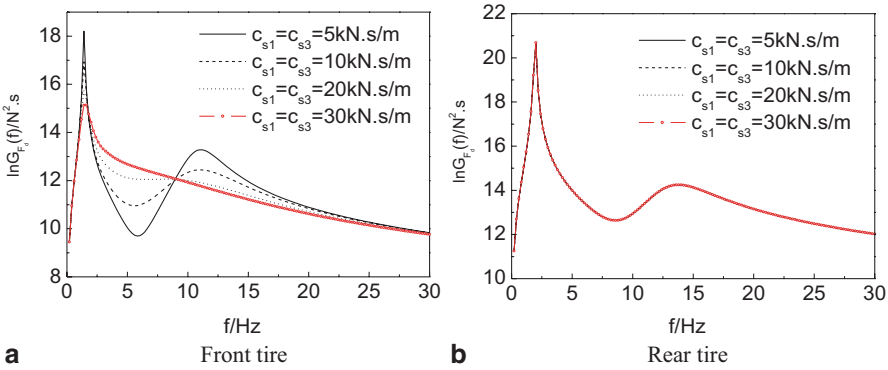

Fig. 2.23 The effect of front suspension damping on the tire force spectral density

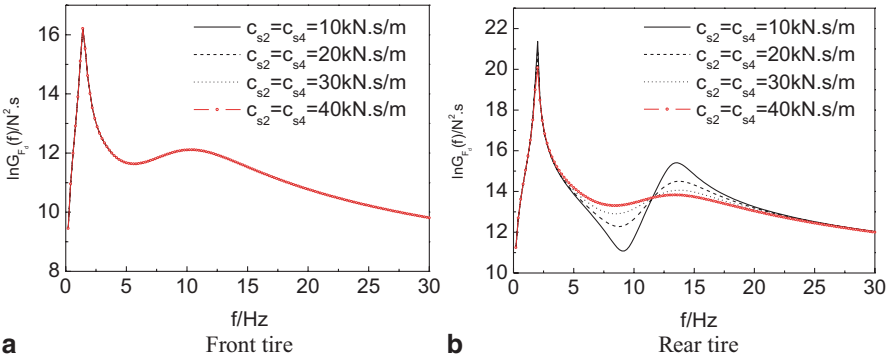

Fig. 2.24 The effect of rear suspension damping on the tire force spectral density

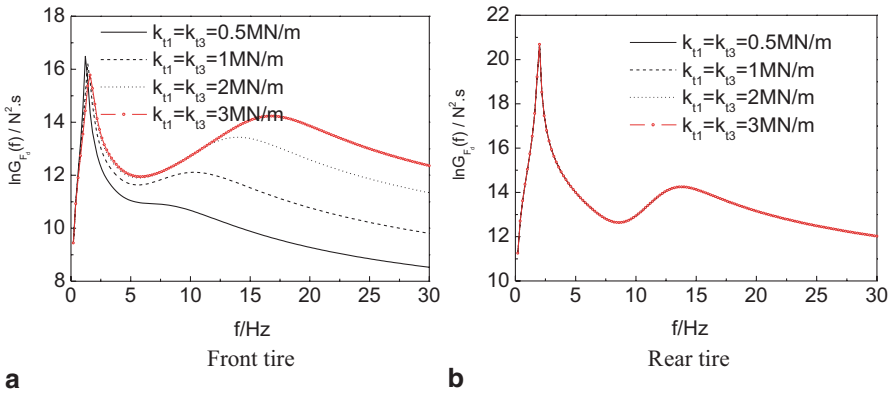

Fig. 2.25 The effect of front tire stiffness on the tire force spectral density

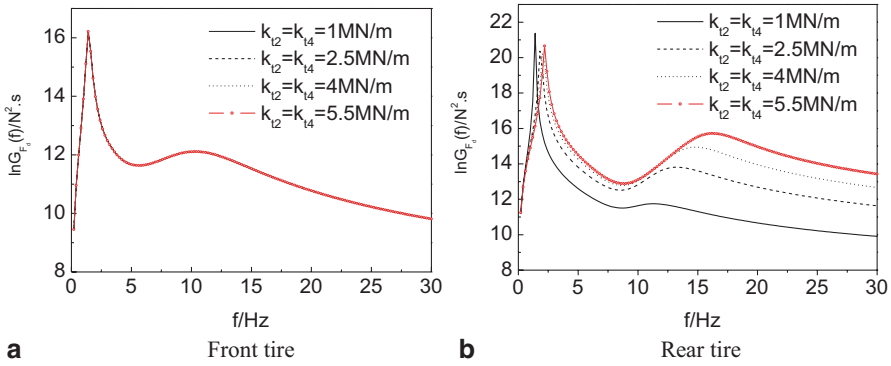

Fig. 2.26 The effect of rear tire stiffness on the tire force spectral density

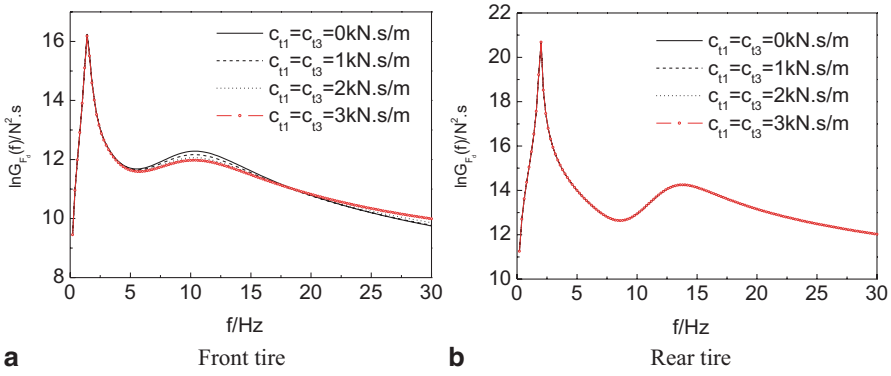

Fig. 2.27 The effect of front tire damping on the tire force spectral density

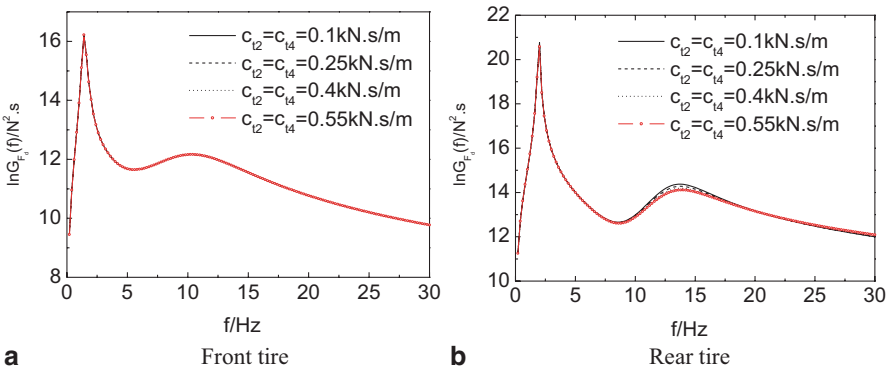

Fig. 2.28 The effect of rear tire damping on the tire force spectral density

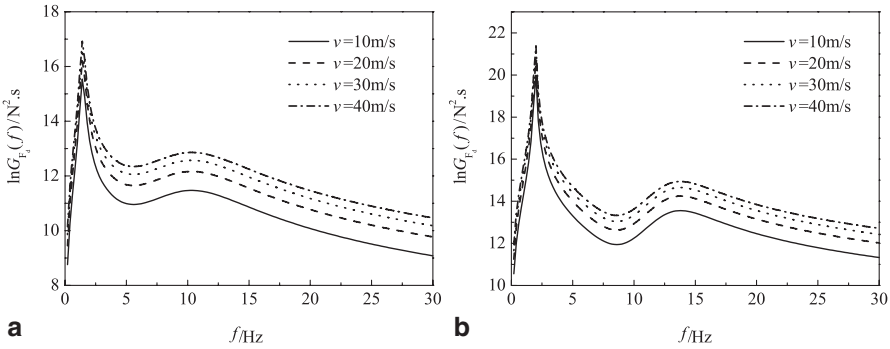

Fig. 2.29 The effect of vehicle moving speed on the tire force spectral density

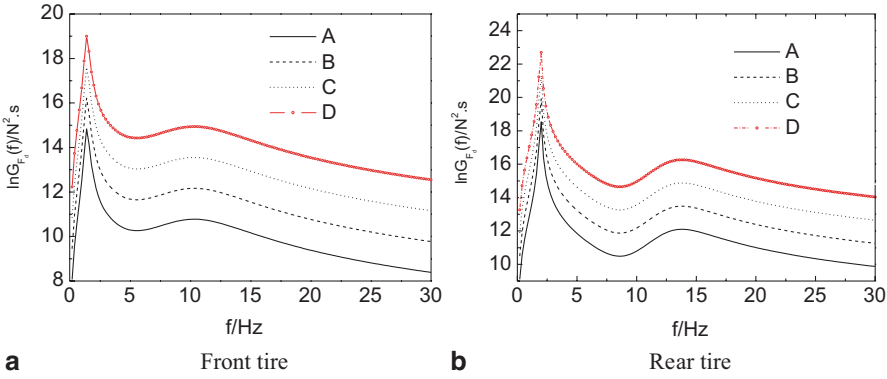

Fig. 2.30 The effect of road grade on the tire force spectral density

These suggest that, as the suspension stiffness increases, the low frequency vibration of the dynamic tire force becomes stronger and the damage to the pavement increases. Therefore, in order to reduce the dynamic tire force and improve pavement service life, a small suspension stiffness should be considered first when designing the suspension, under the condition that the suspension bearing capacity and ride comfort can be completely guaranteed.

2. The effect of suspension damping

The effect of suspension damping on the tire force spectral density can be seen in Figs. 2.23 and 2.24. The variation in the front-suspension damping has little effect on the rear tire force spectral density, and the variation in the rear suspension damping also has little effect on the front tire force spectral density. The frequencies corresponding to the two spectral peaks do not change as the suspension damping changes. As the front suspension damping increases, the first and second spectral peaks of the front tire force all decrease significantly, and when the damping increases to a certain value, the second spectral peak disappears. As the rear suspension damping increases, the second spectral peak of the rear tire force decreases significantly. But the first spectral peak decreases only slightly. These show that increasing suspension damping can reduce the dynamic tire force, which is beneficial for pavement service life.

3. The effect of tire stiffness

Figures 2.25 and 2.26 show the effect of the tire stiffness on the tire force spectral density. The tire stiffness has a great effect on a wheel hop frequency as well as the tire force spectral density beyond the wheel hop frequency, and the larger the tire stiffness, the higher the second spectral peak value. This can be clearly seen in both Figs. 2.25a and 2.26b. However, the tire stiffness only has a moderate effect on the sprung mass resonant frequency as well as on the low-frequency tire force spectral density.

An increase in inflation pressure will cause an increase in the tire stiffness. The larger the tire stiffness, the more severe the vehicle vibration and the higher the dynamic tire force. So, it is necessary to strictly limit tire overpressure.

4. The effect of tire damping

The effect of suspension damping on the tire force spectral density can be seen in Figs. 2.27 and 2.28. The tire damping has little effect on the tire force spectral density in the low-frequency range, but has some effect on the wheel hop frequency and higher frequencies. As the tire damping increases, the first spectral peak remains unchanged, but the second spectral peak decreases slightly. Compared with the other parameters, the effect of tire damping on the tire force spectral density is small, so, most studies of dynamic tire force omit this variable by assuming that the inherent damping of the tire is negligible.

5. The effect of moving speed

As seen in Fig. 2.29, we clearly recognize that the vehicle speed has a significant effect on the tire force spectral density, which significantly increases as the vehicle

speed increases. The higher the speed, the more serious the vehicle vibration and the higher the dynamic tire force.

6. The effect of road roughness

Roughness has a tremendous effect on the tire force spectral density. Figure 2.30 shows the relationship between road grades and the tire force spectral density. Symbols A, B, C, and D denote the road grades. The tire force spectral density significantly increases as the road roughness increases (i.e., the pavement surface condition becomes worse). A lower road grade (going from A to D) will cause larger dynamic tire force and more pavement damage.

2.3 Dynamic Analysis of a Three-Axle Heavy Vehicle

This section presents a mathematical model of the interacting process of a vehicle-tire–road system and attempts to figure out the mechanics of interaction. A nonlinear tri-axle vehicle model with a balanced suspension is first proposed based on a detailed analysis of the structural features of a heavy vehicle. Furthermore, an FRC (flexible rolling contact) tire model with enveloping characteristics is added into the full vehicle model. The tire model considers both the tire contact history with a rough road profile and the uneven distribution characteristics of a vertical load. It is expected that these results can supply new ideas for vehicle–road interaction research.

2.3.1 Modeling for a Three-Axle Vehicle with a Balanced Suspension

A three-axle vehicle dynamic model with 6 degrees of freedom is built, as shown in Fig. 2.31.

The main parameters of the vehicle model are listed as follows:

m_c, m_b, m_p cab mass, body mass, and balanced rod mass.
$I_{b\theta}, I_{p\theta}$ body and balanced suspension moment of inertia.
m_{tf}, m_{tm}, m_{tr} unsprung mass of the steering suspension and balanced suspension.
k_{c1}, k_{c2} front and rear mount stiffness of the cab.
c_{c1}, c_{c2} front and rear mount damping of the cab.
k_{sf}, c_{sf} stiffness and damping of the steering suspension.
k_{sr}, c_{sr} stiffness and damping of the balanced suspension.
k_{tf}, c_{tf} stiffness and damping of the steering suspension tire.
k_{tm}, c_{tm} stiffness and damping of the intermediate tire.
k_{tr}, c_{tr} stiffness and damping of the rear tire.
q_f, q_m, q_r road input to the steering suspension tire and balanced suspension tire.

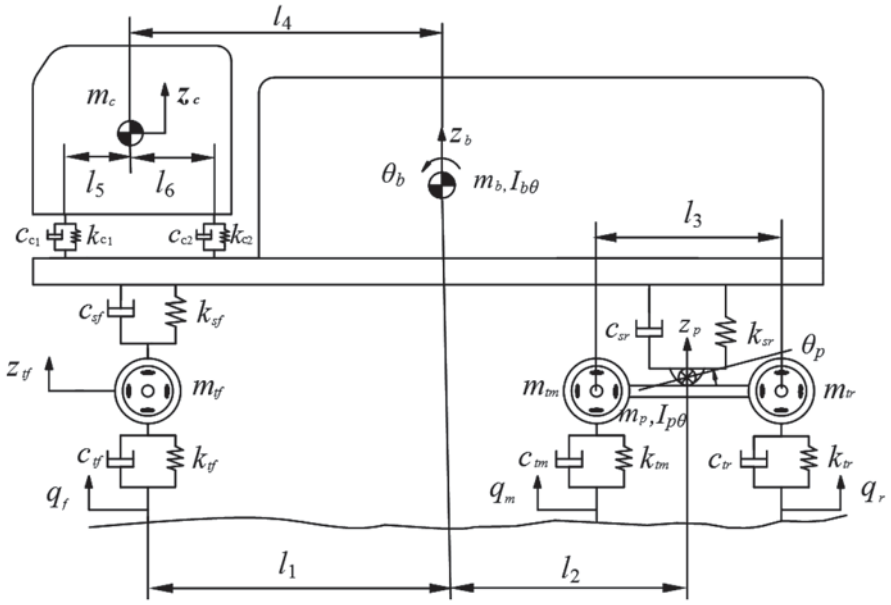

Fig. 2.31 A three-axle vehicle model with a balanced suspension. (Reprinted from ref. [19], with kind permission from Science China Press and Springer-Verlag Berlin Heidelberg)

z_c, z_b, z_{tf}, z_p vertical displacement of the cab, body, front axle, and balanced rod.

θ_b, θ_p angular displacements of the body and balanced suspension.

l_1 distance from the front axle to the center of the vehicle body mass.

l_2 distance from the center of balanced rod to the center of the vehicle body mass.

l_3 distance from the intermediate axle to the rear axle.

l_4 distance from the center of the cab to the center of the vehicle body mass.

l_5 distance from the front cab mount to the center of the cab.

l_6 distance from the rear cab mount to the center of the cab.

According to D'Alembert's principle, the relative displacements between the frame and the cab are

$$\begin{aligned} z_{c1} &= z_b - \theta_b(l_4 + l_5) \\ z_{c2} &= z_b - \theta_b(l_4 - l_6) \end{aligned} \tag{2.39}$$

The relative displacement between the frame and the front steering suspension is

$$z_{ff} = z_b - \theta_b l_1$$

The relative displacement between the frame and the balanced suspension is

$$z_{rr} = z_b - \theta_b l_2 \tag{2.40}$$

The forces between the frame and the cab are

$$F_{c1} = k_{c1}[z_c - z_b + \theta_b(l_4 + l_5)] + c_{c1}[\dot{z}_c - \dot{z}_b + \dot{\theta}_b(l_4 + l_5)] \tag{2.41}$$

$$F_{c2} = k_{c2}[z_c - z_b + \theta_b(l_4 - l_6)] + c_{c2}[\dot{z}_c - \dot{z}_b + \dot{\theta}_b(l_4 - l_6)] \tag{2.42}$$

The force between the frame and the front steering suspension is

$$F_{ff} = k_{sf}[z_{tf} - (z_b - \theta_b l_1)] + c_{sf}[\dot{z}_{tf} - (\dot{z}_b - \dot{\theta}_b l_1)] \tag{2.43}$$

The force between the frame and the balanced suspension is

$$F_{rr} = k_{sr}[z_p - (z_b + \theta_b l_2)] + c_{sr}[\dot{z}_p - (\dot{z}_b + \dot{\theta}_b l_2)] \tag{2.44}$$

The differential equation of vertical motion for the vehicle cab is

$$m_c \ddot{Z}_c + F_{c1} + F_{c2} = 0 \tag{2.45}$$

The differential equation of vertical motion for the vehicle body is

$$m_b \ddot{Z}_b - F_{c1} - F_{c2} - F_{ff} - F_{rr} = 0 \tag{2.46}$$

The differential equation of pitching motion for the vehicle body is

$$I_{b\theta}\ddot{\theta}_b + F_{c1}(l_4 + l_5) + F_{c2}(l_4 - l_6) + F_{ff} l_1 - F_{rr} l_2 = 0 \tag{2.47}$$

The differential equation of vertical motion for the front suspension tire is

$$m_{tf}\ddot{z}_{tf} + F_{ff} + k_{tf}(z_{tf} - q_f) + c_{tf}(\dot{z}_{tf} - q_f) = 0 \tag{2.48}$$

The differential equation of vertical motion for the balanced rod is

$$\begin{aligned}&(m_p + m_{tm} + m_{tr})\ddot{z}_p + k_{sr}[z_p - (z_b + \theta_b l_2)]\\ &+k_{tm}(z_p - \theta_p l_3/2 - q_m) + k_{tr}(z_p + \theta_p l_3/2 - q_r)\\ &+c_{sr}[\dot{z}_p - (\dot{z}_b + \theta_b l_2)] + c_{tm}(\dot{z}_p - \dot{z}_p l_3/2 - q_m)\\ &+c_{tr}(\dot{z}_p + \dot{\theta}_p l_3/2 - \dot{q}_r) = 0\end{aligned} \tag{2.49}$$

The differential equation of pitching motion for the balanced rod is

$$\begin{aligned}&\left(I_{p\theta} + m_{tm} l_3^2/4 + m_{tr} l_3^2/4\right)\ddot{\theta}_{p\theta} - k_{tm}(z_p - \theta_p l_3/2 - q_m) l_3/2\\ &+k_{tr}(z_p - \theta_p l_3/2 - q_r) l_3/2 - c_{tm}(\dot{z}_p - \dot{\theta}_p l_3/2 - q_m) l_3/2\\ &+c_{tr}(\dot{z}_p - \dot{\theta}_p l_3/2 - q_r) l_3/2 = 0\end{aligned} \tag{2.50}$$

The above equations of motion can be written in the form of a matrix of unity

$$M\{\ddot{Z}\}+C\{\dot{Z}\}+K\{Z\}=K_t\{Q\}+C_t\{Q\} \tag{2.51}$$

where $\{Z\}=\{z_c\ z_b\ \theta_b\ z_{tf}\ z_p\ \theta_p\}^T$, in which each matrix can be expressed as

$$M=\begin{bmatrix} m_c & 0 & 0 & 0 & 0 & 0 \\ 0 & m_b & 0 & 0 & 0 & 0 \\ 0 & 0 & I_{b\theta} & 0 & 0 & 0 \\ 0 & 0 & 0 & m_{tf} & 0 & 0 \\ 0 & 0 & 0 & 0 & m_p+m_{tm}+m_{tr} & 0 \\ 0 & 0 & 0 & 0 & 0 & I_{p\theta}+m_{tm}\dfrac{l_3^2}{4}+m_{tr}\dfrac{l_3^2}{4} \end{bmatrix},$$

$$K=\begin{bmatrix} a_{11} & a_{12} & a_{13} & 0 & 0 & 0 \\ a_{21} & a_{22} & a_{23} & a_{24} & a_{25} & 0 \\ a_{31} & a_{32} & a_{33} & a_{34} & a_{35} & 0 \\ 0 & a_{42} & a_{43} & a_{44} & 0 & 0 \\ 0 & a_{52} & a_{53} & 0 & a_{55} & a_{56} \\ 0 & 0 & 0 & 0 & a_{65} & a_{66} \end{bmatrix},\quad C=\begin{bmatrix} b_{11} & b_{12} & b_{13} & 0 & 0 & 0 \\ b_{21} & b_{22} & b_{23} & b_{24} & b_{25} & 0 \\ b_{31} & b_{32} & b_{33} & b_{34} & b_{35} & 0 \\ 0 & b_{42} & b_{43} & b_{44} & 0 & 0 \\ 0 & b_{52} & b_{53} & 0 & b_{55} & b_{56} \\ 0 & 0 & 0 & 0 & b_{65} & b_{66} \end{bmatrix},$$

$$K_t=\begin{bmatrix} 0 & 0 & 0 \\ 0 & 0 & 0 \\ 0 & 0 & 0 \\ k_{tf} & 0 & 0 \\ 0 & k_{tm} & k_{tr} \\ 0 & -\dfrac{b}{2}k_{tm} & \dfrac{b}{2}k_{tr} \end{bmatrix},\quad C_t=\begin{bmatrix} 0 & 0 & 0 \\ 0 & 0 & 0 \\ 0 & 0 & 0 \\ c_{tf} & 0 & 0 \\ 0 & c_{tm} & c_{tr} \\ 0 & -\dfrac{b}{2}c_{tm} & \dfrac{b}{2}c_{tr} \end{bmatrix},\quad \{Q\}=\begin{bmatrix} q_f \\ q_m \\ q_r \end{bmatrix}$$

The coefficients of the matrix are:

$$a_{11}=k_{c1}+k_{c2},\quad a_{12}=-(k_{c1}+k_{c2}),\quad a_{13}=[k_{c1}(l_4+l_5)+k_{c2}(l_4-l_6)],$$

$$a_{21}=-(k_{c1}+k_{c2}),\quad a_{22}=k_{c1}+k_{c2}+k_{sf}+k_{sr},$$
$$a_{23}=-[k_{c1}(l_4+l_5)+k_{c2}(l_4-l_6)+l_1k_{sf}-l_2k_{sr}],$$

$$a_{24}=-k_{sf},\quad a_{25}=-k_{sr},$$

$$a_{31}=[k_{c1}(l_4+l_5)+k_{c2}(l_4-l_6)],\quad a_{32}=-[k_{c1}(l_4+l_5)+k_{c2}(l_4-l_3)+l_1k_{sf}-l_2k_{sr}],$$

$$a_{33} = \left[k_{c1}\left(l_4 + l_5\right)^2 + k_{c2}\left(l_4 - l_6\right)^2 + l_1^2 k_{sf} + l_2^2 k_{sr} \right], \quad a_{34} = l_1 k_{sf}, \quad a_{35} = l_2 k_{sr},$$

$$a_{42} = -k_{sf}, \quad a_{43} = l_1 k_{sf}, \quad a_{44} = k_{sf} + k_{tf},$$

$$a_{52} = -k_{sf}, \quad a_{53} = -l_2 k_{sr}, \quad a_{55} = k_{sr} + k_{tm} + k_{tr}, \quad a_{56} = -l_3 k_{tm} / 2 + l_3 k_{tr} / 2,$$

$$a_{65} = -l_3 k_{tm} / 2 + l_3 k_{tr} / 2, \quad a_{66} = l_3^2 (k_{tm} + k_{tr}) / 4,$$

$$b_{11} = c_{c1} + c_{c2}, \quad b_{12} = -(c_{c1} + c_{c2}),$$
$$b_{13} = [c_{c1}(l_4 + l_5) + c_{c2}(l_4 - l_6)],$$

$$b_{21} = -(c_{c1} + c_{c2}), \quad b_{22} = c_{c1} + c_{c2} + c_{sf} + c_{sr},$$
$$b_{23} = -[c_{c1}(l_4 + l_5) + c_{c2}(l_4 - l_6) + l_1 c_{sf} - l_2 c_{sr}],$$

$$b_{24} = -c_{sf}, \quad b_{25} = -c_{sr},$$

$$b_{31} = [c_{c1}(l_4 + l_5) + c_{c2}(l_4 - l_6)], \quad b_{32} = -[c_{c1}(l_4 + l_5) + c_{c2}(l_4 - l_6) + l_1 c_{sf} - l_2 c_{sr}],$$

$$b_{33} = \left[c_{c1}\left(l_4 + l_5\right)^2 + c_{c2}\left(l_4 - l_6\right)^2 + l_1^2 c_{sf} + l_2^2 c_{sr} \right], \quad b_{34} = l_1 c_{sf}, \quad b_{35} = -l_2 c_{sr},$$

$$b_{42} = -c_{sf}, \quad b_{43} = l_1 c_{sf}, \quad b_{44} = c_{sf} + c_{tf},$$

$$b_{52} = -c_{sf}, \quad b_{53} = -l_2 c_{sr}, \quad b_{55} = c_{sr} + c_{tm} + c_{tr}, \quad b_{56} = -l_3 c_{tm} / 2 + l_3 c_{tr} / 2,$$

$$b_{65} = -l_3 c_{tm} / 2 + l_3 c_{tr} / 2, \quad b_{66} = l_3^2 (c_{tm} + c_{tr}) / 4.$$

2.3.2 Modeling for a Vehicle-Tire–Road Coupling System

Because the tire is the only link between the vehicle and the road besides the air, it can not only support the vehicle load but also attenuate the shock from the uneven road profile. The tire dynamic behavior also has an important influence on vehicle and road dynamics. Therefore, it is necessary to build a tire model to reflect the tire's actual physical features and to satisfy the vehicle–road interaction study. A tire is mainly composed of rubber and cord-rubber composite materials. Consequently, there exists a contact footprint area between the tire and the road caused by the tire's

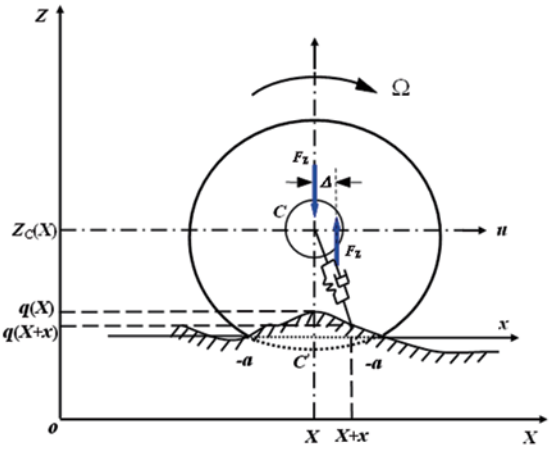

Fig. 2.32 The FRC tire model on an uneven road surface. (Reprinted from ref. [19], with kind permission from Science China Press and Springer-Verlag Berlin Heidelberg)

radial deformation. When a vehicle is travelling on uneven road surface, the height of the wheel center is not the pure sum of the tire free radius and the road original profile elevation. The single point contact (SPC) tire model is often used in vehicle dynamics and road design. However, the contact relationship between tire and road occurs through a finite footprint area rather than at a single point. The SPC model is convenient for calculating the dynamic tire force, but it cannot reflect the real interaction of the vehicle-tire–road system and also cannot filter out the high spatial frequency components from uneven road excitation. The tire property of filtering out the high-frequency excitation component is called the enveloping characteristic, which was initially proposed by Lippmann [17]. A flexible roll contact (FRC) model, proposed by Guo, includes the tire geometry and flexible filtering properties [18], as shown in Fig. 2.32 [19]. The FRC model can reflect the variable contact length on a road surface for a rolling tire. The contact area is not a single point and the contact point is not constrained to lie vertically beneath the wheel center but depends on the local road profile. The model has the ability to envelop small irregularities through local deformations within the footprint.

Some springs are used to simulate the effects of inflation pressure and flexible carcass, and some dampers describe the energy dissipation caused by carcass deformations. Both the tire stiffness and damping are taken into account in this section. The vertical dynamic load at the wheel center is expressed as

$$F_d = \int_{-r_0}^{r_0} k_t(x)\cdot\Delta Z(X,x)dx + \int_{-r_0}^{r_0} c_t(x)\cdot\Delta\dot{Z}(X,x)dx \tag{2.52}$$

where r_0 is the free radius of tire, $k_t(x)$ and $c_t(x)$ are the tire distributive vertical stiffness and damping, respectively, $\Delta Z(X,x)$ and $\Delta\dot{Z}(X,x)$ are the relative deformation and velocity at a particular point within the contact length. $\Delta Z(X,x)$ and $\Delta\dot{Z}(X,x)$ can be expressed as

$$\begin{cases} \Delta Z(X,x) = q(X+x) + \sqrt{r_0^2 - x^2} - r_0 - Z_c(X) \\ \Delta \dot{Z}(X,x) = \dot{q}(X+x) - xu / \sqrt{r_0^2 - x^2} - \dot{Z}_c(X) \end{cases} \tag{2.53}$$

where $q(X)$ is the original road profile, $q(X+x)$ is the local road profile of a particular contact point between the tire and road, $Z_c(X)$ is the vertical displacement of the wheel center. There are two methods that are used to model the distributions of the vertical stiffness and damping: uniform and nonuniform distributions.

1. Uniform distribution:

$$k_t(x) = \frac{K_{ts}}{2a}, \quad c_t(x) = \frac{C_{ts}}{2a} \tag{2.54}$$

where K_{ts} and C_{ts} are the vertical stiffness and damping of the tire, and $2a$ is the length of the footprint.

2. Nonuniform distribution:

$$k_t(x) = \frac{q_z(x)}{\Delta z(x)}, \quad c_t(x) = \frac{q_z(x)}{\Delta \dot{z}(x)} \tag{2.55}$$

where $\Delta z(x)$ and $\Delta \dot{z}(x)$ are the relative deformation and velocity at each point and the road profile along the contact length, and $q_z(x)$ is the distribution function of the vertical load.

The actual distribution of a load on the local contact area is not symmetrically distributed for a moving vehicle, but the load distribution can be approximately assumed as a uniform, symmetrical distribution of a parabolic or trapezoidal shape. Thus, a nonuniform model is adopted to represent the distributions of the vertical stiffness and damping, as Eq. 2.56.

$$\begin{cases} q_2(x) = \frac{F_z}{2a} \cdot \eta(\frac{x}{a}) = \frac{F_z}{2a} \cdot \eta(u) \\ \eta(u) = A \cdot (1 - u^{2n}) \cdot (1 - B \cdot u) \end{cases} \tag{2.56}$$

where F_z is the static vertical load, $\eta(u)$ is the dimensionless function, $u = \frac{x}{a}$ is the relative coordinate within the contact length, $A = \frac{2n+1}{2n}$ and $B = -\frac{3(2n+3)}{2n+1} \cdot \frac{\Delta}{a}$ are fitted coefficients, n is the uniform distribution factor, Δ is the distance from the load distribution center to the footprint center, and $\frac{\Delta}{a}$ is the partial distribution factor. According to Fig. 2.32, the force and the moment equilibrium equations are obtained using the following equations

$$\begin{cases} \int_{-a}^{a} q_z(x)dx = F_Z \\ \int_{-a}^{a} q_z(x)\cdot x\cdot dx = F_Z\cdot\Delta \end{cases} \tag{2.57}$$

Then, the constraint equation is easily deduced as

$$\begin{cases} \eta(1) = \eta(-1) = 0 \\ \eta(u) \geq 0, u \in [-1,1] \\ \eta(u) = 0, u \notin [-1,1] \\ \int_{-1}^{1} \eta(u)\cdot du = 2 \\ \int_{-1}^{1} \eta(u)\cdot u\cdot du = 2\cdot\dfrac{\Delta}{a} \end{cases} \tag{2.58}$$

By combining the three-axle heavy vehicle model with the FRC tire model and the random road excitation, the vehicle-tire–road coupling system can be established, as illustrated in Fig. 2.33.

According to D'Alembert's principle, the differential equation of vertical motion for the vehicle cab is

$$m_c\ddot{z}_c + F_{c1} + F_{c2} = 0 \tag{2.59}$$

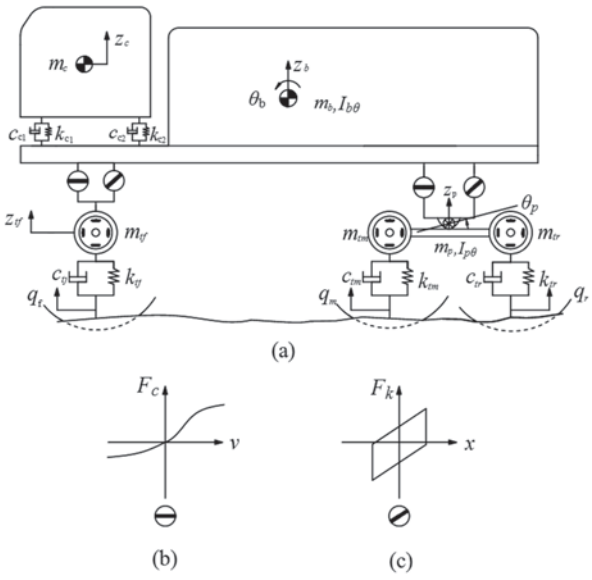

Fig. 2.33 A nonlinear vehicle-tire–road coupling system. (Reprinted from ref. [19], with kind permission from Science China Press and Springer-Verlag Berlin Heidelberg)

where F_{c1} and F_{c2} are the forces between the cab and the frame,

$$F_{c1} = k_{c1}[z_c - z_b + \theta_b(l_3 + l_5)] + c_{c1}[\dot{z}_c - \dot{z}_b + \dot{\theta}_b(l_4 + l_5)] \tag{2.60}$$

$$F_{c2} = k_{c2}[z_c - z_b + \theta_b(l_4 - l_6)] + c_{c2}[\dot{z}_c - \dot{z}_b + \dot{\theta}_b(l_4 - l_6)] \tag{2.61}$$

The differential equation of vertical motion for the vehicle body is

$$m_b\ddot{z}_b - F_{c1} - F_{c2} - F_{ff} - F_{rr} = 0 \tag{2.62}$$

where F_{ff} is the force between the front steering suspension and the frame, F_{rr} is the force between the balanced suspension and the frame. The F_{ff} is composed of the front nonlinear damping force of the shock absorber and the nonlinear restoring force of the leaf springs, and can be expressed as

$$F_{ff} = F_{fc} + F_{fk} \tag{2.63}$$

$$F_{fc} = \begin{cases} \left\{ \dfrac{c_1[\dot{z}_{tf} - (\dot{z}_b - \dot{\theta}_b l_1) - \alpha_f]}{\alpha_f \sqrt{1 + [\dfrac{\dot{z}_{tf} - (\dot{z}_b - \dot{\theta}_b l_1) - \alpha_f}{\alpha_f}]^2}} + c_{2f} \right\} [\dot{z}_{tf} (\dot{z}_b - \dot{\theta}_b l_1)] & \dot{z}_{tf} - (\dot{z}_b - \dot{\theta}_b l_1) < v_{f\lim} \\ C_{ef} v_{f\lim} + C_{bf}[\dot{z}_{tf} - (\dot{z}_b - \dot{\theta}_b l_1) - v_{f\lim}] & \dot{z}_{tf} - (\dot{z}_b - \dot{\theta}_b l_1) \geq v_{f\lim} \end{cases} \tag{2.64}$$

$$F_{fk} = \begin{cases} k_{fu}[z_{tf} - (z_b - \theta_b l_2)] + F_{fu} & z_{tf} - (z_b - \theta_b l_2) > 0 \\ k_{fl}[z_{tf} - (z_b - \theta_b l_2)] + F_{fl} & z_{tf} - (z_b - \theta_b l_2) \leq 0 \end{cases} \tag{2.65}$$

F_{rr} is composed of the rear nonlinear damping force and the nonlinear restoring force as well, and can be expressed as

$$F_{rr} = F_{rc} + F_{rk} \tag{2.66}$$

$$F_{rc} = \begin{cases} \left\{ \dfrac{c_{1r}\left[\dot{z}_p - \left(\dot{z}_b + \dot{\theta}_b l_2\right) - \alpha_r\right]}{\{\alpha_r \sqrt{1 + [\dfrac{\dot{z}_p - \left(\dot{z}_b + \dot{\theta}_b l_2\right) - \alpha_r}{\alpha_r}]^2}} + c_{2r} \right\} \left[\dot{z}_p - \left(\dot{z}_p + \dot{\theta}_b l_2\right)\right] & \dot{z}_p - \left(\dot{z}_b + \dot{\theta}_b l_2\right) < v_{r\lim} \\ C_{er} v_{r\lim} + C_{br}\left[\dot{z}_p - \left(\dot{z}_b + \dot{\theta}_b l_2\right) - v_{r\lim}\right] & \dot{z}_p - \left(\dot{z}_b + \dot{\theta}_b l_2\right) \geq v_{r\lim} \end{cases} \tag{2.67}$$

$$F_{rk} = \begin{cases} k_{ru}[z_p - (z_b + \theta_b l_2)] + F_{ru} & z_p - (z_b + \theta_b l_2) > 0 \\ k_{rl}[z_p - (z_b + \theta_b l_2)] + F_{rl} & z_p - (z_b + \theta_b l_2) \leq 0 \end{cases} \tag{2.68}$$

The differential equation of pitching motion for the vehicle body is also obtained as

$$I_{p\theta}\ddot{\theta}_b + F_{c1}(l_4 + l_5) + F_{c2}(l_4 - l_6) + F_{ff}l_1 - F_{rr}l_2 = 0 \tag{2.69}$$

The differential equation of motion for the unsprung mass of the steering suspension is obtained as

$$m_{tf}\ddot{z}_{tf} + F_{ff} + F_{fd} = 0 \tag{2.70}$$

where F_{fd} is the dynamic tire with the FRC tire model,

$$\begin{aligned} F_{fd} &= \int_{-\tau_0}^{\tau_0} k_{tf}\cdot\Delta z_f(X,x)dx + \int_{-\tau_0}^{\tau_0} c_{tf}\cdot\Delta\dot{z}_f(X,x)dx \\ &= \int_{-\tau_0}^{\tau_0} k_{tf}(x)\cdot[q_f\left(X+x\right) + \sqrt{r_0^2 - x^2} - r_0 - Z_f(X)\Big]dx + \\ &\quad \int_{-\tau_0}^{\tau_0} c_{tf}(x)\cdot[\dot{q}_f\left(X+x\right) + \sqrt{r_0^2 - x^2} - \dot{Z}_f(X)\Big]dx \end{aligned} \tag{2.71}$$

The differential equation of motion for the balanced rod is

$$(m_p + m_{tm} + m_{tr})\ddot{z}_p + F_{rr} + F_{md} + F_{rd} = 0 \tag{2.72}$$

Where F_{md} and F_{rd} are presented respectively as

$$\begin{aligned} F_{md} &= \int_{-\tau_0}^{\tau_0} k_{tm}\cdot\Delta z_m\left(X,x\right)dx + \int_{-\tau_0}^{\tau_0} c_{tm}\cdot\Delta\dot{z}_m\left(X,x\right)dx \\ &= \int_{-\tau_0}^{\tau_0} k_{tm}\left(x\right)\cdot\left[q_m\left(X+x\right) + \sqrt{r_0^2 - x^2} - r_0 - Z_c\left(X\right) + \frac{Z_{\theta 2}\left(X\right)b}{2}\right]dx \\ &\quad + \int_{-\tau_0}^{\tau_0} c_{tm}\left(x\right)\cdot\left[\dot{q}_m\left(X+x\right) - xu/\sqrt{r_0^2 - x^2} - \dot{Z}_c\left(X\right) + \frac{\dot{Z}_{\theta 2}\left(X\right)b}{2}\right]dx \end{aligned} \tag{2.73}$$

$$\begin{aligned} F_{rd} &= \int_{-\tau_0}^{\tau_0} k_{tr}\cdot\Delta z_r\left(X,x\right)dx + \int_{-\tau_0}^{\tau_0} c_{tr}\cdot\Delta\dot{z}_r\left(X,x\right)dx \\ &= \int_{-\tau_0}^{\tau_0} k_{tr}\left(x\right)\cdot\left[q_r\left(X+x\right) + \sqrt{r_0^2 - x^2} - r_0 - Z_c\left(X\right) - \frac{Z_{\theta 2}\left(X\right)b}{2}\right]dx \\ &\quad + \int_{-\tau_0}^{\tau_0} c_{tr}\left(x\right)\cdot\left[\dot{q}_r\left(X+x\right) - xu/\sqrt{r_0^2 - x^2} - \dot{Z}_c\left(X\right) - \frac{\dot{Z}_{\theta 2}\left(X\right)b}{2}\right]dx \end{aligned} \tag{2.74}$$

2.3.3 Numerical Results and Discussions

The interaction of a vehicle and a road is a weakly coupled for two reasons: (1) the displacement response of the pavement system (0–1 mm) is much smaller than the deflection of the tire or suspension (10–20 mm), (2) the speed of propagation of elastic waves along the road profile (100–600 m/s) is much larger than the vehicle's speed (10–50 m/s). So the road profile can be assumed to be unchanged for a vehicle traveling on a road surface. In addition, the vehicle–road system is a nonlinear coupled system. The superposition principle of a linear system is no longer valid and the vibration response cannot be directly analyzed in the frequency domain. Therefore, it is necessary to set up a random roughness model in the time domain.

Generally, there are three methods to build the time-domain road model: the harmonic superposition method, the linear filtered white-noise method, and the numerical simulation for PSD sampling method. The linear filtered white-noise method has the advantage of high precision and a small calculation burden. Therefore, the filtered white-noise method is chosen for setting up the time-domain road model in this section. There are different road inputs to each tire for a three-axle vehicle. Let the front tire road input be $q_1(s)$ and the rear tire road input be $q_1(s)$. Then the rear road input $q_2(s)$ is defined as

$$q_2(S) = q_1(s-b) \tag{2.75}$$

Where s is the distance traveled by the vehicle, and b is the delayed distance. So the transfer function is expressed as

$$H_{12}(n) = \frac{q_2(s)}{q_1(s)} = e^{-\tau s} = e^{-j2\pi nb} \tag{2.76}$$

where $\tau = b/u$ (b is the distance between the front and the rear axles and u is vehicle speed) is the time delay between inputs experienced by the front and the rear wheels. Then one can obtain the power spectral matrix in spatial frequencies as

$$[G_q(n)]_{2\times 2} = G_q(n)\begin{bmatrix} 1 & e^{-j2\pi nb} \\ e^{j2\pi nb} & 1 \end{bmatrix} \tag{2.77}$$

In order to obtain the road input to the rear wheel, a rational function is needed to replace $e^{-\tau s}$ approximately. There are several ways to construct a rational function, such as the Pade's approximation, Bessel functions, Lagrangian polynomial, etc. The Pade's approximation is used to substitute $e^{-\tau s}$ in Eq. (2.77) in this section [20, 21]. Then one can obtain a new transfer function as

$$H_{12}(\omega) = \frac{q_2(\omega)}{q_1(\omega)} = \frac{1-\frac{1}{2}\tau(j\omega)+\frac{1}{12}\tau^2(j\omega)^2}{1+\frac{1}{2}\tau(j\omega)+\frac{1}{12}\tau^2(j\omega)^2} \tag{2.78}$$

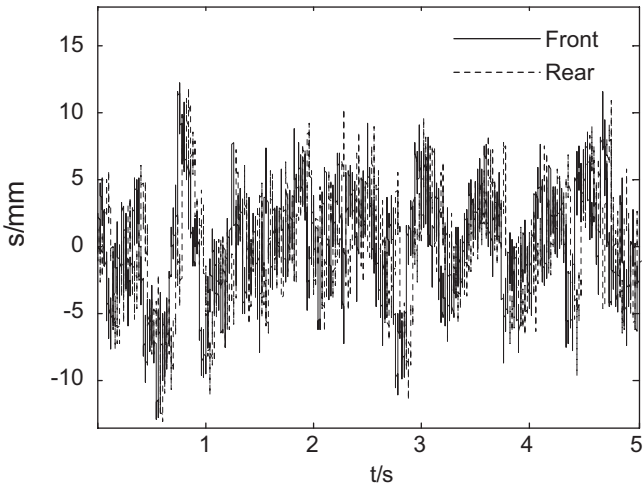

Fig. 2.34 B-class road surfaces. (Reprinted from ref. [19], with kind permission from Science China Press and Springer-Verlag Berlin Heidelberg)

According to control theory, the state equations for Eq. (2.78) can be easily derived as follows

$$\begin{cases} \dot{X}(t) = AX(t) + Bq_1(t) \\ q_2(t) = CX(t) + Dq_1(t) \end{cases} \tag{2.79}$$

where

$$A = \begin{bmatrix} 0 & 1 \\ -\dfrac{12u^2}{b^2} & -\dfrac{6u}{b} \end{bmatrix}, \quad B = \begin{bmatrix} 0 \\ 1 \end{bmatrix}, \quad C = \begin{bmatrix} 0 & -\dfrac{12u}{b} \end{bmatrix}, \quad D = 1;$$

Then the front and the rear wheel inputs of a balanced suspension are obtained for B-class (GB/T 7031—2005/ISO 86) road surfaces, shown in Fig. 2.34.

It can be seen from Fig. 2.35 that the simulated road excitation result is close to theory in the PSD frequency spectrum. The validity of the time-domain input signal is verified.

The schematic diagram for the three road inputs are proposed for a tri-axle vehicle, shown as Fig. 2.36. The road input to the front tire is first simulated using the band-limited white noise module in MATLAB/Simulink. The same principle can be used to simulate another road input to the wheel. Then the intermediate and the rear road inputs are calculated by considering the delay times τ_1 and τ_2. Of course, the rear road input can also be deduced from the intermediate input with a delay time τ_3.

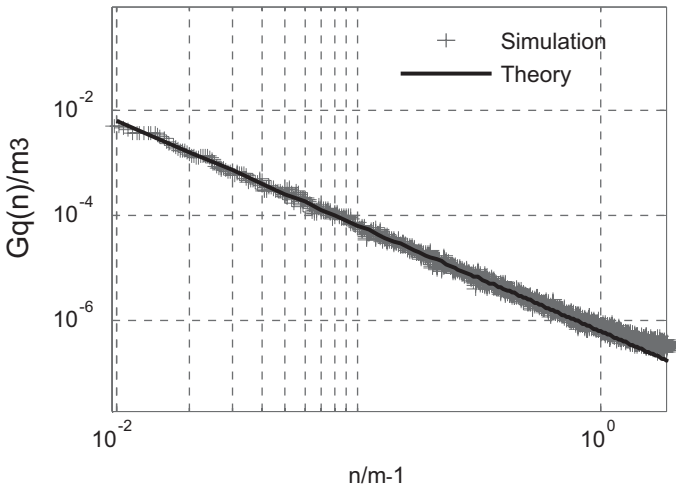

Fig. 2.35 Validation in frequency domain for a B-class road. (Reprinted from ref. [19], with kind permission from Science China Press and Springer-Verlag Berlin Heidelberg)

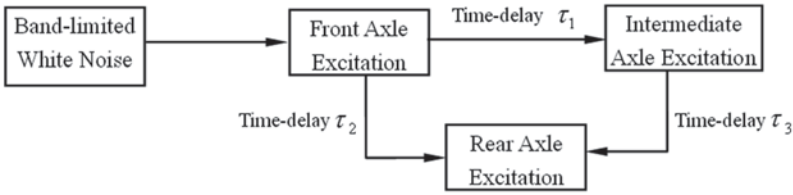

Fig. 2.36 Schematic diagram for the three road inputs. (Reprinted from ref. [19], with kind permission from Science China Press and Springer-Verlag Berlin Heidelberg)

It is very difficult to obtain an approximate analytical solution for a high-dimensional nonlinear system or a nonlinear system under random excitation. Numerical methods are effective ways to solve such problems. Moreover, the specific methods are listed as: the Runge–Kutta method, the central differential method, the Newmark-β method, the Wilson-θ method, and the Houbolt method. The Newmark-β method has an advantage of unconditional stable integration if suitable parameters are chosen. Although the Newmark-β method calculation costs a lot of time, the single-step error $(O(\Delta t^3))$ is smaller than the central differential method's, and has a high precision. Thus, the Newmark-β method is the best choice to solve the above nonlinear model under uneven road excitation.

The main dynamic parameters involved in the vehicle model are shown in Table 2.2.

The cab accelerations and the tire forces are compared based on the FRC and SPC tire models, respectively, as shown in Fig. 2.37, 2.38, 2.39, 2.40 and 2.41.

In Fig. 2.37, it can be observed that the response amplitude of the cab acceleration based on the FRC tire model is much smaller than that based on the SPC tire

Table 2.2 Main parameters of a three-axle vehicle

Parameter	Unit	Symbol	Value	Parameter	Unit	Symbol	Value
Cab mass	kg	m_c	557.5	Front mount damping of cab	N s/m	c_{c1}	3620
Vehicle body mass	kg	m_b	11,523	Rear mount damping of cab	N s/m	c_{c2}	3620
Unsprung mass of steering suspension	kg	m_{tf}	412	Damping of steering suspension	N s/m	c_{tf}	50,636
Balanced rod mass	kg	m_p	177	Damping of balanced suspension	N s/m	c_{sr}	25,320
Unsprung mass of balanced suspneiosn	kg	$m_{tm} = m_{tr}$	676	Damping of steering suspension tire	N.s/m	c_{tf}	3500
Body moment of inertia	kg m^2	$I_{\theta 1}$	55,502	Damping of balanced suspension tire	N s/m	$c_{tm} =$	7000
Balanced suspension moment of inertia	kg m^2	$I_{p\theta}$	351	Distance from front axle to center of vehicle body mass	m	l_1	3.64
Front mount stiffness of cab	N/m	k_{c1}	36,230	Distance from intermediate axle to rear axle	m	l_3	1.3
Rear mount stiffness of cab	N/m	k_{c2}	36,230	Distance from front cab mount to center of cab	m	l_5	1.2
Stiffness of steering suspension	N/m	k_{sr}	251,380	Distance from rear cab mount to center of cab	m	l_6	1.0
Stiffness of balanced suspension	N/m	k_{tf}	206,4000	Distance from center of cab to center of vehicle body mass	m	l_4	2.8

Table 2.2 (continued)

Parameter	Unit	Symbol	Value	Parameter	Unit	Symbol	Value
Stiffness of steering suspension tire	N/m	k_{tf}	1,100,000	Distance from center of balanced rod to center of vehicle body mass	m	l_2	2.71
Stiffness of balanced suspension tire	N/m	$k_{tm} = k_{tr}$	2,200,000				

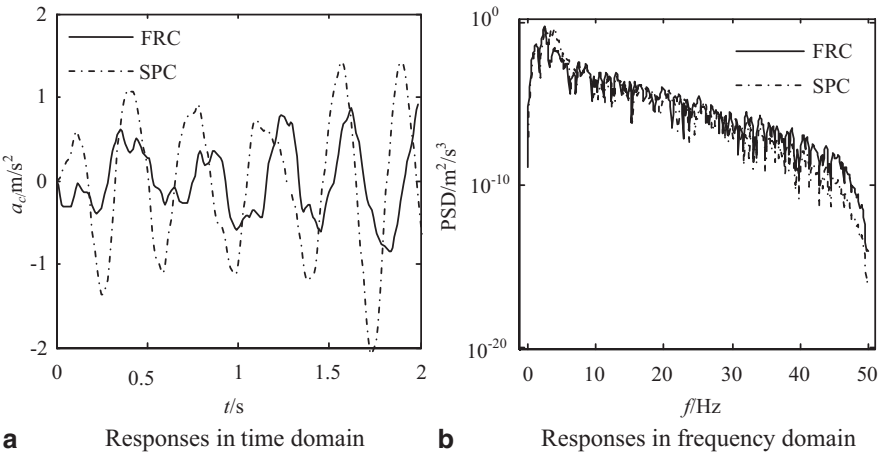

Fig. 2.37 Comparison of cab accelerations with the FRC and SPC models. (Reprinted from ref. [19], with kind permission from Science China Press and Springer-Verlag Berlin Heidelberg)

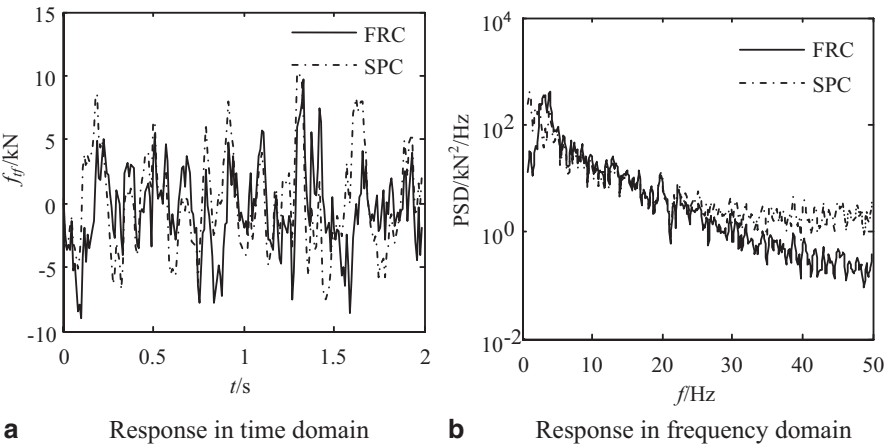

Fig. 2.38 Comparison of front tire forces with the FRC and SPC models. (Reprinted from ref. [19], with kind permission from Science China Press and Springer-Verlag Berlin Heidelberg)

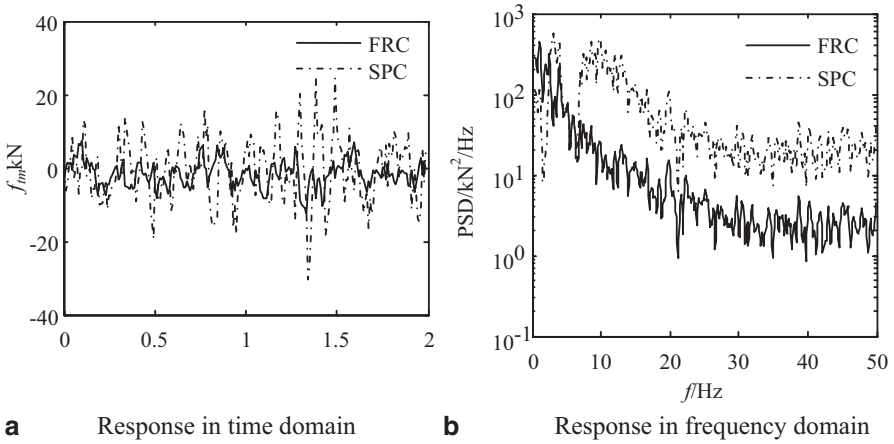

Fig. 2.39 Comparison of intermediate tire forces with the FRC and SPC models. (Reprinted from ref. [19], with kind permission from Science China Press and Springer-Verlag Berlin Heidelberg)

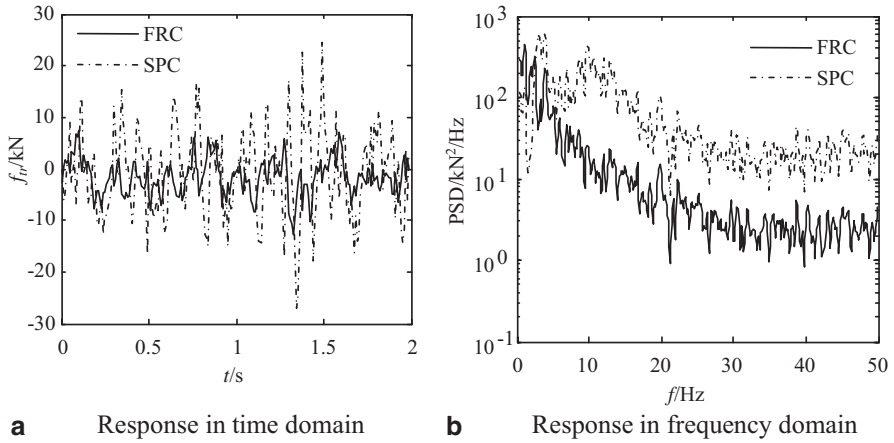

Fig. 2.40 Comparison of the rear tire forces with the FRC and SPC models. (Reprinted from ref. [19], with kind permission from Science China Press and Springer-Verlag Berlin Heidelberg)

model in the time domain. The frequency components show a slight difference and the maximum amplitude of PSD for the FRC model is even bigger than the SPC model's.

Figure 2.38 shows that the response amplitude of the front tire force based on the FRC tire model are slightly smaller than those based on the SPC model. The FRC tire model reduces the amplitude of the PSD significantly at the high-frequency range.

As can be seen from Figs. 2.39 and 2.40, the response amplitudes of the intermediate and rear tire forces based on the SPC tire model are much larger than those

based on the FRC model. The amplitudes of the PSD at the medium- and high-frequency domains are all suppressed by the FRC tire model.

In short, the response amplitude of cab acceleration based on the FRC tire model is much smaller than that based on the SPC tire model in the time domain. In addition, the amplitudes of the PSD for the tire dynamic load at the medium- and high-frequency domains are all suppressed by the FRC tire model. The traditional SPC tire model may bring a large error. The FRC model filters out vibration components of the tire forces at medium and high frequencies and reflects the actual interaction process of vehicle–road.

2.4 Chapter Summary

1. The detail testing scheme of the shock absorber is proposed and the damping characteristics are tested under both sinusoidal and random displacement excitation. The testing data under different excitation frequencies and amplitudes are analyzed. Test results show that the shock absorber has typical features of nonlinearity, nonsymmetry, and hysteresis. In order to satisfy the vehicle dynamics simulation, the nonlinear Besinger model is chosen to describe the shock absorber's nonlinear characteristics. The LSM is utilized to identify seven parameters of the Besinger model based on the experiment results.
2. When the leaf spring is loaded and unloaded repeatedly in vertical direction, the leaf spring will slide longitudinally, generating a viscous friction between the leafs. So when it is loaded and unloaded, the envelope curves of the leaf spring stiffness characteristics are basically two straight lines with different slopes, showing the hysteretic characteristic. The nonlinear model of a leaf spring is established by fitting the experimental results and identifying the parameters, and can provide a reliable and effective parameter source for vehicle dynamics research.
3. The dynamic tire force generated by a heavy vehicle has typical low-frequency features. The energy is concentrated primarily in the range of $0 \sim 4$ Hz. In order to reduce the dynamic tire force and improve pavement service life, small suspension stiffness should be first considered under the condition that the suspension bearing capacity and ride comfort can be completely guaranteed. The increased suspension damping can reduce the dynamic tire force, which is a benefit to pavement service life.
4. The response amplitude of the cab acceleration with the FRC tire model is much smaller than that with the SPC tire model in the time domain. In addition, the amplitudes of PSD for tire dynamic load at the medium- and high-frequency domains are all suppressed by the FRC tire model. The traditional SPC tire model may bring a larger error. The FRC model filters out vibration components of tire forces at medium and high frequencies and reflects the actual interaction process of vehicle–road.

References

1. Dave C, Yu F. Vehicle dynamics and control. China Communications Press; 2004.
2. Erich H. Commercial vehicle technology (in Chinese). Beijing: China Machine Press; 2009.
3. Lu ZH, Li SM. Simulation techniques for nonlinear dynamic characteristics of telescopic hydraulic dampers. J Tsinghua Univ Sci Technol. 2002;42(11):1532–6.
4. Segel L, Lang HH. The mechanics of automotive hydraulic dampers at high stroking frequencies. Veh Syst Dyn. 1981;10(2, 3):82–5.
5. Lang HH. A study of the characteristics of automotive hydraulic dampers at high stroking frequencies. Michigan: University of Michigan; 1977.
6. Eyres RD, Champneys AR, Lieven NAJ. Modelling and dynamic response of a damper with relief valve. Nonlinear Dyn. 2005;40(2):119–47.
7. Adrian S. The influence of damper properties on vehicle dynamic behavior. Society of Automotive Engineers paper: 2002-01-0319; 2002.
8. Šika Z, Bauma V, Valášek M, et al. Identification of phenomenological shock absorber model using neuro-fuzzy. Method Bull Appl Mech. 2008;4(15):88–91.
9. Jia JH, Du JY, Wang Y, et al. Design method for fluid viscous dampers. Arch Appl Mech. 2008;78(9):737–46.
10. Xabier CA, Jordi V, Joan S, et al. A parametric damper model validated on a track. Heavy Veh Syst. 2006;13(3):145–62.
11. Lu YJ, Li SH, Chen N. Research on damping characteristics of shock absorber for heavy vehicle. Res J Appl Sci Eng Technol. 2013;5(3):842–7.
12. Taro countryside. Optimal control and application of random vibration. Beijing: Aerospace Press; 1984.
13. Fancher PS, Ervin RD, MacAdam CC, et al. Measurement and representation of the mechanical properties of truck leaf springs. Warrendale: Technical Paper Series 800905, Society of Automotive Engineers; 1980.
14. Qin PY, Dentel G, Mesh M. Multi-leaf spring and hotchkiss suspension CAE simulation. Haffner: ABAQUS Users' Conference; 2002.
15. Mahmood MS, Davood R. Analysis and optimization of a composite leaf spring. Compos Struct. 2003;60(3):317–25.
16. Ding NG, Ma JJ. Finite element analysis on the hysteresis behavior of a leaf spring. Automot Eng. 2003;25(1):12–4.
17. Lippmann SA, Piccin WA, Baker TP. Enveloping characteristics of truck tires, a laboratory evaluation. Society of Automotive Engineer paper: 650184; 1965.
18. Guo KH. Tire roller contact model for simulation of vehicle vibration input. Society of Automotive Engineer paper: 932008; 1993.
19. Lu YJ, Yang SP, Li SH. Research on dynamics of a class of heavy vehicle-tire-road coupling system. Sci China-technol Sci. 2011;54(8):2054–63.
20. Xu XY, Li JK, Xu GL. Padé approximation introduction. Shanghai: Shanghai Science and Technology Press; 1990.
21. Vajta M. Some remarks on Padé-approximations. Veszprém: 3rd TEMPUS INTCOM Symposium; 2000.

Chapter 3
Dynamic Analysis of a Heavy Vehicle Using Function Virtual Prototype

There are several models used to study vehicle dynamics, such as the lumped parameter model (as shown in Chap. 2 of this book) and the digital simulation model. With the rapid development of computer technology, the function virtual prototype (FVP) technology has been widely utilized to study vehicle riding comfort and road friendliness. In this chapter, the nonlinear virtual prototype model of a heavy vehicle (DFL1250A9) is set up, and an orthogonal optimization program for the virtual heavy vehicle model is presented to analyze the effect of vehicle parameters on riding comfort and road friendliness according to the design of experiment (DOE) method. Through a reasonable choice for the best objects, factors, level and experiment combination, a best matching program of experiment factors could be obtained and the goal of riding comfort and road friendliness could be accomplished. Finally, two kinds of adjustable damper control system are established within MATLAB/Simulink environment. The ADAMS/Matlab cosimulation of the full vehicle system is completed to show that the MR damper under semiactive "on–off" control can minimize seat vertical acceleration, suspension deflection, and dynamic tire force compared with a passive suspension. The semiactive suspension can improve vehicle dynamical performance, weaken vehicle body vibration, and increase riding comfort.

3.1 Modeling of Vehicle Suspension, Tire, and Road

The multibody system (MBS) dynamics is one of the most important theoretical achievements of mechanics. With the development of the theory, corresponding commercial software packages, such as ADAMS [1], have been developed and are conveniently used in modeling and simulation. In the automotive industry, vehicle dynamic modeling and simulation have already been widely used in vehicle performance studies, such as riding, handling, and stability. A complicated heavy vehicle model, including the suspension structures and parameters in more detail, can be conveniently built with the help of the software tools. The FVP technology has

S. Yang et al., *Dynamics of Vehicle-Road Coupled System,*
DOI 10.1007/978-3-662-45957-7_3

been widely applied in the vehicle industry [2, 3]. A moving vehicle is a complex nonlinear vibration system with multiple DOF, and some proper assumptions and simplifications are given, as follows:

1. Internal friction and damping in hinges, except for rotational hinges and prismatic joint, are neglected.
2. In addition to bushings and springs, vehicle parts and components are regarded as rigid bodies.
3. The engine's inner structure is neglected, and only the output rotational speed and torque are included.

The front suspension of a heavy vehicle is composed of the front axle, leaf springs (eight leaves), a shock absorber, a steering knuckle, tie rods and so on. The shock absorber is a major damping element in a suspension system, which is mainly used to attenuate vibration of the vehicle body. The damping force between the two rigid bodies is expressed by the following equation:

$$F_d = f_d(v) \tag{3.1}$$

where f_d is a nonlinear interpolation spline function and v is the relative acceleration between the two rigid bodies. The damping force is a function of the instantaneous relative velocity of the two components. The shock absorber (SACHS F088) of the front suspension was tested on an HT-911 dynamic material testing system. The force–velocity characteristic curve of the shock absorber is shown in Fig. 3.1 [6].

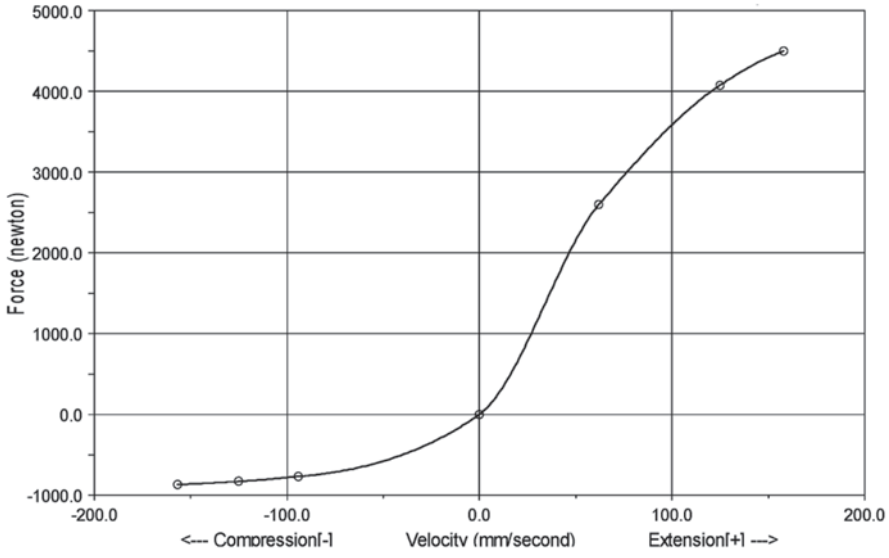

Fig. 3.1 Nonlinear characteristic curve of a shock absorber. Reprinted from ref. [3], Copyright 2010, with permission from Elsevier

The leaf springs for the suspension are built in a module of ADAMS. Each leaf is made up of a series of parts connected with discrete beams. The leaves are connected with bushings at the leaf seat. The beam forces and moments are calculated as follows:

$$\begin{bmatrix} F_x \\ F_y \\ F_z \\ T_x \\ T_y \\ T_z \end{bmatrix} = -\begin{bmatrix} K_{11} & 0 & 0 & 0 & 0 & 0 \\ 0 & K_{22} & 0 & 0 & 0 & K_{26} \\ 0 & 0 & K_{33} & 0 & K_{35} & 0 \\ 0 & 0 & 0 & K_{44} & 0 & 0 \\ 0 & 0 & K_{53} & 0 & K_{55} & 0 \\ 0 & K_{62} & 0 & 0 & 0 & K_{66} \end{bmatrix} \begin{bmatrix} x-l \\ y \\ z \\ a \\ b \\ c \end{bmatrix} - \begin{bmatrix} C_{11} & C_{21} & C_{31} & C_{41} & C_{51} & C_{61} \\ C_{21} & C_{22} & C_{32} & C_{42} & C_{52} & C_{62} \\ C_{31} & C_{32} & C_{33} & C_{43} & C_{53} & C_{63} \\ C_{41} & C_{42} & C_{43} & C_{44} & C_{54} & C_{64} \\ C_{51} & C_{52} & C_{53} & C_{54} & C_{55} & C_{65} \\ C_{61} & C_{62} & C_{63} & C_{64} & C_{65} & C_{66} \end{bmatrix} \begin{bmatrix} V_x \\ V_y \\ V_z \\ w_x \\ w_y \\ w_z \end{bmatrix} \tag{3.2}$$

where F and T are the force and the moment, x, y, z, a, b, c, V_x, V_y, V_z, w_x, w_y, and w_z are the relative displacement, angle, velocity, and angular velocity between the points I and J, respectively, K is and the leaf spring stiffness, C is the damping coefficient, and l is the length of the beam. Given the polar moment of inertia along the x-axis, moment of inertia along the y–y and z–z central axes, cross-sectional area, Young's elastic modulus, and other parameters, the leaf spring forces and moments of each connection portion can be determined.

The leaf spring of the front suspension is established according to the structure of Fig. 3.2. The external dimensions of the front leaf spring are $1600 \times 90 \times 25$ mm.

The front steering suspension is assembled with the shock absorbers, leaf spring, steering knuckles, tie rod tires, and so on, as shown in Fig. 3.3.

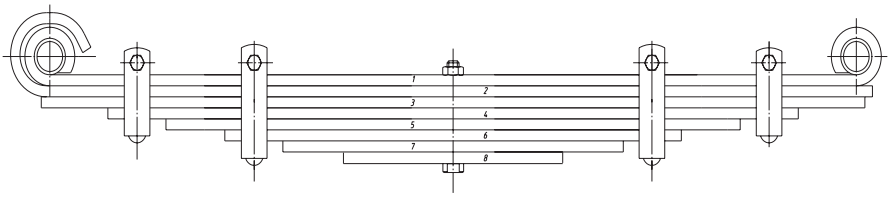

Fig. 3.2 Leaf spring of the front suspension. Reprinted from ref. [3], Copyright 2010, with permission from Elsevier

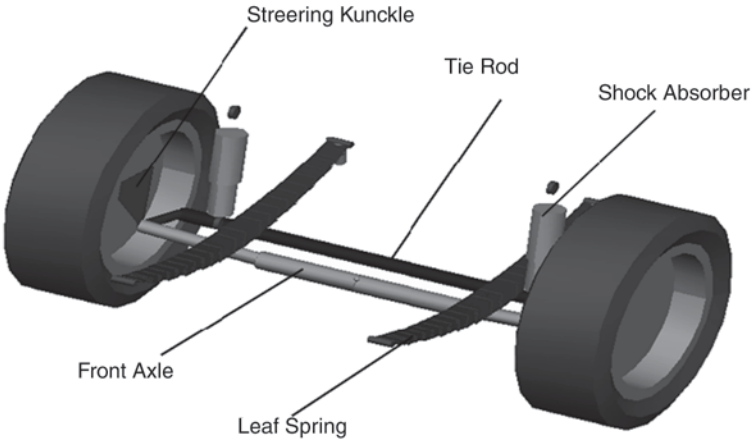

Fig. 3.3 Front steering suspension. Reprinted from ref. [3], Copyright 2010, with permission from Elsevier

A steering subsystem is established to ensure the correct dynamics simulation of the full vehicle model. It is the combination of the steering wheel, the column shaft, the knuckle arm, etc. as shown in Fig. 3.4.

The rear suspension of the heavy vehicle is a nonindependent balanced suspension, which includes the intermediate axle, rear axle, lateral rod, longitudinal road, and leaf spring. The external dimensions of the rear leaf spring are $1720 \times 90 \times 15$ mm, as shown in Fig. 3.5.

The balanced suspension utilizes the "level" principle to distribute the load equally and to reduce the effect of road irregularities. It is difficult to model the guiding mechanism due to the complicated spatial geometric relationship in the

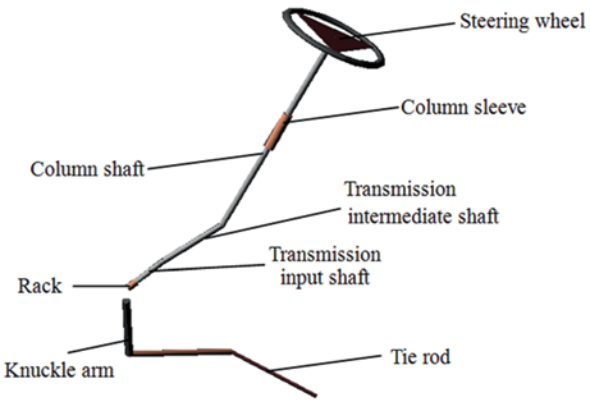

Fig. 3.4 Steering subsystem. Reprinted from ref. [3], Copyright 2010, with permission from Elsevier

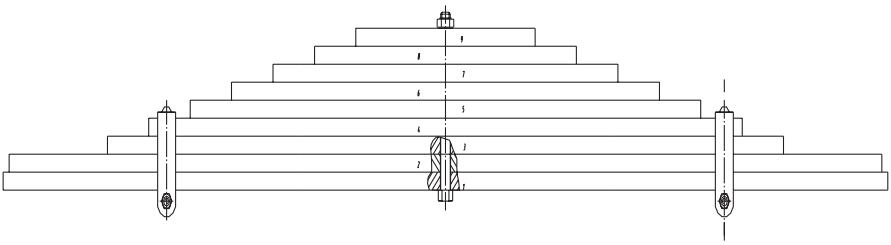

Fig. 3.5 Leaf spring of a balanced suspension. Reprinted from ref. [3], Copyright 2010, with permission from Elsevier

traditional modeling method. The multibody dynamics modeling provides an effective method to solve this problem. The balanced suspension includes tandem driving axles (intermediate axle and rear axle), leaf springs (nine leaves), lateral rods, and longitudinal rods. These templates are also built according to 2D drawings, as shown in Fig. 3.6.

The tire is a very crucial component of the whole vehicle model. There are five general tire models used for the dynamics simulation of a multibody vehicle model [8]: the Fiala model, the University of Arizona (UA) model, the Smithers model, the DELET model and the model proposed in this book. First, the tire is simulated as an elastic ring, which is called the Fiala Tire (FT) model in this book. The FT model is a physical tire model in which the tire carcass is modeled as a beam on an elastic

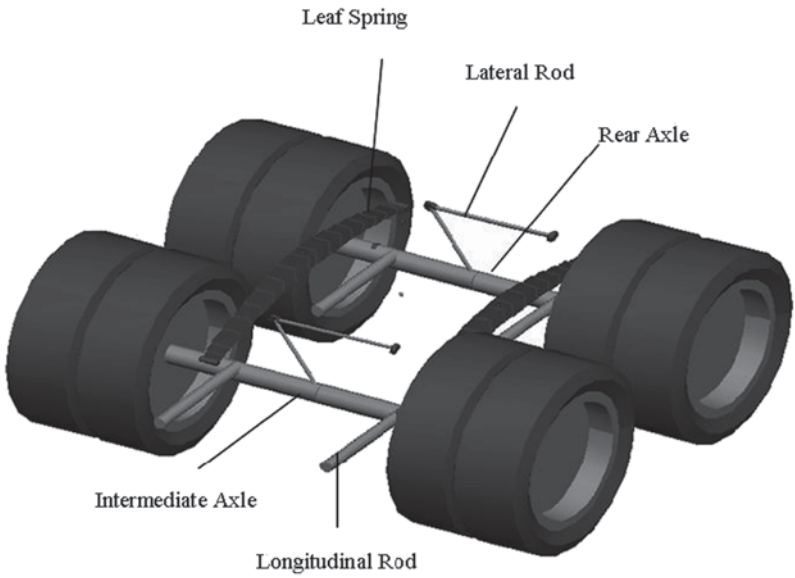

Fig. 3.6 Tandem balanced suspension system. Reprinted from ref. [3], Copyright 2010, with permission from Elsevier

Table 3.1 Main parameters of the tire. (11.00R20)

Parameter	Unit	Value
Free rolling radius	Mm	507
Vertical stiffness	N/mm	1100
Vertical damping	N·s/mm	3.5
Coefficient of rolling resistance moment	Mm	0.015
Cornering stiffness	N/rad	800
Camber stiffness	N/rad	0
Friction coefficient of pure rolling		0.9
Friction coefficient of pure sliding		1.0

foundation in the lateral direction. Although the tire belt ply or buffer layer is simplified as a section beam acted on under a concentrated load, it can well describe the normal, longitudinal, the lateral forces between the tire and the road, with regards to vehicle ride comfort and road damage.

The dimensionless analytical equation of the FT model is

$$\begin{cases} \dfrac{P_y}{P_z \cdot \mu} = \phi - \dfrac{1}{3}\phi^2 + \dfrac{1}{27}\phi^3 \\ \dfrac{3M_a}{P_z \cdot \mu \cdot a} = \dfrac{\phi}{2} - \dfrac{\phi^2}{2} + \dfrac{1}{6}\phi^3 - \dfrac{1}{54}\phi^4 \end{cases} \tag{3.3}$$

where P_y is the lateral force of the tire, P_z is the vertical loading, μ is the tire adhesion coefficient, M_a is the aligning torque, a is the length of the tire footprint, and ϕ is the dimensionless sideslip angle. The sideslip angle can be expressed as

$$\phi = \frac{Ktg\beta}{P_z \cdot \mu} \tag{3.4}$$

where β is the slip angle and K is the cornering stiffness. The types of front and rear tires are both 11.00R20. The parameters are listed in Table 3.1.

The road is not ideally flat and its surface is a mixture of waves with differing wavelength and amplitude. It has been established that most road surface irregularities are normally distributed and may be accurately modeled by a stationary random process. Thus, we often describe road surfaces with a power spectral density (PSD) in a frequency domain. It is difficult to create a road model which not only meets tire requirements but also conforms to stochastic distribution characteristics. At present, there are generally three ways to simulate the road spectrum: harmonic superposition, integral white noise, and noise-shaping filter method. In this section, the random sinusoidal (harmonic wave) superposition method is adopted, which is the method of discrete numerical simulation. According to standard GB/T 7031-2005/ISO 8608, the PSD of road surface roughness can be represented as

$$\begin{aligned} G_d(n) &= G_d(n_0)\left(\frac{n}{n_0}\right)^{-w} \\ G_d(n_0) &= \left(\lim_{\Delta n \to 0} \frac{1}{\Delta n} |X(n)|^2\right)\Big|_{n=n_0} \end{aligned} \quad n > 0, \tag{3.5}$$

where n_0 is the reference spatial frequency, n is the spatial frequency, $G_d(n_0)$ is the road roughness coefficient (the value of the power spectrum density when the reference spatial frequency is n_0), $X(n)$ is the amplitude of the road surface roughness in the spatial domain, and w is the frequency index which depends on the frequency structure of the road spectrum. The w index is found within the range of $1.75 < w < 2.25$, with $w=2$ being a good average value. In a certain spatial frequency range, $n_1 < n < n_2$, the displacement PSD of road roughness is $G_d(n)$. According to the expansion properties of the stationary stochastic process, the variance of road roughness is described by

$$\sigma_Z^2 = \int_{n_1}^{n_2} G_d(n) dn \tag{3.6}$$

The spatial frequency range, $n_1 < n < n_2$, is divided into several uniform intervals which have a width of Δn_i. The power density $G_d(n)$ in every small interval is substituted by $G_d(n_{\text{mid}-i})$, where $n_{\text{mid}-i} (i = 1, 2, \ldots, n)$ is the center frequency of the interval i. Based on such a discrete approximation method, Eq. (3.6) is expressed as

$$\sigma_Z^2 \approx \sum_{i=1}^{n} G_d(n_{\text{mid}-i}) \cdot \Delta n_i \tag{3.7}$$

In order to describe the road model, a sinusoidal function is constructed as follows:

$$\sqrt{2G_d(n_{\text{mid}-i}) \cdot \Delta n_i} \cdot \sin(2\pi n_{\text{mid}-i} x + \theta_i) \tag{3.8}$$

The standard deviation of this function is $\sqrt{G_d(n_{\text{mid}-i}) \cdot \Delta n_i}$ in every small interval. After superposition, the road surface in two-dimensional (2D) space is

$$q(x) = \sum_{i=1}^{n} \sqrt{2G_d(n_{\text{mid}-i}) \cdot \Delta n_i} \cdot \sin(2\pi n_{\text{mid}-i} x + \theta_i) \tag{3.9}$$

where θ is the random phase angle uniformly distributed from 0 to 2π, x is the longitudinal coordinate of a road, and $q(x)$ is the vertical roughness of the road**.** The surface of a B-class road in 2D space and the corresponding 3D virtual road model are shown in Figs. 3.7 and 3.8, respectively. The 3D virtual road model's dimension is 1000 m × 22.5 m and the vertical roughness scale is kept equal with the longitudinal-coordinate scale in Fig. 3.8.

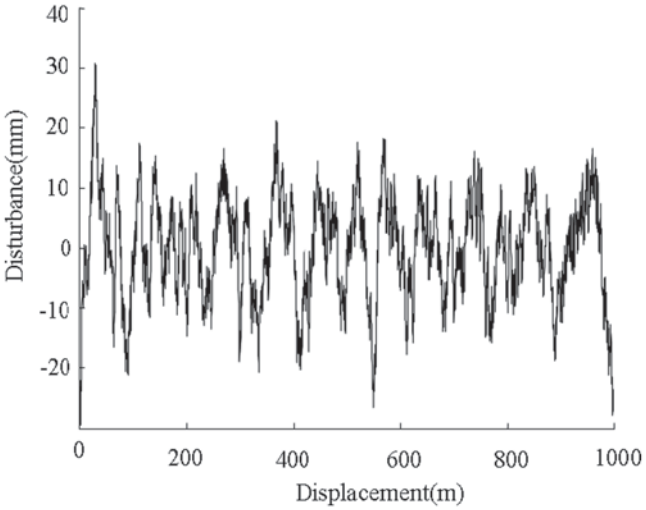

Fig. 3.7 Surface profile of a B-class road. Reprinted from ref. [3], Copyright 2010, with permission from Elsevier

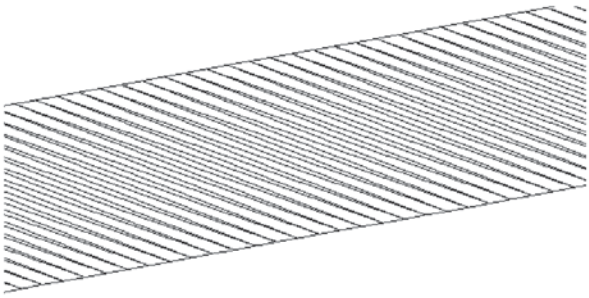

Fig. 3.8 Three-dimensional (3D) virtual road. Reprinted from ref. [3], Copyright 2010, with permission from Elsevier

A full-vehicle model includes a locomotive cab, a chassis frame, a carriage, an engine, an oil tank, and their key subsystems. After a precise definition of the spatial locations of the subsystems, the vehicle model is established through the input and the output communication device. The integration process of a full-vehicle model is shown in Fig. 3.9.

The integrated model can be more accurate and truly reflect the actual fine structure of vehicle systems. Some quasi-static equilibrium simulations are done and implemented to check for redundant constraints. The whole 3D vehicle model is shown in Fig. 3.10. The main parameters of the full vehicle model are listed as follows. The full vehicle mass is 24,900 kg, the axle bases are 5700 and 1300 mm, the wheel bases are 1986/1860/1860 mm, the centric height is 862 mm, the camber angle is 1°, the kingpin inclination is 7°, the toe-in angle is 1°52′.

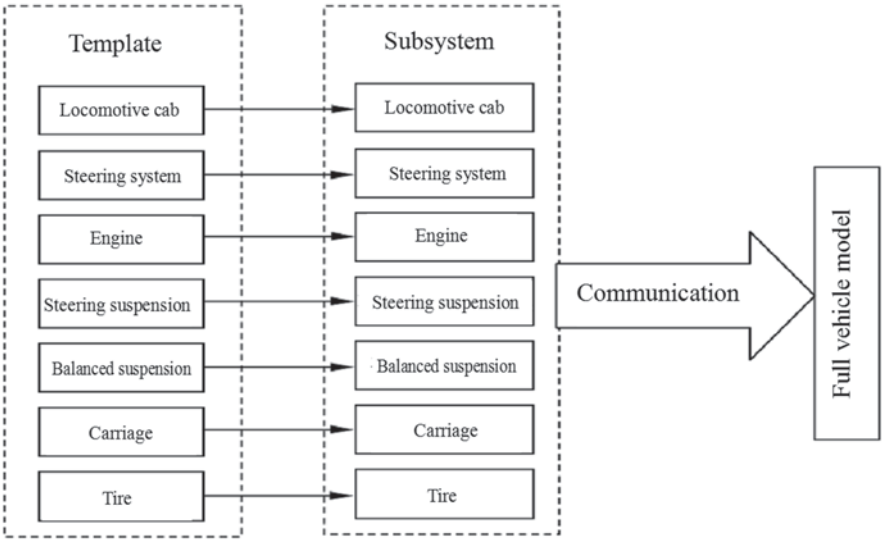

Fig. 3.9 The integration process of a full vehicle model. Reprinted from ref. [3], Copyright 2010, with permission from Elsevier

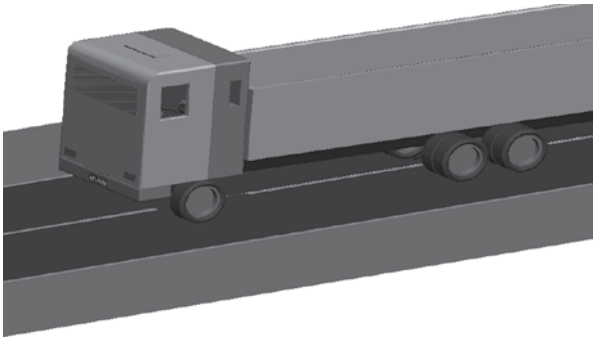

Fig. 3.10 Three-dimensional (3D) multibody vehicle model. Reprinted from ref. [3], Copyright 2010, with permission from Elsevier

3.2 Orthogonal Optimization of a Heavy Vehicle

It is not enough to evaluate a single parameter's (vehicle geometric position, suspension stiffness, and damping characteristics) effect on vehicle performance. According to whether a mathematical model exists, *s*, optimization methods for a target can be divided into two categories: (1) computable optimization, whose mathematical model is known and can be numerically solved directly; (2) experimental optimization, whose mathematical model is unknown and cannot be solved directly—in this case, an optimal parameter combination can be obtained based on experimental

results. DOE for optimization is a discrete optimization method proposed by Fisher. The parametric modeling is the most advantageous for the multibody vehicle model. In order to figure out which vehicle parameter has the most significant impact on vehicle performance and which parameters result in the extremities, several simulation trials of matching parameters should be done. Furthermore, since the vehicle multibody model contains a lot of nonlinear parameters, it is suitable to utilize the experimental optimization method to improve the vehicle ride comfort and road friendliness. The orthogonal experimental design method was first proposed by Tiankou Hongyi from Japan, and is called the International Standard Orthogonal Test. This method has been widely used in detection, earthquake prediction, and product design because of its effective, robust, high-quality characteristics [4, 8].

In this section, an orthogonal optimization program for the multibody heavy vehicle model is presented to analyze the effect of vehicle parameters on ride comfort and road friendliness according to the DOE method. Through a reasonable choice of the best objects, factors, level, and experiment combination, a best matching program of experimental factors can be obtained and the goal of ride comfort and road friendliness can be accomplished.

1. Orthogonal program

The orthogonal DOE method makes use of an orthogonal table to arrange the experiments and analyze the multifactor effects on the objective. The basic characteristic of this method is that full-scale testing is replaced by a representative sample of possible parameter-value combination in the digital experiment. The effect of every factor (system parameter) on the objects can be analyzed and the best matching of levels can also be selected through a full-scale experiment method in detail. But the full-scale experiments have so many combinations that they are hard to accomplish due to the heavy workload. If the main purpose of the experiment is to seek the optimal combination of levels, the orthogonal table can be used to arrange for fewer experiments. The focus of this study on the interaction between the vehicle and the road—the acceleration of the centers of mass of the vehicle and driver seat are chosen to evaluate ride comfort, while the tire dynamic force is used to evaluate road friendliness. So in this orthogonal experiment, the objects are established as the vertical acceleration of the driver seat (Object1), the vertical acceleration of the vehicle's center of mass (Object2), the front tire force (Object3), the intermediate tire force (Object4), and the rear tire force (Object5).

Shock absorbers and leaf springs have a significant impact on vehicle performance and road friendliness. Thus, the suspension's and the cab suspension's damping and stiffness coefficients are selected as the experiment factors. The front steering suspension and the balanced suspension of a heavy vehicle is a nondependent suspension and the left and the right shock absorbers and leaf springs are completely symmetrical. So in this orthogonal experiment, the experiment factors are selected as the front suspension damping (Factor A), the front suspension stiffness (Factor B), the balanced damping (Factor C), the balanced suspension stiffness (Factor D), and the driver seat damping (Factor E). After the selection of the experiment factors, the range of levels for the factors needs to be determined. The nonlinearity of

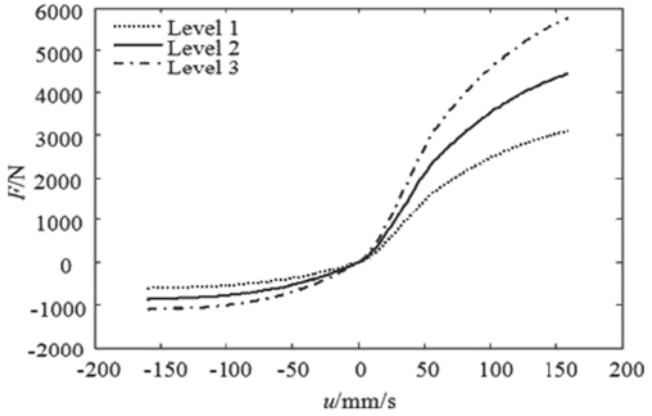

Fig. 3.11 Damping curve of the front suspension. Reprinted from ref. [7], Copyright 2013, with kind permission from CESER Publications

the multibody vehicle model and the comprehensive effect of factors on the objects are taken into account. For example, the three-level curve of the front suspension damping and leaf spring stiffness of a balanced suspension are shown in Figs. 3.11 and 3.12. Each level value of vehicle parameter is 0.7, 1.0, and 1.3 times of the initial value (described in Chap. 2) [7].

According to the established experiment objects, experiment factors, experiment levels, a reasonable orthogonal table is formulated and the experiment matrix is constructed, as the orthogonal table of $L_{27}(3^5)$, listed in Table 3.2.

The orthogonal experiment program is implemented by the flow chart in Fig. 3.13. Through a reasonable choice for the best objects, factors, level and

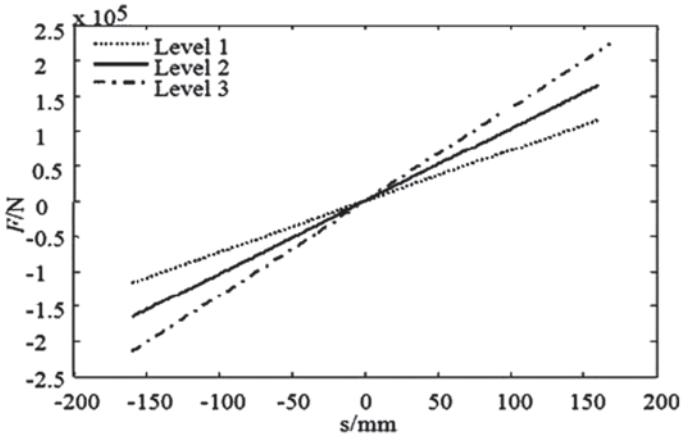

Fig. 3.12 Stiffness curve of a balanced suspension. Reprinted from ref. [7], Copyright 2013, with kind permission from CESER Publications

Table 3.2 $L_{27}(3^5)$ Orthogonal table

Experiment Number	Factor and level				
	A	B	C	D	E
T1	1	1	1	1	1
T2	1	1	2	2	2
T3	1	1	3	3	3
T4	1	2	1	2	2
T5	1	2	2	3	3
T6	1	2	3	1	1
T7	1	3	1	3	3
T8	1	3	2	1	1
T9	1	3	3	2	2
T10	2	1	1	2	3
T11	2	1	2	3	1
T12	2	1	3	1	2
T13	2	2	1	3	1
T14	2	2	2	1	2
T15	2	2	3	2	3
T16	2	3	1	1	2
T17	2	3	2	2	3
T18	2	3	3	3	1
T19	3	1	1	3	2
T20	3	1	2	1	3
T21	3	1	3	2	1
T22	3	2	1	1	3
T23	3	2	2	2	1
T24	3	2	3	3	2
T25	3	3	1	2	1
T26	3	3	2	3	2
T27	3	3	3	1	3

experiment combination, a best matching program of experiment factors can be obtained and the goal of ride comfort and road friendliness can be accomplished.

2. Results of the orthogonal experiment

According to the orthogonal experiment $L_{27}(3^5)$, 27 sets of orthogonal experiments for the parameterized model of a heavy vehicle were done and the results are shown in Table 3.3.

Range analysis is commonly used to study the orthogonal experiment, which can show the optimization results of the orthogonal experiment intuitively. In order to analyze the effect of different levels of experiment factors on vehicle ride comfort

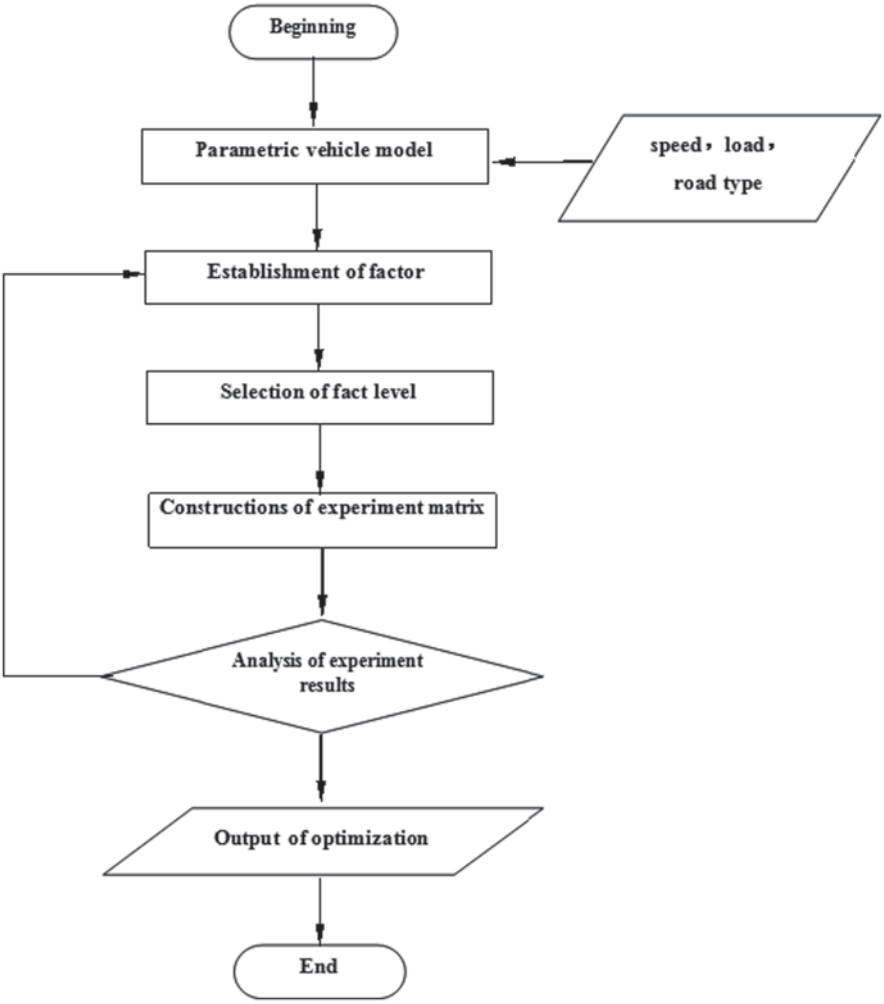

Fig. 3.13 Flow chart of the orthogonal experiment. Reprinted from ref. [7], Copyright 2013, with kind permission from CESER Publications

and road friendliness, the range analysis and judgment of the results of the orthogonal experiment are conducted through a specific process as shown in Fig. 3.14.

The expression for the range analysis is

$$R_j = \max\left\{\overline{y}_{ji}\right\} - \min\left\{\overline{y}_{ji}\right\}, i = 1,2,3 \tag{3.10}$$

where $\overline{y}_{ji}$ is the mean value of the sum of evaluation indexes of all levels for each factor. R_j is defined as the range between the maximum and the minimum value of $\overline{y}_{ji}$, which is used to evaluate the importance on the objects. So the best level

Table 3.3 Orthogonal simulation experiment results

Experiment number	Optimal object				
	Driver seat acceleration/m/s2	Vehicle body acceleration/m/s2	Front tire force/N	Intermediate tire force/*N*	Rear tire force/N
T1	1.2446	1.0153	26,143.8	35,559.9	35,157.4
T2	2.1266	0.9661	26,385.3	34,556.9	34,478.7
T3	1.0682	0.9831	26,310.4	33,890.6	33,785.9
T4	1.6856	1.0672	26,267.6	35,580.2	35,153
T5	1.127	0.9642	26,433.4	34,584.1	34,468.2
T6	1.2348	0.9749	26,365.6	33,867.1	33,845.3
T7	1.3622	0.9984	26,316.6	35,506.5	35,227.5
T8	1.0584	0.9319	26,418.7	34,534.2	34,547.4
T9	1.0486	0.8931	26,374.7	33,872.4	33,825.2
T10	2.5872	1.1432	26,145.7	35,626.6	35,135.5
T11	1.176	1.0006	26,461.2	34,558.8	34,445.7
T12	1.0682	0.9438	26,347.2	33,852.5	33,847.9
T13	1.4994	0.9718	26,237.2	35,588.9	35,109.5
T14	1.0584	0.9504	26,411.3	34,626.9	34,469.1
T15	1.0976	0.9383	26,327.7	33,838.7	33,788.9
T16	1.715	0.9932	26,218.6	35,602.7	35,192.6
T17	1.0878	0.9451	26,496.9	34,547.4	34,507.7
T18	1.1662	0.9641	26,373.8	33,896.9	33,788
T19	1.3818	0.9968	26,194.5	35,621.5	35,142.6
T20	1.078	0.9773	26,450.1	34,596.9	34,438.7
T21	1.1466	0.9742	26,355.5	33,887.9	33,785.4
T22	1.6954	1.0241	26,257.1	35,570.4	35,134.7
T23	1.7542	0.9622	26,415.1	34,542.5	34,465.2
T24	1.0976	0.9873	26,245.4	33,839.5	33,793.8
T25	2.548	1.046	26,264.4	35,591.1	35,216.1
T26	1.0682	0.9436	26,447.1	34,544.4	34,454.5
T27	1.1172	0.9586	26,305.6	33,869.2	33,933.7

for each factor could be achieved when $\overline{y}_{ji}$ is the smallest and the larger R_j means greater significance of the object. The aims of the interaction study of the vehicles and the road is to reduce the driver acceleration, vehicle center of mass acceleration and the dynamic tire forces upon the road surface.

The range analysis of the driver's acceleration is listed in Table 3.4. Figure 3.15 is the comparison chart of each experiment factor's effect on the driver seat acceleration. The degree of importance of the suspension parameters on the first object (driver seat acceleration) is listed in descending order: balanced suspension stiffness (Factor D), front suspension damping (Factor A), driver seat damping (Factor E), front suspension stiffness (Factor B), and balanced suspension damping (Factor C).

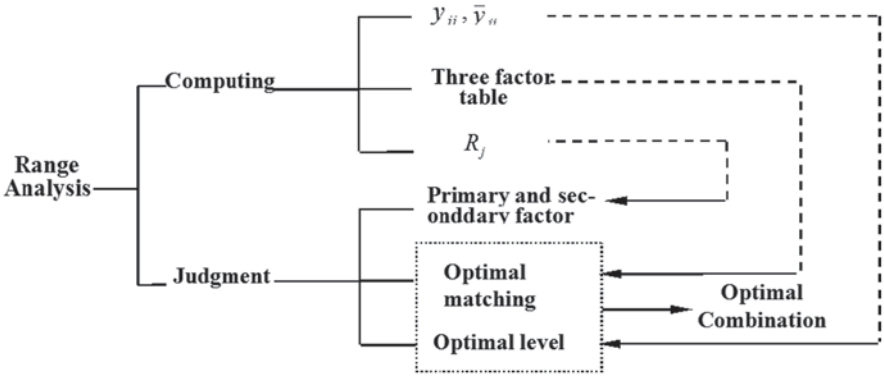

Fig. 3.14 Range analysis diagram. Reprinted from ref. [7], Copyright 2013, with kind permission from CESER Publications

Table 3.4 Range analysis of the driver's acceleration

Range	Factor				
	A	*B*	*C*	*D*	*E*
y_{j1}	11.2700	11.9560	12.8772	15.719	12.4852
y_{j2}	15.0822	12.4558	12.2500	11.5346	13.4358
y_{j3}	10.9466	12.8870	12.1716	10.0450	11.3778
$\bar{y}_{j1}$	1.2522	1.3284	1.4308	1.7466	1.3872
$\bar{y}_{j2}$	1.6758	1.3839	1.3611	1.2816	1.4929
$\bar{y}_{j3}$	1.2163	1.4319	1.3542	1.1161	1.2642
R_j	0.4595	0.1035	0.0766	0.6305	0.2348

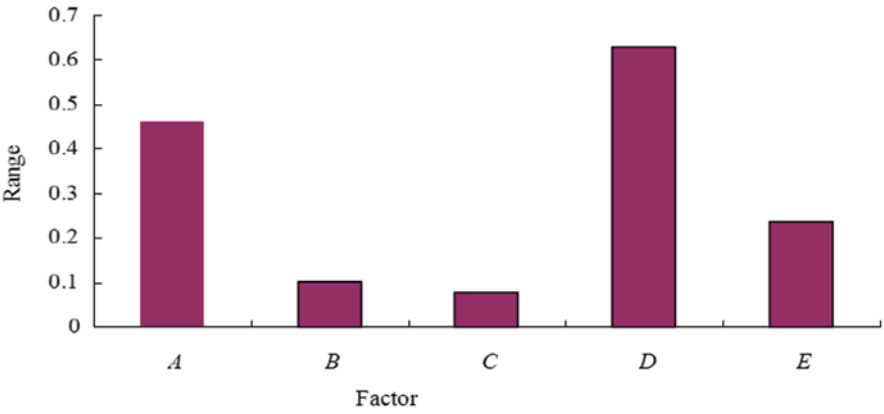

Fig. 3.15 The effect of experiment factors on driver acceleration. Reprinted from ref. [7], Copyright 2013, with kind permission from CESER Publications

Table 3.5 Range analysis of the vehicle body acceleration

Range	Factor				
	A	*B*	*C*	*D*	*E*
y_{j1}	8.7695	8.7942	9.0013	9.2560	8.8479
y_{j2}	8.9354	8.8505	8.8151	8.6414	8.8821
y_{j3}	8.8099	8.8701	8.6740	8.6174	8.7848
$\overline{y}_{j1}$	0.9444	0.9771	1.0001	1.0284	0.9831
$\overline{y}_{j2}$	0.9929	0.9834	0.9795	0.9602	0.9869
$\overline{y}_{j3}$	0.9789	0.9856	0.9638	0.9575	0.9761
R_j	0.0185	0.0085	0.0363	0.0709	0.0108

Thus, the balanced suspension stiffness and the front suspension damping are two dominant factors affecting ride comfort. In short, the best combination of factor levels for lowest driver's acceleration is determined as $A_3B_1C_3D_3E_3$.

The range analysis of the vehicle body acceleration is listed in Table 3.5. Figure 3.16 is the comparison chart of each experiment factor's effect on the vehicle

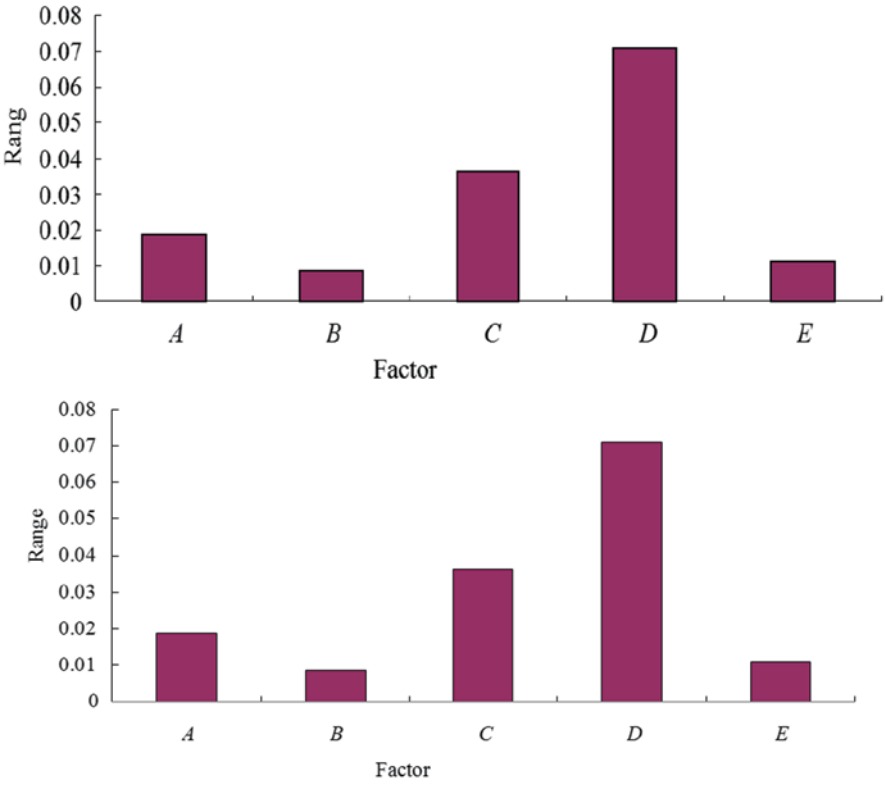

Fig. 3.16 The effect of experiment factors on the vehicle body acceleration. Reprinted from ref. [7], Copyright 2013, with kind permission from CESER Publications

Table 3.6 Range analysis of the front tire force

Range	Factor				
	A	*B*	*C*	*D*	*E*
y_{j1}	236,918.0	237,016.1	236,291.7	236,045.5	236,797.9
y_{j2}	237,032.9	237,019.6	236,960.4	237,919.1	237,034.9
y_{j3}	237,019.6	236,934.8	237,216.4	237,005.9	237,137.7
$\overline{y}_{j1}$	26,324.2	26,335.1	26,310.4	26,227.3	26,310.9
$\overline{y}_{j2}$	26,336.9	26,335.5	26,328.9	26,435.5	26,337.2
$\overline{y}_{j3}$	26,335.5	26,326.1	26,357.4	26,333.9	26,348.6
R_j	12.7	9.4	47.0	208.2	37.7

body acceleration. The degree of importance of the suspension parameter's effect on the second object (vehicle body acceleration) is in sequence of the balanced suspension stiffness (Factor D), the balanced suspension damping (Factor C), the front suspension damping (Factor A), the driver seat damping (Factor E), and the suspension stiffness (Factor B). Thus, the balanced suspension stiffness, damping and the front suspension damping are the dominant factors affecting ride comfort. In short, the best combination of factor levels is determined as $A_1B_1C_3D_3E_3$.

The range analysis of the front tire force is listed in Table 3.6. Figure 3.17 is the comparison chart of each experiment factor's effect on the front tire force. The degree of importance of the suspension parameter's effect on the third object (front tire force) is in sequence of the balanced suspension stiffness (Factor D), the balanced suspension damping (Factor C), the driver seat damping (Factor E), the front suspension damping (Factor A), and the suspension stiffness (Factor B).Thus, the bal-

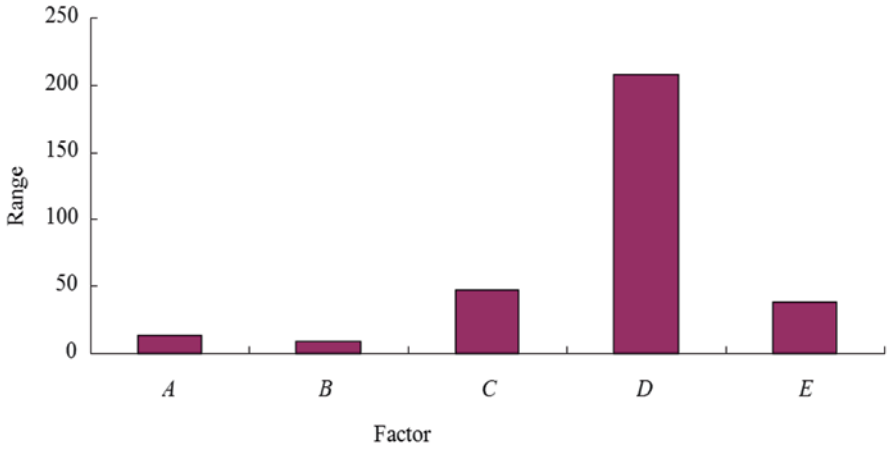

Fig. 3.17 The effect of experiment factors on front tire force. Reprinted from ref. [7], Copyright 2013, with kind permission from CESER Publications

Table 3.7 Range analysis of the intermediate tire force

Range	Factor				
	A	*B*	*C*	*D*	*E*
y_{j1}	312,079.8	311,951.9	312,151.6	320,247.8	312,200
y_{j2}	312,043.7	312,139.4	312,038.3	311,092.1	311,958.2
y_{j3}	312,031.2	312,063.4	311,964.8	304,814.8	311,996.5
$\overline{y}_{j1}$	34,675.5	34,661.3	34,683.5	35,583.1	34,688.9
$\overline{y}_{j2}$	34,671.5	34,682.2	34,670.9	34,565.8	34,662.0
$\overline{y}_{j3}$	34,670.1	34,673.7	34,662.8	33,868.3	34,666.3
R_j	4.0	20.9	20.7	1714.8	26.9

anced suspension stiffness and damping are the dominant factors affecting front tire force. In short, the best combination of factor levels is determined as $A_1B_3C_1D_1E_1$.

The range analysis of the intermediate tire force is listed in Table 3.7. Figure 3.18 is the comparison chart of each experiment factor's effect on the intermediate tire force. The degree of importance of the suspension parameter's effect on the fourth object (intermediate tire force) is in sequence of the balanced suspension stiffness (Factor D), the driver seat damping (Factor E), the suspension stiffness (Factor B), the balanced suspension damping (Factor C), and the front suspension damping (Factor A). Thus, the balanced suspension stiffness is the only dominant factor affecting the intermediate tire force. In short, the best combination of factor levels is determined as $A_3B_1C_3D_3E_2$.

The range analysis of the intermediate tire force is listed in Table 3.8. Figure 3.19 is the comparison chart of each experiment factor's effect on the intermediate tire force. The degree of importance of the suspension parameters effect on the fifth object (rear tire force) is in sequence of the balanced suspension stiffness (Factor D), the balanced suspension damping (Factor C), the front suspension damping

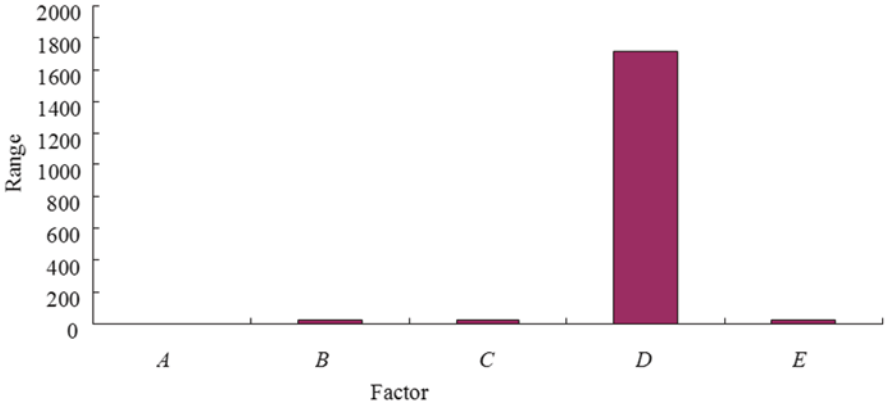

Fig. 3.18 The effect of experiment factors on the intermediate tire force. Reprinted from ref. [7], Copyright 2013, with kind permission from CESER Publications

Table 3.8 Range analysis of the rear tire force

Range	Factor				
	A	*B*	*C*	*D*	*E*
y_{j1}	310,566.8	310,488.6	310,217.8	316,468.9	31,038.9
y_{j2}	310,355.7	310,284.9	310,227.7	310,365.4	310,427.3
y_{j3}	310,215.7	310,364.7	310,692.7	304,394.1	310,326.0
$\overline{y}_{j1}$	34,507.4	34,498.7	34,468.6	35,163.2	34,487.2
$\overline{y}_{j2}$	34,483.9	34,476.1	34,469.7	34,485.0	34,483.9
$\overline{y}_{j3}$	34,468.4	34,484.9	34,521.4	33,821.6	34,468.4
R_j	39.0	22.6	52.8	1341.6	11.2

(Factor A), the suspension stiffness (Factor B), and the driver seat damping (Factor E). Thus, the balanced suspension stiffness is the dominant factor affecting rear tire force. In short, the best combination of factor levels is determined as $A_3B_2C_1D_3E_3$.

Through the range analysis, the best factor and combination of levels are obtained for each object. In order to equalize the five object effects on ride comfort and road friendliness, the final best matching is chosen as $A_1B_1C_3D_2E_3$ according to the major and minor effects on ride comfort and road friendliness.

According to the range analysis method, the best combination of $A_1B_1C_3D_2E_3$ is obtained. The optimized results are shown in Fig. 3.20–3.24.

Based on the calculation of the results, the optimized root mean square (R.M.S) acceleration of the driver and body decreased 8.9 and 7.4 %, respectively, compared with the nonoptimized results, and the dynamic tire force of the front, intermediate and rear wheels decreased 2.3 , 4.3, and 3.8 %, respectively.

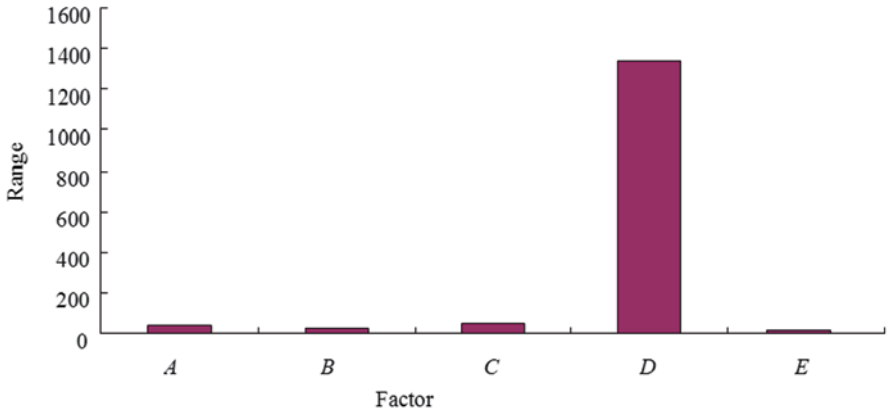

Fig. 3.19 The effect of experiment factors on the rear tire force. Reprinted from ref. [7], Copyright 2013, with kind permission from CESER Publications

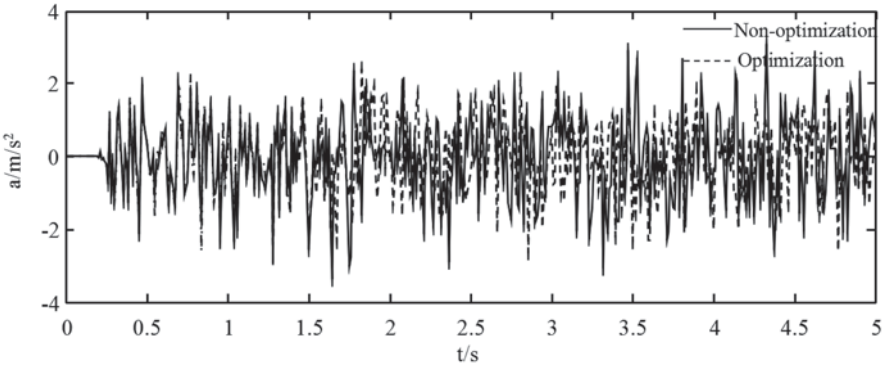

Fig. 3.20 The optimized result of driver acceleration. Reprinted from ref. [7], Copyright 2013, with kind permission from CESER Publications

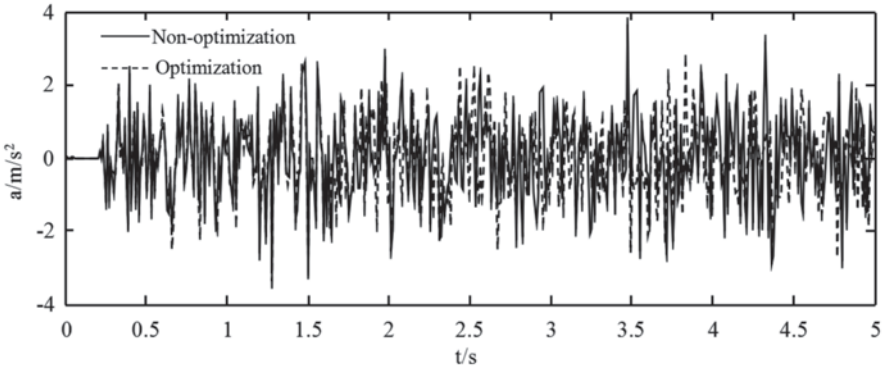

Fig. 3.21 The optimized result of body acceleration. Reprinted from ref. [7], Copyright 2013, with kind permission from CESER Publications

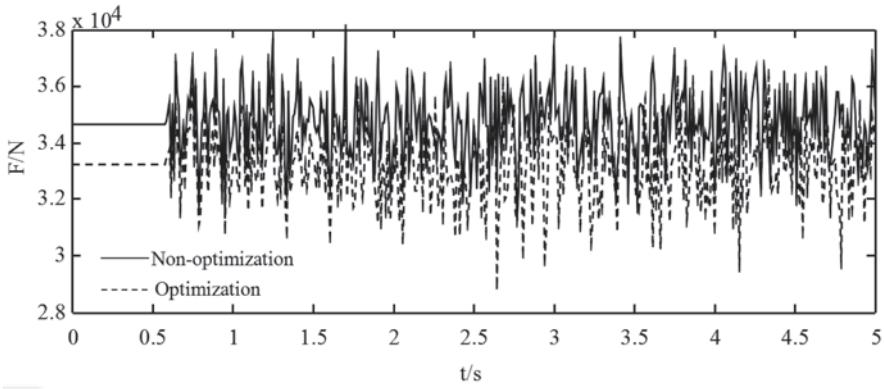

Fig. 3.22 The optimized result of front tire force. Reprinted from ref. [7], Copyright 2013, with kind permission from CESER Publications

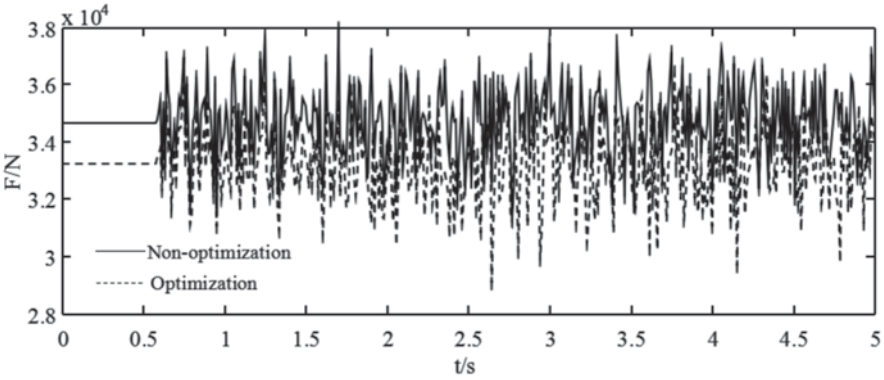

Fig. 3.23 The optimized result of intermediate tire force. Reprinted from ref. [7], Copyright 2013, with kind permission from CESER Publications

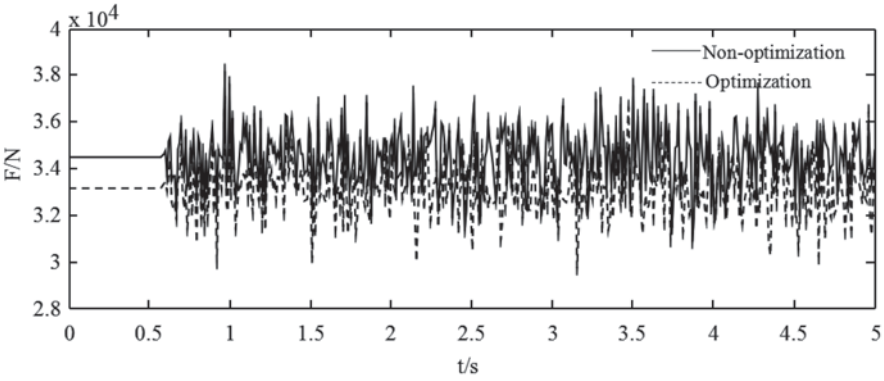

Fig. 3.24 The optimized result of rear tire force. Reprinted from ref. [7], Copyright 2013, with kind permission from CESER Publications

3.3 Semiactive Control of a Heavy Vehicle

In this section, a detailed multibody model of a heavy vehicle is presented in ADAMS/CAR. Two kinds of control algorithms are developed for a semiactive suspension in the MATLAB/Simulink virtual environment, respectively. Thus the ADAMS/Matlab cosimulation of the full truck-system is completed through the establishing interface [5].

1. *Control algorithm*

The designed semiactive control system in this section is shown as follows:

1. Semiactive on–off control

Generally, the semiactive on–off control damping force is

$$F = \begin{cases} C_{\max} \times V & V \times V_{\text{body}} \geq 0 \\ C_{\min} \times V & V \times V_{\text{body}} < 0 \end{cases} \tag{3.11}$$

where V is the velocity between the damper piston and the column casing, which is equal to the velocity between the wheel and the vehicle body, $C_{\max}$ is the damping coefficient when the orifice is fully closed, and is also the passive suspension damping coefficient, and $C_{\min}$ is the damping coefficient when the orifice is fully open. Let $C_{\max} = 3000$ N·s/m, $C_{\min} = 0$.

2. Semiactive MR control based on a revised Bingham model

In recent years, a number of semiactive control label M (Magneto-rheological) R fluid-based dampers have been developed for vehicle suspension applications. The MR damper offers high viscous damping corresponding to low velocities in the preyield condition, while the postyield saturation corresponding to high velocities can be characterized by a considerably lower viscous damping coefficient. The damping properties are considered to be well suited for vibration attenuation applications to achieve the satisfactory compromise among different conflicting requirements. Although the traditional Bingham model can be used to fit the MR damper force–displacement response and energy dissipation ability, this model cannot describe the MR damper nonlinear characters of force and velocity well. Thus, a revised Bingham model with a nonlinear hysteresis loop is used in this section. The MR damping force with this model is expressed by the following equations:

$$F = \begin{cases} C_1 V + F_{y} \operatorname{sgn}(V - V_0) & V' \geq 0 \\ C_1 V + F_{y} \operatorname{sgn}(V + V_0) & V' < 0 \end{cases} \tag{3.12}$$

$$F_y = \begin{cases} F_{y\max} & V \times V_{\text{body}} \geq 0 \\ F_{y\min} & V \times V_{\text{body}} < 0 \end{cases} \tag{3.13}$$

where C_1—MR damper viscous damping coefficient,

F_y—control force,

V_0—MR damper at zero-force velocity, and

V—relative acceleration between the damper piston and the column casing.

The parameters for the damper are chosen as: $C_1 = 800$ N·s/m, $F_{y\max} = 1000$ N, $F_{y\min} = 8$ N, and $V_0 = 1$ m/s. The revised Bingham mechanics model is shown as Fig. 3.25.

2. Controller design

First, some necessary measurements are defined based on the multibody vehicle model in ADAMS/CAR, including the velocity of vehicle body (*V-body*), the velocity between the wheel and the vehicle body (*V-left*, *V-right*). These are three measured signals, which are taken as the output state variables of the vehicle model. Second, the control inputs to the vehicle model are defined as semiactive forces

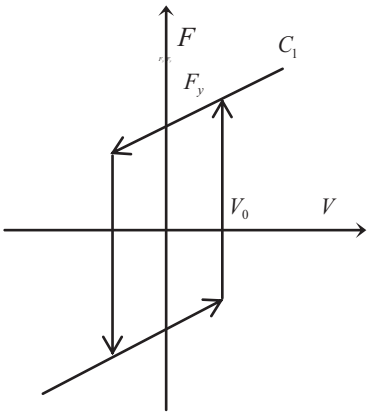

Fig. 3.25 Revised Bingham model. Reprinted from ref. [8], Copyright 2008, with kind permission from IEEE

Force-left and *Force-right*. Third, the full vehicle model is exported as a nonlinear ADAMS plant to MATLAB/Simulink and the designed control algorithm is integrated with the dynamic vehicle model by the control interface. Thus, the cosimulation can be run repeatedly until a more practical controller is achieved. The cosimulation environment in MATLAB/Simulink has been set up to simulate the ADAMS model, and the cosimulation system diagram is shown in Fig. 3.26.

The subsystem of the semiactive "on–off" controller and the semiactive MR controller based on the revised Bingham model are, respectively, shown as Fig. 3.27, 3.28.

3. Cosimulation analysis

The vehicle vertical acceleration directly reflects the passengers' ride comfort. The vehicle suspension dynamic deflection is the displacement between the wheel and

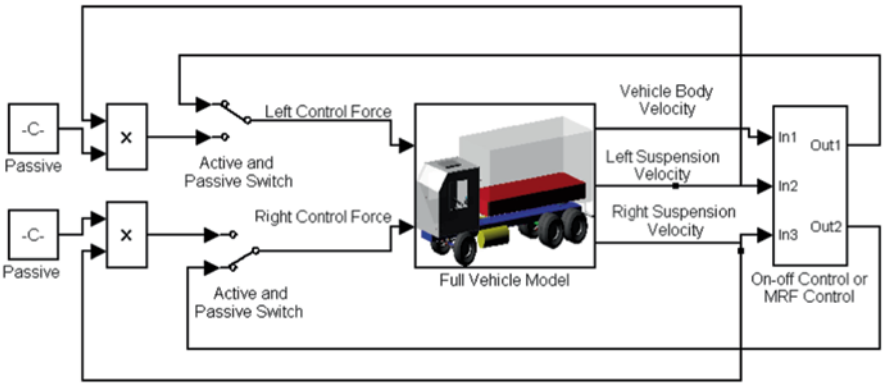

Fig. 3.26 Cosimulation system diagram. Reprinted from ref. [8], Copyright 2008, with kind permission from IEEE

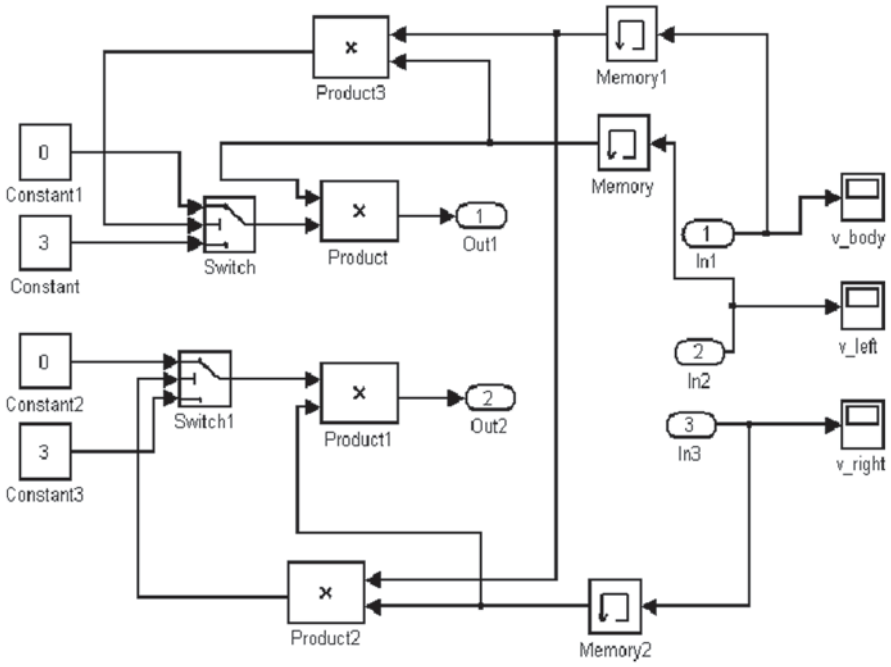

Fig. 3.27 Subsystem of the "on–off" controller. Reprinted from ref. [8], Copyright 2008, with kind permission from IEEE

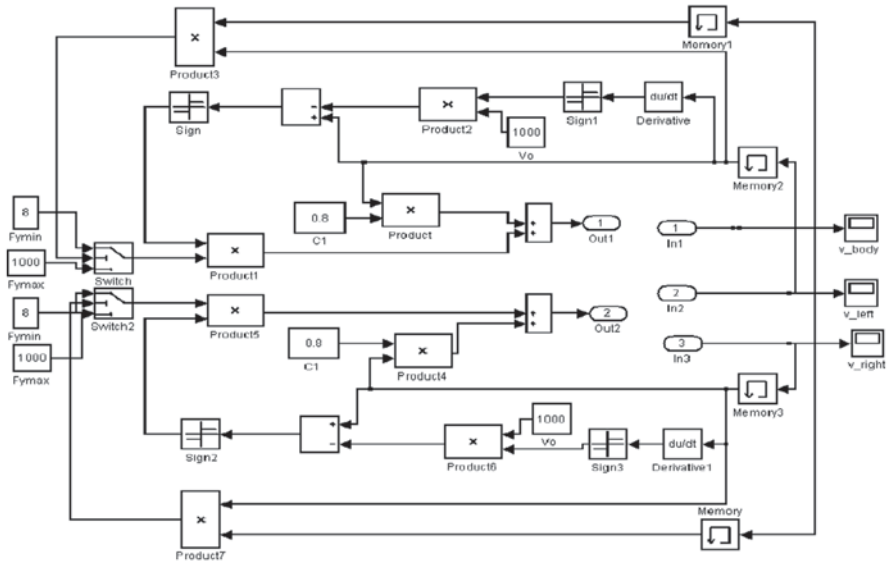

Fig. 3.28 Subsystem of the MR controller. Reprinted from ref. [8], Copyright 2008, with kind permission from IEEE

Table 3.9 Root mean square (R.M.S) of the suspension dynamic performance

Performance index(R.M.S)	Unit	Passive	On–off	MR
Seat vertical acceleration	m/s^{-2}	0.586	0.448	0.430
Left suspension deflection	M	0.055	0.042	0.036
Right suspension deflection	M	0.088	0.077	0.054
Left tire force	N	26,631	24,319	24,185
Right tire force	N	29,177	26,656	26,774

the vehicle body. If the deflection exceeds the designed positive stop, the bumper block would damage the suspension components. Vehicle dynamic tire force seriously affects vehicle driving, braking characteristics and pavement damage. According to these performance indexes, some simulations are done under the national standard C-level road, fully laden, and 40 km/h condition. The vehicle dynamic performances under the passive control, semiactive "on–off" control, and semiactive MR control are analyzed, respectively. The results of every index R.M.S are shown in Table 3.9.

From Table 3.9, it is found that the semiactive "on–off" control can reduce the driver seat acceleration, left suspension deflection, right suspension deflection, left tire force, and right tire dynamic force by 23.6, 23.6, 12.5, 8.7, and 8.6%, respectively, compared to the passive suspension. And the semiactive MRF control based on the revised Bingham model can reduce the same variables by 26.7, 34.3, 38.6, 9.2, and 8.2% compared to the "on–off" control, respectively. Therefore, the semiactive MRF control effects on the revised Bingham model is much better than the traditional passive and "on–off" control strategies and the vehicle dynamic performances are improved.

3.4 Chapter Summary

1. Based on multibody dynamics theory, a nonlinear virtual prototype model of a heavy vehicle is quickly created. According to the orthogonal optimization theory of statistics, the advantage of the parametric model of a multibody vehicle is fully utilized to accomplish the dual optimization goals of ride comfort and road friendliness.
2. Through establishing the interface, the ADAMS/Matlab cosimulation system of the virtual vehicle model is completed. It is found that the adjustable shock absorbers can improve vehicle dynamical performance, weaken vehicle body vibration and increase ride comfort. The cosimulation technology offers a new way to model and control a complex dynamic system.

References

1. Chen J. MSC.ADAMS Examples of technical and engineering analysis. Beijing: China Water-Power Press; 2008.
2. He YP, McPhee J. Application of optimization algorithms and multibody dynamics to ground vehicle suspension design. Int J Heavy Veh Syst. 2007;14(2):158–92.
3. Hegazy S, Rahnejat H, Hussain K. Multi-body dynamics in full-vehicle handling analysis. Procs Inst Mech Eng, Part K: J Multi-body Dyn. 1999;213(1): 19–31.
4. Hu GH, Zhu WH, Cai HX. Mathematical model for abrasive suspension jet cutting based on orthogonal test design. J Shanghai Univ (English Edition). 2009;13(1): 37–44.
5. Lu YJ, Yang SP, Li HY. Dynamic analysis of semi-active vehicle suspensions using a co-simulation approach, 2008IEEE Vehicle Power and Propulsion Conference; 2008, 10394417.
6. Lu YJ, Yang SP, Li SH, Chen LQ. Numerical and experimental investigation on stochastic dynamic load of a heavy duty vehicle. App Math Model. 2010;34(10): 2698–710.
7. Lu YJ, Li SH, Wang CY. Orthogonal test optimization of vehicle smoothness and road friendliness. Int J App Math Stat. 2013; 51(21): 592–600.
8. Snežana P, Ljubomir L. Orthogonal array and virtualization as a method for configuration testing improvement. Novi Sad: First IEEE Eastern European Conference on the Engineering of Computer Based Systems; 2009. p. 148–9.

Chapter 4
Dynamic Analysis of a Pavement Structure Under a Vehicle's Moving Load

With the development of highway transportation, the high speed and heavy duty phenomena have become extraordinarily common. The premature pavement damage caused by the dynamic loads of heavy duty vehicles is becoming more and more serious and is receiving widespread attentions. The static highway design method has met difficulty to meet the traffic requirement. It is a prevailing subject to study the dynamics of pavement structure, to reveal the pavement damage mechanism, and to promote the changing of pavement design criterion from static to dynamic.

This chapter establishes the models of a finite (Sect. 4.1–4.3) and infinite beam (Sect. 4.4) on a nonlinear foundation with viscous damping. Based on the Galerkin method and the integral transform method, the numerical and analytical solutions are derived for the dynamic response of the pavement structure subjected to a moving load. Moreover, the vibration characteristics of the pavement structure under a moving load are discussed through some examples. Furthermore, the coupled nonlinear vibration of the vehicle–pavement system is studied based on a finite Timoshenko beam on the foundation subjected to a spring–mass–damper oscillator.

4.1 The Dynamic Response of a Vehicle–Pavement System Based on a Finite Beam on a Nonlinear Foundation

The dynamic response problem of elastic beams on a nonlinear viscoelastic foundation displays nonlinear and viscous characteristics, which make the analysis difficult. The Galerkin truncation method is a powerful tool for dealing with dynamic problems in such cases. It has been widely used to study free and forced vibration phenomena for elastic materials on nonlinear viscoelastic foundations. Based on the Galerkin method, Li et al. investigated the chaos of a pavement on a viscoelastic foundation subjected to a moving vehicle with the first order discretization and Melnikov's function [1]; Sheng et al. studied the dynamic behavior of Timoshenko beams with damage on a viscoelastic foundation by using 2-term truncation [2];

S. Yang et al., *Dynamics of Vehicle-Road Coupled System,*
DOI 10.1007/978-3-662-45957-7_4

Pellicano and Mastroddi investigated the nonlinear dynamic behavior via 3-term truncation in conjunction with the method of normal forms [3]; Ansari et al. studied train–track interaction via 3-term truncation, considering the internal–external resonance condition and obtained the frequency responses of different harmonics, and found that the nonlinear stiffness plays a positive role in the design of railway tracks because of the delay in the jump phenomenon [4, 5]; Yan et al. studied the dynamic response of functionally graded beams with an open edge crack on an elastic foundation subjected to a transverse moving load via 3-term truncation [6]; Coskun studied the forced vibrations of an elastic beam on a nonlinear tensionless foundation by employing the 5-term truncation [7]; Celep et al. investigated the response of a beam on a tensionless Pasternak foundation subjected to a dynamic load by employing the 5-term truncation [8]; Vassilev and Djondjorov investigated the dynamic stability of viscoelastic pipes lying on a foundation of variable modulus using 10-term truncation [9]; Yang et al. presented the dynamic behavior of the vehicle–pavement-foundation coupled system using the 20-term truncation [10]; Chen and Chen studied steady-state deformations of an infinite beam on a tensionless foundation under a moving point load through 80-term truncation [11]; Senalp et al. studied the dynamic response of a finite length Euler–Bernoulli beam on linear and nonlinear viscoelastic foundations under a concentrated moving force, and 100-term truncation is utilized in order to solve the governing equations of motion [12].

Although the Galerkin truncation has been widely applied to dynamic problems of finite beams on a nonlinear viscoelastic foundation, the convergence of the truncation terms has not been studied. In this section, the convergence of Galerkin's method for dynamic response of finite Euler–Bernoulli beams on a cubic nonlinear foundation with viscous damping is studied. The parametric dependence study is carried out to investigate the effects of different parameters on the convergence of the Galerkin truncation.

The dynamic response of a finite beam on an elastic foundation has been studied through different boundary conditions. Based on the finite element method for the dynamic analysis of beams on an elastic foundation subjected to moving point loads, Thambiratnam and Zhuge proved that the beams of span length $L > 10$ m can accurately approximate the response of the ideal beam of infinite length [13]. In order to study the interaction between train vehicles and railway track, Muscolino and Palmeri scrutinized the response of beams on a viscoelastic foundation under moving single degree-of-freedom (SDOF) oscillators [14]. Based on modal shapes and natural frequencies of the beam-foundation, the effects of boundary conditions and the span length of the beam are investigated through a state–space formulation. Monsalve et al. presented the dynamic analysis of a Timoshenko beam-column on a two-parameter elastic foundation with generalized end conditions. The end conditions allowed simulating any end support condition to the beam-column [15]. The dynamic responses of functionally graded beams on an elastic foundation subjected to a moving load with different end supports are obtained by Yan et al. [6]. The authors found that boundary conditions have significant influence on the dynamic response of the cracked functionally graded materials' beams. However, there are no works on the influences of boundary conditions of finite beams on a foundation on

the dynamic response of the beams excited by a moving load and the convergence of the Galerkin's method. To address the lack of research in this aspect, the dynamic responses are calculated by the Galerkin truncation under three types of the conventional boundary conditions, namely simply-supported (SS), clamped–clamped (CC), and free–free (FF) boundary conditions. In the present work, the effects of the boundary condition and span length of the supporting beam on the dynamic responses and the convergence of the Galerkin truncation are studied.

This section investigates the convergence of Galerkin's method for the dynamic response of a vehicle–pavement system. The pavement is modeled as a finite length Euler–Bernoulli or a Timoshenko beam with uniform cross-section on a nonlinear viscoelastic foundation. The vehicle is simplified as a concentrated force or a spring–mass–damper oscillator. Galerkin's method is utilized to discretize the nonlinear partial differential governing equation of the forced vibration. Moreover, the dependence of the convergence of Galerkin's method on boundary conditions, span length, and other system parameters is studied, respectively.

4.1.1 Equation of Motion [16]

The system under investigation is a finite elastic Euler–Bernoulli beam on a nonlinear viscoelastic foundation and subjected to a moving load. Consider a homogeneous beam with constant cross-section A, moment of inertial I, length L, densityρ, and modulus of elasticity E. The foundation is taken as a nonlinear Winkler's foundation with liner-plus-cubic stiffness and viscous damping with three parameters as follows

$$P = k_1 w + k_3 w^3 + c w_{,T} \tag{4.1}$$

where P represents the force induced by the foundation per unit length of the beam, k_1 and k_3 are the linear and nonlinear foundation parameters, respectively, μ is the damping coefficient of the foundation, T is the time, a comma preceding T denotes the partial differentiation with respect to T.

Using the Hamilton principle and considering the Euler–Bernoulli beam theory, one can develop the governing differential equation of motion for the beam as

$$\rho A w_{,TT} + EI w_{,XXXX} + k_1 w + k_3 w^3 + c w_{,T} = F_z \delta(X - VT) \tag{4.2}$$

where $w(X, T)$ is the vertical displacement function, EI is the flexural rigidity of the beam, X is the spatial coordinate along the axis of the beam, $\delta(X)$ is the Dirac delta function used to deal with the moving concentrated load, a comma preceding X denotes the partial differentiation with respect to X, F_z and v are the magnitudes of the load and load speed, respectively.

Introduce the dimensionless variables and parameters as follows

$$w \leftrightarrow \frac{w}{L}, t = \frac{T}{L}\sqrt{\frac{E}{\rho}}, v = V\sqrt{\frac{\rho}{E}}, x = \frac{X}{L}, k_{\mathrm{b}} = \frac{1}{L}\sqrt{\frac{I}{A}},$$
$$F_z \leftrightarrow \frac{F_z}{EA}, c \leftrightarrow \frac{c}{A}\sqrt{\frac{L^2}{\rho E}}, k_1 \leftrightarrow \frac{k_1 L^2}{EA}, k_3 \leftrightarrow \frac{k_3 L^4}{EA} \tag{4.3}$$

where x is the dimensionless spatial coordinate and t is the dimensionless time. Equation (4.2) can be transformed into the dimensionless equation

$$w_{,tt} + k_{\mathrm{b}}^2 w_{,xxxx} + k_1 w + k_3 w^3 + c w_{,t} = F_z \delta(x - vt) \tag{4.4}$$

Here, the beam considered in the model, is assumed to be simply supported at both ends, and therefore the boundary conditions are given as follows

$$w(0,t) = w(1,t) = 0, w_{,xx}(0,t) = w_{,xx}(1,t) = 0 \tag{4.5}$$

In the present investigation, two other kinds of boundary conditions of the beam are also considered, that is, both clamped ends, as follows

$$w(0,t) = w(1,t) = 0, w_{,x}(0,t) = w_{,x}(1,t) = 0 \tag{4.6}$$

and both free ends as follows

$$w_{,xx}(0,t) = w_{,xx}(1,t) = 0, w_{,xxx}(0,t) = w_{,xxx}(1,t) = 0 \tag{4.7}$$

In all numerical examples here, the initial conditions are

$$w(x,t)\Big|_{t=0} = 0, \quad w_{,t}(x,t)\Big|_{t=0} = 0 \tag{4.8}$$

4.1.2 Galerkin's Discretization

The Galerkin truncation method is used to discretize the system and the series expansion form for $w(x, t)$ is assumed to be

$$w(x,t) = \sum_{k=1}^{\infty} q_k(t)\varphi_k(x) \tag{4.9}$$

where $\varphi_k(x)$ are the trial functions, and $q_k(t)$ are sets of generalized displacements of the beams. In this research, the first n terms of Eq. (4.9) is considered in order to determine $w(x, t)$. Substituting Eq. (4.9) into Eq. (4.4) leads to

$$\begin{aligned}&\sum_{k=1}^{n}\left\{\left[\ddot{q}_k(t)+k_1 q_k(t)+c\dot{q}_k(t)\right]\varphi_k(x)\right\}+k_b^2\sum_{k=1}^{n}\left[q_k(t)\varphi_k''''(x)\right]\\&+k_3\left\{\sum_{k=1}^{n}\left[q_k(t)\varphi_k(x)\right]\right\}^3-F_z\delta(x-vt)=0\end{aligned}\tag{4.10}$$

Multiplying Eq. (4.10) by the weight functions $w_i(x)$ and integrating it over the interval of 0 and 1, the Galerkin procedure leads to the following set of n second-order ordinary differential equations (ODES)

$$\begin{aligned}&\sum_{k=1}^{n}\left\{\left[\ddot{q}_k(t)+k_1 q_k(t)+c\dot{q}_k(t)\right]\int_0^1\varphi_k(x)w_i(x)\mathrm{d}x\right\}\\&+k_b^2\sum_{k=1}^{n}\left[q_k(t)\int_0^1\varphi_k''''(x)w_i(x)\mathrm{d}x\right]\\&+k_3\int_0^1\left\{\sum_{k=1}^{n}\left[q_k(t)\varphi_k(x)\right]\right\}^3 w_i(x)\mathrm{d}x-F_z w_i(vt)=0\\&i=1,2,...,n\end{aligned}\tag{4.11}$$

If the trial functions and the weight functions are both chosen properly, the vertical displacement of the beams $w_n(x,t)$ can be numerically solved via Eq. (4.9).

In the present investigation, both the trial and weight functions are chosen as eigenfunctions of the beam-foundation linear subsystem under the boundary conditions. The natural frequencies and the mode functions of the beam on a linear elastic foundation which is simply supported and without any loads can be derived as follows

$$\omega_k^2=k_b^2\beta_k^4+k_1,\ (k=1,2,\cdots)\tag{4.12}$$

and

$$\phi_k(x)=\sin(\beta_k x),(k=1,2,\cdots)\tag{4.13}$$

where

$$\beta_k=k\pi,(k=1,2,\cdots)\tag{4.14}$$

When the beam is CC at the ends, the kth mode functions is

$$\phi_k(x)=\cosh\beta_k x-\cos\beta_k x+\xi_k(\sin\beta_k x-\sinh\beta_k x),k=1,2,\ldots\tag{4.15}$$

where

$$\xi_k = \frac{\cosh \beta_k - \cos \beta_k}{\sinh \beta_k - \sin \beta_k}, (k = 1, 2, \cdots) \tag{4.16}$$

and the characteristic equation is

$$\cos \beta_k \cosh \beta_k = 1 \tag{4.17}$$

whose nontrivial solutions should be numerically computed: $\beta_1 = 4.73, \beta_2 = 7.85, \ldots$ (notice that $\beta_k \cong (2k+1)\pi/2$ for $k > 2$).

When the beam is FF at the ends, the kth mode functions is

$$\phi_k(x) = \cos \beta_k x + \cosh \beta_k x + \xi_k (\sin \beta_k x + \sinh \beta_k x), k = 1, 2, \cdots \tag{4.18}$$

where

$$\xi_k = -\frac{\cos \beta_k - \cosh \beta_k}{\sin \beta_k - \sinh \beta_k} = -\frac{\cos \beta_k + \cosh \beta_k}{\sin \beta_k + \sinh \beta_k}, k = 1, 2, \cdots \tag{4.19}$$

and the characteristic equation is Eq. (4.17), same as CC boundary conditions. The eigenvalues are $\beta_1 = 0, \beta_2 = 4.73, \beta_3 = 7.85 \ldots$ (notice that $\beta_k \cong (2k-1)\pi/2$ for $k > 3$).

Both the trial and weight functions are chosen as eigenfunctions of the beam-foundation linear subsystem. That is to say, $\varphi_k(x) = \phi_k(x)$, $w_i(x) = \phi_i(x)$. For SS, CC, and FF boundary conditions, the mode functions satisfied

$$\varphi_k'''' = \beta_k^4 \varphi_k(x) \tag{4.20}$$

With the usual orthogonal condition, the CC and FF boundary conditions satisfied

$$\int_0^1 \varphi_k(x) w_i(x) \mathrm{d}x = \begin{cases} 0, & k \neq i \\ 1, & k = i \end{cases} \tag{4.21}$$

Substitution of Eq. (4.21) into Eq. (4.11) yields

$$\begin{aligned} &\ddot{q}_i(t) + c\dot{q}_i(t) + \left(k_1 + k_\mathrm{b}^2 \beta_i^4\right) q_i(t) - F_z w_i(vt) \\ &+ k_3 \int_0^1 \left\{ \sum_{k=1}^{n} \left[q_k(t) \varphi_k(x) \right] \right\}^3 w_i(x) \mathrm{d}x = 0 \end{aligned} \tag{4.22}$$

For a set of given parameters k_b, k_1, k_3, F_z, μ and the initial conditions in Eq. (4.8), $q_k(t)$ can be numerically solved via the Runge–Kutta method (fourth order) from Eq. (4.22) by discretizing the temporal variables. After substituting the numerical solutions into Eq. (4.9), the vertical displacement $w_n(x,t)$ can be solved.

4.1.3 Numerical Results

In this part, the beam is assumed to be the asphalt mixtures D-12 (limestone). The physical and geometric properties and dimensionless parameters' value of the pavement, foundation, and the moving load are listed in Table 4.1.

The results of a few different numbers of Galerkin truncation terms, namely, 50-term Galerkin's truncation, 75-term Galerkin's truncation, 150-term Galerkin's truncation, and 200-term Galerkin's truncation for the vertical deflections of the asphalt pavement while the load moves to the mid-point of the pavement and the vertical deflections of pavement center with time are, respectively, shown in Figs. 4.1 and 4.2. The numerical results demonstrated that there are big differences between the 50-term Galerkin's truncation results with the 150-term ones and the 200-term ones. The comparisons indicate that the 50-term Galerkin's method is not accurate enough for the dynamic response analysis of the asphalt pavement on a soft soil foundation running the vehicle, and there are discernible differences between the results of the 75-term and the 150-term Galerkin's method. The comparisons also predict that the difference between the results of the 150-term and the 200-term Galerkin's method is very small, so the 150-term Galerkin's method yields rather accurate results. The maximum relative differences between the maximum mid-point vertical deflections is 14.29×10^{-2} in the 50-term Galerkin truncation and the 200-term Galerkin truncation, 4.876×10^{-2} in the 75-term Galerkin truncation and the 200-term Galerkin truncation, and 0.3381×10^{-2} in the 150-term Galerkin truncation and 200-term Galerkin truncation.

Table 4.1 Properties of the asphalt mixtures D-12, pavement, foundation, and load [17]. (Reprinted from ref. [16], Copyright 2014, with permission from Elsevier)

Item	Notation	Value	Dimensionless value
Asphalt mixtures (D–12)			
Young's modulus(steel)	E	6.998 GPa	–
Mass density	ρ	2373 kg/m^3	–
Height of pavement	h	0.3 m	–
Width of pavement	b	1.0 m	–
Modulus of elasticity	k_b	–	5.41×10^{-4}
Length	L	160 m	1
Foundation			
Mean stiffness	k_1	8×10^6 N/m^2	97.552
Nonlinear stiffness	k_3	8×10^6 N/m^4	2.497×10^6
Viscous damping	c	0.3×10^6 Ns/m^2	39.263
Moving load			
Load	F_z	212.6 KN	1.013×10^{-4}
Speed	V	20 m/s	0.01165

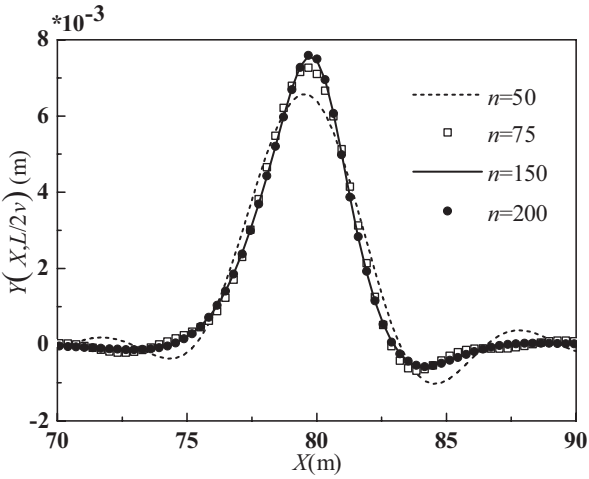

Fig. 4.1 The effects of the Galerkin truncation terms on the vertical deflection of the pavement. (Reprinted from ref. [16], Copyright 2014, with permission from Elsevier)

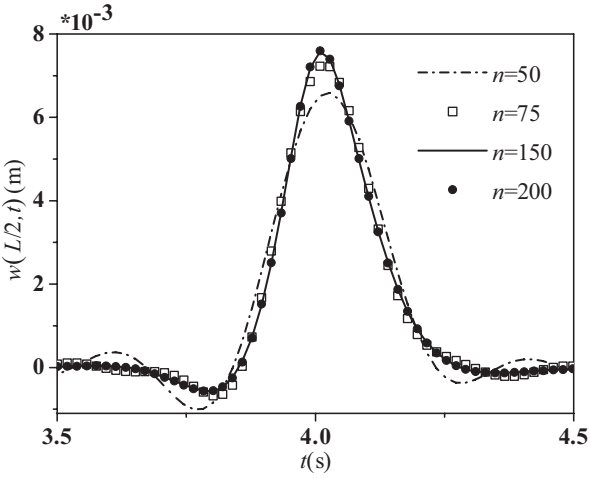

Fig. 4.2 The effects of the Galerkin truncation terms on the vertical displacements of the pavement's midpoint. (Reprinted from ref. [16], Copyright 2014, with permission from Elsevier)

In Figs. 4.3 and 4.4, the effects of three kinds of boundary conditions on the vertical displacements of the pavement midpoint ($X = L/2$) while $T = L/(2V)$ versus the truncation terms and the shape of the pavement while $T = L/(2V)$ are displayed. In Fig. 4.4a, the effects of three kinds of boundary conditions on the vertical displacements of the pavement midpoint ($X = L/2$) while $T = L/(2V)$ versus the truncation terms are displayed. Figure 4.4b shows the kth-order of the natural frequencies. The numerical results also illustrate that the convergence for simply supported boundary conditions is slightly slower, the same as changing tendencies of the natural frequencies. The numerical results which are shown in Fig. 4.4 also illustrate that the convergence can be predicted from the growth in the natural frequencies.

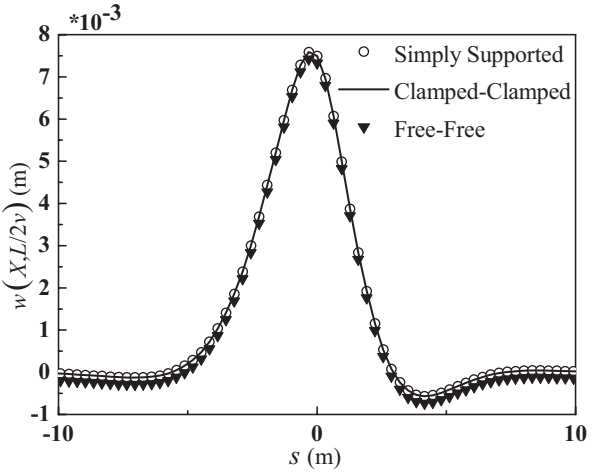

Fig. 4.3 The effects of the boundary conditions on the vertical deflection of the pavement: $n = 200$. (Reprinted from ref. [16], Copyright 2014, with permission from Elsevier)

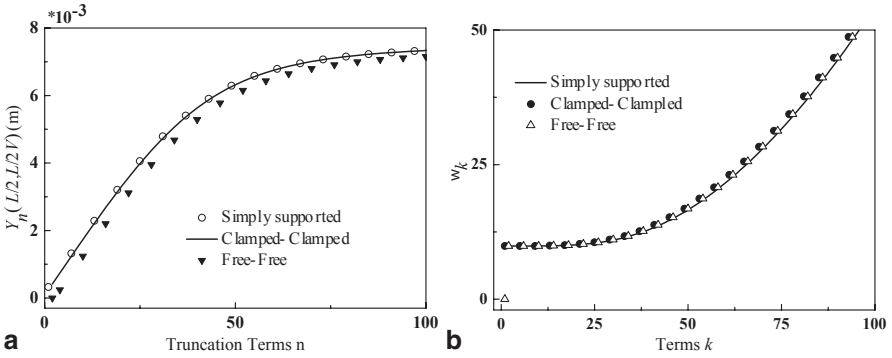

Fig. 4.4 The effects of the boundary conditions: **a** on the vertical displacements of the pavement midpoint versus truncation terms; **b** on the natural frequencies versus terms. (Reprinted from ref. [16], Copyright 2014, with permission from Elsevier)

In the following calculations for the asphalt pavement on a soft soil foundation with a moving vehicle, only the results of the simply supported boundary conditions are shown. Figure 4.5 shows the dependence of the convergence in terms of the vertical deflections of the pavement on the system parameters. There is a little difference among the vertical deflections for different lengths of the beam while the truncation terms are not too large, which means $n < 20$. The numerical results also illustrate that when a longer length of the pavement L is chosen, more truncation terms are required to achieve convergence. The convergence of Galerkin's method depends on the pavement and foundation parameters, including the modulus of elasticity of the pavement, height and width of the pavement, the linear and nonlinear foundation parameters, and the damping coefficient of the foundation, which are displayed in Fig. 4.5, respectively. The numerical results of the asphalt pavement

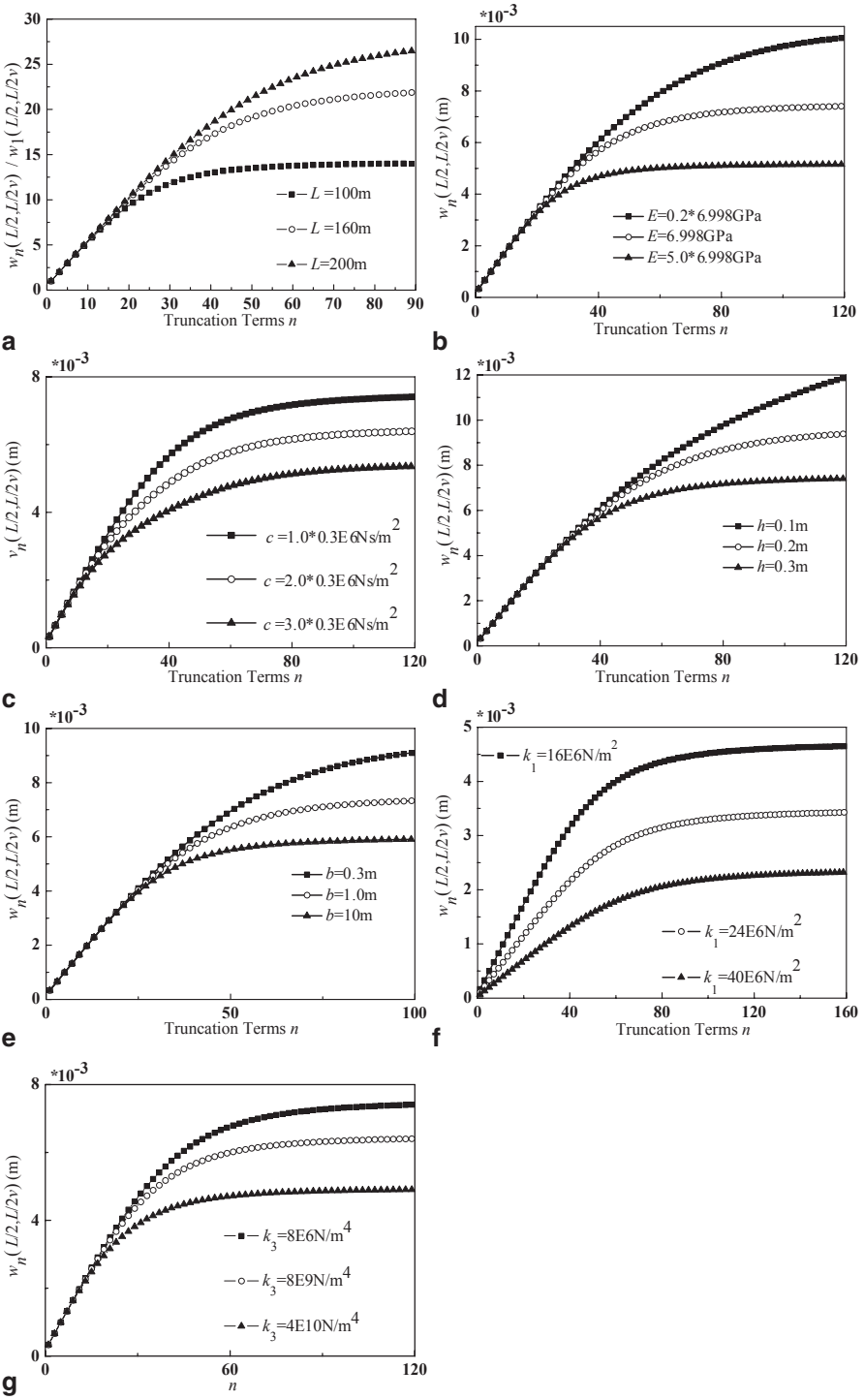

Fig. 4.5 The effects of the parameters on the vertical displacements of the pavement midpoint versus truncation terms. (Reprinted from ref. [16], Copyright 2014, with permission from Elsevier)

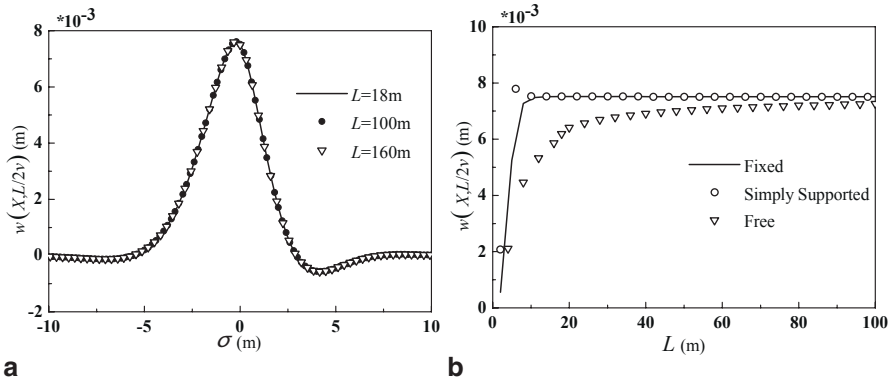

Fig. 4.6 The effects of the span length of the pavement on the vertical deflection of the pavement with $n=200$. (Reprinted from ref. [16], Copyright 2014, with permission from Elsevier)

on a soft soil foundation with a moving vehicle illustrate that the convergence of the Galerkin truncation increases with the growing modulus of elasticity of the pavement, the nonlinear foundation parameters, but decreases with the increase of the linear foundation parameters and the damping coefficient. It is also found that the convergence increases with the height and the width of the pavement. The numerical results also depict that there is a little difference among the vertical deflections of the pavement for not too large truncation terms with the different modulus of elasticity of the pavement, nonlinear foundation parameters, the height and the width of the beam, and the damping coefficient of the foundation. The vertical displacements of the pavement decrease with the increase of these parameters.

The vertical deflections of the asphalt pavement while the load moves to midpoint of the pavement for different lengths of pavement and different boundary conditions are shown in Fig. 4.6a and b, respectively. Figure 4.6a demonstrates that beams of span length $L=18\text{m}$ with SS or CC boundary conditions can accurately approximate the response of the infinite length asphalt pavement on a soft soil foundation with a moving vehicle, and three solutions are overlapped when the span length of the pavement is rather large. Figure 4.6b indicates that the FF boundary conditions are the inefficient ones.

4.2 The Dynamic Response of a Finite Timoshenko Beam on a Nonlinear Viscoelastic Foundation to a Moving Load [18]

4.2.1 Equation of Motion

The system under investigation is a finite elastic Timoshenko beam on a nonlinear viscoelastic foundation subjected to a moving load, as shown in Fig. 4.7. F_0 and V, respectively, represent the magnitude of the load and the load speed. Moreover, V

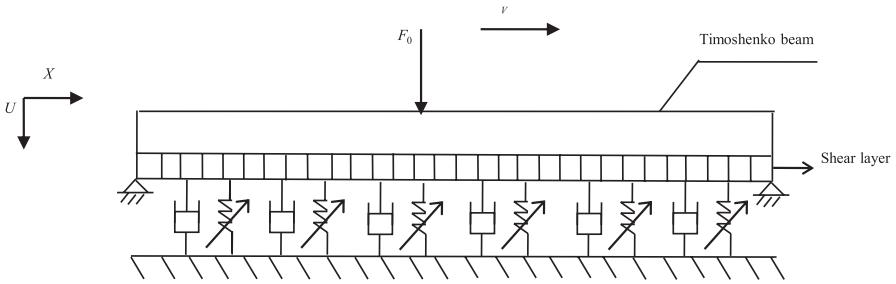

Fig. 4.7 The model of a finite Timoshenko beam on a nonlinear viscoelastic Pasternak foundation. (Reprinted from ref. [18], with kind permission from Springer Science+Business Media)

is assumed to be constant. X and U are the spatial coordinate along the axis of the beam and the vertical displacement function, respectively. Consider a homogeneous beam with constant cross-section A, moment of inertial I, length L, density ρ, modulus of elasticity E, shear modulus G, and effective shear area $k'A$.

The foundation is taken as a nonlinear Pasternak foundation with linear-plus-cubic stiffness and viscous damping as follows:

$$P(x,t) = k_1 U(X,T) + k_3 U^3(X,T) + \mu \frac{\partial U(X,T)}{\partial T} - G_\mathrm{p} \frac{\partial^2 U(X,T)}{\partial X^2} \tag{4.23}$$

where P represents the force induced by the foundation per unit length of the beam. k_1 and k_3 are the linear and nonlinear foundation parameters, respectively. Furthermore, G_p and μ are the shear deformation coefficient and the damping coefficient of the foundation, respectively, and T is the time.

Using the Hamilton principle and considering the Timoshenko beam theory, one can develop the governing differential equations of motion for the beam as

$$\begin{aligned}
&\rho A \frac{\partial^2 U}{\partial T^2} + k'AG\left[\frac{\partial \psi}{\partial X} - \frac{\partial^2 U}{\partial X^2}\right] + k_1 U + k_3 U^3 + \mu \frac{\partial U}{\partial T} - G_\mathrm{p} \frac{\partial^2 U}{\partial X^2} = F_0 \delta(X - VT), \\
&\rho I \frac{\partial^2 \psi}{\partial T^2} - EI \frac{\partial^2 \psi}{\partial X^2} + k'AG\left[\psi - \frac{\partial U}{\partial X}\right] + k_\mathrm{f} \psi + c_\mathrm{f} \frac{\partial \psi}{\partial T} = 0
\end{aligned} \tag{4.24}$$

where k_f and c_f are the foundation rocking stiffness and the damping coefficient, $\psi(X,T)$ is the slope function due to bending of the beam, $\delta(X - VT)$ is the Dirac delta function used to deal with the moving concentrated load.

Introduce the dimensionless variables and parameters as follows

$$\begin{aligned}
&u = \frac{U}{L}, t = \frac{T}{L}\sqrt{\frac{E}{\rho}}, x = \frac{X}{L}, \psi = \psi, v = V\sqrt{\frac{\rho}{E}}, \alpha = \frac{k'G}{E}, \beta = k'AG\frac{L^2}{EI}, k_1 \leftrightarrow \frac{k_1 L^2}{EA}, \\
&k_3 \leftrightarrow \frac{k_3 L^4}{EA}, \mu \leftrightarrow \frac{\mu}{A}\sqrt{\frac{L^2}{\rho E}}, G_\mathrm{p} \leftrightarrow G_\mathrm{p}\frac{1}{EA}, F_0 \leftrightarrow \frac{F_0}{EA}, k_\mathrm{f} \leftrightarrow k_\mathrm{f}\frac{L^2}{EI}, c_\mathrm{f} \leftrightarrow \frac{c_\mathrm{f}}{I}\sqrt{\frac{L^2}{\rho E}}
\end{aligned} \tag{4.25}$$

where x is the dimensionless spatial coordinate and t is the dimensionless time. Equation (4.24) can be transformed into the following dimensionless equation

$$\begin{aligned}&\frac{\partial^2 u}{\partial t^2}+\alpha\left[\frac{\partial \psi}{\partial x}-\frac{\partial^2 u}{\partial x^2}\right]+k_1 u+k_3 u^3+\mu\frac{\partial u}{\partial t}-G_{\mathrm{p}}\frac{\partial^2 u}{\partial x^2}=F_0\delta(x-vt),\\&\frac{\partial^2 \psi}{\partial t^2}-\frac{\partial^2 \psi}{\partial x^2}+\beta\left[\psi-\frac{\partial u}{\partial x}\right]+k_{\mathrm{f}}\psi+c_{\mathrm{f}}\frac{\partial \psi}{\partial t}=0\end{aligned} \tag{4.26}$$

4.2.2 Normal Modes

The harmonic solution can be assumed in the form

$$\begin{aligned}u(x,t)&=\sum_{k=1}^{\infty}\varphi_k(x)e^{\mathrm{i}\omega_k t},\\\psi(x,t)&=\sum_{k=1}^{\infty}\upsilon_k(x)e^{\mathrm{i}\omega_k t}\end{aligned} \tag{4.27}$$

where ω_k are the natural frequencies, and $\varphi_k(x)$ and $\upsilon_k(x)$ are the corresponding mode functions of the beam on a linear Pasternak foundation, which can be derived from Eq. (4.26) as follows

$$\begin{aligned}&\frac{\mathrm{d}^2\varphi_k}{\mathrm{d}x^2}+a\varphi_k-\frac{c}{\beta}\frac{\mathrm{d}\upsilon_k}{\mathrm{d}x}=0,\\&\frac{\mathrm{d}^2\upsilon_k}{\mathrm{d}x^2}+b\upsilon_k+\beta\frac{\mathrm{d}\varphi_k}{\mathrm{d}x}=0\end{aligned} \tag{4.28}$$

where

$$a=(\omega_k{}^2-k_1)/(\alpha+G_{\mathrm{p}}),b=\omega_k{}^2-\beta-k_{\mathrm{f}},c=\alpha\beta/(\alpha+G_{\mathrm{p}})$$

By eliminating the functions U_k from Eq. (4.28), one obtains the Timoshenko beam equations of free vibration in the form

$$\begin{aligned}&\frac{\mathrm{d}^4\varphi_k}{\mathrm{d}x^4}+p\frac{\mathrm{d}^2\varphi_k}{\mathrm{d}x^2}+q\varphi_k=0,\\&p=a+b+c,q=ab\end{aligned} \tag{4.29}$$

Thus the characteristic equation has the form

$$r^4+pr^2+q=0 \tag{4.30}$$

Replacing $z = r^2$ casts Eq. (4.30) in the form

$$z^2 + pz + q = 0 \tag{4.31}$$

Its roots are

$$z_1 = \frac{1}{2}(-p + \sqrt{\Delta}), z_2 = \frac{1}{2}(-p - \sqrt{\Delta}) \tag{4.32}$$

where $\Delta = (-c + a - b)^2 + 4ac$.

Now, one should discuss the sign of the roots z_1 and z_2: $\forall_{\omega k} \Leftrightarrow z_2 < 0; z_1 > 0$ for $q < 0$; $z_1 < 0$ for $q > 0$.

Two possible solutions to Eq. (4.28) can be obtained:

a. For $q < 0$,

$$\begin{aligned} \varphi(x) &= C_1 \cosh \lambda_1 x + C_2 \sinh \lambda_1 x + C_3 \cos \lambda_2 x + C_4 \sin \lambda_2 x, \\ \upsilon(x) &= C_1' \sinh \lambda_1 x + C_2' \cosh \lambda_1 x + C_3' \sin \lambda_2 x + C_4' \cos \lambda_2 x \end{aligned} \tag{4.33}$$

b. For $q > 0$,

$$\begin{aligned} \varphi(x) &= H_1 \cos \lambda_1 x + H_2 \sin \lambda_1 x + H_3 \cos \lambda_2 x + H_4 \sin \lambda_2 x, \\ \upsilon(x) &= H_1' \sin \lambda_1 x + H_2' \cos \lambda_1 x + H_3' \sin \lambda_2 x + H_4' \cos \lambda_2 x \end{aligned} \tag{4.34}$$

where the integration constants C_i, C_i', H_i, and H_i' depend on the boundary conditions.

The simply supported boundary condition analyzed in this research is the most frequently encountered boundary condition for the present problem. The boundary conditions for a simply supported beam are

$$\begin{aligned} &\varphi(0) = \varphi(1) = 0, \\ &\varphi''(0) + a\varphi(0) = \varphi''(1) + a\varphi(1) = 0 \end{aligned} \tag{4.35}$$

a. For $q < 0$, the solution to Eq. (4.29) has the form (4.33). From the boundary conditions at $x = 0$, the following equations are obtained

$$C_1 + C_3 = 0, \lambda_1^2 C_1 - \lambda_2^2 C_3 = 0 \tag{4.36}$$

The system of equations is satisfied when $C_1 = C_3 = 0$, which corresponds to the solution for the Euler–Bernoulli beam.

The boundary conditions at $x = 1$ are expressed by the matrix equation

$$\begin{bmatrix} \sinh \lambda_1 & \sinh \lambda_2 \\ \lambda_1^2 \sinh \lambda_1 & -\lambda_2^2 \sinh \lambda_2 \end{bmatrix} \begin{bmatrix} C_2 \\ C_4 \end{bmatrix} = \begin{bmatrix} 0 \\ 0 \end{bmatrix} \tag{4.37}$$

The nontrivial solution to Eq. (4.37) is obtained from the condition that the main matrix determinant is equal to zero. Thus, one can obtain the frequency equation

$$\sin \lambda_2 = 0 \tag{4.38}$$

Consequently, the corresponding *i*th normal modes with simply supported boundary conditions can be obtained as

$$\begin{aligned} \phi(x) &= C \sin \lambda_2 x, \\ \upsilon(x) &= C' \cos \lambda_2 x \end{aligned} \tag{4.39}$$

b. For $q > 0$, the solution to Eq. (4.29) has the form (4.34). From the boundary conditions at $x = 0$, the following equations are obtained

$$H_1 + H_3 = 0, \lambda_1^2 H_1 + \lambda_2^2 H_3 = 0 \tag{4.40}$$

The system of equations is satisfied when $H_1 = H_3 = 0$.

The boundary conditions at $x = 1$ are expressed by the matrix equation

$$\begin{bmatrix} \sin \lambda_1 & \sin \lambda_2 \\ -\lambda_1^2 \sin \lambda_1 & -\lambda_2^2 \sin \lambda_2 \end{bmatrix} \begin{bmatrix} H_2 \\ H_4 \end{bmatrix} = \begin{bmatrix} 0 \\ 0 \end{bmatrix} \tag{4.41}$$

The nontrivial solution to Eq. (4.41) is obtained from the condition that the main matrix determinant is equal to zero. Thus, one can obtain the frequency equation

$$\sin \lambda_2 = 0 \tag{4.42}$$

Consequently, the corresponding *i*th normal modes with simply supported boundary conditions can be obtained as

$$\begin{aligned} \varphi(x) &= H \sin \lambda_2 x, \\ \upsilon(x) &= H' \cos \lambda_2 x \end{aligned} \tag{4.43}$$

4.2.3 Galerkin's Discretization

The Galerkin truncation method is used to discretize the system and the series expansion forms for $u(x,t)$ and $\psi(x,t)$ with the simply supported boundary conditions are assumed as

$$\begin{aligned} u(x,t) &= \sum_{k=1}^{\infty} q_k(t) \varphi_k(x), \\ \psi(x,t) &= \sum_{k=1}^{\infty} \zeta_k(t) \upsilon_k(x) \end{aligned} \tag{4.44}$$

where $\varphi_k(x)$ and $\nu_k(x)$ are the trial functions, $q_k(t)$ and $\zeta_k(t)$ are the sets of generalized displacements. In this research, the trial functions $\varphi_k(x)$ and $\nu_k(x)$ are chosen as eigenfunctions of the Timoshenko beam linear subsystem with the simply supported boundary conditions as

$$\begin{aligned}\varphi_k(x) &= \sin(\beta_k x),\\ \upsilon_k(x) &= \cos(\beta_k x)\end{aligned} \tag{4.45}$$

The first n terms of Eq. (4.44) are considered in this research. Substituting Eq. (4.44) into Eq. (4.26) leads to

$$\begin{aligned}&\sum_{k=1}^{n}\left\{\left[\ddot{q}_k(t)+\mu\dot{q}_k(t)+\left[k_1+G_p(k\pi)^2+\alpha(k\pi)^2\right]q_k(t)\right]\varphi_k(x)\right\}\\ &-\alpha\left[\sum_{k=1}^{n}(k\pi)\zeta_k(t)\varphi_k(x)\right]+k_3\left[\sum_{k=1}^{n}q_k(t)\varphi_k(x)\right]^3=F_0\delta(x-vt),\\ &\sum_{k=1}^{n}\left\{\left[\ddot{\zeta}_k(t)+c_f\dot{\zeta}_k(t)+\left[k_f+(k\pi)^2+\beta\right]\zeta_k(t)\right]\upsilon_k(x)\right\}-\beta\left[\sum_{k=1}^{n}(k\pi)q_k(t)\upsilon_k(x)\right]=0\end{aligned} \tag{4.46}$$

Multiplying Eq. (4.46) by the weight functions $w_i(x)$ and integrating it over the interval of 0 and 1, the Galerkin procedure leads to the following set of $2n$ second-order ODES

$$\begin{aligned}&\sum_{k=1}^{n}\left\{\left[\ddot{q}_k(t)+\mu\dot{q}_k(t)+\left[k_1+G_p(k\pi)^2+\alpha(k\pi)^2\right]q_k(t)\right]\int_0^1\varphi_k(x)w_i(x)\mathrm{d}x\right\}\\ &-\sum_{k=1}^{n}\left[\alpha(k\pi)\zeta_k(t)\int_0^1\varphi_k(x)w_i(x)\mathrm{d}x\right]+k_3\int_0^1\left[\sum_{k=1}^{n}q_k(t)\varphi_k(x)\right]^3w_i(x)\mathrm{d}x=F_0w_i(vt),\\ &\sum_{k=1}^{n}\left\{\left[\ddot{\zeta}_k(t)+c_f\dot{\zeta}_k(t)+\left[k_f+(k\pi)^2+\beta\right]\zeta_k(t)\right]\int_0^1\upsilon_k(x)\nu_i(x)\mathrm{d}x\right\}\\ &-\sum_{k=1}^{n}\left[\beta(k\pi)q_k(t)\int_0^1\upsilon_k(x)\nu_i(x)\mathrm{d}x\right]=0,i=1,2,\ldots n\end{aligned} \tag{4.47}$$

Here, the weight functions $w_i(x)$ and $v_i(x)$, $i=1,2,\ldots,n$, are also chosen as eigenfunctions of the Timoshenko beam linear subsystem. That is,

$$w_i(x)=\sin(\beta_i x), v_i(x)=\cos(\beta_i x) \tag{4.48}$$

With the usual orthogonal condition, the SS boundary conditions lead to

$$\int_0^1\phi_k(x)w_i(x)\mathrm{d}x=\begin{cases}0, & k\neq i\\ 1/2, & k=i\end{cases}\qquad\int_0^1\upsilon_k(x)\nu_i(x)\mathrm{d}x=\begin{cases}0, & k\neq i\\ 1/2, & k=i\end{cases} \tag{4.49}$$

Substitution of Eq. (4.49) into Eq. (4.47) yields

$$\begin{aligned}&\ddot{q}_i(t)+\left[k_1+G_{\mathrm{p}}(i\pi)^2+\alpha(i\pi)^2\right]q_i(t)+2k_3\int_0^1\left[\sum_{k=1}^{n}q_k(t)\varphi_k(x)\right]^3 w_i(x)\mathrm{d}x\\&+\mu\dot{q}_i(t)-\alpha(i\pi)\zeta_i(t)=2F_0w_i(vt),\\&\ddot{\zeta}_i(t)+c_{\mathrm{f}}\dot{\zeta}_i(t)+\left[k_{\mathrm{f}}+(i\pi)^2+\beta\right]\zeta_i(t)-\beta(i\pi)q_i(t)=0,i=1,2,\ldots n\end{aligned}\tag{4.50}$$

The above mentioned ODES can be solved via the fourth-order Runge–Kutta method. In the numerical computation here, the initial conditions are

$$q(t)\big|_{t=0}=\dot{q}(t)\big|_{t=0}=\zeta(t)\big|_{t=0}=\dot{\zeta}(t)\big|_{t=0}=0\tag{4.51}$$

4.2.4 Numerical Results

In this part, numerical examples are given for parametric research. The physical and geometric properties of the Timoshenko beam, foundation and the moving load are listed in Table 4.2.

The vertical deflection of the beam when the load moves to the mid-point of the beam is shown in Fig. 4.8a, while the vertical deflection of beam center with time is illustrated in Fig. 4.8b. The Galerkin truncation term is set to four values, namely, a 50-term Galerkin's truncation, 75-term Galerkin's truncation, 150-term Galerkin's truncation, and 200-term Galerkin's truncation. As shown in the two plots, the transverse deflection increases for $x<80$ or $t<4$, and the biggest deflection appears at $x=80$ (with $\pm 0.2\%$ variations) or $t=4$ (with $\pm 0.15\%$ variations). After reaching the peak values, the transverse deflection decreases and tends to zero. The growth speed of the transverse deflection is almost the same as the reduced speed. The numerical results also demonstrated that there are large differences between the 50-term Galerkin truncation results with the 150-term ones and the 200-term ones. There is no doubt that the 50-term Galerkin's method is not accurate enough for the dynamic response analysis Timoshenko beams on nonlinear viscoelastic foundations subjected to a moving concentrated load, and there are discernible differences between the results of the 75-term and the 150-term Galerkin's method. Moreover, the results of the 150-term and the 200-term Galerkin's method are almost the same. Therefore, the 150-term Galerkin's method yields rather accurate results. The maximum relative differences between the maximum mid-point vertical deflections is 8.49×10^{-2} in the 50-term Galerkin's truncation and 200-term Galerkin's truncation, 4.06×10^{-2} in the 75-term Galerkin's truncation and 200-term Galerkin's truncation, and 0.74×10^{-2} in the 150-term Galerkin's truncation and 200-term Galerkin's truncation. The results are in good agreement with the research by Ding et al. [16].

Figure 4.9 shows the dependence of the convergence in terms of the vertical deflections of the beam on the system parameters. The abscissa represents the trunca-

Table 4.2 Properties of the beam, foundation, and load. (Reprinted from ref. [18], with kind permission from Springer Science+Business Media)

Item	Notation	Value	Dimensionless Value
Beam			
Young's modulus	E	6.998 GPa	–
Shear modulus	G	77 GPa	
Mass density	ρ	2373 kg/m^3	–
Height of pavement	h	0.3 m	–
Width of pavement	b	1.0 m	–
Length	L	160 m	–
Shear coefficients	k'	0.4	–
–	α	–	4.401
–	β	–	1.502×10^7
Foundation			
Linear stiffness	k_1	8×10^6 N/m^2	97.552
Nonlinear stiffness	k_3	8×10^6 N/m^4	2.497×10^6
Viscous damping	μ	0.3×10^6 Ns/m^2	39.263
Shear deformation coefficient	G_p	6.669×10^7 N	0.0318
Rocking stiffness	k_f	10^8 N	1.626×10^5
Rocking damping coefficient	c_f	1.5×10^6 N·s	2.618×10^4
Moving load			
Load	F_0	2.126×10^5 N	1.01×10^{-4}
Speed	V	20 m/s	0.01165

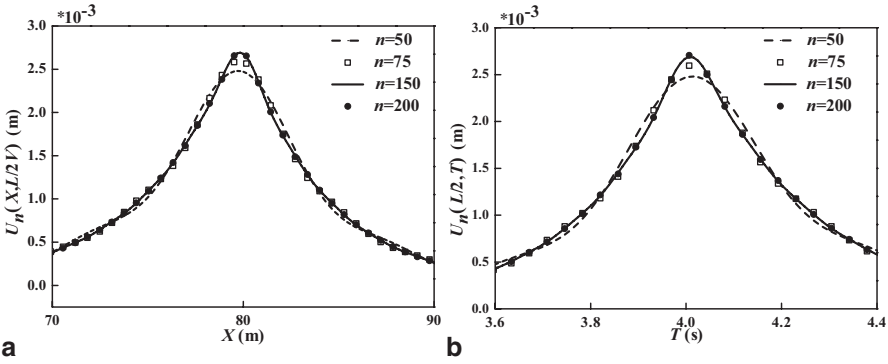

Fig. 4.8 Effects of the Galerkin's truncation terms: **a** The effects on the vertical deflection of the beam; **b** The effects on the vertical deflection of the beam's midpoint. (Reprinted from ref. [18], with kind permission from Springer Science+Business Media)

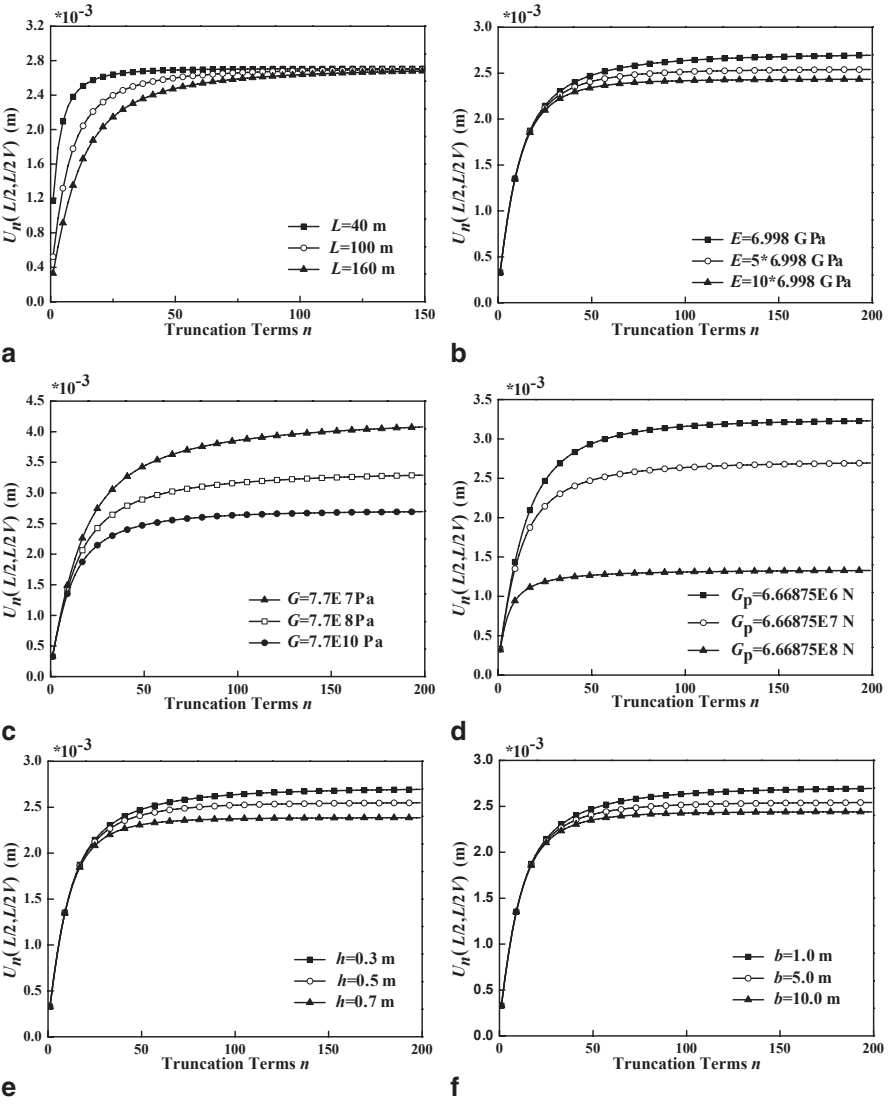

Fig. 4.9 Effects of parameters on the vertical displacements of the beam's midpoint versus the truncation terms. (Reprinted from ref. [18], with kind permission from Springer Science+Business Media)

tion terms n while the ordinate represents the vertical displacements of the beam's midpoint while $X = L/(2V)$, $T = L/(2V)$. As seen in these figures, the vertical deflections of the beam increase with the truncation terms initially, but gradually approach to a stable value. The numerical results illustrate that the convergence of the Galerkin truncation increases with the growing modulus of elasticity of the beam, the shear modulus of the beam, the shear coefficient of the foundation, the height

and the width of the beam, but decreases with the growing length of the beam. That is, the longer the length of the beam that is chosen, the more truncation terms are required to achieve convergence. From the obtained results, it is concluded that the vertical displacements of the beam decrease with the growing of these parameters except the length of the beam. For various values of L, there is little difference among the vertical deflections of the beam when $U_n(L/2, L/(2V))$ has been a stable value in Fig. 4.9a. Moreover, the numerical results also depict that there is little difference among the vertical deflections of the beam for not too large truncation terms with different values of the modulus of elasticity and the height and width of the beam. It should be noted that the effects of the above mentioned parameters have been investigated except the shear modulus of the beam and the shear coefficient of the foundation in Ref. [16]. In this section, similar conclusions are drawn from Fig. 4.9b, e and f. However, the influence of the length of the beam on the vertical deflection of a Timoshenko beam on the Pasternak foundation can be neglected, which is different from Ref. [16], probably because of a model difference.

The above discussions demonstrate that the above mentioned parameters have appreciable influences on the convergence of the Galerkin truncation. However, some parameters do not, including the linear foundation parameters, the rocking stiffness of the foundation, the damping coefficient of the foundation, and the nonlinear foundation parameters. On the other hand, these parameters have greater effects on the vertical displacements than the convergence of the Galerkin truncation. Consequently, it is difficult to demonstrate the dependence of the convergence on these parameters. In order to study the effects of these parameters on the convergence of the Galerkin truncation, δ_n is introduced and described by

$$\delta_n = \frac{U_n(L/2, L/2V) - U_{n-1}(L/2, L/2V)}{U_{n-1}(L/2, L/2V)} \times 100\% \tag{4.52}$$

The effects of other system parameters on the convergence of the Galerkin truncation are investigated in Fig. 4.10. Compared with Fig. 4.9, on the contrary, the numerical results demonstrate that δ_n decreases with the truncation terms until they are zero. From Fig. 4.10a and b, it can be seen that the convergence of the Galerkin truncation decreases with the increasing linear foundation parameters, but increases with the increasing rocking stiffness of the foundation. Furthermore, the 100-term Galerkin's method does not have a convergent numerical solution. This conclusion coincides with that in Ref. [16].

Figure 4.10c and d show a more complicated phenomenon that the convergence of the Galerkin truncation concerns not only the system parameters but also the truncation terms. As seen in Fig. 4.10c, when the truncation term is less than 37, the larger damping coefficient of the foundation performs the faster convergence. Otherwise, the smaller damping coefficient of the foundation leads to the faster convergence. A similar conclusion can be drawn from Fig. 4.10d, whereas the nonlinear foundation parameter has less influence on the convergence of the Galerkin truncation than the damping coefficient of the foundation.

The time history diagrams for the vertical dynamic deflections of the mid-span of the beam for different values of the system parameters are shown in Fig. 4.11. As seen in these figures, the maximum value of the dynamic deflection occurs almost

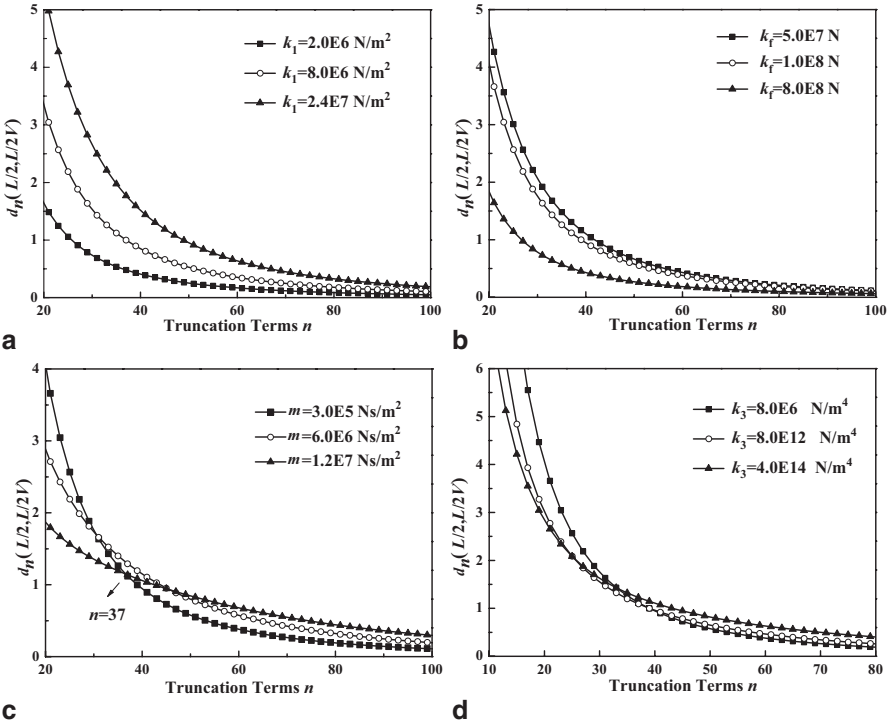

Fig. 4.10 Effects of parameters on δ_n versus truncation terms. (Reprinted from ref. [18], with kind permission from Springer Science+Business Media)

at the mid-span of the beam (with ±0.15% variations), as illustrated in Fig. 4.8b. However, it is worth to note that the peak value occurs at a farther vicinity of the mid-span (with ±0.86% variations) when the damping coefficient of the foundation is a greater one from Fig. 4.11a. Thus, the growth speed of the transverse deflection is far greater than the reduced speed. That is to say, the damping coefficient of the foundation is a reason for time delay. Moreover, as the damping coefficient of the foundation increases, the deflection of the Timoshenko beams decreases accordingly. In Ref. [19], similar results can be found. Above all, the numerical results show that the damping coefficient of the foundation has significant influence on the dynamic response of the Timoshenko beam. In other words, the damping coefficient of the foundation cannot be neglected when studying the dynamic response of finite Timoshenko beams supported by nonlinear viscoelastic Pasternak foundations.

The effects of the shear modulus of the beam and the shear deformation coefficient of the foundation on the deflections of the beams lying on viscoelastic nonlinear foundations are illustrated in Fig. 4.11b and c, respectively. From the simulation results obtained, one can see that the biggest deflections decrease with the increasing shear modulus of the beams and the increasing shear deformation coefficient of the foundations. It should be noted that a Pasternak foundation turns into a Winkler foundation when $G_p = 0$. That is to say, the maximum deflection of a Timoshenko beam on a Pasternak foundation is much smaller than that of a beam on

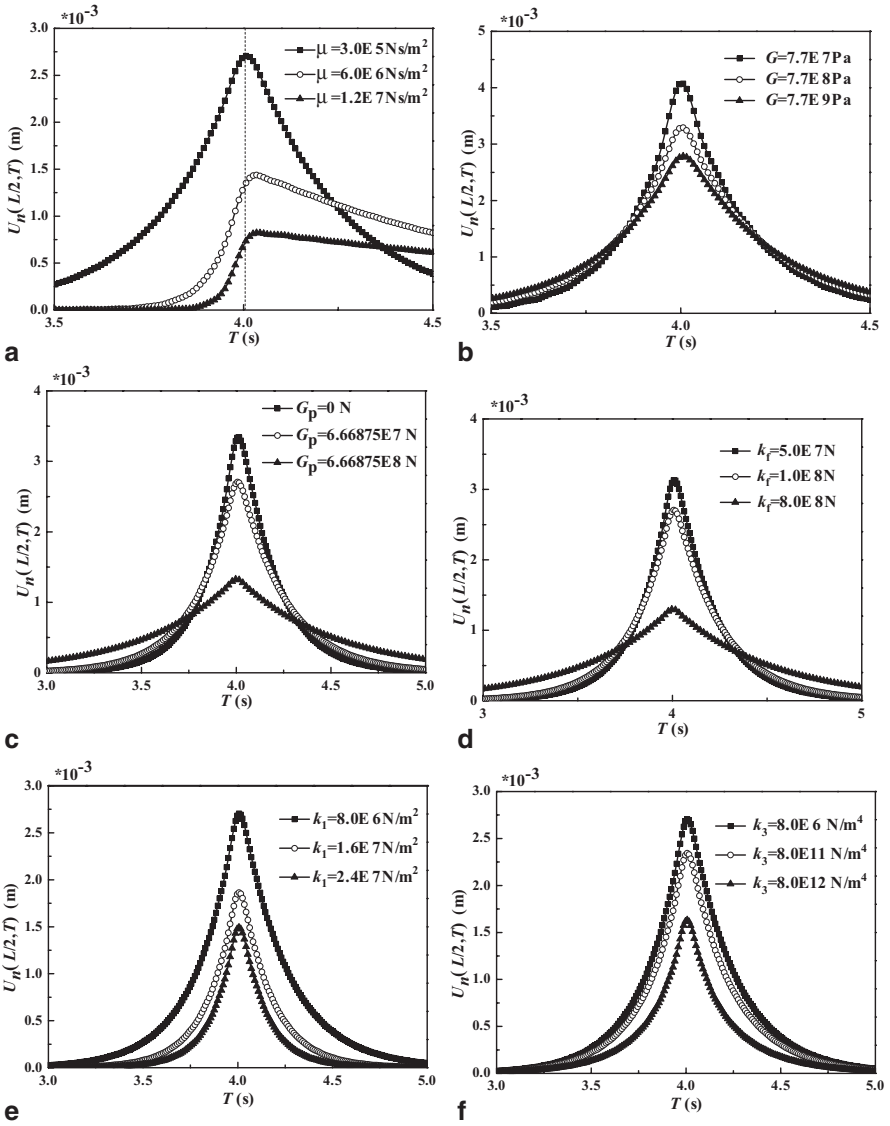

Fig. 4.11 Effects of parameters on the deflection of the beam. (Reprinted from ref. [18], with kind permission from Springer Science+Business Media)

a Winkler foundation. It is noted that this conclusion corresponds with the research in Ref. [20].

From Fig. 4.11d, one can observe that the maximum deflection decreases with the increasing rocking stiffness of the foundation. In Ref. [19], Ding et al. has a similar conclusion. Figure 4.11e and f display the effects of the linear elasticity parameter and the nonlinear elasticity parameter of the foundation on the deflection of Timoshenko beams supported by viscoelastic nonlinear foundations. The numerical

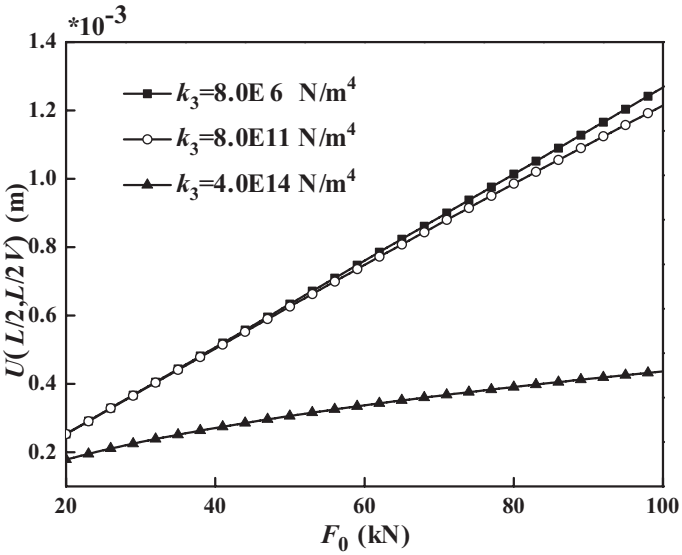

Fig. 4.12 The effects of the nonlinear elasticity parameter on the vertical displacement versus the magnitude of the moving load. (Reprinted from ref. [18], with kind permission from Springer Science+Business Media)

results indicate that the biggest deflections decrease with the increasing linear and nonlinear elasticity parameters of the foundation. The whole form of the deflection has little change with different linear elasticity parameters and nonlinear elasticity parameters of the foundation.

Figure 4.12 shows that the influence of the nonlinear elasticity parameter on the vertical displacements of the beam at mid-span while the load moves to the mid-point of the beam versus the magnitude of the moving load. The figure predicts that the difference between the results of $k_3 = 8.0 \times 10^6\,\mathrm{N/m^4}$ and $k_3 = 8.0 \times 10^{11}\,\mathrm{N/m^4}$ is very small. When compared the results of $k_3 = 8.0 \times 10^6\,\mathrm{N/m^4}$ with $k_3 = 8.0 \times 10^{14}\,\mathrm{N/m^4}$, there are big differences and the deflection decreases with the increasing nonlinear elasticity parameter. Furthermore, the deflection of the Timoshenko beams increases with the increasing magnitude of the moving load.

As far as the effects of the rocking damping coefficient on the dynamic response of finite beams are concerned, one can conclude that the rocking damping coefficient could neither affect greatly on the deflection of the beam nor make a contribution to the convergence of the Galerkin truncation from Fig. 4.13. That is, the rocking damping coefficient can be neglected when studying the dynamic response of finite Timoshenko beams supported by nonlinear viscoelastic Pasternak foundations.

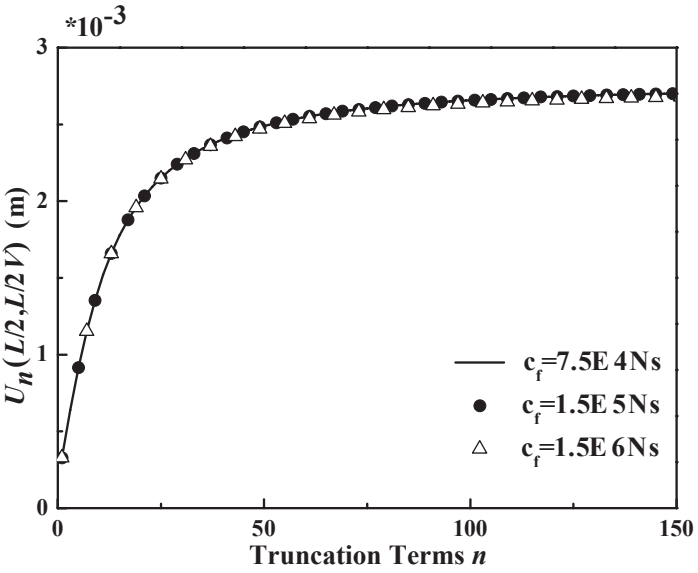

Fig. 4.13 The effects of the rocking damping coefficient on the vertical deflection versus the truncation terms. (Reprinted from ref. [18], with kind permission from Springer Science+Business Media)

4.3 Vibration of a Vehicle–Pavement Coupled System Based on a Finite Timoshenko Beam on a Nonlinear Foundation [21]

4.3.1 The Mathematical Model

The schematic of a finite elastic beam subjected to a moving spring–mass–damper system on a nonlinear foundation is shown in Fig. 4.14. The beam is modeled based on Timoshenko beam theory. $U(X, T)$ and $\psi(X, T)$ are the vertical displacement function and the slope function due to bending of the beam, respectively. T is the time. X and Z are, respectively, the spatial coordinate along the axis of the beam and the vertical spatial coordinate. Shearing strain γ is defined as $\gamma = U_{,X} - \psi$, where the comma preceding X denotes the partial differentiation with respect to X. The foundation model is characterized by linear elastic modulus k_1, nonlinear elastic modulus k_3, Pasternak foundation modulus (shear deformation coefficient) G_p, damping coefficient μ, rocking stiffness k_f, and rocking damping coefficients c_f. V represents the speed of the moving oscillator. k and c are, respectively, the elastic stiffness and the damping coefficients of the moving oscillator. m_1 and m_2 are the masses in the moving oscillator. Z_1 and Z_2 are the vertical displacement functions of the two masses of the oscillator.

Consider the pavement as a homogeneous beam with constant cross-section A, moment of inertial I, length L, densityρ, shear modulus G, effective area $k'A$, and

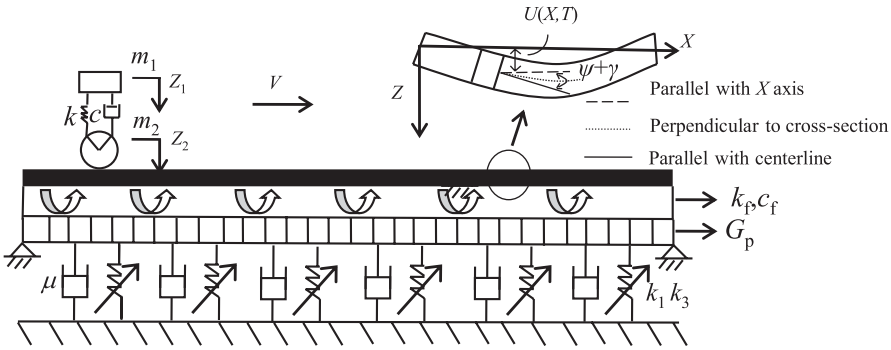

Fig. 4.14 Schematic representation of a Timoshenko beam subjected to a moving oscillator on a nonlinear Pasternak foundation. (Reprinted from ref. [21], Copyright 2014, with permission from Elsevier)

modulus of elasticity E. The equations of motion for the Timoshenko beam can be obtained by the d'Alembert's principle and the Timoshenko beam theory as

$$\begin{aligned}&\rho AU_{,TT}+k'AG\left(\psi_{,X}-U_{,XX}\right)+k_1U+k_3U^3+\mu U_{,T}-G_pU_{,XX}=F_0\delta\left(X-VT\right),\\&\rho I\psi_{,TT}-EI\psi_{,XX}+k'AG\left(\psi-U_{,X}\right)+k_f\psi+c_f\psi_{,T}=0\end{aligned}\tag{4.53}$$

where F_0 represents the force induced by the moving spring–mass–damper oscillator. The comma preceding T denotes the partial differentiation with respect to T. Furthermore, the equations of motion for the moving oscillator can be obtained by Newton's Second Law as

$$\begin{aligned}&m_1\frac{\mathrm{d}^2Z_1}{\mathrm{d}T^2}+k\left(Z_1-Z_2\right)+c\left(\frac{\mathrm{d}Z_1}{\mathrm{d}T}-\frac{\mathrm{d}Z_2}{\mathrm{d}T}\right)=0,\\&m_2\frac{\mathrm{d}^2Z_2}{\mathrm{d}T^2}-k\left(Z_1-Z_2\right)-c\left(\frac{\mathrm{d}Z_1}{\mathrm{d}T}-\frac{\mathrm{d}Z_2}{\mathrm{d}T}\right)=-F_0+m_1g+m_2g\end{aligned}\tag{4.54}$$

In this research, all work is based on the assumption that the moving oscillator stays on the ground. The displacement of the moving oscillator is expressed as the sum of the vertical displacement of the beam and beam's surface roughness as

$$Z_2(T)=U(X,T)|_{X=VT}+\mathrm{Z_p}(X)|_{X=VT}\tag{4.55}$$

where $\mathrm{Z_p}(X)$ represents the road surface roughness, and is defined as

$$\mathrm{Z_p}(X)=a\sin\left(\frac{2\pi X}{L_0}\right)\tag{4.56}$$

in which a is the amplitude of the road surface roughness, and L_0 is the wavelength of harmonic road roughness. Substituting Eq. (4.55) into Eq. (4.54) leads to

$$m_1\frac{\mathrm{d}^2 Z_1}{\mathrm{d}T^2}=-k(Z_1-Z_2)-c\frac{\mathrm{d}Z_1}{\mathrm{d}T}+c\left[U_{,T}+VU_{,X}+V\frac{\mathrm{d}Z_{\mathrm{p}}(X)}{\mathrm{d}X}\right]_{X=VT} \tag{4.57}$$

and

$$\begin{aligned}F_0=&-m_2\left[U_{,TT}+2VU_{,XT}+V^2U_{,XX}+V^2\frac{\mathrm{d}^2 Z_{\mathrm{p}}(X)}{\mathrm{d}X^2}\right]_{X=VT}+k\left(Z_1-Z_2\right)\\&+c\frac{\mathrm{d}Z_1}{\mathrm{d}T}-c\left[U_{,T}+VU_{,X}+V\frac{\mathrm{d}Z_{\mathrm{p}}(X)}{\mathrm{d}X}\right]_{X=VT}+m_1g+m_2g\end{aligned} \tag{4.58}$$

Substitution of Eqs. (4.57) and (4.58) into Eq. (4.53) leads to the following governing differential equations of coupled motion

$$\begin{aligned}&\rho AU_{,TT}+k'AG\left(\psi_{,X}-U_{,XX}\right)+k_1U+k_3U^3+\mu U_{,T}-G_{\mathrm{p}}U_{,XX}=\\&\left\{-m_2\left[Y_{,TT}+2VY_{,XT}+V^2Y_{,XX}+V^2\frac{\mathrm{d}^2 Z_{\mathrm{p}}(X)}{\mathrm{d}T^2}\right]_{X=VT}+\left(m_2+m_1\right)g-m_1\frac{\mathrm{d}^2 Z_1}{\mathrm{d}T^2}\right\}\delta(X-VT),\\&\rho I\psi_{,TT}-EI\psi_{,XX}+k'AG\left(\psi-U_{,X}\right)+k_{\mathrm{f}}\psi+c_{\mathrm{f}}\psi_{,T}=0,\\&m_1\frac{\mathrm{d}^2 Z_1}{\mathrm{d}T^2}=-k\left\{Z_1-\left[U+Z_{\mathrm{p}}(X)\right]_{X=VT}\right\}-c\left\{\frac{\mathrm{d}Z_1}{\mathrm{d}T}-\left[U_{,T}+VU_{,X}+V\frac{\mathrm{d}Z_{\mathrm{p}}(X)}{\mathrm{d}X}\right]_{X=VT}\right\}\end{aligned} \tag{4.59}$$

Here, the beam is assumed to be simply supported at both ends. Therefore, the boundary conditions are given as follows

$$U(X,T)\big|_{X=0}=U(X,T)\big|_{X=L}=0,EI\psi_{,X}(X,T)\big|_{X=0}=EI\psi_{,X}(X,T)\big|_{X=L}=0 \tag{4.60}$$

In order to avoid round-off due to manipulations with large or small numbers in numerical calculations, the following dimensionless variables and parameters are introduced

$$\begin{aligned}&u=\frac{U}{L},t=\frac{T}{L}\sqrt{\frac{E}{\rho}},x=\frac{X}{L},\psi=\psi,v=V\sqrt{\frac{\rho}{E}},\alpha=\frac{k'G}{E},\beta=k'AG\frac{L^2}{EI},\\&\kappa=\frac{(m_2+m_1)g}{EA},z_{\mathrm{p}}=\frac{a}{L}\sin\left(\frac{2\pi xL}{L_0}\right),z_1=\frac{Z_1}{L},k\leftrightarrow\frac{\rho L^2}{m_1E}k,k_1\leftrightarrow\frac{k_1L^2}{EA},\\&k_3\leftrightarrow\frac{k_3L^4}{EA},\mu\leftrightarrow\frac{\mu}{A}\sqrt{\frac{L^2}{\rho E}},G_{\mathrm{p}}\leftrightarrow G_{\mathrm{p}}\frac{1}{EA},k_{\mathrm{f}}\leftrightarrow k_{\mathrm{f}}\frac{L^2}{EI},c_{\mathrm{f}}\leftrightarrow\frac{\mathrm{c}_{\mathrm{f}}}{\mathrm{I}}\sqrt{\frac{L^2}{\rho E}},\\&m_2\leftrightarrow\frac{m_2}{\rho AL},m_1\leftrightarrow\frac{m_1}{\rho AL},c\leftrightarrow\frac{cL}{m_1}\sqrt{\frac{\rho}{E}}\end{aligned} \tag{4.61}$$

Equations (4.59) and (4.60) can be expressed into the dimensionless normalized forms

$$\begin{aligned}
&u_{,tt}+\alpha\left(\psi_{,x}-u_{,xx}\right)+k_1u+k_3u^3+\mu u_{,t}-G_{\mathrm{p}}u_{,xx}\\
&\quad=\left[\kappa-m_1\frac{\mathrm{d}^2z_1}{\mathrm{d}t^2}-m_2\left(y_{,tt}+2vy_{,xt}+v^2y_{,xx}+v^2\frac{\mathrm{d}^2z_{\mathrm{p}}}{\mathrm{d}x^2}\right)_{x=vt}\right]\delta\left(x-vt\right),\\
&\psi_{,tt}-\psi_{,xx}+\beta\left(\psi-u_{,x}\right)+k_{\mathrm{f}}\psi+c_{\mathrm{f}}\psi_{,t}=0,\\
&\frac{\mathrm{d}^2z_1}{\mathrm{d}t^2}+k\left[z_1-\left(u+z_{\mathrm{p}}\right)_{x=vt}\right]+c\left[\frac{\mathrm{d}z_1}{\mathrm{d}t}-\left(u_{,t}+vu_{,x}+v\frac{\mathrm{d}z_{\mathrm{p}}}{\mathrm{d}x}\right)_{x=vt}\right]=0
\end{aligned}\tag{4.62}$$

and

$$u\left(x,t\right)\big|_{x=0}=u\left(x,t\right)\big|_{x=1}=0,\psi_{,x}\left(x,t\right)\big|_{x=0}=\psi_{,x}\left(x,t\right)\big|_{x=1}=0\tag{4.63}$$

4.3.2 The Schemes of Solution

The Galerkin truncation method is used to discretize the governing equations and the series expansion form for $u(x, t)$ and $\psi(x, t)$ which are simply supported at both ends, respectively, are assumed as

$$\begin{aligned}
u\left(x,t\right)&=\sum_{k=1}^{\infty}q_k\left(t\right)\varphi_k\left(x\right),\\
\psi\left(x,t\right)&=\sum_{k=1}^{\infty}\zeta_k\left(t\right)\upsilon_k\left(x\right)
\end{aligned}\tag{4.64}$$

where $q_k(t)$ and $\zeta_k(t)$, respectively, are sets of generalized vertical displacements and slope displacements due to the bending of the beam, $\varphi_k(x)$ and $\nu_k(x)$ are the trial functions of $u(x, t)$ and $\psi(x, t)$, respectively. Moreover, each of the trial functions should satisfy the boundary conditions (4.63). The first n terms of Eq. (4.64) are considered in the following calculations.

In this research, the trial functions $\varphi_k(x)$ and $\nu_k(x)$ are chosen as eigenfunctions of the Timoshenko beam linear subsystem with the simply supported boundary conditions as

$$\begin{aligned}
\varphi_k\left(x\right)&=\sin\left(\beta_kx\right),\\
\upsilon_k\left(x\right)&=\cos\left(\beta_kx\right)
\end{aligned}\tag{4.65}$$

where $\beta_k=k\pi$. Substituting Eqs. (4.64) and (4.65) into Eq. (4.62) leads to

$$\sum_{k=1}^{n}\left\{\left[\ddot{q}_k(t)+\mu\dot{q}_k(t)+\left(k_1+G_p\beta_k{}^2+\alpha\beta_k{}^2\right)q_k(t)\right]\sin(\beta_k x)\right\}-\alpha\sum_{k=1}^{n}\beta_k\zeta_k(t)\sin(\beta_k x)$$
$$+k_3\left[\sum_{k=1}^{n}q_k(t)\sin(\beta_k x)\right]^3+\left\{m_1\ddot{z}_1(t)-\kappa+m_2\left[\sum_{k=1}^{n}\ddot{q}_k(t)\sin(\beta_k vt)+2v\sum_{k=1}^{n}\beta_k\dot{q}_k(t)\cos(\beta_k vt)\right.\right.$$
$$\left.\left.-v^2\sum_{k=1}^{n}\beta_k{}^2q_k(t)\sin(\beta_k vt)-\frac{4\pi^2v^2aL}{L_0{}^2}\sin\left(\frac{2\pi vtL}{L_0}\right)\right]\right\}\delta(x-vt)=0,$$
$$\sum_{k=1}^{n}\left\{\left[\ddot{\zeta}_k(t)+c_f\dot{\zeta}_k(t)+\left(k_f+\beta_k{}^2+\beta\right)\zeta_k(t)\right]\cos(\beta_k x)\right\}-\beta\sum_{k=1}^{n}\beta_k q_k(t)\cos(\beta_k x)=0,$$
$$\ddot{z}_1(t)+kz_1(t)-k\sum_{k=1}^{n}q_k(t)\sin(\beta_k vt)-k\frac{a}{L}z_p(vt)+c\dot{z}_1(t)-c\sum_{k=1}^{n}\dot{q}_k(t)\sin(\beta_k vt)$$
$$-cv\sum_{k=1}^{n}\beta_k q_k(t)\cos(\beta_k vt)-\frac{2\pi cva}{L_0}\cos\left(\frac{2\pi vtL}{L_0}\right)=0 \tag{4.66}$$

Here, the weight functions $w_i(x)$ and $v_i(x)$, $i=1,2,\ldots,n$, are also chosen as eigenfunctions of the Timoshenko beam linear subsystem, i.e.,

$$w_i(x)=\sin(\beta_i x),v_i(x)=\cos(\beta_i x) \tag{4.67}$$

Multiplying the first two equations of Eq. (4.66) by the weight functions $w_i(x)$ and $v_i(x)$, respectively, then integrating the resulting equation over the interval of 0 and 1, the Galerkin procedure leads to the following set of $2n+1$ s-order ODES

$$\ddot{q}_i(t)+\mu\dot{q}_i(t)+\left(k_1+G_p\beta_i{}^2+\alpha\beta_i{}^2\right)q_i(t)-\alpha\beta_i\zeta_i(t)+2k_3\int_0^1\left[\sum_{k=1}^{n}q_k(t)\sin(\beta_k x)\right]^3\sin(\beta_i x)\mathrm{d}x$$
$$-2\kappa\sin(\beta_i vt)+2m_1\ddot{z}_1(t)\sin(\beta_i vt)+2m_2\left[\sum_{k=1}^{n}\ddot{q}_k(t)\sin(\beta_k vt)\right]\sin(\beta_i vt)$$
$$+4m_2v\left[\sum_{k=1}^{n}\beta_k\dot{q}_k(t)\cos(\beta_k vt)\right]\sin(\beta_i vt)-2m_2v^2\left[\sum_{k=1}^{n}\beta_k{}^2q_k(t)\sin(\beta_k vt)\right]\sin(\beta_i vt)$$
$$-\frac{8\pi^2v^2m_2aL}{L_0{}^2}\sin\left(\frac{2\pi vtL}{L_0}\right)\sin(\beta_i vt)=0,$$
$$\ddot{\zeta}_i(t)+c_f\dot{\zeta}_i(t)+\left(k_f+\beta_i{}^2+\beta\right)\zeta_i(t)-\beta\beta_i q_i(t)=0,i=1,2,\ldots n,$$
$$\ddot{z}_1(t)+kz_1(t)-k\sum_{k=1}^{n}q_k(t)\sin(\beta_k vt)-k\frac{a}{L}\sin\left(\frac{2\pi vtL}{L_0}\right)+c\dot{z}_1(t)-c\sum_{k=1}^{n}\dot{q}_k(t)\sin(\beta_k vt)$$
$$-cv\sum_{k=1}^{n}\beta_k q_k(t)\cos(\beta_k vt)-\frac{2\pi cva}{L_0}\cos\left(\frac{2\pi vtL}{L_0}\right)=0 \tag{4.68}$$

In the following simulations, the initial conditions are all set as

$$\begin{aligned}&q(t)\big|_{t=0}=0,q_{,t}(t)\big|_{t=0}=0,\\&\zeta(t)\big|_{t=0}=0,\zeta_{,t}(t)\big|_{t=0}=0,\\&z_1(t)\big|_{t=0}=0,z_{1,t}(t)\big|_{t=0}=0\end{aligned} \tag{4.69}$$

For a set of given physical and geometric parameters of the Timoshenko beam, the foundation and the moving vehicle, $q_k(t)$, $\zeta_k(t)$, and $z_1(t)$ can be numerically solved via the fourth-order Runge–Kutta method from Eq. (4.68) by discretizing the temporal variables based on the initial conditions of Eq. (4.69). After substituting the numerical solutions of $q_k(t)$ and $\zeta_k(t)$ into Eq. (4.64), one can solve the vertical displacement function $u(x, t)$ and the slope function $\psi(x, t)$.

4.3.3 Numerical Case Studies

In the following numerical examples, the physical and geometric properties of the vehicle–pavement coupled system are listed in Table 4.3.

Based on the parameter values, the values of the dimensionless parameters α, β, and κ, are determined by Eq. (4.61) as $\alpha = 4.4013, \beta = 1.502 \times 10^7$, and $k = 1.02172 \times 10^{-4}$.

Ride comfort is one of the most significant dynamic performance characteristics of modern vehicles. Here, the vertical dynamic acceleration of the vehicle body, m_1, is introduced for describing the ride comfort. Therefore, the acceleration A_1 is defined as

Table 4.3 Properties of the Timoshenko beam, foundation and load. (Reprinted from ref. [21], Copyright 2014, with permission from Elsevier)

	Item	Notation	Value	Dimensionless value
Vehicle	Vehicle body mass	m_1	21260 kg	0.18665
	Tire mass	m_2	190 kg	0.00167
	Suspension stiffness	k	2.06×10^6 N/m	0.84114
	Suspension damping	c	3.0×10^4 N s/m	0.13151
	Speed	V	15 m/s	0.00874
Foundation	Linear stiffness	k_1	8×10^6 N/m^2	97.552
	Nonlinear stiffness	k_3	8×10^6 N/m^4	2.497×10^6
	Viscous damping	μ	0.3×10^6 Ns/m^2	39.263
	Shear parameter	G_p	6.66875×10^7 N	0.0318
	Rocking stiffness	k_f	10^6 N	1.6259×10^3
	Rocking damping coefficient	c_f	1.5×10^6 N·s	2.618×10^4
Beam	Young's modulus	E	6.998 GPa	–
	Shear modulus	G	3.2 GPa	–
	Mass density	ρ	2373 kg/m^3	–
	Cross–section of the pavement	A	0.3 m^2	–
	Moment of inertial of the pavement	I	0.00225 m^4	–
	Length	L	160 m	–
	Wavelength of road roughness	L_0	10 m	
	Amplitude of road roughness	a	0.002 m	
	Shear coefficients	k'	0.4	–

$$A_1 = \frac{\mathrm{d}^2 Z_1}{\mathrm{d}T^2} \tag{4.70}$$

Convergence Studies

The modal truncation method has been widely used to investigate the dynamic response of elastic materials on a nonlinear foundation. Theoretically, an exact solution is obtained by considering an infinite number of modes. Ding et al. studied the convergence of Galerkin's method for the Euler–Bernoulli beam [16] and the Timoshenko beam [18] on a nonlinear foundation subjected to a moving force. The authors found that the Galerkin truncation needs super high-order modes. Moreover, Bhattiprolu, Bajaj, and Davies studied the effect of the number of modes due to the nonlinear and viscoelastic behaviors of soils [22]. They found that Galerkin's method needs 20 modes even for the beam on a nonlinear foam foundation. At the beginning of the numerical investigation, the convergence of the modal truncation is studied for determining the validity of the present study.

Figure 4.15 shows the comparison of the dynamic responses of the vehicle–pavement coupled system with different Galerkin truncation terms. The time history of the vertical deflection of the midpoint of the Timoshenko beam, meaning $X = L/2$, is shown in Fig. 4.15a. The vertical deflection $U(X, L/2V)$ of the Timoshenko beam is shown in Fig. 4.15b. As shown in Fig. 4.15a and b, there are significant differences between the results from the 25-term modal truncation with the results from the 100-term truncation and the 200-term truncation. Furthermore, there are some differences that can be discerned from the numerical results of the 50-term modal truncation with the results of the 100-term. Therefore, the dynamic response of the Timoshenko beam on a six-parameter foundation subjected to a moving oscillator needs more than 50 terms of the modal truncation. The comparison also shows that the vertical deflections from the 100-term modal truncation are very close to the results from the 200-term truncation. These conclusions are in good agreement with the study by Yang et al. based on the same pavement and subgrade model subjected to a moving force [18].

Figure 4.15c and d, respectively, display the vertical displacement and the acceleration of the vehicle body with the different terms of the modal truncation. Figure 4.15c shows that there are discernible differences between the time history and the vertical displacement of the vehicle body of 25-term and 200-term modal truncations. Moreover, Fig. 4.14d illustrates that there are almost no differences in the accelerations of the vehicle body between the 25-term and 200-term modal truncation. Therefore, the simulations for the displacement of the vehicle body do not need such a large number of modes as like the calculations for the displacement of the pavement do.

From Fig. 4.15a–d, one can find that the 100-term Galerkin truncation for the dynamic response of the vehicle–pavement coupled system based on a Timoshenko beam on a six-parameter foundation yields rather accurate results. In the following numerical examples, the first 100 modes are considered for the Galerkin truncation. Therefore, $n = 100$.

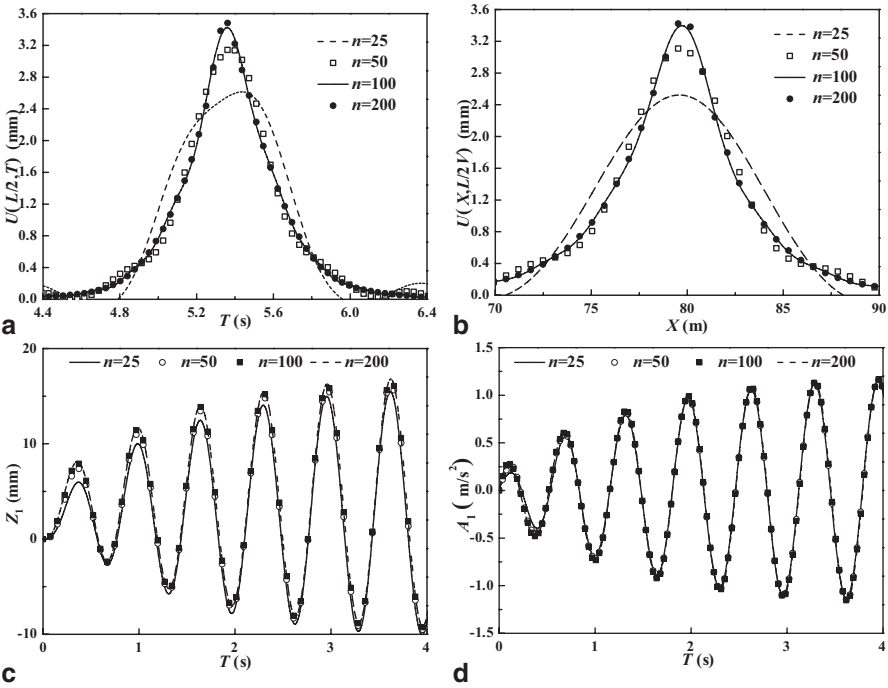

Fig. 4.15 Convergence of the Galerkin's truncation method. (Reprinted from ref. [21], Copyright 2014, with permission from Elsevier)

The Timoshenko beam theory takes into account shear deformation and rotational inertia effects. If the shear deformation and the rotational inertia effects are neglected, the Timoshenko beam theory deduces to the Euler–Bernoulli beam theory. The Euler–Bernoulli beam theory is known as an engineer's beam theory or classical beam theory. The similar Galerkin procedure is applicable in the case of Euler–Bernoulli beams on the same nonlinear foundation. In this case, the equations of motion can be derived as

$$\rho A U_{,TT} + EIU_{,XXXX} + k_1 U + k_3 U^3 + \mu U_{,T} - G_p U_{,XX} =$$

$$\left\{ -m_2 \left[U_{,TT} + 2VU_{,XT} + V^2 U_{,XX} + V^2 \frac{\mathrm{d}^2 Z_p(X)}{\mathrm{d}X^2} \right]_{X=VT} \right.$$

$$\left. + (m_2 + m_1) g - m_1 \frac{\mathrm{d}^2 Z_1}{\mathrm{d}T^2} \right\} \delta(X - VT),$$

$$m_1 \frac{\mathrm{d}^2 Z_1}{\mathrm{d}T^2} = -k\left\{ Z_1 - \left[U + Z_P(X) \right]_{X=VT} \right\} - c\left\{ \frac{\mathrm{d}Z_1}{\mathrm{d}T} - \left[U_{,T} + VU_{,X} + V\frac{\mathrm{d}Z_p(X)}{\mathrm{d}X} \right]_{X=VT} \right\} \tag{4.71}$$

Using the similar Galerkin procedure, the following set of $n+1$ dimensionless second-order ODES leads to

$$\begin{aligned}
&\ddot{q}_i(t)+\mu\dot{q}_i(t)+2k_3\int_0^1\left[\sum_{k=1}^{n}q_k(t)\sin(\beta_k x)\right]^3\sin(\beta_i x)\mathrm{d}x+\sin(\beta_i vt)\\
&\left\{2m_2\left[\sum_{k=1}^{n}\ddot{q}_k(t)\sin(\beta_k vt)\right]+2m_1\ddot{z}_1(t)-2\kappa+4m_2v\left[\sum_{k=1}^{n}\beta_k\dot{q}_k(t)\cos(\beta_k vt)\right]\right.\\
&\left.-2m_2v^2\left[\sum_{k=1}^{n}\beta_k{}^2q_k(t)\sin(\beta_k vt)\right]-8\mathrm{m}_2v^2\frac{\pi^2aL}{L_0{}^2}\sin\left(\frac{2\pi vtL}{L_0}\right)\right\}\\
&+\beta_i{}^2G_{\mathrm{p}}q_i(t)+\beta_i{}^4k_{\mathrm{b}}{}^2q_i(t)+k_1q_i(t)=0,\ \ i=1,2,...n,\\
&\ddot{z}_1(t)=-kz_1(t)+k\sum_{k=1}^{n}q_k(t)\sin(\beta_k vt)+k\frac{a}{L}\sin\left(\frac{2\pi vtL}{L_0}\right)+c\sum_{k=1}^{n}\dot{q}_k(t)\sin(\beta_k vt)\\
&+\frac{2\pi cva}{L_0}\cos\left(\frac{2\pi vtL}{L_0}\right)-c\dot{z}_1(t)+cv\sum_{k=1}^{n}\beta_k q_k(t)\cos(\beta_k vt)
\end{aligned}\tag{4.72}$$

where dimensionless parameter k_{b} is defined as

$$k_{\mathrm{b}}=\frac{1}{L}\sqrt{\frac{I}{A}}\tag{4.73}$$

Based on the parameter values in Table 4.3, k_{b} is determined by Eq. (4.73) as $k_b=5.41\times10^{-4}$. Then, $q_k(t)$ and $z_1(t)$ in Eq. (4.72) are numerically solved via the fourth-order Runge–Kutta method.

In Fig. 4.16a, the effects of two different beam theories on the vertical displacements of the pavement $U(L/2,L/2V)$ versus the truncation terms are shown. Without considering the rocking stiffness and the rocking damping coefficients, the numerical results in Fig. 4.16a illustrate that the convergence of the Galerkin

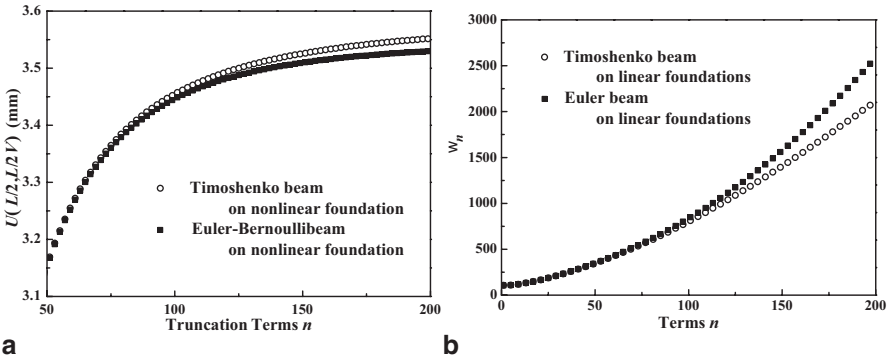

Fig. 4.16 Comparison between the different beam theories of the pavement. (Reprinted from ref. [21], Copyright 2014, with permission from Elsevier)

truncation for the Timoshenko beam on the six-parameter foundation is slightly slower than the Euler–Bernoulli beam on the same foundation. Moreover, Fig. 4.16a shows that the vertical displacements of the Timoshenko beam are slightly larger than those of the Euler–Bernoulli beam. One thing needs to be known, Palmeri and Cicirello also found that the Timoshenko beam theory predicts larger deflections than the Euler–Bernoulli beam theory based on cracked beams under static loads [23]. In Ref. [16], the authors have found that the convergence of the modal truncation is predicted by the natural frequency of the linear subsystem. In order to explore the reason behind the different convergence for the two beam theories, the natural frequencies of the linear subsystem of the two beam models are compared. The natural frequencies of the Euler–Bernoulli beam on a linear elastic Pasternak foundation which is simply supported and without any loads, $\omega \mathrm{E}_k$, are derived as follows

$$\omega_{\mathrm{E}k}^2 = k_{\mathrm{b}}^2 (k\pi)^4 + k_1 + G_{\mathrm{P}} (k\pi)^2 \tag{4.74}$$

where $k = 1,2,\ldots$. The natural frequencies of the Timoshenko beam on the same foundation and with the same boundary conditions, $\omega \mathrm{T}_k$, are calculated from the following equation

$$\sqrt{\sqrt{\left(\frac{\omega_{\mathrm{T}k}^2 - k_1 + (\alpha + G_{\mathrm{p}})(\omega_{\mathrm{T}k}^2 - \beta) + \alpha\beta}{\alpha + G_{\mathrm{p}}}\right)^2 - 4\frac{(\omega_{\mathrm{T}k}^2 - k_1)(\omega_{\mathrm{T}k}^2 - \beta)}{\alpha + G_{\mathrm{p}}}} + \frac{\omega_{\mathrm{T}k}^2 - k_1 + (\alpha + G_{\mathrm{p}})(\omega_{\mathrm{T}k}^2 - \beta) + \alpha\beta}{\alpha + G_{\mathrm{p}}}} = \sqrt{2}k\pi \tag{4.75}$$

The Fig. 4.16b shows that the natural frequencies of the Timoshenko beam on a linear foundation increase slower than the frequencies of the Euler–Bernoulli beam on the same foundation. The comparison between Fig. 4.16a and b shows that the changing tendencies of the natural frequencies not only predict the convergence of the modal truncation, but also predict the differences between the convergences of the different beam theories.

Figure 4.17 shows the effects of the length of the road on the dynamic response of the pavement. Figure 4.17a and b, respectively, depict the effects of the length of the road for the Euler–Bernoulli beam and the Timoshenko beam on a nonlinear foundation. As indicated by Fig. 4.17, the vertical displacement of the pavement does not converge with an increasing length of the road. Furthermore, the no convergence phenomenon appears in the dynamic response based on the Euler–Bernoulli beam and the Timoshenko beam on a nonlinear foundation. The amplitude of the fluctuation of the vertical displacement is about 1/10 of the maximum vertical deflection of the pavement. It should be noted that Thambiratnam and Zhuge found that the finite length of beams can accurately approximate the response of the ideal beam of infinite length based on the dynamic analysis of beams on an elastic foundation subjected to moving point loads [24]. Moreover, based on a moving concentrated load, Ding et al. also found the dynamic responses have good convergence of the length of the pavement [16]. Therefore, the coupling between the oscillator and

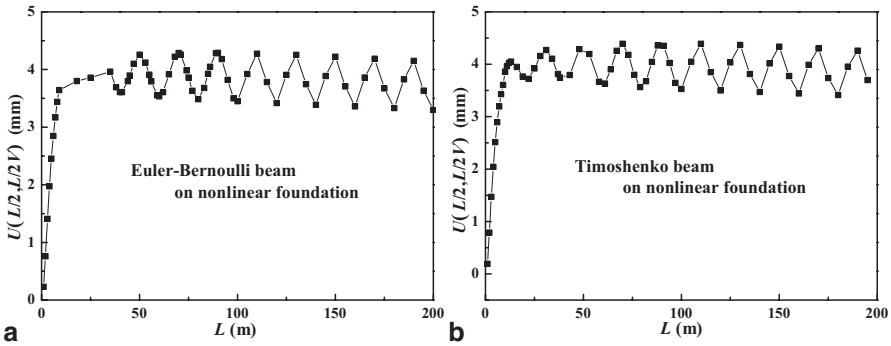

Fig. 4.17 The effects of the length of the road on the vertical displacement of the pavement midpoint. (Reprinted from ref. [21], Copyright 2014, with permission from Elsevier)

the pavement causes the fluctuation of the vertical displacement of the pavement with the increasing length of the road. On the other hand, Fig. 4.17 illustrates that the maximum and the minimum of the fluctuation of the vertical displacement are both convergent with an increasing pavement length. Therefore, the finite length of the pavement can be used to study the vibration of the vehicle–pavement coupled system. In the following calculations, the length of the road, $L = 160$ m.

The Coupling Effect

The effect of coupling between the pavement and the vehicle is examined in this section. Based on Eq. (4.56) and Table 4.3, the excitation frequency from the roughness of the road surface is derived as

$$\omega_P = \frac{2\pi V}{L_0} = 9.425 \tag{4.76}$$

If the suspension damping is neglected, based on Table 4.3, the natural frequency of the moving spring–mass oscillator is derived as

$$\omega_o = \sqrt{\frac{k}{m_1}} = 9.844 \tag{4.77}$$

Therefore, based on the parameter values in Table 4.3, the vehicle body is near to resonance.

The time history of the vertical displacement of the pavement $U(L/2, T)$ is described in Fig. 4.18a. Meanwhile, the time history of the vehicle body is shown in Fig. 4.18b. The speed of the moving vehicle is set to three values, namely, $V = 10$ m/s, $V = 15.667$ m/s, and $V = 20$ m/s. Based on Eq. (4.76) and Table 4.3, the excitation frequencies of the pavement, respectively, are calculated as $\omega_P = 6.283$ rad/s,

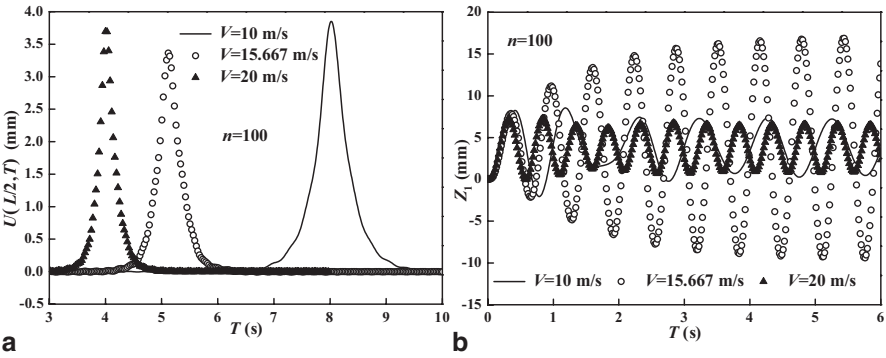

Fig. 4.18 The effects of the speed of the vehicle. (Reprinted from ref. [21], Copyright 2014, with permission from Elsevier)

ω_p=9.844 rad/s, and ω_p=12.566 rad/s. Figure 4.18b shows that the amplitude of the vibration of the vehicle is very large when the vehicle is near to resonance. Based on Eq. (4.76), the vibration of the vehicle will be faster for the greater moving speed. This conclusion is also found from Fig. 4.18b. Figure 4.18a reveals that the amplitude of the dynamic response of the pavement becomes smaller when the vehicle is close to resonance. Furthermore, the response curves of the midpoint of the beam become narrower when the moving speed of the vehicle increases. Therefore, the resonance of the vehicle obviously influences the dynamic response of the pavement.

Figure 4.19a exhibits the biggest displacement of the vehicle body versus the speed of the vehicle. The numerical results clearly show the resonance area of the vehicle body. Moreover, there is only a little change for the biggest displacement of the vehicle body with the different moving speeds of the vehicle while speeding away from the resonance area. Figure 4.19b and c, respectively, show the biggest vertical displacement of the midpoint of the pavement and the biggest acceleration of the vehicle body versus the moving speed of the vehicle. The comparison between Fig. 4.19b and c clearly reveals that the changing tendencies of the vertical deflections of the pavement's midpoint and the acceleration of the vehicle body versus the speed are completely opposite. On the other hand, the changing processes of Fig. 4.19a and b are fully synchronized. Therefore, the dynamic response of the pavement and the vibration of the vehicle are coupled.

Figure 4.20a and b show the time history of the midpoint of the pavement and the vehicle body with different suspension stiffness. Based on Eq. (4.76) and Table 4.3, the natural frequencies of the vehicle are calculated as ω_o=0.9844 rad/s for $k = 2.06 \times 10^4\,\mathrm{N/m}$ and ω_o=31.49 rad/s for $k = 2.06 \times 10^7\,\mathrm{N/m}$. Therefore, the vehicle is far away from resonance when $k = 2.06 \times 10^4\,\mathrm{N/m}$ and $k = 2.06 \times 10^7\,\mathrm{N/m}$. This is the reason why the vibration of the vehicle body is very weak with $k = 2.06 \times 10^4\,\mathrm{N/m}$ and $k = 2.06 \times 10^7\,\mathrm{N/m}$. Figure 4.21 illustrates the influence of the suspension damping on the dynamic response of the vehicle–pavement coupled system. Figure 4.21b shows that the vibration of the vehicle becomes

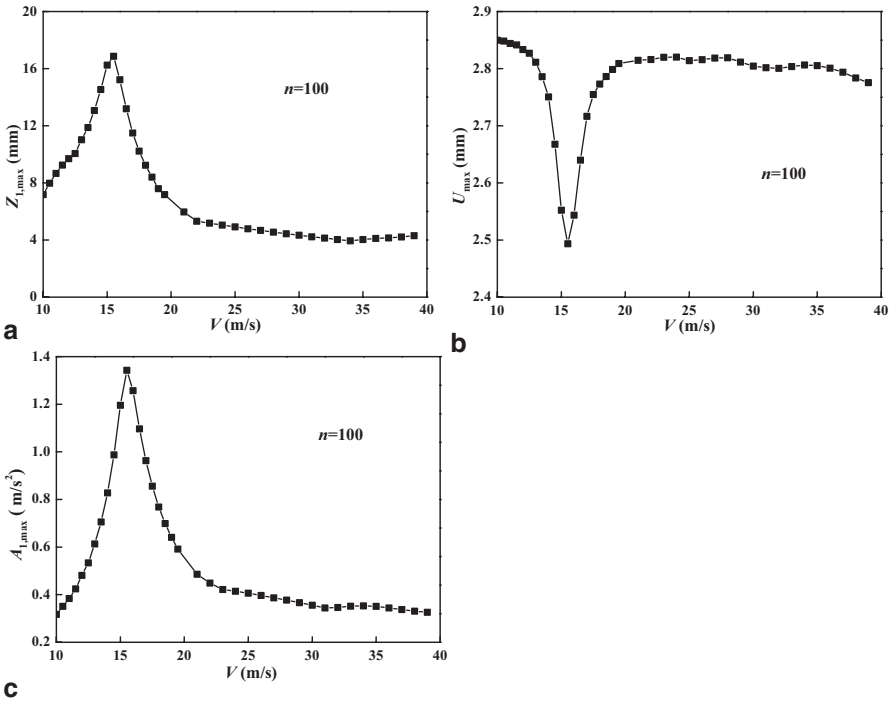

Fig. 4.19 The effects of the speed of the vehicle. (Reprinted from ref. [21], Copyright 2014, with permission from Elsevier)

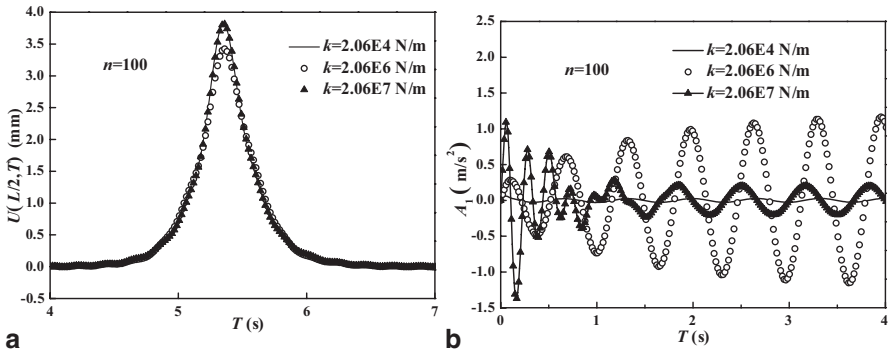

Fig. 4.20 The effects of the suspension stiffness. (Reprinted from ref. [21], Copyright 2014, with permission from Elsevier)

stronger with the decreasing suspension damping. As seen from Fig. 4.21a, the suspension damping has a significant impact on the dynamic response of the pavement. As seen in Figs. 4.18, 4.20 and 4.21 also prove that the dynamic response of the pavement becomes stronger when the vibration of the vehicle becomes weaker.

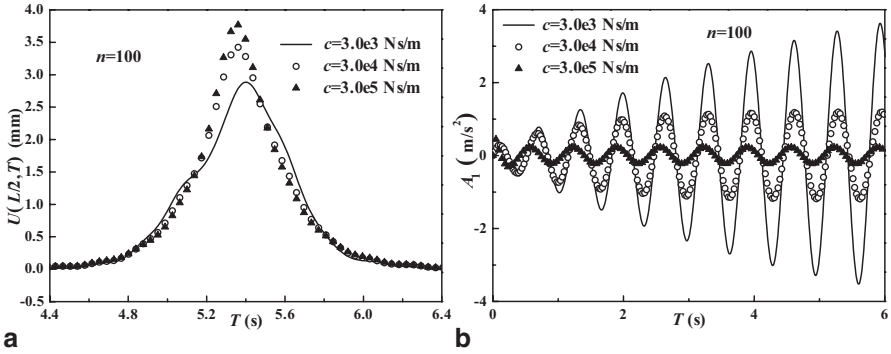

Fig. 4.21 The effects of the suspension damping. (Reprinted from ref. [21], Copyright 2014, with permission from Elsevier)

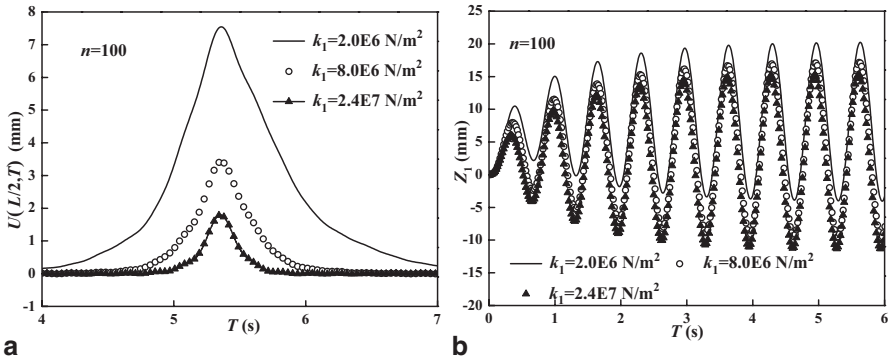

Fig. 4.22 The effects of the linear elastic modulus of the subgrade. (Reprinted from ref. [21], Copyright 2014, with permission from Elsevier)

Physical Parameter Studies

In this section, the effects of the physical parameters of the pavement and the subgrade on the vibration of the vehicle–pavement are investigated by numerical examples. Figure 4.22a and b, respectively, show the effects of the linear elastic modulus of the subgrade on the response of the pavement and the vehicle. The comparison in Fig. 4.22a indicates that the dynamic response of the pavement becomes weaker with the increasing linear elastic modulus of the subgrade. On the other hand, the numerical results in Fig. 4.22b indicate that the parameter of the subgrade changes the response of the pavement faster. The pavement is affected more than the vehicle. Therefore, the authors only show the numerical results of the response of the pavement in the following calculations.

The effects of the other five parameters of the foundation on the dynamic response of the pavement are presented in Fig. 4.23a–e. Meanwhile, the effects of the shear modulus of the pavement are displayed in Fig. 4.23f. Figure 4.23d shows

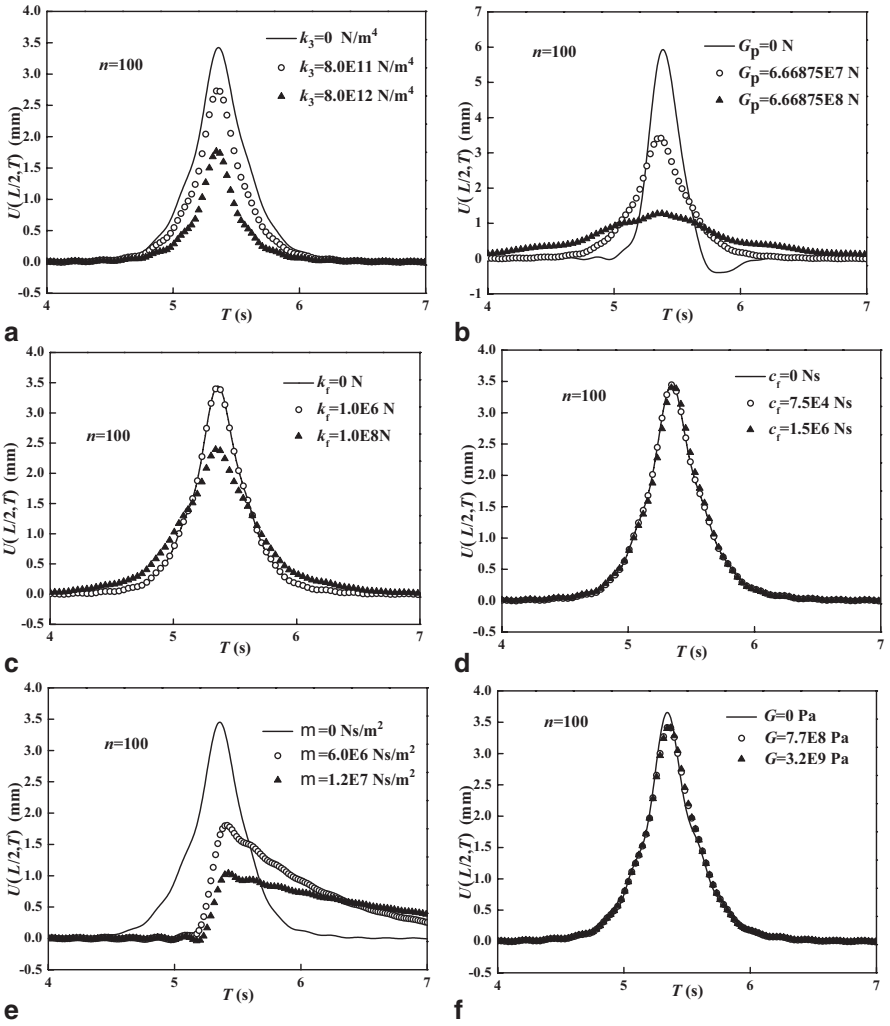

Fig. 4.23 The effects of the physical parameters on the vertical displacements of the pavement's midpoint. (Reprinted from ref. [21], Copyright 2014, with permission from Elsevier)

that the effects of the rocking damping coefficient of the subgrade on the dynamic response of the pavement can be neglected. On the contrary, Fig. 4.23 show that the other five physical parameters, namely, the nonlinear elasticity parameter, the shear deformation coefficient, the rocking stiffness and the damping coefficient of the subgrade, and the shear modulus of the pavement, are all important parameters that influence the dynamic response of the pavement. Furthermore, the response of the pavement decreases with these increasing physical parameters. Therefore, if any of these physical parameters are neglected during the process of modeling, the dynamic analysis overestimates the dynamic response of the pavement.

4.4 The Dynamic Response of an Infinite Timoshenko Beam on a Nonlinear Viscoelastic Foundation [19, 25]

The integral transformation is a powerful tool for dealing with dynamic problems. There are two approaches to deal with a nonlinear term in the governing equations, namely, a perturbation method [26] and the Adomian decomposition method (ADM) without linearization or perturbation [27]. Kargarnovin et al. [26] compared the responses of a nonlinear and an equivalent linear viscoelastic model, and found that the results are completely different at low frequencies. Furthermore, Hryniewicz [27] found that the nonlinearity of the foundation increases the amplitude of vibration under certain conditions. Based on the nonlinear cubic Winkler foundation, Kargarnovin et al. [26] studied the response of an infinite Timoshenko beam subjected to a harmonic moving load, and considered the shear modulus of the beams, without taking into account the shear parameter of the foundation. Hryniewicz [27] discussed the dynamic response of an infinite Rayleigh beam subjected to a moving load without considering the shear modulus of the beam or the foundation. However, there have been no literatures on the dynamic response of an infinite beam on a nonlinear foundation considering the shear deformable beams and shear modulus of the foundation at the same time.

The standard ADM was developed by Adomian for solving linear or nonlinear differential and integral equations [28]. The method has a significant advantage in providing with the solution in a rapid convergent series. Recently several authors have proposed a variety of modifications on the standard ADM. Vahidi and Jalalvand applied the Shanks transformation on the ADM to improve the accuracy of the approximate solutions [29]. Nevertheless, the modified ADM has not been applied to investigate the dynamic response of a beam on a nonlinear foundation.

This section investigates the dynamic response of infinite Timoshenko beams supported by nonlinear viscoelastic foundations to a moving concentrated force. The nonlinearity in the foundation is assumed to be cubic. The nonlinear governing equations of motion are developed by considering the effects of the shear deformable beams and the shear modulus of the foundations at the same time. The differential equations are respectively solved using the ADM and a perturbation method in conjunction with a complex Fourier transformation. An approximate closed form solution is derived in an integral form from the presented Green's function and the theorem of residues, which is used for the calculation of the integral. The dynamic response distribution along the length of the beam is obtained from the closed form solution. The derivation process demonstrates that two methods for the dynamic response of infinite beams on nonlinear foundations to a moving force give a consistent result. The numerical results reveal the influences of the shear deformable beam and the shear modulus of the foundations on dynamic responses. Moreover, the influences on the dynamic response are numerically studied for nonlinearity, viscoelasticity, and other system parameters.

4.4.1 The Mathematical Model

An infinite elastic Timoshenko beam on a nonlinear viscoelastic foundation subjected to a moving load is used to model many engineering devices, as shown in Fig. 4.24, where F_0 and ω are the magnitude and the frequency of the external load, v is the moving speed of the load, t is the time, x is the spatial coordinate along the axis of the beam, $w(X, T)$ is the vertical deflection function of the infinite Timoshenko beam.

The speed of the moving load is assumed to be constant. The nonlinear viscoelastic foundation is taken as a Pasternak foundation with linear-plus-cubic stiffness and viscous damping. Based on these assumptions, the governing differential equations for the displacements $u(x, t)$ and the rotation $\psi(x, t)$ of the beam are

$$\begin{cases} \rho A w_{,TT} + k^* AG\left(\psi_{,X} - w_{,XX}\right) + k_1 w + k_3 w^3 + c w_{,T} - G_p w_{,XX} = F_z\left(X,T\right) \\ \rho I \psi_{,TT} - EI\psi_{,XX} + k^* AG\left(\psi - w_{,X}\right) + k_f \psi + c_f \psi_{,T} = 0 \end{cases} \tag{4.78}$$

where a comma preceding x or t denotes a partial differentiation with respect to x or t, A is the constant cross–section of the homogeneous Timoshenko beam, G, I, ρ, and E are the shear modulus, the second moment of area, the density and the modulus of elasticity of the beam, k^*A is the effective shear area, k_1, k_3, and G_p are the linear, the nonlinear and the shear foundation parameters, c is the damping coefficient of the foundation, k_f and c_f respectively are the rocking stiffness and damping coefficients of the foundation, and the harmonic concentrated moving load is expressed by

$$F_z(X,T) = F_0\, \mathrm{e}^{\mathrm{i}\omega T}\, \delta(X - vT) \tag{4.79}$$

where $\delta(x–vt)$ is the Dirac delta function, which can be defined by

$$\int_{-\infty}^{+\infty} \delta(X - vT) f(X)\, \mathrm{d}X = f(vT) \tag{4.80}$$

for arbitrary function $f(x)$.

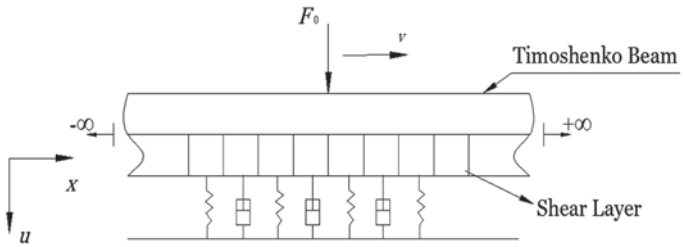

Fig. 4.24 The model of an infinite Timoshenko beam on a nonlinear viscoelastic foundation under a harmonic moving load. (Reprinted from ref. [25], Copyright 2014, with permission from Elsevier)

4.4.2 The Perturbation Method

Introduce a dimensionless variable as follows

$$w(X,T) \leftrightarrow \frac{k_3}{k_1}\sqrt{\frac{I}{A}}w(X,T) \tag{4.81}$$

Substituting Eq. (4.81) into Eq. (4.78) leads to

$$\begin{aligned} &\rho A w_{,TT} + S\psi_{,X} - q w_{,XX} + k_1 w + \varepsilon w^3 + c w_{,T} - G_{\mathrm{p}} w_{,XX} = \frac{F_0 S}{q}\delta(X - vT) \\ &\rho I S\psi_{,TT} - EIS\psi_{,XX} + qS\psi - q^2 w_{,X} + k_{\mathrm{f}} S\psi + c_{\mathrm{f}} S\psi_{,T} = 0 \end{aligned} \tag{4.82}$$

where $q = k^* AG$, $S = q\frac{k_3}{k_1}\sqrt{\frac{I}{A}}$, $\varepsilon = k_3(\frac{q}{S})^2$. Introducing the coordinate transformation

$$\eta = X - vT \tag{4.83}$$

and substituting Eq. (4.83) into Eq. (4.82) yield

$$\begin{aligned} &\left(\rho A v^2 - q - G_{\mathrm{p}}\right)\overline{w}'' - cv\overline{w}' + k_1\overline{w} + \varepsilon\overline{w}^3 + S\overline{\psi}' = \frac{F_0 S}{q}\delta(\eta) \\ &\left(\rho I S v^2 - EIS\right)\overline{\psi}'' - c_{\mathrm{f}} vS\overline{\psi}' + \left(qS + k_{\mathrm{f}} S\right)\overline{\psi} - q^2\overline{w}' = 0 \end{aligned} \tag{4.84}$$

One assumes an expansion of dimensionless displacement

$$\begin{aligned} &\overline{w}(\eta) = \overline{w}_0(\eta) + \overline{w}_1(\eta)\varepsilon + \overline{w}_2(\eta)\varepsilon^2 + \cdots, \\ &\overline{\psi}(\eta) = \overline{\psi}_0(\eta) + \overline{\psi}_1(\eta)\varepsilon + \overline{\psi}_2(\eta)\varepsilon^2 + \cdots \end{aligned} \tag{4.85}$$

Substituting Eq. (4.85) into Eq. (4.84), and then equating coefficient ε^0, ε^1, and ε^2 in the resulting equation, one obtains

$$\varepsilon^0 : F_{\overline{w}0} = \frac{F_0 S}{q}\delta(\eta), F_{\overline{\psi}0} = 0 \tag{4.86}$$

$$\varepsilon^1 : F_{\overline{w}1} = -\overline{w}_0^3, F_{\overline{\psi}1} = 0 \tag{4.87}$$

$$\varepsilon^2 : F_{\overline{w}2} = -3\overline{w}_0^2\overline{w}_1, F_{\overline{\psi}2} = 0 \tag{4.88}$$

where

$$\begin{aligned} F_{\bar{w}k} &= \left(\rho A v^2 - q - G_\mathrm{p}\right)\bar{w}_k'' - cv\bar{w}_k' + k_1\bar{w}_k + S\bar{\psi}_k', \\ F_{\bar{\psi}k} &= \left(\rho I S v^2 - EIS\right)\bar{\psi}_k'' - c_\mathrm{f} v S\bar{\psi}_k' + \left(qS + k_\mathrm{f} S\right)\bar{\psi}_k - q^2\bar{w}_k' \end{aligned} \tag{4.89}$$

$k = 0,1,2$. Then, the application of a complex Fourier transform

$$W_0(\xi) = \int_{-\infty}^{+\infty} \bar{w}_0(\eta)\mathrm{e}^{-\mathrm{i}\eta\xi}\,\mathrm{d}\eta, \Psi_0(\xi) = \int_{-\infty}^{+\infty} \bar{\psi}_0(\eta)\mathrm{e}^{-\mathrm{i}\eta\xi}\,\mathrm{d}\eta \tag{4.90}$$

to Eq. (4.86) leads to

$$\begin{aligned} &\left[\left(-\rho I v^2 + k^* AG + G_\mathrm{p}\right)\xi^2 - \mathrm{i}cv\xi + k_1\right]W_0(\xi) + \mathrm{i}k^* AG\xi\Psi_0(\xi) = F_0, \\ &\left[\left(\rho I v^2 - EI\right)\xi^2 + \mathrm{i}c_\mathrm{f} v\xi - \left(k^* AG + k_\mathrm{f}\right)\right]\Psi_0(\xi) + \mathrm{i}k^* AG\xi W_0(\xi) = 0 \end{aligned} \tag{4.91}$$

$U_0(\xi)$ and $\Psi_0(\xi)$, termed as Green's functions, can be solved from Eq. (4.91)

$$\begin{aligned} W_0(\xi) &= \frac{B_{60}\xi^2 + B_{70}\xi + B_{80}}{B_{10}\xi^4 + B_{20}\xi^3 + B_{30}\xi^2 + B_{40}\xi + B_{50}}, \\ \Psi_0(\xi) &= \frac{\mathrm{i}k^* AGF_0\xi}{B_{10}\xi^4 + B_{20}\xi^3 + B_{30}\xi^2 + B_{40}\xi + B_{50}} \end{aligned} \tag{4.92}$$

where

$$\begin{aligned} B_{10} &= G_\mathrm{p} IE - G_\mathrm{p} v^2\rho I - Av^2 EI\rho + Av^4 I\rho^2 + k^* AGEI - k^* AGv^2\rho I, \\ B_{20} &= -\mathrm{i}vc_\mathrm{f} k^* AG - \mathrm{i}cEIv + \mathrm{i}\rho Icv^3 - \mathrm{i}G_\mathrm{p} vc_\mathrm{f} + \mathrm{i}\rho c_\mathrm{f} v^3 A, \\ B_{30} &= G_\mathrm{p} k^* AG - \rho Av^2 k^* AG + k_\mathrm{f} k^* AG - cc_\mathrm{f} v^2 + EIk_1 - \rho Iv^2 k_1 \\ &\quad + G_\mathrm{p} k_\mathrm{f} - A\rho k_\mathrm{f} v^2, \\ B_{40} &= -\mathrm{i}cvk^* AG - \mathrm{i}vc_\mathrm{f} k_1 - \mathrm{i}cvk_\mathrm{f}, B_{50} = k_1 k^* AG + k_1 k_\mathrm{f}, \\ B_{60} &= EIF_0 - \rho IF_0 v^2, \\ B_{70} &= -\mathrm{i}vc_\mathrm{f} F_0, \\ B_{80} &= F_0 k_\mathrm{f} + F_0 k^* AG \end{aligned} \tag{4.93}$$

Now, if an inverse Fourier transform is taken from both sides of (4.93), then one will get

$$\begin{aligned}\bar{w}_0(\eta) &= \frac{1}{2\pi}\int_{-\infty}^{+\infty} W_0(\xi)\mathrm{e}^{\mathrm{i}\xi\eta}\,\mathrm{d}\xi \\ &= \frac{1}{2\pi}\int_{-\infty}^{+\infty} \frac{B_{60}\xi^2 + B_{70}\xi + B_{80}}{B_{10}\xi^4 + B_{20}\xi^3 + B_{30}\xi^2 + B_{40}\xi + B_{50}}\mathrm{e}^{\mathrm{i}\xi\eta}\,\mathrm{d}\xi \\ \bar{\psi}_0(\eta) &= \frac{1}{2\pi}\int_{-\infty}^{+\infty} \Psi_0(\xi)\mathrm{e}^{\mathrm{i}\xi\eta}\,\mathrm{d}\xi \\ &= \frac{1}{2\pi}\int_{-\infty}^{+\infty} \frac{\mathrm{i}k^* AGF_0\xi}{B_{10}\xi^4 + B_{20}\xi^3 + B_{30}\xi^2 + B_{40}\xi + B_{50}}\mathrm{e}^{\mathrm{i}\xi\eta}\,\mathrm{d}\xi\end{aligned} \tag{4.94}$$

To calculate the integrals of Eq. (4.94), it is necessary to employ the residue theorem. According to the residue theorem, the integrals of Eq. (4.94) are returned to the sum of the residues at the poles. The poles are the roots of $B_{10}\xi^4 + B_{20}\xi^3 + B_{30}\xi^2 + B_{40}\xi + B_{50} = 0$. Since the beam length is considered to be infinite, the boundary conditions are

$$\lim_{\eta\to\pm\infty}\bar{w} = \lim_{\eta\to\pm\infty}\bar{w}' = \lim_{\eta\to\pm\infty}\bar{w}'' = 0,\ \lim_{\eta\to\pm\infty}\bar{\psi} = \lim_{\eta\to\pm\infty}\bar{\psi}' = \lim_{\eta\to\pm\infty}\bar{\psi}'' = 0 \tag{4.95}$$

The closed form solutions are obtained as

$$\begin{aligned}\bar{w}_0(\eta) &= \frac{1}{2\pi}\mathrm{Re}\,s\left\{\frac{B_{60}\xi^2 + B_{70}\xi + B_{80}}{B_{10}\xi^4 + B_{20}\xi^3 + B_{30}\xi^2 + B_{40}\xi + B_{50}}\mathrm{e}^{\mathrm{i}\xi\eta}\right\}\Bigg|_{\xi=\xi_l} \\ &= \frac{1}{2\pi}\left[2\pi\mathrm{i}\sum_{\mathrm{Im}\,\xi_j>0}\lim_{\xi\to\xi_j}(\xi-\xi_j)W_0(\xi)\mathrm{e}^{\mathrm{i}\xi\eta} + \pi\mathrm{i}\sum_{\mathrm{Im}\,\xi_j=0}\lim_{\xi\to\xi_j}(\xi-\xi_j)W_0(\xi)\mathrm{e}^{\mathrm{i}\xi\eta}\right] \\ \bar{\psi}_0(\eta) &= \frac{1}{2\pi}\mathrm{Re}\,s\left\{\frac{\mathrm{i}k^* AGF_0\xi}{B_{10}\xi^4 + B_{20}\xi^3 + B_{30}\xi^2 + B_{40}\xi + B_{50}}\mathrm{e}^{\mathrm{i}\xi\eta}\right\}\Bigg|_{\xi=\xi_l} \\ &= \frac{1}{2\pi}\left[2\pi\mathrm{i}\sum_{\mathrm{Im}\,\xi_j>0}\lim_{\xi\to\xi_j}(\xi-\xi_j)\Psi_0(\xi)\mathrm{e}^{\mathrm{i}\xi\eta} + \pi\mathrm{i}\sum_{\mathrm{Im}\,\xi_j=0}\lim_{\xi\to\xi_j}(\xi-\xi_j)\Psi_0(\xi)\mathrm{e}^{\mathrm{i}\xi\eta}\right]\end{aligned} \tag{4.96}$$

for $\eta \geq 0$, where ξ_j in the first part of Eq. (4.96) is the pole of $W_0(\xi)$ in the upper half part of the complex plane and ξ_j in the second part of Eq. (4.96) is the pole of $\Psi_0(\xi)$ in the upper half part of the complex plane, and

$$\begin{aligned}
\bar{w}_0(\eta) &= \frac{1}{2\pi}\mathrm{Re}\,s\left\{\frac{B_{60}\xi^2+B_{70}\xi+B_{80}}{B_{10}\xi^4+B_{20}\xi^3+B_{30}\xi^2+B_{40}\xi+B_{50}}\mathrm{e}^{\mathrm{i}\xi\eta}\right\}\Bigg|_{\xi=\xi_l} \\
&= \frac{1}{2\pi}\left[-2\pi\mathrm{i}\sum_{\mathrm{Im}\,\xi_j<0}\lim_{\xi\to\xi_j}(\xi-\xi_j)W_0(\xi)\mathrm{e}^{\mathrm{i}\xi\eta}-\pi\mathrm{i}\sum_{\mathrm{Im}\,\xi_j=0}\lim_{\xi\to\xi_j}(\xi-\xi_j)W_0(\xi)\mathrm{e}^{\mathrm{i}\xi\eta}\right] \\
\bar{\psi}_0(\eta) &= \frac{1}{2\pi}\mathrm{Re}\,s\left\{\frac{\mathrm{i}k^*AGF_0\xi}{B_{10}\xi^4+B_{20}\xi^3+B_{30}\xi^2+B_{40}\xi+B_{50}}\mathrm{e}^{\mathrm{i}\xi\eta}\right\}\Bigg|_{\xi=\xi_l} \\
&= \frac{1}{2\pi}\left[-2\pi\mathrm{i}\sum_{\mathrm{Im}\,\xi_j<0}\lim_{\xi\to\xi_j}(\xi-\xi_j)\Psi_0(\xi)\mathrm{e}^{\mathrm{i}\xi\eta}-\pi\mathrm{i}\sum_{\mathrm{Im}\,\xi_j=0}\lim_{\xi\to\xi_j}(\xi-\xi_j)\Psi_0(\xi)\mathrm{e}^{\mathrm{i}\xi\eta}\right]
\end{aligned} \tag{4.97}$$

for $\eta \le 0$, where ξ_j in the first part of Eq. (4.97) is the pole of $W_0(\xi)$ in the lower half part of the complex plane and ξ_j in the second part of Eq. (4.97) is the pole of $\Psi_0(\xi)$ in the lower half part of the complex plane.

When the integrals of Eq. (4.94) have high order poles, the closed form solutions are obtained as

$$\begin{aligned}
\bar{w}_0(\eta) &= \frac{1}{2\pi}\mathrm{Res}\left\{\frac{B_{60}\xi^2+B_{70}\xi+B_{80}}{B_{10}\xi^4+B_{20}\xi^3+B_{30}\xi^2+B_{40}\xi+B_{50}}\mathrm{e}^{\mathrm{i}\xi\eta}\right\}\Bigg|_{\xi=\xi_l} \\
&= \frac{1}{2\pi}\lim_{\xi\to\xi_l}\frac{\mathrm{d}}{\mathrm{d}\xi}\left\{\frac{B_{60}\xi^2+B_{70}\xi+B_{80}}{(\xi-\xi_1)(\xi-\xi_2)}\mathrm{e}^{\mathrm{i}\xi\eta}\right\} \\
\bar{\psi}_0(\eta) &= \frac{1}{2\pi}\mathrm{Res}\left\{\frac{\mathrm{i}k^*AGF_0\xi}{B_{10}\xi^4+B_{20}\xi^3+B_{30}\xi^2+B_{40}\xi+B_{50}}\mathrm{e}^{\mathrm{i}\xi\eta}\right\}\Bigg|_{\xi=\xi_l} \\
&= \frac{1}{2\pi}\lim_{\xi\to\xi_l}\frac{\mathrm{d}}{\mathrm{d}\xi}\left\{\frac{\mathrm{i}k^*AGF_0\xi}{(\xi-\xi_1)(\xi-\xi_2)}\mathrm{e}^{\mathrm{i}\xi\eta}\right\}
\end{aligned} \tag{4.98}$$

where ξ_l in the first part of Eq. (4.98) is the second order pole of $U_0(\xi)$, ξ_1 and ξ_2 are the first order poles. ξ_l in the second part of Eq. (4.98) is the second order pole of $\Psi_0(\xi)$, ξ_1 and ξ_2 are the first order poles.

Using a similar procedure based on appropriate Green's functions and the convolution integral theorem, one obtains the closed form solutions

$$\begin{aligned}
\bar{w}_1(\eta) &= -\int_{-\infty}^{+\infty}\bar{w}_0^3(\eta-\eta^*)\tilde{w}_1(\eta^*)\mathrm{d}\eta^*, \\
\bar{\psi}_1(\eta) &= -\int_{-\infty}^{+\infty}\bar{w}_0^3(\eta-\eta^*)\tilde{\psi}_1(\eta^*)\mathrm{d}\eta^*
\end{aligned} \tag{4.99}$$

$$\begin{aligned}
\bar{w}_2(\eta) &= -3\int_{-\infty}^{+\infty}\bar{w}_0^2(\eta-\eta^*)\bar{w}_1(\eta-\eta^*)\tilde{w}_1(\eta^*)\mathrm{d}\eta^*, \\
\bar{\psi}_2(\eta) &= -3\int_{-\infty}^{+\infty}\bar{w}_0^2(\eta-\eta^*)\bar{w}_1(\eta-\eta^*)\tilde{\psi}_1(\eta^*)\mathrm{d}\eta^*
\end{aligned} \tag{4.100}$$

where $\tilde{w}_1(\eta)$ and $\tilde{\psi}_1(\eta)$ can be determined by

$$\begin{aligned} L_1\tilde{w}_1(\eta)+L_2\tilde{\psi}_1(\eta)&=\delta(\eta)\\ -L_2\tilde{w}_1(\eta)+L_3\tilde{\psi}_1(\eta)&=0 \end{aligned} \tag{4.101}$$

Therefore, the dynamic response of the system can be determined by the following equation

$$\bar{w}(\eta)=\bar{w}_0(\eta)+\bar{w}_1(\eta)+\bar{w}_2(\eta) \tag{4.102}$$

The same procedure is applicable in the case of Euler–Bernoulli beams. In this case, the equations of motion can be derived as

$$EIw_{,XXXX}+\rho Aw_{,TT}-G_pw_{,XX}+k_1w+k_3w^3+cw_{,T}=F_0\delta(X-vT) \tag{4.103}$$

Using the same procedure, one can calculate the closed form solution as

$$\begin{aligned} \bar{w}_0(\eta)&=\frac{F_0}{2\pi}\int_{-\infty}^{+\infty}\frac{\mathrm{e}^{\mathrm{i}\xi\eta}}{EI\xi^4+\left(G_\mathrm{p}-\rho Av^2\right)\xi^2-\mathrm{i}cv\xi+k_1}\mathrm{d}\xi,\\ \bar{w}_1(\eta)&=-\int_{-\infty}^{+\infty}\bar{w}_0^3\left(\eta-\eta^*\right)\tilde{w}_1(\eta^*)\mathrm{d}\eta^*\\ \bar{w}_2(\eta)&=-3\int_{-\infty}^{+\infty}\bar{w}_0^2\left(\eta-\eta^*\right)\bar{w}_1\left(\eta-\eta^*\right)\tilde{w}_1\left(\eta^*\right)\mathrm{d}\eta^* \end{aligned} \tag{4.104}$$

Using the same method of the residue theorem, one will solve Eq. (4.104).

4.4.3 The Modified ADM

The ADM is an iterative method, which has proven successful in dealing with nonlinear equations. This method is based on the search for a solution in the form of a series in which the nonlinear terms are calculated recursively using the Adomian polynomials. The main properties of the method are that it is capable of reducing the size of computational work while still maintaining highly accurate numerical solutions. In this study, a moving harmonic load is considered, and the modified ADM is used to deal with the nonlinear term of the foundation reaction. The complex integral transformations, Green's function, and the theorem of residues are employed for the dynamic response of the Timoshenko beam with an infinite length supported by a nonlinear foundation.

The ADM gives the solutions $u(x, t)$ and $\psi(x, t)$ of Eq. (4.78) in a series form of the infinite sum

$$\begin{aligned} w(X,T)&=\sum_{j=0}^{+\infty}w_j(X,T),\\ \psi(X,T)&=\sum_{j=0}^{+\infty}\psi_j(X,T) \end{aligned} \tag{4.105}$$

Substitution of Eq. (4.105) into the linear terms in Eq. (4.78) yields

$$\begin{aligned} &L_1\sum_{j=0}^{+\infty} w_j\left(X,T\right)+L_2\sum_{j=0}^{+\infty}\psi_j\left(X,T\right)=F_0\,\mathrm{e}^{\mathrm{i}\omega T}\,\delta\left(X-vT\right)-k_3 f\left(w\right)\\ &-L_2\sum_{j=0}^{+\infty} w_j\left(X,T\right)+L_3\sum_{j=0}^{+\infty}\psi_j\left(X,T\right)=0 \end{aligned} \tag{4.106}$$

where $f(w)$ and L_i $(i=1,2,3)$ are called the nonlinear operator and the linear operator and defined by

$$f(w)=w^3 \tag{4.107}$$

$$\begin{aligned} L_1&=\rho A\frac{\partial}{\partial T^2}-k^* AG\frac{\partial}{\partial X^2}+c\frac{\partial}{\partial T}-G_{\mathrm{p}}\frac{\partial}{\partial X^2}+k_1,\\ L_2&=k^* AG\frac{\partial}{\partial X},\\ L_3&=\rho I\frac{\partial}{\partial T^2}-EI\frac{\partial}{\partial X^2}+c_{\mathrm{f}}\frac{\partial}{\partial T}+k^* AG+k_{\mathrm{f}} \end{aligned} \tag{4.108}$$

In order to solve Eq. (4.106) via the ADM, the nonlinear operator $f(w)$ can be decomposed into the form of the infinite sum of series

$$f(w)=\sum_{j=0}^{+\infty}\overline{A}_j \tag{4.109}$$

where $\overline{A}_j$ are called Adomian polynomials of $w_1, w_2, \ldots, w_j$. So that Eq. (4.106) is rewritten as the recursive form

$$\begin{aligned} &L_1 w_0\left(X,T\right)+L_2\psi_0\left(X,T\right)=F_0\,\mathrm{e}^{\mathrm{i}\omega T}\,\delta\left(X-vT\right)\\ &-L_2 w_0\left(X,T\right)+L_3\psi_0\left(X,T\right)=0 \end{aligned} \tag{4.110}$$

for $j=0$, and

$$\begin{aligned} &L_1 w_j\left(X,T\right)+L_2\psi_j\left(X,T\right)=-k_3\overline{A}_{j-1}\\ &-L_2 w_j\left(X,T\right)+L_3\psi_j\left(X,T\right)=0 \end{aligned} \tag{4.111}$$

for $j\geq 1$.

The modified ADM suggests that the nonlinear operator $f(w)$ can be decomposed by the following polynomials

$$
\begin{aligned}
&\overline{A}_0 = f(w_0) = w_0^3 \\
&\overline{A}_1 = w_1 \frac{\mathrm{d}f(w_0)}{\mathrm{d}w_0} + \frac{1}{2!} w_1^2 \frac{\mathrm{d}^2 f(w_0)}{\mathrm{d}w_0^2} + \frac{1}{3!} w_1^3 \frac{\mathrm{d}^3 f(w_0)}{\mathrm{d}w_0^3} + \cdots \\
&\overline{A}_2 = w_2 \frac{\mathrm{d}f(w_0)}{\mathrm{d}w_0} + \frac{w_1^2}{2!}\left(w_2^2 + 2w_1 w_2\right) \frac{\mathrm{d}^2 f(w_0)}{\mathrm{d}w_0^2} + \frac{1}{3!}\left(3\left(w_1^2 w_2 + w_1 w_2^2\right) + w_2^3\right) \frac{\mathrm{d}^3 f(w_0)}{\mathrm{d}w_0^3} + \cdots \\
&\overline{A}_3 = w_3 \frac{\mathrm{d}f(w_0)}{\mathrm{d}w_0} + \frac{1}{2!}(w_3^2 + 2w_1 w_3 + 2w_2 w_3) \frac{\mathrm{d}^2 f(w_0)}{\mathrm{d}w_0^2} + \frac{1}{3!}\Big[w_1^3 + 3w_3^2\left(w_1 + w_2\right) \\
&\quad + 3w_3\left(w_1 + w_2\right)^2\Big] \frac{\mathrm{d}^3 f(w_0)}{\mathrm{d}w_0^3} + \cdots \\
&\quad \vdots
\end{aligned}
\tag{4.112}
$$

So here $\overline{A}_j$ are given as

$$
\begin{aligned}
&\overline{A}_0 = w_0^3, \\
&\overline{A}_1 = 3w_0^2 w_1 + w_1^2 w_0 + w_1^3, \\
&\vdots
\end{aligned}
\tag{4.113}
$$

Since the beam is infinitely long and the transverse load moves in the positive x direction with a constant velocity v, a moving coordinate η can be defined by

$$
\eta = x - vt \tag{4.114}
$$

For an infinite Timoshenko beam in the steady-state dynamic response, one can assume the form of the solution for (4.110) as

$$
\begin{aligned}
w_0(X,T) &= \overline{w}_0(\eta) = \tilde{w}_0(\eta)\mathrm{e}^{\mathrm{i}\omega T}, \\
\psi_0(X,T) &= \overline{\psi}_0(\eta) = \tilde{\psi}_0(\eta)\mathrm{e}^{\mathrm{i}\omega T}
\end{aligned}
\tag{4.115}
$$

The following results can be obtained

$$
\begin{aligned}
&w_{0,T} = \left(-v\tilde{w}_0' + \mathrm{i}\omega\tilde{w}_0\right)\mathrm{e}^{\mathrm{i}\omega T}, \\
&w_{0,TT} = \left(v^2\tilde{w}_0'' - 2\mathrm{i}\omega v\tilde{w}_0' - \omega^2 w_0\right)\mathrm{e}^{\mathrm{i}\omega T}, \\
&w_{0,T} = \tilde{w}_0'\mathrm{e}^{\mathrm{i}\omega T}, \\
&w_{0,TT} = \tilde{w}_0''\mathrm{e}^{\mathrm{i}\omega T} \\
&\psi_{0,T} = \left(-v\tilde{\psi}_0' + \mathrm{i}\omega\tilde{\psi}_0\right)\mathrm{e}^{\mathrm{i}\omega T}, \\
&\psi_{0,TT} = \left(v^2\tilde{\psi}_0'' - 2\mathrm{i}\omega v\tilde{\psi}_0' - \omega^2\psi_0\right)\mathrm{e}^{\mathrm{i}\omega T}, \\
&\psi_{0,X} = \tilde{\psi}_0'\mathrm{e}^{\mathrm{i}\omega T}, \psi_{0,XX} = \tilde{\psi}_0''\mathrm{e}^{\mathrm{i}\omega T}
\end{aligned}
\tag{4.116}
$$

where the prime indicates differentiation with respect to η. Substitution of Eq. (4.116) into Eq. (4.110) yields

$$\begin{aligned}
&\left(\rho A v^2 - k^* AG - G_\mathrm{p}\right)\tilde{w}_0'' + \left(-2\mathrm{i}\omega v\rho A - cv\right)\tilde{w}_0' + \left(-\omega^2\rho A + k_1 + \mathrm{i}c\omega\right)\tilde{w}_0 \\
&\qquad + k^* AG\tilde{\psi}_0' = F_0\delta(\eta) \\
&\left(\rho I v^2 - EI\right)\tilde{\psi}_0'' + \left(-2\mathrm{i}\omega v\rho I - vc_\mathrm{f}\right)\tilde{\psi}_0' + \left(-\omega^2\rho I + k^* AG + k_\mathrm{f} + \mathrm{i}\omega c_\mathrm{f}\right)\tilde{\psi}_0 \\
&\qquad - k^* AG\tilde{w}_0' = 0
\end{aligned} \tag{4.117}$$

Considering the boundary conditions of an infinite beam and applying the complex Fourier transform to (4.117), one will get

$$\begin{aligned}
W_0(\xi) &= \int_{-\infty}^{+\infty} \tilde{w}_0(\eta)\mathrm{e}^{-\mathrm{i}\eta\xi}\,\mathrm{d}\eta = \frac{B_{60}\xi^2 + B_{70}\xi + B_{80}}{B_{10}\xi^4 + B_{20}\xi^3 + B_{30}\xi^2 + B_{40}\xi + B_{50}}, \\
\Psi_0(\xi) &= \int_{-\infty}^{+\infty} \tilde{\psi}_0(\eta)\mathrm{e}^{-\mathrm{i}\eta\xi}\,\mathrm{d}\eta = \frac{-\mathrm{i}k^* AGF_0\xi}{B_{10}\xi^4 + B_{20}\xi^3 + B_{30}\xi^2 + B_{40}\xi + B_{50}}
\end{aligned} \tag{4.118}$$

where $W_0(\xi)$ and $\tilde{w}_0(\eta)$ are a couple of Fourier transforms, $\Psi_0(\xi)$ and $\tilde{\psi}_0(\eta)$ are also a couple of Fourier transforms. $B_{10} - B_{80}$ are determined by the following terms

$$\begin{aligned}
B_{10} &= -G_\mathrm{p}IE + G_\mathrm{p}v^2\rho I + Av^2EI\rho - Av^4I\rho^2 - k^* AGEI + k^* AGv^2\rho I, \\
B_{20} &= \mathrm{i}cEIv - \mathrm{i}\rho Icv^3 - 2G_\mathrm{p}v\omega\rho I - 2Av\omega EI\rho + 4Av^3\omega\rho^2 I + \mathrm{i}G_\mathrm{p}vc_\mathrm{f} \\
&\quad - \mathrm{i}\rho c_\mathrm{f}v^3 A - 2AG\omega\rho Ik^* + \mathrm{i}vc_\mathrm{f}k^* AG, \\
B_{30} &= -\mathrm{i}c\omega EI + 3Icv^2\omega\rho I + G_\mathrm{p}\omega^2\rho I + A\omega^2 EI\rho - 6Av^2\omega^2 I\rho^2 + cc_\mathrm{f}v^2 - \mathrm{i}G_\mathrm{p}\omega c_\mathrm{f} \\
&\quad + 3\mathrm{i}Av^2\omega\rho c_\mathrm{f} - EIk_1 + \rho Iv^2k_1 - G_\mathrm{p}k_\mathrm{f} + \rho Av^2k_\mathrm{f} - G_\mathrm{p}k^* AG + A^2Gv^2\rho k^* \\
&\quad + AG\omega^2\rho Ik^* - \mathrm{i}AG\omega c_\mathrm{f}k^* - AGk_\mathrm{f}k^*, \\
B_{40} &= -3\mathrm{i}cv\omega^2\rho I + 4Av\omega^3 I\rho^2 - 2cv\omega c_\mathrm{f} - 3\mathrm{i}Av\omega^2\rho c_\mathrm{f} - 2v\omega I\rho k_1 \\
&\quad + \mathrm{i}vc_\mathrm{f}k_1 + \mathrm{i}cvk_\mathrm{f} - 2Av\omega\rho k_\mathrm{f} + \mathrm{i}AcGvk^* - 2A^2Gv\omega\rho k_1, \\
B_{50} &= -k_1k^* AG - k_1k_\mathrm{f} + \mathrm{i}c\omega^3 I\rho - A\omega^4 I\rho^2 + c\omega^2 c_\mathrm{f} + \mathrm{i}A\omega^3\rho c_\mathrm{f} + \omega^2 I\rho k_1 - \mathrm{i}\omega c_\mathrm{f}k_1 \\
&\quad - \mathrm{i}c\omega k_\mathrm{f} + A\omega^2\rho k_\mathrm{f} - \mathrm{i}AcG\omega k^* + A^2G\omega^2\rho k^*, \\
B_{60} &= -EIF_0 + \rho IF_0v^2, \\
B_{70} &= -2v\omega I\rho F_0 + \mathrm{i}vc_\mathrm{f}F_0, \\
B_{80} &= \omega^2 I\rho F_0 - \mathrm{i}\omega c_\mathrm{f}F_0 - F_0k_\mathrm{f} - F_0k^* AG
\end{aligned} \tag{4.119}$$

Now, if an inverse Fourier transform is taken from both sides of Eq. (4.119), then one will get

$$\tilde{w}_0(\eta)=\frac{1}{2\pi}\int_{-\infty}^{+\infty}\frac{B_{60}\xi^2+B_{70}\xi+B_{80}}{B_{10}\xi^4+B_{20}\xi^3+B_{30}\xi^2+B_{40}\xi+B_{50}}\mathrm{e}^{\mathrm{i}\xi\eta}\,\mathrm{d}\,\xi \tag{4.120}$$
$$\tilde{\psi}_0(\eta)=\frac{1}{2\pi}\int_{-\infty}^{+\infty}\frac{-\mathrm{i}k^*AGF_0\xi}{B_{10}\xi^4+B_{20}\xi^3+B_{30}\xi^2+B_{40}\xi+B_{50}}\mathrm{e}^{\mathrm{i}\xi\eta}\,\mathrm{d}\,\xi$$

Equation (4.120) can be calculated via employing the residue theorem. According to the residue theorem, the integrals of Eq. (4.120) are the sum of residues at the poles. The poles are the roots of the denominator in Eq. (4.120). The closed form solutions are obtained as

$$\begin{aligned}\tilde{w}_0(\eta)&=\mathrm{i}\sum_{\mathrm{Im}\,\xi_j>0}\lim_{\xi\to\xi_j}\frac{(\xi-\xi_j)\left(B_{60}\xi^2+B_{70}\xi+B_{80}\right)}{B_{10}\xi^4+B_{20}\xi^3+B_{30}\xi^2+B_{40}\xi+B_{50}}\mathrm{e}^{\mathrm{i}\xi\eta}\\&\quad+\frac{\mathrm{i}}{2}\sum_{\mathrm{Im}\,\xi_j=0}\lim_{\xi\to\xi_j}\frac{(\xi-\xi_j)\left(B_{60}\xi^2+B_{70}\xi+B_{80}\right)}{B_{10}\xi^4+B_{20}\xi^3+B_{30}\xi^2+B_{40}\xi+B_{50}}\mathrm{e}^{\mathrm{i}\xi\eta}\\\tilde{\psi}_0(\eta)&=\mathrm{i}\sum_{\mathrm{Im}\,\xi_n>0}\lim_{\xi\to\xi_n}\frac{(\xi-\xi_n)\left(-\mathrm{i}k^*AGF_0\xi\right)}{B_{10}\xi^4+B_{20}\xi^3+B_{30}\xi^2+B_{40}\xi+B_{50}}\mathrm{e}^{\mathrm{i}\xi\eta}\\&\quad+\frac{\mathrm{i}}{2}\sum_{\mathrm{Im}\,\xi_n=0}\lim_{\xi\to\xi_n}\frac{(\xi-\xi_n)\left(-\mathrm{i}k^*AGF_0\xi\right)}{B_{10}\xi^4+B_{20}\xi^3+B_{30}\xi^2+B_{40}\xi+B_{50}}\mathrm{e}^{\mathrm{i}\xi\eta}\end{aligned} \tag{4.121}$$

for $\eta\geq 0$, where ξ_j and ξ_n are the poles of $W_0(\xi)$ and $\Psi_0(\xi)$ in the upper half part of the complex plane, and

$$\begin{aligned}\tilde{w}_0(\eta)&=\mathrm{i}\sum_{\mathrm{Im}\,\xi_j<0}\lim_{\xi\to\xi_j}\frac{(\xi-\xi_j)\left(B_{60}\xi^2+B_{70}\xi+B_{80}\right)}{B_{10}\xi^4+B_{20}\xi^3+B_{30}\xi^2+B_{40}\xi+B_{50}}\mathrm{e}^{\mathrm{i}\xi\eta}\\&\quad+\frac{\mathrm{i}}{2}\sum_{\mathrm{Im}\,\xi_j=0}\lim_{\xi\to\xi_j}\frac{(\xi-\xi_j)\left(B_{60}\xi^2+B_{70}\xi+B_{80}\right)}{B_{10}\xi^4+B_{20}\xi^3+B_{30}\xi^2+B_{40}\xi+B_{50}}\mathrm{e}^{\mathrm{i}\xi\eta}\\\tilde{\psi}_0(\eta)&=\mathrm{i}\sum_{\mathrm{Im}\,\xi_n<0}\lim_{\xi\to\xi_n}\frac{(\xi-\xi_n)\left(-\mathrm{i}k^*AGF_0\xi\right)}{B_{10}\xi^4+B_{20}\xi^3+B_{30}\xi^2+B_{40}\xi+B_{50}}\mathrm{e}^{\mathrm{i}\xi\eta}\\&\quad+\frac{\mathrm{i}}{2}\sum_{\mathrm{Im}\,\xi_n=0}\lim_{\xi\to\xi_n}\frac{(\xi-\xi_n)\left(-\mathrm{i}k^*AGF_0\xi\right)}{B_{10}\xi^4+B_{20}\xi^3+B_{30}\xi^2+B_{40}\xi+B_{50}}\mathrm{e}^{\mathrm{i}\xi\eta}\end{aligned} \tag{4.122}$$

for $\eta\leq 0$, where ξ_j and ξ_n are the poles of $w_0(\xi)$ and $\Psi_0(\xi)$ in the lower half part of the complex plane. When the integrals of Eq. (4.120) have high order poles, the sum of residues at the poles are obtained as

$$\operatorname{Res}\left\{\frac{B_{60}\xi^2+B_{70}\xi+B_{80}}{B_{10}\xi^4+B_{20}\xi^3+B_{30}\xi^2+B_{40}\xi+B_{50}}\mathrm{e}^{\mathrm{i}\xi\eta}\right\}\Bigg|_{\xi=\xi_l}\lim_{\xi\to\xi_l}\frac{\mathrm{d}}{\mathrm{d}\xi}\left\{\frac{B_{60}\xi^2+B_{70}\xi+B_{80}}{(\xi-\xi_1)(\xi-\xi_2)}\mathrm{e}^{\mathrm{i}\xi\eta}\right\}$$
$$\operatorname{Res}\left\{\frac{\mathrm{i}k'AGF_0\xi}{B_{10}\xi^4+B_{20}\xi^3+B_{30}\xi^2+B_{40}\xi+B_{50}}\mathrm{e}^{\mathrm{i}\xi\eta}\right\}\Bigg|_{\xi=\xi_m}=\lim_{\xi\to\xi_m}\frac{\mathrm{d}}{\mathrm{d}\xi}\left\{\frac{\mathrm{i}k'AGF_0\xi}{(\xi-\xi_1)(\xi-\xi_2)}\mathrm{e}^{\mathrm{i}\xi\eta}\right\} \tag{4.123}$$

where ξ_l and ξ_m are the second order poles of $w_0(\xi)$ and $\Psi_0(\xi)$, respectively, ξ_1 and ξ_2 are the first order poles.

As pointed out by Wazwaz [30], the modified decomposition method may give the exact solution for nonlinear equations by only using two iterations. In the following computations, the infinite series $\overline{A}_j$ only keeps the first three terms for the modified ADM. Now, consider Eq. (4.111). For $j=1$ and 2, Eq. (4.111) can be rewritten as

$$\begin{aligned}&\left(\rho Av^2-k^*AG-G_\mathrm{p}\right)\tilde{w}_1''-cv\tilde{w}_1'+k_1\tilde{w}_1+k^*AG\tilde{\psi}_1'=-k_3\tilde{w}_0^3\\&\left(\rho Iv^2-EI\right)\tilde{\psi}_1''-c_\mathrm{f}v\tilde{\psi}_1'+\left(k^*AG+k_\mathrm{f}\right)\tilde{\psi}_1-k^*AG\tilde{w}_1'=0\end{aligned} \tag{4.124}$$

and

$$\begin{aligned}&\left(\rho AV^2-k^*AG-G_\mathrm{p}\right)\tilde{w}_2''-cV\tilde{w}_2'+k_1\tilde{w}_2+k^*AG\tilde{\psi}_2'=-3k_3\tilde{w}_0^2\tilde{w}_1-3k_3\tilde{w}_1^2\tilde{w}_0-k_3\tilde{w}_1^3\\&\left(\rho IV^2-EI\right)\tilde{\psi}_2''-c_\mathrm{f}V\tilde{\psi}_2'+\left(k^*AG+k_\mathrm{f}\right)\tilde{\psi}_2-k^*AG\tilde{w}_2'=0\end{aligned} \tag{4.125}$$

Using a similar procedure for Eq. (4.117) and the convolution integral theorem, one obtains the closed form solutions of Eqs. (4.124) and (4.125)

$$\begin{aligned}\tilde{w}_1(\eta)&=-k_3\int_{-\infty}^{+\infty}\tilde{w}_0^3\left(\eta-\eta^*\right)\hat{w}_{11}\left(\eta^*\right)\mathrm{d}\eta^*,\\\tilde{\psi}_1(\eta)&=-k_3\int_{-\infty}^{+\infty}\tilde{w}_0^3\left(\eta-\eta^*\right)\bar{\psi}_{11}\left(\eta^*\right)\mathrm{d}\eta^*\end{aligned} \tag{4.126}$$

and

$$\begin{aligned}\tilde{w}_2(\eta)&=-k_3\int_{-\infty}^{+\infty}\left[3\tilde{w}_0^2\left(\eta-\eta^*\right)\tilde{w}_1\left(\eta-\eta^*\right)+3\tilde{w}_1^2\left(\eta-\eta^*\right)\tilde{w}_0\left(\eta-\eta^*\right)+\tilde{w}_1^3\left(\eta-\eta^*\right)\right]\hat{w}_{21}\left(\eta^*\right)\mathrm{d}\eta^*,\\\tilde{\psi}_2(\eta)&=-k_3\int_{-\infty}^{+\infty}\left[3\tilde{w}_0^2\left(\eta-\eta^*\right)\tilde{w}_1\left(\eta-\eta^*\right)+3\tilde{w}_1^2\left(\eta-\eta^*\right)\tilde{w}_0\left(\eta-\eta^*\right)+\tilde{w}_1^3\left(\eta-\eta^*\right)\right]\bar{\psi}_{21}\left(\eta^*\right)\mathrm{d}\eta^*\end{aligned} \tag{4.127}$$

where $\hat{w}_{j1}(\eta)$ and $\bar{\psi}_{j1}(\eta)$ ($j=1, 2$) are the dynamic responses of $\mathrm{e}^{i\omega_j T}\,\delta(X-vT)$, $\omega_1=3\omega$ and $\omega_2=5\omega$. Using the same method of the residue theorem, the Eqs. (4.126) and (4.127) will be solved. According to the procedure for solving Eq. (4.117), $B_{1j}-B_{8j}$ are determined by the following terms

$$
\begin{aligned}
B_{1j} &= -G_{\mathrm{p}}IE + G_{\mathrm{p}}v^2\rho I + Av^2EI\rho - Av^4I\rho^2 - k^*AGEI + k^*AGv^2\rho I,\\
B_{2j} &= \mathrm{i}cEIv - \mathrm{i}\rho Icv^3 - 2G_{\mathrm{p}}v\omega_jI\rho - 2Av\omega_jEI\rho + 4Av^3\omega_j\rho^2I + \mathrm{i}G_{\mathrm{p}}vc_{\mathrm{f}} - \mathrm{i}\rho c_{\mathrm{f}}v^3A\\
&\quad - 2AG\omega_j\rho Ik^* + \mathrm{i}vc_{\mathrm{f}}k^*AG,\\
B_{3j} &= -\mathrm{i}c\omega_jEI + 3Icv^2\omega_j\rho I + G_{\mathrm{p}}\omega_j^2\rho I + A\omega_j^2EI\rho - 6Av^2\omega_j^2I\rho^2 + cc_{\mathrm{f}}v^2 - \mathrm{i}G_{\mathrm{p}}\omega_jc_{\mathrm{f}}\\
&\quad + 3\mathrm{i}Av^2\omega_j\rho c_{\mathrm{f}} - EIk_1 + \rho Iv^2k_1 - G_{\mathrm{p}}k_{\mathrm{f}} + \rho Av^2k_{\mathrm{f}} - G_{\mathrm{p}}k^*AG + A^2Gv^2\rho k^*\\
&\quad + AG\omega_j^2\rho Ik^* - \mathrm{i}AG\omega_jc_{\mathrm{f}}k^* - AGk_{\mathrm{f}}k^*,\\
B_{4j} &= -3\mathrm{i}cv\omega_j^2\rho I + 4Av\omega_j^3I\rho^2 - 2cv\omega_jc_{\mathrm{f}} - 3\mathrm{i}Av\omega_1^2\rho c_{\mathrm{f}} - 2v\omega_jI\rho k_1 + \mathrm{i}vc_{\mathrm{f}}k_1 + \mathrm{i}cvk_{\mathrm{f}}\\
&\quad - 2Av\omega_j\rho k_{\mathrm{f}} + \mathrm{i}AcGvk^* - 2A^2Gv\omega_j\rho k_1,\\
B_{5j} &= -k_1k^*AG - k_1k_{\mathrm{f}} + \mathrm{i}c\omega_j^3I\rho - A\omega_j^4I\rho^2 + c\omega_j^2c_{\mathrm{f}} + \mathrm{i}A\omega_j^3\rho c_{\mathrm{f}} + \omega_j^2I\rho k_1 - \mathrm{i}\omega_jc_{\mathrm{f}}k_1\\
&\quad - \mathrm{i}c\omega_jk_{\mathrm{f}} + A\omega_j^2\rho k_{\mathrm{f}} - \mathrm{i}AcG\omega_jk^* + A^2G\omega_j^2\rho k^*,\\
B_{6j} &= -EI + \rho Iv^2,\\
B_{7j} &= -2V\omega_jI\rho + \mathrm{i}vc_{\mathrm{f}},\\
B_{8j} &= \omega_j^2I\rho - \mathrm{i}\omega_jc_{\mathrm{f}} - k_{\mathrm{f}} - k^*AG
\end{aligned}
\tag{4.128}
$$

where $j=1, 2$. The steady-state response $w(X, T)$ can be solved by the following equation based on the solutions of Eqs. (4.117), (4.126), and (4.127)

$$
w(X,T) = \tilde{w}_0(\eta)\,\mathrm{e}^{i\omega T} + \tilde{w}_1(\eta)\,\mathrm{e}^{i\omega_1 T} + \tilde{w}_2(\eta)\,\mathrm{e}^{i\omega_2 T} \tag{4.129}
$$

In the standard ADM, the infinite series of the decomposition for the nonlinear operator $w(u)$ is suggested as follows

$$
\overline{A}_j = \sum_{n=1}^{j} c(n,j)(w_0{}^3)^{(n)} \tag{4.130}
$$

It should be noted that in this scheme, the sum of the subscripts in each term of A_j are equal to j. The $c(n, j)$ are products of n components of u whose subscripts sum to j, divided by the factorial of the number of repeated subscripts. Thus

$$
\begin{aligned}
c(1,3) &= w_3,\\
c(2,3) &= w_1w_2,\\
c(3,3) &= \frac{1}{6}w_1^3
\end{aligned}
\tag{4.131}
$$

So here $\overline{A}_j$ are given as

$$
\begin{aligned}
\overline{A}_0(\eta) &= w_0^3,\\
\overline{A}_1(\eta) &= 3w_0^2w_1,\\
\overline{A}_2(\eta) &= 3w_0^2w_2 + 3w_1^2w_0,\\
\overline{A}_3(\eta) &= w_1^3 + 3w_0^2w_3 + 6w_0w_1w_2,\\
&\vdots
\end{aligned}
\tag{4.132}
$$

Compared with the procedure of the modified ADM, Eq. (4.110) and Eq. (4.111) for $j=1$ are exactly the same as Eqs. (4.117) and (4.124), while Eq. (4.110) should be

$$\begin{aligned}\left(\rho Av^2-k^*AG-G_{\mathrm{p}}\right)\tilde{w}_2''-cv\tilde{w}_2'+k_1\tilde{w}_2+k^*AG\tilde{\psi}_2'&=-3k_3\tilde{w}_0^2\tilde{w}_1\\ \left(\rho Iv^2-EI\right)\tilde{\psi}_2''-c_{\mathrm{f}}v\tilde{\psi}_2'+\left(k^*AG+k_{\mathrm{f}}\right)\tilde{\psi}_2-k^*AG\tilde{w}_2'&=0\end{aligned} \tag{4.133}$$

for $j=2$, and Eq. (4.127) should be

$$\begin{aligned}\tilde{w}_2(\eta)&=-3k_3\int_{-\infty}^{+\infty}\tilde{w}_0^2\left(\eta-\eta^*\right)\tilde{w}_1\left(\eta-\eta^*\right)\hat{w}_{21}\left(\eta^*\right)\mathrm{d}\eta^*,\\ \tilde{\psi}_2(\eta)&=-3k_3\int_{-\infty}^{+\infty}\tilde{w}_0^2\left(\eta-\eta^*\right)\tilde{w}_1\left(\eta-\eta^*\right)\hat{\psi}_{21}\left(\eta^*\right)\mathrm{d}\eta^*\end{aligned} \tag{4.134}$$

After comparing Eq. (4.125) with Eq. (4.132) and Eq. (4.127) with Eq. (4.133), one can find that the modified ADM includes more terms than the standard ADM. The extra terms cause a huge number of calculations for the steady-state response, and the calculations for the closed form solutions are more complicated.

4.4.4 The Moving Force

In this part, numerical examples are given for parametric research. The physical and geometric properties of the Timoshenko beam, the foundation and the moving load are listed in Table 4.4.

In part three, the decomposition series for the Adomian decomposition were found. But the convergence of the decomposition series has not been determined. Accordingly, let

$$\alpha_j=\begin{cases}\dfrac{\left\|w_{j+1}\right\|}{\left\|w_j\right\|},\left\|w_j\right\|\neq 0\\ 0,\left\|w_j\right\|=0\end{cases} \tag{4.135}$$

$$\left\|w_j\right\|=\max_{\eta}\mathrm{Abs}[w_j(\eta)] \tag{4.136}$$

The decomposition series Eq. (4.129) will converge rapidly to an exact solution for $0\le\alpha_j<1,\ j=0,1,2,\ldots$. According to Table 4.4 and Eqs. (4.89) and (4.135), one can obtain

$$\left\|w_0\right\|=0.000345 \tag{4.137}$$

$$\left\|w_1\right\|=0.000046454 \tag{4.138}$$

Table 4.4 Properties of the beam, foundation, and load. (Reprinted from ref. [19], with kind permission from Springer Science+Business Media)

Item	Notation	Value
Beam		
Young's modulus(steel)	E	201 GPa
Shear modulus	G	77 GPa
Mass density	ρ	7850 kg/m^3
Cross sectional area	A	7.69×10^{-3} m^2
Second moment of area	I	3.055×10^{-5} m^4
Shear coefficients	k'	0.4
Foundation		
Linear stiffness	k_1	3.5×10^7 N/m^2
Nonlinear stiffness	k_3	4×10^{14} N/m^4
Viscous damping	μ	1732.5×10^3 Ns/m^2
Shear parameter	G_p	66687500 N
Rocking stiffness	k_f	10^8 N/m^2
Rocking Damping coefficients	c_f	1.5×10^6 N·s/m^2
Moving load		
Load	F_0	65 KN
Speed	v	50 m/s

$$\|w_2\| = 0.0000294 \tag{4.139}$$

$$\alpha_0 = \frac{\|w_1\|}{\|w_0\|} \approx 0.1346 < 1 \tag{4.140}$$

$$\alpha_1 = \frac{\|w_2\|}{\|w_1\|} \approx 0.633 < 1 \tag{4.141}$$

In the following computations, the infinite decomposition series Eq. (4.105) only keeps the first three terms.

Based on the prescribed method, a computer program has been provided to solve the problem. To realize the steady–state response, it is sufficient to study the vibration of any point of the beam. Hence, the point $x=0$ is used in the following numerical examples. As the first example, the dynamic response of the infinite Timoshenko beam is considered during passage of a moving load. Figure 4.25 shows the time history of the Timoshenko beam subjected to the moving concentrated force. For $t<0$, the transverse deflection increases with time, and the largest deflection does not appear in $t=0$, but there is a little delay. After reaching the largest deflection, the transverse deflection decreases and tends toward zero while the growth speed of the transverse deflection is far greater than the reduced speed.

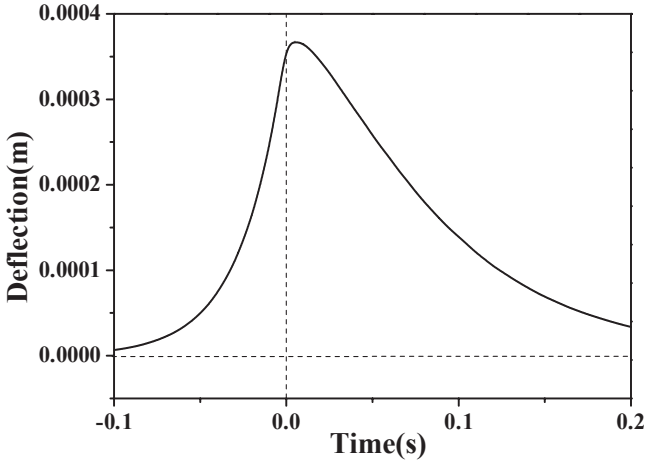

Fig. 4.25 The approximate analytical solution of the deflection of the beam. (Reprinted from ref. [19], with kind permission from Springer Science+Business Media)

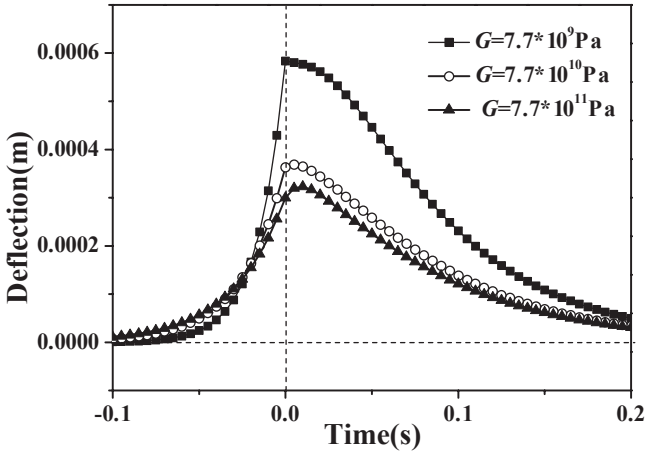

Fig. 4.26 Effect of the shear modulus of the Timoshenko beam on the deflection of the beam Timoshenko. (Reprinted from ref. [19], with kind permission from Springer Science+Business Media)

The effects of the shear modulus of the Timoshenko beam and the shear modulus of the foundation on the deflection of the beam on the viscoelastic nonlinear foundation are illustrated in Figs. 4.26 and 4.27, respectively. From the observation of Figs. 4.26 and 4.27, it is found that the largest deflection of the Timoshenko beam decreases with the increasing shear moduli of the beam and the foundation. Furthermore, Figs. 4.26 and 4.27 show that the contributions of the shear moduli of the beam and the foundation on the deflection are significant, especially when the

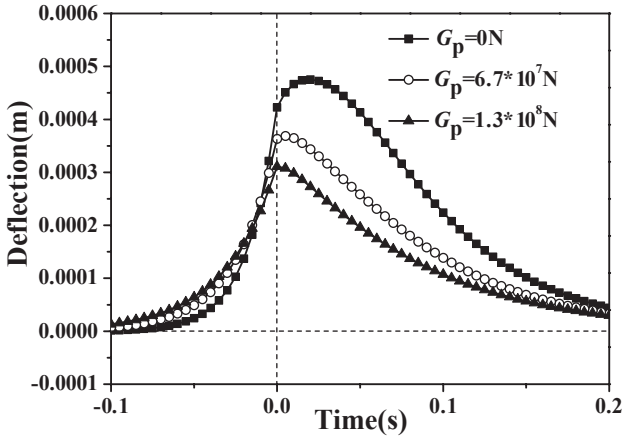

Fig. 4.27 Effect of the shear modulus of the foundation on the deflection of the beam. (Reprinted from ref. [19], with kind permission from Springer Science+Business Media)

shear moduli of the beams and the foundations are small. That is, the shear moduli of both the beams and the foundations cannot be neglected for the dynamic response of infinite beams on nonlinear viscoelastic foundations. In this section, the effects of the shear moduli of the beams and the foundations are investigated at the same time, and similar results are found at the above mentioned two references. On the other hand, the numerical results also indicate that the shear modulus of Timoshenko beams is not sensitive to the time delays of the largest deflection while the time delays decrease with the increasing shear modulus of the foundations.

Figure 4.28 shows the effect of the modulus of the elasticity of the beam on the deflection of the Timoshenko beam on the viscoelastic nonlinear foundation. As it

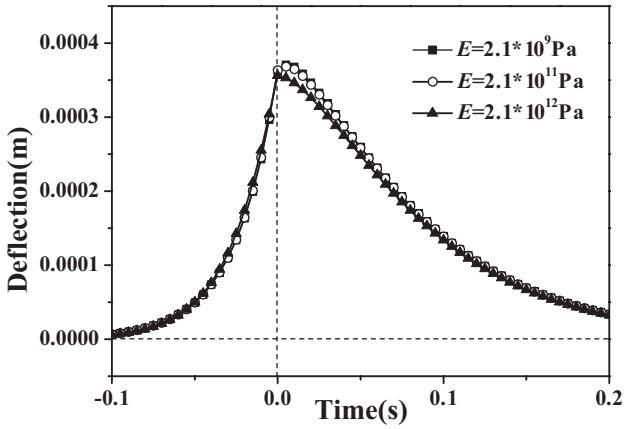

Fig. 4.28 The effect of the modulus of the elasticity of the Timoshenko beam on the deflection of the beam. (Reprinted from ref. [19], with kind permission from Springer Science+Business Media)

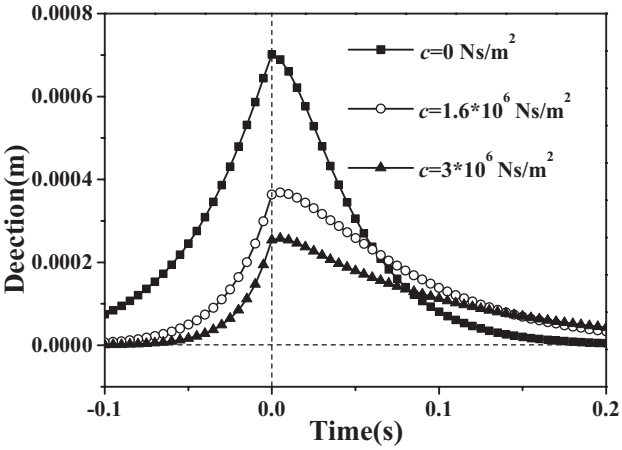

Fig. 4.29 The effect of the damping coefficient of the foundation on the deflection of the beam. (Reprinted from ref. [19], with kind permission from Springer Science+Business Media)

is seen in this figure, the modulus of the elasticity of the Timoshenko beam has little effect on the transverse deflection of the Timoshenko beam. Specifically, there are only discernible differences between the results for rather large and different modulus of the elasticity of the Timoshenko beam.

Figure 4.29 illustrates the effect of the damping coefficient of the foundation on the deflection of the Timoshenko beam on the viscoelastic nonlinear foundation. It should be noted that the viscoelastic foundation turns into an elastic Pasternak foundation when $c=0$. The numerical result shows that the damping coefficient of the foundation has significant influence on the dynamic response of the deflection of the Timoshenko beam and the deflection decreases with the increasing damping coefficient. Furthermore, the numerical result shows that the largest deflection of the Timoshenko beam on the elastic Pasternak foundation appears at $t=0$. Moreover, the time of the largest deflection appearing is delayed with the increasing damping coefficient of foundations. Hence a larger value of the damping coefficient of foundations leads to a smaller deflection of the beam and the damping is one of the reasons for the time delay.

The effects of the linear and the nonlinear elasticity parameters of the foundations on the deflection of the Timoshenko beam on the viscoelastic nonlinear foundation are displayed in Figs. 4.30 and 4.31. Figures 4.30 and 4.31 show that the form of the deflection of the beam has little change with different linear and nonlinear elasticity parameters of the foundations. Furthermore, the numerical results of Figs. 4.30 and 4.31 show that the largest deflection of the beams decreases with the increasing linear elasticity parameter of the foundation and the decreasing nonlinear elasticity parameter.

Figures 4.32 and 4.33 show that the dynamic responses of the Timoshenko beam on the viscoelastic nonlinear foundation change with the rocking stiffness and the damping coefficients of foundation. As seen in this figures, the shape has little

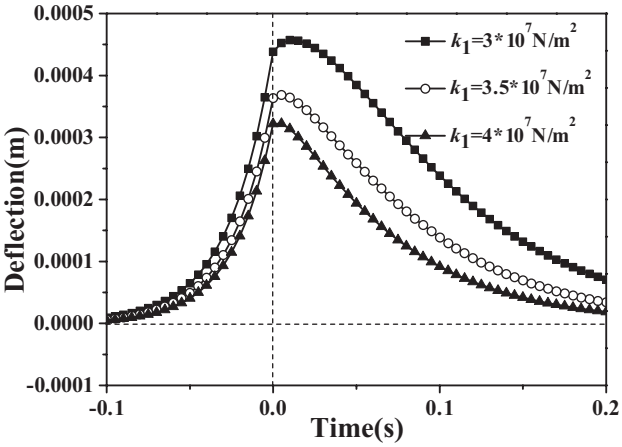

Fig. 4.30 The effect of the linear elasticity parameter of the foundation on the deflection of the beam. (Reprinted from ref. [19], with kind permission from Springer Science+Business Media)

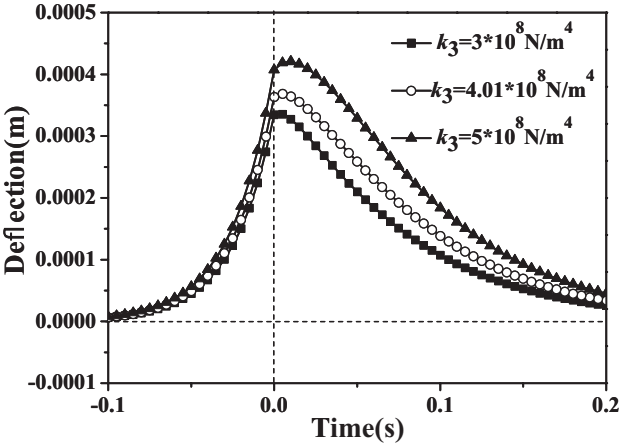

Fig. 4.31 The effect of the nonlinear elasticity parameter of the foundation on the deflection of the beam. (Reprinted from ref. [19], with kind permission from Springer Science+Business Media)

change and the largest deflection decreases with the increasing foundation rocking stiffness and damping coefficients. It proves that the influences of the rocking stiffness and damping coefficients of the foundation on the transverse deflection of the infinite beam on the foundation cannot be neglected.

The effect of the velocity of the moving concentrated force on the deflection of the Timoshenko beam on the viscoelastic nonlinear foundation is displayed in Fig. 4.34. Figure 4.34 indicates that the largest deflection of the Timoshenko beam decreases with the increasing moving velocity. Furthermore, the deflection of the beam is sensitive to the changing moving velocity. On the other hand, the numerical

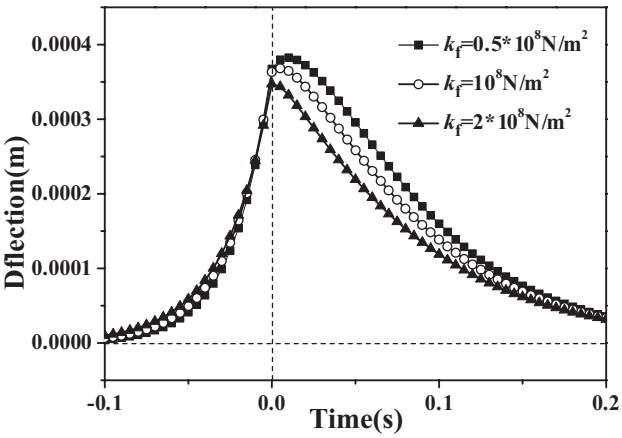

Fig. 4.32 The effect of the foundation rocking stiffness on the deflection of the beam. (Reprinted from ref. [19], with kind permission from Springer Science+Business Media)

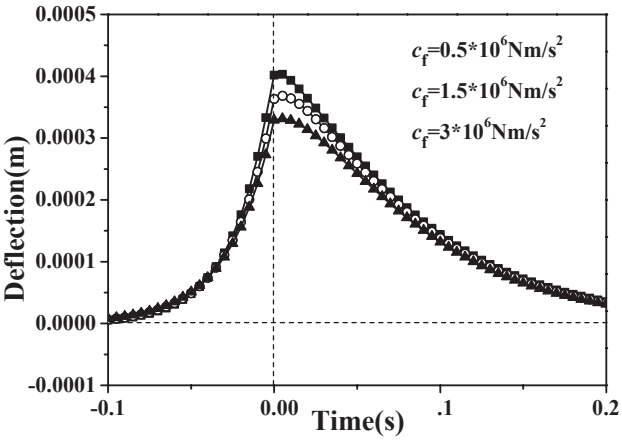

Fig. 4.33 The effect of the foundation damping coefficient on the deflection of the beam. (Reprinted from ref. [19], with kind permission from Springer Science+Business Media)

results in Fig. 4.34 prove that the whole form of the deflection of the Timoshenko beam on the viscoelastic nonlinear foundation has little change under different velocities of the moving concentrated force.

The deflections of two different beam models on the viscoelastic nonlinear foundation are compared in Fig. 4.35. As it is seen from the figure, the deflection of the Timoshenko beam near the region of $t=0$ is smaller than that of the Euler–Bernoulli beam. Furthermore, the deflection of the Timoshenko beam on the foundation is larger than that of the Euler–Bernoulli beam in other regions. Nevertheless, the Euler–Bernoulli beam is more acceptable for the dynamic response of the beam on the foundation in this investigation, because the Euler–Bernoulli beam overestimates the results of the dynamic response. In other words, the numerical results in

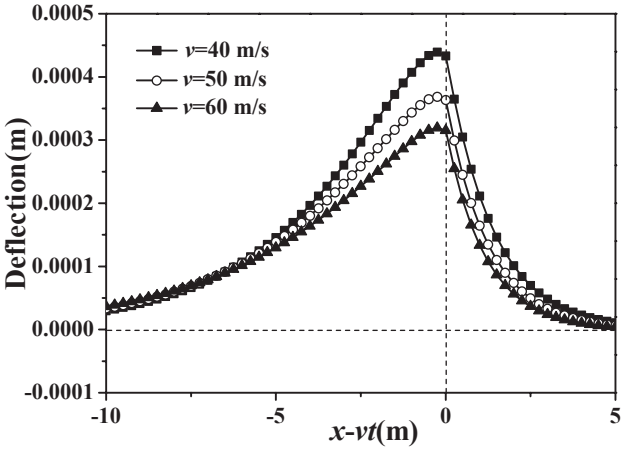

Fig. 4.34 Influence of the moving velocity of the load on the deflection of the beam. (Reprinted from ref. [19], with kind permission from Springer Science+Business Media)

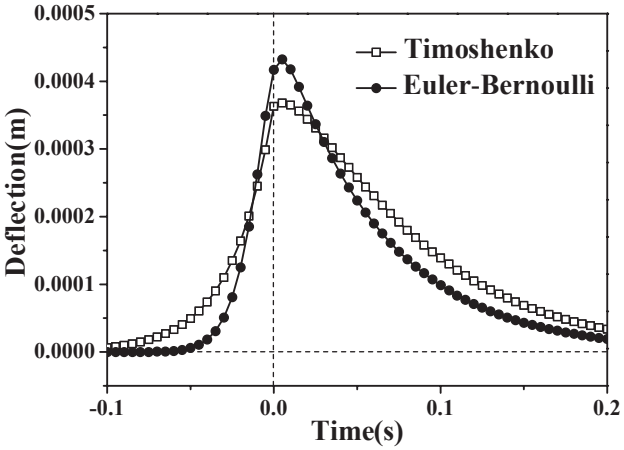

Fig. 4.35 Comparison of two different beam models from the deflection of the beam. (Reprinted from ref. [19], with kind permission from Springer Science+Business Media)

Fig. 4.35 illustrate that the dynamic response based on the Euler–Bernoulli beam theory provides a more conservative estimate in road design.

4.4.5 Parametric Studies

In this part, numerical examples are given for parametric research. The physical and geometric properties of the beam, the foundation and the moving load are listed in Table 4.4.

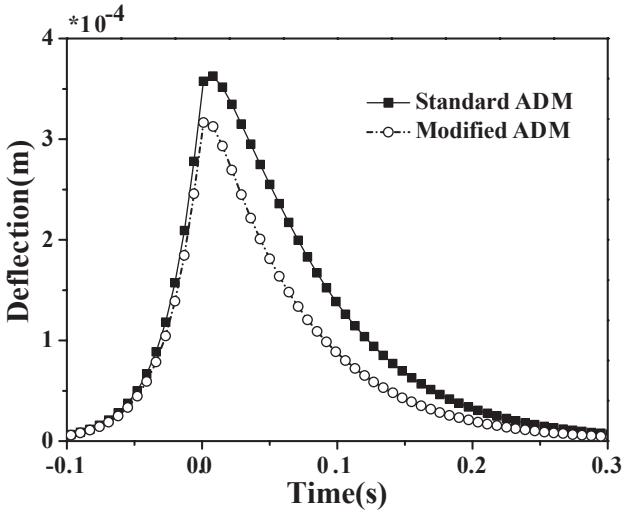

Fig. 4.36 The approximate analytic solution of deflection of the beam. (Reprinted from ref. [25], Copyright 2014, with permission from Elsevier)

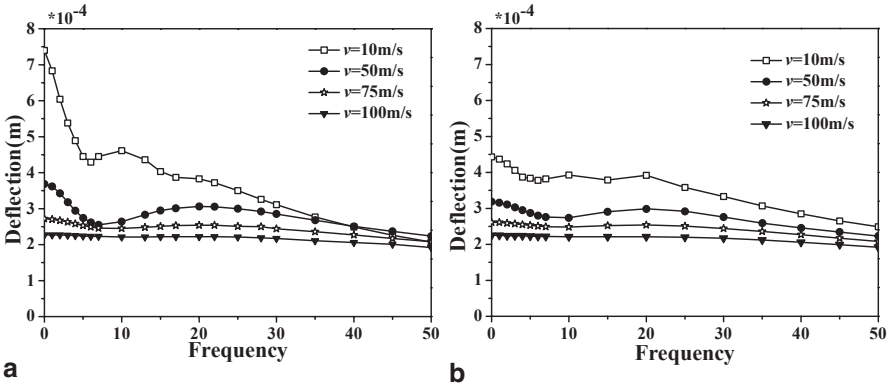

Fig. 4.37 The effects of the moving speed on the approximate analytic solution of deflection of the beams: **a** the standard ADM; **b** the modified ADM. (Reprinted from ref. [25], Copyright 2014, with permission from Elsevier)

The steady-state responses of a point at $x=0$ of the Timoshenko beam on a viscoelastic nonlinear foundation based on the modified ADM and the standard ADM are compared in Fig. 4.36. As pointed out by Wazwaz [30], the modification demonstrated a rapid convergence of the series solution if compared with the standard ADM. As it can be seen from the figure, the largest deflections of the Timoshenko beam via the modified ADM are smaller than those via the standard ADM. Although the modified ADM may give more accurate results, in the investigations of dynamic response of beams on a foundation, the standard ADM is more conservative.

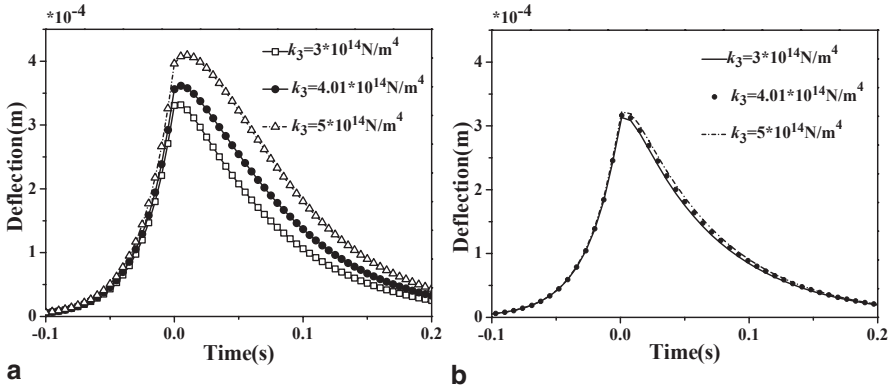

Fig. 4.38 The effects of the nonlinear elasticity parameter of foundations on the deflection of the beams: **a** the standard ADM; **b** the modified ADM. (Reprinted from ref. [25], Copyright 2014, with permission from Elsevier)

Figure 4.37 illustrates the effects of the speed of the moving load on the dynamic responses of the beam changing with the frequency of the external load. Figure 4.37a and b show the numerical results solved by the standard ADM and the modified ADM, respectively. The numerical results indicate that the largest deflection of the beams decreases with the increasing moving speed for both ADMs. Furthermore, Fig. 4.37a and b both show that the responses are more sensitive to the frequency of the external load for the smaller moving speed. The figures also demonstrate that the two kinds of ADM yield the qualitatively same results, while there are quantitative differences.

Based on the two kinds of ADMs, the effects of the nonlinear elasticity parameter of the foundations on the deflection of the infinite beams on a nonlinear foundation are displayed in Fig. 4.38a and b, respectively. Figure 4.38 shows that the shapes of the time history of the Timoshenko beam center are almost the same for different nonlinear parameters of the foundation. Moreover, the numerical results of Fig. 4.38 show that the largest deflections of the beams increase with the increasing nonlinear elasticity parameter of the foundation. The numerical results also indicate that the results from the two ADMs qualitatively predict the same tendencies with the changing parameters, while quantitatively there are certain differences. The results via the standard ADM are more sensitive to nonlinear parameters than those via the modified ADM.

The effects of the shear modulus of the foundation, the shear modulus of Timoshenko beams and the rocking damping coefficients on the deflection of the infinite Timoshenko beams on a nonlinear viscoelastic Pasternak foundation with $v=50$ m/s and $\omega=1$ Hz are shown in Figs. 4.39, 4.40 and 4.41, respectively. The numerical results show that the largest deflections of beams decrease with the shear modulus of the beam, the shear modulus of the foundation and the rocking damping coefficient, and the shear moduli of the beams and the foundation cannot be neglected. The numerical simulations also indicate results via the standard ADM are more sensitive to shear modulus parameters than those via the modified ADM.

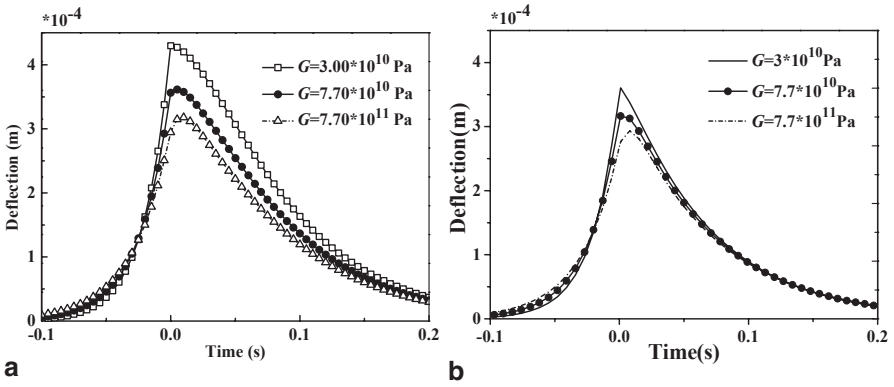

Fig. 4.39 The effects of the shear modulus of beams on the deflection of the beams: **a** the standard ADM; **b** the modified ADM. (Reprinted from ref. [25], Copyright 2014, with permission from Elsevier)

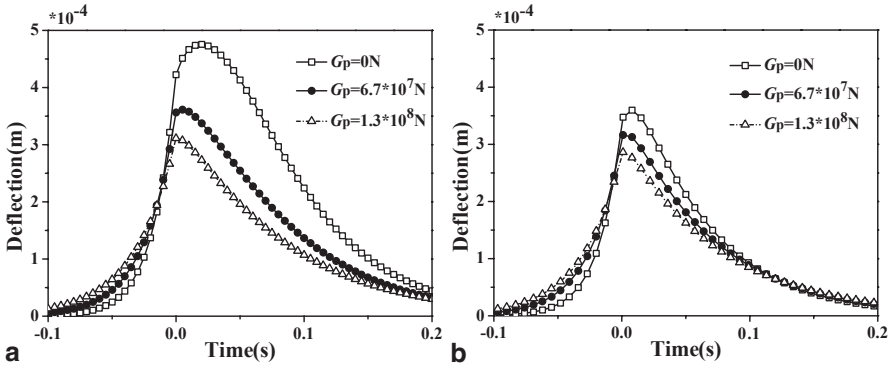

Fig. 4.40 The effects of the shear modulus of foundations on the deflection of the beams: **a** the standard ADM; **b** the modified ADM. (Reprinted from ref. [25], Copyright 2014, with permission from Elsevier)

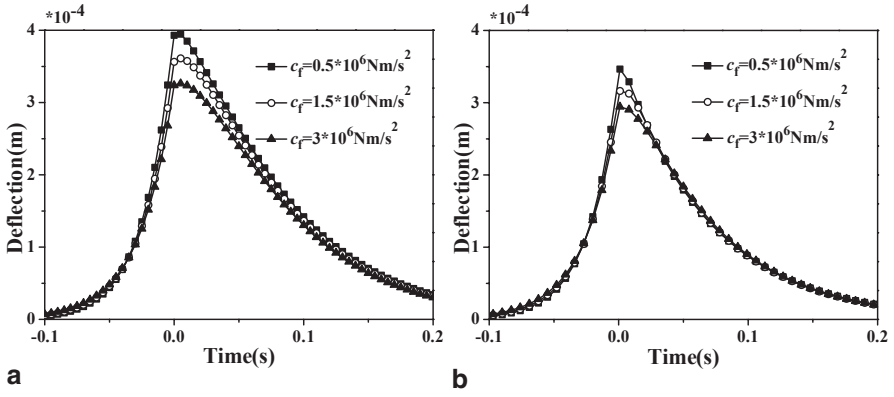

Fig. 4.41 The effects of the rocking damping coefficients on the deflection of the beams: **a** the standard ADM; **b** the modified ADM. (Reprinted from ref. [25], Copyright 2014, with permission from Elsevier)

4.5 Chapter Summary

This chapter is devoted to the dynamic analysis of a pavement structure under a vehicle's moving load. The pavement structure is modeled as a finite Euler–Bernoulli beam on a nonlinear foundation, a finite Timoshenko beam on a nonlinear Pasternak foundation and an infinite Timoshenko beam on a nonlinear foundation with viscous damping. Moreover, three types of the conventional boundary conditions, namely SS, CC, and FF boundary conditions are investigated. The numerical simulation found that the vertical deflections of the pavement for three boundary conditions are overlapped with a rather large length of the pavement. The vehicle's moving load is considered as a moving concentrated load, a harmonic moving load and a moving spring-mass-damper oscillator, respectively.

Based on the dynamic response of the pavement-vehicle system, the convergence of the Galerkin truncation and the dependences on the system parameters are numerically studied. It was found that the convergence of the Galerkin truncation can be predicted by the natural frequencies, the slow growth in the natural frequency of the pavement causes lack of convergence, and investigation into dynamical responses of the vehicle–pavement-foundation system needs large truncation terms. Furthermore, the convergence increases with growing of the moduli of elasticity of the pavement and the nonlinear foundation parameters but decrease with the increasing linear foundation parameters and the damping coefficient. Moreover, the convergence of the Galerkin truncation for Timoshenko beams on foundations is slightly slower than that of the Euler–Bernoulli beam. Nevertheless, the vertical deflections of the Timoshenko beam are slightly larger.

To account for shear deformations of the pavement and the subgrade, the shear modulus of the beam and the shear deformation coefficient of the foundation are considered at the same time. Therefore, nonlinear coupled dynamics of the vehicle–pavement system is investigated with a Timoshenko beam on a linear-plus-cubic Pasternak-type foundation under a moving spring-mass-damper oscillator. The numerical examples revealed that the amplitude of the vibratory responses of the pavement becomes smaller when the vehicle is close to resonance.

In conjunction with complex Fourier transformation, the ADM and a perturbation method are, respectively, used to deal with the nonlinear term from the foundation reaction for the dynamic analysis of infinite Timoshenko beams on the nonlinear foundation. This chapter proves that the ADM and the perturbation method give the consistent result for current issues.

References

1. Li SH, Yang SP, Xu BQ, Xing HJ. Chaos of a beam on a nonlinear elastic foundation under moving loads. 2007 International Symposium on Nonlinear Dynamics. J Phys Conf Ser. 2008;96(1):012116.
2. Sheng DF, Zhang Y, Cheng CJ. Dynamic behavior of nonlinear viscoelastic Timoshenko beams with damage on a viscoelastic foundation. J Shanghai Univ (English Edition). 2004;8(3):245–51.

3. Pellicano F, Mastroddi F. Nonlinear dynamics of a beam on an elastic foundation. Nonlinear Dyn. 1997;14(4):335–55.
4. Ansari M, Esmailzadeh E, Younesian D. Internal-external resonance of beams on a non-linear viscoelastic foundation traversed by a moving load. Nonlinear Dyn. 2010;61(1–2):163–82.
5. Ansari M, Esmailzadeh E, Younesian D. Frequency analysis of finite beams on a nonlinear Kelvin–Voight foundation under moving loads. J Sound Vib. 2011;330(7):1455–71.
6. Yan T, Kitipornchai S, Yang J. Dynamic behavior of edge-cracked shear deformable functionally graded beams on an elastic foundation under a moving load. Compos Struct. 2011;93(11):2992–3001.
7. Coskun I. Non-linear vibrations of a beam on a tensionless Winkler foundation. J Sound Vib. 2000;236(3):401–11.
8. Celep Z, Güler K, Demir F. Response of a completely free beam on a tensionless Pasternak foundation subjected to dynamic load. Struct Eng Mech. 2011;37(1):61–77.
9. Vassilev VM, Djondjorov PA. Dynamic stability of viscoelastic pipes on elastic foundations of variable modulus. J Sound Vib. 2006;297(1–2):414–9.
10. Yang SP, Li SH, Lu YJ. Investigation on dynamic interaction between a heavy vehicle and road pavement. Veh Syst Dyn. 2010;48(8):923–44.
11. Chen JS, Chen YK. Steady state and stability of a beam on a damped tensionless foundation under a moving load. Int J Non-Linear Mech. 2011;46(1):180–5.
12. Senalp AD, Arikoglu A, Ozkol I. Dynamic response of a finite length Euler–Bernoulli beam on linear and nonlinear viscoelastic foundations to a concentrated moving force. J Mech Sci Technol. 2010;24(10):1957–61.
13. Thambiratnam D, Zhuge Y. Dynamic analysis of beams on an elastic foundation subjected to moving loads. J Sound Vib. 1996;198(2):149–69.
14. Muscolino G, Palmeri A. Response of beams on viscoelastically damped foundation to moving oscillators. Int J Solids Struct. 2007;44(5):1317–36.
15. Arboleda-Monsalve LG, Zapata-Medina DG, Aristizabal-Ochoa JD. Timoshenko beam-column with generalized end conditions on an elastic foundation: dynamic-stiffness matrix and load vector. J Sound Vib. 2008;310(4–5):1057–79.
16. Ding H, Chen LQ, Yang SP. Convergence of Galerkin truncation for dynamic response of finite beams on nonlinear foundations under a moving load. J Sound Vib. 2012;331(10):2426–42.
17. Contreras JN, Castro-Fresno D, Vega-Zamanillo A. Dynamic modulus of an asphalt mixture by ultrasonic direct test. NDT E Int. 2010;43(7):629–34.
18. Yang Y, Ding H, Chen LQ. Dynamic response to a moving load of a Timoshenko beam on a nonlinear viscoelastic foundation. Acta Mech Sin. 2013;29(5):718–27.
19. Ding H, Shi KL, Chen LQ, Yang SP. Dynamic response of an infinite Timoshenko beam on a nonlinear viscoelastic foundation. Nonlinear Dyn. 2013;73:285–98.
20. Cao CY, Zhong Y. Dynamic response of a beam on a Pasternak foundation under a moving load. J Chongqing Univ. 2008;7:311–6.
21. Ding H, Yang Y, Chen LQ, Yang SP. Vibration of vehicle–pavement coupled system based on a Timoshenko beam on a nonlinear foundation. J Sound Vib. 2014;333(24):6623–36.
22. Bhattiprolu U, Bajaj AK, Davies P. An efficient solution methodology to study the response of a beam on a viscoelastic and nonlinear unilateral foundation: static response. Int J Solids Struct. 2013;50:2328–39.
23. Palmeri A, Cicirello A. Physically-based Dirac's delta functions in the static analysis of multi-cracked Euler–Bernoulli and Timoshenko beams. Int J Solids Struct. 2011;48:2184–95.
24. Thambiratnam D, Zhuge Y. Dynamic analysis of beams on an elastic foundation subjected to moving loads. J Sound Vib. 1996;198:149–69.
25. Ding H, Shi KL, Chen LQ, Yang SP. Adomian polynomials for nonlinear response of supported Timoshenko beams subjected to a moving harmonic load. Acta Mech Solida Sin. 2014;27(4):383–93.
26. Kargarnovin MH, Younesian D, Thompson DJ. Response of beams on nonlinear viscoelastic foundations to harmonic moving loads. Comput Struct. 2005;83(23–24):1865–77.

27. Hryniewicz Z. Dynamics of a Rayleigh beam on a nonlinear foundation due to a moving load using Adomian decomposition and coiflet expansion. Soil Dyn Earthq Eng. 2011;31(8):1123–31.
28. Adomian G. A new approach to nonlinear partial differential equations. J Math Anal Appl. 1984;102(2):420–34.
29. Vahidi AR, Jalalvand B. Improving the accuracy of the Adomian decomposition method for solving nonlinear equations. Appl Math Sci. 2012;6(10):487–97.
30. Wazwaz AM. A reliable modification of the Adomian decomposition method. Appl Math Comput. 1999;102(1):77–86.

Chapter 5
Road Dynamic Responses Under Moving Vehicle Loads Based on Double-Layer Plate Model

A beam and a plate on different kinds of foundations have been widely adopted to predict the deflections and the stresses of the road [1–3]. Chapter 4 in this book established a finite and an infinite beam models on nonlinear foundations, and discussed the effect of nonlinear parameters on beam responses. The road structure, from top to bottom, consists of surface course, base course, subbase course, as well as subgrade and natural foundation. A multilayered medium is close to the actual road system.

Based on the previous researches, this chapter improves the traditional single infinite Kirchhoff plate model and establishes an infinite double-layer plate on a Kelvin foundation and an elastic half-space to model the road's layered system. An analytical approach is developed to investigate the dynamic response of the road subjected to moving vehicle loads. The shape of the tire–road contact area is assumed to be rectangular spatial distributed, and the load pressure within the contact area is assumed to be uniformly distributed. The Fourier transform is used to derive the Green's function of the road under the unit impulse load. Based on the superposition principle of linear system, the analytical solutions of the dynamic responses in time domain are then derived by integrating the generalized Duhamel integral over the Green's function of the double-layer plate under the unit impulse load. The vibration characteristics of the road under a moving constant and harmonic load are then analyzed.

5.1 Description of the Moving Vehicle Loads

5.1.1 Mathematical Model of the Moving Vehicle Loads

It is the tire on the road surface that actually applies vehicle loads to the road. Therefore, the tire contact shape and pressure is important in computing the dynamic responses of the road system. A lot of field tests have been done to measure the actual contact shape and contact pressure between the tire and the road surface. The

S. Yang et al., *Dynamics of Vehicle-Road Coupled System,*
DOI 10.1007/978-3-662-45957-7_5

available data shows that the contact shape is between rectangular and circular, and the contact pressure distributions are typically nonuniform and vary with vehicle loads, tire type, tire pressure, and vehicle moving speed [4–6]. The precise description of the tire contact shape and the contact pressure using a mathematical formula is very difficult. But for the truck tire, especially, when the load is large enough, the contact shape is more similar to a rectangular. So, in order to simplify the following calculation, in this chapter and chap. 6, the rectangular tire contact shape with uniform vertical contact pressure is assumed to simulate the tire–road contact forces generated by moving heavy vehicles.

If the vertical (z direction) vehicle load $F(x,y,t)$ is uniformly distributed in a rectangular area $\{-l_1 \le x \le l_1, \quad -l_2 \le y \le l_2\}$, and is moving in the positive x direction with a constant advance velocity v, Then, this vehicle load $F(x,y,t)$ can be characterized by

1. Moving constant load

$$F(x,y,t) = \frac{F}{4l_1 l_2} H\left(l_1^2 - (x-vt)^2\right) H\left(l_2^2 - y^2\right) H(t) \tag{5.1}$$

For the steady state response of the road, Eq. (5.1) can be simplified as

$$F(x,y,t) = \frac{F}{4l_1 l_2} H\left(l_1^2 - (x-vt)^2\right) H\left(l_2^2 - y^2\right) \tag{5.2}$$

where F is the magnitude of the moving constant load, $H(\cdot)$ represents the Heaviside unit step function.

2. Moving harmonic load

$$F(x,y,t) = \frac{F_0}{4l_1 l_2} e^{j\omega_0 t} H\left(l_1^2 - (x-vt)^2\right) H\left(l_2^2 - y^2\right) H(t) \tag{5.3}$$

For the steady state response of the road, Eq. (5.3) can be simplified as

$$F(x,y,t) = \frac{F_0}{4l_1 l_2} e^{j\omega_0 t} H\left(l_1^2 - (x-vt)^2\right) H\left(l_2^2 - y^2\right) \tag{5.4}$$

where F_0 is the amplitude of the moving harmonic load, and $\omega_0 = 2\pi f_0$ is the frequency of the moving harmonic load.

5.1.2 Calculation of the Tire Contact Area

When a single-axle single-tire is considered, the tire contact shape can be a combination of a rectangle of $0.4L \times 0.6L$ and two semicircles whose radiuses are width 0.3 L of the rectangle [6, 7]. The layout of the contact area is shown in Fig. 5.1a. So, the tire contact area can be expressed as

$$A_c = 0.4L \times 0.6L + \pi \times (0.3L)^2 \tag{5.5}$$

where A_c is the contact area of the single-tire, $A_c = F / p$, F is the tire–road contact force generated by the single-tire, p is the tire–road contact pressure.

The size L can be obtained from Eq. (5.5)

$$L = \sqrt{\frac{A_c}{0.5227}} \tag{5.6}$$

The contact area A_c is converted into an equivalent rectangle with a length of $2\,l_1$ and a width of $2l_2 = 0.6L$. The length $2l_1$ can be calculated as follow

$$2l_1 = \frac{A_c}{2l_2} = \frac{A_c}{0.6L} \tag{5.7}$$

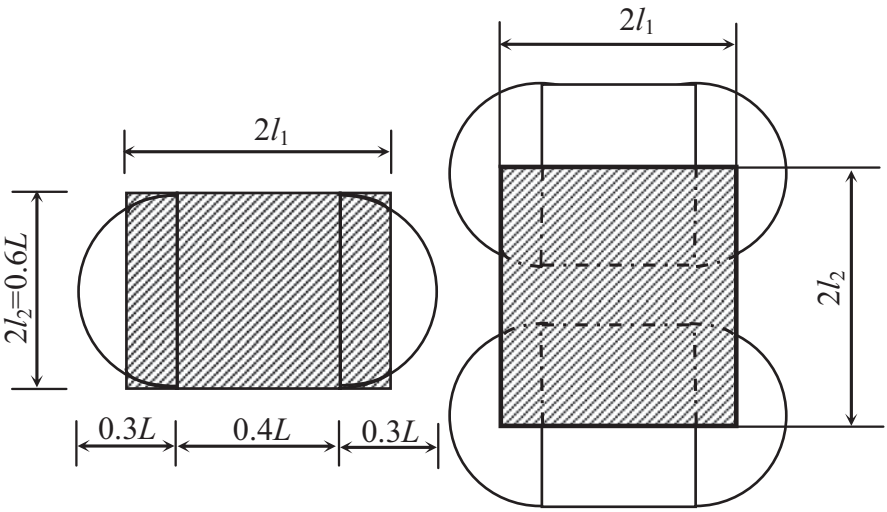

Fig. 5.1 Contact area of the tire. **a** single-tire, **b** dual-tire

When a single-axle dual-tire is considered, the layout of the contact area is shown in Fig. 5.1b. The length and the width of the contact rectangle are $2l_1$ and $2l_2$, respectively. The calculation of l_1 is the same as the abovementioned single-tire contact, the size l_2 is half of the distance between the two tires' centers, $2l_2 = 1.5d_s$, in which d_s is the equivalent circle diameter of single-tire contact area under full load.

$$d_s = \sqrt{\frac{4A_c}{\pi}} \tag{5.8}$$

5.2 Dynamic Responses of an Infinite Double-Layer Plate on a Kelvin Foundation

5.2.1 Governing Equations of the Infinite Double-Layer Plate

The infinite double-layer plate on a Kelvin foundation, shown in Fig. 5.2, is employed as a road model. The upper layer of the plate models the surface course, and the lower layer models the base course. Each layer is assumed to extend to infinity horizontally and to be of uniform thickness. The material of each layer is considered to be linear elastic with elastic modulus E_1 and E_2, shear modulus G_1 and G_2, Poisson's ratio μ_1 and μ_2, mass density ρ_1 and ρ_2, thickness h_1 and h_2. In a Cartesian coordinate system $\{x, y, z\}$, based on the assumptions of plate theory, the motion of the double-layer thin plate is governed as follows.

1. Displacement components

$$\begin{cases} u(x,y,z,t) = -z\dfrac{\partial w}{\partial y} \\ v(x,y,z,t) = -z\dfrac{\partial w}{\partial y} \\ w(x,y,t) = w(x,y,t) \end{cases} \tag{5.9}$$

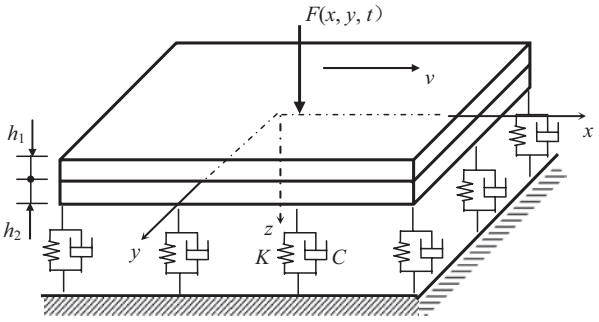

Fig. 5.2 An infinite double-layer plate on a Kelvin foundation

2. Strain components

$$\varepsilon_x = -z\frac{\partial^2 w}{\partial x^2} \quad \varepsilon_y = -z\frac{\partial^2 w}{\partial y^2} \quad \gamma_{xy} = -2z\frac{\partial^2 w}{\partial x \partial y} \tag{5.10}$$

3. Stress components

$$\begin{cases} \sigma_x = -\dfrac{E(z)}{1-\mu^2(z)} z\left[\dfrac{\partial^2 w}{\partial x^2} + \mu(z)\dfrac{\partial^2 w}{\partial y^2}\right] \\ \sigma_y = -\dfrac{E(z)}{1-\mu^2(z)} z\left[\dfrac{\partial^2 w}{\partial y^2} + \mu(z)\dfrac{\partial^2 w}{\partial x^2}\right] \\ \tau_{xy} = -2G(z)z\dfrac{\partial^2 w}{\partial x \partial y} = -\dfrac{E(z)}{1+\mu(z)} z\dfrac{\partial^2 w}{\partial x \partial y} \end{cases} \tag{5.11}$$

where $E(z)$, $G(z)$, and $\mu(z)$ represents the change of elastic modulus, shear modulus, and Poisson's ratio along the direction z.

4. Internal force components

Let h_0 be the distance between the stress neutral layer and the upper surface of the double-layer plate and take the stress neutral layer as plane $z = 0$ as shown in Fig. 5.2. So, the stress components of the double-layer plate satisfies the following functions

$$\sigma_{1x} = E_1 \frac{z}{r}, \ \sigma_{2x} = E_2 \frac{z}{r} \tag{5.12}$$

where r is the curvature radius of the stress neutral layer.

Since the stress of the neutral layer is zero, it can be gained

$$\int_{A_1} \sigma_{1x} \mathrm{d}A_1 + \int_{A_2} \sigma_{2x} \mathrm{d}A_2 = 0 \tag{5.13}$$

Substituting Eq. (5.12) into Eq. (5.13), one gets

$$E_1 \int_{h_0-h_1}^{h_0} z\mathrm{d}z + E_2 \int_{h_0-h_1-h_2}^{h_0-h_1} z\mathrm{d}z = 0 \tag{5.14}$$

By integrating the above equation, the vertical position of the stress neutral layer can be obtained.

$$h_0 = \frac{E_1 h_1^2 + E_2(2h_1 + h_2)h_2}{2E_1 h_1 + 2E_2 h_2} \tag{5.15}$$

The internal force components can be expressed as

$$\begin{cases} M_x = \int_{h_0-h_1-h_2}^{h_0} z\sigma_x \mathrm{d}z = -D\dfrac{\partial^2 w}{\partial x^2} - D_{xy}\dfrac{\partial^2 w}{\partial y^2} \\ M_y = \int_{h_0-h_1-h_2}^{h_0} z\sigma_y \mathrm{d}z = -D\dfrac{\partial^2 w}{\partial y^2} - D_{xy}\dfrac{\partial^2 w}{\partial x^2} \\ M_{xy} = \int_{h_0-h_1-h_2}^{h_0} z\tau_{xy} \mathrm{d}z = -2D_k\dfrac{\partial^2 w}{\partial x \partial y} \end{cases} \tag{5.16}$$

in which,

$$\begin{cases} D = \int_{h_0-h_1}^{h_0} \dfrac{E_1}{1-\mu_1^2} z^2 \mathrm{d}z + \int_{h_0-h_1-h_2}^{h_0-h_1} \dfrac{E_2}{1-\mu_2^2} z^2 \mathrm{d}z \\ D_{xy} = \int_{h_0-h_1}^{h_0} \dfrac{E_1\mu_1}{1-\mu_1^2} z^2 \mathrm{d}z + \int_{h_0-h_1-h_2}^{h_0-h_1} \dfrac{E_2\mu_2}{1-\mu_2^2} z^2 \mathrm{d}z \\ D_k = \int_{h_0-h_1}^{h_0} G_1 z^2 \mathrm{d}z + \int_{h_0-h_1-h_2}^{h_0-h_1} G_2 z^2 \mathrm{d}z \end{cases} \tag{5.17}$$

5. Dynamic equation

Integrating the 3D equilibrium equation of variable-density in direction z, one can obtain

$$\begin{cases} \dfrac{\partial M_x}{\partial x} + \dfrac{\partial M_{xy}}{\partial y} - Q_x = 0 \\ \dfrac{\partial M_{xy}}{\partial x} + \dfrac{\partial M_y}{\partial y} - Q_y = 0 \\ \dfrac{\partial Q_x}{\partial x} + \dfrac{\partial Q_y}{\partial y} - \rho h\dfrac{\partial^2 w}{\partial t^2} + q(x,y,t) = 0 \end{cases} \tag{5.18}$$

where $q(x,y,t)$ is the external load applied on the surface layer of the double-layer plate, $q(x,y,t) = F(x,y,t) - Kw - C\dfrac{\partial w}{\partial t}$, where K and C are the vertical stiffness coefficient and damping coefficient, and ρh is the mass density of the double-layer plate per unit area, $\rho h = \int_{h_0-h_1}^{h_0} \rho_1 \mathrm{d}z + \int_{h_0-h_1-h_2}^{h_0-h_1} \rho_2 \mathrm{d}z = \rho_1 h_1 + \rho_2 h_2$.

Substituting Eq. (5.16) into the first two equations of Eq. (5.18) leads to expressions of the shear components

$$\begin{cases} Q_x = -\dfrac{\partial}{\partial x}\left[D\dfrac{\partial^2 w}{\partial x^2} + (D_{xy} + 2D_k)\dfrac{\partial^2 w}{\partial y^2} \right] \\ Q_y = -\dfrac{\partial}{\partial y}\left[D\dfrac{\partial^2 w}{\partial y^2} + (D_{xy} + 2D_k)\dfrac{\partial^2 w}{\partial x^2} \right] \end{cases} \tag{5.19}$$

Substituting Eq. (5.19) into the third of Eq. (5.18), together with some arrangement, one obtains the partial differential equation of the double-layer thin plate on a viscoelastic Kelvin foundation under moving vehicle loads in terms of vertical displacement w as

$$D\left(\frac{\partial^4 w}{\partial x^4} + \frac{\partial^4 w}{\partial y^4} \right) + 2(D_{xy} + 2D_k)\frac{\partial^4 w}{\partial x^2 \partial y^2} + \rho h \frac{\partial^2 w}{\partial t^2} + Kw + C\frac{\partial w}{\partial t} = F(x, y, t) \tag{5.20}$$

The boundary conditions for $x \to \pm\infty$, $y \to \pm\infty$ and the initial condition for $t = 0$ are represented by

$$\begin{cases} \lim\limits_{x\to\pm\infty} \dfrac{\partial^n w}{\partial x^n} = 0; \quad \lim\limits_{y\to\pm\infty} \dfrac{\partial^n w}{\partial y^n} = 0 \quad n = 0, 1, 2\cdots. \\ w(x, y, t)\big|_{t=0} = \left.\dfrac{\partial w(x, y, t)}{\partial t}\right|_{t=0} = 0 \end{cases} \tag{5.21}$$

5.2.2 *The Displacement and the Stress of the Double-Layer Plate Under Moving Vehicle Loads Supported by a Kelvin Foundation*

1. Vertical displacement Green's functions of the double-layer plate

The triple Fourier transform and its inversion are defined as follows

$$\begin{cases} \overline{f}(k_1, k_2, \omega) = \displaystyle\int_{-\infty}^{+\infty}\int_{-\infty}^{+\infty}\int_{-\infty}^{+\infty} f(x, y, t) e^{-j(k_1 x + k_2 y + \omega t)} \mathrm{d}x\mathrm{d}y\mathrm{d}t \\ f(x, y, t) = \dfrac{1}{(2\pi)^3}\displaystyle\int_{-\infty}^{+\infty}\int_{-\infty}^{+\infty}\int_{-\infty}^{+\infty} \overline{f}(k_1, k_2, \omega) e^{j(k_1 x + k_2 y + \omega t)} \mathrm{d}k_1\mathrm{d}k_2\mathrm{d}\omega \end{cases} \tag{5.22}$$

By replacing $F(x,y,t)$ on the right side of Eq. (5.20)with the unit impulse load $F_\delta(x,y,t;0,0,0)=\delta(x)\delta(y)\delta(t)$, which acts at the origin of the coordinates for time t=0, and applying the triple Fourier transform with respect to x,y,t in Eq. (5.20), one obtains the algebraic equation of vertical displacement in the transformed domain.

$$\left[D(k_1^4+k_2^4)+2(D_{xy}+2D_k)k_1^2k_2^2\right]\overline{w}-\rho h\omega^2\overline{w}+K\overline{w}+jC\omega\overline{w}=1 \tag{5.23}$$

The following property of the Fourier transform is used in deriving the above equation

for $$|x|\to+\infty, f(x)\to 0:\ \overline{f}^{(n)}(x)=(jk)^n\overline{f}(x), \overline{\delta}(t)=1 \tag{5.24}$$

Rewriting Eq. (5.23) leads to

$$\overline{w}=\frac{1}{\left[D(k_1^4+k_2^4)+2(D_{xy}+2D_k)k_1^2k_2^2\right]-\rho h\omega^2+K+jC\omega} \tag{5.25}$$

Applying an inverse Fourier transform in Eq. (5.25) leads to

$$\begin{aligned} w=&\frac{1}{(2\pi)^3}\int_{-\infty}^{+\infty}\int_{-\infty}^{+\infty}\int_{-\infty}^{+\infty} \\ &\frac{e^{j(k_1x+k_2y+\omega t)}}{\left[D(k_1^4+k_2^4)+2(D_{xy}+2D_k)k_1^2k_2^2\right]-\rho h\omega^2+K+jC\omega}\mathrm{d}k_1\mathrm{d}k_2\mathrm{d}\omega \\ =&G\ (x,y,0,t) \end{aligned} \tag{5.26}$$

Equation (5.26) is the vertical displacement of the double-layer plate on a viscoelastic Kelvin foundation under unit impulse load, namely, vertical displacement Green's functions of the double-layer plate.

According to the theory of linear partial differential equation, the dynamic response of the double-layer plate to an external moving load $F(x,y,t)$ can be calculated by a generalized Duhamel integral, which integrates the Green's functions in all dimensions [8,9].

$$u_{ki}(x,y,z,t)=\int_S\int_0^t F(\zeta_1,\zeta_2,\tau)\times G_{ki}(x-\zeta_1,y-\zeta_2,z,t-\tau)\mathrm{d}\tau\mathrm{d}S \tag{5.27}$$

where the left-hand-side of Eq. (5.27) is the convolution integral of the moving load F and Green's function, u_{ki} on the right-hand-side of Eq. (5.27) represents the dynamic responses along the e_i direction for the observation x,y,z of the

viscoelastic body under the moving load F acting on the surface of the viscoelastic body along the e_k direction, and S is the distribution area of the moving load F.

2. Displacement and stress of the double-layer plate under a moving constant load

The vertical displacements of the double-layer plate under a moving constant load can be obtained by substituting Eq. (5.2) and Eq. (5.26) into Eq. (5.27), that is

$$w=\int_s\int_{-\infty}^{t}\frac{F}{4l_1l_2}H\left[l_1^2-(\zeta_1-v\tau)^2\right]H\left[l_2^2-\zeta_2^2\right]\frac{1}{(2\pi)^3}\int_{-\infty}^{+\infty}\int_{-\infty}^{+\infty}\int_{-\infty}^{+\infty}\frac{e^{j[k_1(x-\zeta_1)+k_2(y-\zeta_2)+\omega(t-\tau)]}}{\left[D(k_1^4+k_2^4)+2(D_{xy}+2D_k)k_1^2k_2^2\right]-\rho h\omega^2+K+jC\omega}\mathrm{d}k_1\mathrm{d}k_2\mathrm{d}\omega\mathrm{d}\tau\mathrm{d}S \tag{5.28}$$

letting $\zeta_1'=\zeta_1-v\tau$ and performing some integral calculation, one rewites Eq. (5.28) as

$$\begin{aligned}
w&=\frac{F}{(2\pi)^3}\int_{-l_1}^{l_1}\int_{-l_2}^{l_2}\int_{-\infty}^{t}\frac{1}{4l_1l_2}\int_{-\infty}^{+\infty}\int_{-\infty}^{+\infty}\int_{-\infty}^{+\infty}\\
&\frac{e^{j(k_1x+k_2y+\omega t)}e^{-j(\omega+vk_1)\tau}e^{-jk_1\zeta_1'}e^{-jk_2\zeta_2}}{\left[D(k_1^4+k_2^4)+2(D_{xy}+2D_k)k_1^2k_2^2\right]-\rho h\omega^2+K+jC\omega}\mathrm{d}k_1\mathrm{d}k_2\mathrm{d}\omega\mathrm{d}\tau\mathrm{d}\zeta_1'\mathrm{d}\zeta_2\\
&=\frac{F}{(2\pi)^3}\int_{-\infty}^{t}\int_{-\infty}^{+\infty}\int_{-\infty}^{+\infty}\int_{-\infty}^{+\infty}\frac{\sin(k_1l_1)}{k_1l_1}\frac{\sin(k_2l_2)}{k_2l_2}\\
&\frac{e^{j(k_1x+k_2y+\omega t)}e^{-j(\omega+vk_1)\tau}}{\left[D(k_1^4+k_2^4)+2(D_{xy}+2D_k)k_1^2k_2^2\right]-\rho h\omega^2+K+jC\omega}\mathrm{d}k_1\mathrm{d}k_2\mathrm{d}\omega\mathrm{d}\tau\\
&=\frac{F}{(2\pi)^2}\int_{-\infty}^{+\infty}\int_{-\infty}^{+\infty}\int_{-\infty}^{+\infty}\frac{\sin(k_1l_1)}{k_1l_1}\frac{\sin(k_2l_2)}{k_2l_2}\\
&\frac{e^{j(k_1x+k_2y+\omega t)}\delta(\omega+vk_1)}{\left[D(k_1^4+k_2^4)+2(D_{xy}+2D_k)k_1^2k_2^2\right]-\rho h\omega^2+K+jC\omega}\mathrm{d}k_1\mathrm{d}k_2\mathrm{d}\omega\\
&=\frac{F}{4\pi^2}\int_{-\infty}^{+\infty}\int_{-\infty}^{+\infty}\frac{\sin(k_1l_1)}{k_1l_1}\frac{\sin(k_2l_2)}{k_2l_2}\\
&\frac{e^{j[k_1(x-vt)+k_2y]}}{\left[D(k_1^4+k_2^4)+2(D_{xy}+2D_k)k_1^2k_2^2\right]+K-\rho hv^2k_1^2-jCvk_1}\mathrm{d}k_1\mathrm{d}k_2
\end{aligned} \tag{5.29}$$

In the derivation of Eq. (5.29), the following equality properties of the Dirac delta function are used

$$\begin{cases} \int_{-\infty}^{+\infty} e^{-j\omega t}\mathrm{d}t = 2\pi\delta(\omega) \\ \int_{-\infty}^{+\infty} e^{-j(\omega-\omega_0)t}\mathrm{d}t = 2\pi\delta(\omega-\omega_0) \\ \int_{-\infty}^{+\infty} \delta(t-t_0)f(t)\mathrm{d}t = f(t_0) \end{cases} \tag{5.30}$$

The stress components in the upper layer can be expressed as

$$\begin{aligned} \sigma_x &= -\frac{E_1 z}{1-\mu_1^2}\left[\frac{\partial^2 w}{\partial x^2} + \mu_1 \frac{\partial^2 w}{\partial y^2}\right] \\ &= \frac{E_1 z}{1-\mu_1^2}\frac{F}{4\pi^2}\int_{-\infty}^{+\infty}\int_{-\infty}^{+\infty}\frac{\sin(k_1 l_1)}{k_1 l_1}\frac{\sin(k_2 l_2)}{k_2 l_2}\times \\ &\frac{(k_1^2+\mu_1 k_2^2)e^{j[k_1(x-vt)+k_2 y]}}{\left[D(k_1^4+k_2^4)+2(D_{xy}+2D_k)k_1^2 k_2^2\right]+K-\rho h v^2 k_1^2 - jCvk_1}\mathrm{d}k_1\mathrm{d}k_2 \end{aligned} \tag{5.31}$$

$$\begin{aligned} \sigma_y &= -\frac{E_1 z}{1-\mu_1^2}\left[\frac{\partial^2 w}{\partial y^2} + \mu_1 \frac{\partial^2 w}{\partial x^2}\right] \\ &= \frac{E_1 z}{1-\mu_1^2}\frac{F}{4\pi^2}\int_{-\infty}^{+\infty}\int_{-\infty}^{+\infty}\frac{\sin(k_1 l_1)}{k_1 l_1}\frac{\sin(k_2 l_2)}{k_2 l_2}\times \\ &\frac{(\mu_1 k_1^2+k_2^2)e^{j[k_1(x-vt)+k_2 y]}}{\left[D(k_1^4+k_2^4)+2(D_{xy}+2D_k)k_1^2 k_2^2\right]+K-\rho h v^2 k_1^2 - jCvk_1}\mathrm{d}k_1\mathrm{d}k_2 \end{aligned} \tag{5.32}$$

$$\begin{aligned} \tau_{xy} &= -\frac{E_1 z}{1+\mu_1}\frac{\partial^2 w}{\partial x \partial y} \\ &= \frac{E_1 z}{1+\mu_1}\frac{F}{4\pi^2}\int_{-\infty}^{+\infty}\int_{-\infty}^{+\infty}\frac{\sin(k_1 l_1)}{k_1 l_1}\frac{\sin(k_2 l_2)}{k_2 l_2}\times \\ &\frac{k_1 k_2 e^{j[k_1(x-vt)+k_2 y]}}{\left[D(k_1^4+k_2^4)+2(D_{xy}+2D_k)k_1^2 k_2^2\right]+K-\rho h v^2 k_1^2 - jCvk_1}\mathrm{d}k_1\mathrm{d}k_2 \end{aligned} \tag{5.33}$$

By exchanging E_1 and μ_1 in Eq. (5.31)–(5.33) for E_2 and μ_2, one can obtain the stress components in the lower layer.

3. Displacement and stress of the double-layer plate under a moving harmonic load

The vertical displacements of the double-layer plate under a moving harmonic load can be obtained by substituting Eq. (5.4) and Eq. (5.26) into Eq. (5.27), that is

$$w=\int_s\int_{-\infty}^{t}\frac{F_0}{4l_1l_2}e^{j\omega_0\tau}H\left[l_1^2-(\zeta_1-v\tau)^2\right]H\left[l_2^2-\zeta_2^2\right]\frac{1}{(2\pi)^3}\int_{-\infty}^{+\infty}\int_{-\infty}^{+\infty}\int_{-\infty}^{+\infty}\frac{e^{j[k_1(x-\zeta_1)+k_2(y-\zeta_2)+\omega(t-\tau)]}}{\left[D(k_1^4+k_2^4)+2(D_{xy}+2D_k)k_1^2k_2^2\right]-\rho h\omega^2+K+jC\omega}\mathrm{d}k_1\mathrm{d}k_2\mathrm{d}\omega\mathrm{d}\tau\mathrm{d}S \tag{5.34}$$

Performing the same derivation process as Eq. (5.29) leads to

$$w=\frac{F_0}{4\pi^2}e^{j\omega_0t}\int_{-\infty}^{+\infty}\int_{-\infty}^{+\infty}\frac{\sin(k_1l_1)}{k_1l_1}\frac{\sin(k_2l_2)}{k_2l_2}\times\frac{e^{j[k_1(x-vt)+k_2y]}}{\left[D(k_1^4+k_2^4)+2(D_{xy}+2D_k)k_1^2k_2^2\right]+K-\rho h(\omega_0-vk_1)^2+jC(\omega_0-vk_1)}\mathrm{d}k_1\mathrm{d}k_2 \tag{5.35}$$

The stress components in the upper layer can be expressed as

$$\begin{aligned}\sigma_x&=-\frac{E_1z}{1-\mu_1^2}\left[\frac{\partial^2w}{\partial x^2}+\mu_1\frac{\partial^2w}{\partial y^2}\right]\\&=\frac{E_1z}{1-\mu_1^2}\frac{F_0}{4\pi^2}e^{j\omega_0t}\int_{-\infty}^{+\infty}\int_{-\infty}^{+\infty}\frac{\sin(k_1l_1)}{q_1l_1}\frac{\sin(k_2l_2)}{q_2l_2}\times\\&\frac{(k_1^2+\mu_1k_2^2)e^{j[k_1(x-vt)+k_2y]}}{\left[D(k_1^4+k_2^4)+2(D_{xy}+2D_k)k_1^2k_2^2\right]+K-\rho h(\omega_0-vk_1)^2+jC(\omega_0-vk_1)}\mathrm{d}k_1\mathrm{d}k_2\end{aligned} \tag{5.36}$$

$$\begin{aligned}\sigma_y&=-\frac{E_1z}{1-\mu_1^2}\left[\frac{\partial^2w}{\partial y^2}+\mu_1\frac{\partial^2w}{\partial x^2}\right]\\&=\frac{E_1z}{1-\mu_1^2}\frac{F_0}{4\pi^2}e^{j\omega_0t}\int_{-\infty}^{+\infty}\int_{-\infty}^{+\infty}\frac{\sin(k_1l_1)}{k_1l_1}\frac{\sin(k_2l_2)}{k_2l_2}\times\\&\frac{(\mu_1k_1^2+k_2^2)e^{j[k_1(x-vt)+k_2y]}}{\left[D(k_1^4+k_2^4)+2(D_{xy}+2D_k)k_1^2k_2^2\right]+K-\rho h(\omega_0-vk_1)^2+jC(\omega_0-vk_1)}\mathrm{d}k_1\mathrm{d}k_2\end{aligned} \tag{5.37}$$

$$\begin{aligned}\tau_{xy} &= -\frac{E_1 z}{1+\mu_1}\frac{\partial^2 w}{\partial x \partial y} \\ &= \frac{E_1 z}{1+\mu_1}\frac{F_0}{4\pi^2} e^{j\omega_0 t}\int_{-\infty}^{+\infty}\int_{-\infty}^{+\infty}\frac{\sin(k_1 l_1)}{k_1 l_1}\frac{\sin(k_2 l_2)}{k_2 l_2}\times \\ &\quad \frac{k_1 k_2 e^{j[k_1(x-vt)+k_2 y]}}{\left[D(k_1^4+k_2^4)+2(D_{xy}+2D_k)k_1^2 k_2^2\right]+K-\rho h(\omega_0 - vk_1)^2 + jC(\omega_0 - vk_1)}\mathrm{d}k_1\mathrm{d}k_2\end{aligned} \tag{5.38}$$

By exchanging E_1 and μ_1 in Eq. (5.36)–(5.38) for E_2 and μ_2, one can obtain the stress components in the lower layer.

5.3 Numerical Simulations of an Infinite Double-Layer Plate on a Kelvin Foundation

Computation of dynamic responses of the double-layer plate to the moving loads requires numerical evaluation of Eq. (5.29), (5.31)–(5.33) and Eqs. (5.35)–(5.38), which involve the double integrals in the infinite intervals. These integrals are highly oscillatory in nature as they contain complex indexes. Such integrals require a great deal of sophistication in the numerical computation. Usually, researchers tend to evaluate these integrals by the fast Fourier transform. In this section, an efficient computer program based on the adaptive Simpson numerical algorithm is developed to perform the integrals and the program is coded and implemented via Mathmatica. The parameters used in the numerical calculation are chosen to be: $E_1 = 1500\text{MPa}$, $E_2 = 1200\text{MPa}$, $\mu_1 = \mu_2 = 0.35$, $h_1 = 0.15\text{m}$, $h_2 = 0.2\text{m}$, $\rho_1 = 2613\text{kg/m}^3$, $\rho_2 = 2083\text{kg/m}^3$, $K = 50\text{MN/m}^3$, $v = 25\text{m/s}$.

5.3.1 Result Verification

The single-layer plate is the model frequently adopted by researchers in their study of vehicle-induced road vibrations. Furthermore, a single-layer plate is a special case of a double-layer plate when the material properties of each layer are identical. The steady-state response of a single-layer plate on a Winkler foundation under a moving rectangular distributed constant load is available in the literature of Kim [10], which is used to compare it with the solution of this section. Kim's numerical result was obtained by using the fast Fourier transform. In Kim's paper, the parameters used in the numerical calculation are chosen to be: $E = 1516\text{MPa}$, $\mu = 0.35$, $h = 0.15\text{m}$, $\rho = 2440\text{kg/m}^3$, $K = 95\text{MN/m}^3$, $C = 0$, $F = 175\text{N}$, $l_1 = l_2 = 0.075\text{m}$. By using the parameters in Kim's paper, the vertical displacements under three different speeds are also calculated and plotted in Fig. 5.3. It can

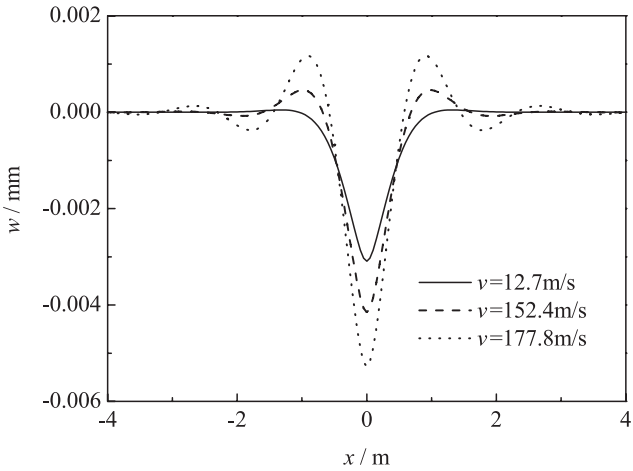

Fig. 5.3 Vertical displacement calculated using the parameters in Kim's paper

be seen that the results obtained in this section are in good agreement with Fig. 2(a) in Kim's paper.

5.3.2 The Dynamic Response of the Double-Layer Plate

1. The dynamic response of the double-layer plate under a moving constant load

If we consider the vehicle load $F = 50\text{kN}$ and the contact pressure $p = 0.7\text{MPa}$, the length $l_1 = 0.11\text{m}$, and the width $l_2 = 0.16\text{m}$, the tire contact rectangle can be evaluated from Eqs. (5.5)–(5.8). The vertical displacement w and the longitudinal normal stress σ_x at the bottom of the double-layer plate for different values of the damping coefficient are shown in Fig. 5.4, 5.5 5.6, when the load is moving at a constant speed. From Fig. 5.4–5.6, we can see:

a. With the extension of the time and the space, the dynamic responses attenuate rapidly. The dynamic responses are symmetric with respect to the two axes(x- and y-axes) and time $t = 0$ when there is no damping in the system. The maximum of the dynamic responses occur at the center of the load. When there exists damping, the dynamic responses are symmetric with respect to the x- axis, but no longer symmetric with respect to the y-axis and time $t = 0$. As the damping increases, the asymmetry of the dynamic responses become more obvious. The maximum of the longitudinal normal stress still occurs at the center of the load. However there exists a significant delay in the vertical displacement and the maximum of the vertical displacement lags behind the center of the load. The distance and the time of the lag become more apparent when the damping increases.

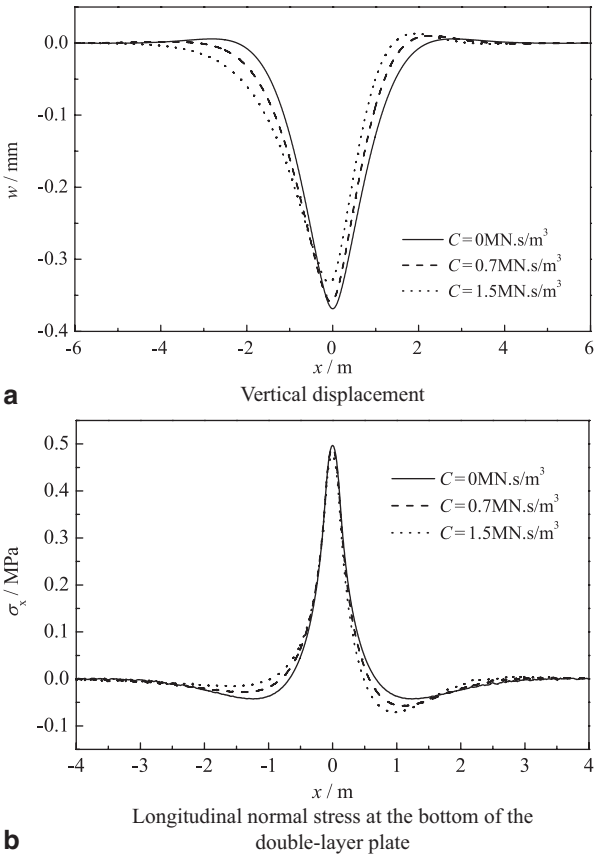

Fig. 5.4 The dynamic response of the double-layer plate along the x-axis under a moving constant load. **a** Vertical displacement, **b** Longitudinal normal stress at the bottom of the double-layer plate

b. Before and after the load passes through the observation point which is located at the bottom of the double-layer plate, the longitudinal normal stress of this point is negative. When the load is passing through the observation point, the longitudinal normal stress of this point is positive. So, when the vehicle is traveling on the road, each point of the road must go through an alternating process from compression to tension, then from tension to compression, which is extremely adverse to the road fatigue life.
c. When there exists damping in the system, the plate vibration is propagating forward along the moving direction in the space domain, the plate vibration ahead of the load is greater than that behind the load. The plate vibration before the load passing through is greater than that after the load passing through in the time domain.

2. The dynamic response of the double-layer plate under a moving harmonic load

The vertical displacement and the longitudinal normal stress at the bottom of the double-layer plate under a moving harmonic load with respect to different loading frequencies and amplitudes for the observation point ($x = 0$, $y = 0$) are shown in

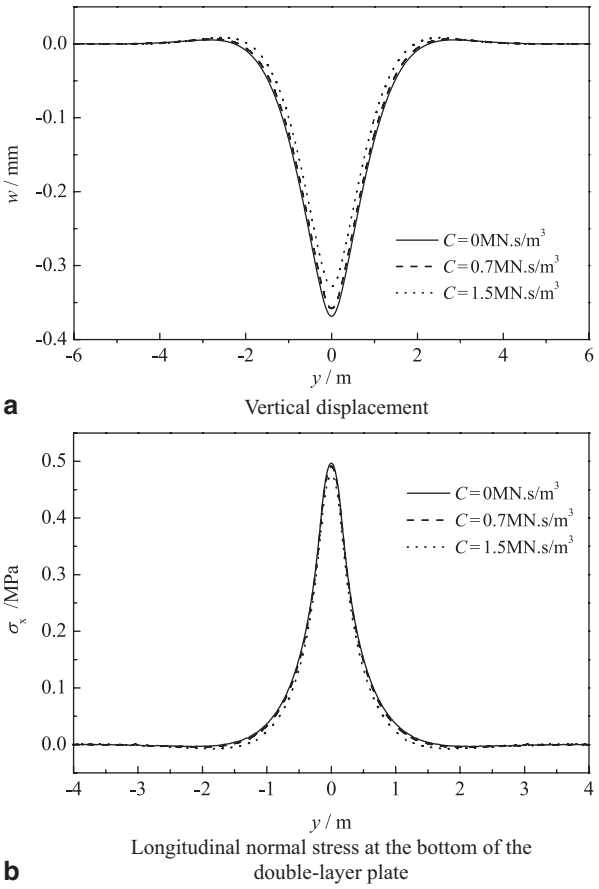

Fig. 5.5 The dynamic response of the double-layer plate along the y-axis under a moving constant load. **a** Vertical displacement, **b** Longitudinal normal stress at the bottom of the double-layer plate

Fig. 5.7 and 5.8, respectively, where $C = 600\text{kN}\cdot\text{s}/\text{m}^3$. From Fig. 5.7 and 5.8, we can see:

a. The plate vibration frequency increases as the loading frequency increases, and the vibration amplitude before the load passes through is larger than that after the load passes through, but the influence region of the displacement and stress in the time domain is becoming narrower as the loading frequency increases.
b. As the loading frequency increases, the negative maximum of the vertical displacement decreases and the positive maximum of the vertical displacement increases, the increase of positive maximum is greater than the decrease of negative maximum. Also, the maximum longitudinal tensile stress decreases and the maximum longitudinal compressive stress increases as the loading frequency increases. The influence of the loading frequency on the vertical displacement is greater than that on the longitudinal normal stress at the bottom of the double-layer plate.

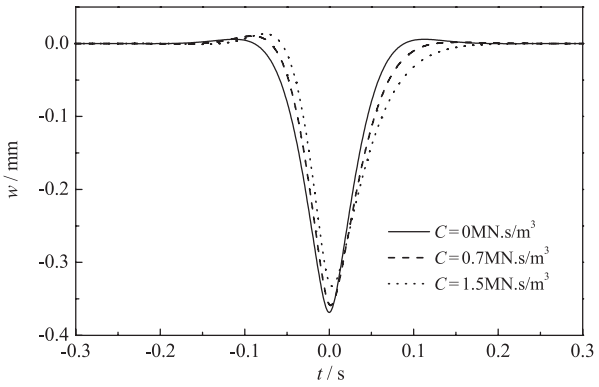

a Vertical displacement

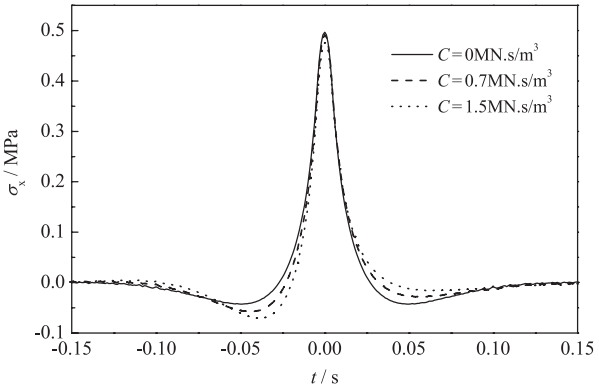

b Longitudinal normal stress at the bottom of the double-layer plate

Fig. 5.6 The dynamic response of the double-layer plate verses time under a moving constant load. **a** Vertical displacement, **b** Longitudinal normal stress at the bottom of the double-layer plate

c. As the harmonic load amplitude increases, the plate vibration amplitude also increases, which causes a significant increase in the negative and positive maximum of the vertical displacement and the maximum longitudinal tensile and compressive stress.

5.4 Dynamic Responses of an Infinite Double-Layer Plate on an Elastic Half Space Foundation

5.4.1 Governing Equations of the Infinite Double-Layer Plate

The double-layer thin plate on an elastic half-space foundation, shown in Fig. 5.9 is employed as a road model. The upper layer of the plate models the surface course,

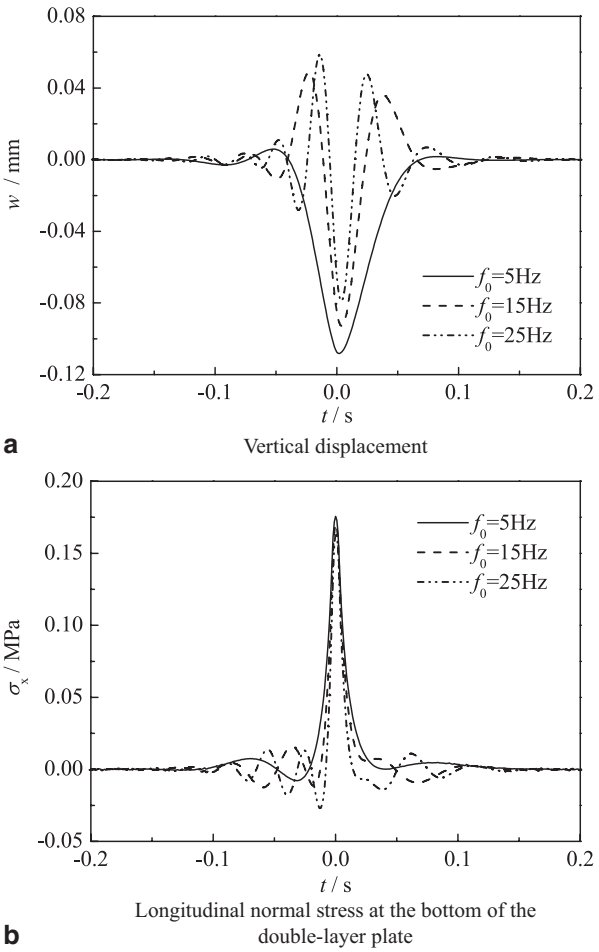

Fig. 5.7 The dynamic response of the double-layer plate vs. time under different frequencies of harmonic load. **a** Vertical displacement, **b** Longitudinal normal stress at the bottom of the double-layer plate

and the lower layer models the base course. The contact condition between the plate and the elastic half-space foundation is assumed to be smooth. Each layer is assumed to extend to infinity horizontally, and to be of uniform thickness. E_1, E_2, μ_1, μ_2, ρ_1, ρ_2, h_1, and h_2 denote the elastic modulus, Poisson's ratio, mass density, and thickness of the two layers, respectively. $F(x,y,t)$ is the load moving at a constant speed v along the x direction, $P(x,y,t)$ is the foundation reaction. The partial differential equation of the vertical vibration of the double-layer plate can be obtained from Eq. (5.20)

$$D\left(\frac{\partial^4 w}{\partial x^4}+\frac{\partial^4 w}{\partial y^4}\right)+2\left(D_{xy}+2D_k\right)\frac{\partial^4 w}{\partial x^2\partial y^2}+\rho h\frac{\partial^2 w}{\partial t^2}=F(x,y,t)-P(x,y,t) \quad (5.39)$$

in which, D, D_{xy}, D_k, and ρh have the same meaning as sect. 5.2.

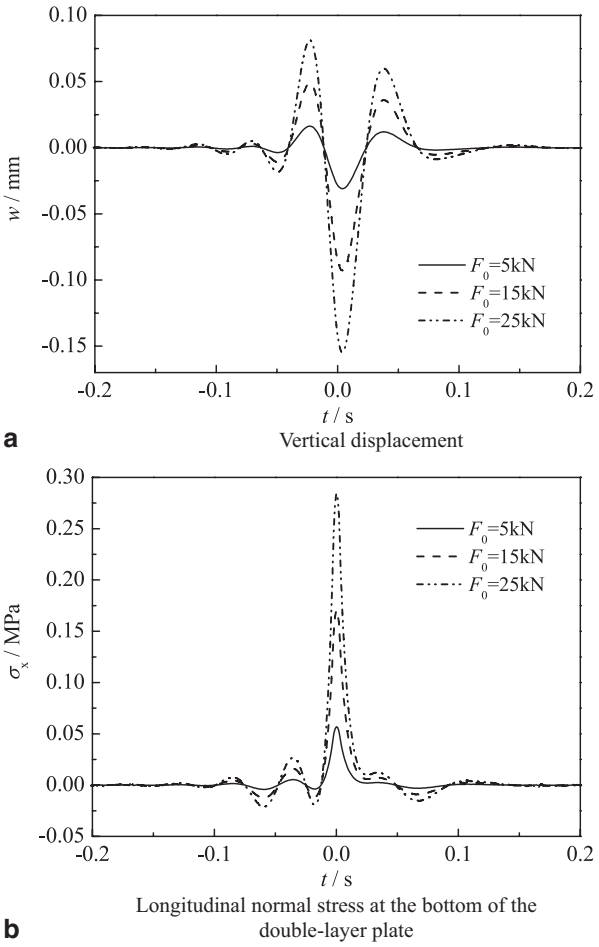

Fig. 5.8 The dynamic response of the double-layer plate vs. time under different amplitudes of harmonic load. **a** Vertical displacement, **b** Longitudinal normal stress at the bottom of the double-layer plate

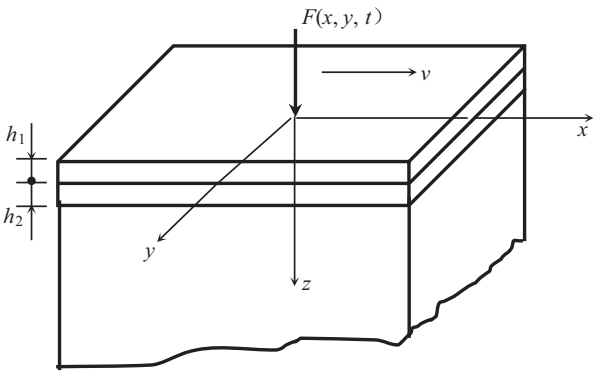

Fig. 5.9 An infinite double-layer plate on an elastic half-space foundation

The boundary conditions for $x \to \pm\infty$, $y \to \pm\infty$ and the initial condition for $t = 0$ are represented by

$$\begin{cases} \lim\limits_{x\to\pm\infty} \dfrac{\partial^n w}{\partial x^n} = 0; \quad \lim\limits_{y\to\pm\infty} \dfrac{\partial^n w}{\partial y^n} = 0 \quad n = 0,1,2\cdots \\ w(x,y,t)\big|_{t=0} = \left.\dfrac{\partial w(x,y,t)}{\partial t}\right|_{t=0} = 0 \end{cases} \tag{5.40}$$

5.4.2 Governing Equations of the Elastic Half-Space Foundation

The mass density, Poisson's ratio, elastic modulus, and Lamé constant of the elastic half-space foundation are symbolized by ρ, μ, E, λ, and G. u_b, v_b, and w_b are the displacement components along the three directions x, y, z. Based on elasto-dynamics, the motion of the homogeneous isotropic elastic medium is governed by the following equations.

1. Motion differential equations

$$\begin{cases} \dfrac{\partial \sigma_x}{\partial x} + \dfrac{\partial \tau_{yx}}{\partial y} + \dfrac{\partial \tau_{zx}}{\partial z} = \rho \dfrac{\partial^2 u_b}{\partial t^2} \\ \dfrac{\partial \sigma_y}{\partial y} + \dfrac{\partial \tau_{zy}}{\partial z} + \dfrac{\partial \tau_{xy}}{\partial x} = \rho \dfrac{\partial^2 v_b}{\partial t^2} \\ \dfrac{\partial \sigma_z}{\partial z} + \dfrac{\partial \tau_{xz}}{\partial x} + \dfrac{\partial \tau_{yz}}{\partial y} = \rho \dfrac{\partial^2 w_b}{\partial t^2} \end{cases} \tag{5.41}$$

2. Geometric equations

$$\begin{cases} \varepsilon_x = \dfrac{\partial u_b}{\partial x} \quad \varepsilon_y = \dfrac{\partial v_b}{\partial y} \quad \varepsilon_z = \dfrac{\partial w_b}{\partial z} \\ \gamma_{yz} = \dfrac{\partial w_b}{\partial y} + \dfrac{\partial v_b}{\partial z} \quad \gamma_{zx} = \dfrac{\partial u_b}{\partial z} + \dfrac{\partial w_b}{\partial x} \quad \gamma_{xy} = \dfrac{\partial v_b}{\partial x} + \dfrac{\partial u_b}{\partial y} \end{cases} \tag{5.42}$$

3. Physical equations

$$\begin{cases} \sigma_x = \lambda e + 2G\varepsilon_x \quad \sigma_y = \lambda e + 2G\varepsilon_y \quad \sigma_z = \lambda e + 2G\varepsilon_z \\ \tau_{yz} = G\gamma_{yz} \quad \tau_{zx} = G\gamma_{zx} \quad \tau_{xy} = G\gamma_{xy} \end{cases} \tag{5.43}$$

4. Navier's equations of motion

$$\begin{cases} (\lambda+G)\dfrac{\partial e}{\partial x}+G\nabla^2 u_b=\rho\dfrac{\partial^2 u_b}{\partial t^2} \\ (\lambda+G)\dfrac{\partial e}{\partial y}+G\nabla^2 v_b=\rho\dfrac{\partial^2 v_b}{\partial t^2} \\ (\lambda+G)\dfrac{\partial e}{\partial z}+G\nabla^2 w_b=\rho\dfrac{\partial^2 w_b}{\partial t^2} \end{cases} \tag{5.44}$$

where $e=\dfrac{\partial u_b}{\partial x}+\dfrac{\partial v_b}{\partial y}+\dfrac{\partial w_b}{\partial z}$ is the relative change of volume, $\nabla^2=\dfrac{\partial^2}{\partial x^2}+\dfrac{\partial^2}{\partial y^2}+\dfrac{\partial^2}{\partial z^2}$ is the Laplase operator.

The boundary conditions for $x=\pm\infty,\ y=\pm\infty,\ z=+\infty$ are represented by

$$u_b=0,\ v_b=0,\ w_b=0,\ \frac{\partial u_b}{\partial x}=0,\ \frac{\partial v_b}{\partial y}=0,\ \frac{\partial w_b}{\partial z}=0 \tag{5.45}$$

The stress boundary conditions for the plane $z=0$ are expressed as

$$\sigma_z=-P(x,y,t),\quad \tau_{xz}=0,\quad \tau_{yz}=0 \tag{5.46}$$

The displacement on the interface between the elastic half-space foundation and the double-layer plate must satisfy

$$w_b(x,y,0,t)=w(x,y,t) \tag{5.47}$$

5.4.3 The Solutions of a Half-Space Foundation in a Number-Frequency Domain

Based on the Helmholtz potential[11], the displacement field of a half-space foundation can be represented as

$$\boldsymbol{U}(u_b,v_b,w_b)=\nabla\Phi+\nabla\times\boldsymbol{\Psi}(\Psi_1,\Psi_2,\Psi_3) \tag{5.48}$$

in which, Φ and Ψ are the scalar potential function and vector potential function of the displacement field U, respectively. Letting $g=\nabla\times\Psi$ [1] and expanding Eq. (5.48) lead to

$$\begin{cases} u_b = \dfrac{\partial \Phi}{\partial x} + g_1 \\ v_b = \dfrac{\partial \Phi}{\partial y} + g_2 \\ w_b = \dfrac{\partial \Phi}{\partial z} + g_3 \end{cases} \tag{5.49}$$

Substituting Eqs. (5.49) into Navier's equations of motion (5.44) yields relationships satisfied by functions Φ and g

$$\begin{cases} \nabla^2 \Phi - \dfrac{1}{C_p^2} \dfrac{\partial^2 \Phi}{\partial t^2} = 0 \\ \nabla^2 g_i - \dfrac{1}{C_s^2} \dfrac{\partial^2 g_i}{\partial t^2} = 0, \qquad i = 1,2,3 \end{cases} \tag{5.50}$$

in which, $C_p = \sqrt{(\lambda + 2G)/\rho}$ is the compression (P wave) wave speed, $C_s = \sqrt{G/\rho}$ is the shear (S wave) wave speed.

Simultaneously, the vector potential function $g = \nabla \times \Psi$ must satisfy $\nabla g = \nabla . \nabla \times \Psi = 0$, that is

$$\Theta = \frac{\partial g_1}{\partial x} + \frac{\partial g_2}{\partial y} + \frac{\partial g_3}{\partial z} = 0 \tag{5.51}$$

By applying the triple Fourier transform with respect to x, y, t in Eqs. (5.50), one can transform the problem from the time-space domain to the wave-frequency domain. The transformed wave equations are

$$\begin{cases} \dfrac{\partial^2 \bar{\Phi}(k_1, k_2, \omega)}{\partial z^2} - B_p^2 \bar{\Phi}(k_1, k_2, \omega) = 0 \\ \dfrac{\partial^2 \bar{g}_i(k_1, k_2, \omega)}{\partial z^2} - B_s^2 \bar{g}_i(k_1, k_2, \omega) = 0 \qquad i = 1,2,3 \end{cases} \tag{5.52}$$

in which, $B_p^2 = k_1^2 + k_2^2 - k_p^2, k_p = \omega / C_p, B_s^2 = k_1^2 + k_2^2 - k_s^2, k_s = \omega / C_s$, k_1 and k_2 are the wave numbers along the x and y axes.

The solutions to the transformed differential equations (5.52) can be given as

$$\begin{cases} \overline{\Phi} = A_4 e^{-B_p z} \\ \overline{g}_i = A_i e^{-B_s z} \quad i = 1,2,3 \end{cases} \tag{5.53}$$

where A_1, A_2, A_3, and A_4 are the integration constants which can be determined by the stress boundary condition Eq (5.46) for the plane $z = 0$ and the Eq (5.51). The exponentially increasing terms $e^{B_p z}$ and $e^{B_s z}$ have been discarded because the boundary condition for $z = +\infty$ must be considered.

Solving the geometric Eq (5.42), physical Eq (5.43), and the Eq (5.49) simultaneously, one expresses the stress components in terms of Φ ϕ and g_i as

$$\begin{cases} \sigma_z = \lambda \dfrac{1}{C_p^2} \dfrac{\partial^2 \Phi}{\partial t^2} + 2G \dfrac{\partial^2 \Phi}{\partial z^2} + 2G \dfrac{\partial g_3}{\partial z} \\ \tau_{zx} = G\left(2 \dfrac{\partial^2 \Phi}{\partial x \partial z} + \dfrac{\partial g_1}{\partial z} + \dfrac{\partial g_3}{\partial x} \right) \\ \tau_{zy} = G\left(2 \dfrac{\partial^2 \Phi}{\partial y \partial z} + \dfrac{\partial g_2}{\partial z} + \dfrac{\partial g_3}{\partial y} \right) \end{cases} \tag{5.54}$$

By applying the triple Fourier transform with respect to x, y, t in Eqs. (5.54) and Eq. (5.51), one can get

$$\begin{cases} \overline{\sigma}_z = -\lambda \dfrac{\omega^2}{C_p^2} \overline{\Phi} + 2G \dfrac{\partial^2 \overline{\Phi}}{\partial z^2} + 2G \dfrac{\partial \overline{g}_3}{\partial z} \\ \overline{\tau}_{zx} = G\left(2jk_1 \dfrac{\partial \overline{\Phi}}{\partial z} + \dfrac{\partial \overline{g}_1}{\partial z} + jk_1 \overline{g}_3 \right) \\ \overline{\tau}_{zy} = G\left(2jk_2 \dfrac{\partial \overline{\Phi}}{\partial z} + \dfrac{\partial \overline{g}_2}{\partial z} + jk_2 \overline{g}_3 \right) \\ \overline{\Theta} = jk_1 \overline{g}_1 + jk_2 \overline{g}_2 + \dfrac{\partial \overline{g}_3}{\partial z} = 0 \end{cases} \tag{5.55}$$

Substituting Eqs. (5.53) into Eqs. (5.55) leads to

$$\begin{cases} \overline{\sigma}_z = -\lambda k_p^2 A_4 e^{-B_p z} + 2GB_p{}^2 A_4 e^{-B_p z} - 2GB_s A_3 e^{-B_s z} \\ \overline{\tau}_{zx} = G\left(-2jk_1 B_p A_4 e^{-B_p z} - B_s A_1 e^{-B_s z} + jk_1 A_3 e^{-B_s z} \right) \\ \overline{\tau}_{zy} = G\left(-2jk_2 B_p A_4 e^{-B_p z} - B_s A_2 e^{-B_s z} + jk_2 A_3 e^{-B_s z} \right) \\ \overline{\Theta} = jk_1 A_1 e^{-B_s z} + jk_2 A_2 e^{-B_s z} - B_s A_3 e^{-B_s z} = 0 \end{cases} \tag{5.56}$$

5.4.4 Displacement Green's Functions of the Elastic Half-Space Foundation

By replacing $F(x,y,t)$ on the right side of Eq. (5.39) with the unit impulse load $F(x,y,t)=\delta(x)\delta(y)\delta(t)$, and applying a triple Fourier transform with respect to x,y,t in Eq. (5.39), the algebraic equation of the vertical displacement in the transformed domain can be obtained.

$$\left[D\left(k_1^4+k_2^4\right)+2(D_{xy}+2D_k)k_1^2k_2^2-\rho h\omega^2\right]\overline{w}=1-\overline{P}(k_1,k_2,\omega) \tag{5.57}$$

From Eq. (5.47), Eq. (5.49) and Eq. (5.53), we can know

$$\overline{w}=\overline{w}_b\big|_{z=0}=\frac{\partial\overline{\Phi}}{\partial z}+\overline{g}_3=-B_pA_4e^{-B_pz}+A_3e^{-B_sz}\Big|_{z=0}=-B_pA_4+A_3 \tag{5.58}$$

Substituting Eq. (5.58) into Eq. (5.57) leads to

$$-\overline{P}(k_1,k_2,\omega)=\left[D\left(k_1^4+k_2^4\right)+2(D_{xy}+2D_k)k_1^2k_2^2-\rho h\omega^2\right](-B_pA_4+A_3)-1 \tag{5.59}$$

From the stress boundary conditions Eq. (5.46), it can be known that Eq. (5.59) is the transformed vertical stress σ_z on the surface of the half-space foundation for the plane $z=0$, that is $\overline{\sigma}_z=-\overline{P}(k_1,k_2,\omega)$.

By letting $D_1=D\left(k_1^4+k_2^4\right)+2(D_{xy}+2D_k)k_1^2k_2^2-\rho h\omega^2$, and substituting Eq. (5.59) into Eq. (5.56), together with some arrangement, Eq. (5.56) can be rewritten in a form of a matrix for the plane $z=0$

$$\begin{bmatrix} 0 & 0 & -2B_s-D_1/G & \left(k_1^2+k_2^2+B_s^2\right)+D_1B_p/G \\ -B_s & 0 & jk_1 & -2jk_1B_p \\ 0 & -B_s & jk_2 & -2jk_2B_p \\ k_1 & k_2 & jB_s & 0 \end{bmatrix}\begin{bmatrix} A_1 \\ A_2 \\ A_3 \\ A_4 \end{bmatrix}=\begin{bmatrix} -1/G \\ 0 \\ 0 \\ 0 \end{bmatrix} \tag{5.60}$$

Solving Eq. (5.60) leads to

$$\begin{cases} A_1=\dfrac{2jk_1B_pB_s}{G\Delta} \\ A_2=\dfrac{2jk_2B_pB_s}{G\Delta} \\ A_3=-\dfrac{2B_p(k_1^2+k_2^2)}{G\Delta} \\ A_4=-\dfrac{(k_1^2+k_2^2+B_s^2)}{G\Delta} \end{cases} \tag{5.61}$$

in which,

$$\Delta = \left[(k_1^2 + k_2^2 + B_s^2) + D_1 B_p / G \right] (k_1^2 + k_2^2 + B_s^2) - 2B_p (2B_s + D_1 / G)(k_1^2 + k_2^2) \cdot$$

By applying the Fourier transformation to Eqs. (5.49), along with the substitution of Eqs. (5.53) and Eqs. (5.61), the transformed displacement can be expressed as

$$\begin{cases} \overline{u}_b = \dfrac{j}{G\Delta}\left[-k_1 (k_1^2 + k_2^2 + B_s^2) e^{-B_p z} + 2k_1 B_p B_s e^{-B_s z} \right] \\ \overline{v}_b = \dfrac{j}{G\Delta}\left[-k_2 (k_1^2 + k_2^2 + B_s^2) e^{-B_p z} + 2k_2 B_p B_s e^{-B_s z} \right] \\ \overline{w}_b = \dfrac{1}{G\Delta}\left[B_p (k_1^2 + k_2^2 + B_s^2) e^{-B_p z} - 2B_p (k_1^2 + k_2^2) e^{-B_s z} \right] \end{cases} \tag{5.62}$$

By considering the geometric equations and the physical equations, the transformed stress can be expressed as

$$\begin{cases} \overline{\sigma}_x = \dfrac{1}{G\Delta}\left[(\lambda k_p^2 + 2Gk_1^2)(k_1^2 + k_2^2 + B_s^2) e^{-B_p z} - 4Gk_1^2 B_p B_s e^{-B_s z} \right] \\ \overline{\sigma}_y = \dfrac{1}{G\Delta}\left[(\lambda k_p^2 + 2Gk_2^2)(k_1^2 + k_2^2 + B_s^2) e^{-B_p z} - 4Gk_2^2 B_p B_s e^{-B_s z} \right] \\ \overline{\sigma}_z = -\dfrac{1}{\Delta}\left[(k_1^2 + k_2^2 + B_s^2)^2 e^{-B_p z} - 4B_p B_s (k_1^2 + k_2^2) e^{-B_s z} \right] \end{cases} \tag{5.63}$$

$$\begin{cases} \overline{\tau}_{xy} = \dfrac{1}{\Delta}\left[2k_1 k_2 (k_1^2 + k_2^2 + B_s^2) e^{-B_p z} - 4k_1 k_2 B_p B_s e^{-B_s z} \right] \\ \overline{\tau}_{yz} = \dfrac{1}{\Delta} 2jk_2 B_p (k_1^2 + k_2^2 + B_s^2)(e^{-B_p z} - e^{-B_s z}) \\ \overline{\tau}_{zx} = \dfrac{1}{\Delta} 2jk_1 B_p (k_1^2 + k_2^2 + B_s^2)(e^{-B_p z} - e^{-B_s z}) \end{cases} \tag{5.64}$$

The expression of the displacement and stress of the elastic half-space foundation under a unit impulse load can be obtained by employing the inverse Fourier transformation to Eqs. (5.62)–(5.64). Limited by space, we present here only the expression of the displacement and the longitudinal stress σ_x, those are

$$\begin{aligned} u_b = G_u(x, y, 0, t) = \frac{j}{(2\pi)^3 G} \int_{-\infty}^{+\infty} \int_{-\infty}^{+\infty} \int_{-\infty}^{+\infty} \\ \frac{1}{\Delta}\left[-k_1 (k_1^2 + k_2^2 + B_s^2) e^{-B_p z} + 2k_1 B_p B_s e^{-B_s z} \right] e^{j(k_1 x + k_2 y + \omega t)} \mathrm{d}k_1 \mathrm{d}k_2 \mathrm{d}\omega \end{aligned} \tag{5.65}$$

$$v_b = G_v(x,y,0,t) = \frac{j}{(2\pi)^3 G}\int_{-\infty}^{+\infty}\int_{-\infty}^{+\infty}\int_{-\infty}^{+\infty} \frac{1}{\Delta}\left[-k_2(k_1^2+k_2^2+B_s^2)e^{-B_p z} + 2k_2 B_p B_s e^{-B_s z}\right] e^{j(k_1 x + k_2 y + \omega t)} \mathrm{d}k_1 \mathrm{d}k_2 \mathrm{d}\omega \tag{5.66}$$

$$w_b = G_w(x,y,0,t) = \frac{1}{(2\pi)^3 G}\int_{-\infty}^{+\infty}\int_{-\infty}^{+\infty}\int_{-\infty}^{+\infty} \frac{1}{\Delta}\left[B_p(k_1^2+k_2^2+B_s^2)e^{-B_p z} - 2B_p(k_1^2+k_2^2)e^{-B_s z}\right] e^{j(k_1 x + k_2 y + \omega t)} \mathrm{d}k_1 \mathrm{d}k_2 \mathrm{d}\omega \tag{5.67}$$

$$\sigma_x = G_{\sigma_x}(x,y,0,t) = \frac{1}{(2\pi)^3 G}\int_{-\infty}^{+\infty}\int_{-\infty}^{+\infty}\int_{-\infty}^{+\infty} \frac{1}{\Delta}\left[(\lambda k_p^2 + 2Gk_1^2)(k_1^2+k_2^2+B_s^2)e^{-B_p z} - 4Gk_1^2 B_p B_s e^{-B_s z}\right] e^{j(k_1 x + k_2 y + \omega t)} \mathrm{d}k_1 \mathrm{d}k_2 \mathrm{d}\omega \tag{5.68}$$

Equations (5.65)–(5.68) are namely the displacement and stress Green's functions of the elastic half-space foundation.

5.4.5 *The Displacement and Stress of the Double-Layer Plate Under Moving Vehicle Loads Supported by Elastic Half-Space*

1. The displacement and stress of the double-layer plate on an elastic half-space foundation under a moving constant load

Substituting Eq. (5.2) and Eqs. (5.65)–(5.68) into Eq. (5.27) and calculating by a generalized Duhamel integral, then performing the same derivation process as Eq. (5.29), the expression of the displacement and the longitudinal stress of the elastic half-space foundation under a moving constant load can be obtained as

$$u_b = \frac{jF}{(2\pi)^2 G}\int_{-\infty}^{+\infty}\int_{-\infty}^{+\infty} \frac{\sin(k_1 l_1)}{k_1 l_1}\frac{\sin(k_2 l_2)}{k_2 l_2} \frac{1}{\Delta}\left[-k_1(k_1^2+k_2^2+B_s^2)e^{-B_p z} + 2k_1 B_p B_s e^{-B_s z}\right] e^{j[k_1(x-vt)+k_2 y]} \mathrm{d}k_1 \mathrm{d}k_2 \tag{5.69}$$

$$v_b = \frac{jF}{(2\pi)^2 G}\int_{-\infty}^{+\infty}\int_{-\infty}^{+\infty} \frac{\sin(k_1 l_1)}{k_1 l_1}\frac{\sin(k_2 l_2)}{k_2 l_2} \frac{1}{\Delta}\left[-k_2(k_1^2+k_2^2+B_s^2)e^{-B_p z} + 2k_2 B_p B_s e^{-B_s z}\right] e^{j[k_1(x-vt)+k_2 y]} \mathrm{d}k_1 \mathrm{d}k_2 \tag{5.70}$$

$$w_b = \frac{F}{(2\pi)^2 G}\int_{-\infty}^{+\infty}\int_{-\infty}^{+\infty}\frac{\sin(k_1 l_1)}{k_1 l_1}\frac{\sin(k_2 l_2)}{k_2 l_2} \\ \frac{1}{\Delta}\left[B_p(k_1^2+k_2^2+B_s^2)e^{-B_p z} - 2B_p(k_1^2+k_2^2)e^{-B_s z}\right]e^{j[k_1(x-vt)+k_2 y]}\mathrm{d}k_1\mathrm{d}k_2 \tag{5.71}$$

$$\sigma_x = \frac{F}{(2\pi)^2 G}\int_{-\infty}^{+\infty}\int_{-\infty}^{+\infty}\frac{\sin(k_1 l_1)}{k_1 l_1}\frac{\sin(k_2 l_2)}{k_2 l_2} \\ \frac{1}{\Delta}\left[(\lambda k_p^2 + 2Gk_1^2)(k_1^2+k_2^2+B_s^2)e^{-B_p z} - 4Gk_1^2 B_p B_s e^{-B_s z}\right]e^{j[k_1(x-vt)+k_2 y]}\mathrm{d}k_1\mathrm{d}k_2 \tag{5.72}$$

in which, $k_p = -vk_1/C_p$, $k_s = -vk_1/C_s$, B_p, B_s, and Δ must also be modified correspondingly.

By considering Eq. (5.47) of the displacement compatibility and by letting $z = 0$ in Eq. (5.71), the vertical displacement of the double-layer plate can be expressed as

$$w = \frac{F}{(2\pi)^2 G}\int_{-\infty}^{+\infty}\int_{-\infty}^{+\infty}\frac{\sin(k_1 l_1)}{k_1 l_1}\frac{\sin(k_2 l_2)}{k_2 l_2} \\ \frac{1}{\Delta}\left[B_p(k_1^2+k_2^2+B_s^2) - 2B_p(k_1^2+k_2^2)\right]e^{j[k_1(x-vt)+k_2 y]}\mathrm{d}k_1\mathrm{d}k_2 \tag{5.73}$$

The stress components in the upper layer can be expressed as

$$\begin{aligned}\sigma_x &= -\frac{E_1 z}{1-\mu_1^2}\left[\frac{\partial^2 w}{\partial x^2} + \mu_1\frac{\partial^2 w}{\partial y^2}\right] \\ &= \frac{E_1 z}{1-\mu_1^2}\frac{F}{4\pi^2 G}\int_{-\infty}^{+\infty}\int_{-\infty}^{+\infty}\frac{\sin(k_1 l_1)}{k_1 l_1}\frac{\sin(k_2 l_2)}{k_2 l_2}\times(k_1^2+\mu_1 k_2^2) \\ &\quad \frac{1}{\Delta}\left[B_p(k_1^2+k_2^2+B_s^2) - 2B_p(k_1^2+k_2^2)\right]e^{j[k_1(x-vt)+k_2 y]}\mathrm{d}k_1\mathrm{d}k_2\end{aligned} \tag{5.74}$$

$$\begin{aligned}\sigma_y &= -\frac{E_1 z}{1-\mu_1^2}\left[\frac{\partial^2 w}{\partial y^2} + \mu_1\frac{\partial^2 w}{\partial x^2}\right] \\ &= \frac{E_1 z}{1-\mu_1^2}\frac{F}{4\pi^2 G}\int_{-\infty}^{+\infty}\int_{-\infty}^{+\infty}\frac{\sin(k_1 l_1)}{k_1 l_1}\frac{\sin(k_2 l_2)}{k_2 l_2}\times(\mu_1 k_1^2+k_2^2) \\ &\quad \frac{1}{\Delta}\left[B_p(k_1^2+k_2^2+B_s^2) - 2B_p(k_1^2+k_2^2)\right]e^{j[k_1(x-vt)+k_2 y]}\mathrm{d}k_1\mathrm{d}k_2\end{aligned} \tag{5.75}$$

$$\begin{aligned}\tau_{xy} &= -\frac{E_1 z}{1+\mu_1}\frac{\partial^2 w}{\partial x \partial y} \\ &= \frac{E_1 z}{1+\mu_1}\frac{F}{4\pi^2 G}\int_{-\infty}^{+\infty}\int_{-\infty}^{+\infty}\frac{\sin(k_1 l_1)}{k_1 l_1}\frac{\sin(k_2 l_2)}{k_2 l_2}\times k_1 k_2 \\ &\frac{1}{\Delta}\left[B_p(k_1^2+k_2^2+B_s^2)-2B_p(k_1^2+k_2^2)\right]e^{j[k_1(x-vt)+k_2 y]}\mathrm{d}k_1\mathrm{d}k_2\end{aligned} \tag{5.76}$$

By exchanging E_1 and μ_1 in Eqs. (5.74)–(5.76) for E_2 and μ_2, the stress components in the lower layer can be obtained.

2. The displacement and stress of the double-layer plate on an elastic half-space foundation under a moving harmonic load

Substituting Eq. (5.4) and Eqs. (5.65)–(5.68) into Eq. (5.27)and calculating by a generalized Duhamel integral, then performing the same derivation process as Eq. (5.29), the expression of the displacement and the longitudinal stress of the elastic half-space foundation under a moving harmonic load can be obtained as

$$\begin{aligned}u_b &= \frac{jF_0}{(2\pi)^2 G}e^{j\omega_0 t}\int_{-\infty}^{+\infty}\int_{-\infty}^{+\infty}\frac{\sin(k_1 l_1)}{k_1 l_1}\frac{\sin(k_2 l_2)}{k_2 l_2} \\ &\frac{1}{\Delta}\left[-k_1(k_1^2+k_2^2+B_s^2)e^{-B_p z}+2k_1 B_p B_s e^{-B_s z}\right]e^{j[k_1(x-vt)+k_2 y]}\mathrm{d}k_1\mathrm{d}k_2\end{aligned} \tag{5.77}$$

$$\begin{aligned}v_b &= \frac{jF_0}{(2\pi)^2 G}e^{j\omega_0 t}\int_{-\infty}^{+\infty}\int_{-\infty}^{+\infty}\frac{\sin(k_1 l_1)}{k_1 l_1}\frac{\sin(k_2 l_2)}{k_2 l_2} \\ &\frac{1}{\Delta}\left[-k_2(k_1^2+k_2^2+B_s^2)e^{-B_p z}+2k_2 B_p B_s e^{-B_s z}\right]e^{j[k_1(x-vt)+k_2 y]}\mathrm{d}k_1\mathrm{d}k_2\end{aligned} \tag{5.78}$$

$$\begin{aligned}w_b &= \frac{F_0}{(2\pi)^2 G}e^{j\omega_0 t}\int_{-\infty}^{+\infty}\int_{-\infty}^{+\infty}\frac{\sin(k_1 l_1)}{k_1 l_1}\frac{\sin(k_2 l_2)}{k_2 l_2} \\ &\frac{1}{\Delta}\left[B_p(k_1^2+k_2^2+B_s^2)e^{-B_p z}-2B_p(k_1^2+k_2^2)e^{-B_s z}\right]e^{j[k_1(x-vt)+k_2 y]}\mathrm{d}k_1\mathrm{d}k_2\end{aligned} \tag{5.79}$$

$$\begin{aligned}\sigma_x &= \frac{F_0}{(2\pi)^2 G}e^{j\omega_0 t}\int_{-\infty}^{+\infty}\int_{-\infty}^{+\infty}\frac{\sin(k_1 l_1)}{k_1 l_1}\frac{\sin(k_2 l_2)}{k_2 l_2} \\ &\frac{1}{\Delta}\left[(\lambda k_p^2+2Gk_1^2)(k_1^2+k_2^2+B_s^2)e^{-B_p z}-4Gk_1^2 B_p B_s e^{-B_s z}\right]e^{j[k_1(x-vt)+k_2 y]}\mathrm{d}k_1\mathrm{d}k_2\end{aligned} \tag{5.80}$$

in which, $k_p = (\omega_0 - vk_1)/C_p$, $k_s = (\omega_0 - vk_1)/C_s$, B_p, B_s, and Δ must also be modified correspondingly.

By setting $z = 0$ in Eq. (5.79), the vertical displacement of the double-layer plate can be expressed as

$$w = \frac{F_0}{(2\pi)^2 G} e^{j\omega_0 t} \int_{-\infty}^{+\infty}\int_{-\infty}^{+\infty} \frac{\sin(k_1 l_1)}{k_1 l_1}\frac{\sin(k_2 l_2)}{k_2 l_2} \frac{1}{\Delta}\left[B_p(k_1^2 + k_2^2 + B_s^2) - 2B_p(k_1^2 + k_2^2)\right] e^{j[k_1(x-vt)+k_2 y]} \mathrm{d}k_1 \mathrm{d}k_2 \tag{5.81}$$

The stress components in the upper layer can be expressed as

$$\sigma_x = \frac{E_1 z}{1-\mu_1^2}\frac{F_0}{(2\pi)^2 G} e^{j\omega_0 t} \int_{-\infty}^{+\infty}\int_{-\infty}^{+\infty} \frac{\sin(k_1 l_1)}{k_1 l_1}\frac{\sin(k_2 l_2)}{k_2 l_2} \frac{(k_1^2 + \mu k_2^2)}{\Delta}\left[B_p(k_1^2 + k_2^2 + B_s^2) - 2B_p(k_1^2 + k_2^2)\right] e^{j[k_1(x-vt)+k_2 y]} \mathrm{d}k_1 \mathrm{d}k_2 \tag{5.82}$$

$$\sigma_y = \frac{E_1 z}{1-\mu_1^2}\frac{F_0}{(2\pi)^2 G} e^{j\omega_0 t} \int_{-\infty}^{+\infty}\int_{-\infty}^{+\infty} \frac{\sin(k_1 l_1)}{k_1 l_1}\frac{\sin(k_2 l_2)}{k_2 l_2} \frac{(k_2^2 + \mu k_1^2)}{\Delta}\left[B_p(k_1^2 + k_2^2 + B_s^2) - 2B_p(k_1^2 + k_2^2)\right] e^{j[k_1(x-vt)+k_2 y]} \mathrm{d}k_1 \mathrm{d}k_2 \tag{5.83}$$

$$\tau_{xy} = -\frac{E_1 z}{1+\mu_1}\frac{\partial^2 w}{\partial x \partial y} = \frac{E_1 z}{1+\mu_1}\frac{F_0}{(2\pi)^2 G} e^{j\omega_0 t} \int_{-\infty}^{+\infty}\int_{-\infty}^{+\infty} \frac{\sin(k_1 l_1)}{k_1 l_1}\frac{\sin(k_2 l_2)}{k_2 l_2} \frac{k_1 k_2}{\Delta}\left[B_p(k_1^2 + k_2^2 + B_s^2) - 2B_p(k_1^2 + k_2^2)\right] e^{j[k_1(x-vt)+k_2 y]} \mathrm{d}k_1 \mathrm{d}k_2 \tag{5.84}$$

By exchanging E_1 and μ_1 in Eqs. (5.82)–(5.84) for E_2 and μ_2, the stress components in the lower layer can be obtained.

5.5 Numerical Simulations of an Infinite Double-Layer Plate on an Elastic Half Space Foundation

The analytical solutions of the dynamic responses of the double-layer plate on an elastic half-space foundation to moving loads are all generalized double integrals in the infinite intervals. The integrands are highly oscillatory and singular

in nature as they contain complex indexes. The numerical evaluation of these integrals is a formidable task. In this section, an efficient computer program based on an adaptive Simpson numerical algorithm is developed to perform the integrals and the program is coded and implemented via Mathmatica. The parameters used in the numerical calculation are chosen to be: $E_1 = 1500\text{MPa}$, $E_2 = 1200\text{MPa}$, $\mu_1 = \mu_2 = 0.35$, $h_1 = 0.15\text{m}$, $h_1 = 0.2\text{m}$, $\rho_1 = 2613\text{kg/m}^3$, $\rho_2 = 2083\text{kg/m}^3$, $E = 50\text{MPa}$, $\rho = 2000\text{kg/m}^3$, $\mu = 0.35$, $v = 25\text{m/s}$, $F = 50\text{kN}$, $F_0 = 15\text{kN}$, $f_0 = 15\text{Hz}$,$l_1 = 0.11\text{m}$, and $l_2 = 0.16\text{m}$.

In actual calculation, the material damping can be taken into account through use of the linear hysteretic damping theory (complex damping theory) [12]. That is multiplying all the material parameters by the hysteretic damping coefficient

$$\begin{aligned} &E^* = (1+2j\xi)E,\ G^* = (1+2j\xi)G,\ \lambda^* = (1+2j\xi)\lambda, \\ &C_p{}^* = C_p\sqrt{1+2j\xi} \approx (1+j\xi)C_p,\ C_s{}^* = C_s\sqrt{1+2j\xi} \approx (1+j\xi)C_s, \\ &k_p{}^* = k_p \Big/ \sqrt{1+2j\xi} \approx (1-j\xi)k_p,\ k_s{}^* = k_s \Big/ \sqrt{1+2j\xi} \approx (1-j\xi)k_s \end{aligned} \tag{5.85}$$

where ξ denotes the hysteretic damping ratio, and here $\xi = 0.05$.

5.5.1 Result Verification

The dynamic response of an elastic half-space to a moving point load was presented by Hung via the direct integral transform method. In Hung's paper [13], the parameters used in the numerical calculation are chosen to be: $G = 20\text{MPa}$, $\mu = 0.25$, $\rho = 2000\text{kg/m}^3$, $\xi = 0.02$. The normalized vertical displacement W and longitudinal displacement U are defined by

$$W = \frac{2\pi Gz}{F} w_b, U = \frac{2\pi Gz}{F} u_b \tag{5.86}$$

By setting the plate thickness equal to zero, the double-layer plate on an elastic half-space foundation can be easily degenerated to an elastic half-space, which is used to verify the accuracy of the present theory and procedure. By using Hung' material parameters, the normalized vertical displacement W and longitudinal displacement U of an elastic half-space under a moving point load for the observation point $(x, y, z) = (0, 0, 1\text{m})$ are calculated and plotted in Fig. 5.10a and b. It can be seen that the results obtained in this section are in good agreement with Figs. 6 and 7 in Hung's paper. This fact indicates the correctness of the analytical derivation and procedure developed in this study.

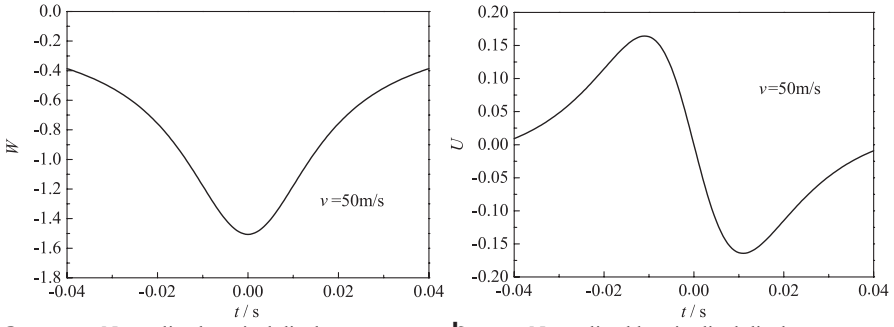

Fig. 5.10 Normalized displacements calculated using the parameters in Hung's paper. **a** Normalized vertical displacement, **b** Normalized longitudinal displacement

5.5.2 The Dynamic Response of the Double-Layer Plate

The longitudinal normal stress σ_x at the bottom of the double-layer plate under a moving constant load for the observation point $(x = 0, y = 0)$ is shown in Fig. 5.11a against time t. The vertical displacement and the longitudinal normal stress of the elastic half-space foundation for the observation point $(x = 0, y = 0)$ with respect to the different depth values are shown in Figs. 5.11b and c against time t. According to the displacement compatibility condition, the vertical displacement of the elastic half-space foundation for $z = 0$ in Fig. 5.11b is the vertical displacement of the double-layer plate. The vertical displacement and the longitudinal normal stress at the bottom of the double-layer plate under a moving harmonic load for the observation point $(x = 0, y = 0)$ are shown in Fig. 5.12 against time t. From Fig. 5.11 and 5.12, we can see:

1. The longitudinal normal stress at the bottom of the double-layer plate presents an alternating process from compression to tension, then from tension to compression. The longitudinal normal stress is compressive before and after the load passes through the observation point, but when the load is passing through the observation point, the longitudinal normal stress is tensile, and the maximum tensile stress is much larger than the maximum compression stress.
2. As the depth increases, the displacement and the stress of the elastic half-place foundation attenuates very rapidly. For the given material parameters, the maximum vertical displacement $w_{b\max}$ is -0.2735 mm and the maximum longitudinal tensile stress $\sigma_{x\max}$is 9459.97 Pa when $z = 0$m, the maximum vertical displacement $w_{b\max}$ is -0.1100 mm and the maximum longitudinal tensile stress $\sigma_{x\max}$ is 36.85 Pa when $z = 2$m. The rate of decrease of the vertical displacement and longitudinal tensile stress reaches up to 59.78 and 99.61 %, respectively.
3. The maximum longitudinal tensile stress appears on both sides of the load center and the curve of the longitudinal tensile stress presents an obvious "saddle" type.

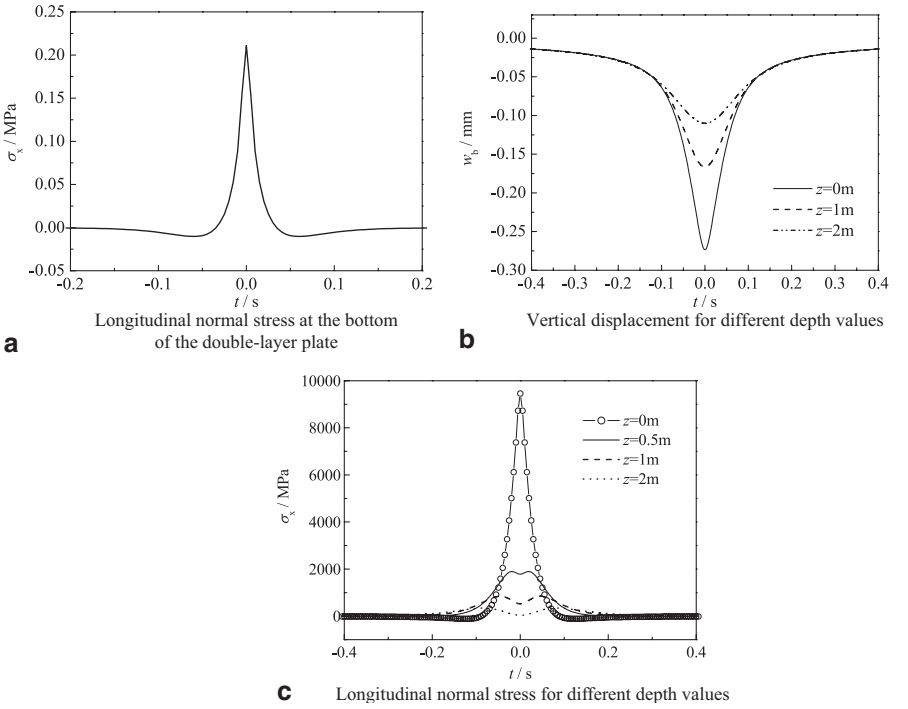

Fig. 5.11 The dynamic response of the double-layer plate on an elastic half-space foundation under a moving constant load. **a** Longitudinal normal stress at the bottom of the double-layer plate, **b**Vertical displacement for different depth values, **c** Longitudinal normal stress for different depth values

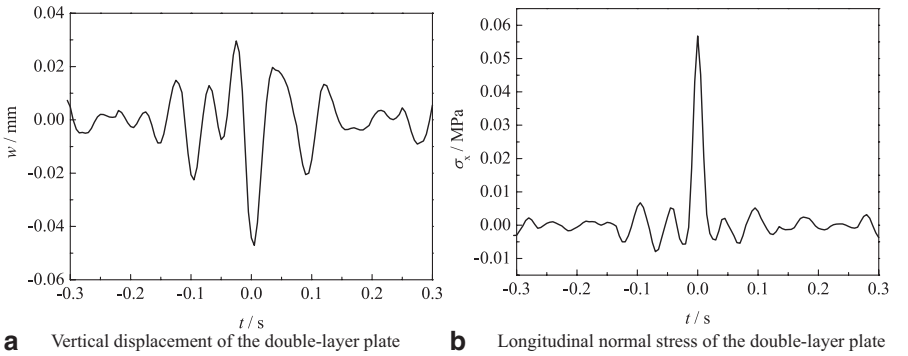

Fig. 5.12 The dynamic response of the double-layer plate on an elastic half-space foundation under a moving harmonic load. **a** Vertical displacement of the double-layer plate, **b** Longitudinal normal stress of the double-layer plate

4. The vibration frequency of the double-layer plate increases under a harmonic load, the vertical displacement and longitudinal normal stress in the front and rear of the load center present an obvious fluctuation trend.

5.6 Chapter Summary

In this chapter, the road is regarded as an infinite double-layer plate on a Kelvin foundation and on an elastic half-space, and the steady-state response of the road subjected to moving vehicle loads is studied. The governing equations of motion are analytically solved by integral transforms, together with the generalized Duhamel integral integrated over the Green's function of the double-layer plate under the unit impulse load. The dynamic responses in the time-space domain are evaluated by the efficient computer program, which is developed via Mathmatica and have been validated by comparing with results available in the literatures. The following conclusions can be drawn from the studies.

1. With the extension of the time and the space, the road dynamic responses attenuate rapidly. As the foundation damping increases, the asymmetry of the road dynamic responses before and after the load passes through become more obvious. The road dynamic response before the load passes through is greater than that after the load passes through. The maximum vertical displacement lags behind the center of the load. The distance and the time of the lag become more apparent when the damping increases.
2. The longitudinal normal stress at the bottom of the double-layer plate presents a tension and a compression alternating process. When the load is passing through the observation point, the longitudinal normal stress is tensile. However, before and after the load passes through the observation point, the longitudinal normal stress is compressive. This goes against the road fatigue life.
3. The vibration frequency of the double-layer plate increases under a moving harmonic load. The vertical displacement and longitudinal normal stress in the front and rear of the load center present an obvious fluctuation trend.
4. As the depth increases, the displacement and the stress of the elastic half-place foundation attenuates very rapidly. The maximum longitudinal tensile stress doesn't appear at the load center, but appear on both sides of the load center. So, the curve of the longitudinal tensile stress shows obviously saddle-like.

References

1. Frýba L. Vibration of solids and structures under moving loads. London: Thomas Telford; 1999.
2. Yang SP, Li SH, Lu YJ. Investigation on dynamic interaction between a heavy vehicle and road pavement. Veh Syst Dyn. 2010;48(8):923–44.

3. Beskou ND, Theodorakopoulos DD. Dynamic effects of moving loads on road pavements: a review. Soil Dynamics and Earthquake Engineering. 2011;31:547–67.
4. Bee M De. Measurement of tyre/pavement interface stresses under moving wheel loads. Heavy Systems. 1996;3(1–4):97–115.
5. Drakos CA, Roque R, Birgisson B. Effect of measured tire contact stresses on near-surface rutting. Transp Res Rec. 2001;1764:59–69.
6. Huang YH. Pavement analysis and design. 2nd ed. Prentice Hall, 2003.
7. Chen J. Basic research on vehicle and pavement interaction. Changchun: Jilin University Press; 2002.
8. Sun L. Dynamics of plate generated by moving harmonic loads. J Appl Mech. 2005;72:772–7.
9. Zhou HF, Jiang JQ. Dynamic response of rigid pavements to moving vehicles. China Civ Eng J. 2006;39(8):117–25.
10. Kim SM, Roesset JM. Moving loads on a plate on elastic foundation. J Eng Mech. 1998;124(9):1010–7.
11. Yang GT. Basis of elastic plastic kinetics. Beijing: Science Press; 2008.
12. Liao ZP. Introduction of engineering vibration theory. Beijing: Science Press; 2002.
13. Hung HH, Yang YB. Elastic waves in viscoelastic half-space generated by various vehicle loads. Soil Dyn Earthq Eng. 2001;21:1–17.

Chapter 6
Road Dynamic Responses Under Moving Vehicle Loads Based on Three-Dimensional Finite Element Model

Chapter 4 and Chap. 5 studied the road dynamic responses under moving loads by the analytical method. The deficiency of the analytical method lies in: (1) The road system model is relatively simple, the beam and the plate models, which are based on the small deformation theory and cannot reflect the real road structure. (2) The analytical method takes the road as a continuum body of infinite length in the horizontal direction and cannot reflect the size effect of the road. (3) It is difficult for the analytical method to treat the nonlinearity of constitutive relations and the nonlinear dynamic behavior between the vehicle and the road.

In this chapter, based on the layered plate theory, a 3-D finite element model of the road system is established by ANSYS10.0 software. The time-dependent deflection, stress and strain of the road are obtained by linking together the road surface roughness, a moving heavy duty vehicle, and a multilayered road system. The road fatigue life is calculated by taking the tensile strain at the bottom of the asphalt surface as the evaluation index. A parametric investigation is then conducted to show the effects of vehicle load, road grade, vehicle moving speed and vehicle parameters on the road fatigue life. The fatigue-induced failure regularity and mechanism of the road system under a moving stochastic load is elucidated.

6.1 Three-Dimensional Finite Element Model of Road System

6.1.1 Road Model of a Layered Plate and Its Basic Assumptions

When using the finite element method to establish the layered system of the road system, it is necessary to simplify the real road by ignoring the secondary factors and focusing on the key issues. Here, it is assumed that [1, 2]:

S. Yang et al., *Dynamics of Vehicle-Road Coupled System,*
DOI 10.1007/978-3-662-45957-7_6

1. The material of each layer is homogeneous and isotropic.
2. The soil base is infinite in both the horizontal direction and the depth direction. Other layers resting on the soil base are infinite in the horizontal direction, but finite in the depth direction.
3. When the vehicle is moving, the stress and displacement of the road at an infinite distance from the vehicle load are zero.
4. The contact condition between each layer is completely continuous.

Based on the above assumptions, a four-layer medium, consisting of the surface course, the base course, the subbase and the soil base, is employed as a road model to account for the real situation of the road system. The asphalt mixture is a typical viscoelastic material highly sensitive to temperature. The properties of the asphalt mixture depend on the time, the temperature and the stress. So the Burgers model is used to characterize the viscosity in the asphalt concrete surface course. The soil will generate a large plastic deformation under an external force. The Drucker–Prager model is used to handle the behavior of the soil base. The semi-rigid base and subbase course are enforced to behave as linear elastic.

6.1.2 Three Dimensional Finite Element Model of the Road System

1. The finite element model

The actual road system extends horizontally and vertically to infinity. It is implemented in ANSYS by choosing a cube of finite size along the x, y and z axis. This will unavoidably cause additional computational errors. To mitigate such errors, the model must be large enough. However, the larger the model, the longer the computation time as it requires more elements and computational resources if the same level of precision is to be maintained. After using other models in the existing literature for reference and trying a number of model dimensions for analysis [3–5],we found that, when the model length and width along the x and y axis exceeds 5 m, and the model depth along the z axis exceeds 3 m, the maximum vertical displacement at the top of the surface course becomes stable and no apparent change can be found. Finally, the model dimension (x, y, z) is selected to be 16.35 m × 6 m × 6 m. Where, the x-axis is the longitudinal direction, the y-axis is the transverse direction, and the z-axis is the vertical direction (depth).

The finite element model of the road is set up layer by layer from the bottom to the top. First, establish the left side of the soil base for $x = 0$, then stretch the left side for 16.35 m along the x-axis to establish the soil base. Next, stretch orderly upward to establish the subbase, base course, and surface course. Element Solid 45 is used to simulate the structural behavior of the base course, subbase and soil base, and element Solid 186, which allows large viscoelastic deformation, is employed to simulate the behavior of the asphalt surface course. The contact condition between each layer is completely continuous.

As the moving load on the road surface is localized, subdivision is required near the loaded area to capture the step-stress and strain gradient in these areas. So along

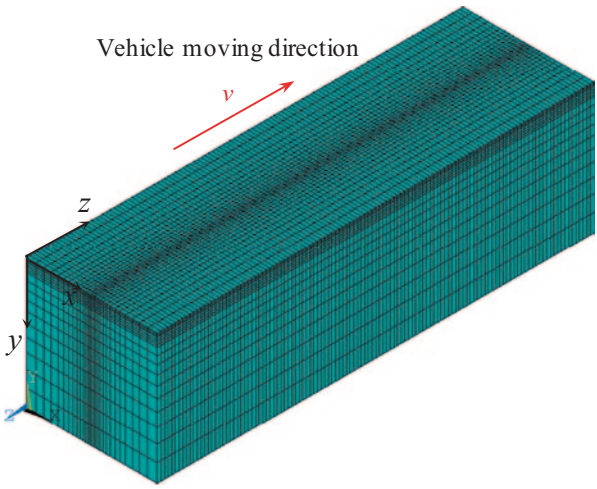

Fig. 6.1 Finite element mesh of the road system

the transverse y axis, the middle part uses dense elements while the outer part uses spare elements. Along the vertical z axis, the surface and base layers use a dense element while the soil foundation uses spare elements. There are 65,424 nodes and 59,024 elements in the road finite element model. The finite element mesh of the road system is shown in Fig. 6.1.

2. The boundary conditions

The boundary conditions have a great influence on the calculation results, so it is important to select the correct boundary conditions. When the vehicle is moving on the road, there are no responses at infinity. Therefore, according to Saint Venant's Principle, the boundary conditions are adopted as follows: the x-axis displacements of the two longitudinal sections are constrained to be zero, the y-axis displacements of the two transverse sections are constrained to be zero, and the displacements at the bottom of the road are constrained to be zero along the x, y, and z directions.

6.1.3 A Transient Dynamic Analysis of Road System Vibration

The full method is used to fulfill the transient dynamic finite element analysis of the road system, and the Consistent Mass Matrices (CMM) is used in the calculation.

1. Modal analysis to determine the Rayleigh damping coefficient

The damping mechanism is very complicated, which is related to the structure itself, the viscosity of the surrounding medium, the energy dissipation of the soil base, and so on. It is very difficult to determine accurately the damping matrix in the finite element analysis. Therefore, Rayleigh damping assumes that the damping matrix is a linear combination of the stiffness matrix and the mass matrix is adopted in the finite element analysis of this chapter. That is,

$$[C] = \alpha[M] + \beta[K] \tag{6.1}$$

where, α is Alpha damping, also known as the mass damping coefficient, and β is Beta damping, also known as the stiffness damping coefficient. According to the orthogonal condition, these two damping coefficients can be calculated by the vibration modes and the damping ratios. That is,

$$\alpha = \frac{2\omega_i\omega_k(\xi_i\omega_k - \xi_k\omega_i)}{\omega_k^2 - \omega_i^2} \quad \beta = \frac{2(\xi_k\omega_k - \xi_i\omega_i)}{\omega_k^2 - \omega_i^2} \tag{6.2}$$

where, ω_i and ω_k are the natural frequencies of the order i and order k mode, ξ_i and ξ_k, which must be determined by the test, are the damping ratios corresponding to the order i and order k mode, in general, the value of i and k can be chosen as $i = 1,\ k = 2$. The damping ratio is approximated as a constant in a certain frequency range, that is $\xi_i = \xi_k = \xi$, then Eq. (6.2) can be simplified as

$$\alpha = \frac{2\omega_1\omega_2\xi}{\omega_2 + \omega_1} \quad \beta = \frac{2\xi}{\omega_2 + \omega_1} \tag{6.3}$$

The block Lanczos's method is used to carry out the modal analysis of the finite element model. The frequencies corresponding to the modes of the first five orders are 6.5037, 7.4609, 8.4101, 8.5306, and 9.4529 Hz, respectively. Then,

$$\omega_1 = 2\pi f_1 = 2\pi \times 6.5307 = 40.864 \text{ rad/s} \tag{6.4}$$

$$\omega_2 = 2\pi f_2 = 2\pi \times 7.4609 = 46.878 \text{ rad/s} \tag{6.5}$$

The damping ratio of the road system is usually between 0.02 and 0.2. By letting $\xi = 0.05$, the damping coefficient can be calculated to be $\alpha = 2.183,\ \beta = 0.00114$.

2. The integration time step

In the ANSYS transient dynamic analysis, the Newmark-β method is used to solve the equation of motion on the discrete time point. The integration time step (Δt) affects not only the computational efficiency but also the solution accuracy and the convergence of the transient dynamic analysis. The smaller the time step, the higher the accuracy. An integration time step that is too large will affect the response of the higher order modes, and an integration time step that is too small will increase the computation cost. In this section, the step load is used to carry out the transient dynamic analysis. In order to describe the step load, Δt should be selected as follow [6]

$$\Delta t \le \frac{1}{180 f_1} = \frac{1}{180 \times 6.5307} = 0.00085\text{s} \tag{6.6}$$

In which, f_1 is the first order frequency of the finite elementmodel, determined by the above modal analysis.

3. The viscoelastic constitutive model

An asphalt mixture is a typical viscoelastic material with properties that depend on the time, the temperature, and the stress. The Burgers model is commonly used for characterizing viscosity in road [7–9]. The Burgers model is a combination of the Maxwell model and the Kelvin models in series. Both the Maxwell model and the Kelvin model experience identical stress σ, and their strain are ε_1 and ε_2, respectively. So, the total strain ε is composed of two parts

$$\varepsilon = \varepsilon_1 + \varepsilon_2 \tag{6.7}$$

The stress–strain relationship of the Bergers model can be further expressed as,

$$\sigma + p_1 \dot{\sigma} + p_2 \ddot{\sigma} = q_1 \dot{\varepsilon} + q_2 \ddot{\varepsilon} \tag{6.8}$$

where $p_1 = \frac{\eta_1}{E_1} + \frac{\eta_1 + \eta_2}{E_2}$, $p_2 = \frac{\eta_1 \eta_2}{E_1 E_2}$, $q_1 = \eta_1$, $q_2 = \frac{\eta_1 \eta_2}{E_2}$, where E_1 and E_2 are elastic constants, and η_1 and η_2 are viscosity constants.

The viscoelastic material has a creep and stress relaxation process, and the strain and stress responses are a function of time. Under the constant strain $\varepsilon = \varepsilon_0 H(t)$, the stress response, which varies with the time, can be expressed as:

$$\sigma = Y(t)\varepsilon_0 \tag{6.9}$$

where, $H(t)$ is the Heaviside unit step function, $Y(t)$ is the relaxation modulus representing the stress under unit strain,

$$Y(t) = \frac{E_1}{\alpha - \beta}\left[\left(\frac{E_2}{\eta_2} - \beta\right)e^{-\beta t} - \left(\frac{E_2}{\eta_2} - \alpha\right)e^{-\alpha t}\right] \tag{6.10}$$

$$\text{where, } \alpha = \frac{p_1 + \sqrt{p_1^2 - 4p_2}}{2p_2}; \quad \beta = \frac{p_1 - \sqrt{p_1^2 - 4p_2}}{2p_2}$$

4. Loading

The dynamic random tire force in the time domain can be obtained by using the procedure presented in Sect. 2.2. That is, building up the whole vehicle model of 8 degrees of freedom, considering the road random roughness, and using the Newmark-β method to solve the differential equation of vehicle motion. The moving random load equals the sum of the vehicle static load and the dynamic random tire force in the time domain. Due to the fact that the rear axle load is greater than the front axle load, only the moving random load of the left-side rear tire is taken into consideration in the finite element analysis of this chapter. The vehicle model refers to the structure of Dongfeng DFL1250A9, which is plotted in Fig. 6.2. Dongfeng

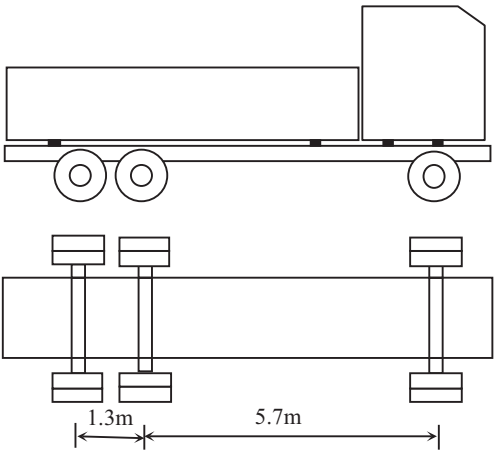

Fig. 6.2 Schematic diagram of the vehicle model

DFL1250A9 has double rear axles, which is combined into a single axle in the whole vehicle model of 8 degrees of freedom. When the dynamic response of the road system is calculated, the moving random load will be divided equally into two parts, which are distributed on the road at intervals of 1.3 m.

Suppose, the moving random load is uniformly distributed in a rectangular contact area, the contact pressure p is 0.7 MPa, and the contact area, which is $0.218\text{m} \times 0.314\text{m}$, can be calculated by Eqs. (5.5)–(5.8). The contact area is divided into 8 rectangular elements, 2 along the x axis, 4 along the y axis.

When the step load is adopted, the loading process is shown in Fig. 6.3. The first step load is applied in rows 1, 2 of elements, the second step load is applied in rows 2, 3 of elements, and so on. The vehicle moving speed can be changed by changing the load duration time in each unit.

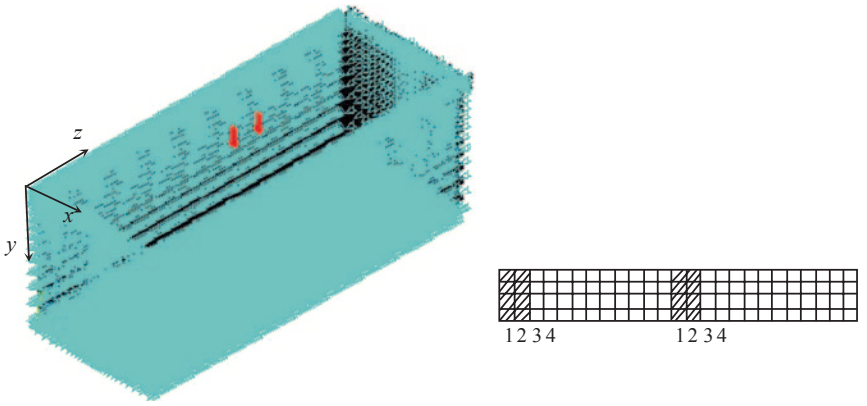

Fig. 6.3 Loading process of a moving vehicle. **a** Effect diagram of loading. **b** Schematic diagram of loading elements

Table 6.1 Material parameters of each layer of the road system

Layer	Thickness /m	Elastic moduli /MPa	Poisson's ratio	Internal friction angle/^{0}	Dilatancy angle/^{0}	Cohesion/ kPa	Density /kgm^{-3}	Damping ratio /%
Surface course	0.15	1400	0.35	60		350	2500	0.05
Base course	0.30	1200	0.35	40		250	2200	0.05
Subbase	0.25	650	0.4	35		200	2000	0.05
Soil base		35	0.4	22	30	55	1930	0.05

6.2 Dynamic Responses of Road System to the Moving Vehicle Loads

The 8 degrees of freedom vehicle model shown in Fig. 2.18 of Chap. 2 is used here to generate the stochastic dynamic tire force in the time domain. The vehicle calculation parameters refer to Sect. 2.2.3.

The material parameters of each layer of the road system are given in Table 6.1. The material parameters of the Burgers model are chosen to be: $E_1 = 350\text{MPa}$, $E_2 = 164.7\text{MPa}$, $\eta_1 = 233.4658\text{GPa}\cdot\text{s}$, $\eta_2 = 5.0317\text{GPa}\cdot\text{s}$

6.2.1 Vertical Displacement Analysis of Road System

The vertical displacement (road deflection) can reflect the overall strength and rigidity of the road system. It is an important mechanical index of asphalt pavement design in China. Figure 6.4 shows the vertical displacement of each layer against the time. Figure 6.5 illustrates the relationship between the maximum vertical displace-

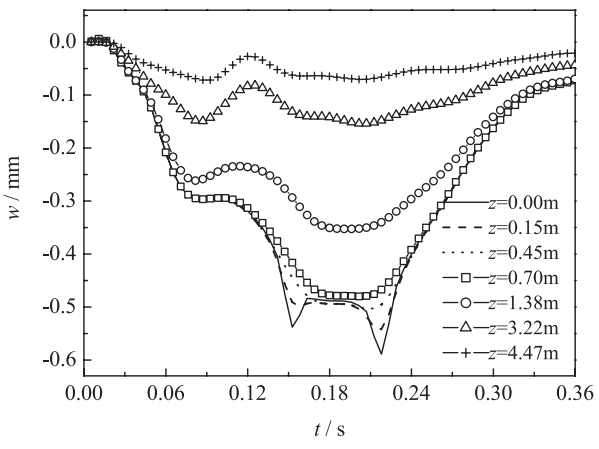

Fig. 6.4 Vertical displacement w vs. time

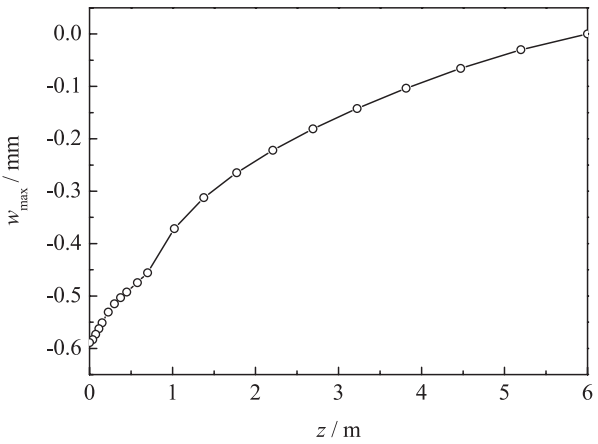

Fig. 6.5 Maximum vertical displacement w_{zmax} vs. depth

ments of each layer and the road system depth. The maximum vertical displacement is 0.5889 mm, occurring on the surface of the asphalt. The vertical displacement decreases as the depth increases. The maximum vertical displacement on the top of the soil base is 0.4798 mm. The deflection caused by the soil base is about 77.35% of that on the surface of the asphalt. Therefore, increasing the soil compaction can effectively reduce the surface deflection

6.2.2 Stress Analysis of Road System

1. The vertical normal stress

Figure 6.6 shows the vertical normal stress of each layer against time. Figure 6.7 illustrates the relationship between the maximum vertical normal stresses of all layers and the road system depth. Each layer of the road system is mainly under pressure in the vertical direction. The maximum vertical compressive stress appears in the asphalt surface course. As the load approaches and leaves the observation point, there is very little tensile stress in each layer. As the depth increases, the vertical compressive stress decreases rapidly in the base and the subbase. The maximum vertical compressive stress on the surface of the asphalt is 0.745 MPa. The maximum vertical compressive stress at the junction of the base and the subbase is 0.0585 MPa, only 7.85% of that is on the surface of the asphalt. The compressive stress has dropped to a very small value (0.0127 MPa) on the top of the soil base. This shows that the asphalt surface course is easiest to produce compaction deformation. Thus during road paving, attention must be paid to the compaction quality.

2. The longitudinal normal stress

Figure 6.8 shows the longitudinal (vehicle moving direction) normal stress of each layer against the time. Figure 6.9 illustrates the relationship between the maximum

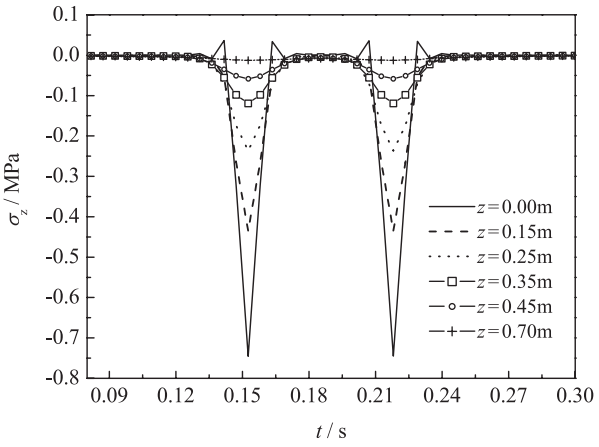

Fig. 6.6 Vertical normal stress σ_z vs. time

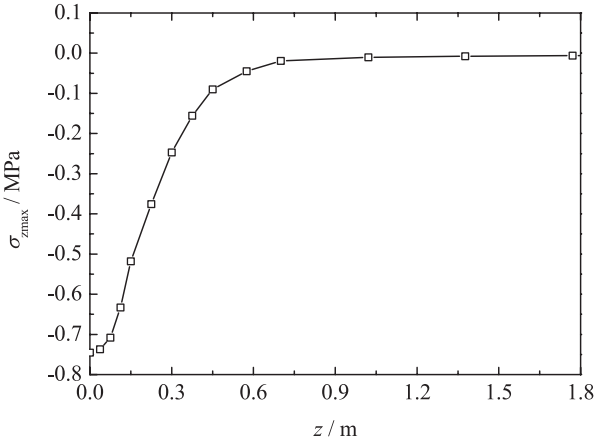

Fig. 6.7 Maximum vertical normal stress $\sigma_{z\max}$ vs. depth

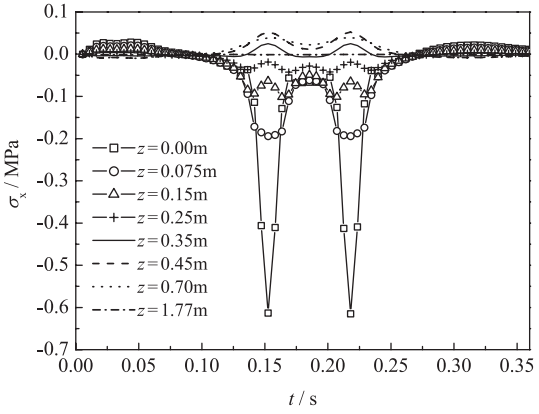

Fig. 6.8 Longitudinal normal stress σ_x vs. time

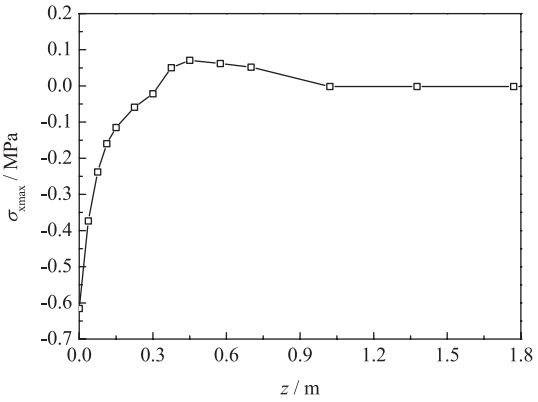

Fig. 6.9 Maximum longitudinal normal stress $\sigma_{x\max}$ vs. depth

longitudinal normal stresses of all layers and the road system depth. The longitudinal normal stress is alternating, and there is both tensile stress and compressive stress in each layer. The asphalt surface course is primarily under pressure, the longitudinal compressive stress decays rapidly in the surface course, the maximum longitudinal compressive stress on the surface of the asphalt is 0.61528 MPa, but the maximum longitudinal compressive stress at the junction of the surface course and base course is only 0.11499 MPa. The lower part of the base and the subbase are mainly under tensile stress, the maximum longitudinal tensile stress occurs at the junction of the base and the subbase, with a value of 0.0712 MPa.

3. The transverse normal stress

Figure 6.10 shows the transverse normal stress of each layer against the time. Figure 6.11 illustrates the relationship between the maximum transverse normal stresses of all layers and the road system depth. The asphalt surface course is primarily under pressure, the transverse compressive stress also decays rapidly in the surface course, the maximum transverse compressive stress on the surface of the asphalt is

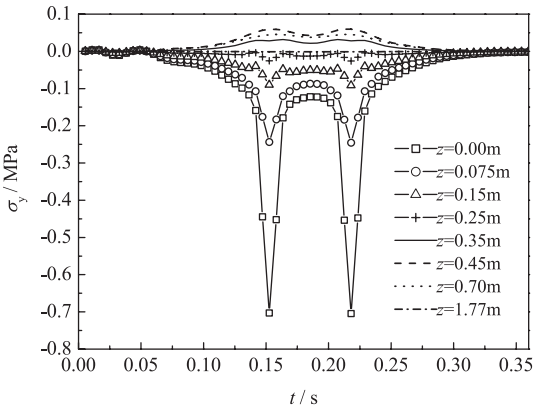

Fig. 6.10 Transverse normal stress σ_y vs. time

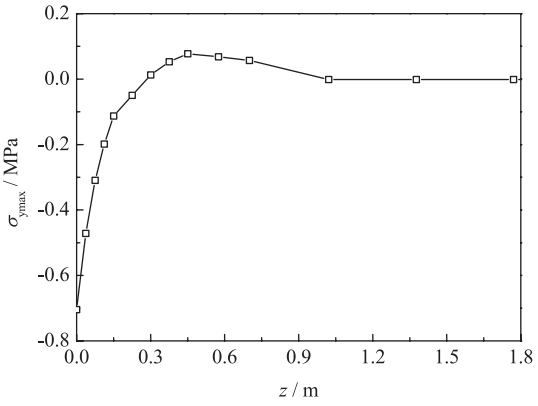

Fig. 6.11 Maximum transverse normal stress $\sigma_{y\max}$ vs. depth

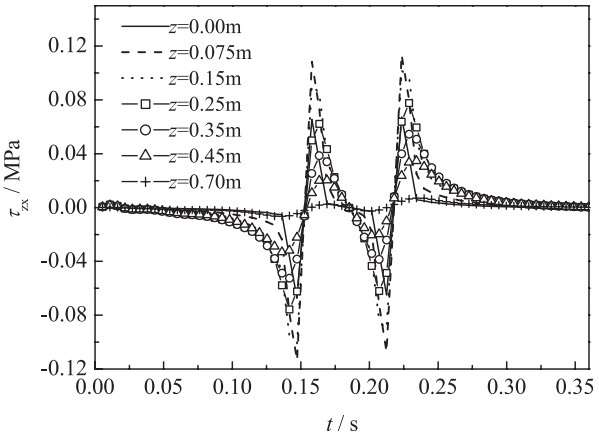

Fig. 6.12 Longitudinal shear stress τ_{zx} vs. time

0.70453 MPa, but the maximum transverse compressive stress at the junction of the surface course and base course is only 0.11249 MPa. The base and the subbase are mainly under tensile stress, the maximum transverse tensile stress also occurs at the junction of the base and the subbase, the maximum value is 0.0775 MPa, which is 8.85% larger than the maximum longitudinal tensile stress.

4. The longitudinal shear stress

Figure 6.12 shows that the longitudinal shear stress of each layer against the time. Figure 6.13 illustrates the relationship between the maximum longitudinal shear stress of all layers and the road system depth. As the traffic load approaches and leaves the observation point, the longitudinal shear stress τ_{zx} of each layer experiences two changes in the opposite direction. The longitudinal shear stress varies significantly in the asphalt surface course. First, it increases as the depth increases, and reaches the maximum value in the lower part of the asphalt surface course. Then, it decreases significantly as the depth increases. The maximum shear stress at the junction of the base and the subbase is 0.37 times that in the surface course. The

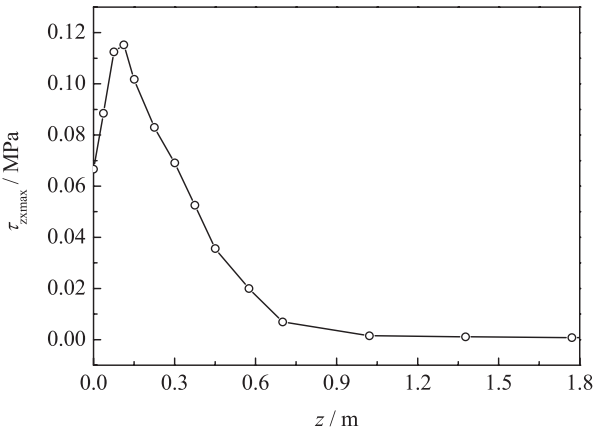

Fig. 6.13 Maximum longitudinal shear stress $\tau_{zx\max}$ vs. depth

shear stress of the soil base is approximately zero. So it is particularly important to improve the anti-shear ability in the asphalt surface.

6.2.3 Stain Analysis of Road System

1. The vertical linear strain

Figure 6.14 shows the vertical linear strain of each layer against the time. In the asphalt surface course, the vertical linear strain is alternating. When the load is approaching or leaving the observation point, it bears vertical tensile strain, but when the traffic load is passing through the observation point, it bears vertical compressive strain. The vertical tensile strain decreases gradually as the depth increases. An alternative variation of the vertical strain can easily make the asphalt surface course

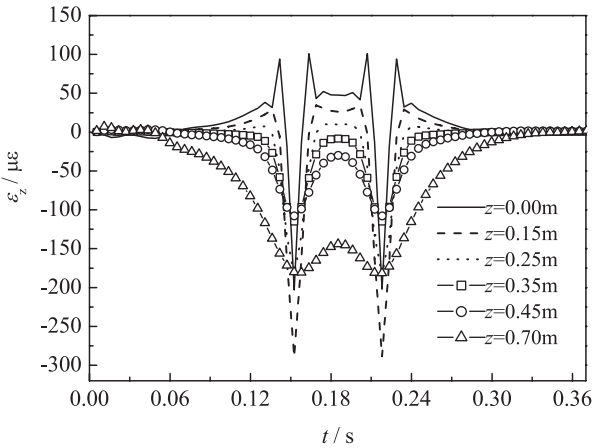

Fig. 6.14 Vertical normal strain ε_z vs. time

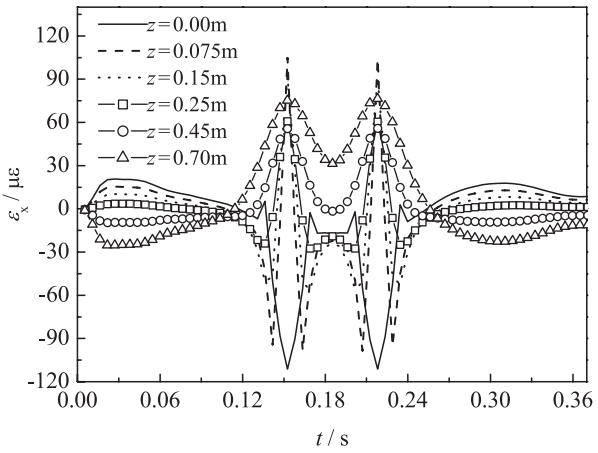

Fig. 6.15 Longitudinal normal strain ε_x vs. time

detach from the base course. The base and the subbase mainly bear vertical compressive strain. From the analysis of the stress response in the above subsection, we know that the vertical compressive stress is very small in the base and the subbase compared with that in the surface course. From Fig. 6.14, we know that the vertical compressive strain should not be ignored, and the vertical compressive strain at the junction of the base and the subbase is larger than that at the junction of the surface course and the base. This is mainly because the elasticity modulus of the base and the subbase materials, which deforms easily under the load action, is less than that of the surface course material.

2. The longitudinal linear strain

Figure 6.15 shows the longitudinal linear strain of each layer against the time. The longitudinal linear strain is alternating, and there is both tensile strain and compressive strain in each layer. The surface of the asphalt mainly bears compressive strain. In the surface course, when the load is approaching or leaving the observation point, it bears longitudinal compressive strain, but when the traffic load is passing through the observation point, it bears longitudinal tensile strain. The base and the subbase mainly bear tensile strain.

3. The transverse linear strain

Figure 6.16 shows the transverse linear strain of each layer against the time. The surface of the asphalt mainly bears compressive strain. The interior of the surface course, the base, and the subbase bear tensile strain. The maximum transverse tensile strain occurs at the junction of the subbase and the soil base.

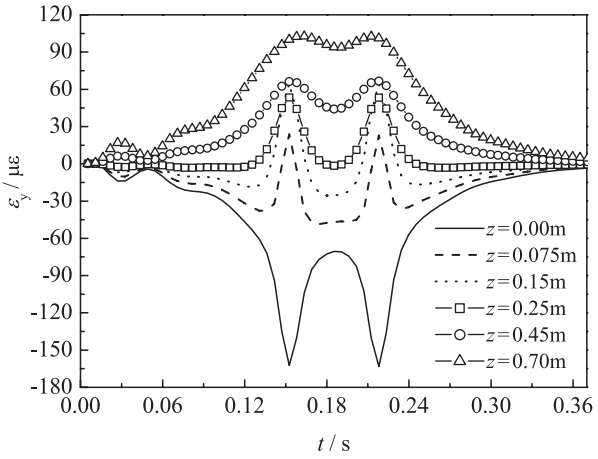

Fig. 6.16 Transverse normal strain ε_y vs. time

6.3 Analysis of Asphalt Pavement Fatigue Life Under Moving Vehicle Loads

6.3.1 Prediction Model of Asphalt Pavement Fatigue Life

When the vehicle is traveling repeatedly on the road, not only the road surface performance, such as smoothness and anti-slide, but also the structural strength will decrease step by step, until fatigue failure occurs. It is very important to study the fatigue properties of asphalt pavements, which receives widespread attention from road scientists and engineers all over the world. In order to ensure the asphalt pavement to maintain good practicability and durability, the fatigue life is taken as the basic design principle in asphalt pavement design in many countries of the world.

Because there have many factors affecting the asphalt pavement fatigue life, it is very difficult to establish directly the relation between the asphalt pavement fatigue life and the various influencing factors. Therefore, at present, almost all of the researchers adopt the approach which firstly establishes the prediction model of asphalt mixture through the indoor accelerated loading test, and then revises the indoor fatigue life model to establish the prediction model of asphalt pavement fatigue life in view of various influencing factors. However, because the testing instrument and method, the pavement structure, environmental and operational conditions are different, it is difficult to get a fatigue life equation suitable for a variety of conditions, and it is more difficult to establish a stable and reliable relationship between the indoor fatigue test and the asphalt pavement fatigue life. At present, the commonly used fatigue life model is divided into the strain model and the strain–stiffness model [10].

The strain model takes the tensile strain ε_t as a parameter variable, and the equation can be expressed as

$$N_f = k_1 \left(\frac{1}{\varepsilon_t} \right)^{k_2} \tag{6.11}$$

in which N_f is the fatigue life of the road system, represented by the number of loading cycles, ε_t is the tensile strain at the bottom of the surface course, and k_1 and k_2 are experimentally measured constants.

The strain–stiffness model, which is recommended by Monismith, takes the stiffness modulus of the asphalt mixture as a parameter variable. Considering the influence of asphalt aging and temperature change, the equation can be expressed as

$$N_f = k_1 \left(\frac{1}{\varepsilon_t}\right)^{k_2} \left(\frac{1}{E}\right)^{k_3} \tag{6.12}$$

where E is the stiffness modulus of the asphalt mixture (or dynamic stiffness modulus), and k_3 is a constant depending on the temperature.

When a single vehicle is passing through the road, David Cebon [11] puts forward fatigue life prediction models, which take longitudinal tensile strain at the bottom of the asphalt concrete surface course as a parameter variable. That is,

$$\log N_f(10\%) = 15.947 - 3.291 \log\left(\frac{\varepsilon}{10^{-6}}\right) - 0.854 \log\left(\frac{E}{10^3}\right) \tag{6.13}$$

$$\log N_f(45\%) = 16.086 - 3.291 \log\left(\frac{\varepsilon}{10^{-6}}\right) - 0.854 \log\left(\frac{E}{10^3}\right) \tag{6.14}$$

where N_f is the fatigue life of the road system, at which the fatigue fracture area is equal to 10 or 45 % of the wheel path area, ε is the maximum tensile strain at the bottom of the asphalt concrete surface course, and E, in psi (6.89 kPa) is the elasticity modulus of the asphalt concrete surface course.

Equations (6.13) and (6.14) have been widely used in fatigue life analysis of road system. In this section, the fatigue life of the road system is calculated by Eq. (6.13), and the parametric study follows to show the effects of the vehicle load, the road grade, the vehicle moving speed, the suspension stiffness, the suspension damping, the tire stiffness and the tire damping on the road fatigue life.

6.3.2 Parameter Influence Analysis of Asphalt Pavement Fatigue Life

1. The effect of the vehicle load

Figure 6.17 illustrates the relationship between the vehicle load and the road fatigue life. As the load increases, the static load and the dynamic tire force distributed on the road all increase, and the road fatigue life decreases severely. For example, the fatigue life for 80 % overload is 27.81 % of that for full load. It has been shown that overloading is one of the main reasons for early damage to the road.

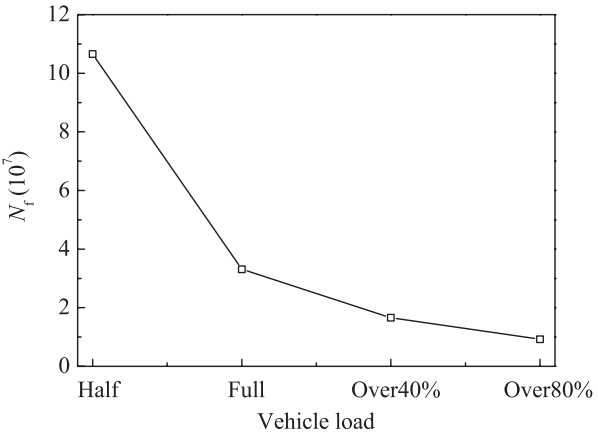

Fig. 6.17 Effect of the vehicle load

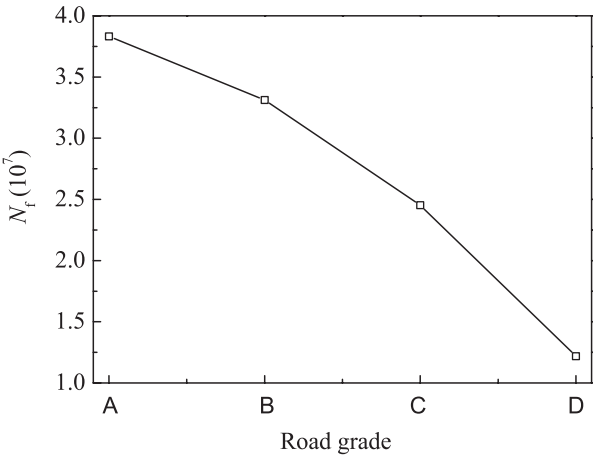

Fig. 6.18 Effect of the road grade

2. The effect of the road grade

The effect of the road grade on the road fatigue life can be seen in Fig. 6.18. As the road grade decreases from A to D, the dynamic tire force distributed on the road increases continuously, and the road fatigue life decreases with a parabolic correlation. The fatigue life for C grade is 64 % of that for A grade, but the fatigue life for D grade is only 31.83 % of that for A grade. Therefore, improving the road roughness grade is an effective measure to reduce the dynamic tire force and improve the road fatigue life.

3. The effect of the suspension parameters

Figures 6.19 and 6.20 show the effect of the rear suspension stiffness and the rear suspension damping on the road fatigue life, respectively. When the suspension stiffness is small, the road fatigue life increases slightly as the suspension stiffness

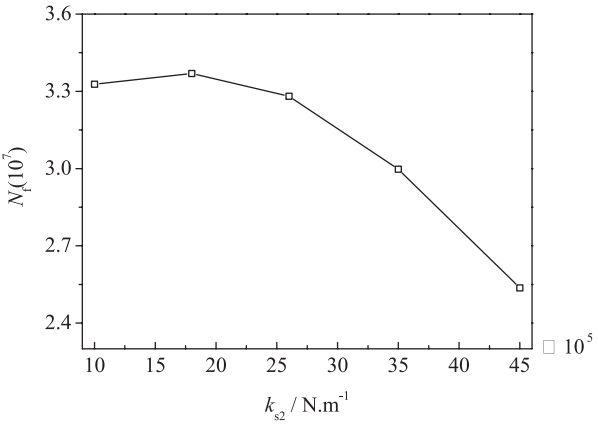

Fig. 6.19 Effect of the suspension stiffness

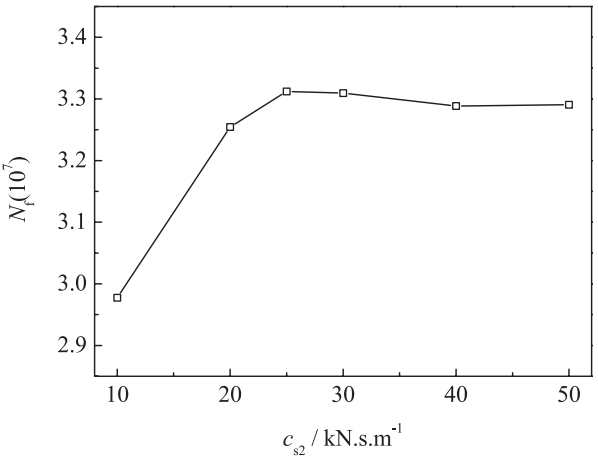

Fig. 6.20 Effect of the suspension damping

increases, and then it decreases approximately in a parabolic arc as the suspension stiffness increases. In general, increasing the suspension stiffness will reduce the road fatigue life.

As the suspension damping increases, the road fatigue life increases rapidly at first, and then remains unchanged. This implies that increasing suspension damping is beneficial to improve the road fatigue life. In addition, according to vehicle dynamics, reducing the suspension stiffness and increasing the suspension damping can effectively inhibit vehicle vibration.

4. The effect of the tire stiffness

The effect of the rear tire stiffness on road fatigue life can be seen in Fig. 6.21. The road fatigue life decreases as the tire stiffness increases. Because the tire stiffness and the inflation pressure are closely related, an increase in inflation pressure will cause an increase in tire stiffness. The greater the tire stiffness, the more severe the

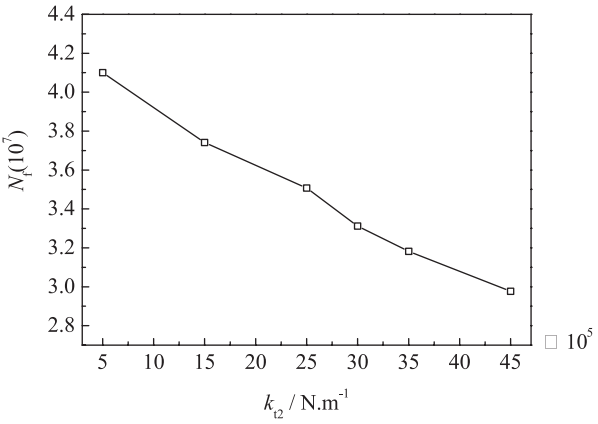

Fig. 6.21 Effect of the tire stiffness

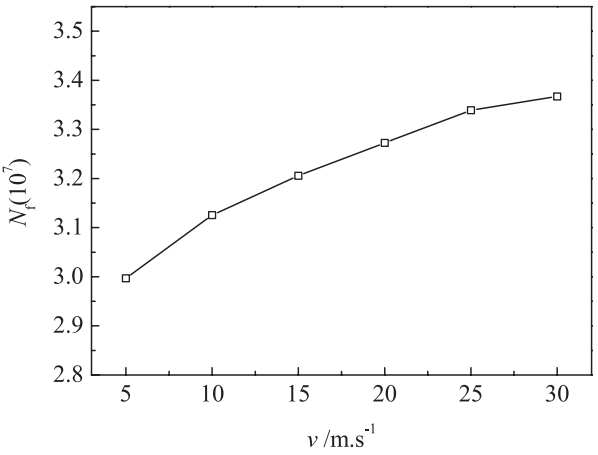

Fig. 6.22 Effect of the vehicle moving speed

vehicle vibration and the larger the dynamic tire force. In order to avoid early road damage, it is necessary to strictly limit tire overpressure.

5. The effect of the vehicle moving speed

Figure 6.22 shows the effect of the vehicle moving speed on the road fatigue life. As the vehicle moving speed increases, the tensile strain at the bottom of the asphalt surface course decreases, and the road fatigue life increases. But the increase in moving speed will worsen vehicle vibration, which is disadvantageous to driving safety. In addition, high-speed vehicles will generate greater horizontal forces while braking and turning. These horizontal forces may cause the increase of shear stress in the road system, destroy the adhesion among layers, and make the road produce rutting, shoving, and wave. So, the effect of vehicle speed should be considered from all aspects.

6.4 Chapter Summary

This chapter establishes a 3D viscoelastic finite element model of the asphalt pavement system. In view of the interaction between the vehicle and the road, the displacement, the stress and the strain in the road system under a moving random load are numerically simulated, and the effects of loading capacity, road grade, vehicle moving speed, and vehicle parameters on the road fatigue life are discussed in details. The analysis results point to the following conclusions:

1. The asphalt surface course is under a pressure state in all three dimensions, and the shear stress in this layer is the main cause for its failure.
2. The base and the subbase are under a tensile state in the longitudinal and the transverse directions, the maximum longitudinal and transverse tensile stress occurs at the junction of the base and the subbase. So, the road fatigue failure caused by tensile stress under a moving load should first appear at the junction of the base and the subbase.
3. The road fatigue life decreases sharply as the road grade decreases and the vehicle load increases. Thus, improving the road roughness grade and strictly enforcing restrictions on overloading are effective measures to avoid early road damage and to prolong the road fatigue life.
4. Reducing the suspension and the tire stiffness, and increasing suspension damping can inhibit vehicle vibration and improve the road fatigue life.
5. Increasing the vehicle moving speed is beneficial to improve the road fatigue life. However increasing the vehicle moving speed will worsen vehicle vibration and increase the road shear failure while braking and turning. So, the effect of vehicle speed should be considered from all aspects.

References

1. Chen J. Basic research on vehicle and pavement interaction. Changchun: Jilin University; 2002.
2. Wang X. Study on the dynamical response of flexible pavement foundations under random loads. Changsha: Central South University; 2006.
3. Saad B, Mitri H, Poorooshasb H. Three-Dimensional dynamic analysis of flexible conventional pavement foundation. J Transp Eng. 2005;131(6):460–9.
4. Mulungye RM, Owende PMO, Mellon K. Finite element modeling of flexible pavements on soil subgrades. Mater Des. 2007;28:739–56.
5. Shan JX, Huang XM, Liao GY. Dynamic response analysis of pavement structure under moving load. J Highw Transp Res Dev. 2007;24(1):10–3.
6. Wang XM. ANSYS numerical analysis of engineering structures. Beijing: China Communications Press; 2007.
7. Guo DZ, Ren YB. Mechanics of multilayered viscoelastic systems. Harbin: Harbin Industry Press; 2001.
8. Lv PM, Dong ZH. A model to study the dynamic response of visco-elastic layered system under moving load. Eng Mech. 2011;28(12):153–9.

9. Sun L, Luo FQ. Transient wave propagation in multilayered viscoelastic media: theory, numerical computation, and validation, J Appl Mech. 2008;75:031007.
10. Lv PM, Dong ZH. Mechanical analysis of vehicle-asphalt pavement system. Beijing: China Communications Press; 2010.
11. Cebon D. Handbook of vehicle-road interaction. England: Swets and Zeitlinger; 1999.

Chapter 7
Modeling and Dynamic Analysis of Vehicle–Road Coupled Systems

With the increase of road traffic and vehicle loads, earlier damage of asphalt pavement on expressways has become more and more serious, which has greatly shortened the effective lifespan of the pavement. Road damage causes dynamic tire-force to increase greatly, which may reduce the passenger's ride comfort and safety. Thus it is necessary to investigate the interaction between vehicle and pavement intently and compute vehicle loads accurately. However at present, vehicle and road are investigated separately in vehicle dynamics and road dynamics. In vehicle dynamics, road surface roughness is generally regarded as an excitation to a vehicle, and the dynamic behavior and the parameter optimization of vehicles are investigated. In road dynamics, the vehicle is generally regarded as a moving load acting on the pavement, and the pavement is modeled as a beam, a plate and a multilayer system on viscous elastic foundations. It is necessary to propose a new vehicle–road coupled system to investigate the responses of the vehicle and road simultaneously.

In this chapter, the two- and three-dimensional vehicle–road coupled systems are built and coupled system responses are simulated with the methods of mode superposition, Galerkin's method and numerical integration. The differences between the coupled system and the traditional systems are also investigated.

7.1 Modeling of A Two-Dimensional Vehicle–Road Coupled System

7.1.1 Model of Tire-Road Contact

The characteristics of contact between tire and road, which is one of the key issues that affect vehicle dynamics and dynamic pavement forces, have received more and more attention. Many tire models have been proposed during the past decades. The simplest and most popular one is the point contact tire model which describes the

S. Yang et al., *Dynamics of Vehicle-Road Coupled System,*
DOI 10.1007/978-3-662-45957-7_7

vertical force of the tire. However, the contact characteristics between tire and road are rather complicated. Considering the effect of geometric size and elastic filter of a tire, the enveloping effect on the road should not be neglected when a vehicle is running on rough ground. In addition, the contact print length between tire and road varies in time and the tire may jump away from the ground. Thus when the road surface roughness is complex, the point contact tire model may pose rather large uncertainties.

Guo presented a flexible roller contact tire model, and carried out simulations of a vehicle vibration system based on a rigid and flexible roller contact tire model [1–3]. The compressing deformation between tire and road is expressed as

$$\Delta z(x, x_a) = \begin{cases} q(x + x_a) + \sqrt{r_0^2 - x_a^2} - r_0 - z_2(x) & \Delta z \geq 0 \\ 0 & \Delta z \leq 0 \end{cases} \tag{7.1}$$

where $q(x, x_a)$ is the road surface roughness, r_0 is the tire radius, $z_2(x)$ and x are the vertical and lengthwise displacements of the wheel center, x_a is the local lengthwise coordinate in the tire contact print, and $-r_0 \leq x \leq r_0$.

The vertical dynamic force between the tire and pavement is

$$F_{zd}(x) = \int_a k_t(x) \cdot \Delta z(x, x_a) dx_a \tag{7.2}$$

where k_t is the tire vertical distributing stiffness coefficient, and a is the length of the tire contact print.

The flexible roller model considers three assumptions, including the multipoint contact between the tire and the road, the varying tire print length and the probability of the tire jumping away from the road. But the model does not consider the effect of tire damping and pavement vibration on tire force. Moreover, when computing the effective road input, this model has the assumption that a vehicle runs slowly on the road and uses a static tire load to replace the dynamic tire load.

Based on the above analysis, a revised flexible roller contact model (RFRC tire model) is proposed, as shown in Fig. 7.1 [4].

The proposed model is composed of three equations. The compressing deformation between tire and road is expressed as

$$\Delta z(x, x_a) = \begin{cases} w(x, x_a) + q(x + x_a) + \sqrt{r_0^2 - x_a^2} - r_0 - z_2(x) & \Delta z \geq 0 \\ 0 & \Delta z \leq 0 \end{cases} \tag{7.3}$$

where w is the vertical vibration displacement of the pavement.

The relative velocity between the tire and the pavement is

$$\Delta \dot{z}(x, x_a) = \begin{cases} \dfrac{\partial w(x, x_a)}{\partial t} + \dfrac{\partial q(x + x_a)}{\partial t} + \dfrac{x_a v}{\sqrt{r_0^2 - x_a^2}} - \dfrac{\partial z_2(x)}{\partial t} & \Delta z \geq 0 \\ 0 & \Delta z \leq 0 \end{cases} \tag{7.4}$$

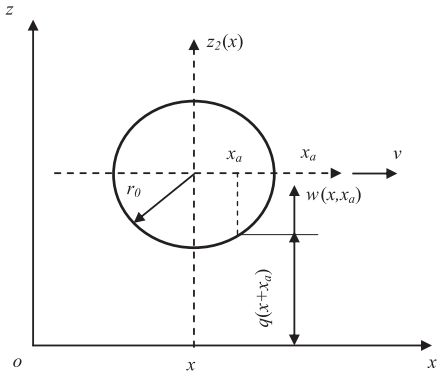

Fig. 7.1 The revised flexible roller tire model. (Reprinted from ref. [4], with kind permission from Springer Science+Business Media)

where, v is the vehicle running speed.

The vertical dynamic force between the tire and the pavement is

$$F_{zd}(x) = \int_a \left[k_t(x) \cdot \Delta z(x, x_a) + c_t(x) \cdot \Delta \dot{z}(x, x_a) \right] dx_a \tag{7.5}$$

where k_t and c_t are the tire vertical distributing stiffness and damping coefficient respectively.

Substituting Eq. (7.5) into the vehicle–road coupled system equations of motion, the tire force can be determined and the dynamics of the system can be studied with no need to compute the effective road input.

7.1.2 Equations of a Two-Dimensional Vehicle–Road Coupled System

The vehicle–pavement-foundation coupled system built in this work is shown in Fig. 7.2. A two DOF oscillator and a Bernoulli–Euler beam on a viscoelastic Kelvin foundation with two simply supported ends are employed to model the vehicle and the pavement. The vehicle begins to move along the beam at a constant velocity in the lengthwise direction from the midpoint of the beam when $t = 0$.

Let the vehicle's static equilibrium and the pavement's neutral position be the coordinate origins. The system equations of motion can be obtained by d'Alembert's principle as follows,

$$\begin{bmatrix} m_1 & 0 \\ 0 & m_2 \end{bmatrix} \cdot \begin{bmatrix} \ddot{z}_1 \\ \ddot{z}_2 \end{bmatrix} + \begin{bmatrix} c_1 & -c_1 \\ -c_1 & c_1 \end{bmatrix} \cdot \begin{bmatrix} \dot{z}_1 \\ \dot{z}_2 \end{bmatrix} + \begin{bmatrix} k_1 & -k_1 \\ -k_1 & k_1 \end{bmatrix} \cdot \begin{bmatrix} z_1 \\ z_2 \end{bmatrix} = \begin{bmatrix} 0 \\ F_{zd} - m_1 g - m_2 g \end{bmatrix} \tag{7.6}$$

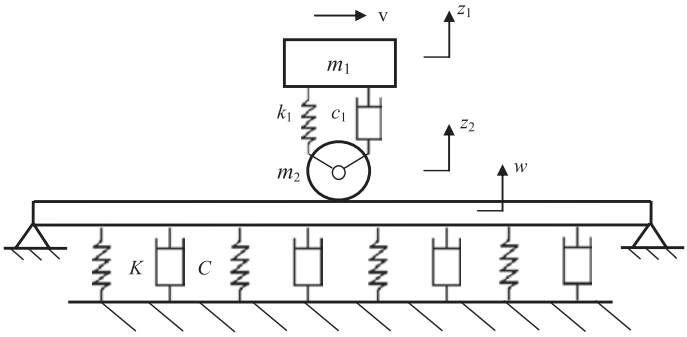

Fig. 7.2 Two-dimensional vehicle–road coupled system with roller tire-road contact. (Reprinted from ref. [4], with kind permission from Springer Science+Business Media)

$$EI\frac{\partial^4 w}{\partial x^4}+Kw+C\frac{\partial w}{\partial t}+m\frac{\partial^2 w}{\partial t^2}=-F_{zd}\delta(x-x_t) \tag{7.7}$$

where z_1 z_2 and w are the vertical displacements of the body, wheel, and pavement, respectively. E, I, F_{zd}, and L are the modulus of elasticity, the cross-sectional moment of inertia, the tire vertical force, and the road length respectively. X_0 is the wheel center lengthwise position at any time, which is expressed as $x_t = L/2+vt$

The harmonic road excitation takes the following form,

$$q_0 = B_0\sin(2\pi vt/L_0) = B_0\sin\Omega t \tag{7.8}$$

where B_0 and L_0 are the amplitude and wavelength of road roughness respectively.

The initial conditions and boundary conditions of the beam are

$$w(x,t)\big|_{t=0} = \left.\frac{\partial w(x,t)}{\partial t}\right|_{t=0} = 0 \tag{7.9}$$

$$w(0) = w(L) = \frac{\partial^2 w(0)}{\partial x^2} = \frac{\partial^2 w(L)}{\partial x^2} = 0 \tag{7.10}$$

Let

$$w(x,t) = \sum_{i=1}^{N} U_i(x)\eta_i(t) \tag{7.11}$$

where the normal mode $U_i(x)$ can be obtained by boundary conditions (7.9) and (7.10) as

$$U_i(x) = \sqrt{\frac{2}{mL}}\sin\frac{i\pi x}{L} \tag{7.12}$$

The road partial differential Eq. (7.7) can be discretized into many ordinary differential equations with the method of mode superposition,

$$\ddot{\eta}_j(t)+2\xi_j\omega_j\dot{\eta}_j(t)+\omega_j^2\eta_j(t)=F_j(t) \tag{7.13}$$

where

$$\omega_j=\sqrt{\left(\frac{j\pi}{L}\right)^4\frac{EJ}{m}+\frac{K}{m}},\ \xi_j=\frac{C}{2m\omega_j} \tag{7.14}$$

$$F_j(t)=\int_0^L F_{zd}(t)\delta\left(x-x_t\right)Y_j(x)dx=F_{zd}(t)Y_j\left(x_t\right) \tag{7.15}$$

7.1.3 Interaction of Tire and Road

Substituting road roughness Eq. (7.8) and road vertical displacement (7.11) into Eqs. (7.3) and (7.4), one gets the relative displacement and velocity between the tire and the pavement as follows,

$$\Delta z(x,x_a)=\begin{cases}\sum_{i=1}^{N}\sqrt{\frac{2}{mL}}\sin\frac{i\pi x_t}{L}\eta_i(t)+B_0\sin\frac{2\pi}{L_0}(x_t+x_a) & \\ \quad+\sqrt{r_0^2-x_a^2}-r_0-z_2(t)-z_{2s} & \Delta z\geq 0\\ 0 & \Delta z<0\end{cases} \tag{7.16}$$

$$\Delta\dot{z}\left(x,x_a\right)=\begin{cases}\sum_{i=1}^{N}\sqrt{\frac{2}{mL}}\sin\frac{i\pi x_t}{L}\dot{\eta}_i(t)+\sum_{i=1}^{N}\sqrt{\frac{2}{mL}}\frac{i\pi v}{L}\cos\frac{i\pi x_t}{L}\eta_i(t) & \\ \quad+B_0v\frac{2\pi}{L_0}\cos\frac{2\pi}{L_0}\left(x_t+x_a\right)+\frac{x_av}{\sqrt{r_0^2-x_a^2}}-\dot{z}_2(t) & \Delta z\geq 0\\ 0 & \Delta z<0\end{cases} \tag{7.17}$$

where z_{2s} is the tire static deformation.

By using even distributing stiffness and damping, the vertical tire force using the revised flexible roller contact (RFRC) tire model can be expressed as

$$F_{zd}(t)=\int_{a_1}^{a_2}\left[\frac{k_t}{a_2-a_1}\cdot\Delta z(x,x_a)+\frac{c_t}{a_2-a_1}\cdot\Delta\dot{z}(x,x_a)\right]dx_a \tag{7.18}$$

where a_1 and a_2 are the start point and the end point of the tire contact print, which are varying every moment. When $\Delta Z\leq 0$, the tire jumps away from the pavement. When $\Delta Z\geq 0$, the tire contacts with the pavement.

The vertical tire force using the traditional single point contact (SPC) tire model is

$$\begin{aligned} F_{zd}(t) &= k_t(w(t)+q(t)-z_2(t))+c_t\left(\frac{\partial w(t)}{\partial t}+\dot{q}(t)-\dot{z}_2(t)\right) \\ &= k_t\left(\sum_{i=1}^{N}\sqrt{\frac{2}{mL}}\sin\frac{i\pi x_t}{L}\eta_i(t)+B_0\sin\frac{2\pi x_t}{L_0}-z_2(t)\right) \\ &\quad + c_t\left(\begin{array}{l}\sum_{i=1}^{N}\sqrt{\frac{2}{mL}}\sin\frac{i\pi x_t}{L}\dot{\eta}_i(t)+\sum_{i=1}^{N}\sqrt{\frac{2}{mL}}\frac{i\pi v}{L}\cos\frac{i\pi x_t}{L}\eta_i(t) \\ +B_0 v\frac{2\pi}{L_0}\cos\frac{2\pi x_t}{L_0}-\dot{z}_2(t)\end{array}\right) \end{aligned} \tag{7.19}$$

Equations (7.18) and (7.19) show that the tire force is influenced by wheel vibration, pavement vibration, and road surface roughness. Thus the vehicle equations are coupled with the road equations. Combining the vehicle ordinary differential Eq. (7.6) and the road Eq. (7.13) leads to the vehicle–pavement coupled system equation,

$$[M]\{\ddot{Z}\}+[C]\{\dot{Z}\}+[K]\{Z\}=\{R\} \tag{7.20}$$

where, $\{Z\}=\{z_1 \quad z_2 \quad \eta_1 \quad \eta_2 \quad \cdots\}^T$ is the displacement column vector of the vehicle–road system. $[M]$, $[C]$, $[K]$ are the matrices of mass, damping, and stiffness respectively. $[R]$ is the force vector.

Since it is difficult to remove the coupled terms from the above vehicle–road coupled equations, the numerical integral is the best method to solve the equation.

7.1.4 Calculation Program and Model Verification

A computer program was designed to get the dynamic responses of the coupled system by the quick direct integral method [5, 6]. The routines of the calculation program are outlined as follows,

1. Input system parameters, integral step Δt , integral step number n, and modal superposition order of the pavement NM.
2. Create mass, stiffness, and the force matrix.
3. Set initial conditions when $t=0$.

Let the initial displacement and initial velocity be $\begin{cases}\{Z\}_0=\{Z(0)\}\\ \{\dot{Z}\}_0=\{\dot{Z}(0)\}\end{cases}$.

Initial acceleration can be obtained from Eq. (7.20) as

$$\{\ddot{Z}\}_0=[M]^{-1}\left(\{R\}_0-[K]_0\{Z\}_0-[C]_0\{\dot{Z}\}_0\right) \tag{7.21}$$

4. Calculate the displacement and velocity when $t = (n + 1)\Delta t$.

Let $\varphi = \psi = 0$ when $n = 0$ and $\varphi = \psi = 1/2$ when $n \geq 1$. One can build the following relations:

$$\begin{cases} \{Z\}_{n+1} = \{Z\}_n + \{\dot{Z}\}_n \Delta t + (1/2 + \psi)\{\ddot{Z}\}_n \Delta t^2 - \psi\{\ddot{Z}\}_{n-1} \Delta t^2 \\ \{\dot{Z}\}_{n+1} = \{\dot{Z}\}_n + (1 + \varphi)\{\ddot{Z}\}_n \Delta t - \varphi\{\ddot{Z}\}_{n-1} \Delta t \end{cases} \tag{7.22}$$

5. Calculate the tire force when $t = (n + 1)\Delta t$.

a. Applying the RFRC tire model

The pavement displacement when $t = (n + 1)\Delta t$ at the position of $x_t + x$ can be obtained by Eq. (7.11). Here, the value of x is between $-$r0 and r0. Tire deformation at the position of $x_t + x$ can be obtained by Eq. (7.16). When $\Delta Z \geq 0$, the tire contacts the pavement and the start (a_1) and end (a_2) of the tire contact print can be found. Thus, the start point and end point of the tire print when $t = (n + 1)\Delta t$ can be determined. The tire force when $t = (n + 1)\Delta t$ can be obtained by Eq. (7.18) and the force matrix $\{R\}_{n+1}$ when $t = (n + 1)\Delta t$ can be obtained by Eq. (7.15).

b. Applying the SPC tire model

Pavement displacement, tire force, and the force matrix $\{R\}_{n+1}$ when $t = (n + 1)\Delta t$ can be obtained by Eqs. (7.11), (7.19) and (7.15).

6. Calculate acceleration when $t = (n + 1)\Delta t$.

Substituting Eq. (7.22) into the coupled system Eq. (7.20) when $t = (n + 1)\Delta t$ leads to

$$[M]\{\ddot{Z}\}_{n+1} + [C]_{n+1}\{\dot{Z}\}_{n+1} + [K]_{n+1}\{Z\}_{n+1} = \{R\}_{n+1} \tag{7.23}$$

Thus one can obtain the acceleration matrix of the coupled system when $t = (n + 1)\Delta t$ as

$$\begin{aligned} \{\ddot{Z}\}_{n+1} = [M]^{-1}(\{R\}_{n+1} - [K]_{n+1}\{Z\}_n - ([C]_{n+1} + [K]_{n+1}\Delta t)\{\dot{Z}\}_n \\ - \{(1 + \varphi)[C]_{n+1} + (1/2 + \psi)[K]_{n+1}\Delta t\}\{\ddot{Z}\}_n \Delta t \\ + (\varphi[C]_{n+1} + \psi[K]_{n+1}\Delta t)\{A\}_{n-1}\Delta t \end{aligned} \tag{7.24}$$

7. Repeating steps (4), (5), and (6), one can get the displacement, velocity, force, and acceleration matrixes of the coupled system step by step.
8. Output time histories of the vehicle's body acceleration, suspension deformation, tire force, pavement displacement and pavement acceleration.

Figure 7.3 shows the calculating block diagram for this two-dimensional vehicle–road coupled system.

Parameters of the pavement structure are chosen as follows: $E = 1.6 \times 10^9$ N/m^2, $\rho = 2.5 \times 10^3$ kg/m^3 , $K = 48 \times 10^6$ N/m^2, $C = 0.3 \times 10^5$ N·s/m^2, $NM = 140$, the width of the pavement is 6 m and the height of the pavement is 0.1 m. The cross section is rectangular.

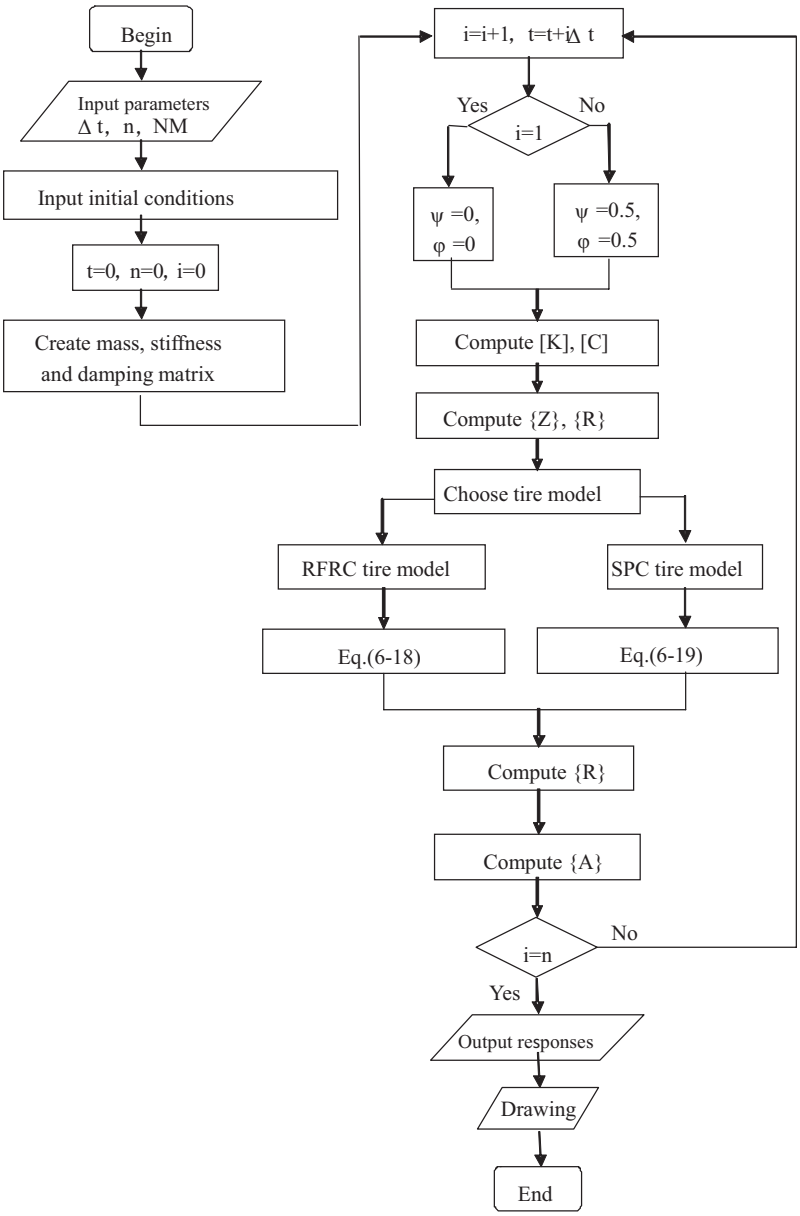

Fig. 7.3 The calculating block diagram

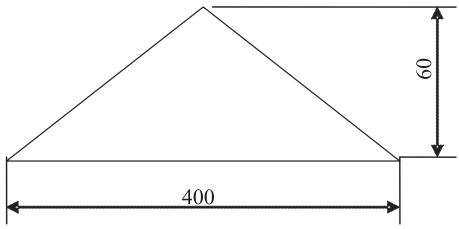

Fig. 7.4 Triangular bump in [7] (Unit:mm)

Parameters of the vehicle system are the same as found in reference [7], $m_2 = 637.5$ kg, $m_1 = 75$ kg, $K_2 = 70{,}360$ N/m, $K_1 = 286{,}500$ N/m, $C_2 = 1530.7$ N · s^2/m, $C_1 = 7760.2$ N · s^2/m, $R_0 = 0.36675$ m. The tire type is 235/75R15.

Road impulse excitation was simulated by a triangular bump that is the same as reference [7], as shown in Fig. 7.4.

The vertical accelerations of the vehicle body at different velocities were calculated based on the two tire models at speeds of 10, 20, 30, 40, 50, 60, 70, and 80 km/h, as shown in Fig. 7.5. The dashed and the solid lines represent the results of SPC and RFRC tire models respectively.

Maximum vehicle body vertical acceleration obtained from simulation results and test data by reference [7] are listed in Table 7.1 and shown in Fig. 7.6.

It can be seen from Fig. 7.6 and Table 7.1 that

1. Results of the proposed RFRC tire model are closer to the test data than those of the traditional SPC tire model except in the case of 60 km/h. Thus, the validity of the RFRC tire model is basically verified.
2. The results of the SPC tire model are always greater than the test data.
3. The margin of error of the RFRC tire model is greatest when $v = 60$ km/h. The reason for this may be that the roughness of the road leads to vehicle resonance and enlarges the vehicle body acceleration. However, the roughness of the road is neglected here because of the lack of a test of road roughness in reference [7].

7.2 Effects of the Two Tire Models on the Responses of the Vehicle–Road Coupled System

To investigate the difference between the two tire models in dynamics analysis, parameters of a heavy vehicle system were chosen as [8]

$m_1 = 10{,}109$ kg, $m_2 = 190$ kg, $k_1 = 75{,}000$ N/m, $k_t = 2{,}060{,}000$ N/m, $c_1 = 30{,}000$ N · s/m, $c_t = 900$ N · s/m, $r_0 = 559$ mm, $v = 20$ m/s and a tire type of 12.00R20.

The vehicle–road system responses under harmonic, impulse, and random road excitation using the SPC and RFRC tire models are computed and shown in Figs. 7.7, 7.8, 7.9, 7.10, 7.11, and 7.12. The dashed and solid lines represent the results of the SPC and RFRC tire models respectively.

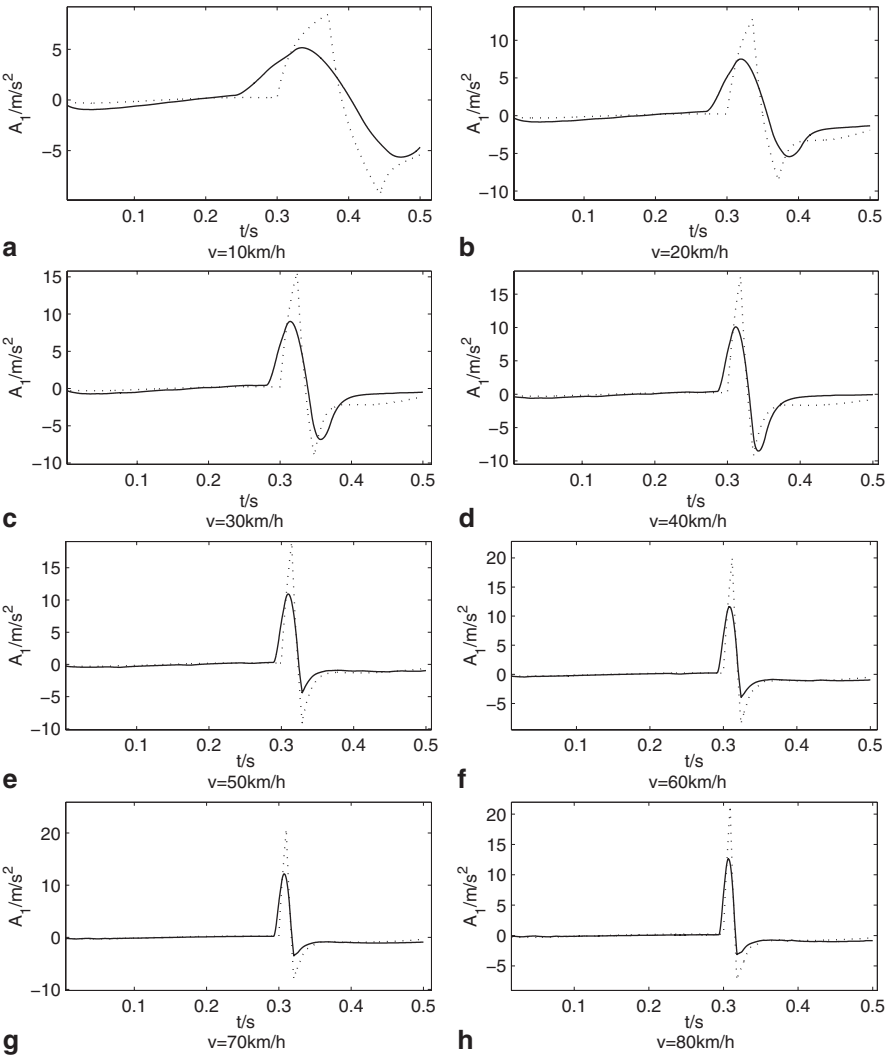

Fig. 7.5 Vehicle body vertical accelerations using two tire models. (Reprinted from ref. [4], with kind permission from Springer Science+Business Media)

1. *Harmonic response*s

With a road roughness harmonic wavelength of $L_0 = 10$ m and amplitude of $B_0 = 0.01$ m, the vehicle body acceleration A_1, suspension deformation *sd*, tire force F_t, pavement displacement w, and pavement acceleration A_r are all shown in Fig. 7.7. From Fig. 7.7 it can be seen that

1. Values derived for the vehicle body acceleration and tire force which are based on the proposed RFRC model are in general smaller than those based on the

Table 7.1 Maximum vehicle body vertical acceleration

Vehicle speed *(km/h)*	SPC model *(m/s^2)*	Error *(%)*	RFRC model *(m/s^2)*	Error *(%)*	Test data *(m/s^2)*
10	8.4540	+68.07	5.1627	+2.64	5.03
20	12.8837	+82.75	7.5082	+6.50	7.05
30	15.6314	+74.85	9.0087	+0.77	8.94
40	17.6742	+51.45	10.0967	−13.48	11.67
50	19.0164	+41.60	10.9328	−18.59	13.43
60	20.0244	+18.84	11.6198	−31.04	16.85
70	20.8145	+34.90	12.1762	−21.09	15.43
80	21.4072	+44.84	12.6114	−14.67	14.78

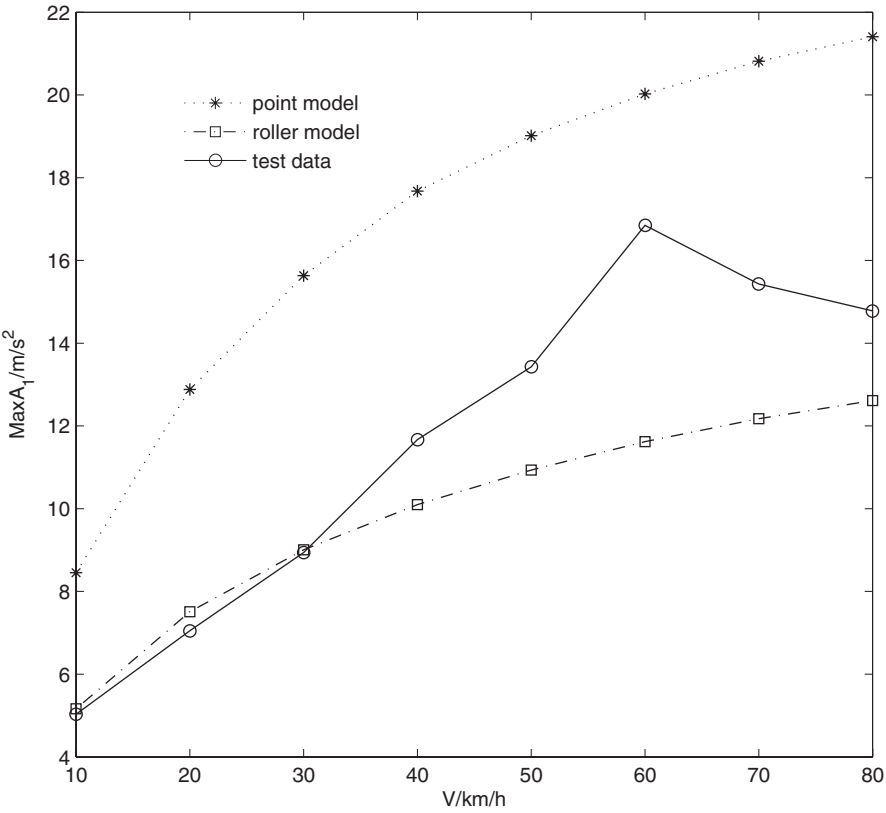

Fig. 7.6 Comparison between the two tire models and the test data

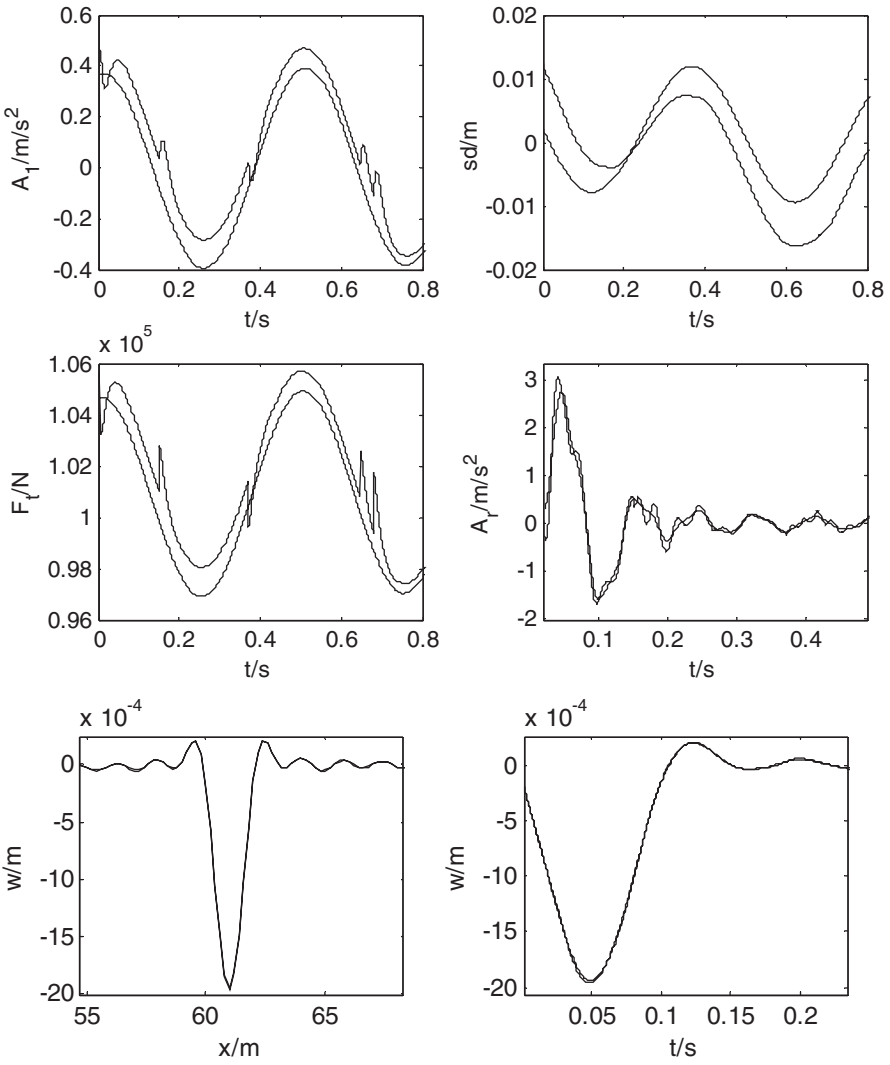

Fig. 7.7 Harmonic responses to basic parameters (L_0=10 m, B_0=0.01 m). (Reprinted from ref. [4], with kind permission from Springer Science+Business Media)

single point contact tire model. The reason may be that the flexible roller contact reflects the elastic characteristic of the tire.

2. Suspension deformation based on the RFRC tire model is different from that based on the SPC model. But the two results have the same varying rule.
3. The effect of tire models on pavement displacement is very small.
4. The effect of tire models on pavement acceleration is greater than on pavement displacement. The peak value of pavement acceleration based on the RFRC model is higher than that based on the SPC model. This may be explained by the

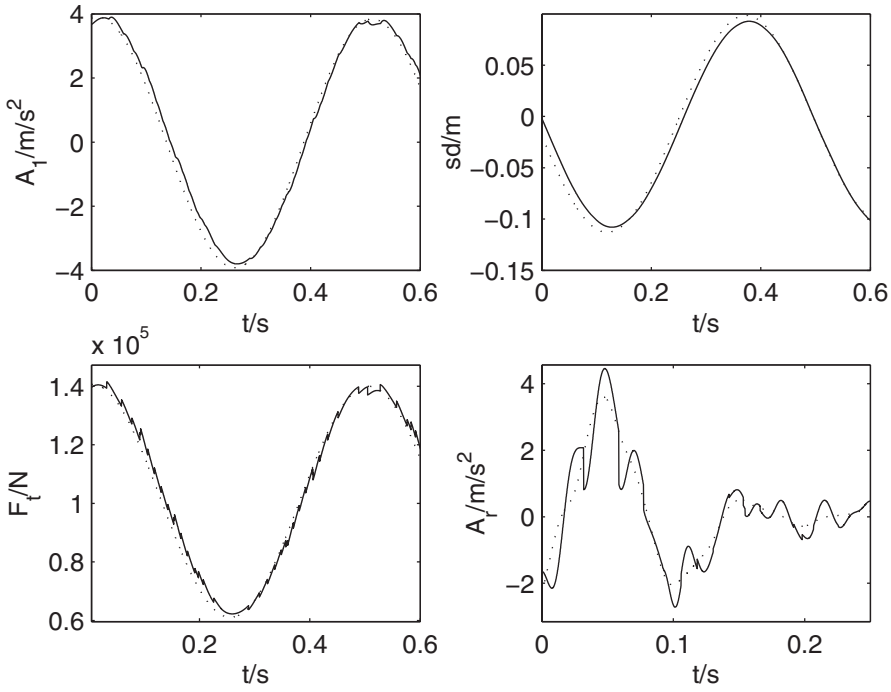

Fig. 7.8 Harmonic responses with $B_0 = 0.1$ m. (Reprinted from ref. [4], with kind permission from Springer Science+Business Media)

ability of the RFRC model to describe a tire jumping away from the pavement and then impacting it.

With a road surface roughness amplitude of $B_0 = 0.1$m and the remaining parameters being unchanged, the responses of the coupled system are shown in Fig. 7.8, from which it can be seen that

1. The effects of tire models on vehicle body acceleration, tire force, and suspension deformation decrease with the increase of the road surface roughness amplitude. Vehicle body acceleration, tire force, and suspension deformation based on the RFRC model are smaller than those based on the SPC model.
2. With the increase in the road surface roughness amplitude, the effect of the tire models on pavement acceleration increases.

With a road surface roughness wavelength of $L_0 = 2.3$m and the remaining parameters being unchanged, the coupled system responses are shown in Fig. 7.9, where it can be seen that

1. The effects of tire models on vehicle body acceleration, tire force, suspension deformation, and pavement acceleration increase with the decrease in the road surface roughness wave length.

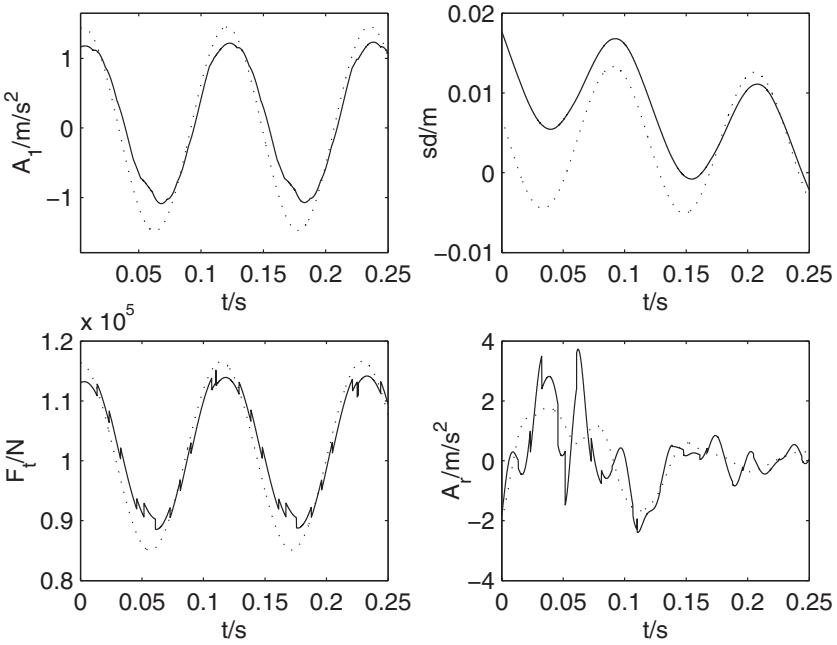

Fig. 7.9 Harmonic responses with $L_0 = 2.3$ m. (Reprinted from ref. [4], with kind permission from Springer Science+Business Media)

2. Vehicle body acceleration and tire force based on the flexible roller contact tire model are smaller than those based on the single contact tire model. The effect of tire models on suspension deformation becomes complicated.

With a vehicle running speed of $v = 40$ m/s, the responses of the coupled system are shown in Fig. 7.10, where it can be seen that

1. The effects of tire models on vehicle body acceleration, tire force, suspension deformation, and pavement acceleration increase with the increase in the vehicle running speed.
2. The effects of tire models on vehicle body acceleration, tire force, and suspension deformation become complicated. This is because the vehicle speed influences not only the frequency of road excitation but also the lengthwise position of the vehicle and pavement.

2. *Impulse responses*

According to GB5902-86, the height of the triangle protruding block for a heavy vehicle is 0.12 m. The impulse responses of the coupled system are shown in Fig. 7.11. From Fig. 7.11 it can be seen that

1. Peak values for vehicle body acceleration and tire force based on the RFRC tire model are much smaller than those based on the SPC tire model. The impulse

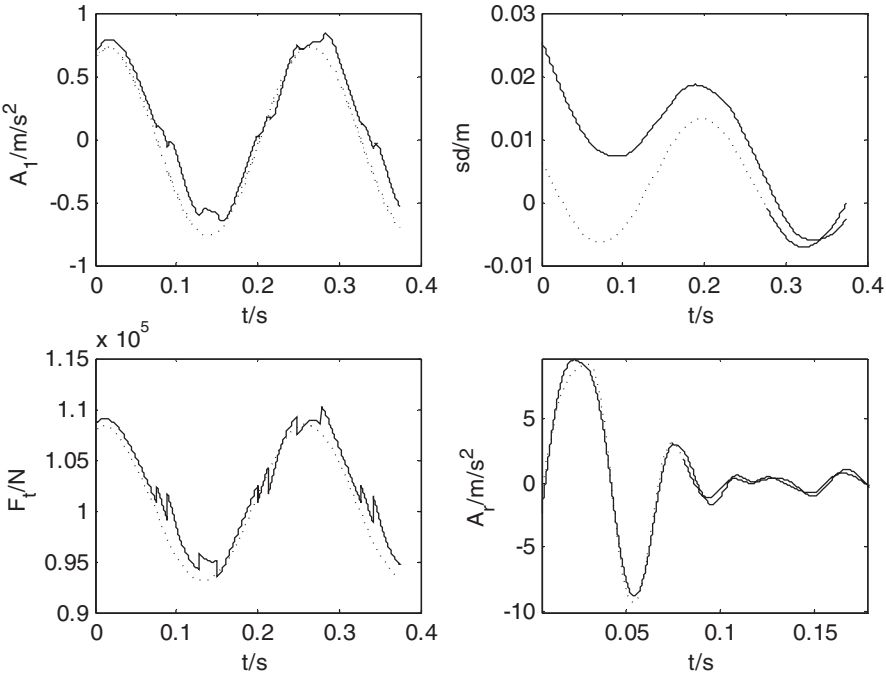

Fig. 7.10 Harmonic responses with v=40 m/s. (Reprinted from ref. [4], with kind permission from Springer Science+Business Media)

action time of the RFRC model is longer than that of the SPC model. This demonstrates that the RFRC tire model is able to reflect the tire's elastic deformation, geometric size, and vibration absorption.

2. Effect of tire models on suspension deformation is small. The peak value for suspension deformation based on the RFRC model is smaller than that based on the SPC tire model. The peak time value for suspension deformation obtained from the RFRC model lags behind that obtained from the SPC tire model.
3. The RFRC tire model's peak values for pavement displacement and acceleration are smaller than those of the SPC tire model. But the effect of tire models on pavement acceleration is greater than that of the pavement displacement. At different times and different positions, the pavement displacement and acceleration of the RFRC model may be larger or smaller than that of the SPC model.

3. *Stochastic responses*

According to GB7031-87 [9], the time-domain data of C-class road roughness is simulated with the method proposed by Liu [10]. The stochastic responses of the vehicle–road coupled system are shown in Fig. 7.12.

From Fig. 7.12 it can be seen that

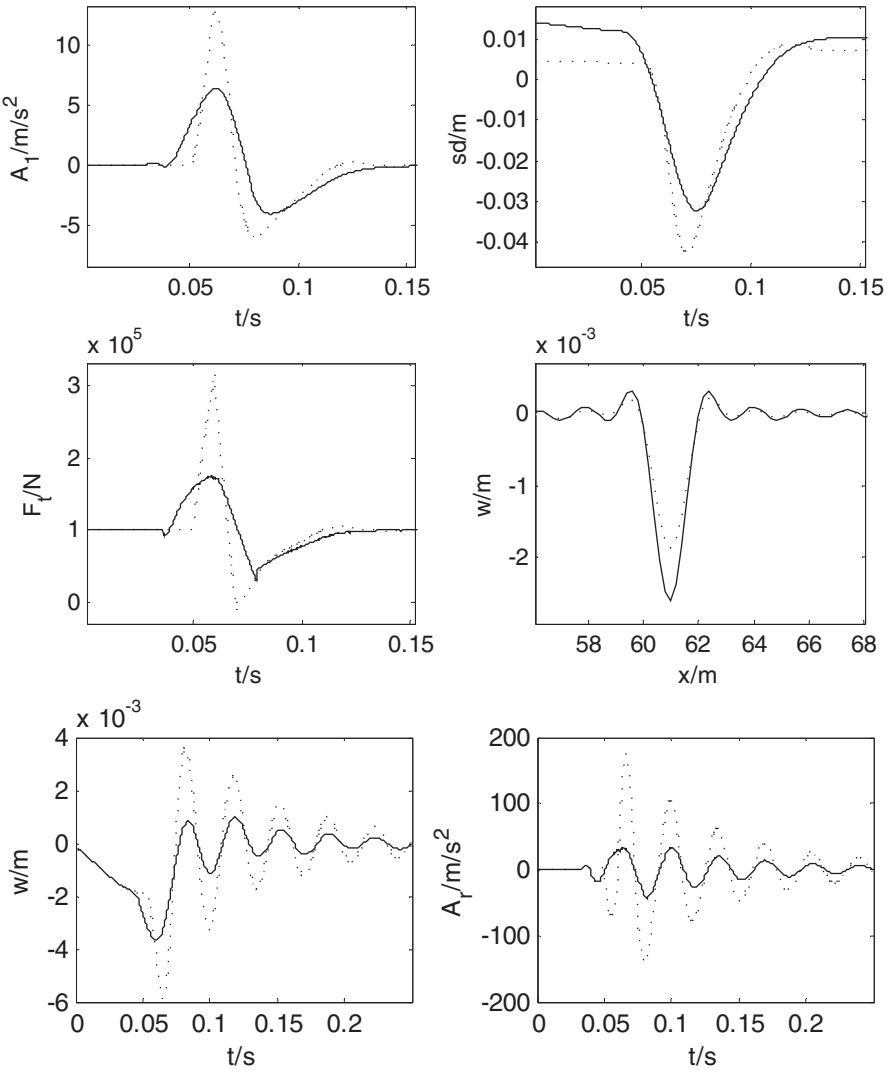

Fig. 7.11 Impulse responses of the vehicle–road coupled system. (Reprinted from ref. [4], with kind permission from Springer Science+Business Media)

1. The effects of tire models on the stochastic responses of the vehicle–road coupled system are greater than that on the harmonic responses.
2. The peak values of the vehicle body responses and tire force obtained by the RFRC model are much smaller than that by the SPC model.
3. The peak value of suspension deformation obtained by the RFRC model is smaller than that obtained by the SPC model. The peak time value for suspension

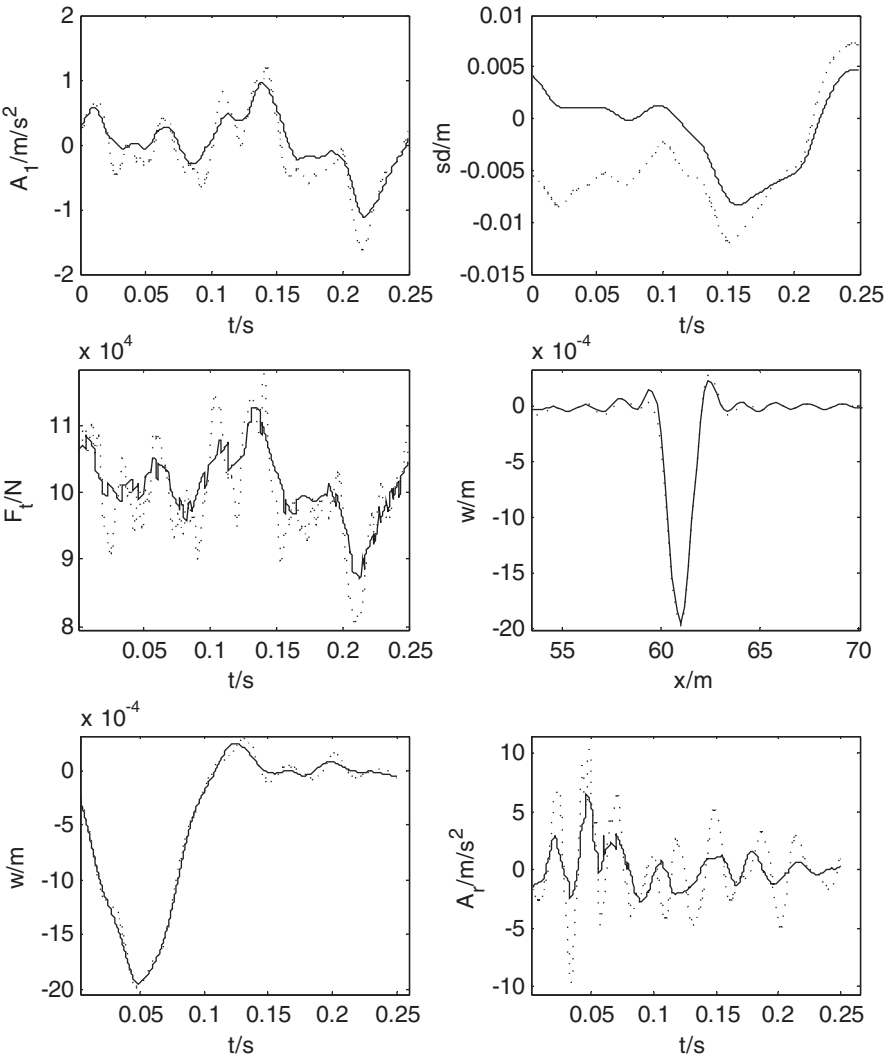

Fig. 7.12 Stochastic responses of the vehicle–road coupled system

deformation obtained from the RFRC model lags behind that from the SPC tire model.

4. The RFRC tire model's peak value for pavement displacement and acceleration are smaller than those of the SPC tire model. But the effect of tire models on pavement acceleration is greater than that of the pavement displacement. At different times and different positions, the RFRC model's pavement displacement and acceleration may be larger or smaller than the SPC model.

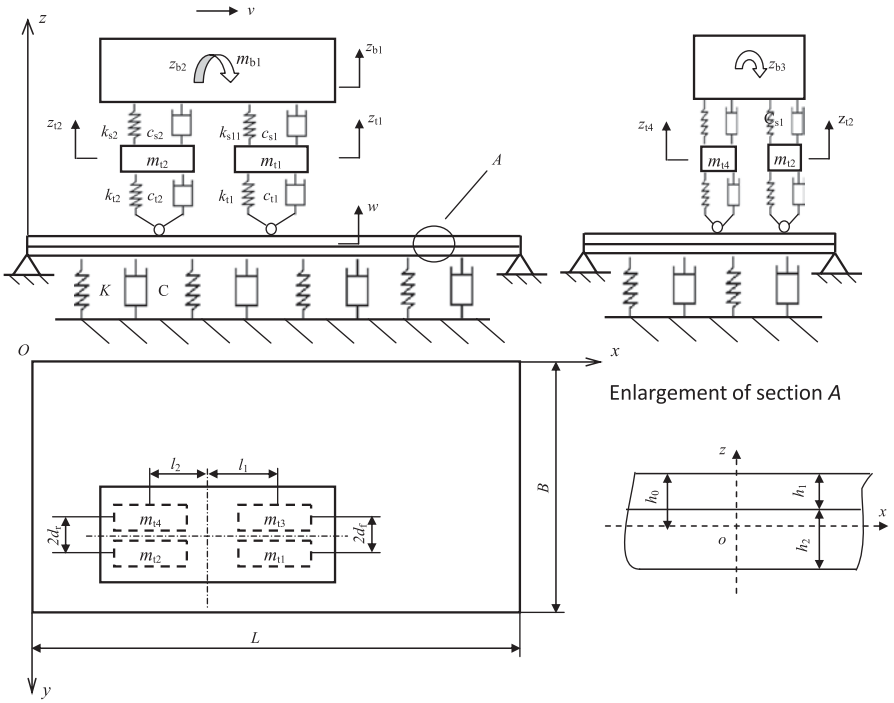

Fig. 7.13 The three-dimensional vehicle–road coupled system. (Reprinted from ref. [11] by permission of Taylor & Francis Ltd)

7.3 Modeling of a Three-Dimensional Vehicle–Road Coupled System

The three-dimensional (3D) vehicle–road coupled system considered in this work is shown in Fig. 7.13. A seven DOF vehicle and a double-layer rectangular thin plate on a viscoelastic foundation with four simply supported boundaries are employed to model the vehicle and pavement. The upper layer of the plate models an asphalt topping, the lower layer models the base course, and the viscoelastic foundation stands for the sub grade of the pavement. The pavement roughness is assumed to be sinusoidal and the material for the topping and base course is assumed to be isotropic and elastic. The vehicle is moving along the plate at a constant velocity in a lengthwise direction.

7.3.1 Equations of Motion for the Vehicle

The vehicle equations can be obtained by using Dalembert's principle.

The vertical vibration equation for the vehicle body is

$$\begin{aligned}
&m_{b1}\ddot{z}_{b1}+c_{s1}(\dot{z}_{b1}-\dot{z}_{t1}-\dot{z}_{b2}l_1-\dot{z}_{b3}d_f)+k_{s1}(z_{b1}-z_{t1}-z_{b2}l_1-z_{b3}d_f)\\
&+c_{s2}(\dot{z}_{b1}-\dot{z}_{t2}+\dot{z}_{b2}l_2-\dot{z}_{b3}d_r)+k_{s1}(z_{b1}-z_{t2}+z_{b2}l_2-z_{b3}d_r)\\
&+c_{s3}(\dot{z}_{b1}-\dot{z}_{t3}-\dot{z}_{b2}l_1+\dot{z}_{b3}d_f)+k_{s1}(z_{b1}-z_{t3}-z_{b2}l_1+z_{b3}d_f)\\
&+c_{s4}(\dot{z}_{b1}-\dot{z}_{t4}+\dot{z}_{b2}l_2+\dot{z}_{b3}d_r)+k_{s4}(z_{b1}-z_{t4}+z_{b2}l_2+z_{b3}d_r)=0
\end{aligned} \tag{7.25}$$

The pitch vibration equation for the vehicle body is

$$\begin{aligned}
&m_{b2}\ddot{z}_{b2}-l_1c_{s1}(\dot{z}_{b1}-\dot{z}_{t1}-\dot{z}_{b2}l_1-\dot{z}_{b3}d_f)-l_1k_{s1}(z_{b1}-z_{t1}-z_{b2}l_1-z_{b3}d_f)\\
&+l_2c_{s2}(\dot{z}_{b1}-\dot{z}_{t2}+\dot{z}_{b2}l_2-\dot{z}_{b3}d_r)+l_2k_{s2}(z_{b1}-z_{t2}+z_{b2}l_2-z_{b3}d_r)\\
&-l_1c_{s3}(\dot{z}_{b1}-\dot{z}_{t3}-\dot{z}_{b2}l_1+\dot{z}_{b3}d_f)-l_1k_{s3}(z_{b1}-z_{t3}-z_{b2}l_1+z_{b3}d_f)\\
&+l_2c_{s4}(\dot{z}_{b1}-\dot{z}_{t4}+\dot{z}_{b2}l_2+\dot{z}_{b3}d_r)+l_2k_{s4}(z_{b1}-z_{t4}+z_{b2}l_2+z_{b3}d_r)=0
\end{aligned} \tag{7.26}$$

The rolling vibration equation for the vehicle body is

$$\begin{aligned}
&m_{b3}\ddot{z}_{b3}-d_fc_{s1}(\dot{z}_{b1}-\dot{z}_{t1}-\dot{z}_{b2}l_1-\dot{z}_{b3}d_f)-d_fk_{s1}(z_{b1}-z_{t1}-z_{b2}l_1-z_{b3}d_f)\\
&-d_rc_{s2}(\dot{z}_{b1}-\dot{z}_{t2}+\dot{z}_{b2}l_2-\dot{z}_{b3}d_r)-d_rk_{s2}(z_{b1}-z_{t2}+z_{b2}l_2-z_{b3}d_r)\\
&+d_fc_{s3}(\dot{z}_{b1}-\dot{z}_{t3}-\dot{z}_{b2}l_1+\dot{z}_{b3}d_f)+d_fk_{s3}(z_{b1}-z_{t3}-z_{b2}l_1+z_{b3}d_f)\\
&+d_rc_{s4}(\dot{z}_{b1}-\dot{z}_{t4}+\dot{z}_{b2}l_2+\dot{z}_{b3}d_r)+d_rk_{s4}(z_{b1}-z_{t4}+z_{b2}l_2+z_{b3}d_r)=0
\end{aligned} \tag{7.27}$$

The vertical vibration equation for the right front wheel is

$$\begin{aligned}
&m_{t1}\ddot{z}_{t1}-c_{s1}(\dot{z}_{b1}-\dot{z}_{t1}-\dot{z}_{b2}l_1-\dot{z}_{b3}d_f)-k_{s1}(z_{b1}-z_{t1}-z_{b2}l_1-z_{b3}d_f)\\
&+F_{t1}=0
\end{aligned} \tag{7.28}$$

The vertical vibration equation for the right rear wheel is

$$\begin{aligned}
&m_{t2}\ddot{z}_{t2}-c_{s2}(\dot{z}_{b1}-\dot{z}_{t2}+\dot{z}_{b2}l_2-\dot{z}_{b3}d_r)-k_{s2}(z_{b1}-z_{t3}+z_{b2}l_2-z_{b3}d_r)\\
&+F_{t2}=0
\end{aligned} \tag{7.29}$$

The vertical vibration equation for the left front wheel is

$$\begin{aligned}
&m_{t3}\ddot{z}_{t3}-c_{s3}(\dot{z}_{b1}-\dot{z}_{t3}-\dot{z}_{b2}l_1+\dot{z}_{b3}d_f)-k_{s3}(z_{b1}-z_{t3}-z_{b2}l_1+z_{b3}d_f)\\
&+F_{t3}=0
\end{aligned} \tag{7.30}$$

The vertical vibration equation for the left rear wheel is

$$\begin{aligned}
&m_{t4}\ddot{z}_{t4}-c_{s4}(\dot{z}_{b1}-\dot{z}_{t4}+\dot{z}_{b2}l_2+\dot{z}_{b3}d_r)-k_{s4}(z_{b1}-z_{t4}+z_{b2}l_2+z_{b3}d_r)\\
&+F_{t4}=0
\end{aligned} \tag{7.31}$$

where z_{b1}, z_{b2}, z_{b3} are the vehicle body's vertical, pitching and rolling displacements. z_{t1}, z_{t2}, z_{t3}, z_{t4} are the wheel's vertical displacements. mb_1 is the mass of the vehicle body, and mb_2 and mb_3 are the moment of inertia of the vehicle body in the pitching

and rolling directions respectively. $c_{s1} \sim c_{s4}$ are the suspension damping coefficients, $k_{s1} \sim k_{s4}$ are the suspension stiffness's, $m_{t1} \sim m_{t4}$ are the wheel's masses, and $F_{t1} \sim F_{t4}$ are the tire forces. d_f is half of the front wheel track, d_t is half of the rear wheel track and $l_1 + l_2$ is the wheel space.

The above vehicle equations can be rewritten in matrix form,

$$M_v \ddot{Z}_v + C_v \dot{Z}_v + K_v Z_v = R_v \tag{7.32}$$

where

$$M_v = diag[m_{b1} \quad m_{b2} \quad m_{b3} \quad m_{t1} \quad m_{t2} \quad m_{t3} \quad m_{t4}] \tag{7.33}$$

$$K_v = \begin{bmatrix} \sum_{i=1}^{4} k_{si} & \begin{matrix} -k_{s1}l_1 + k_{s2}l_2 - \\ k_{s3}l_1 + k_{s4}l_2 \end{matrix} & \begin{matrix} -k_{s1}d_f - k_{s2}d_r + \\ k_{s3}d_f + k_{s4}d_r \end{matrix} & -k_{s1} & -k_{s2} & -k_{s3} & -k_{s4} \\ & \begin{matrix} k_{s1}l_1^2 + k_{s2}l_2^2 + \\ k_{s3}l_1^2 + k_{s4}l_2^2 \end{matrix} & \begin{matrix} k_{s1}l_1 d_f - k_{s2}l_2 d_r - \\ k_{s3}l_1 d_f + k_{s4}l_2 d_r \end{matrix} & k_{s1}l_1 & -k_{s2}l_2 & k_{s3}l_1 & -k_{s4}l_2 \\ & & \begin{matrix} k_{s1}d_f^2 + k_{s2}d_r^2 + \\ k_{s3}d_f^2 + k_{s4}d_r^2 \end{matrix} & k_{s1}d_f & k_{s2}d_r & -k_{s3}d_f & -k_{s4}d_r \\ & & & k_{s1} & 0 & 0 & 0 \\ & & & & k_{s2} & 0 & 0 \\ & & & & & k_{s3} & 0 \\ & & & & & & k_{s4} \end{bmatrix} \tag{7.34}$$

Symmetric

$$C_v = \begin{bmatrix} \sum_{i=1}^{4} c_{si} & \begin{matrix} -c_{s1}l_1 + c_{s2}l_2 - \\ c_{s3}l_1 + c_{s4}l_2 \end{matrix} & \begin{matrix} -c_{s1}d_f - c_{s2}d_r + \\ c_{s3}d_f + c_{s4}d_r \end{matrix} & -c_{s1} & -c_{s2} & -c_{s3} & -c_{s4} \\ & \begin{matrix} c_{s1}l_1^2 + c_{s2}l_2^2 + \\ c_{s3}l_1^2 + c_{s4}l_2^2 \end{matrix} & \begin{matrix} c_{s1}l_1 d_f - c_{s2}l_2 d_r - \\ c_{s3}l_1 d_f + c_{s4}l_2 d_r \end{matrix} & c_{s1}l_1 & -c_{s2}l_2 & c_{s3}l_1 & -c_{s4}l_2 \\ & & \begin{matrix} c_{s1}d_f^2 + c_{s2}d_r^2 + \\ c_{s3}d_f^2 + c_{s4}d_r^2 \end{matrix} & c_{s1}d_f & c_{s2}d_r & -c_{s3}d_f & -c_{s4}d_r \\ & & & c_{s1} & 0 & 0 & 0 \\ & & & & c_{s2} & 0 & 0 \\ & & & & & c_{s3} & 0 \\ & & & & & & c_{s4} \end{bmatrix} \tag{7.35}$$

Symmetric

$$R_v = [0 \quad 0 \quad 0 \quad -F_{t1} \quad -F_{t2} \quad -F_{t3} \quad -F_{t4}]^T \tag{7.36}$$

$$Z_v = [z_{b1} \quad z_{b2} \quad z_{b3} \quad z_{t1} \quad z_{t2} \quad z_{t3} \quad z_{t4}]^T \tag{7.37}$$

7.3.2 Equations of Motion for the Road

The two layers' height, elastic modulus, shear modulus, Poisson ratio, and density are symbolized by h_1, h_2, E_1, E_2, G_1, G_2, μ_1, μ_2, ρ_1, and ρ_2. Let h_0 be the distance between the stress neutral layer and the upper surface of the double-layer plate. Take the stress neutral layer as the coordinate axial x and vertical direction as coordinate axial z. The coordinate system is built, as shown in Fig. 7.13.

The partial differential equation of the double-layer thin plate on the viscoelastic foundation subjected to moving vehicle loads can be gained

$$\begin{aligned} &D\left(\frac{\partial^4 w}{\partial x^4}+\frac{\partial^4 w}{\partial y^4}\right)+2(D_{xy}+2D_k)\frac{\partial^4 w}{\partial x^2\partial y^2}+\rho h\frac{\partial^2 w}{\partial t^2}+Kw+C\frac{\partial w}{\partial t} \\ &=\sum_{s=1}^{4}F_{ts}\delta(x-x_{ts})\delta(y-y_{ts}) \end{aligned} \tag{7.38}$$

where, F_{ts} is the s-th wheel's tire force.

The displacement of the double-layer thin plate with four simply supported boundaries can be expressed as

$$w(x,y,t)=\sum_{m=1}^{NM}\sum_{n=1}^{NN}U_{mn}(t)\sin\frac{m\pi x}{L}\sin\frac{n\pi y}{B} \tag{7.39}$$

where, L and B are the pavement's length and width.

Substituting Eq. (7.39) into Eq. (7.38) leads to the residual value R,

$$\begin{aligned} R=&D\left(\frac{\partial^4 w}{\partial x^4}+\frac{\partial^4 w}{\partial y^4}\right)+2(D_{xy}+2D_k)\frac{\partial^4 w}{\partial x^2\partial y^2}+\rho h\frac{\partial^2 w}{\partial t^2}+Kw+C\frac{\partial w}{\partial t} \\ &-\sum_{i=1}^{4}F_{ti}\delta(x-x_{ti})\delta(y-y_{ti}) \end{aligned} \tag{7.40}$$

By limiting the residual value R the following equation can be got by Galerkin's method

$$\int_0^L\int_0^B R\sin(i\pi x/L)\sin(j\pi y/B)dxdy=0 \tag{7.41}$$

As a simplification of the above equation, Eq. (7.38) can be discretized as a set of ordinary differential equations

$$M_{mn}\ddot{U}_{mn}+C_{mn}\dot{U}_{mn}+K_{mn}U_{mn}=R_{mn} \tag{7.42}$$

where $m=1\sim NM$, $n=1\sim NN$,

$$M_{mn}=\frac{LB}{4}\rho h, \tag{7.43}$$

$$C_{mn} = \frac{LB}{4}C, \tag{7.44}$$

$$K_{mn} = \left[D\left(\left(\frac{m\pi}{L} \right)^4 + \left(\frac{n\pi}{B} \right)^4 \right) + 2\left(D_{xy} + 2D_k \right) \left(\frac{m\pi}{L} \right)^2 \left(\frac{n\pi}{B} \right)^2 + K \right] \frac{LB}{4} \tag{7.45}$$

$$R_{mn} = \int_0^L \int_0^B \sum_{s=1}^{4} F_{ts} \delta\left(x - x_{ts} \right) \delta\left(y - y_{ts} \right) \sin(m\pi x / L) \sin(n\pi y / B)\, dx dy \tag{7.46}$$

7.3.3 Interaction Between the Vehicle and the Road

The vertical contact force between the tire and the pavement is related to not only tire motion and road surface roughness but also road vibration. Thus the vertical contact force between the tire and the pavement can be expressed as

$$F_{ts} = k_{ts}\left[x_{ts} - r_{ts} - w(x_{ts}, y_{ts}, t) \right] + c_{ts}\left[\dot{x}_{ts} - \dot{r}_{ts} - \frac{\partial w(x_{ts}, y_{ts}, t)}{\partial t} \right] \tag{7.47}$$

where $s = 1 \sim 4$ and r_{ts} is the road surface roughness satisfying the following functions

$$\begin{aligned} r_{t1} &= r_{t3} = B_0 \sin\left(\frac{2\pi v t}{L_0} \right), \\ r_{t2} &= r_{t4} = B_0 \sin\left[\frac{2\pi}{L_0}\left(vt + l_1 + l_2 \right) \right] \end{aligned} \tag{7.48}$$

Where, B_0 is the amplitude of the road surface roughness, and L_0 is the wavelength of the road roughness.

Substituting Eq. (7.39) into Eq. (7.47), one gets

$$\begin{aligned} F_{ts} = {} & k_{ts}(z_{ts} - r_{ts}) + c_{ti}(\dot{z}_{ts} - \dot{r}_{ts}) - k_{ts} \sum_{m=1}^{NM} \sum_{n=1}^{NN} U_{mn}(t) \sin\frac{m\pi x}{L} \sin\frac{n\pi y}{B} \\ & - c_{ts} \sum_{m=1}^{NM} \sum_{n=1}^{NN} \dot{U}_{mn}(t) \sin\frac{m\pi x}{L} \sin\frac{n\pi y}{B} \\ & - c_{ts} \sum_{m=1}^{NM} \sum_{n=1}^{NN} U_{mn}(t) \frac{m\pi v}{L} \cos\frac{m\pi x}{L} \sin\frac{n\pi y}{B} \end{aligned} \tag{7.49}$$

Substituting Eq. (7.39) into Eq. (7.46) leads to

$$R_{mn}=\int_0^L\int_0^B\sum_{s=1}^{4}\begin{bmatrix}k_{ts}(z_{ts}-r_{ts})+c_{ts}(\dot{z}_{ts}-\dot{r}_{ts})\\-k_{ts}\sum_{m=1}^{NM}\sum_{n=1}^{NN}U_{mn}(t)\sin\frac{m\pi x}{L}\sin\frac{n\pi y}{B}\\-c_{ts}\sum_{m=1}^{NM}\sum_{n=1}^{NN}\dot{U}_{mn}(t)\sin\frac{m\pi x}{L}\sin\frac{n\pi y}{B}\\-c_{ts}\sum_{m=1}^{NM}\sum_{n=1}^{NN}U_{mn}(t)\frac{m\pi v}{L}\cos\frac{m\pi x}{L}\sin\frac{n\pi y}{B}\end{bmatrix}\delta(x-x_{ts})\,\delta(y-y_{ts})\sin(m\pi x/L)\sin(n\pi y/B)\,dxdy \tag{7.50}$$

It is clear that the contact force between tire and pavement is influenced not only by wheel displacement, wheel velocity and road roughness, but also by the pavement vibration mode's displacement and velocity. In addition, the force upon the pavement is related to wheel track and wheel spacing. Equations (7.32) and (7.42) will compose the ordinary differential equations of the vehicle–road coupled system.

Omitting the coupling action of the vehicle and the pavement, one can simplify the contact forces between tire and pavement

$$\hat{F}_{ts}=k_{ts}\left(x_{ts}-r_{ts}\right)+c_{ts}\left(\dot{x}_{ts}-\dot{r}_{ts}\right) \tag{7.51}$$

$$\begin{aligned}\hat{R}_{mn}&=\int_0^L\int_0^B\sum_{s=1}^{4}\left[k_{ts}(z_{ts}-r_{ts})+c_{ts}(\dot{z}_{ts}-\dot{r}_{ts})\right]\\&\delta\left(x-x_{ts}\right)\delta\left(y-y_{ts}\right)\sin(m\pi x/L)\sin(n\pi y/B)dxdy\end{aligned} \tag{7.52}$$

The coupled system equations take the following expression

$$[M]\{\ddot{Z}\}+[C]\{\dot{Z}\}+[K]\{Z\}=\{R\} \tag{7.53}$$

where, $[M]$, $[C]$, $[K]$ are the matrices of mass, damping, and stiffness respectively. $\{Z\}$ and $\{R\}$ are displacements and force excitations of the vehicle–pavement coupled system respectively, which are expressed by

$$\{Z\}_i=\begin{cases}\{Z_v\}_i & i=1\sim 7\\ U_{mn} & i=8\sim NM\times NN+7\end{cases} \tag{7.54}$$

$$\{R\}_i=\begin{cases}0 & i=1\sim 3\\ \hat{F}_{ts} & i=4\sim 7, s=i-3\\ \hat{R}_{mn} & i=8\sim NM\times NN+7\end{cases} \tag{7.55}$$

Here, i, m, and n are subscripts, and the relation of Z_i and U_{mn} is shown in Table 7.2.

$[C]$ and $[K]$ are the damping and the stiffness matrixes of the vehicle–pavement coupled system, and the configuration of $[K]$ for the coupled system is

Table 7.2 Relation of Z_i and U_{mn}. (Reprinted from ref. [11] by permission of Taylor & Francis Ltd)

I	N				
M	1	2	…	NM×NN-1	NM×NN
1	8	9		NM×NN+6	NM×NN+7
2	NM×NN+8	NM×NN+9		2×NM×NN+6	2×NM×NN+7
⋮					
NM×NN-1	(NM×NN-2)×(NM×NN)+8	(NM×NN-2)×(NM×NN)+9		(NM×NN-1)×(NM×NN)+6	(NM×NN-1)×(NM×NN)+7
NM×NN	(NM×NN-1)×(NM×NN)+8	(NM×NN-1)×(NM×NN)+9		(NM×NN)×(NM×NN)+6	(NM×NN)×(NM×NN)+7

$$[K]=$$

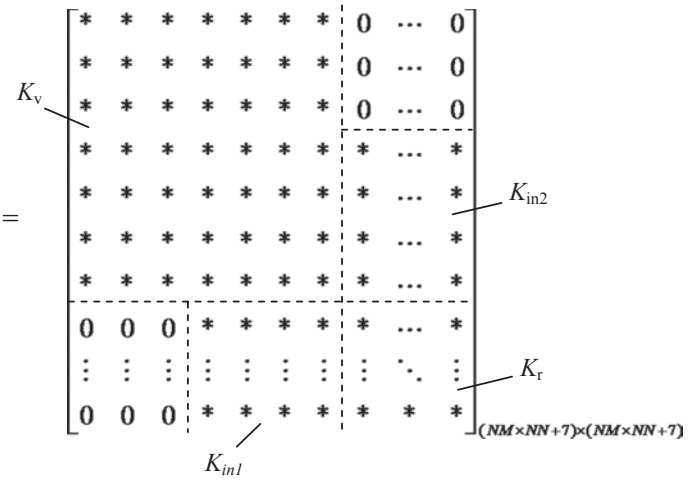

where, K_v is the stiffness matrix of the vehicle subsystem, K_r is the stiffness matrix of the pavement subsystem, K_{in1} and K_{in2} are the coupled stiffness matrixes between the vehicle and pavement.

K_v is expressed by Eq. (7.34). Diagonal elements of K_r are expressed by

$$\begin{aligned}[K_r]_{ii} &= K_{mn} + \sum_{s=1}^{4} k_{ts}\left(\sin\frac{m\pi x_{ts}}{L}\sin\frac{n\pi y_{ts}}{B}\right)^2 \\ &+ \sum_{s=1}^{4} c_{ts}\frac{m\pi v}{L}\cos\frac{m\pi x_{ts}}{L}\sin\frac{m\pi x_{ts}}{L}\left(\sin\frac{n\pi y_{ts}}{B}\right)^2\end{aligned} \tag{7.56}$$

where, $i = 8 \sim NM \times NN + 7$. The value of *m* and *n* can be determined by *i* according to Table 7.2.

Off-diagonal elements of K_r are expressed by

$$\begin{aligned}\left[K_r\right]_{ij} &= \sum_{s=1}^{4} k_{ts} \sin\frac{\bar{m}\pi x_{ts}}{L}\sin\frac{\bar{n}\pi y_{ts}}{B}\sin\frac{m\pi x_{ts}}{L}\sin\frac{n\pi y_{ts}}{B} \\ &+ \sum_{s=1}^{4} c_{ts}\frac{\bar{m}\pi v}{L}\cos\frac{\bar{m}\pi x_{ts}}{L}\sin\frac{\bar{n}\pi y_{ts}}{B}\sin\frac{m\pi x_{ts}}{L}\sin\frac{n\pi y_{ts}}{B}\end{aligned} \tag{7.57}$$

where, $i = 8 \sim NM \times NN + 7$, $j = 8 \sim NM \times NN + 7$, and $i \neq j$. The value of m and n can be decided by i and the value of $\bar{m}$ and $\bar{n}$ can be determined by j according to Table 7.2.

K_{in1} and K_{in2} are symmetric and the expression of K_{in1} is

$$[K_{in1}]_{ij} = -k_{ts}\sin\frac{m\pi x_{ts}}{L}\sin\frac{n\pi y_{ts}}{B} - c_{ts}\cos\frac{m\pi x_{ts}}{L}\sin\frac{n\pi y_{ts}}{B} \tag{7.58}$$

where, $i = 8 \sim NM \times NN + 7, j = 4 \sim 7, s = j - 3$ The value of m and n can be determined by i according to Table 7.2.

Since K_{r}, K_{in1}, and K_{in2} are related to the tire positions x_{ts} and y_{ts} $[K]$ is a time-varying matrix. With the same configuration as $[K]$, $[C]$ is also a time-varying matrix.

The configuration of $[K]$ for a separated system is

$$[K]=\left[\begin{array}{ccccccc:ccc} * & * & * & * & * & * & * & 0 & \cdots & 0 \\ * & * & * & * & * & * & * & 0 & \cdots & 0 \\ * & * & * & * & * & * & * & 0 & \cdots & 0 \\ * & * & * & * & * & * & * & 0 & \cdots & 0 \\ * & * & * & * & * & * & * & 0 & \cdots & 0 \\ * & * & * & * & * & * & * & 0 & \cdots & 0 \\ * & * & * & * & * & * & * & 0 & \cdots & 0 \\ \hdashline 0 & 0 & 0 & 0 & 0 & 0 & 0 & * & \cdots & * \\ \vdots & \vdots & \vdots & \vdots & \vdots & \vdots & \vdots & \vdots & \ddots & \vdots \\ 0 & 0 & 0 & 0 & 0 & 0 & 0 & * & * & * \end{array}\right]_{(NM\times NN+7)\times(NM\times NN+7)}$$

K_{v} K_{r}

By comparing the stiffness and damping matrix configurations for a coupled system and a separated system, the difference between these two systems is whether to consider the coupling of the tire and pavement displacements, namely, whether the coefficients K_{ij}, K_{ji} C_{ij} and C_{ji} $(i = 8 \sim NM \times NN + 7, j = 4 \sim 7)$ are all zero. Due to the high dimensional matrix and time-varied parameters, the equations are solved by direct numerical integration.

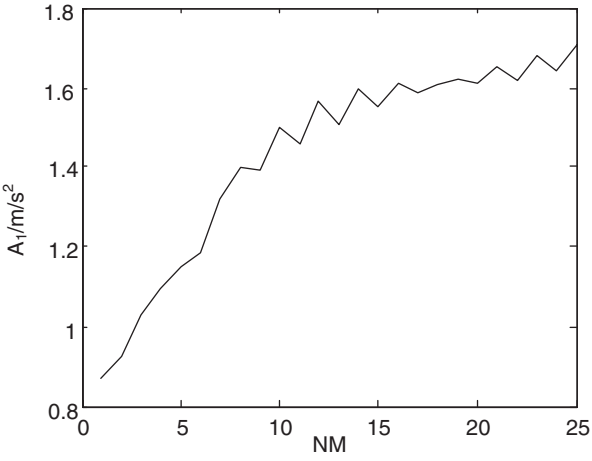

Fig. 7.14 The effects of the mode number on vehicle body acceleration

7.4 Response Comparison of the Coupled System with the Traditional Separated System

Parameters for the heavy vehicle system are chosen as follows [11, 12]:

$m_{b1}=21{,}260$ kg, $m_{b2}=3\times10^5$ kg · m^2, $m_{b3}=0.6\times10^5$ kg · m^2, $m_{t1}=m_{t3}=220$ kg, $m_{t2}=m_{t4}=1500$kg, $k_{s1}=k_{s3}=2\times10^6$N/m, $k_{s2}=k_{s4}=5\times10^6$N/m, $c_{s1}=c_{s3}=5000$N · s/m, $c_{s2}=c_{s4}=40{,}000$ N · s/m, $k_{t1}=k_{t3}=1.73\times10^6$ N/m, $k_{t2}=k_{t4}=4.6\times10^6$ N/m, $c_{t1}=c_{t3}=1200$ N · s/m, $c_{t2}=c_{t4}=4300$ N · s/m。

Parameters for the pavement and foundation are chosen as follows [13, 14]:

$h_1=0.1$ m, $\mu_1=0.25$, $E_1=1600$ MPa, $\rho_1=2.5\times10^3$ kg/m^3, $h_2=0.2$ m, $E_2=700$ MPa, $\mu_2=0.25$, $\rho_2=2.2\times10^3$ kg/m^3, $K=8\times10^6$ N/m^3, $C=0.3\times10^5$ N · s/m^2, $v=20$ m/s, $B_0=0.002$ m, $L_0=10$ m, $L=160$ m, $B=24$ m。

To confirm the validity of the integration results, two numerical tests have been done for choosing a suitable mode number for the pavement and integral time step. The effects of the mode number on the vertical accelerations of the vehicle body and pavement are shown in Figs. 7.14 and 7.15. It is found that when the mode number of the pavement is larger than 20, system dynamic responses change very little. Thus, the suitable value of NM is 20. With a similar numerical test, the suitable value for Δt can be obtained as 0.1 ms.

By comparing the dynamics of the coupled vehicle–pavement-foundation system with that of a traditional system, the effect of coupling action on vehicle body acceleration, tire forces, suspension deformations, and pavement displacements can be found.

In order to minimize effects of initial conditions and boundary conditions, three techniques are applied. First, integrate the system equations with zero initial conditions from t=0 to t=0.25 s, which means a vehicle begins running from the position of x=75 m to x=80 m at a velocity of 20 m/s. Then, let t=0 and choose for the initial condition displacements and velocities at a time where the vehicle passing

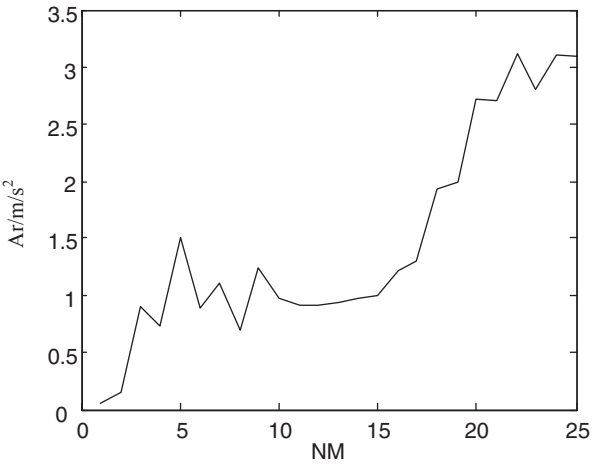

Fig. 7.15 The effects of the mode number on pavement acceleration

position is x = 80 m. Finally, integrate the system equations again. Thus the dynamic response of a coupled system and a traditional system can be obtained, as shown in Figs. 7.16, 7.17, 7.18, and 7.19. Solid lines represent the coupled system's response and dashed lines represent the traditional system's response.

Figure 7.16 shows the vertical, pitch and roll acceleration of the vehicle body, and vertical displacement of the pavement at the position of y = 18 m when $t = 0.08\text{s}$. In Fig. 4, the road surface roughness amplitude is $B_0 = 0.002\text{m}$ and the foundation reaction modulus is $K = 8\times10^6\,\text{N/m}^3$. From Fig. 7.16 it can be seen that

1. Vehicle–pavement coupling affects the vertical acceleration of the vehicle body most largely. The coupled system amplitude of vertical acceleration is 26% larger than that of the traditional system.
2. The effect of the coupling action on pitching acceleration of the vehicle body and vertical displacement of the pavement is very small.
3. Though road surface roughness used in this work does not change in traverse direction *y*, the coupled system can reflect the roll acceleration of the vehicle body. However, the effect of the coupled action on the roll acceleration of the vehicle body needs further investigation.

Let road surface roughness amplitude of $B_0 = 0.01\text{m}$. Accelerations of the vehicle body and vertical displacement of the pavement are shown in Fig. 7.17. Comparing Fig. 7.16 with Fig. 7.17, one can find that

1. The amplitude of vertical acceleration for a coupled system is 5.0% larger than that for a traditional system, but the amplitude of the pavement displacement for a coupled system is 18.9% smaller than that for a traditional system.
2. With the increase of road surface roughness amplitude, the effect of coupling action on vehicle body accelerations decrease, but the effect of coupling action on pavement displacement increase.

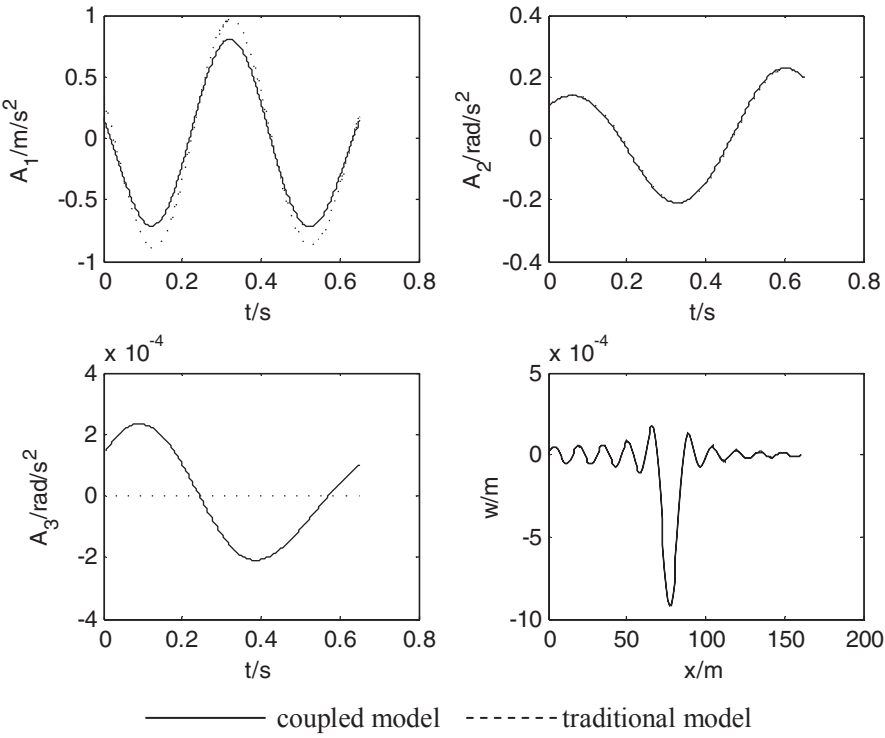

Fig. 7.16 Vehicle body accelerations with B_0=0.002 m. (Reprinted from ref. [11] by permission of Taylor & Francis Ltd)

3. The effect of the coupled action on the vertical displacement of the pavement is much larger at a position where the vehicle is passing than at other positions.

Figure 7.18 shows suspension deformations between vehicle body and right front wheel, right rear wheel, left front wheel, and left rear wheel with B_0=0.002 m. From Fig. 7.18 it can be seen that

1. The coupling action causes front and rear suspension deformations to increase 6.7 and 35.3 % respectively.
2. The effect of the coupling action on the rear suspension is much more dramatic than on the front suspension.

Figure 7.19 shows vehicle suspension deformations in the case of $B_0 = 0.01\text{m}$ and $K = 8\times10^6\,\text{N/m}^3$. It can be seen from Fig. 7.19 that the coupling action causes the front and rear suspension deformations to increase 0.4 and 9.7 % respectively. Thus the effect of the coupling action on suspension deformations becomes smaller with the increase in road surface roughness amplitude.

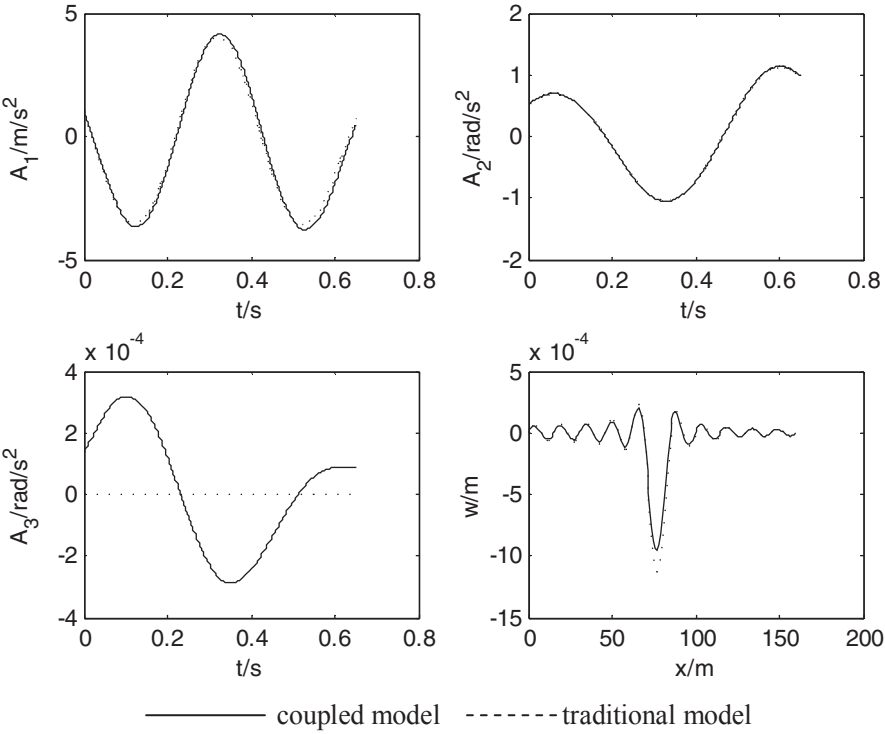

Fig. 7.17 Vehicle body accelerations with $B_0 = 0.01$ m. (Reprinted from ref. [11] by permission of Taylor & Francis Ltd)

Figure 7.20 shows the tire forces of the right front wheel, right rear wheel, left front wheel, and left rear wheel with $B_0 = 0.002\text{m}$. From Fig. 7.20 it can be seen that

1. After considering the coupling action, the tire force amplitudes of the front and rear wheel increase 1.0 and 16.3 % respectively.
2. The effects of the coupling action on the rear wheel's tire forces are much more significant than on the front wheel's tire forces.
3. The right tire force is not the same as the left tire force. This is because the pavement displacement at the right wheels is not the same as that at the left wheels.

Figure 7.21 shows the tire forces in the case of $B_0 = 0.01\text{m}$. From Fig. 7.21 it can be seen that after considering the coupling action, the tire force amplitudes of the front and rear wheel increase 0.3 and 2.1 % respectively. Thus with the increase in road surface roughness amplitude, the effect of the coupling action on the tire forces becomes smaller.

Figure 7.22 shows the pavement displacements at the four wheels with $B_0 = 0.002$ m. From Fig. 7.22 it can be seen that

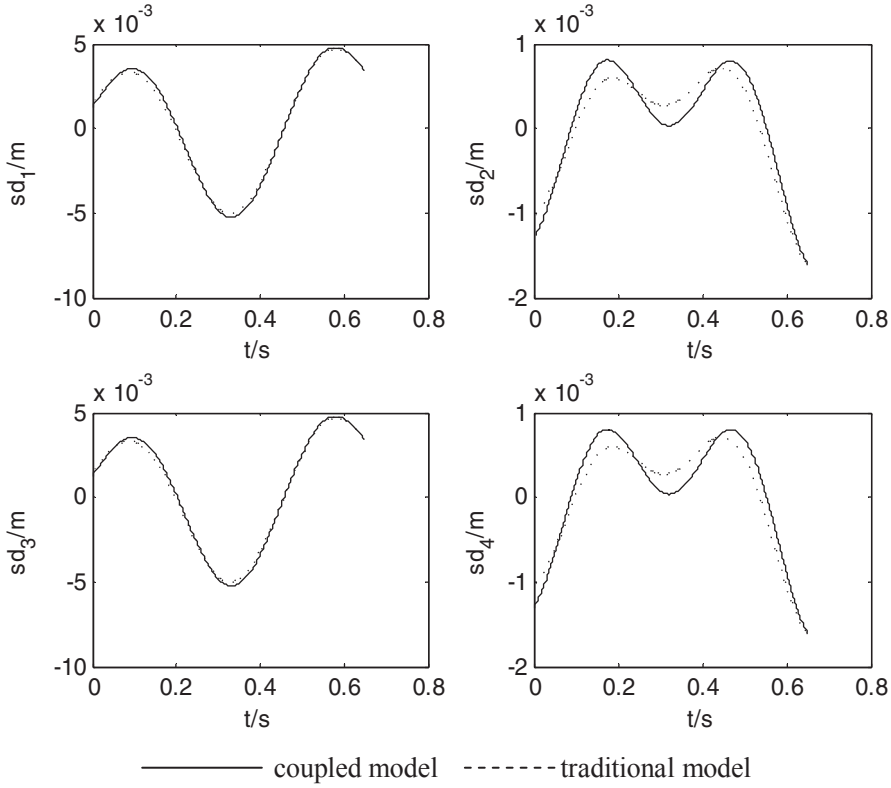

Fig. 7.18 Suspension deformations with $B_0 = 0.002$ m. (Reprinted from ref. [11] by permission of Taylor & Francis Ltd)

1. After considering the coupling action, the pavement displacement amplitudes at the front wheels and rear wheels both increase 15.2 and 5.8%, respectively.
2. The pavement displacement at the rear wheel of the traditional system is delayed behind the coupled system for about 0.15 s. The time delay at the front wheel is difficult to see.

Figure 7.23 shows the pavement displacements in the case of $B_0 = 0.01\text{m}$. From Fig. 7.23 it can be seen that

1. After considering the coupling action, the amplitudes of the pavement displacement at the front and rear wheels increase 45.8 and 4.3%, respectively. Thus with the increase in the road surface roughness amplitude, the effect of the coupling action on the pavement displacement at the front wheels becomes larger, but the effect of the coupling action on the pavement displacement at the rear wheels becomes smaller.

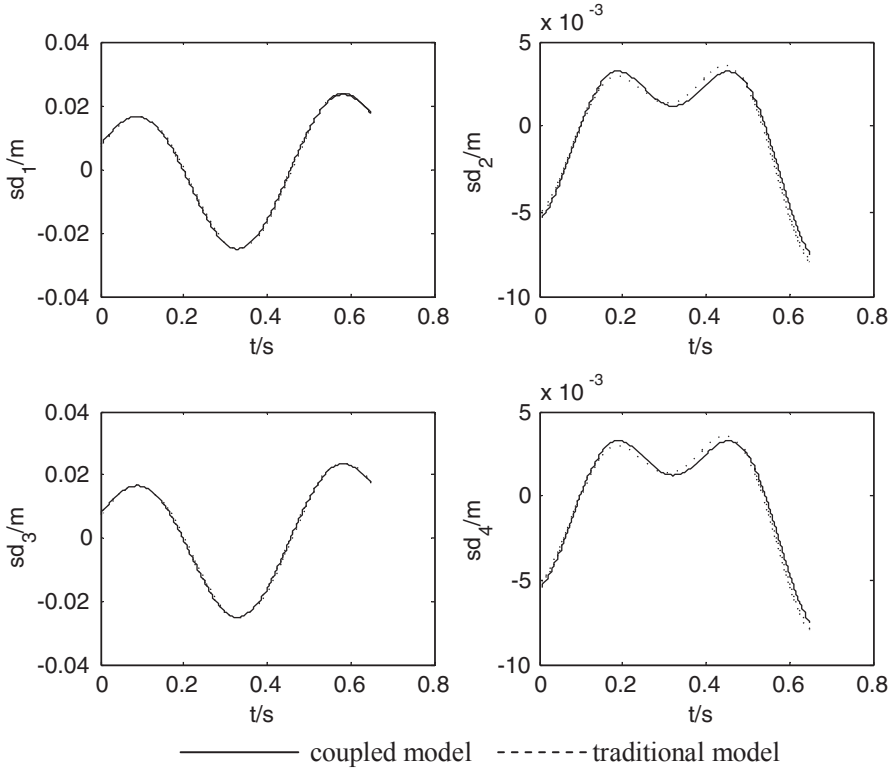

Fig. 7.19 Suspension deformations with B_0=0.01 m. (Reprinted from ref. [11] by permission of Taylor & Francis Ltd)

2. The pavement displacements of the traditional system are delayed behind the coupled system for 0.21 s at the front wheel and 0.18 s at the rear wheel. The time delay of the traditional system can be seen more easily on a rough road surface than on a smooth road surface.

7.5 Chapter Summary

In this chapter, a two-dimensional and a three-dimensional vehicle–road coupled system are built and a revised roller tire model is proposed. The responses of the vehicle and road are computed simultaneously and the effects of the vehicle–road coupling on responses are also analyzed. It can be found that

1. Under harmonic, impulse, or stochastic road excitations, the vehicle body acceleration and the tire force obtained from the RFRC tire model are smaller than those obtained from the SPC tire model. As to the pavement acceleration, the comparison result is on the contrary. Under short wave length harmonic excitation, high running speed, impulse or stochastic road excitation, the two tire models' results are very different. In these cases, the flexible roller contact tire model should be used to compute the tire force and system responses.
2. The dynamic response of the coupled system changes similarly with that of the traditional system, including the vehicle body vertical acceleration, tire forces and suspension deformations. The role of vehicle–road coupling in the vehicle and road dynamic computation depends mainly on the relation between the road

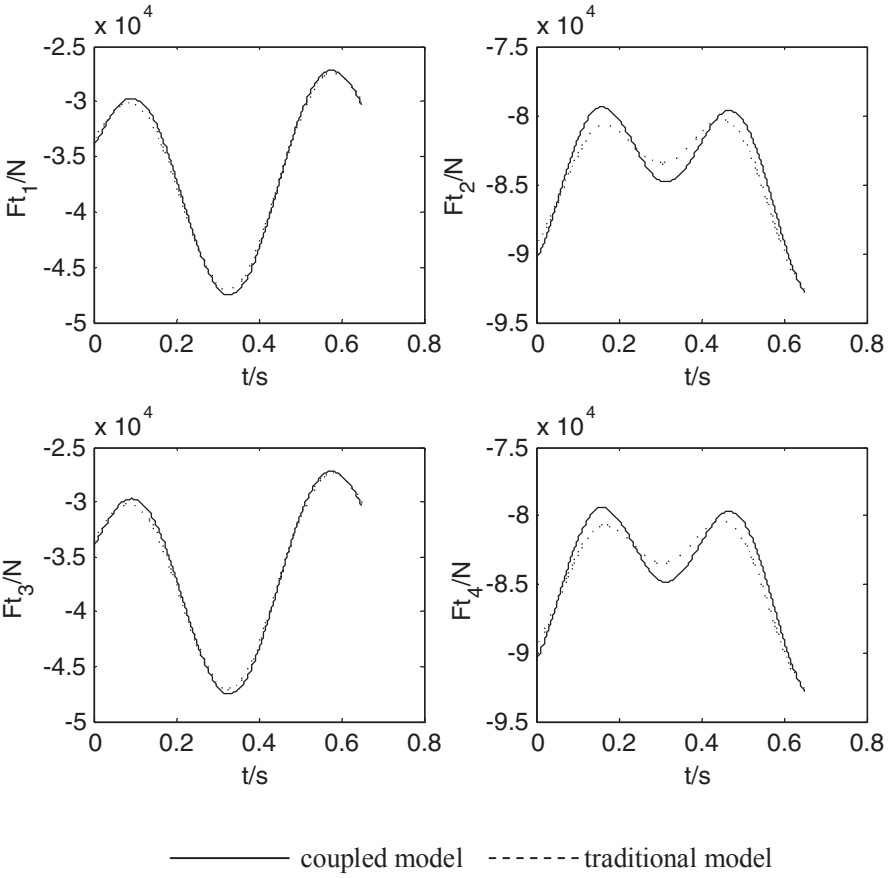

Fig. 7.20 Tire forces with B_0=0.002 m. (Reprinted from ref. [11] by permission of Taylor & Francis Ltd)

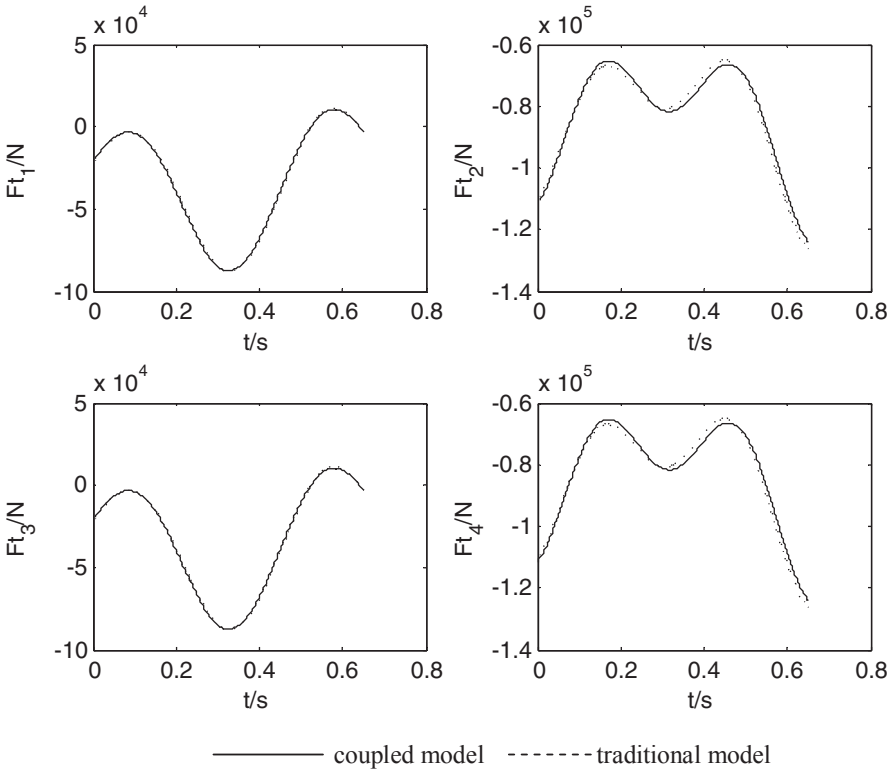

Fig. 7.21 Tire forces with $B_0 = 0.01$ m. (Reprinted from ref. [11] by permission of Taylor & Francis Ltd)

roughness amplitude and the pavement displacement. In the case of a heavy-duty vehicle, a soft subgrade or a higher running speed, the pavement displacement may be near the amplitude of road roughness and vehicle–road coupling should be considered.

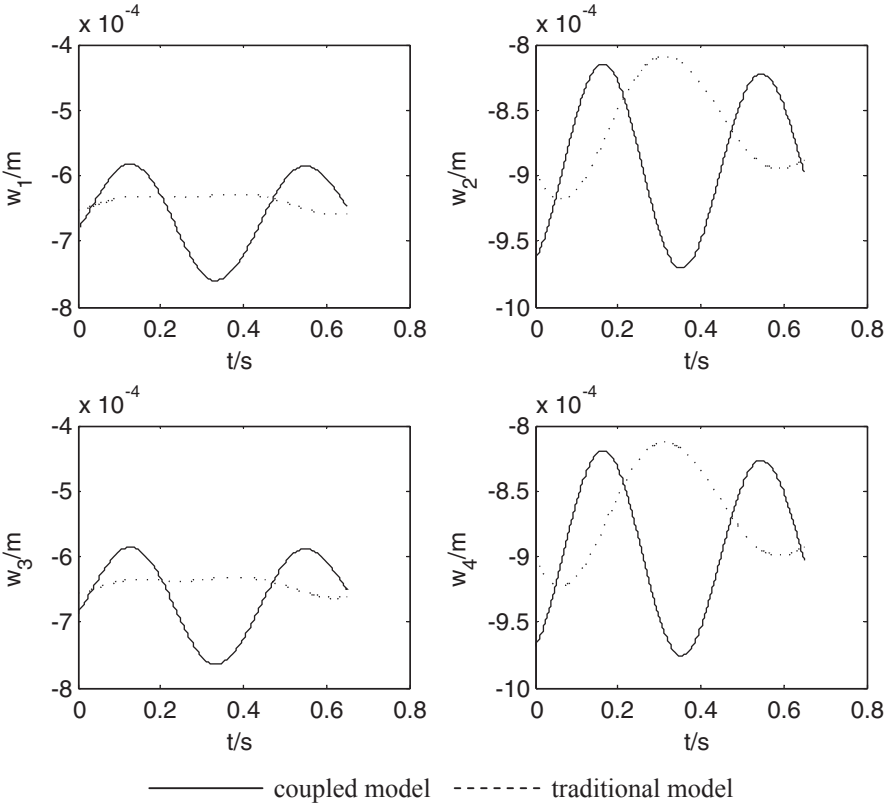

Fig. 7.22 Pavement displacements with $B_0 = 0.002$ m. (Reprinted from ref. [11] by permission of Taylor & Francis Ltd)

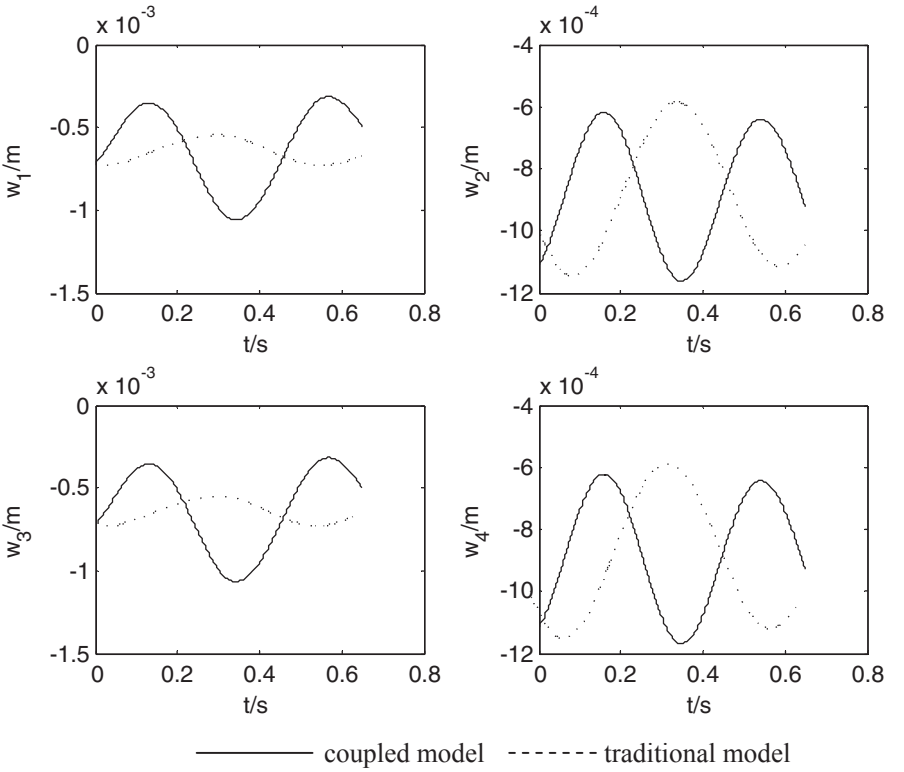

Fig. 7.23 Pavement displacements with $B_0 = 0.01$ m. (Reprinted from ref. [11] by permission of Taylor & Francis Ltd)

References

1. Guo KH. Tire roller contact model for simulation of vehicle vibration input. Soc Automot Eng (SAE 932008). 1993;991:45–51.
2. Guo KH, Liu Q, Ding GF. Influences of loading and inflation pressure on tire enveloping properties. Trans CSAE. 1998;14(3):53–5.
3. Guo KH, Liu Q, Ding GF. Analysis of tire enveloping properties and its application in modeling of vehicle vibration systems. Automot Eng. 1999;21(2):65–71, 80.
4. Yang SP, Li SH, Lu YJ. Dynamics of Vehicle-pavement coupled system based on a revised flexible roller contact tire model. Sci China, Ser E. 2009;52(3):721–30.
5. Zhai WM. Two simple fast integration methods for large-scale dynamic problems in engineering. Int J Numer Methods Eng. 1996;39:4199–214.
6. Zhai WM. Vehicle-track coupled dynamics. Beijing: China Railway Publishing House; 2002.
7. Chen LQ, Wang QR. Simulation and analysis of ride comfort on pulse road based on ADAMS. Comput Simul. 2006;23(12):212–15.
8. Wang JJ, Zhang W, Wu WX. Analysis of dynamic response of simply supported girder bridge under heavy moving vehicles. Cent South Highw Eng. 2005;30(2):55–62.
9. Automobile handbook. Beijing: China Communications Press; 2001.

10. Liu XD, Deng ZD, Gao F. Research on the method of simulating road roughness numerically. J Beijing Univ Aeronaut Astronaut. 2003;29(9):843–46.
11. Yang SP, Li SH, Lu YJ. Investigation on the dynamic interaction between a heavy vehicle and road pavement. Veh Syst Dyn. 2010;48(8):923–44.
12. Law SS, Zhu XQ. Bridge dynamic responses due to road surface roughness and braking of vehicle. J Sound Vib. 2005;282:805–30.
13. Deng XJ. Subgrade and pavement engineering. Beijing: China Communications Press; 2000.
14. Deng XJ, Huang XM. Principles of pavement design. Beijing: China Communications Press; 2001.

Chapter 8
Parameter Design of Vehicle–Road System with Low Dynamic Interaction

At present, parameter design of the vehicle and pavement with the aim of reducing the vehicle–pavement dynamic interaction is usually studied respectively in vehicle dynamics and road dynamics. It is seldom to study the low dynamic design of vehicle and road parameters simultaneously.

By using the new theory of vehicle–pavement coupled system proposed in Chap. 7, effects of system parameters on dynamic characteristics of vehicle and pavement are simulated and analyzed in detail. Based on the simulation results, some low dynamic design measures are suggested for choosing system parameters, which may contribute to the ride comfort of heavy vehicle and the life of asphalt pavement [1].

8.1 Verification of the New Theory of Vehicle–Road Coupled System

In order to investigate the low dynamic design of vehicle and road parameters, the validity of the new theory of vehicle–road coupled system must be verified first. A response comparison with the finite element method given by Wu [2] is made here. Wu considered the interaction between pavements and the underlying soil foundation and researched the effects of a finite element grid, pavement thickness and foundation stiffness on pavement displacement by using the 3D finite element method [2].

After applying the same parameters and boundary conditions to Wu's model, the pavement displacements are obtained by the above quick direct integral method based on the vehicle–pavement coupled model. Simulation results of this work are shown in Fig. 8.1 and Table 8.1[3].

From Fig. 8.1 and Table 8.1 it can be seen that the results in two methods are very close. Thus, the validation of this vehicle–pavement coupled model and the quick

S. Yang et al., *Dynamics of Vehicle-Road Coupled System,*
DOI 10.1007/978-3-662-45957-7_8

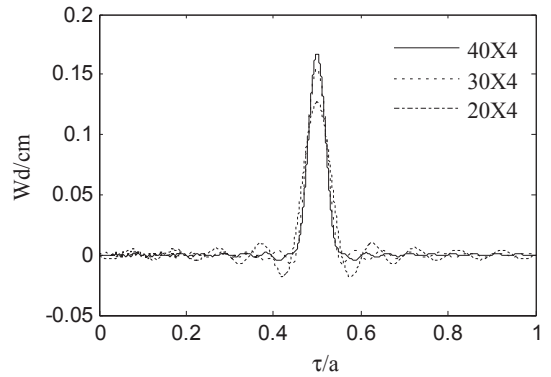

a The effect of a mode superposition number

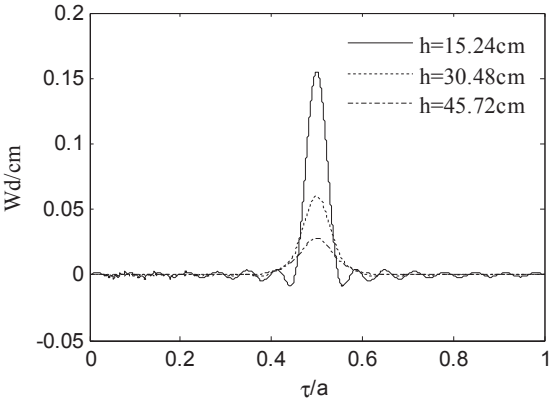

b The effect of pavement thickness

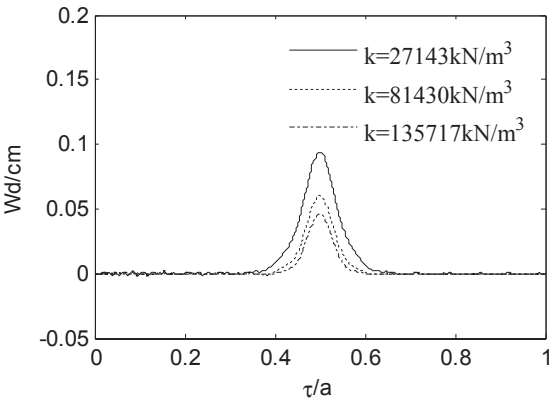

c The effect of foundation stiffness

Fig. 8.1 Results of this work. **a** The effect of a mode superposition number. **b** The effect of pavement thickness. **c** The effect of foundation stiffness. Reprinted from ref. [3], with kind permission from Taylor & Francis Ltd

Table 8.1 The amplitude of pavement displacement at the midpoint obtained by two methods(cm). Reprinted from ref. [3], with kind permission from Taylor & Francis Ltd

Parameters Methods	h (cm)			K (kN/m^3)		
	15.24	30.48	45.72	27,143	81,430	135,717
Wu[2]	0.165	0.065	0.035	0.125	0.065	0.050
This work	0.155	0.060	0.028	0.100	0.060	0.046

direct integral method is tested. However, both methods have a sensitive parameter, grid division or mode superposition number, which influences the simulation results greatly. Hence, the numerical test is necessary to choose the suitable parameter in order to assure the correctness of the results and to improve computation efficiency.

8.2 Evaluation Criterions of Low Dynamic Interaction

The dynamic interaction between tire and pavement plays an important role in vehicle and road dynamic responses. Low dynamic interaction will lead to a better vehicle riding comfort and a longer road fatigue life. The research on rail vehicle/track systems with low dynamic interaction has attracted scholars' attention and some basic rules for reducing dynamic interaction have been proposed for designing parameters [4–5].

However, the research on low dynamic parameters design of vehicle–road systems is still seldom found. The present studies on vehicle and road parameters design are often separated in vehicle dynamics and road dynamics, respectively.

In vehicle dynamics, the dynamic load coefficient (DLC) has been widely adopted as an evaluation criterion for dynamic interaction, which is expressed by [6],

$$DLC = F_d / F_s \tag{8.1}$$

where, F_d is the root mean square (RMS) value of the dynamic tire force, and F_s is the static tire force.

However, DLC is unable to reflect the spatial distribution of tire forces and may lead to a calculation error. Hence, Cebon and Cole put forward a fourth power aggregate force to evaluate the road damage induced by tire dynamic forces [7–8].

In road dynamics, the tensile strain at the bottom of an asphalt surface has been a widely used evaluation criterion for dynamic interaction. Road fatigue life can be predicted using the tensile strain [9]

$$N_f = k_1 \left(\frac{1}{\varepsilon_t} \right)^{k_2} \tag{8.2}$$

where N_f is the fatigue life of the pavement structure, represented by the number of loading cycles, ε_t is the tensile strain at the bottom of the surface course, k_1 and k_2 are experimentally measured constants.

In addition, the stiffness modulus of the asphalt mixture and longitudinal tensile strain at the bottom of the asphalt concrete surface course has been used to predict road fatigue life [5, 10]. When the pavement material is geometrically linear, the pavement displacement can also be used as an evaluation criterion for road damage.

In this work, four criteria are used for evaluating the dynamic interaction between tire and pavement. The pavement displacement and DLC are computed to evaluate the influence of system parameters on the road damage. In addition, RMS of the vertical and pitching vehicle body acceleration are chosen as the criterions for vehicle riding comfort.

8.3 Effects of Vehicle System Parameters

Let the integral step be 0.1 ms and the mode superposition order NM = 20. Effects of vehicle parameters, such as vehicle speed, vehicle load, wheel mass, tire stiffness, suspension stiffness, tire damping, suspension damping, wheelbase and wheel tread, on RMS of the vertical vehicle body acceleration A_1, RMS of the pitching vehicle body acceleration A_2, DLC of the wheels, and the maximum amplitude of the pavement displacement w are obtained. In the DLC results, the square marker stands for the DLC of the front wheel and the circle marker stands for the DLC of the rear wheel.

8.3.1 The Effect of Vehicle Speed

The effect of the vehicle running speed on vehicle riding comfort and pavement damage is shown in Fig. 8.2. It can be seen from Fig. 8.2 that the effect of the vehicle speed on vehicle riding comfort and pavement damage is fluctuant and the front wheel DLC is greater than the rear wheel DLC. The reason for this fluctuation is that the change in road excitation frequency induced by a change in vehicle speed leads to resonance of the vehicle system.

8.3.2 The Effect of Vehicle Load

Figure 8.3 shows the effect of the vehicle load on vehicle riding comfort and pavement damage. It can be seen from Fig. 8.3 that

1. With an increase in the vehicle load, the vertical acceleration of the vehicle body first increases and then decreases, while the pitching acceleration changes a little. Thus, there may exist a load value at which the vehicle's riding comfort is the worst.

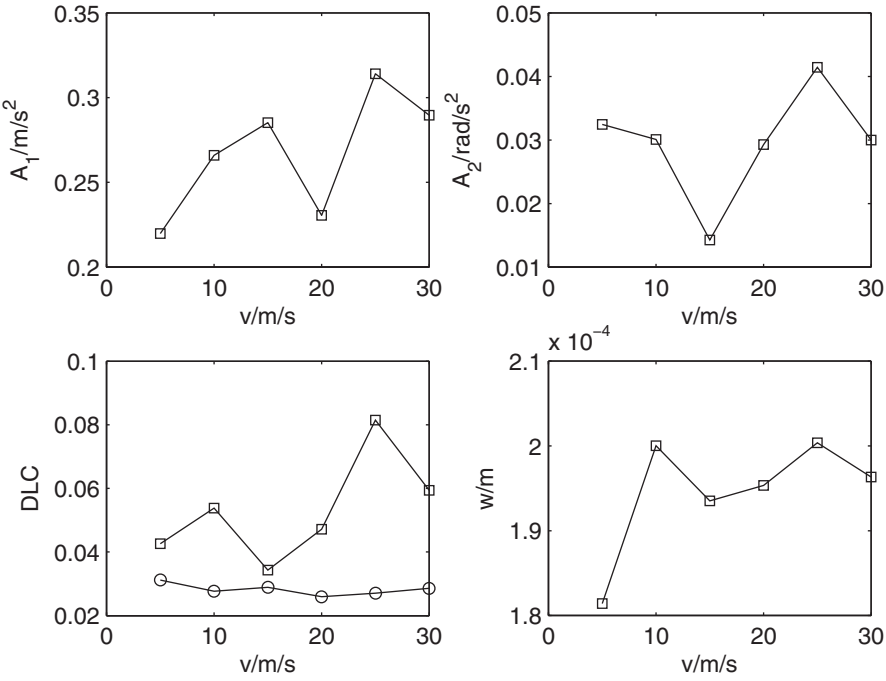

Fig. 8.2 The effect of vehicle speed. Reprinted from ref. [1], with kind permission from Inderscience Enterprises Limited

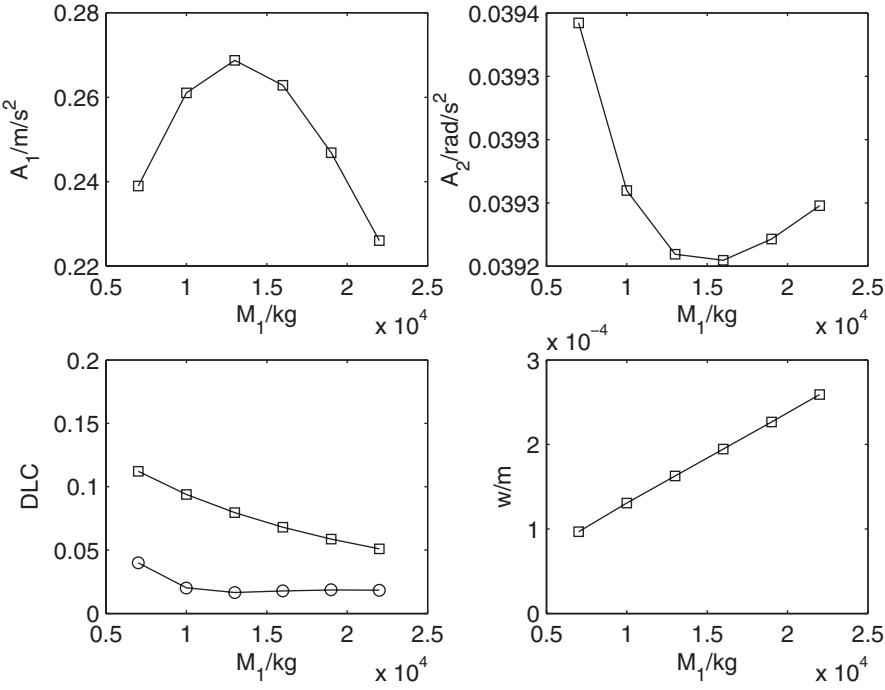

Fig. 8.3 The effect of the vehicle load. Reprinted from ref. [1], with kind permission from Inderscience Enterprises Limited

2. With an increase in the vehicle load, the DLC decreases and the amplitude of pavement displacement increases.

It should be noted that the conclusion concerning the DLC and pavement displacement contradict each other. Many present studies show that the increase of the vehicle load will aggravate the probability of road damage. Hence, it may be said that the pavement displacement is more suitable to be a criterion for road damage than the DLC.

8.3.3 The Effect of Wheel Mass

The effects of the front and rear wheel masses are given in Figs. 8.4 and 8.5.
Figures 8.4 and 8.5 show that

1. With the increase in the front wheel mass, the vertical acceleration of the vehicle body and pavement displacement increases, the front wheel DLC decreases, but the pitch acceleration of the vehicle body rises first and then decreases.
2. With the rise of rear wheel mass, all responses increase, such as the vertical and pitch acceleration of the vehicle body, the front and rear wheel DLC, and the pavement displacement.

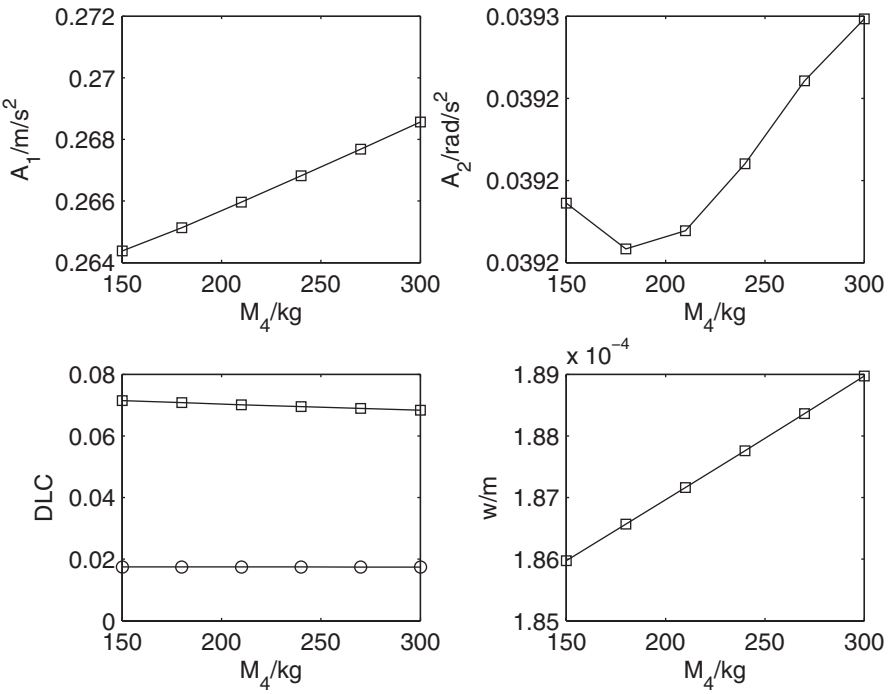

Fig. 8.4 The effect of the front wheel mass

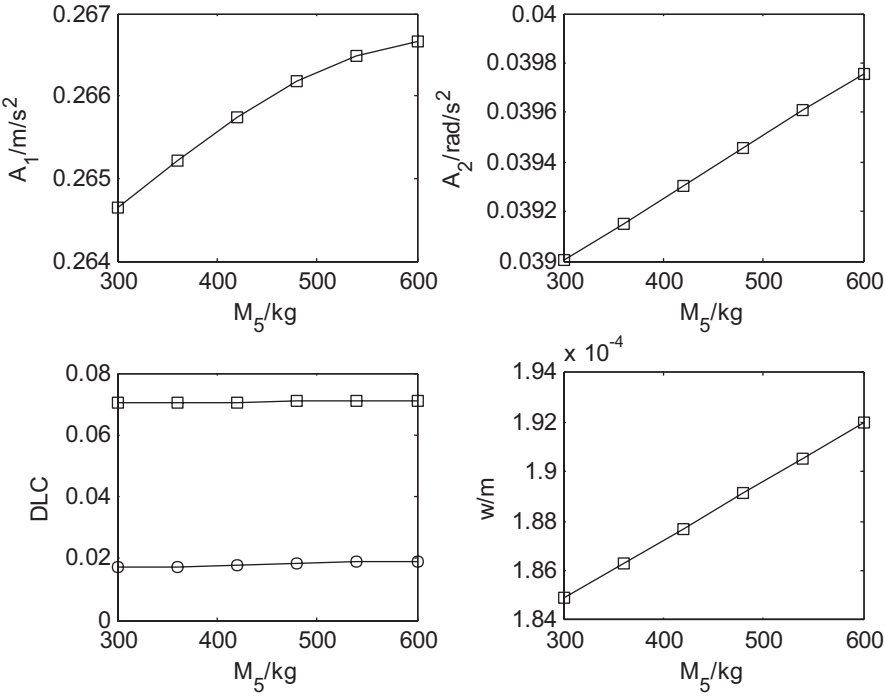

Fig. 8.5 The effect of the rear wheel mass

Thus, a light wheel is beneficial to riding comfort and road fatigue life. However, the design of the wheel mass should also consider other factors, including structure strength and tire–road adhesion characteristics.

8.3.4 The Effects of Tire Stiffness

The effects of the front and rear tire stiffness are shown in Figs. 8.6 and 8.7. From these two figures, it can be seen that

1. The effect of the tire stiffness on vertical acceleration of the vehicle body is contradicted by that on the pitching acceleration of the vehicle body. In order to guarantee vehicle riding comfort, a reasonable value for rear suspension stiffness should be chosen according to a compromise between the vertical and pitching acceleration of the vehicle body.
2. With the increase of front or rear tire stiffness, the DLC of the front or rear wheel and the pavement displacement increase. Moreover, the increase in front tire stiffness hardly influences the DLC of the rear wheel and vice versa. Thus, small tire stiffness contributes to a decrease in road damage.

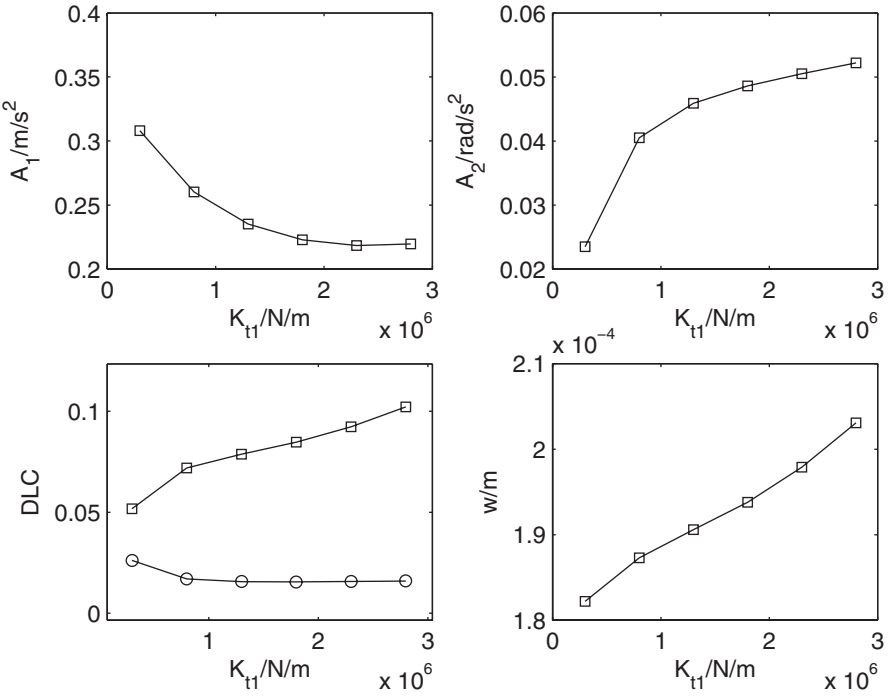

Fig. 8.6 The effect of front tire stiffness

8.3.5 The Effects of Suspension Stiffness

The effects of the front and rear vehicle suspension stiffness are shown in Figs. 8.8 and 8.9. From these two figures, it is found that

1. With the rise in the front suspension stiffness, the vertical and the pitching accelerations of the vehicle body, DLC and pavement displacement all increase. Thus, small front suspension stiffness is a benefit to both vehicle riding comfort and a reduction in road damage.
2. With the rise in rear suspension stiffness, the vertical acceleration of the vehicle body and DLC increase, but the pitching acceleration of the vehicle body decreases slightly, and the pavement displacement first decreases and then increases. Thus, the effect of rear suspension stiffness on riding comfort is complicated and a reasonable value for rear suspension stiffness should be chosen through a trade-off between vertical and pitching accelerations of the vehicle body. In addition, the small rear suspension stiffness may increase road damage.

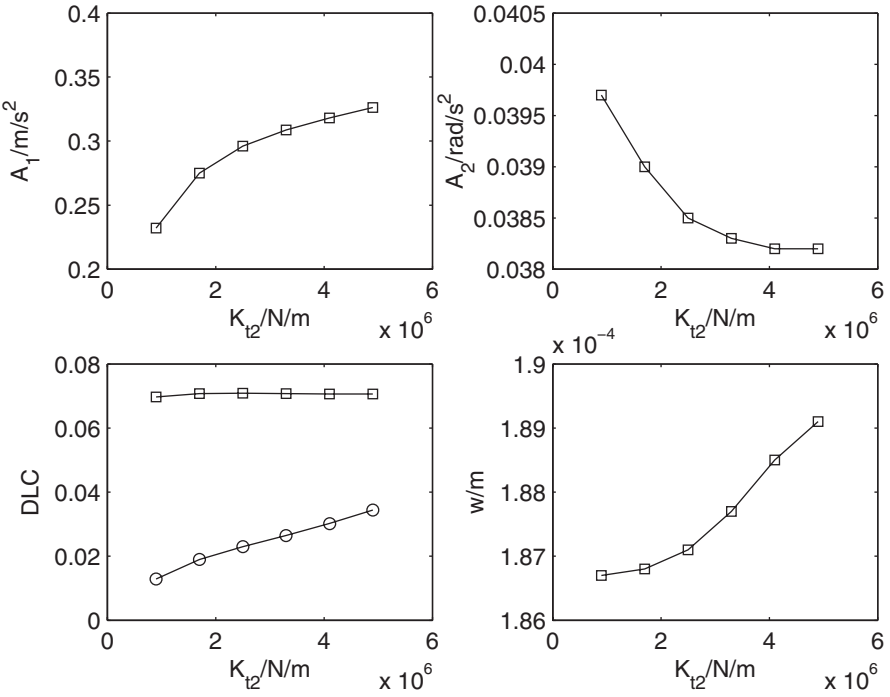

Fig. 8.7 The effect of rear tire stiffness. Reprinted from ref. [1], with kind permission from Inderscience Enterprises Limited

8.3.6 The Effects of Tire Damping

The effects of front and rear tire damping are shown in Figs. 8.10 and 8.11. From these two figures, it is found that

1. With an increase in front or rear tire damping, the vertical and pitch accelerations of the vehicle body decrease which is beneficial to vehicle riding comfort.
2. With an increase in front tire damping, the DLC of the front wheel and the pavement displacement decrease, but the DLC of the rear wheel rises slightly.
3. A rise in rear tire damping leads to an enlargement of pavement displacement, but reduces the DLC of the rear wheel.

Thus, the effect of rear suspension stiffness on riding comfort is complicated and a reasonable value for rear suspension stiffness should be chosen through a trade-off between the vertical and pitching acceleration of the vehicle body. In addition, it should also be noted that the conclusion concerning the DLC and pavement displacement is contradictory. Taking the pavement displacement as a criterion, big front tire damping and small rear tire damping may contribute to a reduction in road damage.

On the other hand, big front or rear tire damping can improve riding comfort.

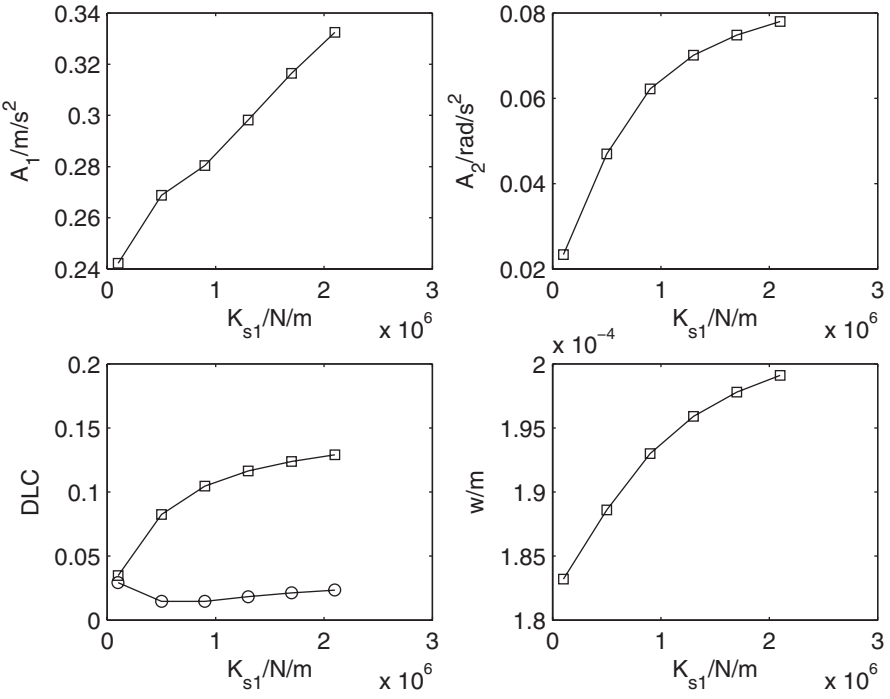

Fig. 8.8 The effect of front suspension stiffness. Reprinted from ref. [1], with kind permission from Inderscience Enterprises Limited

8.3.7 The Effects of Suspension Damping

The effects of front and rear suspension damping are shown in Figs. 8.12 and 8.13. From these two figures, it is found that

1. With the increase of front suspension damping, the vertical acceleration of vehicle body decreases but the pitch acceleration increases.
2. With an increase in front suspension damping, the DLC of the front wheel and the pavement displacement first goes down and then goes up, but the DLC of the rear wheel rises slightly.
3. With an increase in rear suspension damping, the vertical acceleration of the vehicle body increases but the pitch acceleration decreases.
4. With an increase in rear suspension damping, the DLC of the rear wheel and the pavement displacement increase, but the DLC of the rear wheel decreases slightly.

Hence, a small amount of suspension damping is beneficial in reducing road damage. While there exists a most suitable value for the front suspension damping in order to reduce road damage, the effect of suspension damping on comfort is compli-

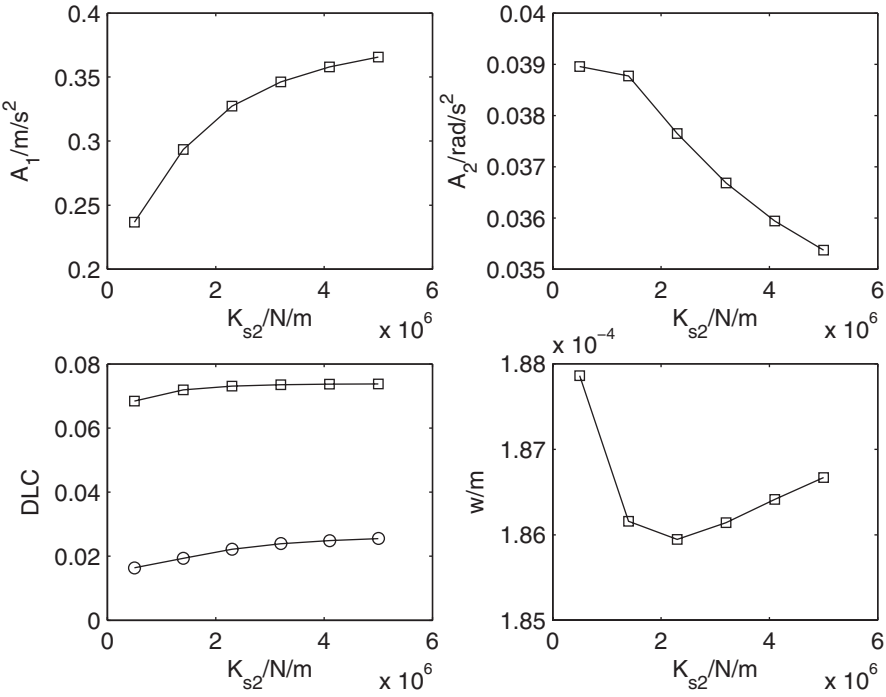

Fig. 8.9 The effect of rear suspension stiffness. Reprinted from ref. [1], with kind permission from Inderscience Enterprises Limited

cated. A reasonable value for rear suspension damping should be chosen according to a compromise between the vertical and pitching acceleration of the vehicle body.

8.3.8 The Effect of Wheelbase

The effect of wheelbase is shown in Fig. 8.14. From Fig. 8.14, it is found that

1. A large wheelbase leads to a small vertical acceleration and a big pitch acceleration for the vehicle body, and a small pavement displacement.
2. An increase in wheelbase will result in the enlargement of the front and rear wheel DLC.

Here, it should also be noted that the conclusion concerning the DLC and pavement displacement is contradictory. Taking the pavement displacement as a criterion, a large wheelbase may contribute to a reduction in road fatigue damage. The effect of wheelbase on riding comfort is complicated. Thus, a reasonable value for the wheelbase should be chosen according to a compromise between the vertical and pitching acceleration of the vehicle body.

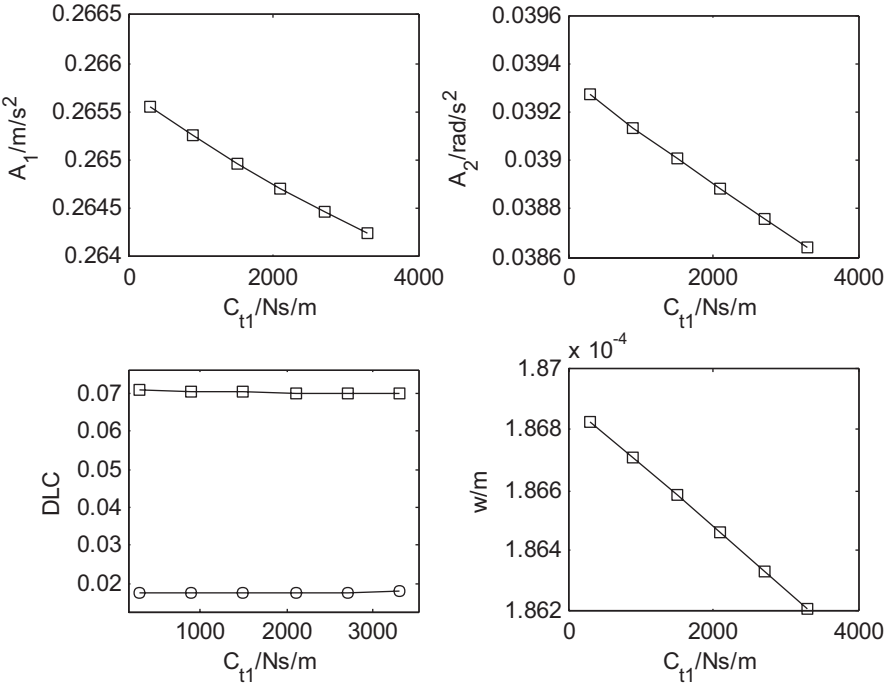

Fig. 8.10 The effects of front tire damping

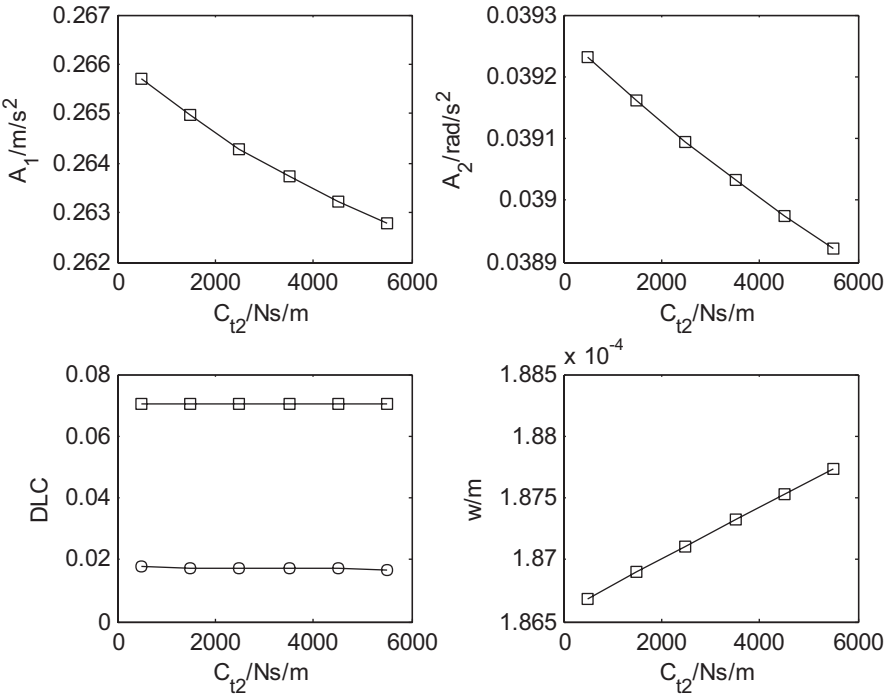

Fig. 8.11 The effects of rear tire damping

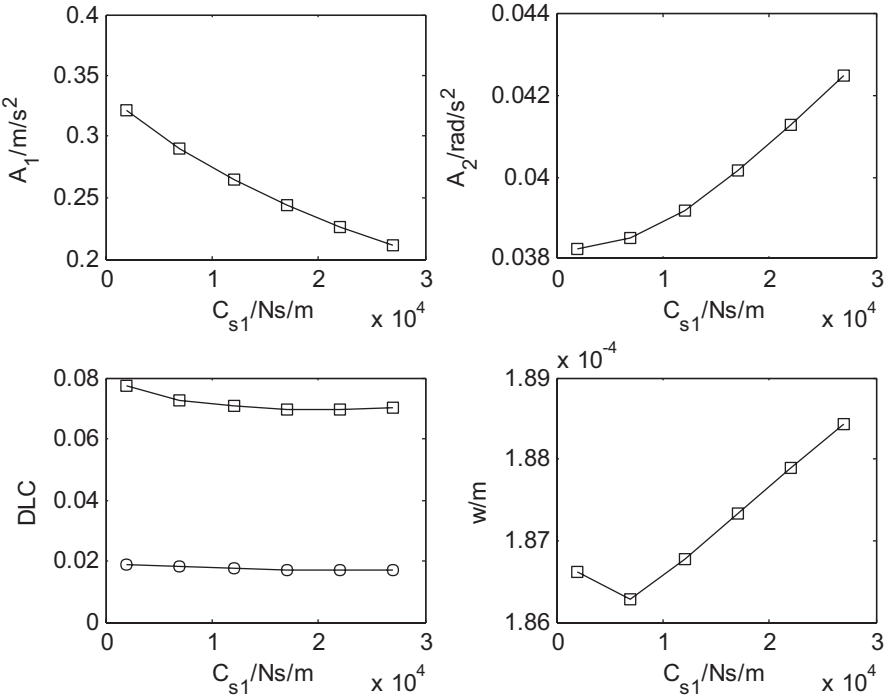

Fig. 8.12 The effects of front suspension damping

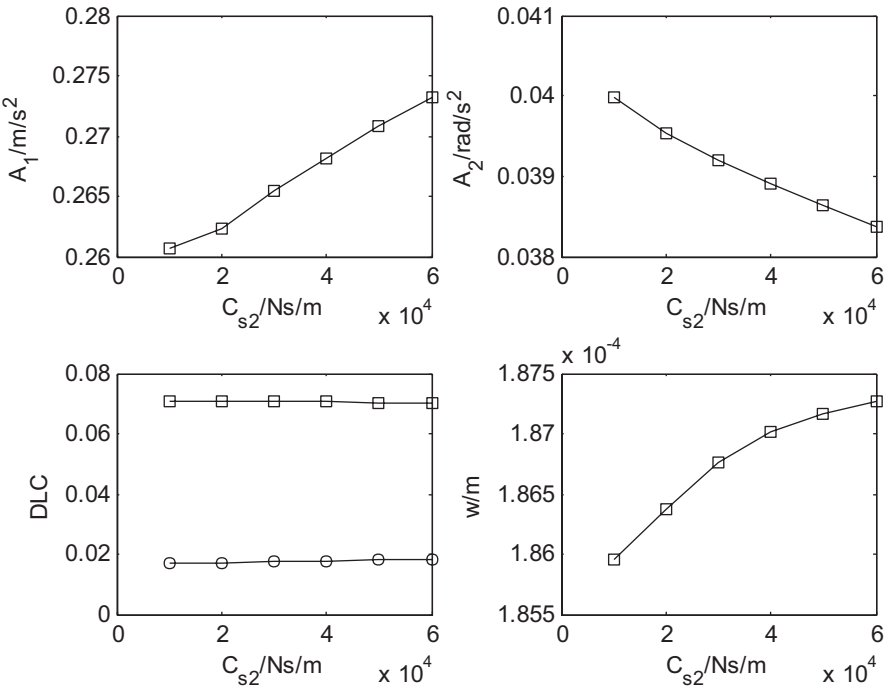

Fig. 8.13 The effects of rear suspension damping

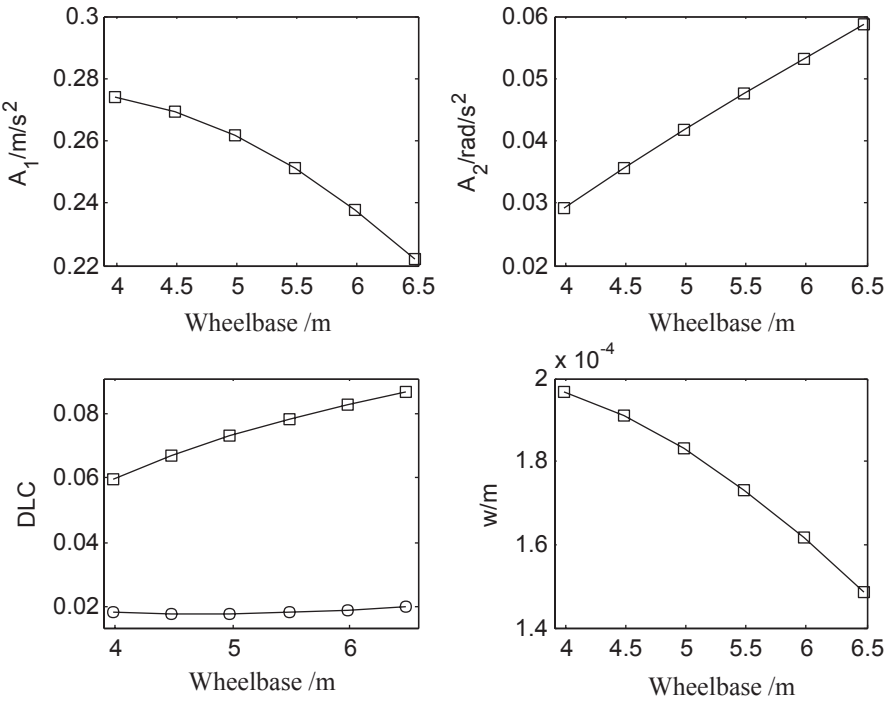

Fig. 8.14 The effect of wheelbase. Reprinted from ref. [1], with kind permission from Inderscience Enterprises Limited

8.3.9 The Effect of Wheel Tread

The effect of wheel tread is shown in Fig. 8.15. From Fig. 8.15, it is found that

1. A large wheel tread leads to a large vertical acceleration and a small pitch acceleration for the vehicle body, but the effect is very small.
2. With an increase in wheel tread, the pavement displacement decreases, the front wheel DLC increases slightly and the rear wheel DLC decreases slightly.

Here, it should also be noted that the conclusion concerning the DLC and pavement displacement is contradictory. Taking the pavement displacement as a criterion, a large wheel tread will improve road fatigue life but does harm to riding comfort.

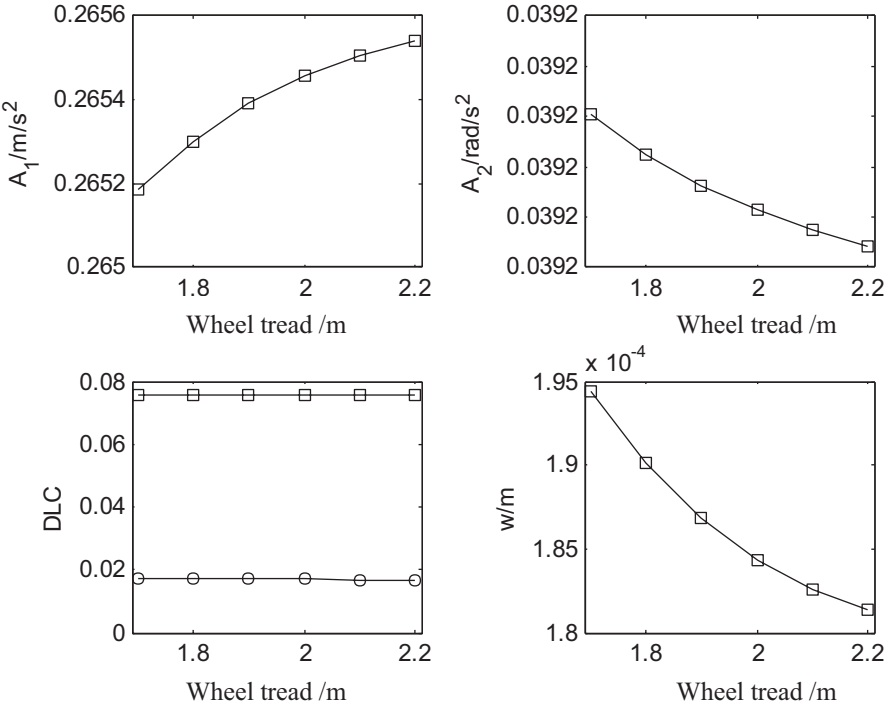

Fig. 8.15 The effect of wheel tread. Reprinted from ref. [1], with kind permission from Inderscience Enterprises Limited

8.4 Effects of Road System Parameters

Effects of road parameters on vehicle riding comfort and road fatigue damage are also obtained, including density, height, elastic modulus, and Poisson ratio of pavement, the foundation response modulus and the foundation damping coefficient. In the DLC results, the square marker stands for the DLC of the front wheel and the circle marker stands for the DLC of the rear wheel.

8.4.1 The Effects of Pavement Density

The effects of pavement density are shown in Fig. 8.16 and 8.17. From these two figures, it is found that

1. The effects of pavement density on vehicle responses, such as the vertical and pitch acceleration of the vehicle body and DLC of the wheels, is slight.
2. With a rise in pavement density, the pavement displacement fluctuates slightly.

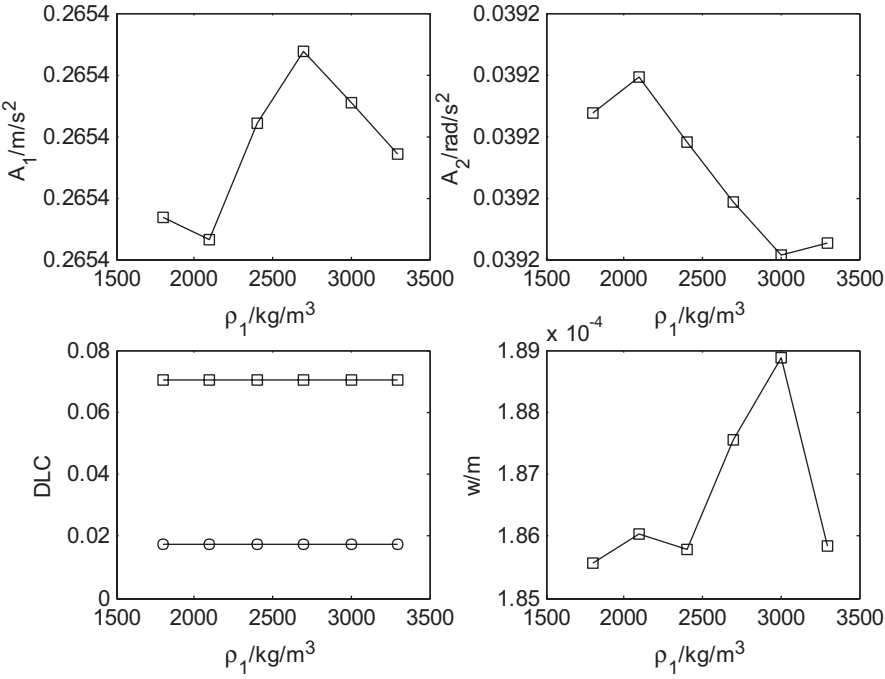

Fig. 8.16 The effect of the topping course density. Reprinted from ref. [1], with kind permission from Inderscience Enterprises Limited

Hence, in order to reduce road damage, the density of the topping and base course should be chosen reasonably and a parameter value inducing peak pavement displacement must be avoided. The effect of the pavement density on riding comfort is too small to be considered.

8.4.2 The Effects of Pavement Height

Figures 8.18 and 8.19 show the effects of the pavement topping height and base course height. From these two figures, it can be noted that

1. With an increase in the topping or base course height, the vertical acceleration of the vehicle body increases. But the effect of these two parameters on the pitching acceleration of the vehicle body is slight.
2. With an increase in the topping or base course height, the DLC of the front wheel increases and the DLC of the rear wheel changes slightly.
3. An increase in the topping or base course height leads to a decrease in the pavement displacement.

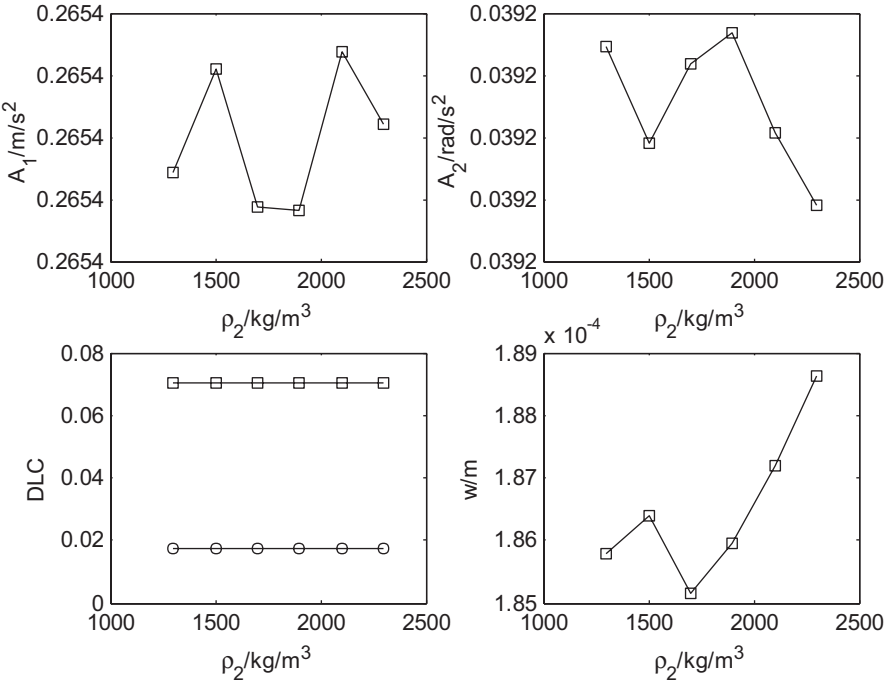

Fig. 8.17 The effect of the base course density. Reprinted from ref. [1], with kind permission from Inderscience Enterprises Limited

Thus, a large topping or base course height contributes to a decrease in road damage but does harm to riding comfort.

8.4.3 The Effects of Elastic Modulus

Figures 8.20 and 8.21 show the effects of the pavement elastic modulus. From these two figures, it can be noted that

1. With an increase in the topping or base course elastic modulus, the vertical acceleration of the vehicle body increases. But the effect of these two parameters on the pitching acceleration of the vehicle body is slight.
2. With an increase in the topping or base course elastic modulus, the DLC of the front wheel increases and the DLC of the rear wheel decreases slightly.
3. An increase in the topping or base course elastic modulus leads to a decrease in the pavement displacement.

Taking the pavement displacement as a criterion, a large topping or base course elastic modulus will improve road fatigue life but do harm to riding comfort.

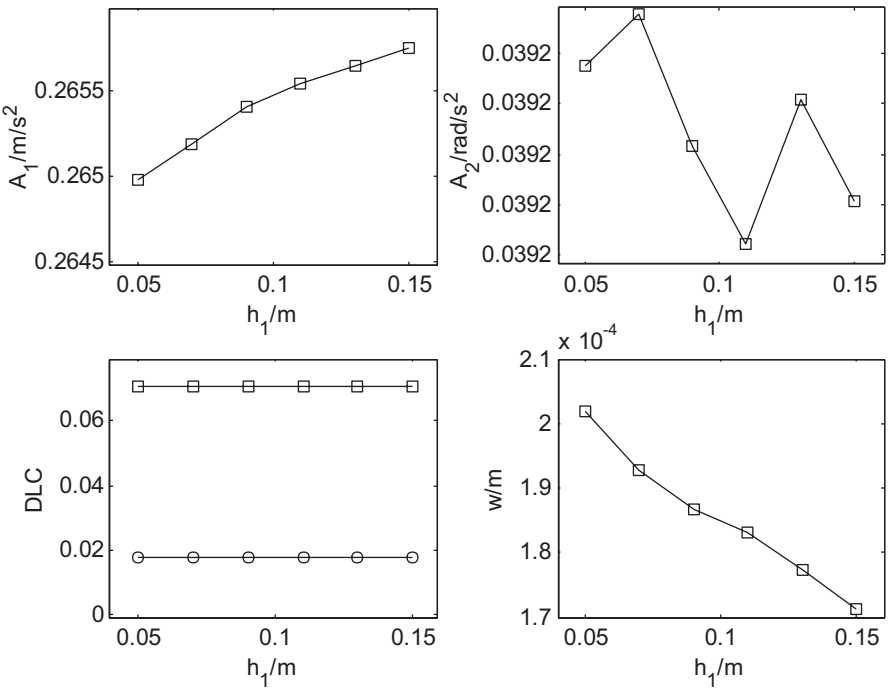

Fig. 8.18 The effect of the topping course height

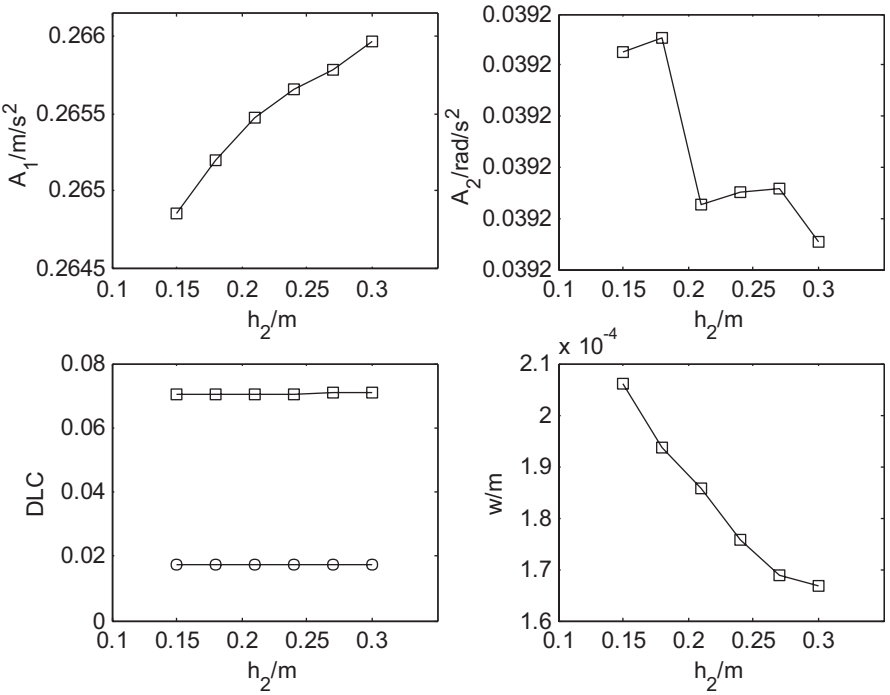

Fig. 8.19 The effect of the base course height

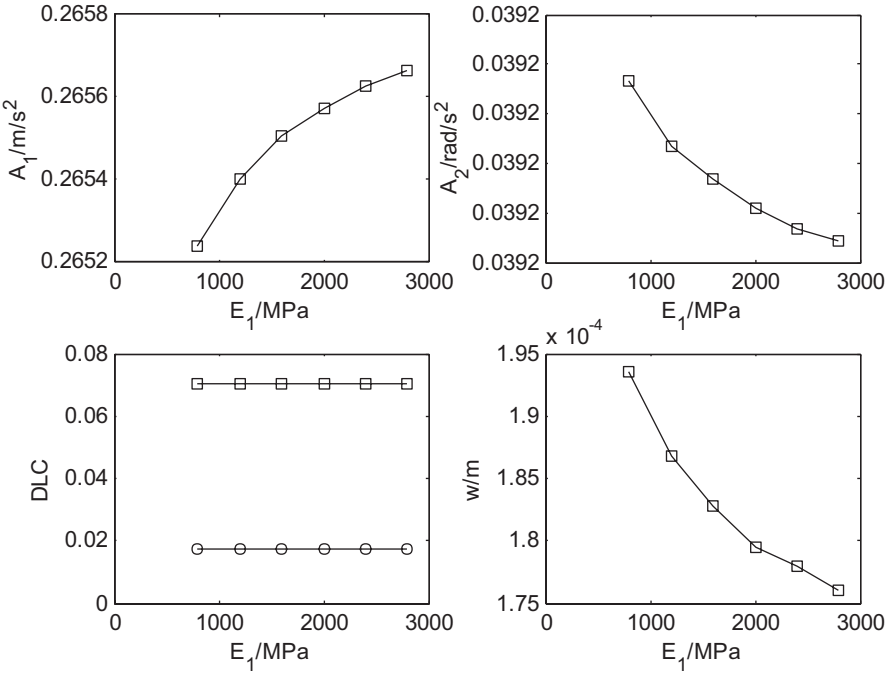

Fig. 8.20 The effect of the topping course elastic modulus

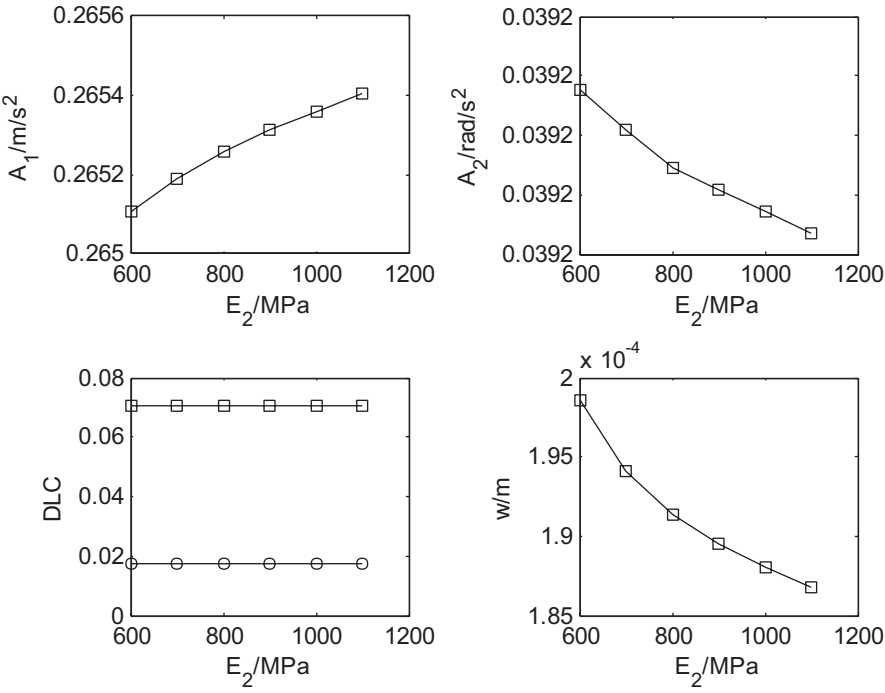

Fig. 8.21 The effect of the base course elastic modulus

8.4.4 The Effects of the Pavement Poisson Ratio

Figures 8.22 and 8.23 show the effects of the pavement Poisson ratio. From these two figures, it can be found that

1. With an increase in the topping or base course Poisson ratio, the vertical acceleration of the vehicle body increases. But the effect of these two parameters on the pitching acceleration of the vehicle body is slight.
2. With an increase in the topping or base course elastic modulus, the DLC of the front wheel increases and the DLC of the rear wheel decreases slightly.
3. An increase in the topping or base course elastic modulus leads to a decrease in the pavement displacement.

Taking the pavement displacement as a criterion, a large topping or base course Poisson ratio will improve road fatigue life but do harm to riding comfort.

8.4.5 The Effect of the Foundation Response Modulus

The effect of the foundation response modulus is shown in Fig. 8.24. It can be seen that

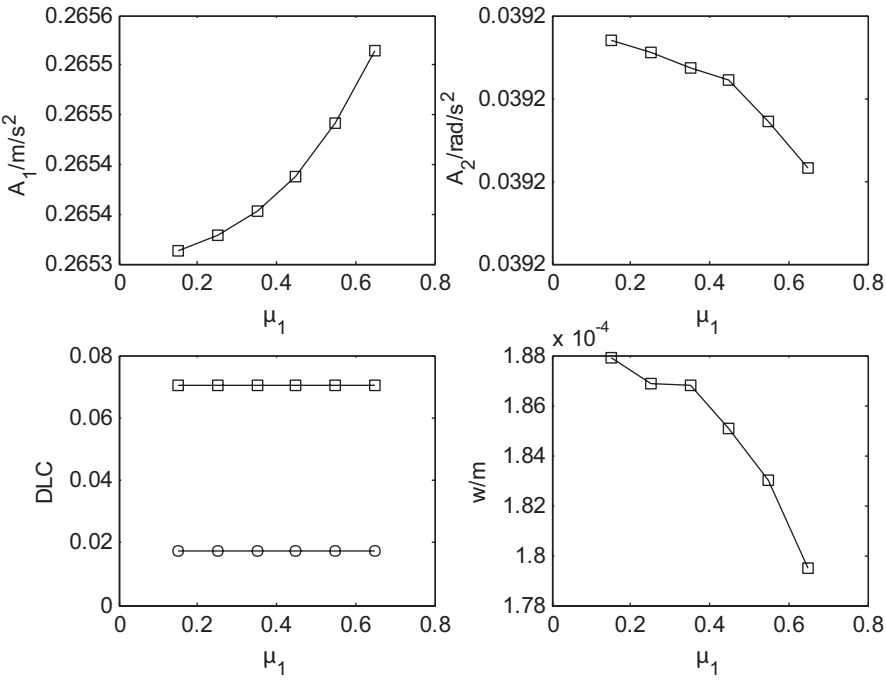

Fig. 8.22 The effect of the topping course Poisson ratio

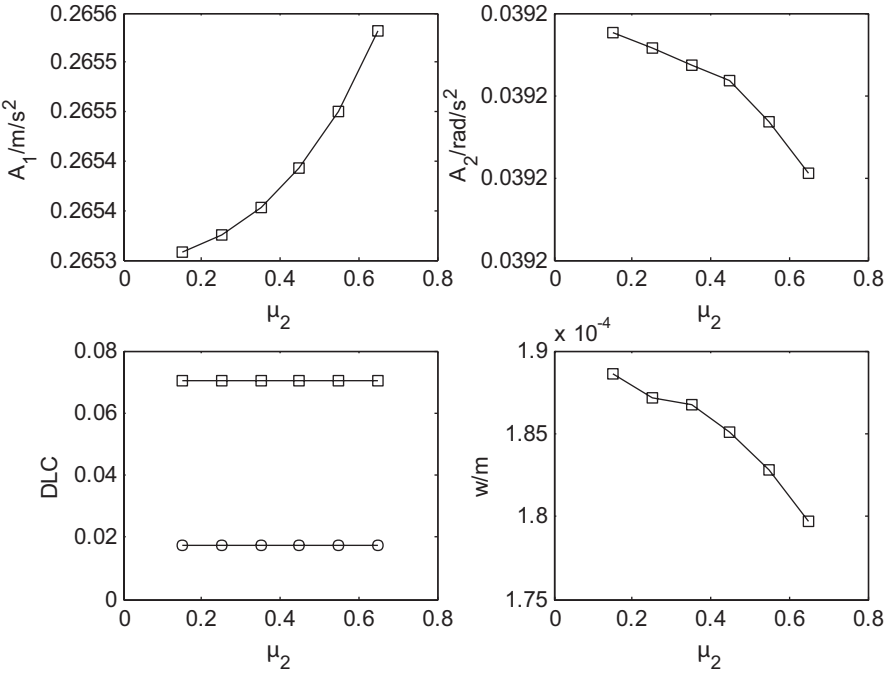

Fig. 8.23 The effect of the base course Poisson ratio

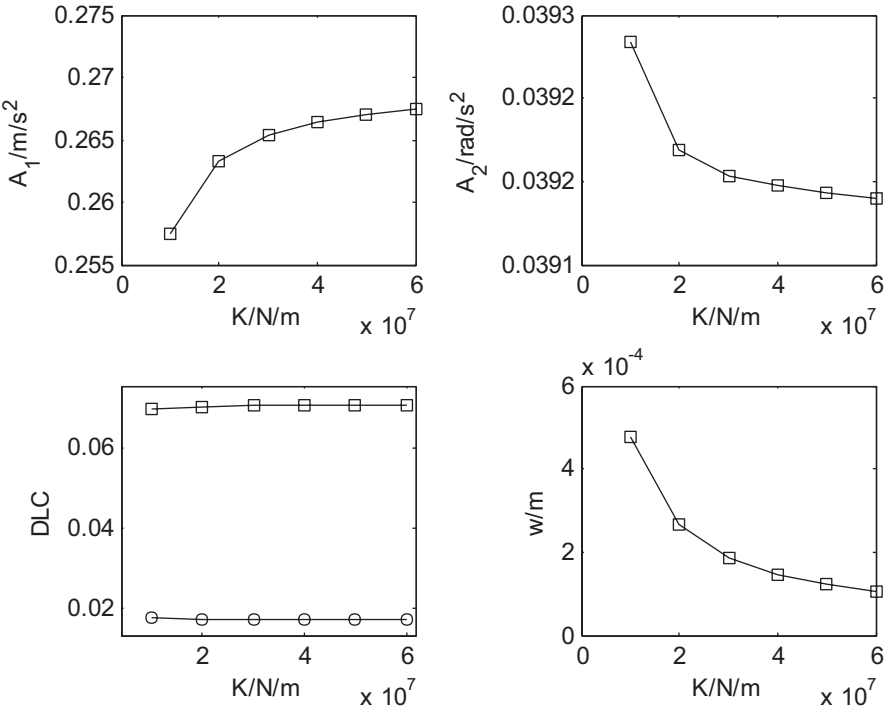

Fig. 8.24 The effect of the foundation response modulus

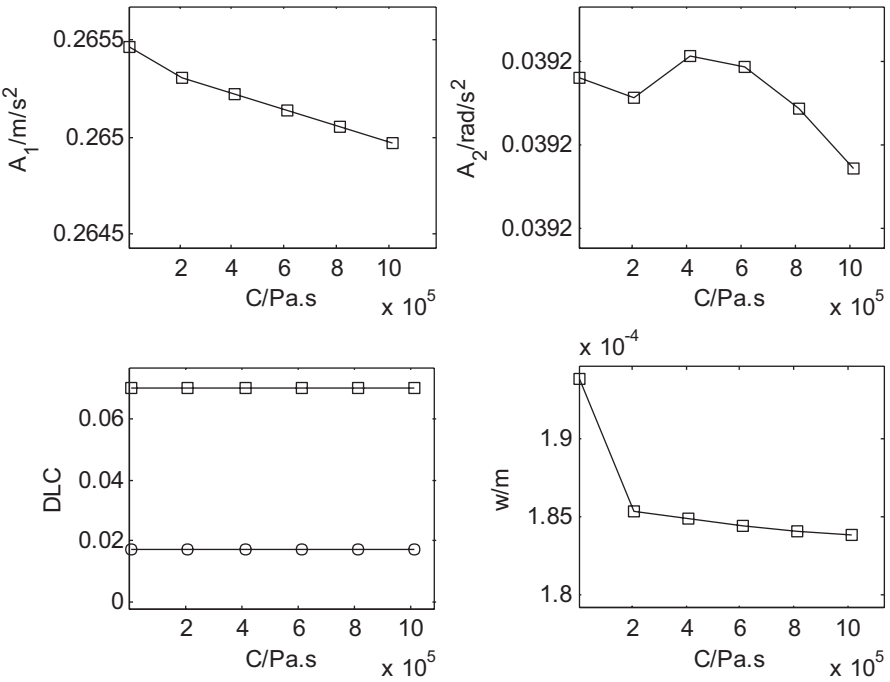

Fig. 8.25 The effect of the foundation damping coefficient

1. With an increase in the foundation response modulus, the vertical acceleration of the vehicle body increases, but the pitching acceleration of the vehicle body decreases.
2. With an increase in the foundation response modulus, the DLC of the front wheel increases and the DLC of the rear wheel decreases slightly.
3. An increase in the foundation response modulus results in a reduction of the pavement displacement.

Taking the pavement displacement as a criterion, a large foundation response modulus is beneficial to road fatigue life but harmful to riding comfort.

8.4.6 The Effect of the Foundation Damping coefficient

The effect of the foundation damping coefficient is shown in Fig. 8.25. It can be seen that

1. With an increase in the foundation damping coefficient, the vertical acceleration of the vehicle body decreases, but the pitching acceleration of the vehicle body only varies slightly.

2. With an increase in the foundation damping coefficient, the DLC of the front and rear wheel decreases slightly, and the pavement displacement also decreases.

Hence, a large foundation damping coefficient is beneficial to both road fatigue life and riding comfort.

8.5 Chapter Summary

In this chapter, vehicle–road coupled system is compared with the finite element model first so as to verify the validity of this coupled system. Then the effects of the vehicle–road coupling and system parameters on vehicle riding comfort and road fatigue damage were analyzed. Some rules of choosing parameters for low dynamic action can be suggested that

1. The effect of vehicle running velocity on vehicle riding comfort and pavement damage is fluctuant. Thus, those velocities inducing the maximum of vehicle body acceleration or pavement displacement should be calculated beforehand and drivers should be informed the risk of these velocities.
2. Increase of the vehicle load may further intensify road damage. However, there exists an unreasonable load value near to half gauge load which will induce resonance of vehicle body and be harmful to riding comfort.
3. It is favorable to decrease tire stiffness or suspension stiffness for controlling road damage. Increase of wheel track or wheelbase also leads to the decrease of road damage.
4. In order to improve riding comfort, the suspension stiffness should be decreased and the tire damping increased. Effects of wheel track, wheelbase, and tire stiffness on vertical acceleration of vehicle body contradict with that on pitching acceleration of vehicle body. Thus, the effect of these three parameters on ride comfort is complex.
5. Increase of topping height, base course height, topping density, base course density, topping Poisson ratio, base course Poisson ratio, or foundation response modulus is favorable to both improving ride comfort and decreasing road fatigue damage.

References

1. Li SH, Yang SP, Chen LQ. Effects of parameters on dynamic responses for a heavy vehicle-pavement-foundation coupled system. Int J Heavy Veh Sys. 2012;19(2):207–24.
2. Wu CP, Shen PA. Dynamic analysis of concrete pavements subjected to moving loads. J Transp Eng, ASCE. 1996, 122(5): 367–73.
3. Yang SP, Li SH, Lu YJ. Investigation on the dynamic interaction between a heavy vehicle and road pavement. Veh Syst Dyn. 2010;48(8):923–44.

4. Zhai WM, Sun X. Analysis and design of vertical dynamic parameters of wheel/rail system with low dynamic interactions. J China Railw Soc. 1993;15(3):1–9.
5. Zhai WM. Vehicle-track coupled dynamics. Beijing: China Railway Publishing House; 2002.
6. Cebon D. Interaction between heavy vehicles and roads SAE 930001. (SEA/SP—93/951); 1993.
7. Cole DJ. Truck suspension design to minimize road damage. Proceedings of the Institution of Mechanical Engineers, Part D: Journal of Automobile Engineering. 1996;210(D):95–107.
8. Yan TY, Liu DW, Chen HM. Road-friendless of heavy vehicles based on an active suspension system. Chin J Mech Eng. 2007;43(2):163–7.
9. Ren WQ. A virtual prototype in vehicle-road system dynamics -MSC.ADAMS applicant and practice. Beijing: Publishing House of Electronics Industry; 2005.
10. Lv PM, Dong ZH. Mechanical analysis of vehicle-asphalt pavement Systems. Beijing: China Communications Press; 2004.

Chapter 9
Modeling and Interaction of a Vehicle–Road System with Nonlinearity and Viscoelasticity

This chapter presents a nonlinear vehicle–road coupled model which is composed of a seven-degree-of-freedom (DOF) vehicle and a simply supported double-layer rectangular thin plate on a nonlinear viscoelastic foundation. The nonlinearity of the suspension stiffness, suspension damping, and tire stiffness is considered and the Leaderman constitutive relation and Burgers model are applied to describe the nonlinear and viscoelastic properties of the asphalt pavement material.

The equations of motion for the vehicle–road system are derived and the partial differential equation of the road pavement is discretized into an infinite number of second-order ordinary differential equations and first-order ordinary differential equations by Galerkin's method and a mathematical transform. A numerical integration method for solving this coupled system is developed and the nonlinear dynamic behaviors of the system are analyzed. In addition, the simulation results of the nonlinear viscoelastic model are compared to those of the linear or elastic model. The effects of system parameters on vehicle riding comfort and road damage are investigated [1, 2].

9.1 System Models and Equations of Motion

9.1.1 Modeling Nonlinearity and Viscoelasticity

A seven-DOF nonlinear vehicle and a double-layer rectangular thin plate on a nonlinear viscoelastic foundation with four simply supported boundaries are used to model the vehicle and the pavement. Figure 9.1 shows the nonlinear vehicle–road coupled system built in this work. In this model, the nonlinearity of tire and suspension and the viscoelasticity of pavement material are considered.

The nonlinear dynamic tire force can be formulated as

$$F_{tk} = k_t Z_t + \beta_1 k_t Z_t^2 + c_t \dot{Z}_t \tag{9.1}$$

S. Yang et al., *Dynamics of Vehicle-Road Coupled System,*
DOI 10.1007/978-3-662-45957-7_9

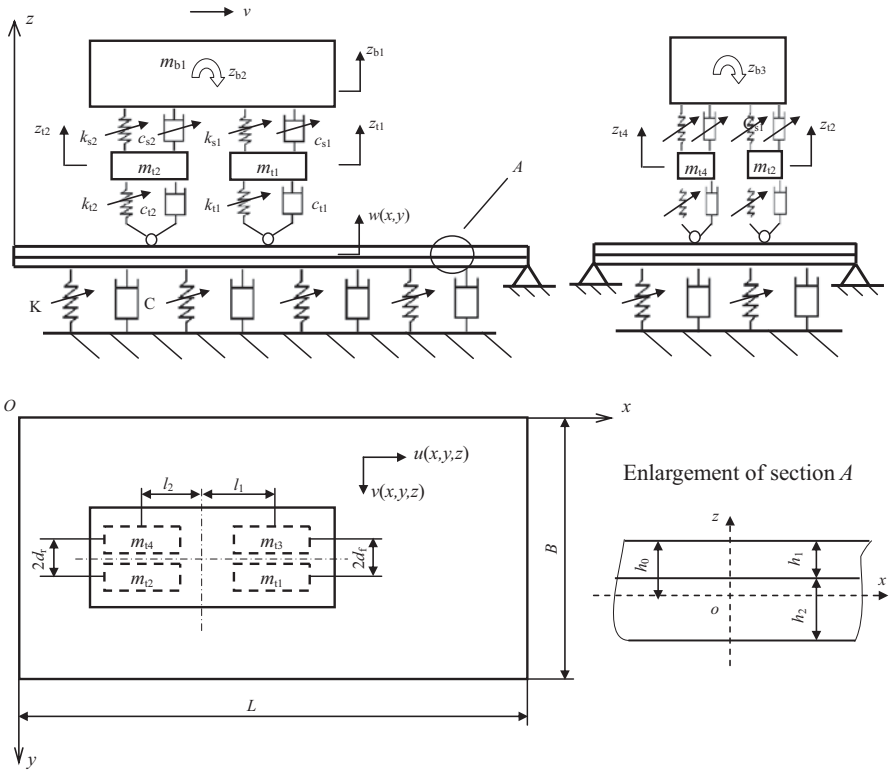

Fig. 9.1 The three-dimensional nonlinear vehicle–road coupled system. (Reprinted from [1], with kind permission from ASME)

where k_t is the linear tire stiffness, β_1 is the nonlinear tire stiffness coefficient, c_t is the tire damping coefficient, Z_t and $\dot{Z}_t$ are the relative vertical displacement and velocity between the wheel and the road surface, respectively.

The nonlinear spring force of the vehicle suspension is modeled as

$$F_{sk} = k_s z_s + \beta_2 k_s z_s^2 + \beta_3 k_s z_s^3 \tag{9.2}$$

where k_s is the linear stiffness coefficient of the suspension, β_2 and β_3 are the square and cubic nonlinear stiffness coefficients of the suspension, Z_s is the relative vertical displacement between the wheel and the vehicle body.

The hydraulic damper of the vehicle suspension is modeled as

$$F_{sc} = C_s(1+\beta_4 sig(\dot{Z}_s))\dot{Z}_s^{1.25} \tag{9.3}$$

where c_s is the linear damping coefficient of the suspension, β_4 is the asymmetry coefficient, $\dot{z}_s$ is the relative vertical velocity between the wheel and the vehicle body.

The upper and lower layers of the plate and the viscoelastic foundation stand for the asphalt topping, base course, and subgrade of the road, respectively. The Leaderman constitutive relation and the Burgers model are applied here to model the nonlinear viscous behaviors of the asphalt topping. The base course is assumed to be linear elastic. The Leaderman constitutive relation [3–5]can be expressed as

$$\begin{aligned}\sigma &= E_0(\varepsilon(x,z,t)+\beta_5\varepsilon(x,z,t)^2+\beta_6\varepsilon(x,z,t)^3)\\ &+\int_0^t \dot{E}(t-\tau)(\varepsilon(x,z,\tau)+\beta_4\varepsilon(x,z,\tau)^2+\beta_5\varepsilon(x,z,\tau)^3)d\tau\end{aligned} \tag{9.4}$$

where E_0 is the initial elastic modulus, β_5 is the square nonlinear coefficient, β_6 is the cubic nonlinear coefficient, and $E(t)$ is the relax function which is derived from the Burgers model for the asphalt mix. The Burgers model [6–8] is shown in Fig. 9.2 and can be written as

$$\sigma + p_1\dot{\sigma} + p_2\ddot{\sigma} = q_1\dot{\varepsilon} + q_2\ddot{\varepsilon} \tag{9.5}$$

where

$$\begin{aligned}p_1 &= \frac{\eta_2}{E_1}+\frac{\eta_2+\eta_3}{E_3},\\ p_2 &= \frac{\eta_2\eta_3}{E_1E_3},\\ q_1 &= \eta_2,\\ q_2 &= \frac{\eta_2\eta_3}{E_3}.\end{aligned} \tag{9.6}$$

The relax function obtained from Eq. (9.6) is

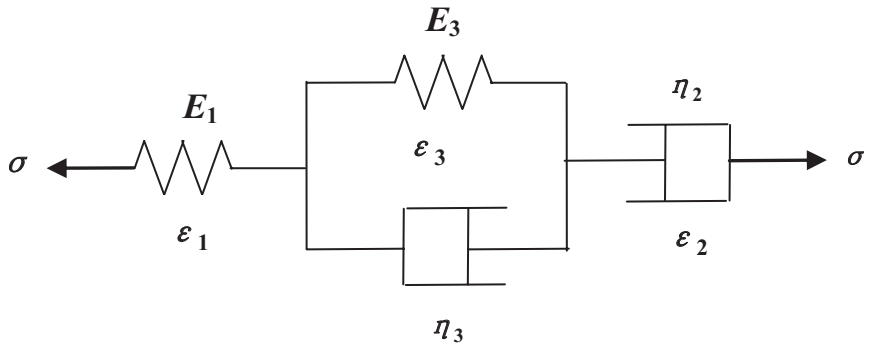

Fig. 9.2 The Burgers model. (Reprinted from [1], with kind permission from ASME)

$$E(t) = Ae^{-\alpha t} + Be^{-\beta t} \tag{9.7}$$

where

$$\begin{aligned} &\alpha = \frac{p_1 + \sqrt{p_1^2 - 4p_2}}{2p_2}, \beta = \frac{p_1 - \sqrt{p_1^2 - 4p_2}}{2p_2}, \\ &A = \frac{1}{\sqrt{p_1^2 - 4p_2}}(\alpha q_2 - q_1), B = \frac{1}{\sqrt{p_1^2 - 4p_2}}(q_1 - \beta q_2). \end{aligned} \tag{9.8}$$

The road subgrade is modeled by a nonlinear Kelvin foundation [9, 10] and the reaction force of the subgrade is

$$P = kZ_r + \beta_7 kz_r^3 + c\dot{z}_r \tag{9.9}$$

where K is the foundation response modulus, β_7 is the cubic nonlinear coefficient, and C is the foundation damping coefficient.

9.1.2 The Equations of Motion for a Nonlinear Vehicle

The vehicle equations of motion can be obtained by d'Alembert's principle

$$M_v\ddot{Z}_v + C_v\dot{Z}_v + K_vZ_v = R_v \tag{9.10}$$

where

$$M_v = diag[m_{b1} \quad m_{b2} \quad m_{b3} \quad m_{t1} \quad m_{t2} \quad m_{t3} \quad m_{t4}] \tag{9.11}$$

$$K_v = \begin{bmatrix} \sum_{i=1}^{4} k_{si} & -k_{s1}l_1 + k_{s2}l_2 - k_{s3}l_1 + k_{s4}l_2 & -k_{s1}d_f - k_{s2}d_r + k_{s3}d_f + k_{s4}d_r & -k_{s1} & -k_{s2} & -k_{s3} & -k_{s4} \\ & k_{s1}l_1^2 + k_{s2}l_2^2 + k_{s3}l_1^2 + k_{s4}l_2^2 & k_{s1}l_1d_f - k_{s2}l_2d_r - k_{s3}l_1d_f + k_{s4}l_2d_r & k_{s1}l_1 & -k_{s2}l_2 & k_{s3}l_1 & -k_{s4}l_2 \\ & & k_{s1}d_f^2 + k_{s2}d_r^2 + k_{s3}d_f^2 + k_{s4}d_r^2 & k_{s1}d_f & k_{s2}d_r & -k_{s3}d_f & -k_{s4}d_r \\ & & & k_{s1} & 0 & 0 & 0 \\ & & & & k_{s2} & 0 & 0 \\ & & & & & k_{s3} & 0 \\ & & & & & & k_{s4} \end{bmatrix} \tag{9.12}$$

$$C_v=\begin{bmatrix}
\sum_{i=1}^{4}c_{si} & -c_{s1}l_1+c_{s2}l_2-c_{s3}l_1+c_{s4}l_2 & -c_{s1}d_f-c_{s2}d_r+c_{s3}d_f+c_{s4}d_r & -c_{s1} & -c_{s2} & -c_{s3} & -c_{s4}\\
 & c_{s1}l_1^2+c_{s2}l_2^2+c_{s3}l_1^2+c_{s4}l_2^2 & c_{s1}l_1d_f-c_{s2}l_2d_r-c_{s3}l_1d_f+c_{s4}l_2d_r & c_{s1}l_1 & -c_{s2}l_2 & c_{s3}l_1 & -c_{s4}l_2\\
 & & c_{s1}d_f^2+c_{s2}d_r^2+c_{s3}d_f^2+c_{s4}d_r^2 & c_{s1}d_f & c_{s2}d_r & -c_{s3}d_f & -c_{s4}d_r\\
 & & & c_{s1} & 0 & 0 & 0\\
 & & & & c_{s2} & 0 & 0\\
 & & & & & c_{s3} & 0\\
 & & & & & & c_{s4}
\end{bmatrix} \tag{9.13}$$

$$R_v=[0\quad 0\quad 0\quad -F_{t1}\quad -F_{t2}\quad -F_{t3}\quad -F_{t4}]^T \tag{9.14}$$

$$Z_v=\left[z_{b1}\quad z_{b2}\quad z_{b3}\quad z_{t1}\quad z_{t2}\quad z_{t3}\quad z_{t4}\right]^T. \tag{9.15}$$

$z_{b1}, z_{b2},$ and z_{b3} are the vehicle body's vertical, pitching, and rolling displacements respectively and $z_{t1}, z_{t2}, z_{t3}, z_{t4}$ are the wheel's vertical displacements. Furthermore, m_1 is the mass of the vehicle body, m_2 and m_3 are the moments of inertia of the vehicle body in the pitching and rolling directions respectively, and $m_{t1}, m_{t2}, m_{t3}, and\, m_{t4}$ are the wheels' masses. $F_{t1}, F_{t2}, F_{t3},$ and F_{t4} are the tire forces, which will be expressed by Eq. (9.56) in Sect. 9.1.4. d_f is half of the front wheel track, d_r is half of the rear wheel track, and l_1+l_2 is the wheel space. $k_{ti}, k_{si}, c_{si}(i=1\sim 4)$ are equivalent nonlinear coefficients of the tire stiffness, suspension stiffness, and damping, which are expressed by

$$k_{ti}=k_{tli}+\beta_1 k_{tli}[Z_{ti}-r_{ti}-w(x_{ti},y_{ti},t)] \tag{9.16}$$

$$k_{si}=k_{sli}+\beta_2 k_{sli}(Z_{b1}-Z_{ti})+\beta_3 k_{sli}(Z_{b1}-Z_{ti})^2 \tag{9.17}$$

$$c_{si}=c_{sli}(1+\beta_4 sig(\dot{Z}_{b1}-\dot{Z}_{ti})\left|\dot{Z}_{b1}-\dot{Z}_{ti}\right|^{0.25} \tag{9.18}$$

where $i=1\sim 4$, k_{tli}, k_{sli}, c_{sli} are linear coefficients of the stiffness or damping, r_{ti} and $w(x_{ti},y_{ti},t)$ are the road roughness and pavement displacements at the midpoint of the tire print.

9.1.3 The Equations of Motion for the Nonlinear and Viscoelastic Pavement

The directions of the vertical, longitudinal, and transverse pavement displacements are shown in Fig. 9.1. According to elastic dynamics [11, 12], the pavement displacements take the following form

$$\begin{cases} u(x,y,z,t) = -z\dfrac{\partial w}{\partial y} \\ v(x,y,z,t) = -z\dfrac{\partial w}{\partial y} \\ w(x,y,t) \quad = w(x,y,t) \end{cases} . \tag{9.19}$$

The relationship between the pavement strains and displacements is

$$\begin{cases} \varepsilon_x \ = -z\dfrac{\partial^2 w}{\partial x^2} \\ \varepsilon_y \ = -z\dfrac{\partial^2 w}{\partial y^2} \\ \gamma_{xy} = -2z\dfrac{\partial^2 w}{\partial x \partial y} \end{cases} . \tag{9.20}$$

With the Leaderman constitutive relation Eq. (9.4), the asphalt topping stresses can be written as

$$\begin{cases} \sigma_x = \dfrac{E_1}{1-\mu_1^2}[g_1(x,y,z,t) + \int_0^t \dfrac{E(t-\tau)}{E_1} g_1(x,y,z,\tau)d\tau] \\ \sigma_y = \dfrac{E_1}{1-\mu_1^2}[g_2(x,y,z,t) + \int_0^t \dfrac{E(t-\tau)}{E_1} g_2(x,y,z,\tau)d\tau] \\ \tau_{xy} = G_1(g_3(x,y,z,t) + \int_0^t \dfrac{E(t-\tau)}{G_1} g_3(x,y,z,\tau)d\tau) \end{cases} \tag{9.21}$$

where E_1, G_1, and μ_1 are the elastic modulus, the shear modulus, and Poisson's ratio of the asphalt pavement, respectively. The expressions of g_1, g_2, and g_3 are

$$\begin{aligned} g_1(x,y,z,t) = &-z\frac{\partial^2 w}{\partial x^2} + \beta_5 z^2 (\frac{\partial^2 w}{\partial x^2})^2 - \beta_6 z^3 (\frac{\partial^2 w}{\partial x^2})^3 \\ &+ \mu_1(-z\frac{\partial^2 w}{\partial y^2} + \beta_5 z^2 (\frac{\partial^2 w}{\partial y^2})^2 - \beta_6 z^3 (\frac{\partial^2 w}{\partial y^2})^3) \end{aligned} \tag{9.22}$$

$$\begin{aligned} g_2(x,y,z,t) = &-z\frac{\partial^2 w}{\partial y^2} + \beta_5 z^2 (\frac{\partial^2 w}{\partial y^2})^2 - \beta_6 z^3 (\frac{\partial^2 w}{\partial y^2})^3 \\ &+ \mu_1(-z\frac{\partial^2 w}{\partial x^2} + \beta_5 z^2 (\frac{\partial^2 w}{\partial x^2})^2 - \beta_6 z^3 (\frac{\partial^2 w}{\partial x^2})^3) \end{aligned} \tag{9.23}$$

$$g_3(x,y,z,t) = -2z\frac{\partial^2 w}{\partial x \partial y} + 4\beta_5 z^2 (\frac{\partial^2 w}{\partial x \partial y})^2 - 8\beta_6 z^3 (\frac{\partial^2 w}{\partial x \partial y})^3. \tag{9.24}$$

For the linear constitutive relation, the stresses of the base course are

$$\begin{cases} \sigma_x = -\dfrac{E_1}{1-\mu_2^2} z[\dfrac{\partial^2 w}{\partial x^2} + \mu_2 \dfrac{\partial^2 w}{\partial y^2}] \\ \sigma_y = -\dfrac{E_1}{1-\mu_2^2} z[\dfrac{\partial^2 w}{\partial y^2} + \mu_2 \dfrac{\partial^2 w}{\partial x^2}] \\ \tau_{xy} = -2G_2 z \dfrac{\partial^2 w}{\partial x \partial y} \end{cases} \tag{9.25}$$

where E_2, G_2, and μ_2 are the elastic modulus, the shear modulus, and Poisson's ratio of the base course, respectively.

The position of the stress-neutral layer is shown in Fig. 9.1 and has been determined in Chap. 5,

$$h_0 = \frac{E_1 h_1^2 + E_2(2h_1 + h_2)h_2}{2E_1 h_1 + 2E_2 h_2}. \tag{9.26}$$

The internal forces of the double-layer, thin plate satisfy the following equation

$$\begin{cases} M_x = \int_{h_0-h_1-h_2}^{h_0} \sigma_x z dz \\ = -D_{x1}\dfrac{\partial^2 w}{\partial x^2} - D_{x2}(\dfrac{\partial^2 w}{\partial x^2})^2 - D_{x3}(\dfrac{\partial^2 w}{\partial x^2})^3 - D_{y1}\dfrac{\partial^2 w}{\partial y^2} \\ \quad - D_{y2}(\dfrac{\partial^2 w}{\partial y^2})^2 - D_{y3}(\dfrac{\partial^2 w}{\partial y^2})^3 - \int_0^t E(t-\tau) D_{E1}(x,y,\tau) d\tau \\ M_y = \int_{h_0-h_1-h_2}^{h_0} \sigma_y z dz \\ = -D_{y1}\dfrac{\partial^2 w}{\partial x^2} - D_{y2}(\dfrac{\partial^2 w}{\partial x^2})^2 - D_{y3}(\dfrac{\partial^2 w}{\partial x^2})^3 - D_{x1}\dfrac{\partial^2 w}{\partial y^2} \\ \quad - D_{x2}(\dfrac{\partial^2 w}{\partial y^2})^2 - D_{x3}(\dfrac{\partial^2 w}{\partial y^2})^3 - \int_0^t E(t-\tau) D_{E2}(x,y,\tau) d\tau \\ M_{xy} = \int_{h_0-h_1-h_2}^{h_0} \tau_{xy} z dz = -D_{xy1}\dfrac{\partial^2 w}{\partial x \partial y} - D_{xy2}(\dfrac{\partial^2 w}{\partial x \partial y})^2 - D_{xy3}(\dfrac{\partial^2 w}{\partial x \partial y})^3 \\ \quad - \int_0^t E(t-\tau) D_{Exy}(x,y,\tau) d\tau \end{cases} \tag{9.27}$$

where

$$D_{x1} = \frac{h_1(h_1^2 E_1 - 3h_0 h_1 E_1 + 3h_0^2 E_1)}{3(1-\mu_1^2)} + \frac{E_2[(h_0-h_1)^3 - (h_0-h_1-h_2)^3]}{3(1-\mu_2^2)} \tag{9.28}$$

$$D_{x2} = \frac{h_1\beta_5 E_1(h_1^3 + 6h_0^2 h_1 - 4h_0 h_1^2 - 4h_0^3)}{4(1-\mu_1^2)} \tag{9.29}$$

$$D_{x3} = \frac{h_1\beta_6 E_1(-5h_0 h_1^3 + 10h_0^2 h_1^2 - 10h_0^3 h_1 + 5h_0^4 + h_1^4)}{5(1-\mu_1^2)} \tag{9.30}$$

$$D_{y1} = \frac{\mu_1 h_1(h_1^2 E_1 - 3h_0 h_1 E_1 + 3h_0^2 E_1)}{3(1-\mu_1^2)} + \frac{\mu_2 E_2[(h_0-h_1)^3 - (h_0-h_1-h_2)^3]}{3(1-\mu_2^2)} \tag{9.31}$$

$$D_{y2} = \frac{\mu_1 h_1\beta_5 E_1(h_1^3 + 6h_0^2 h_1 - 4h_0 h_1^2 - 4h_0^3)}{4(1-\mu_1^2)} \tag{9.32}$$

$$D_{y3} = \frac{\mu_1 h_1\beta_6 E_1(-5h_0 h_1^3 + 10h_0^2 h_1^2 - 10h_0^3 h_1 + 5h_0^4 + h_1^4)}{5(1-\mu_1^2)} \tag{9.33}$$

$$\begin{aligned} D_{xy1} = {} & -2G_1 h_1^2 h_0 + 2G_1 h_1 h_0^2 + \frac{2}{3}G_1 h_1^3 + 2G_2 h_0^2 h_2 - 4G_2 h_0 h_1 h_2 - 2G_2 h_0 h_2^2 \\ & + 2G_2 h_1^2 h_2 + 2G_2 h_1 h_2^2 + \frac{2}{3}G_2 h_2^3 \end{aligned} \tag{9.34}$$

$$D_{xy2} = G_1 h_1\beta_6(h_1^3 + 6h_0^2 h_1 - 4h_0 h_1^2 - 4h_0^3) \tag{9.35}$$

$$D_{xy3} = \frac{5}{8}G_1 h_1\beta_6(-5h_0 h_1^3 + 10h_0^2 h_1^2 - 10h_0^3 h_1 + 5h_0^4 + h_1^4) \tag{9.36}$$

$$D_{E1}(x,y,\tau) = -\int_{h_0-h_1}^{h_0} g_1(x,y,z,\tau)z/(1-\gamma_1^2)dz \tag{9.37}$$

$$D_{E2}(x,y,\tau) = -\int_{h_0-h_1}^{h_0} g_2(x,y,z,\tau)z/(1-\gamma_1^2)dz \tag{9.38}$$

$$D_{Exy}(x,y,\tau) = -\int_{h_0-h_1}^{h_0} g_3(x,y,z,\tau)zdz. \tag{9.39}$$

By integrating the three-dimensional balance equations of the double-layer, thin plate with the vertical-varied density along Z, one may obtain

$$\begin{cases} \dfrac{\partial M_x}{\partial x}+\dfrac{\partial M_{xy}}{\partial x}-Q_x=0 \\ \dfrac{\partial M_{xy}}{\partial x}+\dfrac{\partial M_y}{\partial y}-Q_y=0 \\ \dfrac{\partial Q_x}{\partial x}+\dfrac{\partial Q_y}{\partial y}-\rho h\dfrac{\partial^2 w}{\partial t^2}+q(x,y,t)=0 \end{cases} \tag{9.40}$$

where

$$\rho h=\int_{h_0-h_1}^{h_0}\rho_1 dz+\int_{h_0-h_1-h_2}^{h_0-h_1}\rho_2 dz=\rho_1 h_1+\rho_2 h_2. \tag{9.41}$$

From Eq. (9.40), one may obtain the partial differential equation of the pavement vertical vibration induced by the moving vehicle loads,

$$\begin{aligned} &D_{x1}\left(\frac{\partial^4 w}{\partial x^4}+\frac{\partial^4 w}{\partial y^4}\right)+2(D_{y1}+2D_{xy1})\frac{\partial^4 w}{\partial x^2\partial y^2} \\ &+2D_{x2}\left[\left(\frac{\partial^3 w}{\partial x^3}\right)^2+\frac{\partial^2 w}{\partial x^2}\frac{\partial^4 w}{\partial x^4}+\left(\frac{\partial^3 w}{\partial y^3}\right)^2+\frac{\partial^2 w}{\partial y^2}\frac{\partial^4 w}{\partial y^4}\right] \\ &+2D_{y2}\left[\left(\frac{\partial^3 w}{\partial x\partial y^2}\right)^2+\frac{\partial^2 w}{\partial y^2}\frac{\partial^4 w}{\partial x^2\partial y^2}+\left(\frac{\partial^3 w}{\partial x^2\partial y}\right)^2+\frac{\partial^2 w}{\partial x^2}\frac{\partial^4 w}{\partial x^2\partial y^2}\right] \\ &+4D_{xy2}\left[\frac{\partial^3 w}{\partial x^2\partial y}\frac{\partial^3 w}{\partial x\partial y^2}+\frac{\partial^2 w}{\partial x\partial y}\frac{\partial^4 w}{\partial x^2\partial y^2}\right] \\ &+3D_{x3}\left[2\frac{\partial^2 w}{\partial x^2}\left(\frac{\partial^3 w}{\partial x^3}\right)^2+2\frac{\partial^2 w}{\partial y^2}\left(\frac{\partial^3 w}{\partial y^3}\right)^2+\left(\frac{\partial^2 w}{\partial x^2}\right)^2\frac{\partial^4 w}{\partial x^4}+\left(\frac{\partial^2 w}{\partial y^2}\right)^2\frac{\partial^4 w}{\partial y^4}\right] \\ &+3D_{y3}\left[2\frac{\partial^2 w}{\partial y^2}\left(\frac{\partial^3 w}{\partial x\partial y^2}\right)^2+2\frac{\partial^2 w}{\partial x^2}\left(\frac{\partial^3 w}{\partial x^2\partial y}\right)^2+\left(\frac{\partial^2 w}{\partial y^2}\right)^2\frac{\partial^4 w}{\partial x^2\partial y^2}\right. \\ &\left.+\left(\frac{\partial^2 w}{\partial x^2}\right)^2\frac{\partial^4 w}{\partial x^2\partial y^2}\right] \\ &+6D_{xy3}\left[2\frac{\partial^2 w}{\partial x\partial y}\frac{\partial^3 w}{\partial x\partial y^2}\frac{\partial^3 w}{\partial x^2\partial y}+\left(\frac{\partial^2 w}{\partial x\partial y}\right)^2\frac{\partial^4 w}{\partial x^2\partial y^2}\right] \\ &+\int_0^t \dot{E}(t-\tau)\left(\frac{\partial^2 D_{E1}}{\partial x^2}+2\frac{\partial^2 D_{Exy}}{\partial x\partial y}+\frac{\partial^2 D_{E2}}{\partial y^2}\right)d\tau \\ &+Kw+C\frac{\partial w}{\partial t}+\rho h\frac{\partial^2 w}{\partial t^2}=L(w)+\rho h\frac{\partial^2 w}{\partial t^2}=\sum_{s=1}^{4}F_{ts}\delta(x-x_{ts})\delta(y-y_{ts}) \end{aligned} \tag{9.42}$$

where F_{ts} is the s th tire force.

The displacement of the double-layer, thin plate with four simply supported boundaries can be expressed as

$$w(x,y,t)=\sum_{m=1}^{NM}\sum_{n=1}^{NN}U_{mn}(t)\sin\frac{m\pi x}{L}\sin\frac{n\pi y}{B}. \tag{9.43}$$

The substitution of Eq. (9.43) into Eq. (9.42) leads to a residual value. By limiting the residual value, the following equation can be obtained using Galerkin's method,

$$\int_0^L\int_0^B (L(w)+\rho h\frac{\partial^2 w}{\partial t^2}-\sum_{i=1}^{4}F_{ti}\delta(x-x_{ti})\delta(y-y_{ti}))\sin(i\pi x/L) \sin(j\pi y/B)dxdy=0. \tag{9.44}$$

By simplifying the above equation, one can discretize Eq. (9.42) into a set of ordinary differential equations with an integral item,

$$M_{ij}\ddot{U}_{ij}+C_{ij}\dot{U}_{ij}+K_{1ij}U_{ij}+K_{2ij}U_{ij}^2+K_{3ij}U_{ij}^3+\int_0^t\dot{E}(t-\tau)G(\tau)d\tau=R_{ij} \tag{9.45}$$

where $i=1\sim NM$, $j=1\sim NN$,

$$M_{ij}=\frac{LB}{4}\rho h,\ C_{ij}=\frac{LB}{4}C, \tag{9.46}$$

$$K_{1ij}=D_{1ij}+\frac{LB}{4}K, K_{2ij}=D_{2ij}, K_{3ij}=D_{3ij}+\frac{LB}{4}\beta_7 K \tag{9.47}$$

$$\begin{aligned}G(\tau)&=\int_0^L\int_0^B(\frac{\partial^2 D_{E1}}{\partial x^2}+2\frac{\partial^2 D_{Exy}}{\partial x\partial y}+\frac{\partial^2 D_{E2}}{\partial y^2})\sin(i\pi x/L)\sin(j\pi y/B)dxdy \\ &=A_{1ij}U_{ij}+A_{2ij}U_{ij}^2+A_{3ij}U_{ij}^3\end{aligned} \tag{9.48}$$

$$R_{ij}=\int_0^L\int_0^B\sum_{s=1}^{4}F_{ts}\delta(x-x_{ts})\delta(y-y_{ts})\sin(i\pi x/L)\sin(j\pi y/B)dxdy \tag{9.49}$$

where D_{1ij}, D_{2ij}, D_{3ij}, A_{1ij}, A_{2ij}, and A_{3ij} are expressions of the system parameters.

Due to the integral term in Eq. (9.45), the following transformation [3–5] is applied,

$$x_{1ij}+x_{2ij}=\int_0^t\dot{E}(t-\tau)G(\tau)d\tau \tag{9.50}$$

By substituting Eq. (9.7) into Eq. (9.45), one obtains

$$\begin{cases} x_{1ij} = \int_0^t -A\alpha e^{-\alpha(t-\tau)} G(\tau) d\tau \\ x_{2ij} = \int_0^t -B\beta e^{-\beta(t-\tau)} G(\tau) d\tau \end{cases}. \tag{9.51}$$

The first derivation of Eq. (9.51) is

$$\begin{cases} \dot{x}_{1ij} = -\alpha x_{1ij} - A\alpha(A_{1ij}U_{ij} + A_{2ij}U_{ij}^2 + A_{3ij}U_{ij}^3) \\ x_{2ij} = -\beta x_{2ij} - B\beta(A_{1ij}U_{ij} + A_{2ij}U_{ij}^2 + A_{3ij}U_{ij}^3) \end{cases}. \tag{9.52}$$

The substitution of Eq. (9.50) into Eq. (9.45) leads to

$$M_{ij}\ddot{U}_{ij} + C_{ij}\dot{U}_{ij} + K_{1ij}U_{ij} + K_{2ij}U_{ij}^2 + K_{3ij}U_{ij}^3 + x_{1ij} + x_{2ij} = R_{ij}. \tag{9.53}$$

Thus Eq. (9.45) turns into one second-order ordinary differential equation, Eq. (9.53), and two first-order ordinary differential equations, Eq. (9.52). By re-writing them as matrix equations, one obtains

$$\begin{cases} \dot{X}_1 = -\alpha X_1 - A\alpha(A_1U + A_2U^2 + A_3U^3) = f(t, X_1, U) \\ \dot{X}_2 = -\beta X_2 - B\beta(A_1U + A_2U^2 + A_3U^3) = f(t, X_2, U) \end{cases} \tag{9.54}$$

$$M_r\ddot{U} + C_r\dot{U} + K_rU = R_r - X_1 - X_2 \tag{9.55}$$

where $\{X_1\}$, $\{X_2\}$, $\{AU\}$, $\{U\}$, and $\{R_f - X_1 - X_2\}$ are the column vectors with $NM \times NN$ lines. The components of these column vectors are x_{1ij}, x_{2ij}, $A_{1ij}U_{ij} + A_{2ij}U_{ij}^2 + A_{3ij}U_{ij}^3$, U_{ij}, and $R_{ij} - x_{1ij} - x_{2ij}$ respectively. The row subscript n_r of these column vectors depends on the mode numbers i and j through the expression $n_r = (i-1) \times NN + j$. $[M_r]$, $[C_r]$, and $[K_r]$ are square matrixes of order $NM \times NN$. Here, $K_r = [K_1 + K_2U + K_3U^2]$.

9.1.4 The Interaction Between the Vehicle and the Pavement

In regards to the coupling action of the vehicle and the road, the vertical contact force between the tire and the pavement is related not only to the tire motion and road surface roughness, but also to the road vibration. Based on Eq. (9.1), the vertical contact force between the tire and the pavement may be expressed as

$$F_{ts} = k_{ts}[x_{ts} - r_{ts} - w(x_{ts}, y_{ts}, t)] + c_{ts}[\dot{x}_{ts} - \dot{r}_{ts} - \frac{\partial w(x_{ts}, y_{ts}, t)}{\partial t}] \tag{9.56}$$

where $w(x_{ts}, y_{ts}, t)$ is the pavement displacement of the point under the s th tire and r_{ts} is the road surface roughness satisfying the following functions $r_{t1} = r_{t3} = B_0 \sin(\frac{2\pi vt}{L_0}),\quad r_{t2} = r_{t4} = B_0 \sin[\frac{2\pi}{L_0}(vt + l_1 + l_2)]$.

By substituting Eq. (9.43) into Eq. (9.56), one obtains

$$\begin{aligned} F_{ts} &= k_{ts}(z_{ts} - r_{ts}) + c_{ti}(\dot{z}_{ts} - \dot{r}_{ts}) - k_{ts}\sum_{m=1}^{NM}\sum_{n=1}^{NN} U_{mn}(t)\sin\frac{m\pi x}{L}\sin\frac{n\pi y}{B} \\ &-c_{ts}\sum_{m=1}^{NM}\sum_{n=1}^{NN}\dot{U}_{mn}(t)\sin\frac{m\pi x}{L}\sin\frac{n\pi y}{B} - c_{ts}\sum_{m=1}^{NM}\sum_{n=1}^{NN} U_{mn}(t)\frac{m\pi v}{L}\cos\frac{m\pi x}{L}\sin\frac{n\pi y}{B}. \end{aligned} \tag{9.57}$$

From Eq. (9.49) one may get

$$\begin{aligned} R_{ij} &= \int_0^L\int_0^B \sum_{s=1}^{4}[k_{ts}(z_{ts} - r_{ts}) + c_{ts}(\dot{z}_{ts} - \dot{r}_{ts}) - k_{ts}\sum_{m=1}^{NM}\sum_{n=1}^{NN} U_{mn}(t)\sin\frac{m\pi x}{L}\sin\frac{n\pi y}{B} \\ &-c_{ts}\sum_{m=1}^{NM}\sum_{n=1}^{NN}\dot{U}_{mn}(t)\sin\frac{m\pi x}{L}\sin\frac{n\pi y}{B} - c_{ts}\sum_{m=1}^{NM}\sum_{n=1}^{NN} U_{mn}(t)\frac{m\pi v}{L}\cos\frac{m\pi x}{L}\sin\frac{n\pi y}{B}] \\ &\delta(x - x_{ts})\delta(y - y_{ts})\sin(i\pi x/L)\sin(j\pi y/B)dxdy. \end{aligned} \tag{9.58}$$

It is clear from the above two equations that the contact forces between the tire and the road pavement are not only influenced by the wheel displacement, wheel velocity, and road roughness, but also by the pavement vibration mode's displacement and velocity. Thus, Z_{ts}, the four wheel displacements, are coupled with U_{mn}, the pavement vibration mode's displacements.

Equation (9.10) and Eq. (9.55) can be rewritten in the following form,

$$[M]\{\ddot{Z}\} + [C]\{\dot{Z}\} + [K]\{Z\} = \{R\} \tag{9.59}$$

where

$$[M] = \begin{bmatrix} M_v & 0 \\ 0 & M_r \end{bmatrix},\quad \{R\} = \begin{Bmatrix} R_v \\ R_r - X_1 - X_2 \end{Bmatrix} \tag{9.60}$$

The scheme of $[C]$ is

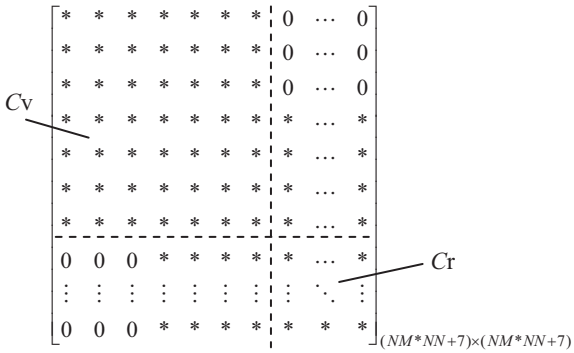

The scheme of [K] is

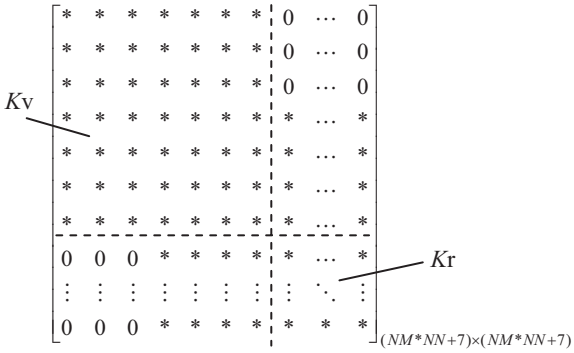

Consequently, Eq. (9.54) and Eq. (9.59) compose the first- and second-order ordinary differential equations of the nonlinear vehicle–road coupled system. Since the stiffness matrix K and damping matrix C of Eq. (9.59) have coupled items and time-varied parameters, the following numerical integration method is used to solve the equations.

9.2 Dynamic Responses of the Nonlinear Vehicle–Road Coupled System

The quick direct integral method and the Runge–Kutta method of order 4 can be combined to solve the system of equations. The routines of the calculation program in this study are as follows:

1. Establish the initial conditions

Assume the initial displacement and initial velocity of Eq. (9.59) are $\begin{cases}\{Z\}_0 = \{Z(0)\} \\ \{\dot{Z}\}_0 = \{\dot{Z}(0)\}\end{cases}$.

Assume the initial displacements of Eq. (9.54) are $\begin{cases}\{X_1\}_0 = \{X_1(0)\} \\ \{X_2\}_0 = \{X_2(0)\}\end{cases}$.

The initial acceleration can be obtained from Eq. (9.59),

$$\{\ddot{Z}\}_0 = [M]^{-1}(\{R\}_0 - [K]_0\{Z\}_0 - [C]_0\{\dot{Z}\}_0). \tag{9.61}$$

2. Compute the displacement, velocity, and acceleration of the vehicle–road coupled system when $t = (n+1)\Delta t$. Here, $n+1$ is the number of steps, and $n = 0,1,2,3\ldots$

Let $\phi = \psi = 0$ when $n = 0$ and $\phi = \psi = 1/2$ when $n \geq 1$. Given the integration time step Δt, one can build the following relations:

$$\begin{cases}\{Z\}_{n+1} = \{Z\}_n + \{\dot{Z}\}_n \Delta t + (1/2+\psi)\{\ddot{Z}\}_n \Delta t^2 - \psi\{\ddot{Z}\}_{n-1}\Delta t^2 \\ \{\dot{Z}\}_{n+1} = \{\dot{Z}\}_n + (1+\phi)\{\ddot{Z}\}_n \Delta t - \phi\{\ddot{Z}\}_{n-1}\Delta t\end{cases} \tag{9.62}$$

$$\begin{cases}\{X_1\}_{n+1} = \{X_1\}_n + \dfrac{\Delta t}{6}(f_{11} + 2f_{12} + 2f_{13} + f_{14}) \\ \{X_2\}_{n+1} = \{X_2\}_n + \dfrac{\Delta t}{6}(f_{21} + 2f_{22} + 2f_{23} + f_{24})\end{cases} \tag{9.63}$$

where

$$\begin{aligned}
&f_{11} = f_1(t_n, X_{1n}, U_n), f_{12} = f_1\left(t_n + \frac{\Delta t}{2}, X_{1n} + \frac{\Delta t}{2} f_{11}, U_n\right), \\
&f_{13} = f_1\left(t_n + \frac{\Delta t}{2}, X_{1n} + \frac{\Delta t}{2} f_{12}, U_n\right), f_{14} = f_1(t_n + \Delta t, X_{1n} + \Delta t f_{13}, U_n) \\
&f_{21} = f_2(t_n, X_{1n}, U_n), f_{22} = f_2\left(t_n + \frac{\Delta t}{2}, X_{1n} + \frac{\Delta t}{2} f_{21}, U_n\right), \\
&f_{23} = f_2\left(t_n + \frac{\Delta t}{2}, X_{1n} + \frac{\Delta t}{2} f_{22}, U_n\right), f_{24} = f_2(t_n + \Delta t, X_{1n} + \Delta t f_{23}, U_n).
\end{aligned} \tag{9.64}$$

By substituting Eq. (9.62) and Eq. (9.63) into Eq. (9.59) when $t = (n+1)\Delta t$, one can obtain

$$\begin{aligned}
\{\ddot{Z}\}_{n+1} = [M]^{-1}(&\{R\}_{n+1} - [K]_{n+1}\{Z\}_n - ([C]_{n+1} + [K]_{n+1}\Delta t)\{\dot{Z}\}_n \\
&- \{(1+\phi)[C]_{n+1} + (1/2+\psi)[K]_{n+1}\Delta t\}\{\ddot{Z}\}_n \Delta t \\
&+ (\phi[C]_{n+1} + \psi[K]_{n+1}\Delta t)\{A\}_{n-1}\Delta t.
\end{aligned} \tag{9.65}$$

3. By repeating process (2), one can get the displacement, velocity, and acceleration of the system step by step.

The convergence criterion of this method is

$$\Delta t < 2/\omega \text{ when } \quad \phi = \psi = 1/2\, fa \tag{9.66}$$

where Δt is the integration time step, and ω is the natural angular frequency of the system.

During the dynamic simulation, the vehicle parameters correspond to those of a heavy truck. Parameters for the vehicle system are as follows [12, 13]:

$m_b1 = 15280$ kg, $m_b2 = 3 \times 10^5$ kg m^2, $m_b3 = 0.6 \times 10^5$ kg m^2, $m_t1 = m_t3 = 190$ kg, $m_t2 = m_t4 = 380$ kg, $k_{sl}1 = k_{sl}3 = 370 \times 10^3$ N/m, $k_{sl}2 = k_{sl}4 = 920 \times 10^3$ N/m, $c_{sl}1 = c_{sl}3 = 12{,}000$ N s/m, $c_{sl}2 = c_{sl}4 = 30{,}000$ N s/m, $k_{tl}1 = k_{tl}3 = 0.73 \times 10^6$ N/m, $k_{tl}2 = k_{tl}4 = 1.46 \times 10^6$ N/m, $c_t1 = c_t3 = 600$ N s/m, $c_t2 = c_t4 = 900$ N s/m, $l_1 = 3.29$ m, $l_2 = 1.48$ m, $l_f = 1.90$ m, $l_r = 1.80$ m, $\beta_1 = 0.01$, $\beta_2 = 0.1$, $\beta_3 = 0.6$, $\beta_4 = 1/3$.

Parameters of the pavement and foundation are given below [14, 15]:

$L = 600$ m, $B = 24$ m, $h_1 = 0.09$ m, $E_1 = 2400$ MPa, $E_3 = 2400$ MPa, $\eta_2 = 3159.32$ MPa s, $\eta_3 = 509.61$ MPa s, $\mu_1 = 0.35$, $\rho_1 = 2.613 \times 10^3$ kg/m^3, $h_2 = 0.2$ m, $E_2 = 1100$ MPa, $\mu_2 = 0.35$, $\rho_2 = 2.083 \times 10^3$ kg/m^3, $K = 48 \times 10^6$ N/m^2, $C = 0.3 \times 10^4$ N s/m^2, $\beta_5 = 0.1$, $\beta_6 = 0.1$, $\beta_7 = 0.01$, $L_0 = 2.3$ m, $B_0 = 0.002$ m.

In order to confirm the validity of the integration results, two numerical tests were done to choose a suitable mode number for the pavement displacement and an integration time step. It is found that, when the time step is smaller than 1 ms and the mode number of the pavement is larger than 10, dynamic responses of the system vary slightly. Thus, a suitable value of NM is 10 and a suitable value of Δt is 1 ms.

The natural frequencies of the derived system are calculated with the system parameters selected above. The vertical, pitching, and rolling natural frequencies of the vehicle body and the vertical natural frequencies of the four wheels are 1.6314, 0.8076, 0.7562, 12.1137, 12.1357, 12.6053, and 12.6492 Hz, respectively. The natural frequencies of the road range from 34.1739 to 143.3673 Hz. By substituting the highest natural frequency of the coupled system 143.3673 Hz into Eq. (9.66), one obtains $\Delta t < 2/(2\pi \times 143.3673) = 2.2\text{ms}$. Because the time step Δt is 1 ms, the convergence criterion is well satisfied.

In addition, the responses that occur during the first 5 s are removed so as to minimize the effect of the transitional course. When $v = 10$ m/s and $B_0 = 0.002$ m, the time history of the vehicle body's vertical acceleration, phase trajectories, and Poincaré maps of the vehicle body's vertical motion, along with the power spectrum of the vehicle body's vertical displacement can be obtained, as shown in Fig. 9.3. From Fig. 9.3, it can be seen that the time history is periodic, the phase trajectories are a closed curve, the Poincaré map is a point, and the power spectrum consists of discrete lines. Thus it can be concluded that the vertical motion of the vehicle body is periodic. It has also been found that the peak frequencies in the power spectrum include 4.38, 8.73, 13.1, and 1.6 Hz, which correspond to one time, two times, and

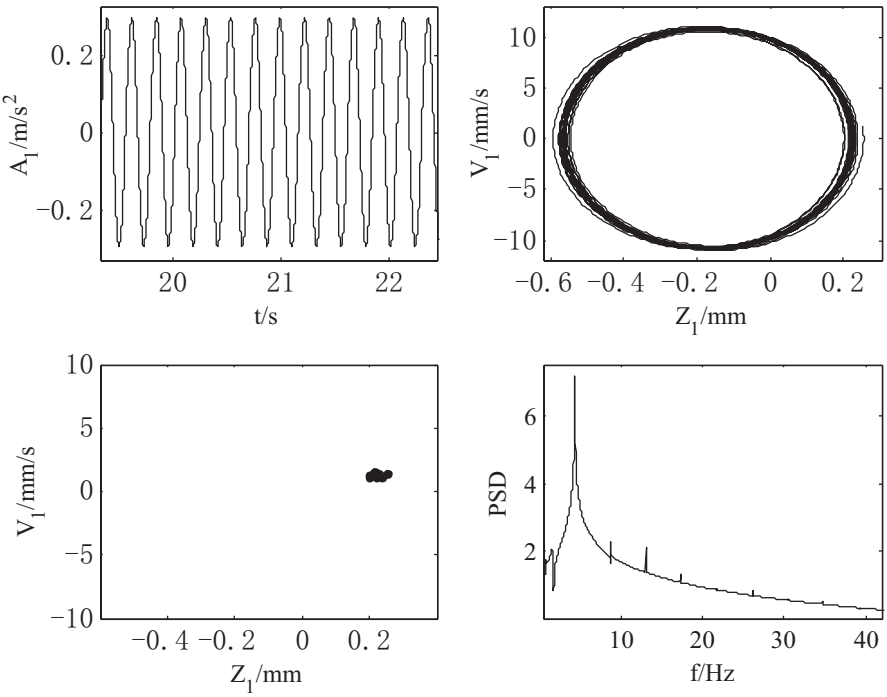

Fig. 9.3 Vehicle responses with B_0=0.002 m. (Reprinted from [1], with kind permission from ASME)

three times the road roughness excitation frequency, as well as the vertical natural frequency of the vehicle body respectively. The 4.38 and 1.6 Hz values may be easily explained using vibration theory: the frequency components of forced vibration include the excitation frequency and natural frequency of the system. The 8.73 and 13.1 Hz values may be the result of the square and cubic nonlinearities of the system, which result in two and three times the excitation frequency, respectively.

Figure 9.4 shows the time history, phase trajectories, Poincaré maps, and power spectrum of the pavement vertical displacement when B_0=0.002 m. It may be observed from Fig. 9.4 that the time history is not periodic, the phase trajectories are complicate and irregular, the Poincaré map is an unclosed curve, and the power spectrum consists of discrete lines. According to nonlinear vibration theory, the largest Lyapunov exponent may be used as a criterion for motion type. If the largest Lyapunov exponent is larger than zero, the system motion is possibly chaotic. On the other hand, if the largest Lyapunov exponent is zero, the system will have a periodic or quasiperiodic motion. When B_0=0.002 m, the largest Lyapunov exponent of the pavement displacement is computed using the method of Wolf [16, 17], and the result is zero. Thus it may be concluded that the vertical motion of the pavement is quasiperiodic. It is also found that the spectral peak frequencies are 4.38, 8.73, and 13.1 Hz, corresponding to one time, two times, and three times the road excitation

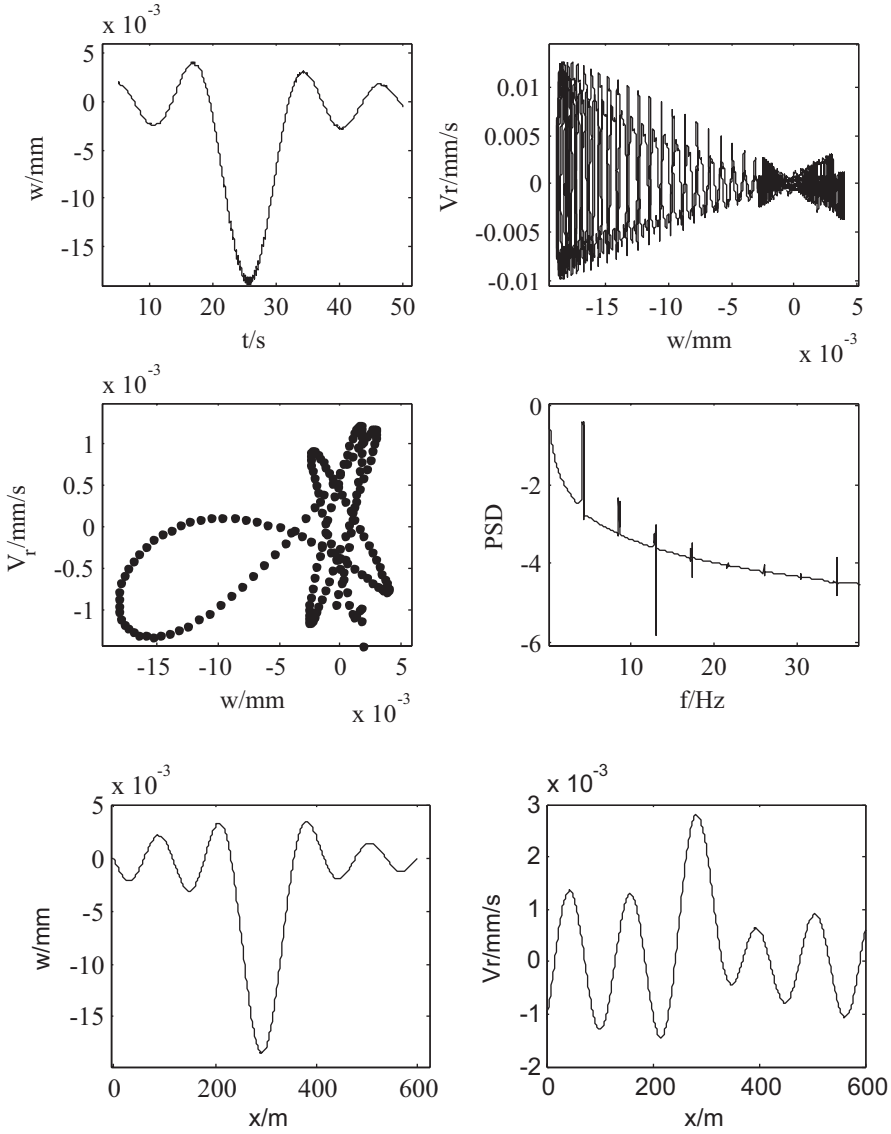

Fig. 9.4 Pavement responses with B_0=0.002 m. (Reprinted from [1], with kind permission from ASME)

frequency, respectively. Similarly, the square and cubic nonlinearity of the system cause the existence of two and three times the excitation frequency.

The dynamic responses of the vehicle body and the pavement in a vertical direction when B_0=0.02 and 0.1 m are also simulated. It is found that the vertical motion of the vehicle body is always periodic in all three cases, but the vertical motion of

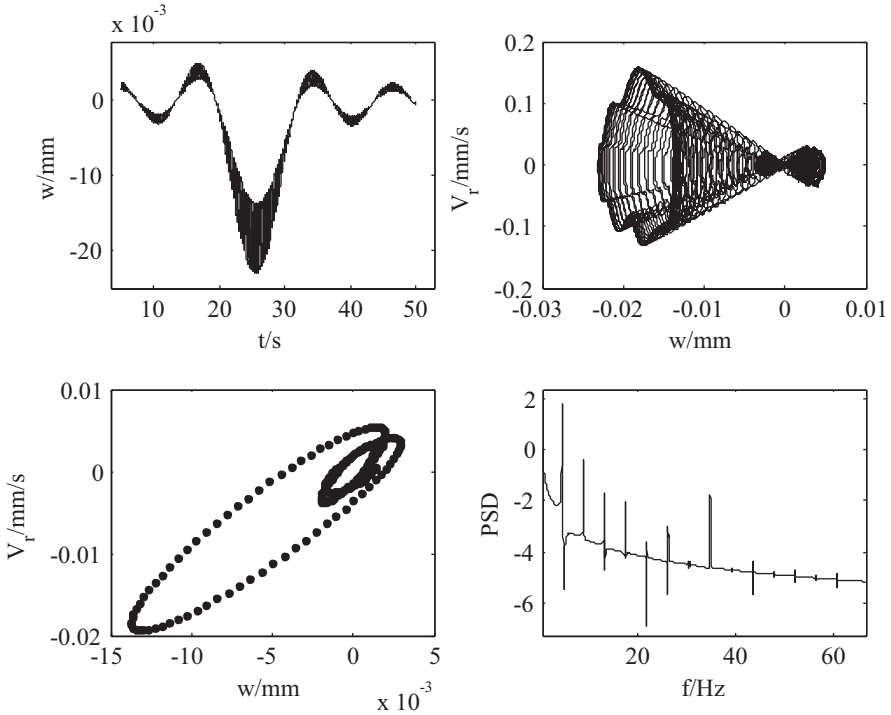

Fig. 9.5 Pavement responses with B_0=0.02 m. (Reprinted from [1], with kind permission from ASME)

the pavement is different in the three cases. Figures 9.5 and 9.6 show the pavement responses in the three cases.

It can be seen from the above two figures that

1. When B_0=0.02 m, the time history of the pavement vertical displacement is similar to that of when B_0=0.002 m. An exception is the appearance of a high-frequency wave. Then, the Poincaré map is a closed curve, and the power spectrum consists of more peaks than when B_0=0.002 m.
2. When B_0=0.1 m, the time history and phase trajectories of the pavement vertical motion are complicated and irregular, the Poincaré map looks like a narrow band, and the power spectrum consists not only of many peaks, but also of continuous broadband stochastic curves.

The largest Lyapunov exponents corresponding to these two cases (B_0=0.02 m, 0.1 m) are also computed and found to be 0 and 0.1912. Hence it may be concluded that the vertical motion of the pavement when B_0=0.02 m is quasiperiodic and the vertical motion of the pavement when B_0=0.1 m is chaotic.

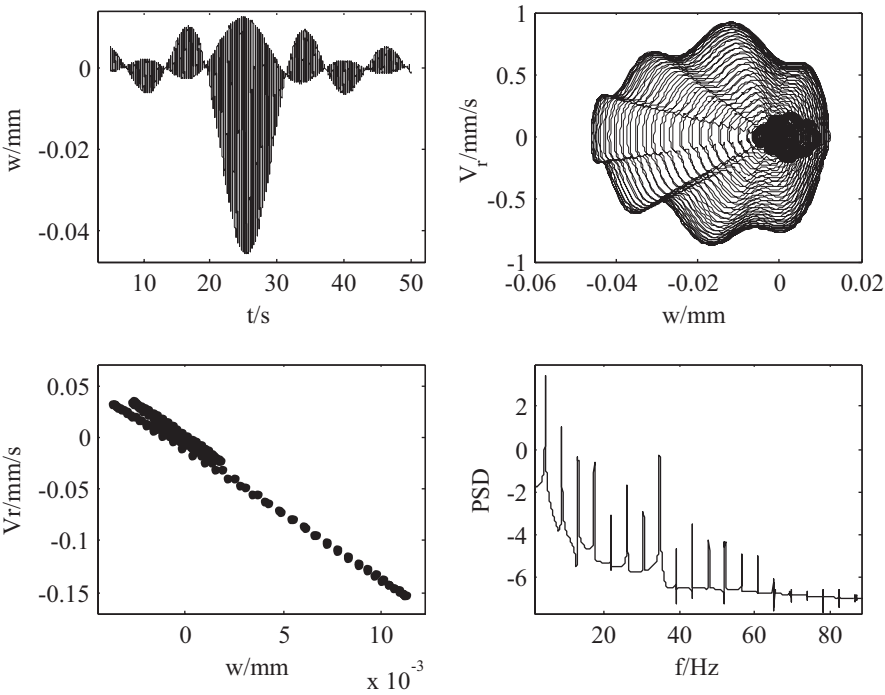

Fig. 9.6 Pavement responses with $B_0 = 0.1$ m

9.3 The Effects of Nonlinearity and Viscoelasticity on Vehicle and Road Responses

To investigate the effect of nonlinearity on vehicle and pavement responses, the amplitude–frequency response curves of the vehicle body's vertical acceleration and the pavement vertical displacement for a linear and nonlinear system are drawn, as shown in Fig. 9.7. In order to obtain a frequency range from 0.5 to 40 Hz, the wave length L_0 varies from 0.5 to 40 m, and the vehicle velocity V is set to 20 m/s. From Fig. 9.7 it can be seen that the effect of nonlinearity on the vehicle body vertical acceleration is greater than the effect on the pavement vertical displacement. At lower frequencies, the responses of the nonlinear system are larger than those of the linear system. However, in higher frequencies, the responses of the nonlinear system are smaller than that of the linear system.

In addition, Fig. 9.8 compares the amplitude–frequency response curves of the vehicle body vertical acceleration and the pavement vertical displacement for the linear elastic and viscoelastic asphalt topping. It may be observed from Fig. 9.8 that the effect of the viscoelastic pavement material on the vehicle response is much smaller than its effect on the pavement response. The response of the pavement with the viscoelastic material is greater than the response of the pavement with the linear elastic material.

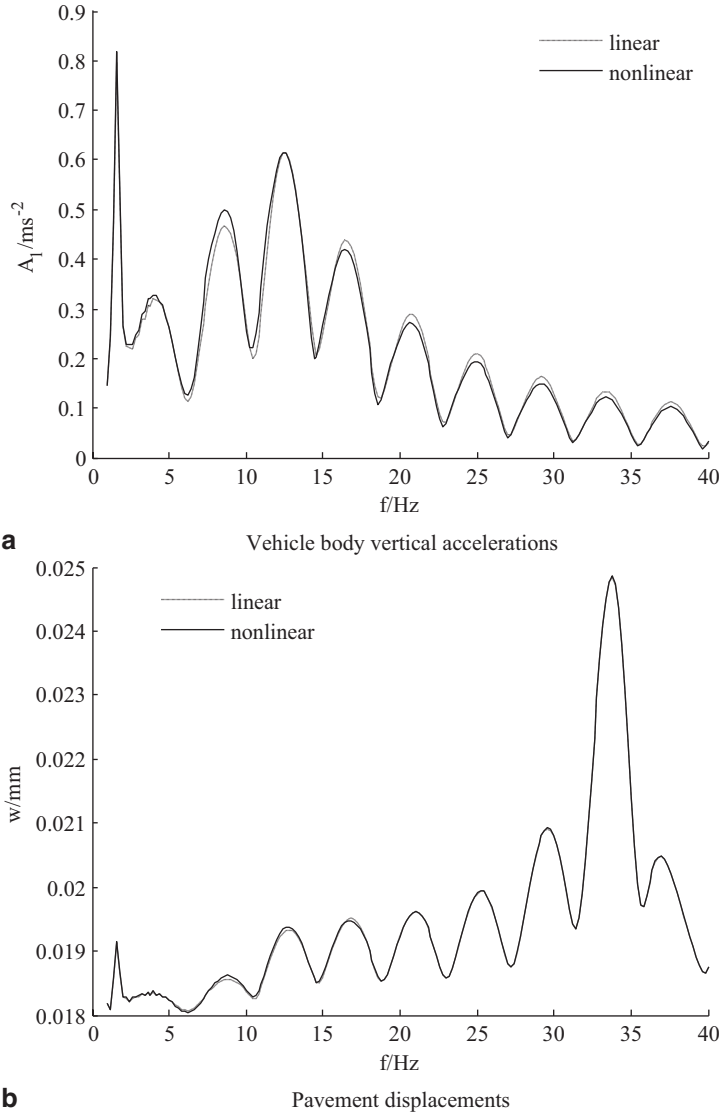

Fig. 9.7 The effect of nonlinearity on amplitude–frequency responses. **a** Vehicle body vertical accelerations. **b** Pavement displacements. (Reprinted from [1], with kind permission from ASME)

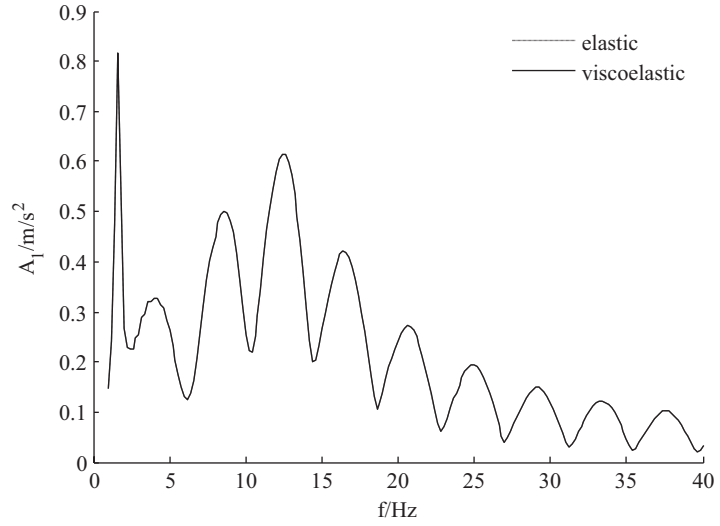

a Vehicle body vertical accelerations

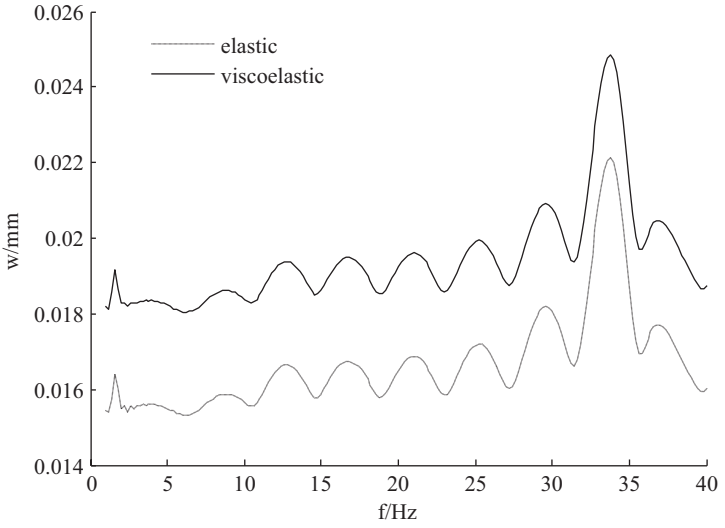

b Pavement displacements

Fig. 9.8 The effect of viscoelasticity on amplitude–frequency responses. **a** Vehicle body vertical accelerations. **b** Pavement displacements. (Reprinted from [1], with kind permission from ASME)

The effects of seven nonlinear parameters β_1, β_2, β_3, β_4, β_5, β_6, β_7, and four viscoelastic parameters E_1, E_3, η_2, η_3 on the vehicle body vertical acceleration, and the pavement displacement are studied, as shown in Fig. 9.9, 9.10, 9.11, 9.12, 9.13, 9.14, 9.15, 9.16, 9.17, 9.18, and 9.19. The main conclusions are listed here,

1. In four of the nonlinear parameters of the vehicle system, the effect of the suspension damper asymmetry coefficient β_4 is the greatest, the effects of the square nonlinear tire stiffness β_1 and the square nonlinear suspension stiffness β_2 are the second, and the effect of the cubic nonlinear suspension stiffness β_3 is the least. A large β_1 or small β_4 both benefit vehicle riding comfort and road service life. Small β_2 may improve vehicle riding comfort but hardly influences the pavement displacement.
2. The effects of the pavement nonlinear parameters β_5, β_6, and β_7 on the responses of the vehicle and pavement is very small. Therefore, these three nonlinear parameters may be omitted in order to simplify the calculations.
3. In four of the viscoelastic parameters of the pavement asphalt topping, the effect of E_1 on system response is greater than that of E_3, and the effect of η_2 on system response is greater than that of η_3. A small E_1, large E_3, large η_2, or large η_3 may not only improve vehicle riding comfort but also extend road service life.

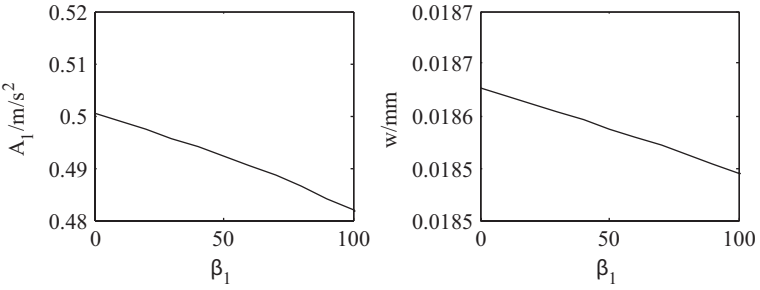

Fig. 9.9 The effect of square nonlinear tire stiffness β_1. (Reprinted from [2], with kind permission from Academy Publisher)

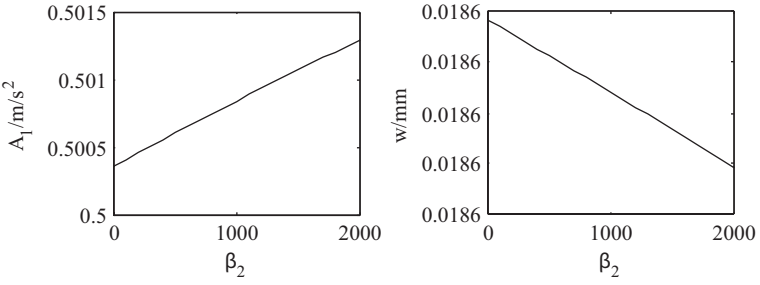

Fig. 9.10 The effect of square nonlinear suspension stiffness β_2. (Reprinted from [2], with kind permission from Academy Publisher)

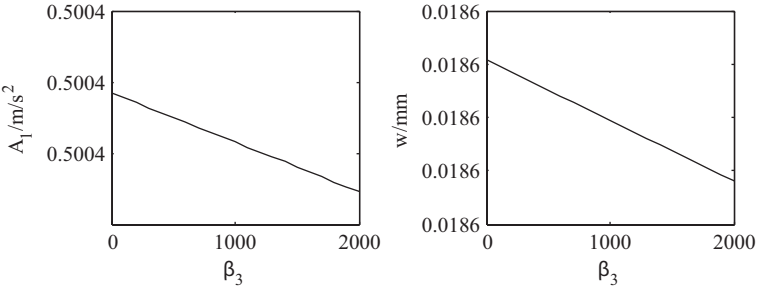

Fig. 9.11 The effect of cubic nonlinear suspension stiffness β_3. (Reprinted from [2], with kind permission from Academy Publisher)

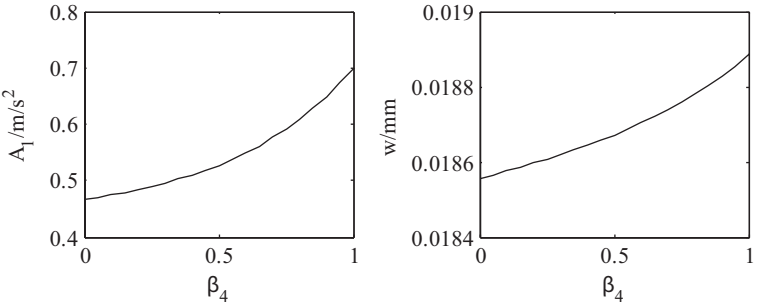

Fig. 9.12 The effect of suspension damper asymmetry coefficient β_4. (Reprinted from [2], with kind permission from Academy Publisher)

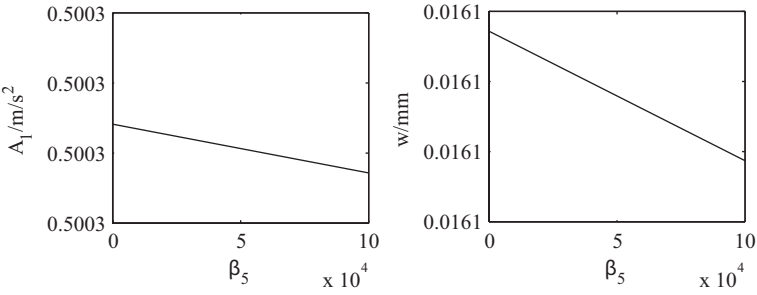

Fig. 9.13 The effect of square nonlinear pavement topping elastic β_5. (Reprinted from [2], with kind permission from Academy Publisher)

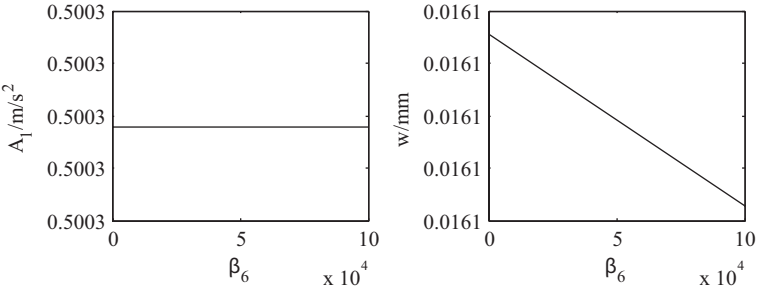

Fig. 9.14 The effect of cubic nonlinear pavement topping elastic β_6. (Reprinted from [2], with kind permission from Academy Publisher)

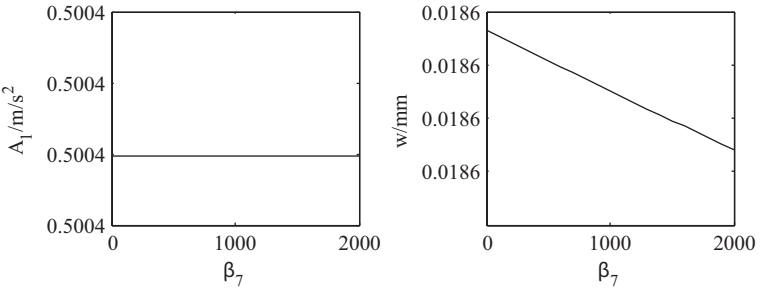

Fig. 9.15 The effect of nonlinear foundation stiffness β_7. (Reprinted from [2], with kind permission from Academy Publisher)

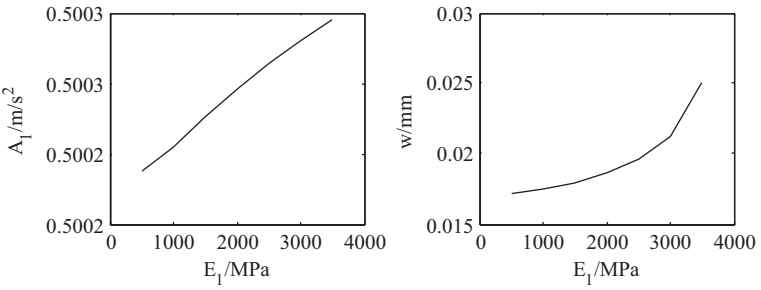

Fig. 9.16 The effect of pavement topping elastic modulus E_1. (Reprinted from [2], with kind permission from Academy Publisher)

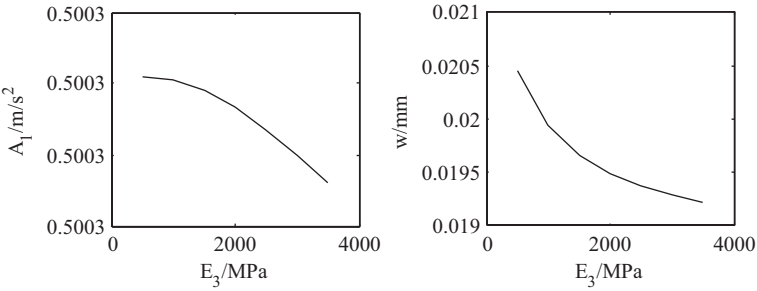

Fig. 9.17 The effect of pavement topping elastic modulus E_3. (Reprinted from [2], with kind permission from Academy Publisher)

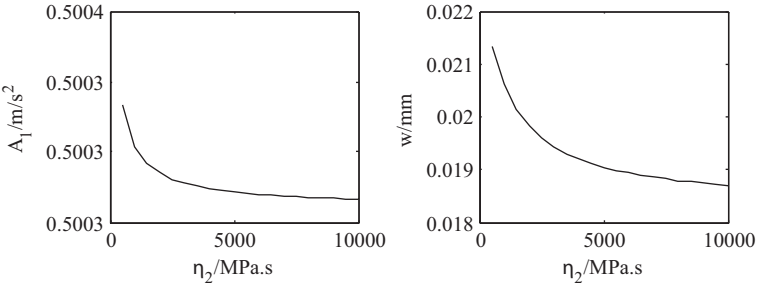

Fig. 9.18 The effect of pavement topping damping η_2. (Reprinted from [2], with kind permission from Academy Publisher)

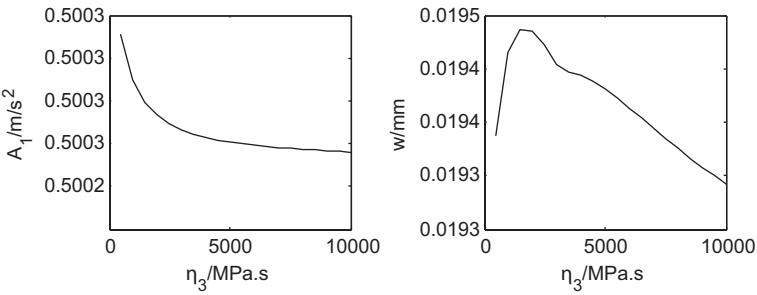

Fig. 9.19 The effect of pavement topping damping η_3. (Reprinted from [2], with kind permission from Academy Publisher)

9.4 Chapter Summary

In this chapter, a 3D vehicle–road coupled system with nonlinearity and viscoelasticity is built and the nonlinear responses of the vehicle and road are computed simultaneously. The effects of the nonlinear and viscous parameters on vehicle riding comfort and road damage are also analyzed. It can be found that

1. The effect of nonlinearity on the vehicle body vertical acceleration is greater than the effect on the pavement vertical displacement. At lower frequencies, the responses of the nonlinear system are greater than those of the linear system. However, at higher frequencies, the responses of the nonlinear system are smaller than those of the linear system. Hence, it is necessary to take into account the nonlinearity of the vehicle suspension to research the nonlinear dynamic phenomena of the vehicle and to improve computational accuracy. On the other hand, the nonlinearity of the pavement material may be neglected if one calculates only the amplitude of the pavement response.
2. The influence of the viscoelastic pavement material on the vehicle response is much smaller than that on the pavement response. The response of the pavement with viscoelastic asphalt topping is greater than the response with linear elastic material. Thus, the viscoelastic characteristic of asphalt topping should be considered in order to estimate the pavement response more accurately.

References

1. Li SH, Yang SP, Chen LQ. A nonlinear vehicle-road coupled model for dynamics research. J Comput Nonlinear Dyn. 2013;8(2):1–14.
2. Li SH, Lu YJ, Li HY. Effects of parameters on dynamics of a nonlinear vehicle-road coupled system. J Comput. 2011;6(12):2656–61.
3. Chen LQ, Cheng CJ, Zhang NH. Chaotic motion of viscoelastic beams with geometric and physical nonlinearities. Eng Mech. 2001;18(1):1–6.
4. Chen LQ, Cheng CJ. Dynamical behavior of nonlinear viscoelastic beams. Appl Math Mech. 2000;21(9):897–902.
5. Potapov VD, Marasanov AY. The investigation of the stability of elastic and viscoelastic rods under a stochastic excitation. Int J Solids Struct. 1997;34(11):1367–77.
6. Marynowski K, Kapitaniak T. Kelvin-Voigt versus burgers internal damping in modeling of axiallymoving viscoelastic web. Int J Non-linear Mech. 2002;37:1147–61.
7. Zheng JL. Application of Burgers model to the analysis of fatigue characteristic of bituminous mixtures. J Changsha Commun Inst. 1995;11(3):32–42.
8. Feng JL, Huang XM. Study on the method of determining viscoelastic parameters of asphalt binder. J Highw Transp Res Dev. 2006;23(5):16–22.
9. Qiu P, Wang XZ, Ye KY. Bifurcation and chaos of the circular plates on the nonlinear elastic foundation. Appl Math Mech. 2003;24(8):779–84.
10. Yang ZA, Zhao XJ, Xi XY. Nonlinear vibration and singularities analysis of a thin rectangular plate on a nonlinear elastic foundation. J Vib Shock. 2006;25(5):69–73.
11. Cao ZY. A Nonlinear dynamic analysis of functionally graded material plates. Acta Mech Solida Sin. 2006;27(1):21–5.
12. Cao ZY. Vibration theory of plates and shells [M]. Beijing: China Railway Press; 1989.

13. Xu B., Shi YB, Wang GD. Suspension non-linear components influence upon ride comfort and road friendliness. Veh Power Technol. 2005;1:46–51.
14. Chen J. A basic study on the interaction between vehicle and roadway [D]. Changchun: Jilin University, 2002.
15. Ke JP, Ding P. A study on the stress relaxation performance of an asphalt mixture. Highw Automot Appl. 2004;4:64–6.
16. Hu HY. Applied nonlinear dynamics. Beijing: Aero Industrial Press, 2000.
17. Wolf A, et al. Determining Lyapunov exponents from a time series. Physica D. 1985;16:285–317.

Chapter 10
The Construction of a Highway Fieldtest Section for Vehicle–Road Interaction

The interaction between a heavy truck and a road system is theoretically studied in the previous chapters. However, field tests of both vibration performance of the vehicle and the road system response have been very few due to the limitation of technical conditions. In order to study further the interaction between a vehicle and the pavement, to master the failure pattern of the road structure under vehicle loads, to improve vehicle driving safety and to verify the theoretical analysis and numerical simulations, a field test section for vehicle–road interaction was built on the ShenZhou to DaMing segment of the DaGuang (Daqing to Guangzhou) highway. The field test of vehicle random dynamic load response and road dynamic response were conducted.

10.1 The Experiment Scheme of the Vehicle–Road System

For the study of the interaction between vehicles and a road structure, various kinds of sensors in every layer of the test section are embedded and some sensors are installed in the tested vehicle. Under different axle load conditions (weight empty, half load, or full load) and various vehicle speeds (10, 20, 30, 40, 50, 60 km/h), the responses of the vehicle and the road system are recorded simultaneously. The speed of each point on the vehicle, the dynamic pressure, static pressure, the longitudinal and transverse dynamic strain data of the road's different layers are all collected. These data are long-term remotely monitored and collected in long-term to study the dynamic response rules of each structural layer of the road during the highway operation.

S. Yang et al., *Dynamics of Vehicle-Road Coupled System,*
DOI 10.1007/978-3-662-45957-7_10

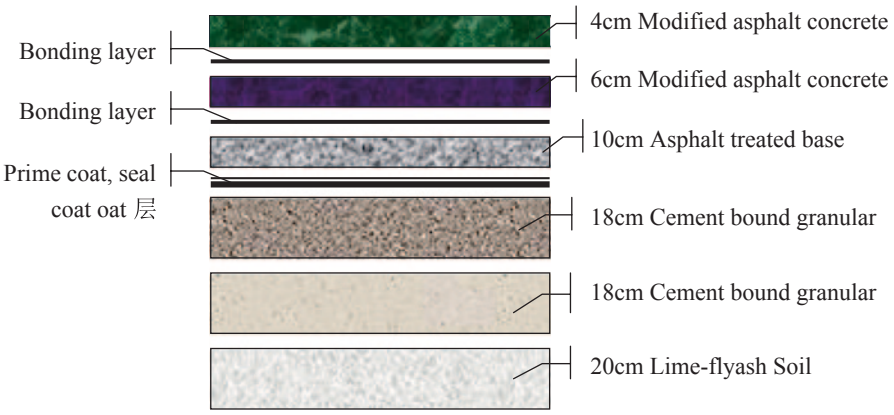

Fig. 10.1 Road structure and material design

10.2 The Highway Field Test System

10.2.1 Introduction of the Highway Road Structure

The total length of the trial section chosen from ShenZhou to DaMing of the DaGuang highway is 220.429 km, 33.4 km of which is expanded as a two-way six-lane highway. The structure scheme of the road is summarized as below: the total width of the roadbed is 34.5 m, in which the width of a one-way lane is 3 × 3.75 m, the width of the middle strip is 4.5 m (including 3 m central dividing strip and two 0.75 m curbs), the paved shoulder is 3.0 m (including 0.5 m width curb), and the soil shoulder width is 0.75 m. The road structure and material design is shown in Fig. 10.1.

10.2.2 The Testing System of the Road

Targeting the problem of fatigue cracking in asphalt pavement, the strain transducer is used for real-time dynamic monitoring of pavement strain. The transverse strain sensors and the longitudinal strain sensors are installed at the bottom of a modified asphalt AC layer, coated macadam, and cement stabilized macadam. Considering the need for comparative analysis, two rows of transverse strain sensors and longitudinal strain sensors are symmetrically laid along the center of the vehicle load track. In order to evaluate the stress of the road structure layers effectively, dynamic and static pressure sensors are embedded in each layer [1, 2].

1. The strain sensor

Along the center line of the tire, the transverse and the longitudinal strain sensors are buried at the bottom of a modified asphalt concrete and asphalt treated base, forming the transverse and longitudinal strain test matrix. These sensors are used for monitoring the longitudinal and transverse strain of the road.

2. The load sensor

The dynamic pressure sensors are embedded successively at the bottom of a modified asphalt concrete layer, asphalt treated base, cement bound granular and on the top of the soil base, which are used for testing the vertical dynamic stress of each layer. The static pressure sensors are set on the top of the soil base to test the vertical static pressure.

The total length of the test road is 100 m and the sensors of each pavement layer and signal acquisition system are shown in Fig. 10.2.

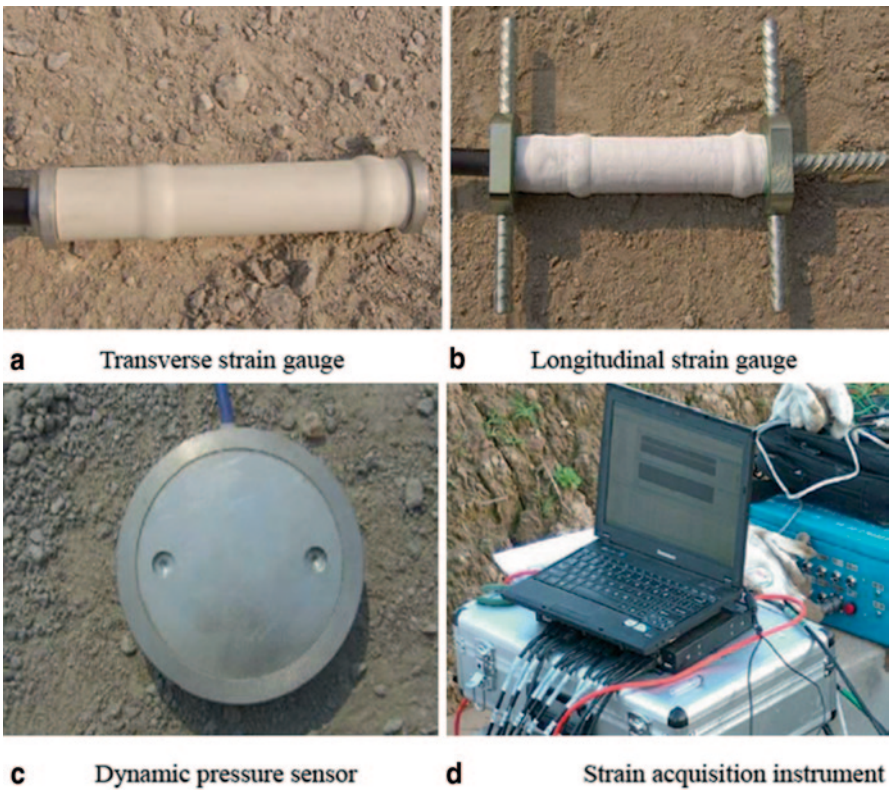

Fig. 10.2 Pavement sensor and signal acquisition analyzer. **a** Transverse strain gauge. **b** Longitudinal strain gauge. **c** Dynamic pressure sensor. **d** Strain acquisition instrument

The signal acquisition system for strain utilizes the Beijing Andy Iotech strain collection device which includes a high performance, multichannel parallel data collection and analysis system. The device includes 48 channels, which can carry out long, continuous data collection (sampling frequency at 1600 Hz). When a vehicle is traveling on the road surface, the computer can record all sensors' electric signals simultaneously. The signals are then transformed to a dynamic strain wave of the measuring point.

10.2.3 The Laying Process of the Sensor

During the construction of each layer of the highway, some sensors are placed at the structure layers in accordance with the design drawing simultaneously, which can ensure the reliability of the data, and also reflect the road dynamic response of every layer [3]. Based on the coring specimens collected at the site, the road physical parameters of each layer are obtained through laboratory experiments. The calibration site and sampling process of the road parameter are shown in Fig. 10.3

On the basis of large-scale research and investigation [4–7] the specific process of laying out the sensors is listed as follows:

1. Calibration of the sensor installation position

In the process of sensor installation, the position of the vehicle wheel tracks is determined to identify each sensor's position relative to the wheel track line. The sensors are embedded in sequence from the subbase to the surface layer of the road. The measuring instruments are used to assist positioning and make the benchmark strict.

2. Overall layout and circuit layout

Due to the large quantity, the various types of sensors, and the high standards of the sensors, the embedding scheme must be designed in advance before the compaction

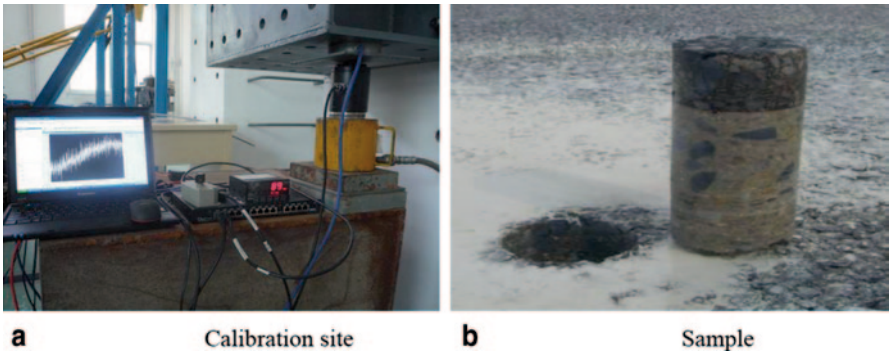

Fig. 10.3 **a** Calibration site. **b** Sample

of the road structure. The embedding position and direction of the sensor should be checked to make sure the arrangement of the sensors' circuit is reasonable. It can reduce unnecessary loss in the process of sensor installation.

3. Artificial digging and circuit slotting

After determining the sensor location, a Luoyang shovel is used to dig the holes, then the circuit is slotted along with the mark. The holes must be dug according to the sensor embedded scheme. It can ensure the precision of the data acquisition.

4. Sensor placement and debugging

The influence of coefficient of loose paving material should be taken into account. A layer of the same mixture dug is covered at the bottom of the hole. Due to the sensibility of the surrounding environment and the fragile structure of the sensors, direct use of mechanical compaction is prone to damage the sensors, destroy the circuits, or lead to other issues. So it is necessary to use the method of artificial ramming preloading. The buried sensors are preliminarily debugged to observe whether the transmission of the signal is normal and to examine the survival rate of the sensor simultaneously.

5. Mechanical paving and compaction

After the completion of artificial ramming preloading of the sensors, the mechanical paving and compaction of the upper structure construction is carried out in accordance with the road construction schedule requirements. To ensure the effect of compaction, the original structure layer must be repeatedly compacted using the rolling machinery. A technician is assigned to protect the wire connector in order to avoid sensor damage by the paving compaction machinery.

6. Wire connector labeled

The initial arrangement of the sensors is finished after the mechanical paving rolling. At this time, sensors are categorized, packaged, and waterproofed to adapt to the requirements of long-term acquisition work.

The installation, connection, and debugging process of the sensors on the scene is shown in Fig. 10.4:

In this experiment, there is an inspection chamber equipped with instruments near the road test section. It not only allows the researchers to connect the instrument of each section to all the test sections on the shared data acquisition system, but also can guarantee the sensor connectors are dry, clean, and easy to identify. The inspection chamber is shown in Fig. 10.5.

Fig. 10.4 Sensor layout process. **a** Location. **b** Digging. **c** Wiring. **d** Placement. **e** Preliminary debugging. **f** Mechanical paving

Fig. 10.5 Inspection chamber

10.3 Vehicle Test System

10.3.1 Introduction of the Vehicle System

On the investigation basis of the traffic in our country at present, a Dongfeng medium-sized truck with three axles is selected as a typical domestic transportation vehicle. There are three types of working conditions: empty load, half load, and full load. In the experimental stage, the vehicle axle load is under strict control to ensure the reliability of the test results.

10.3.2 Introduction of Vehicle Test System

The vehicle test signal acquisition system mainly includes a three-speed sensor, a charge amplifier, a signal acquisition instrument, and a computer [8]. The TSC-D3 speed sensor produced by Chengdu Zhongke Measurement and Control Co., LTD is operated in the 1–500 Hz frequency range. The signal acquisition instrument converts the piezoelectric signals into digital signals. The INV360DF intelligent acquisition analyzer is produced by Beijing Orient Institute of Noise & Vibration. The testing site and collection device is shown in Fig. 10.6.

Figures 10.7–10.10 show each velocity measuring point sensor arrangement on the driver's seat, front steering axle head, intermediate axle head, and rear axle head, respectively.

Fig. 10.6 Testing site and collection device

Fig. 10.7 Driver's seat

Fig. 10.8 Front steering axle head

Fig. 10.9 Intermediate axle head

Fig. 10.10 Rear axle head

10.4 Analysis of the Road Test Results

10.4.1 Analysis of Road Dynamic Strain Response

1. Road dynamic strain under different vehicle speeds

It is discovered from the large amount of measured data that the longitudinal and the transverse flexural strains at the bottom of asphalt concrete show alternation between tensile and compressive strain states under different vehicle axle loads and speeds.

Under the condition of a full load and a speed of 10 km/h, the test result of longitudinal strain of the bottom surface is shown in Fig. 10.11. Under the condition of a full load and a speed of 60 km/h, the test result of the transverse strain at the bottom of the surface layer is shown in Fig. 10.13. The finite element model from chapter two is used to obtain the simulation results; the longitudinal and the transverse strains of the bottom are shown in Figs. 10.12 and 10.14, respectively.

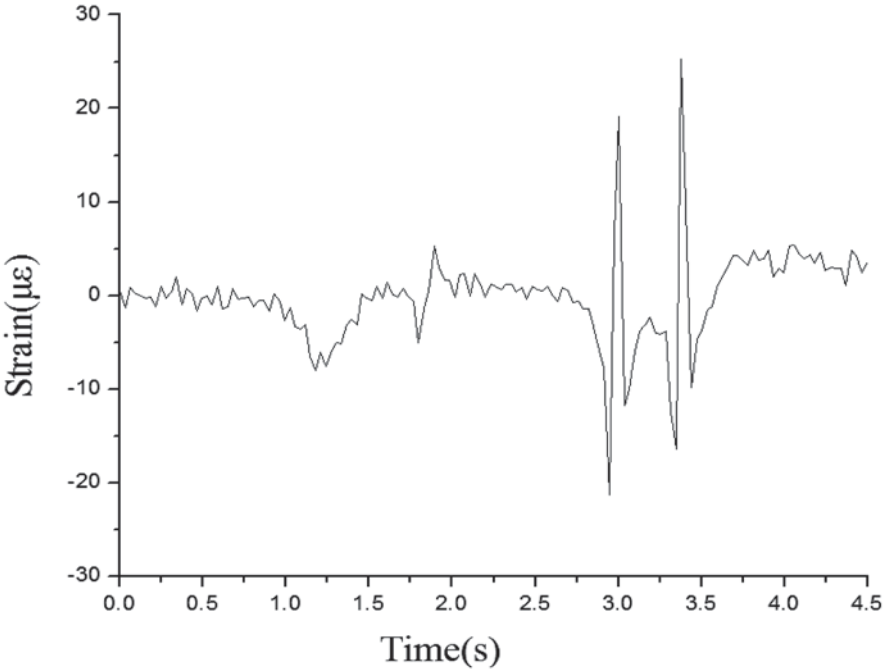

Fig. 10.11 Longitudinal tensile strain at the bottom of asphalt concrete (experiment)

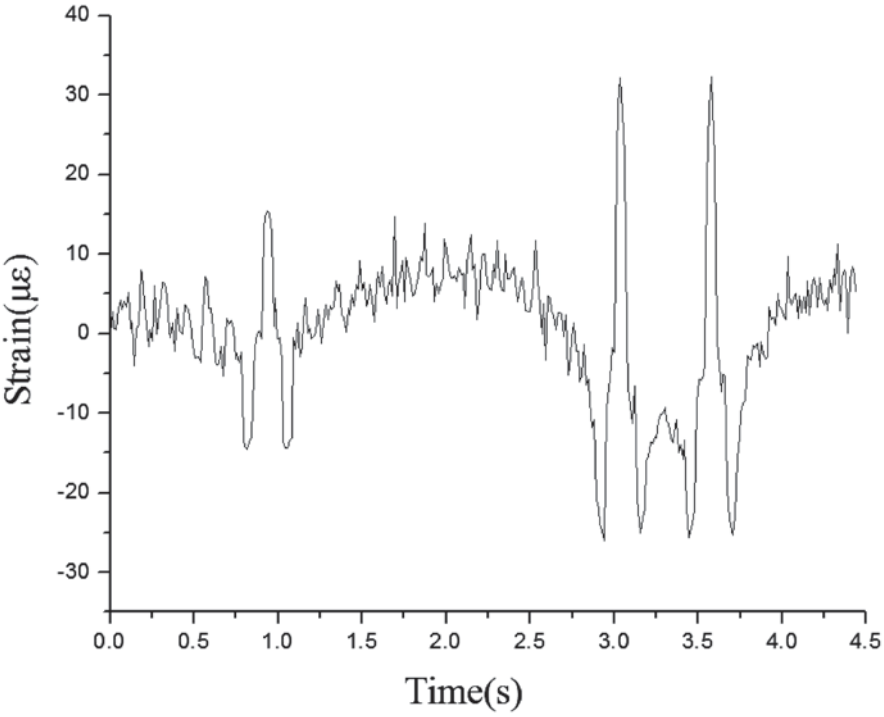

Fig. 10.12 Longitudinal tensile strain at the bottom of asphalt concrete (simulation)

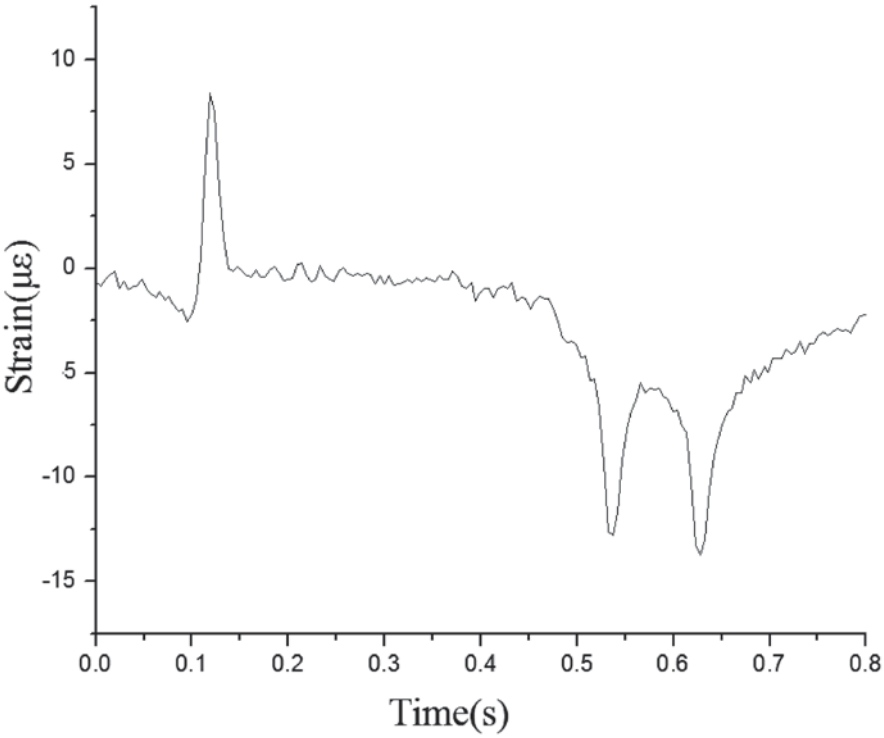

Fig. 10.13 Transverse tensile strain at the bottom of asphalt concrete (experiment)

From Figs. 10.11–10.14, it can be observed that:

1. When the wheels arrive at and leave a point on the pavement, the longitudinal strain at the bottom of the asphalt concrete layer is negative. When the wheels just go past the point, the longitudinal strain becomes positive. This indicates that the asphalt concrete layer mainly bears the longitudinal tensile strain coming from the wheel loading. The conclusion is consistent with the results of previous researcher [9–11].The transverse strain at the bottom of the asphalt concrete includes both tensile strain and compressive strain and the behavior is more complex.
2. The maximum values of the test results of the longitudinal and the transverse tensile strains at the bottom of the asphalt concrete are 26.3 με and13.8 με respectively. The simulation results are 31.9 με, 17.1 με and the relative error is 21.3 %, 23.2 %. The results between the experiment and the simulation are consistent.

Under the condition of a full load at different vehicle speeds, the maximum longitudinal and the transverse tensile strains of the road surface are shown in Fig. 10.14. Figure 10.15 shows that, with an increase in speed, the longitudinal and the

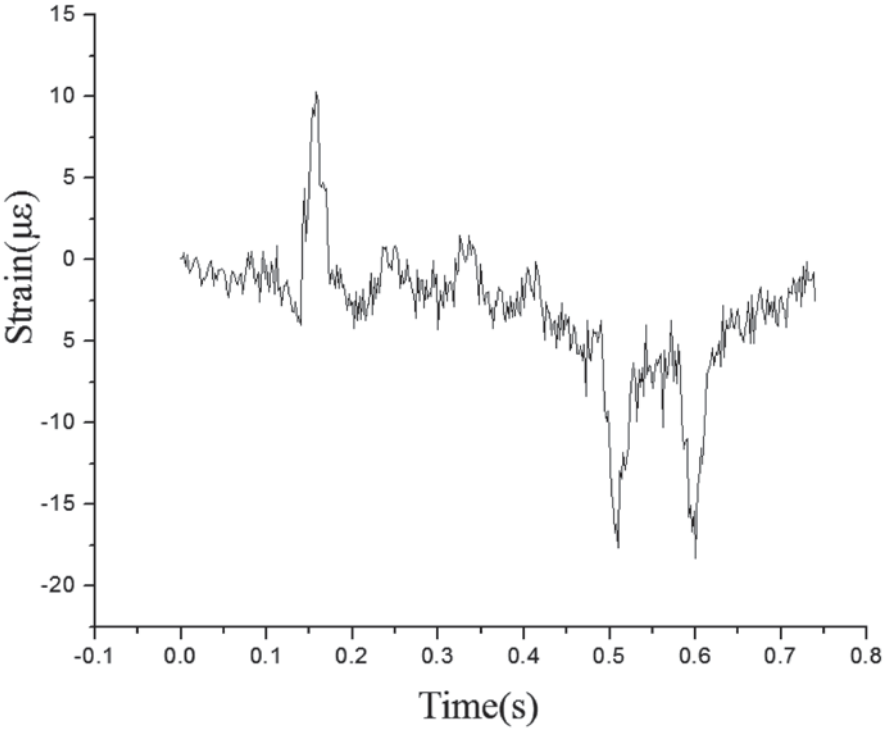

Fig. 10.14 Transverse tensile strain at the bottom of asphalt concrete (simulation)

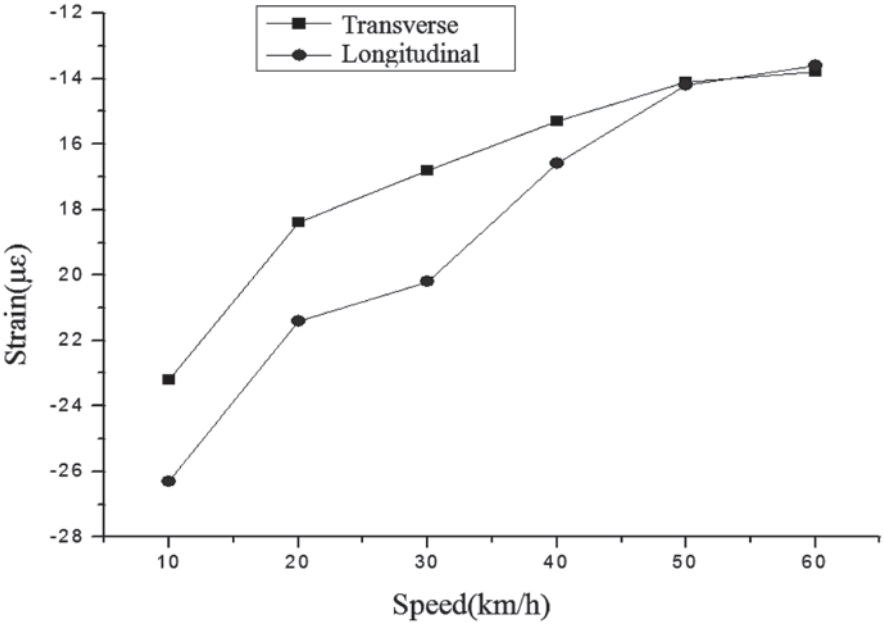

Fig. 10.15 Maximum longitudinal and transverse strain at different vehicle speeds (experiment)

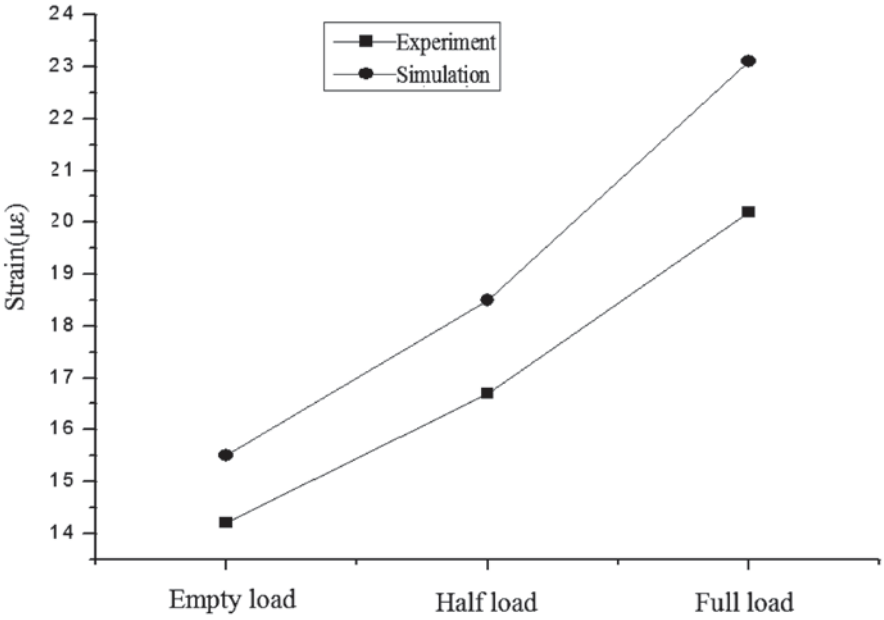

Fig. 10.16 Longitudinal strain comparison between experiment and simulation

transverse strains at the bottom of the surface layer decrease continuously. When the vehicle speed increases from 10 to 30 km/h, the longitudinal tensile strain of the road surface decreases 23.2% while the transverse compressive strain is reduced 27.5%. The reduced magnitude of the longitudinal strain is larger than the transverse strain when the speed is over 30 km/h.

2. Road dynamic strain under different loads

At a speed of 30 km/h under different loading conditions, the tested longitudinal strain results at the bottom of the asphalt concrete are compared with the simulation results, shown in Fig. 10.16. It shows that the longitudinal tensile strain increases with an increase in load. The pattern of the experiment and simulation is the same, and the maximum relative error is 14.3%.

10.4.2 Analysis of Road Vertical Dynamic Stress

1. Vertical dynamic stress of the road at different speeds

Under the condition of a full load, at a speed of 10 km/h, the experimental and simulation results of the vertical dynamic stress at the bottom of the asphalt concrete layer are shown in Figs. 10.17 and 10.18. The experimental and simulation results show the same pattern. The maximum tested compressive stress is −139 kPa and

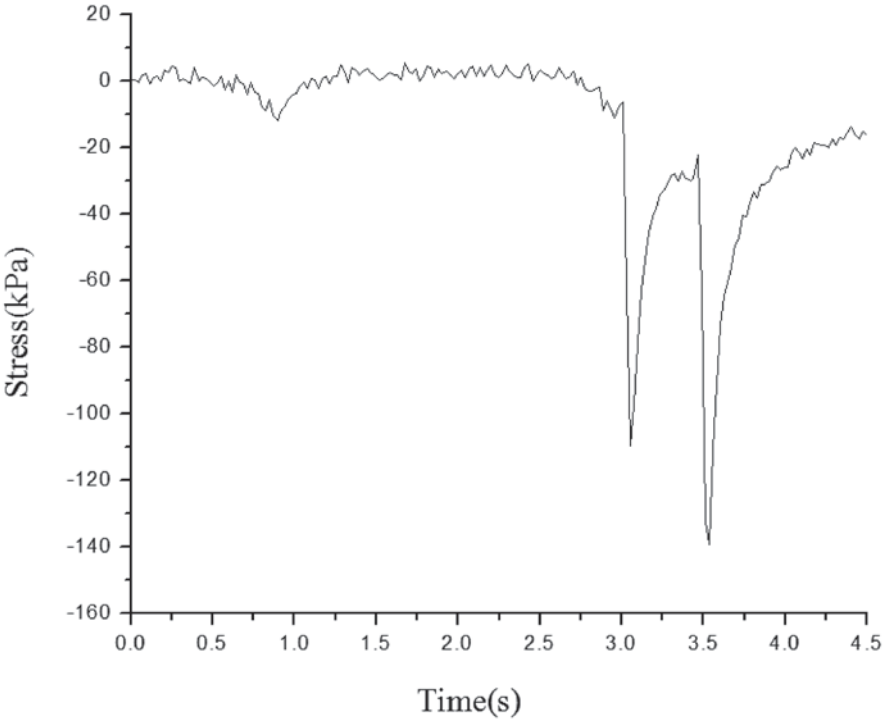

Fig. 10.17 Vertical dynamic stress at the bottom of the asphalt concrete (experiment)

the simulation result is −163 kPa. The relative error is 14.7%, which shows that the simulation result is consistent with the experiment result.

Under the condition of a full load with a respective speed of 10, 20, 40, 60 km/h, the curve is mapped on the basis of the maximum vertical dynamic stress, shown in Fig. 10.19.

Figures 10.17–10.19 show that, under a constant vehicle load, the bottom of the asphalt concrete layer bears vertical compression. Under the same axle load, the compressive stress at the bottom of the surface decreases with an increase in vehicle speed.

2. Vertical dynamic stress of the road under different loads

Under different loading conditions with a constant speed of 30 km/h, the curve of the maximum vertical dynamic stress at the bottom of the asphalt concrete layer is plotted in 10.20. It can be seen that the vertical compressive stress increases with an increase in load, and it presents an approximate linear relationship.

3. Road vertical compressive stress of different structural layers

Under the working condition of a full load and a speed of 60 km/h, the time history curves of the vertical dynamic stress of each road layer are shown in Fig. 10.21. The maximum vertical dynamic stress is shown in Fig. 10.22.

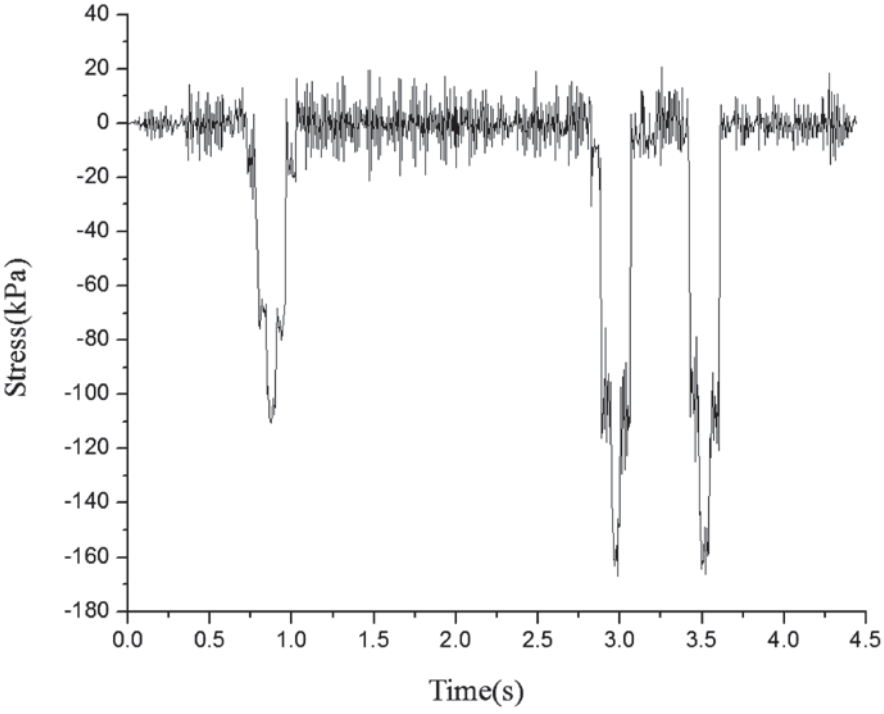

Fig. 10.18 Vertical dynamic stress at the bottom of the asphalt concrete (simulation)

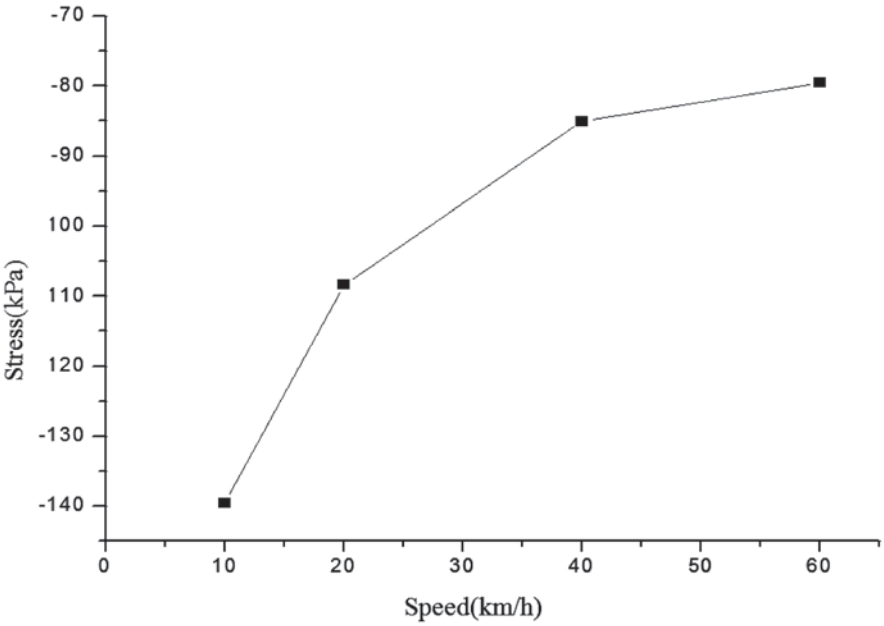

Fig. 10.19 Maximum vertical dynamic stress at different vehicle speeds (experiment)

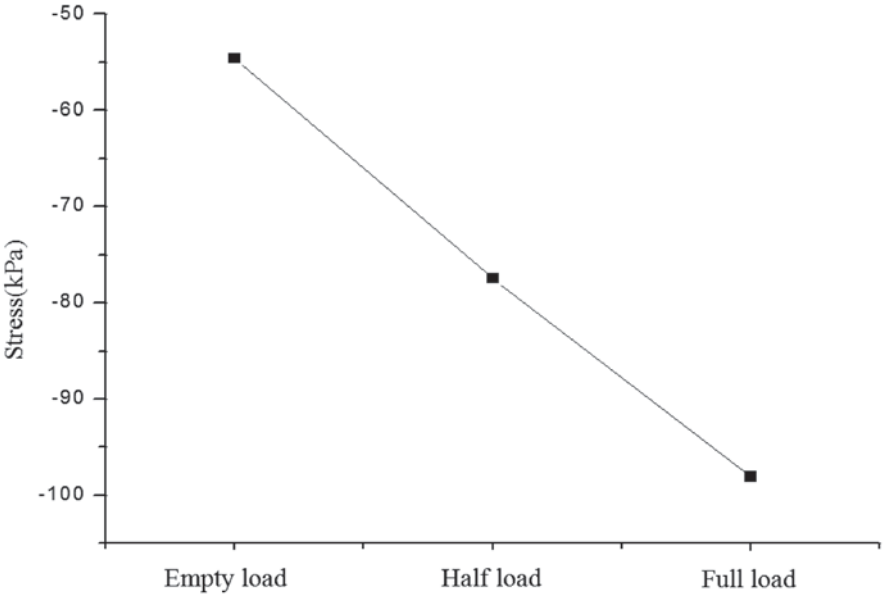

Fig. 10.20 Maximum vertical dynamic stress under different loading (experiment)

Some conclusions can be obtained from Figs. 10.21 and 10.22:

1. Under different vehicle loads, the vertical compressive stress of different road layers continuously decreases with an increase in depth, but its distribution range increases gradually. This conclusion is consistent with the results of previous researches [12, 13].
2. The vertical compressive stress decays quickly in the road structural layers. It reduced 46.7% from the bottom of the asphalt concrete to the bottom of the asphalt treated base layer. The dynamic stress of the cement bound granular layer is very small. Thus, the vertical compressive stress is mainly borne by the asphalt concrete layer. The semi-rigid base can be used to greatly reduce the vertical dynamic stress, which can improve the bearing capacity of the road structure.

10.5 Analysis of the Vehicle Test Results

Under the conditions of empty load, half load, and full load, the vehicle travels at a constant speed of 10, 20, 30, 40, 50, 60 km/h separately on the test section (Class-B road). The curves of vertical acceleration measured from the different points of the

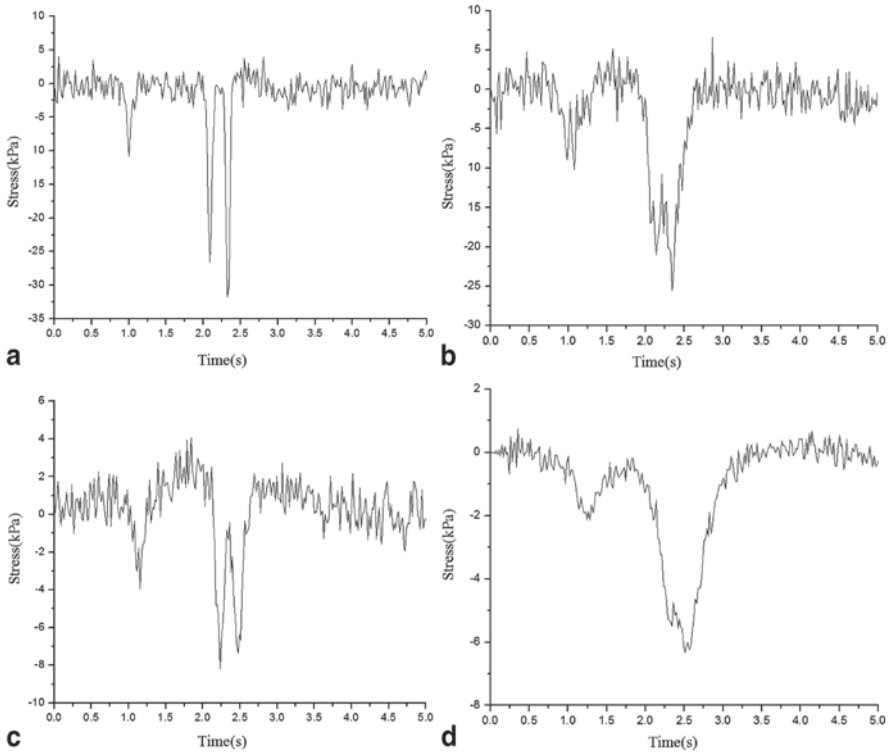

Fig. 10.21 Vertical dynamic stress of different road structure layers. **a** Dynamic stress at the bottom of the asphalt treated base layer. **b** Dynamic stress at the bottom of the upper cement bound granular layer. **c** Dynamic stress at the bottom of the lower cement bound granular layer. **d** Dynamic stress of the upper soil base

vehicle are plotted in Figs. 10.23–10.26. It can be observed that the vehicle vertical acceleration of each measuring point shows an increasing trend. So the working condition of high speed and being overloaded will be unfavorable to the vehicle's riding comfort.

Under the condition of a full load with a speed of 60 km/h, the time domain results of the experiment and the simulation are compared, as shown in Figs. 10.27–10.30. The vehicle simulation model adopts the virtual prototype model from chapter one. The dynamic simulation analysis of the vehicle model is carried out on a random road surface. The default gear stiff integrator (GSTIFF) is adopted to solve the coupled nonlinear differential-algebraic equations (DAE). Through the

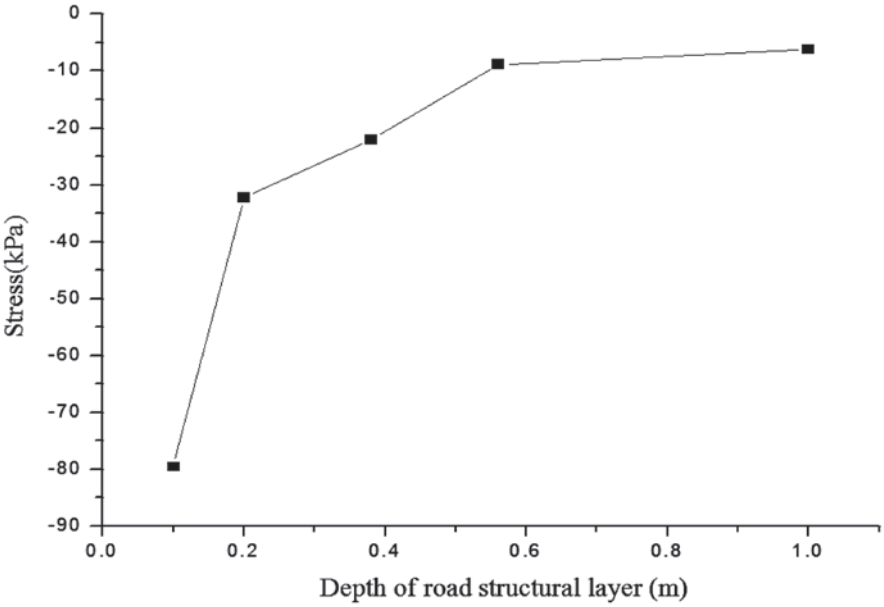

Fig. 10.22 Maximum dynamic stress of each road layer

Fig. 10 23 Vertical acceleration of the driver cab at different speeds and vehicle loads

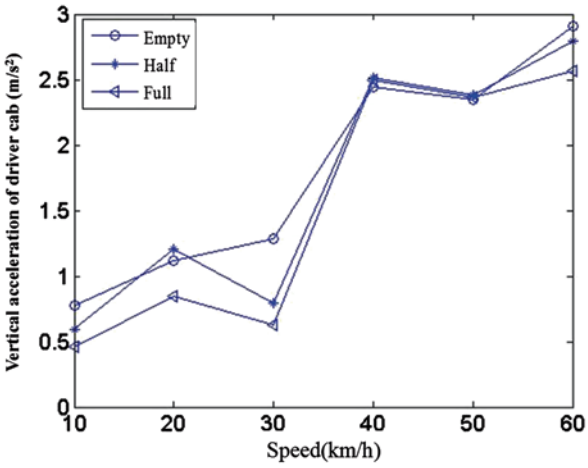

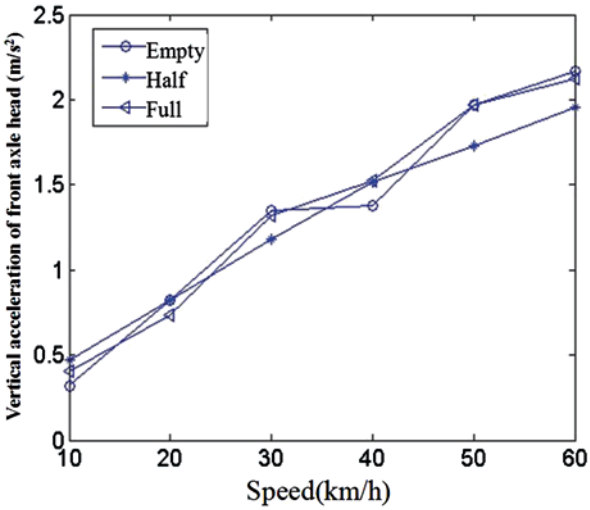

Fig. 10.24 Vertical acceleration of the front axle head at different speeds and loads

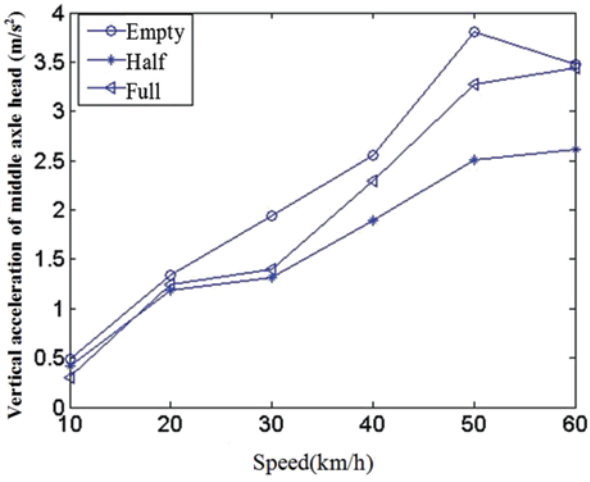

Fig. 10.25 Vertical acceleration of the middle axle head at different speeds and loads

contrasting of Figs. 10.27–10.30, it can be seen that the results of the time trend and distribution of the experiment and simulation are the same.

In order to compare the experimental and simulation results in the time domain and the frequency domain, the acceleration signals are analyzed by utilizing fast Fourier transform (FFT) and a Hanning window is applied to all spectral analyses to inhibit frequency leakage.

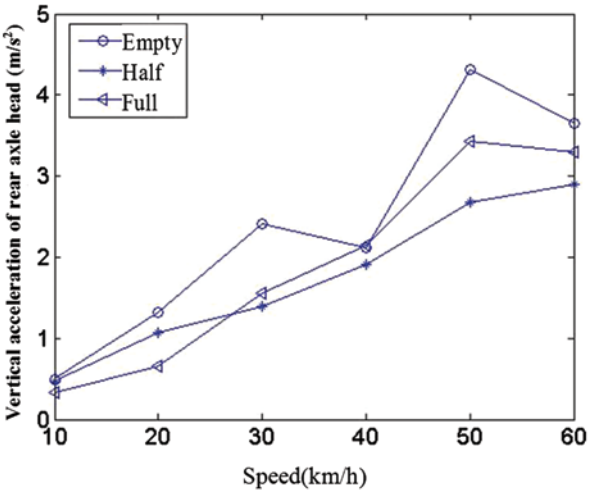

Fig. 10.26 Vertical acceleration of the rear axle head at different speeds and loads

The results of the simulation and the experiment are compared in Table 10.1.

As seen from Table 10.1, the main peak frequency and the amplitude of the simulation results and test results are basically identical. But there are some differences: the maximum relative error of the peak frequency of the power spectral density is 11 % and the maximum relative error of the RMS acceleration is 17 %. In short, the overall trend of simulation results and test results are consistent.

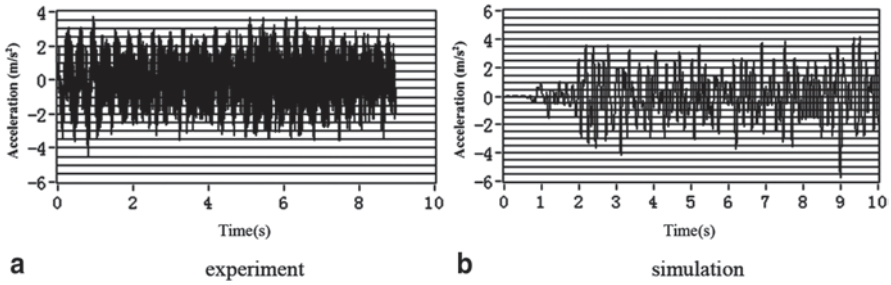

Fig. 10.27 Vertical acceleration of the driver cab in the time domain. **a** experiment. **b** simulation

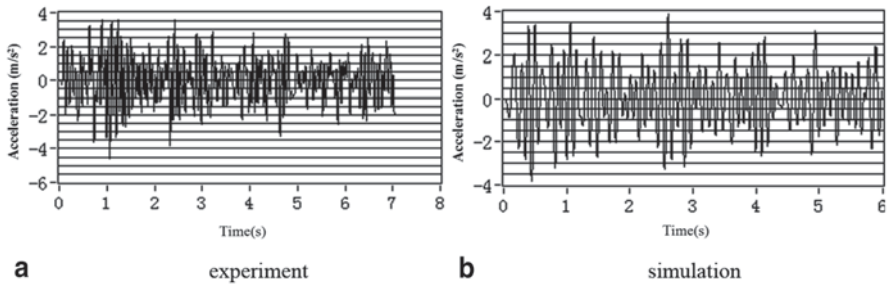

Fig. 10.28 Vertical acceleration of the front axle head in the time domain. **a** experiment. **b** simulation

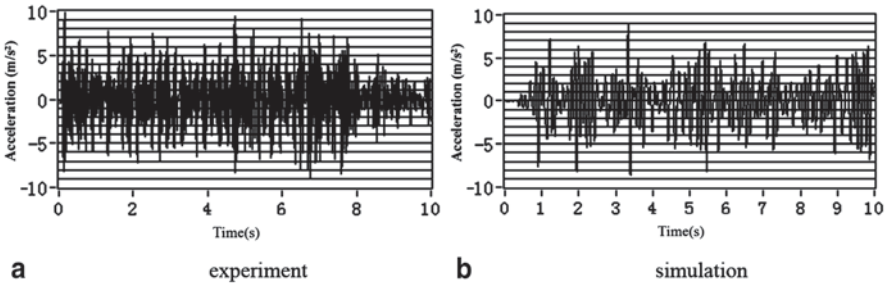

Fig. 10.29 Vertical acceleration of the middle axle head in the time domain. **a** experiment. **b** simulation

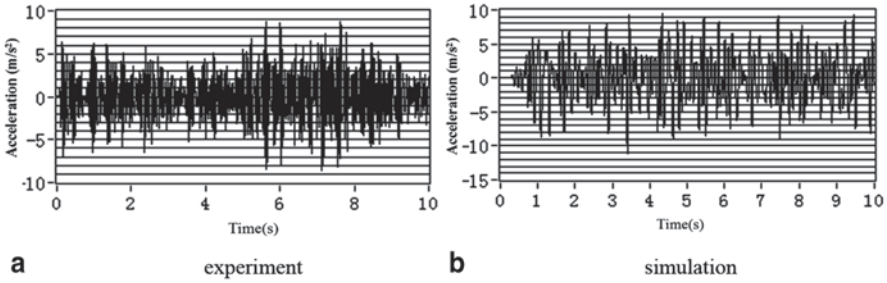

Fig. 10.30 Vertical acceleration of the rear axle head in the time domain. **a** experiment. **b** simulation

Table 10.1 Comparison of the results (experiment and simulation)

Measuring point	Peak frequency of power spectral density(Hz)		RMS of acceleration (m/s^2)	
	Simulation	Experiment	Simulation	Experiment
Driver cab	3.82	3.39	2.12	2.57
Front axle head	10.81	9.98	2.19	1.97
Middle axle head	9.60	10.00	3.51	3.14
Rear axle head	10.01	10.10	3.50	3.37

10.6 Chapter Summary

In order to reveal comprehensively the failure characteristics and the asphalt pavement structure, a section of an expressway is built as a test section. The specific methods of arrangement of different kinds of sensors are put forward for various layers of the road. Based on the test section of the vehicle–road system, the dynamic response data of the vehicle and the road are acquitted. The transverse stress, the longitudinal stress, the dynamic pressure, and the static pressure of each road layer

are collected in details. It provides significant data for the analysis of the dynamic interaction between a vehicle and a road.

References

1. Huang YX. Pavement analysis and design. Beijing: People's Communications Press; 1998.
2. Sun LJ. Structural behavior theory of asphalt pavement. Beijing: People's Communications Press; 2005.
3. Kumara MW, Tia M, Bergin M. Evaluation of early strength requirement of concrete for slab replacement using accelerated pavement testing. J Transp Eng. 2006;132(10):781–9.
4. Qian ZD, Zhang L, Chen LL. Pavement structural dynamics. Najing: Southeast University Press; 2010.
5. Potter TEC, Cebon D, Cole DJ. An investigation of road damage due to measured dynamic tire forces. Proc Inst Mech Eng Part D, J Automob Eng. 1995;209(1):9–24.
6. Pei JZ. Microstructural properties and decay behavior of asphalt pavement. Science Press; 2010.
7. Hunaidi O, Guan W, Nicks J. Building vibrations and dynamic pavement loads induced by transit buses. Soil Dyn Earthq Eng. 2000;19(64):435–45.
8. Dong ZJ, Liu H, Tan YQ. Field measurement of three-directional strain response of asphalt pavement. JSCUT. 2009;(7):46–51.
9. Jeongho O, Fernando EG, Lytton RL. Evaluation of damage potential for pavements due to overweight truck traffic. J Transp Eng. 2007;133(5):308–17.
10. Kim SM, Roesset JM. Moving loads on a plate on an elastic foundation. J Eng Mech. 1998;124(9):1010–17.
11. Lv PM. Mechanical analysis of vehicle-asphalt pavement. Beijing: People's Communications Press; 2010.
12. Kim SM, Mccullough BF. Dynamic response of a plate on a viscous Winkler foundation to moving loads of varying amplitude. Eng Struct. 2003;25(9):1179–88.
13. Kim SM. Influence of horizontal resistance at plate bottom on vibration of plates on an elastic foundation under moving loads. Eng Struct. 2004;26:519–29.

Index

S. Yang et al., *Dynamics of Vehicle-Road Coupled System,*
DOI 10.1007/978-3-662-45957-7